

1 Muon ($g - 2$) Conceptual Design Report

2 E989 Collaboration

3 P. Winter

4 *Argonne National Laboratory, Lemont, IL, USA*

5 E.J. Barnes, R.M. Carey, E. Hazen, J.P. Miller, and B.L. Roberts¹

6 *Boston University, Boston, MA, USA*

7 J. Benante, W.M. Morse, Y.K. Semertzidis, and V. Tishchenko

8 *Brookhaven National Laboratory, Upton, NY, USA*

9 V.P. Druzhinin, B.I. Khazin, I.A. Koop, I. Logashenko, Y.M. Shatunov, and E. Solodov

10 *Budker Institute of Nuclear Physics, Novosibirsk, Russia*

11 D. Newton and A. Wolski

12 *The Cockcroft Institute, Daresbury and University of Liverpool, Liverpool, United Kingdom²*

13 R. Bjorkquist, L. Gibbons, A. Mikhailichenko, and D. Rubin

14 *Cornell University, Ithaca, NY, USA*

15 D. Allspach, G. Annala, L. Bartoszek, B.C.K. Casey, M.E. Convery, B. Drendel,

16 T. Gadfort, S.U. Hansen, K. Hardin, D. Harding, C. Johnstone, J. Johnstone, B. Kiburg,

17 A. Klebaner, I. Kourbanis, K. Krempetz, A. Leveling, A.L. Lyon, N. Mokhov, J.P. Morgan,

18 D. Neuffer, H. Nguyen, J-F. Ostiguy, A. Para, C.C. Polly³, M. Popovic, M. Rominsky,

19 P. Rubinov, R. Schultz, D. Still, A.K. Soha, S. Strigonov, G. Velez, and J-Y. Wu

20 *Fermi National Accelerator Laboratory, Batavia, IL, USA*

21 P.T. Debevec, M. Kasten, S. Leo, and K. Pitts

22 *University of Illinois at Urbana-Champaign, Urbana, IL, USA*

23 S. Donati, C. Ferrari, F. Scuri, F. Spinella, and S. Veronesi

24 *INFN, Sezione di Pisa, Pisa, Italy²*

25 P. Camarri, G. Di Sciascio, and R. Iuppa
26 *INFN, Sezione Roma Tor Vergata, Roma, Italy²*

27 K. Giovanetti
28 *James Madison University, Harrisonburg, VA, USA*

29 N. Khomutov and N. Kuchinskiy
30 *Joint Institute for Nuclear Research, Dubna, Russia*

31 C. Crawford, R. Fatemi, W.P. Gohn, T.P. Gorringer, W. Korsch, and B. Plaster
32 *University of Kentucky, Lexington, KY, USA*

33 T. Bowcock, B. King, S. Maxfield, and T. Teubner
34 *University of Liverpool, Liverpool, United Kingdom²*

35 K. Jungmann and C.J.G. Onderwater
36 *University of Groningen, Groningen, The Netherlands*

37 M. Cordelli, S. Giovannella, F. Happacher, A. Luca', M. Martini, S. Miscetti, A. Palladino,
38 I. Sarra, and G. Venanzoni
39 *Laboratori Nazionali di Frascati, Frascati, Italy*

40 M. Lancaster and E. Motuk
41 *University College London, London, United Kingdom²*

42 D. Kawall
43 *University of Massachusetts, Amherst, MA, USA*

44 T. Chupp and R. Raymond
45 *University of Michigan, Ann Arbor, MI, USA*

46 C. Ankenbrandt, M.A. Cummings, R.P. Johnson, and C. Yoshikawa
47 *Muons Inc., Batavia, IL, USA*

48 M. Eads, M. Fortner, D. Hedin, and N. Pohlman
49 *Northern Illinois University, DeKalb, IL, USA*

50 A. de Gouvea, H. Schellman, and L. Welty-Rieger
51 *Northwestern University, Evanston, IL, USA*

52 T. Itahashi and Y. Kuno
53 *Osaka University, Osaka, Japan*

54 F. Azfar and S. Henry
55 *University of Oxford, Oxford, United Kingdom²*

56 G.D. Alkhozov, V.L. Golovtsov, P.V. Neustroev, L.N. Uvarov, A.A. Vasilyev,
57 A.A. Vorobyov, and M.B. Zhalov
58 *Petersburg Nuclear Physics Institute, Gatchina, Russia*

59 L. Cerrito
60 *Queen Mary, University of London, London, United Kingdom²*

61 F. Gray
62 *Regis University, Denver, CO, USA*

63 D. Moricciani
64 *Università di Roma Tor Vergata, Roma, Italy*

65 C. Fu, X. Ji, L. Li, and H. Yang
66 *Shanghai Jiao Tong University, Shanghai, China*

67 V. Bayliss, T. Bradshaw, S. Canfer, and D. Clarke
68 *STFC Rutherford Appleton Laboratory, Didcot, United Kingdom²*

69 D. Stöckinger
70 *Technische Universität Dresden, Dresden, Germany*

71 G. Pauletta
72 *Università di Udine, Udine, Italy²*

73 S. Baeßler, M. Bychkov, E. Frlez, and D. Pocanic
74 *University of Virginia, Charlottesville, VA, USA*

75 L.P. Alonzi, J. Crnkovic, N. Froemming, A. Garcia, D.W. Hertzog¹, P. Kammel, M. Smith,
76 E. Swanson, and T. Zhao
77 *University of Washington, Seattle, WA, USA*

78 K. Lynch
79 *York College, CUNY, Jamaica, NY, USA*

80 Tuesday 21st May, 2013

¹Co-spokesperson

²Provisional membership pending the outcome of their funding request

³Project Manager

DISCLAIMER

82 This work was prepared as an account of work sponsored by an agency of the United
83 States Government. Neither the United States Government nor any agency thereof, nor any
84 of their employees, nor any of their contractors, subcontractors, or their employees makes any
85 warranty, express or implied, or assumes any legal liability or responsibility for the accuracy,
86 completeness, or any third party's use or the results of such use of any information, apparatus,
87 product, or process disclosed, or represents that its use would not infringe privately owned
88 rights. Reference herein to any specific commercial product, process, or service by trade
89 name, trademark, manufacturer, or otherwise, does not necessarily constitute or imply its
90 endorsement, recommendation, or favoring by the United States Government or any agency
91 thereof or its contractors or subcontractors. The views and opinions of authors expressed
92 herein do not necessarily state or reflect those of the United States Government or any
93 agency thereof.

94

Executive Summary

95 The Muon $g - 2$ Experiment, E989 at Fermilab, will measure the muon anomalous mag-
 96 netic moment, $a_\mu \equiv (g - 2)/2$, to unprecedented precision: the goal is 0.14 parts per million
 97 (ppm). The worth of such an undertaking is coupled to the fact that the Standard Model
 98 (SM) prediction for a_μ can also be determined to similar precision. As such, the comparison
 99 between experiment and theory provides one of the most sensitive tests of the completeness
 100 of the model. The Brookhaven-based E821 experiment, which completed data taking in
 101 2001, determined $a_\mu(\text{Expt})$ to 0.54 ppm. Steady improvements in theory since that time
 102 have resulted in a present SM uncertainty on $a_\mu(\text{SM})$ of 0.42 ppm. The experimental mea-
 103 surement and SM predictions differ by 3.3 to 3.6 standard deviations, depending on which
 104 evaluation of the lowest-order hadronic contribution in the SM is used:

$$\Delta a_\mu(\text{Expt} - \text{SM}) = (286 \pm 80) \times 10^{-11} \quad (1)$$

$$= (260 \pm 78) \times 10^{-11} \quad (2)$$

105 (see Chapter 2 for details). This is a highly cited result, owing in part to the many natural
 106 SM extensions from supersymmetry to dark photons that could cause such an effect. The
 107 planned four-fold improvement in experimental precision compared to E821, could establish
 108 beyond doubt a signal for new physics—if the central value of the measurement remains
 109 unchanged. During the time it will require to mount, run and analyze the data, the SM
 110 hadronic predictions are expected to become even more precise; thus the comparison of
 111 experiment to theory will be quite powerful, no matter what final values are found. The
 112 Motivation for the new experiment and a detailed exposition on the SM theory is provided
 113 in Chapter 2 of this document.

114 The original E989 Proposal, and the additional design work now completed in preparation
 115 of this Conceptual Design Report (CDR), outline a credible plan to achieve the experimental
 116 goal in a timely and cost-efficient manner. The approach is anchored by the re-use of the
 117 existing precision muon storage ring, an efficient and parasitic deployment of the Fermilab
 118 proton complex and beamlines, and strategic upgrades or replacements of outdated or under-
 119 performing components from E821. The experiment will be carried out by a collaboration of
 120 accelerator, atomic, nuclear and particle physicists, drawing from domestic and international
 121 universities and national laboratories. The collaboration retains a strong core of experienced
 122 participants from BNL E821, augmented by many new groups selected for their expertise in
 123 areas that are required to mount a next-generation experiment.

124 In many ways, E989 is a unique, large-scale Project. Several core aspects involve proven
 125 elements from E821 that will be retained in whole or with minor upgrades. This is especially
 126 true for the storage ring elements and the magnetic field measuring tools, which will be
 127 relocated, re-assembled and restored to operation. Many of these items are well beyond a
 128 normal CDR stage in terms of design; indeed, they exist and often require no more than
 129 testing and minor repair. In contrast, several items have been identified as requiring a new
 130 approach to meet the demands of a higher rate experiment with lower systematic uncertain-
 131 ties. Chief among them is a new storage ring kicker and, ultimately, a new inflector magnet.
 132 The storage-ring electrostatic quadrupoles will undergo an operational upgrade and one set
 133 will be redesigned to better allow for the beam passage through them as it enters the storage

134 ring. The beam position mapping will employ a unique in-vacuum tracking system and the
135 instrumentation for the precession frequency measurement—calorimeters, fast digitizers and
136 modern data acquisition—will all be new. Naturally, the entire pion-to-muon beam path
137 from target to storage ring is unique at Fermilab.

138 The BNL experiment was statistics limited. With a persistent and tantalizing hint of new
139 physics, it has been recognized for many years that a next-generation effort is required to
140 lead to a true discovery. A number of informal studies led to the realization that relocation
141 of the storage ring to Fermilab would provide the ideal environment for the next generation
142 experiment. The Booster, the Recycler, and the existing antiproton target station can be
143 used to acquire a 20-fold increase in statistics in a timely manner. One can take direct
144 advantage of the experience with the unique and well-understood storage ring developed
145 for E821. The proposed beam environment and relatively modest experimental upgrades
146 would provide a better measurement environment that will lead to reduced systematic unce
147 rtainties. The E989 Proposal was presented to the Fermilab PAC in March 2009. Cost
148 evaluations by an independent committee followed, and beam delivery studies were initiated.
149 Following the completion of the Proton Improvement Plan, Fermilab can service the NO ν A
150 experiment fully and provide excess proton cycles to adequately meet the unique needs of the
151 $g-2$ experiment. The experimental technical approach described in this CDR is conservative.
152 It is built on the foundation and lessons learned from several generations of $g-2$ experiments
153 at CERN and then Brookhaven, and we retain key personnel that provide necessary overlap
154 with the most recent effort.

155 The beam-use plan has evolved further such that it now largely overlaps with the needs
156 of the Mu2e Experiment. Together, $g-2$ and Mu2e have become the first tenants of the new
157 Muon Campus, which involves several buildings, beamlines and infrastructure support. A
158 new general purpose building, MC-1, has been designed with specific attention to the needs
159 of the $g-2$ experiment—e.g., stable floor, temperature control to $\pm 2^\circ$ F, and the necessary
160 services. Ground-breaking for MC-1 occurred in May, 2013 and beneficial occupancy is
161 expected in early 2014.

162 Following the Project Overview, the CDR is organized as follows. We begin with chapters
163 on the physics motivation—including the discussion standard-model and non-standard-model
164 physics—and the experimental strategy. The measurement involves ambitious statistical
165 and systematic uncertainty goals. Chapter 5 then provides a roadmap that summarizes our
166 plans to meet the statistical and systematic uncertainty targets. The factors contributing
167 to these estimates are distributed throughout the document, as they fall into different WBS
168 categories, so this chapter also provides both short descriptions of the factors that underlie
169 the uncertainty targets, and pointers to the specific sections that discuss the topics in detail.
170 The bulk of the CDR then describes the experimental design that can reach those targets,
171 from production and delivery of the muon beam through to the slow controls and monitoring
172 of the data taking process.

Contents

174	1 Project Overview	17
175	1.1 Mission and Scope	18
176	1.1.1 Muon Beam	18
177	1.1.2 Storage Ring	18
178	1.1.3 Precision Magnetic Field	18
179	1.1.4 Detectors	18
180	1.2 $(g - 2)$ and the Muon Campus	18
181	1.3 Conventional Facilities	18
182	1.4 Organization	18
183	1.4.1 Management	18
184	1.4.2 WBS	18
185	1.4.3 Controls	18
186	1.4.4 Quality Assurance	18
187	1.4.5 ES&H	18
188	1.4.6 Configuration Management	18
189	1.4.7 Risk Management	18
190	1.4.8 Cost and Schedule	18
191	1.5 References	18
192	2 Introduction and Physics Motivation	19
193	2.1 Introduction	19
194	2.2 Magnetic and Electric Dipole Moments	19
195	2.2.1 The Muon	20
196	2.2.2 The Muon Magnetic Moment	20
197	2.2.3 The Muon Electric Dipole Moment	20
198	2.3 Quick Summary of the Experimental Technique	22
199	2.4 Results from E821	23
200	2.4.1 Measurement of a_μ	23
201	2.5 The Standard-Model Value of a_μ	23
202	2.5.1 Introduction	24
203	2.5.2 QED Contribution	25
204	2.5.3 Weak contributions	26
205	Hadronic contribution	27
206	Lowest- and next-lowest-order hadronic contribution	29
207	$a_\mu^{\text{had;LO}}$ from hadronic τ decay	29

208	Hadronic light-by-light contribution	32
209	2.5.4 Summary of the Standard-Model Value and Comparison with Experi-	
210	ment	33
211	2.5.5 Expected Improvements in the Standard-Model Value	34
212	2.6 Physics Beyond the Standard Model	35
213	Varieties of physics beyond the Standard Model	35
214	a_μ and supersymmetry	39
215	a_μ and model selection and parameter measurement	41
216	References	45
217	3 Overview of the Experimental Technique	53
218	3.1 Production and Preparation of the Muon Beam	54
219	3.2 Injection into the Storage Ring	54
220	3.3 The Spin Equations	56
221	3.4 Vertical Focusing with Electrostatic Quadrupoles	58
222	3.5 Muon Decay	58
223	3.6 The Magnetic Field	63
224	References	66
225	4 Beam Dynamics and Beam Related Systematic Errors	69
226	4.1 Introduction	69
227	4.2 The Weak Focusing Betatron	69
228	4.3 Weak Focusing with Discrete Quadrupoles	71
229	4.3.1 Monitoring the Beam Profile	74
230	4.4 Corrections to ω_a : Pitch and Radial Electric Field	77
231	4.5 Systematic Errors from the Pion and Muon Beamlines	80
232	4.5.1 Simulation plan and timeline	83
233	References	85
234	5 Statistical and Systematic Errors for E989	87
235	5.1 Event Rate Calculation Methodologies	88
236	5.1.1 Event Rate by a Relative Comparison to E821	88
237	5.1.2 Bottom-Up Event Rate Calculation	91
238	5.2 ω_a systematic uncertainty summary	93
239	5.3 ω_p systematic uncertainty summary	93
240	References	95
241	6 Civil Construction Off-Project	97
242	6.1 The MC1 Building	97
243	7 Accelerator and Muon Delivery	101
244	7.1 Overall Strategy	101
245	7.2 Protons from Booster	103
246	7.2.1 Proton Improvement Plan	103
247	7.3 Recycler	106

248	7.3.1	Recycler RF	106
249	7.4	Target station	108
250	7.4.1	The $(g - 2)$ production target and optimization of production	109
251	7.4.2	Focusing of secondaries from the target	115
252	7.4.3	Pulsed magnet (PMAG) and collimator	118
253	7.4.4	Target station beam dump	119
254	7.5	Beam Transport Lines	120
255	7.5.1	Overview of $(g - 2)$ beamlines	120
256	7.5.2	Beamline Changes from Collider Operation	120
257	7.5.3	Proton Beam Transport to the Target Station	124
258		Recycler Ring to P1 line stub	124
259		Beamline Design	124
260		Kickers	125
261		Lambertson	125
262		Recycler orbit	126
263		Apertures	126
264	7.5.4	P1, P2 and AP1 Aperture Improvements	129
265		Final Focus Region	130
266	7.5.5	Pion to muon decay beamlines	132
267		Design layout	132
268		Optics	133
269	7.5.6	Delivery Ring	138
270		Rings Lattice and Acceptance	138
271		Kickers and Septa	140
272		Delivery Ring D30 straight section	141
273		Injection	141
274		Extraction	143
275		Proton Removal (Abort) System	143
276		Vacuum Systems	145
277		Infrastructure Improvements	146
278	7.5.7	Muon transport to storage ring	146
279		Considerations	146
280		Civil Layout	147
281		Beam Properties	149
282		Beam Optics	149
283		Beamline Sections	150
284		Extraction from the Delivery Ring	150
285		Horizontal Bend String	155
286		The FODO-cell transport section	158
287		The Final Focus and Injection into the Storage Ring	159
288	7.6	Controls and beam monitoring	162
289	7.6.1	Accelerator controls	162
290		CAMAC and links	162
291		Hot-Link Rack Monitor	164
292		Ethernet	165

293	Controls connectivity	167
294	Restoring connectivity	167
295	Establish connectivity to MC-1	167
296	Possible upgrades for legacy networks	168
297	Safety system	169
298	7.6.2 Accelerator instrumentation	169
299	Beam types	169
300	Primary proton beam	171
301	Mixed secondaries	172
302	Proton Secondaries	175
303	Muon Secondaries	176
304	Accelerator instrumentation summary	178
305	7.7 ES&H, Quality Assurance, Value Management, Risk	179
306	7.7.1 ES&H	179
307	7.7.2 Quality Assurance	179
308	7.7.3 Value Management	179
309	7.7.4 Risk	180
310	References	181
311	8 Beam Rate Simulations	183
312	8.1 Pion Production at the Target	183
313	8.2 Muon capture in the straight section of the decay line	184
314	8.3 G4Beamline simulations of beam transport and muon capture	185
315	8.4 Muon Transmission and Storage Simulations	188
316	8.4.1 Simulation Overview	189
317	8.4.2 Results for Beam Starting at Upstream Entrance of the Inflector	193
318	9 Relocation of the E821 Storage Ring Magnet	195
319	9.1 Preparations for Shipping	196
320	9.2 The Coil Shipping Fixture and Transportation	197
321	References	200
322	10 The Muon Storage Ring Magnet	201
323	10.1 Introduction	201
324	10.2 Yoke Steel	203
325	10.3 Poles and Wedges	204
326	10.3.1 Poles	204
327	10.3.2 Wedges	206
328	10.4 Thermal Effects	206
329	10.5 The Superconducting Coil System	207
330	10.5.1 Overview	207
331	10.5.2 Preparations Prior to Transportation	214
332	10.5.3 Cryostat Vacuum Chambers	216
333	10.5.4 Vacuum Pumps	216
334	10.5.5 Power Supply and Quench Protection	217

335	10.5.6 Cryogenics	221
336	10.5.7 Super Conducting Coils	222
337	10.6 ES&H, Quality Assurance, Value Management, Risks	223
338	10.6.1 Yoke, Pole, and Shims	223
339	10.6.2 Power Supply and Quench Protection System	224
340	Hazards	224
341	Risks	224
342	Quality Assurance	225
343	Value Management	225
344	10.6.3 The Cryogenic and Related Systems	225
345	10.6.4 The Superconducting Coil System	226
346	References	227
347	11 The Superconducting Inflector Magnet	229
348	11.1 Introduction to Inflection Challenges	229
349	11.2 The E821 Inflector Design and Operation	231
350	11.2.1 Magnetic Design of the E821 Inflector	231
351	11.2.2 Shielding the residual fringe field	236
352	11.2.3 Performance of the E821 Inflector	238
353	11.3 Lessons for E989 from the E821 Inflector	238
354	11.4 A New Inflector	240
355	11.4.1 A New Double Cosine Theta Magnet	240
356	11.4.2 Double magnet, using the serpentine winding technique	240
357	11.4.3 Inflector Superconducting Passive Shield	241
358	11.5 Muon Storage Simulations Using a New Inflector	242
359	11.5.1 E821 Inflector Simulation	243
360	11.5.2 Open-ended vs. Closed-ended Inflector Geometry	243
361	11.5.3 Sensitivity to Beam Phase-space Matching	244
362	11.5.4 Increased Horizontal Aperture	244
363	11.5.5 Future Simulations	245
364	11.6 ES&H	245
365	11.7 Risks	246
366	11.7.1 Relocation Risk	246
367	11.7.2 Other Risks	246
368	11.8 Quality Assurance	246
369	11.9 Value Engineering	247
370	References	248
371	12 Beam Vacuum Chambers	251
372	12.1 Changes to the E821 Design	253
373	12.2 Vacuum Chambers	255
374	12.3 Vacuum Pumps	256
375	12.4 Mechanical Interface	257
376	12.5 ES&H, Quality Assurance, Value Management, Risk	258
377	References	259

378	13 The Fast Muon Kicker	261
379	13.1 Requirements for the E989 Kicker	263
380	13.1.1 The E821 Kicker and its Limitations	263
381	13.2 New Kicker Design	264
382	13.3 New Pulseforming Network	266
383	13.4 New Kicker Plate Design	268
384	13.5 Kicker R&D at Cornell	268
385	13.6 Kicker Field Measurement	270
386	13.7 Risks	271
387	13.7.1 Performance Risk	271
388	13.8 Quality Assurance	272
389	13.9 ES& H	272
390	13.10 Value management	273
391	References	278
392	14 The Electrostatic Quadrupoles	279
393	14.1 Introduction	279
394	14.2 E821 Design and Limitations	282
395	14.3 Improvements that Permit Higher n -Value Operation	289
396	14.3.1 Coherent Betatron Oscillations	292
397	14.3.2 Electric Field and Pitch Correction	293
398	14.4 Collimators and Lost Muon Systematic Error	295
399	14.5 ES&H	297
400	14.6 Risks	299
401	14.7 Quality Assurance	300
402	14.8 Value Management	300
403	14.9 R&D	301
404	References	302
405	15 Ring Instrumentation and Controls	303
406	15.1 Cryogenic/Vacuum Control System	303
407	15.1.1 Programmable Logic Controller	303
408	15.1.2 Human Machine Interface	304
409	15.2 Life Safety and System Reliability	305
410	ODH Control System	305
411	15.2.1 Uninterruptible Power Supply (U.P.S.)	306
412	15.2.2 PLC Reliability and Redundancy	306
413	References	307
414	16 The Precision Magnetic Field: ω_p	309
415	16.1 Precision Magnetic Field Measurement	309
416	16.1.1 Relation between a_μ and ω_p	309
417	16.1.2 Physics Requirements on ω_p	310
418	16.1.3 Error budget for the ω_p measurement	311
419	16.2 Recommended Design	311

420	16.2.1	Overview of field measurement using NMR	312
421		Field measurement with NMR	312
422	16.2.2	The Fixed Probe NMR system	313
423	16.2.3	Fixed Probes for E989	316
424		Refurbishing existing probes:	316
425		Constructing new probes:	317
426		Testing the probes:	317
427	16.2.4	Multiplexers	317
428	16.2.5	Pulser and Mixer	318
429	16.2.6	Frequency Reference	318
430	16.2.7	NMR VME System and DAQ	320
431	16.2.8	Digitizer	322
432	16.3	Trolley	323
433		Magnetic Field Maps	323
434		Fixed probe tracking of the magnetic field	326
435		Uncertainty from the muon distribution	328
436	16.3.1	General trolley requirements	329
437		Trolley measurement of B_0	329
438	16.3.2	Garage	331
439	16.3.3	Drive	331
440	16.3.4	Position Measurement	333
441	16.3.5	Probes	334
442	16.3.6	Frequency Measurement	335
443	16.3.7	DAQ	336
444	16.4	Absolute calibration of the trolley probes	336
445	16.4.1	Principles of calibration	336
446		Absolute calibration probe	337
447		Cross-calibration of the trolley with the plunging probe	339
448	16.4.2	^3He Magnetometry	341
449	16.5	Feedback to the magnet power supply	342
450	16.6	Time-dependent perturbations to the B field	343
451	16.7	Other effects on the field determination	344
452	16.8	Magnet Shimming	345
453	16.8.1	Overview	345
454	16.8.2	Passive Shims	345
455		Procedure	347
456		Yoke Iron	347
457		Pole Piece Alignment	347
458		Wedge Shims	347
459		Edge Shims	348
460		Gap shims	349
461		Radial Field	350
462	16.8.3	Active Shims	352
463		Main Current	352
464		Surface Correction coils	352

465	Dipole correction loops	354
466	Gap correction loops	354
467	16.8.4 E821 results	354
468	16.9 Alternatives	354
469	16.10ES&H	356
470	16.11Risks	356
471	Fixed Probe System	356
472	Absolute Calibration System	357
473	Trolley	357
474	Other Performance Risks	358
475	Shimming	358
476	16.12Quality Assurance	359
477	16.13Value Management	360
478	References	361
479	17 The ω_a Measurement	363
480	17.1 Measurement Overview	363
481	17.1.1 Muon Decay and Boost Kinematics	363
482	17.1.2 Analysis Methods Summary	364
483	17.2 Statistical Uncertainty	365
484	17.3 Detector-related Systematic Uncertainties	367
485	17.3.1 Gain Changes and Energy-Scale Stability	369
486	17.3.2 Pileup	370
487	17.4 Detector Systems Overview	372
488	17.4.1 Calorimeter Subsystem Considerations	373
489	17.4.2 Projected Rates in Calorimeter	375
490	17.4.3 Electronics and Data Acquisition Subsystems Considerations	377
491	References	379
492	18 Calorimeter	381
493	18.1 Physics Goals and Requirements	381
494	18.2 Evaluation Methodologies: Test Beams and Simulations	382
495	18.3 Recommended Calorimeter Design	382
496	18.3.1 Absorber Subsystem	385
497	18.3.2 Photodetection Subsystem – SiPM	388
498	Bias voltage system for the SiPMs	391
499	18.3.3 Laser Calibration Subsystem	395
500	18.3.4 Mechanical Subsystem	398
501	18.4 Alternative Design Considerations	399
502	18.5 ES&H	401
503	18.6 Risks	401
504	18.6.1 Performance Risks	401
505	18.6.2 Schedule Risks	401
506	18.7 Quality Assurance	401
507	18.8 Value Management	402

508	18.9 R&D	402
509	References	403
510	19 Tracking Detectors	405
511	19.1 Physics Goals	405
512	19.2 Requirements	406
513	19.3 Recommended Design	407
514	19.3.1 Mechanical Design	409
515	19.3.2 Readout Electronics	412
516	19.4 Performance	417
517	19.5 Alternatives	423
518	19.6 ES&H	424
519	19.7 Risks	425
520	19.7.1 Performance Risk	425
521	19.7.2 Technical and Operational Risk	425
522	19.8 Quality Assurance	427
523	19.9 Value Management	427
524	19.10 R&D	428
525	References	430
526	20 Auxiliary detectors	431
527	20.1 Fiber beam monitors	431
528	20.1.1 Requirements	431
529	20.1.2 Recommended Design	432
530	20.2 Entrance counters	434
531	20.2.1 Requirements	434
532	20.2.2 Recommended design	434
533	20.3 Performance	435
534	20.4 Alternatives	435
535	20.5 ES&H	436
536	20.6 Risks	436
537	20.7 Quality Assurance	437
538	20.8 Value Management	437
539	20.9 R&D	437
540	References	438
541	21 Calorimeter Backend Electronics	439
542	21.1 Backend Electronics	439
543	21.1.1 Physics Goals	439
544	21.1.2 Requirements	440
545	Clock and synchronization distribution	440
546	Waveform Digitization	440
547	21.1.3 Recommended Design	442
548	Clock distribution	442
549	Waveform digitization	442

550	21.1.4 Performance	446
551	21.1.5 Alternatives and Value Engineering	446
552	21.1.6 ES&H	448
553	21.1.7 Risks	448
554	21.1.8 Quality Assurance	449
555	References	451
556	22 Data Acquisition System	453
557	22.1 Physics Goals	453
558	22.2 Overall Requirements	453
559	22.3 Recommended Design	454
560	22.4 Design Performance	460
561	22.5 Alternatives	460
562	22.5.1 ES&H	461
563	22.6 Risks	461
564	22.7 Quality Assurance	462
565	22.8 R&D	462
566	References	467
567	23 Slow Controls	469
568	23.1 Overview and general requirements	469
569	23.2 Recommended Design	470
570	23.2.1 Software and hardware architecture	470
571	23.2.2 Sensors and controls	472
572	23.2.3 Communication with external systems	476
573	23.2.4 Alarm system	478
574	23.2.5 Backend server	479
575	23.2.6 Data storage and access tools	480
576	23.3 Alternative Design Considerations	480
577	23.4 ES&H	481
578	23.5 Risks	482
579	23.6 Quality Assurance	482
580	23.7 Value Management	483
581	23.8 R&D	483
582	References	484

Chapter 1

Project Overview

1.1 Mission and Scope

1.1.1 Muon Beam

1.1.2 Storage Ring

1.1.3 Precision Magnetic Field

1.1.4 Detectors

1.2 $(g - 2)$ and the Muon Campus

1.3 Conventional Facilities

1.4 Organization

1.4.1 Management

1.4.2 WBS

1.4.3 Controls

1.4.4 Quality Assurance

1.4.5 ES&H

1.4.6 Configuration Management

1.4.7 Risk Management

1.4.8 Cost and Schedule

1.5 References

Chapter 2

Introduction and Physics Motivation

2.1 Introduction

This chapter gives the physics context of magnetic moment measurements, the Standard Model expectations, along with the reach of such experiments to identify and constrain physics beyond the Standard Model. Except for a broad-brush mention of the experimental technique, the details are left for later chapters. Chapter 3 gives an overview of the experimental method, and the subsequent chapters give the details. We attempt to follow the WBS structure in those later chapters.

2.2 Magnetic and Electric Dipole Moments

The study of magnetic moments of subatomic particles grew up with the development of quantum mechanics. For fermions the magnetic dipole moment (MDM) is related to the spin by

$$\vec{\mu} = g \frac{Qe}{2m} \vec{s}. \quad (2.1)$$

where $Q = \pm 1$ and $e > 0$. Our modern interpretation of the Stern-Gerlach experiments [1] is that their observation: “to within 10% the magnetic moment of the silver atom is one Bohr magneton” was telling us that the g -factor of the un-paired electron is equal to 2. However, reaching this conclusion required the discovery of spin [3], quantum mechanics [4] along with with Thomas’ relativistic correction [5]. Phipps and Taylor [6] repeated the Stern-Gerlach experiment in hydrogen, and mentioned the electron spin explicitly. One of the great successes of Dirac’s relativistic theory [7] was the prediction that $g \equiv 2$.

For some years, the experimental situation remained the same. The electron had $g = 2$, and the Dirac equation seemed to describe nature. Then a surprising and completely unexpected result was obtained. In 1933, against the advice of Pauli who believed that the proton was a pure Dirac particle [8], Stern and his collaborators [9] showed that the g -factor of the proton was ~ 5.5 , not the expected value of 2. Even more surprising was the discovery in 1940 by Alvarez and Bloch [10] that the neutron had a large magnetic moment.

In 1947, motivated by measurements of the hyperfine structure in hydrogen that obtained splittings larger than expected from the Dirac theory [11, 12, 13], Schwinger [14] showed that

630 from a theoretical viewpoint these “discrepancies can be accounted for by a small additional
 631 electron spin magnetic moment” that arises from the lowest-order radiative correction to the
 632 Dirac moment¹,

$$\frac{\delta\mu}{\mu} = \frac{1}{2\pi} \frac{e^2}{\hbar c} = 0.001162. \quad (2.2)$$

633 It is useful to break the magnetic moment into two terms:

$$\mu = (1 + a) \frac{e\hbar}{2m}, \quad \text{where } a = \frac{(g - 2)}{2}. \quad (2.3)$$

634 The first term is the Dirac moment, 1 in units of the appropriate magneton $e\hbar/2m$. The
 635 second term is the anomalous (Pauli) moment [15], where the dimensionless quantity a
 636 (Schwinger’s $\delta\mu/\mu$) is sometimes referred to as the *anomaly*.

637 2.2.1 The Muon

638 The muon was first observed in a Wilson cloud chamber by Kunze[16] in 1933, where it was
 639 reported to be “a particle of uncertain nature.” In 1936 Anderson and Neddermeyer[17]
 640 reported the presence of “particles less massive than protons but more penetrating than
 641 electrons” in cosmic rays, which was confirmed in 1937 by Street and Stevenson[18], Nishina,
 642 Tekeuchi and Ichimiya[19], and by Crussard and Leprince-Ringuet[20]. The Yukawa theory
 643 of the nuclear force had predicted such a particle, but this “mesotron” as it was called,
 644 interacted too weakly with matter to be the carrier of the strong force. Today we understand
 645 that the muon is a second generation lepton, with a mass about 207 times the electron’s.
 646 Like the electron, the muon obeys quantum electrodynamics, and can interact with other
 647 particles through the electromagnetic and weak forces. Unlike the electron which appears
 648 to be stable, the muon decays through the weak force predominantly by $\mu^- \rightarrow e^- \nu_\mu \bar{\nu}_e$. The
 649 muon’s long lifetime of $\simeq 2.2 \mu\text{s}$ permits precision measurements of its mass, lifetime, and
 650 magnetic moment.

651 2.2.2 The Muon Magnetic Moment

652 The magnetic moment of the muon played an important role in the discovery of the generation
 653 structure of the Standard Model (SM). The pioneering muon spin rotation experiment at
 654 the Nevis cyclotron observed parity violation in muon decay [21], and also showed that g_μ
 655 was consistent with 2. Subsequent experiments at Nevis [24] and CERN [25] showed that
 656 $a_\mu \simeq \alpha/(2\pi)$, implying that in a magnetic field, the muon behaves like a heavy electron. Two
 657 additional experiments at CERN required that contributions from higher-order QED [26],
 658 and then from virtual hadrons [27] be included into the theory in order to reach agreement
 659 with experiment.

660 2.2.3 The Muon Electric Dipole Moment

661 Dirac [7] discovered an electric dipole moment (EDM) term in his relativistic electron theory.
 662 Like the magnetic dipole moment, the electric dipole moment must be along the spin. We

¹A misprint in the original paper has been corrected here.

663 can write an EDM expression similar to Eq. (2.1),

$$\vec{d} = \eta \left(\frac{Qe}{2mc} \right) \vec{s}, \quad (2.4)$$

664 where η is a dimensionless constant that is analogous to g in Eq. (2.1). While magnetic
665 dipole moments (MDMs) are a natural property of charged particles with spin, electric
666 dipole moments (EDMs) are forbidden both by parity and by time reversal symmetry.

667 The search for an EDM dates back to the suggestion of Purcell and Ramsey [28] in 1950,
668 well in advance of the paper by Lee and Yang [29], that a measurement of the neutron EDM
669 would be a good way to search for parity violation in the nuclear force. An experiment
670 was mounted at Oak Ridge [30] soon thereafter that placed a limit on the neutron EDM of
671 $d_n < 5 \times 10^{-20}$ e-cm, although the result was not published until after the discovery of parity
672 violation.

673 Once parity violation was established, Landau [31] and Ramsey [32] pointed out that
674 an EDM would violate both P and T symmetries. This can be seen by examining the
675 Hamiltonian for a spin one-half particle in the presence of both an electric and magnetic
676 field,

$$\mathcal{H} = -\vec{\mu} \cdot \vec{B} - \vec{d} \cdot \vec{E}. \quad (2.5)$$

677 The transformation properties of \vec{E} , \vec{B} , $\vec{\mu}$ and \vec{d} are given in Table 2.2.3, and we see that
678 while $\vec{\mu} \cdot \vec{B}$ is even under all three symmetries, $\vec{d} \cdot \vec{E}$ is odd under both P and T . Thus the
679 existence of an EDM implies that both P and T are not good symmetries of the interaction
680 Hamiltonian, Eq. (2.5). The EDM is a CP -odd quantity, and if observed, would be the
681 manifestation of a new source of CP violation. The search for a muon EDM provides a
682 unique opportunity to search for an EDM of a second-generation particle.

Table 2.1: Transformation properties of the magnetic and electric fields and dipole moments.

	\vec{E}	\vec{B}	$\vec{\mu}$ or \vec{d}
P	-	+	+
C	-	-	-
T	+	-	-

683 Concerning these symmetries, Ramsey states [32]:

684 “However, it should be emphasized that while such arguments are appealing
685 from the point of view of symmetry, they are not necessarily valid. Ultimately
686 the validity of all such symmetry arguments must rest on experiment.”

687 Fortunately this advice has been followed by many experimental investigators during the
688 intervening 50 years. Since the Standard Model CP violation observed in the neutral kaon
689 and B-meson systems is inadequate to explain the predominance of matter over antimatter in
690 the universe, the search for new sources of CP violation beyond that embodied in the CKM
691 formalism takes on a certain urgency. Searches for a permanent electric dipole moment of

692 the electron, neutron, and of an atomic nucleus have become an important part of the search
 693 for physics beyond the Standard Model. The present limits on subatomic EDMs is given in
 694 Table 2.2.3.

Table 2.2: EDM Limits for various systems

Particle	EDM Limit (e-cm)	SM value (e-cm)
p [33]	7.9×10^{-25}	
n [34]	2.9×10^{-26}	$\simeq 10^{-32}$
^{199}Hg [33]	3.1×10^{-29}	$\simeq 10^{-32}$
e^- [35]	1.05×10^{-27}	$< 10^{-41}$
μ [36]	1.8×10^{-19}	$< 10^{-38}$

695 2.3 Quick Summary of the Experimental Technique

696 Polarized muons are produced (see Chapter 7) and injected into the storage ring (see Chap-
 697 ter 13). The magnetic field is a dipole field, shimmed to ppm level uniformity. Vertical
 698 focusing is provided by electrostatic quadrupoles (see Chapter 14).

699 Two frequencies are measured experimentally: The rate at which the muon polarization
 700 turns relative to the momentum, called ω_a , and the value of the magnetic field normalized
 701 to the Larmor frequency of a free proton, ω_p .

702 The rate at which the spin² turns relative to the momentum, $\vec{\omega}_a = \vec{\omega}_S - \vec{\omega}_C$, where S and
 703 C stand for spin and cyclotron. These two frequencies are given by

$$\omega_S = -g \frac{Qe}{2m} B - (1 - \gamma) \frac{Qe}{\gamma m} B; \quad (2.6)$$

$$\omega_C = -\frac{Qe}{m\gamma} B; \quad (2.7)$$

$$\omega_a = \omega_S - \omega_C = -\left(\frac{g-2}{2}\right) \frac{Qe}{m} B = -a \frac{Qe}{m} B \quad (2.8)$$

704 (where $e > 0$ and $Q = \pm 1$). There are two important features of ω_a : (i) It only depends on
 705 the anomaly rather than on the full magnetic moment; (ii) It depends linearly on the applied
 706 magnetic field. In the presence of an electric field ω_a is modified

$$\vec{\omega}_a = -\frac{Qe}{m} \left[a_\mu \vec{B} + \left(a_\mu - \left(\frac{m}{p}\right)^2 \right) \frac{\vec{\beta} \times \vec{E}}{c} \right] \quad (2.9)$$

707 If operated at the ‘magic’ momentum $p_{magic} = m/\sqrt{a_\mu} \simeq 3.09$ GeV/c the electric field
 708 contribution cancels in first order, and requires a small correction in second order.

²The term ‘spin’ is often used in place of the more accurate term ‘polarization’

709 The magnetic field is weighted by the muon distribution, and also averaged over the
 710 running time weighed by the number of stored muons to determine the value of ω_p which
 711 is combined with the average ω_a to determine a_μ . The reason for the use of these two
 712 frequencies, rather than B measured in tesla can be understood from Eq. 2.9. To obtain a_μ
 713 from this relationship requires precise knowledge of the muon charge to mass ratio.

714 To determine a_μ from the two frequencies ω_a and ω_p , we use the relationship

$$a_\mu = \frac{\omega_a/\omega_p}{\lambda_+ - \omega_a/\omega_p} = \frac{\mathcal{R}}{\lambda_+ - \mathcal{R}}, \quad (2.10)$$

715 where the ratio $\lambda_+ = \mu_{\mu^+}/\mu_p = 3.183\,345\,137(85)$ is the muon-to-proton magnetic mo-
 716 ment ratio [41] measured from muonium (the μ^+e^- atom) hyperfine structure[43] (see Sec-
 717 tion 16.1.1 for further details). Of course, to use λ_+ to determine a_{μ^-} requires the assumption
 718 of *CPT* invariance, *viz.* ($a_{\mu^+} = a_{\mu^-}$; $\lambda_+ = \lambda_-$). The comparison of \mathcal{R}_{μ^+} with \mathcal{R}_{μ^-} provides
 719 a *CPT* test. In E821

$$\Delta\mathcal{R} = \mathcal{R}_{\mu^-} - \mathcal{R}_{\mu^+} = (3.6 \pm 3.7) \times 10^{-9} \quad (2.11)$$

720 2.4 Results from E821

721 2.4.1 Measurement of a_μ

722 The E821 Collaboration working at the Brookhaven Laboratory AGS used an electric quadrupole
 723 field to provide vertical focusing in the storage ring, and shimmed the magnetic field to ± 1
 724 ppm uniformity on average. The storage ring was operated at the “magic” momentum,
 725 $p_{magic} = 3.094$ GeV/c, ($\gamma_{magic} = 29.3$), such that $a_\mu = (m/p)^2$ and the electric field did not
 726 contribute to ω_a .³ The result is [38, 39]

$$a_\mu^{E821} = 116\,592\,089(54)_{stat}(33)_{syst}(63)_{tot} \times 10^{-11} \quad (\pm 0.54 \text{ ppm}). \quad (2.12)$$

727 The results from E821 are shown in Fig. 2.1 along with the Standard-Model value which is
 728 discussed below in Section 2.5

729 2.5 The Standard-Model Value of a_μ

730 In this section we present the standard model (SM) theory of the muon anomalous magnetic
 731 moment (anomaly). In the following section we discuss physics beyond the standard model
 732 (BSM) that could contribute to the anomaly at a measurable level. The conclusion is that
 733 muon ($g - 2$) will play a powerful role in the interpretation of new phenomena that might
 734 be discovered at the LHC. If new phenomena are not discovered there, then muon ($g - 2$)
 735 becomes even more important, since it would provide one of the few remaining ways to search
 736 for new physics at the TeV scale.

³The magic momentum was first employed by the third CERN collaboration [27].

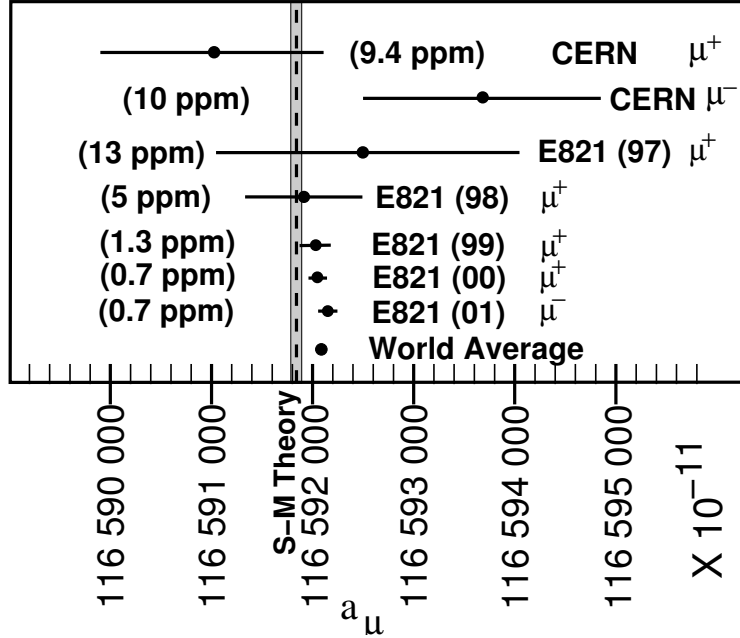


Figure 2.1: Measurements of a_μ from CERN and BNL E821. The vertical band is the SM value using the hadronic contribution from Ref. [47] (see Table 2.3).

2.5.1 Introduction

The magnetic moment of the muon (or electron), which is aligned with its spin, is given by

$$\vec{\mu} = g \frac{Qe}{2m_{\mu,e}} \vec{s}, \quad \underbrace{g = 2(1 + a_\mu)}_{\text{Dirac}}; \quad (2.13)$$

where the quantity g is exactly 2 in the Dirac theory, $Q = \pm 1$ with e a positive number. The small number a , the anomaly, arises from quantum fluctuations, with the largest contribution coming from the single loop diagram in Fig. 2.2(a). This contribution was first calculated by Schwinger [14], who obtained $a = (\alpha/2\pi) = 0.00116\dots$. These calculations have been extended to higher powers in α/π , with the fourth- $(\alpha/\pi)^2$ and sixth-order $(\alpha/\pi)^3$ contributions having been carried out analytically.

The electron anomaly is relatively insensitive to heavier physics, so in principle the 0.03 ppb measurement of the electron anomaly [68] should provide a test of QED, but the 0.6 ppb precision of the *independent* measurement of α limits this comparison. Alternately, one can accept that QED is valid and use the electron anomaly to determine the most precise measurement of α [69].

The muon anomaly is an entirely different case. The relative contribution to the muon anomaly of heavier virtual particles goes as $(m_\mu/m_e)^2 \simeq 43000$, so with much less precision when compared with the electron, the muon anomaly is sensitive to mass scales in the several hundred GeV region. This not only includes the expected contribution of the W and Z bosons, but perhaps contributions from new, as yet undiscovered, particles such as the supersymmetric partners of the electro-weak gauge bosons (see Fig. 2.2(c)).

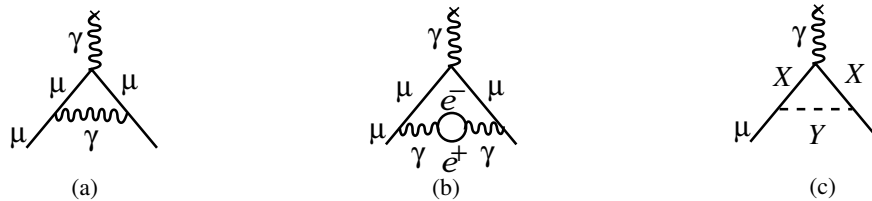


Figure 2.2: The Feynman graphs for: (a) The lowest-order (Schwinger) contribution to the lepton anomaly ; (b) The vacuum polarization contribution, which is one of five fourth-order, $(\alpha/\pi)^2$, terms; (c) The schematic contribution of new particles X and Y that couple to the muon.

756 The standard-model value of a_μ has three contributions from radiative processes: QED
 757 loops containing leptons (e, μ, τ) and photons; loops containing hadrons in vacuum polariza-
 758 tion loops where the e^+e^- pair in Fig 2.2(b) is replaced by hadrons; and weak loops involving
 759 the weak gauge bosons W, Z , and Higgs such as is shown in Fig. 2.2(c) where $X = W$ and
 760 $Y = \nu$, or $X = \mu$ and $Y = Z$. Thus

$$a_\mu^{\text{SM}} = a_\mu^{\text{QED}} + a_\mu^{\text{hadronic}} + a_\mu^{\text{weak}}. \quad (2.14)$$

761 The QED and weak contributions to the muon anomaly are now well understood at the level
 762 needed for the comparison of Standard-Model theory with experiment.

763 The hadronic contribution must be determined from a dispersion relation using experimental
 764 data, namely the cross sections for electron-positron annihilation to hadrons. The determi-
 765 nation of this contribution represents a worldwide effort which was driven primarily by the
 766 existence of BNL experiment E821. The possibility of a new Fermilab experiment has already
 767 stimulated further work that will increase as E989 comes on-line.

768 2.5.2 QED Contribution

769 The QED contribution to a_μ is well understood. Recently the four-loop QED contribution
 770 has been updated and the full five-loop contribution has been calculated [67]. The present
 771 QED value is

$$a_\mu^{\text{QED}} = 116\,584\,718.951 (0.009)(0.019)(0.007)(.077) \times 10^{-11} \quad (2.15)$$

772 where the uncertainties are from the lepton mass ratios, the eight-order term, the tenth-
 773 order term, and the value of α taken from the ^{87}Rb atom $\alpha^{-1}(\text{Rb}) = 137.035\,999\,049(90)$
 774 [0.66 ppb]. [70].

2.5.3 Weak contributions

The electroweak contribution (shown in Fig. 2.3) is now calculated through two loops [50, 51, 52, 53, 56]. The single loop result

$$\begin{aligned}
 a_\mu^{\text{EW}(1)} &= \frac{G_F m_\mu^2}{\sqrt{2} 8\pi^2} \left\{ \underbrace{\frac{10}{3}}_W + \underbrace{\frac{1}{3}(1-4\sin^2\theta_W)^2 - \frac{5}{3}}_Z \right. \\
 &\quad \left. + \mathcal{O}\left(\frac{m_\mu^2}{M_Z^2} \log \frac{M_Z^2}{m_\mu^2}\right) + \frac{m_\mu^2}{M_H^2} \int_0^1 dx \frac{2x^2(2-x)}{1-x + \frac{m_\mu^2}{M_H^2} x^2} \right\} \\
 &= 194.8 \times 10^{-11}, \tag{2.16}
 \end{aligned}$$

was calculated by five separate groups shortly after the Glashow-Salam-Weinberg theory was shown by 't Hooft to be renormalizable. With the present limit on the Higgs boson mass, only the W and Z contribute to the lowest-order electroweak at a measurable level.

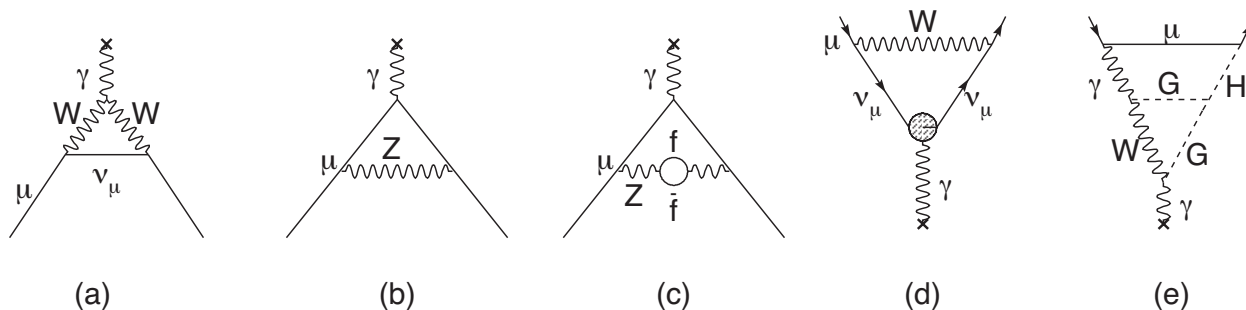


Figure 2.3: Weak contributions to the muon anomalous magnetic moment. Single-loop contributions from (a) virtual W and (b) virtual Z gauge bosons. These two contributions enter with opposite sign, and there is a partial cancellation. The two-loop contributions fall into three categories: (c) fermionic loops which involve the coupling of the gauge bosons to quarks, (d) bosonic loops which appear as corrections to the one-loop diagrams, and (e) a new class of diagrams involving the Higgs where G is the longitudinal component of the gauge bosons. See Ref. [54] for details. The \times indicates the virtual photon from the magnetic field.

The two-loop electroweak contribution⁴ (see Figs. 2.3(c-e) for examples) is negative, and the total electroweak contribution is [76]

$$a_\mu^{\text{EW}} = 154(1) \times 10^{-11} \tag{2.17}$$

where the error comes from hadronic effects in the second-order electroweak diagrams with quark triangle loops. mass [52, 51, 50, 17, 55]. The leading logs for the next-order term have been shown to be small [56]. The weak contribution is about 1.3 ppm of the anomaly, so the experimental uncertainty on a_μ of ± 0.54 ppm now probes the weak scale of the standard model.

⁴We update this contribution by $+1 \times 10^{-11}$ using the LHC value of the Higgs mass [55].

788 **Hadronic contribution**

789 The hadronic contribution to a_μ is about 60 ppm of the total value. The lowest-order diagram
 790 shown in Fig. 2.4(a) dominates this contribution and its error, but the hadronic light-by-light
 791 contribution Fig. 2.4(e) is also important. We discuss both of these contributions below.

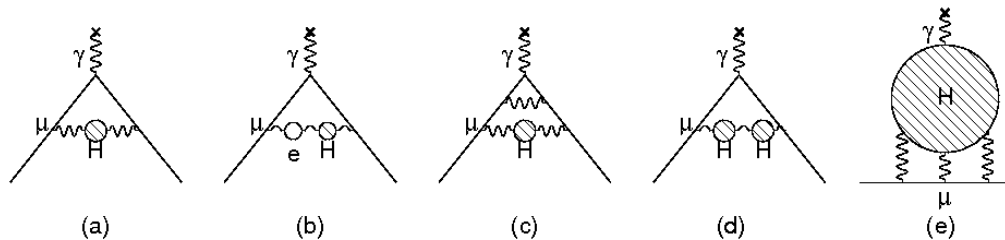


Figure 2.4: The hadronic contribution to the muon anomaly, where the dominant contribu-
 tion comes from the lowest-order diagram (a). The hadronic light-by-light contribution is
 shown in (e).

792 The energy scale for the virtual hadrons is of order $m_\mu c^2$, well below the perturbative
 793 region of QCD. Thus it must be calculated from the dispersion relation shown pictorially in
 794 Fig. 2.5,

$$a_\mu^{\text{had;LO}} = \left(\frac{\alpha m_\mu}{3\pi}\right)^2 \int_{4m_\pi^2}^\infty \frac{ds}{s^2} K(s) R(s), \quad \text{where} \quad R \equiv \frac{\sigma_{\text{tot}}(e^+e^- \rightarrow \text{hadrons})}{\sigma(e^+e^- \rightarrow \mu^+\mu^-)}, \quad (2.18)$$

795 using the measured cross sections for $e^+e^- \rightarrow \text{hadrons}$ as input, where $K(s)$ is a kinematic
 796 factor ranging from 0.63 at $s = 4m_\pi^2$ to 1 at $s = \infty$. This dispersion relation relates the
 797 bare cross section for e^+e^- annihilation into hadrons to the hadronic vacuum polarization
 798 contribution to a_μ . Because the integrand contains a factor of s^{-2} , the values of $R(s)$ at low
 799 energies (the ρ resonance) dominate the determination of $a_\mu^{\text{had;LO}}$, however at the level of
 800 precision needed, the data up to 2 GeV are very important. This is shown in Fig. 2.6, where
 801 the left-hand chart gives the relative contribution to the integral for the different energy
 802 regions, and the right-hand gives the contribution to the error squared on the integral. The
 803 contribution is dominated by the two-pion final state, but other low-energy multi-hadron
 804 cross sections are also important.

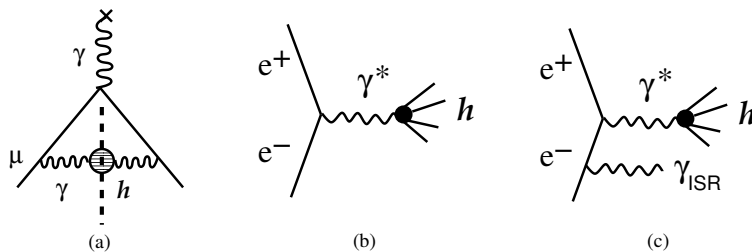


Figure 2.5: (a) The “cut” hadronic vacuum polarization diagram; (b) The e^+e^- annihilation
 into hadrons; (c) Initial state radiation accompanied by the production of hadrons.

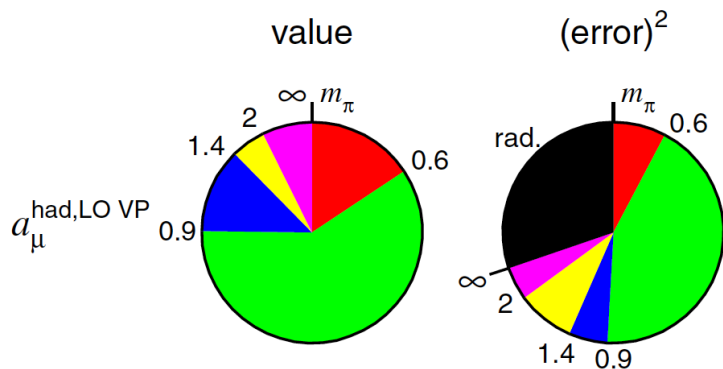


Figure 2.6: Contributions to the dispersion integral, and to the error on the dispersion integral. Taken from Hagirawa, et al., [48]

805 These data for e^+e^- annihilation to hadrons are also important as input into the deter-
 806 mination of $\alpha_s(M_Z)$ and other electroweak precision measurements, including the limit on
 807 the Higgs mass [72].

808 In the 1980s when E821 was being proposed at Brookhaven, the hadronic contribution was
 809 known to about 10 ppm. It now is known to about 0.4 ppm. This improvement has come from
 810 the hard work of many experimental and theoretical physicists. The low energy e^+e^- data
 811 of the 80s have been replaced by very precise data from the CMD2 and SND collaborations
 812 in Novosibirsk, the KLOE collaboration at Frascati, and the BaBar collaboration at SLAC.
 813 The new VEPP-2000 collider in Novosibirsk has been operational for several years, with two
 814 upgraded detectors, CMD-3 and SND-2000. This new facility will permit both energy scans,
 815 and the use of initial-state radiation to measure cross sections up to 2.0 GeV. Additional
 816 data on multi-hadron final states are expected from the Belle detector at KEK and BES-III
 817 at BEPC.

818 In addition to the collider experiments, significant theoretical work has been carried out
 819 in generating the radiator functions used in the initial-state radiation (ISR) experiments, as
 820 KLOE and BaBar [82, 83], as well as on the hadronic light-by-light contribution shown in
 821 Fig. 2.4(e).

822 The worldwide effort to improve our knowledge of the hadronic contribution continues
 823 to this day [91, 92]. The most recent $\pi\pi$ -final state measurements were reported by the
 824 BaBar [84] and KLOE [87, 88] collaborations. An independent analysis of KLOE data using
 825 the direct measurement of $\sigma(e^+e^- \rightarrow \pi^+\pi^-)/\sigma(e^+e^- \rightarrow \mu^+\mu^-)$, which agreed well with their
 826 previous analysis using the luminosity measurement and QED calculations, has been recently
 827 published [93].

828 Muon ($g-2$), and the determination of the hadronic contribution continues to feature
 829 prominently in the international workshops Tau [85] and PHIPSI [86], where sessions were
 830 devoted to all issues around muon ($g-2$). We emphasize that while this is a difficult subject,
 831 progress will continue to be made as E989 progresses at Fermilab.

832 **Lowest- and next-lowest-order hadronic contribution**

833 The cross sections at low energies dominate the dispersion relation, and until recently the
 834 low-energy electron-positron storage rings in Novosibirsk and Frascati provided the bulk of
 835 the new measurements. The Novosibirsk experiments CMD2 (cryogenic magnetic detector)
 836 and SND (spherical neutral detector) collected data up to 1.4 GeV using the traditional
 837 e^+e^- energy scan. The KLOE experiment ran at a fixed energy around 1 GeV, either on
 838 the ϕ -resonance or just below it, using initial-state radiation to lower the collision energy
 839 and provide the full energy range in a single measurement (see Fig. 2.5(c)). The BaBar
 840 experiment also used the ISR technique, but operated at a much higher energy at or near
 841 the $\Upsilon(4s)$, which easily permitted observation of the ISR photon. At Tau2012 the Belle
 842 experiment reported new results on the $\pi^+\pi^-\pi^0$ final state [90] using ISR data. The ISR
 843 (sometimes called “radiative return”) technique is possible because of the development of
 844 the necessary theory [82, 83], which provides the effective virtual photon spectrum, called
 845 the “radiator function.”

846 While the KLOE experiment was limited to the $\pi\pi\gamma$ channel, the higher energy of the
 847 PEP-2 collider permitted BaBar to detect the ISR photon and to measure many multiple
 848 hadron final states along with the $\pi\pi\gamma$ final state, thus providing important data from
 849 channels which were either very imprecise, or simply not available before. The first $\pi^+\pi^-$
 850 data from BaBar were released in August 2009 [84], and covered the energy range from
 851 threshold to 3 GeV. Unlike the other experiments that used a calculated $\mu\mu$ cross section for
 852 the denominator in Eq. (2.18), the BaBar experiment measured the $\mu\mu$ production directly
 853 and took the ratio of experimental numbers to determine $R(s)$ directly.

854 Published $e^+e^- \rightarrow \pi^+\pi^-$ cross sections from the BaBar, KLOE, CMD2 and SND experi-
 855 ments are shown in Fig. 2.7. The KLOE re-analysis of their small-angle data using the ratio
 856 of the $\pi\pi$ $\mu\mu$ cross sections, compared large-angle data[88], and are displayed in Fig. 2.8 as
 857 the pion form factor $|F_\pi|^2$, which is related to the cross section by

$$\sigma_{e^+e^- \rightarrow \pi^+\pi^-} = \frac{\pi\alpha^2}{3s} \beta_\pi^3 |F_\pi|^2. \quad (2.19)$$

858 They were analyzed by a different group of collaborators who worked independently from
 859 those involved in the the KLOE08 [87] analysis.

860 Two recent analyses [47, 48] of the e^+e^- hadroproduction data obtained:

$$a_\mu^{\text{had;LO}} = 6\,923 \pm 42 \times 10^{-11}. \quad (2.20)$$

$$a_\mu^{\text{had;LO}} = 6\,949 \pm 43 \times 10^{-11}. \quad (2.21)$$

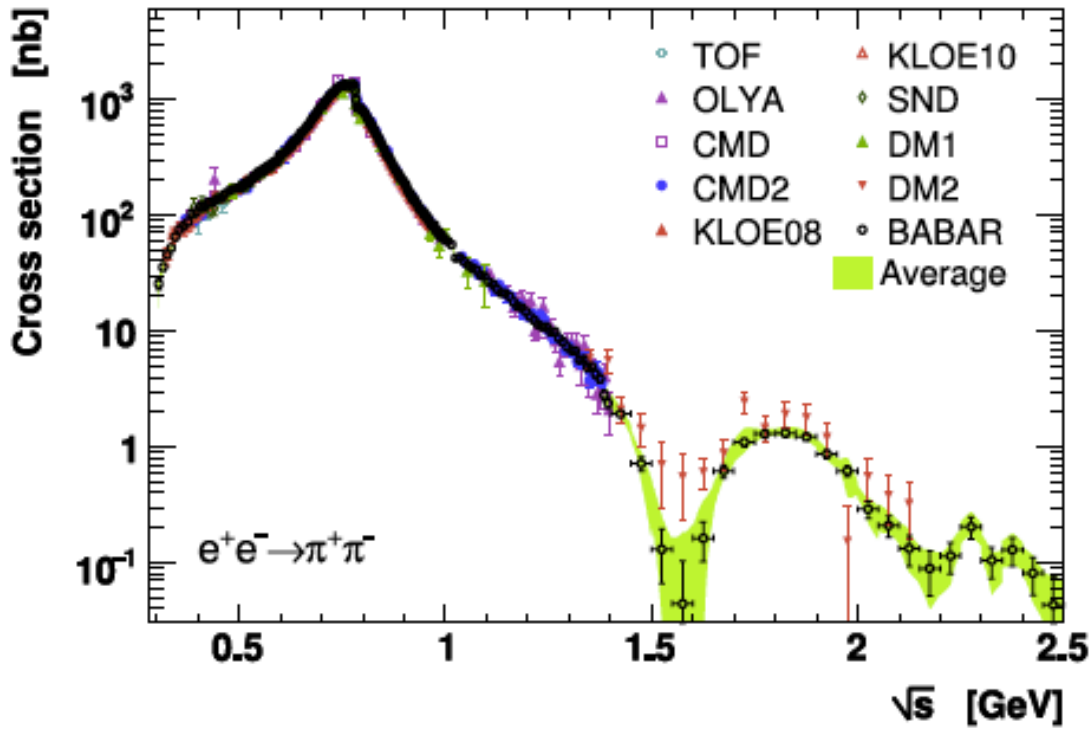
861 Important earlier global analyses include those of HMNT [73], Davier, et al., [74], Jegerlehner [75].

862 The most recent evaluation of the next-order hadronic contribution shown in Fig. 2.4(b-d)
 863 can also be determined from a dispersion relation, and the result is [48]

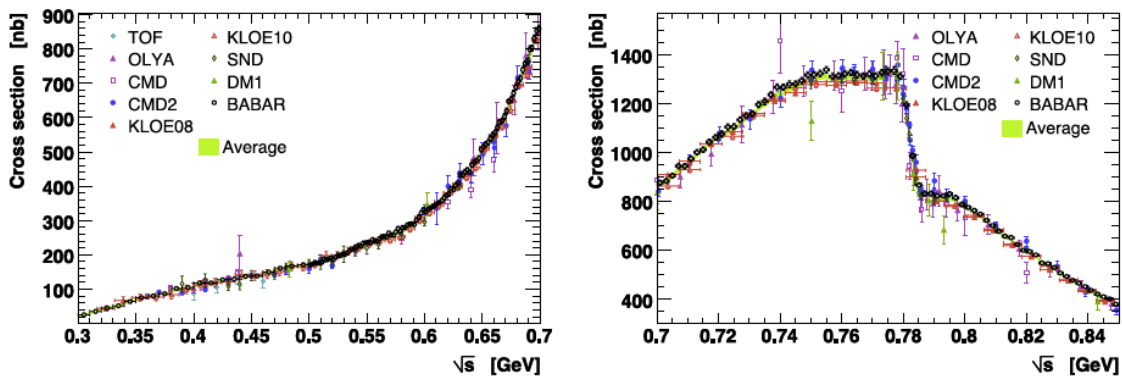
$$a_\mu^{\text{had:NLO}} = (-98.4 \pm 0.6_{\text{exp}} \pm 0.4_{\text{rad}}) \times 10^{-11}. \quad (2.22)$$

864 $a_\mu^{\text{had;LO}}$ from hadronic τ decay

865 The value of $a_\mu^{\text{had;LO}}$ from threshold up to m_τ could in principle be obtained from hadronic
 866 τ^- decays (See Fig. 2.5.3), provided that the necessary isospin corrections are known. This



(a)



(b)

Figure 2.7: The $\pi\pi$ cross section from BaBar, CMD2, KLOE and SND. The lower left-hand figure shows the threshold region, the right-hand figure shows a blowup of the ρ resonance region. The sharp cusp comes from $\rho - \omega$ interference.

867 was first demonstrated by Almany, Davier and Höcker [77]. In the absence of second-class
 868 currents, hadronic τ decays to an *even* number of pions such as $\tau^- \rightarrow \pi^- \pi^0 \nu_\tau$ goes through
 869 the vector part of the weak current, and can be related to e^+e^- annihilation into $\pi^+\pi^-$
 870 through the CVC hypothesis and isospin conservation (see Fig. 2.5.3) [77, 81]. The τ -data

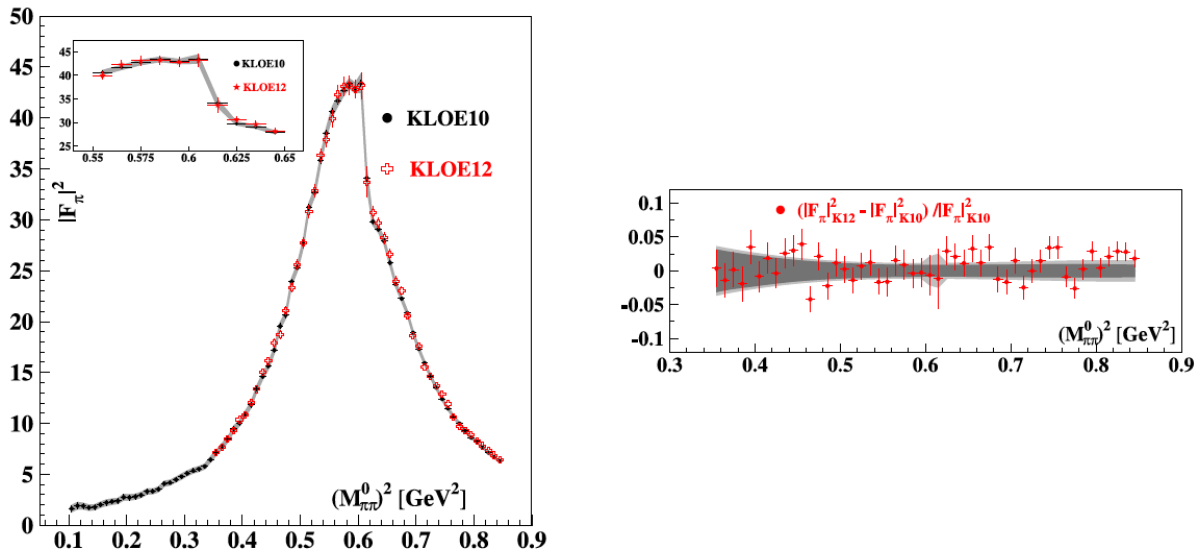


Figure 2.8: The pion form factor $|F_\pi|^2$ from KLOE2010 [88] and the re-analysis of the 2008 data [87] using the cross-section ratio described above [89]. The right-hand side shows the fractional difference between the two analyses.

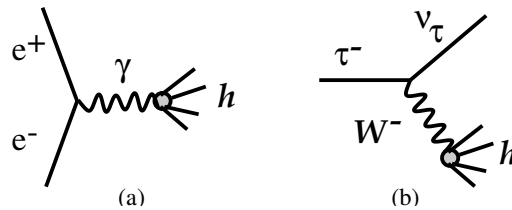


Figure 2.9: e^+e^- annihilation into hadrons (a), and hadronic τ decay (b).

871 only contain an isovector piece, and the isoscalar piece present in e^+e^- annihilation has to be
 872 put in “by hand” to evaluate $a_\mu^{\text{had};\text{LO}}$. Until recently there were 3.5 to 4.5 standard deviation
 873 differences when e^+e^- data and the CVC hypothesis were used to determine the $\tau^- \rightarrow \nu_\tau \pi^- \pi^0$
 874 or $\tau^- \rightarrow \nu_\tau 2\pi^- \pi^+ \pi^0$ branching fractions, when compared with the experimental values. Thus
 875 until recently most authors [48, 76, 75] concluded that there are unresolved issues, most likely
 876 incorrect isospin breaking corrections, that make it difficult to use the τ data on an equal
 877 footing with the e^+e^- data. New isospin corrections reduced the disagreement between the
 878 two methods [47]. However, none of the analyses using tau data have tried to combine
 879 the CVC determined part with that obtained from e^+e^- data. Were this to be done, the
 880 addition of the e^+e^- data would decrease the overall tau-based evaluation of to a_μ^{had} . Even
 881 so, the tau-based evaluation has to use e^+e^- data to determine the isoscalar part, so that
 882 the tau-based evaluation by Davier, et al., [47] can never be completely independent of the
 883 e^+e^- data.

884 More recently, Jegerlehner and Szafron [78] appear to have resolved this problem by

885 calculating the correction from $\rho - \gamma$ mixing, which had not been included correctly in the
 886 previous evaluations. A subsequent hidden local symmetry calculation [79, 80] further refines
 887 these ideas and includes the τ -data in a combined analysis. They conclude that their analysis
 888 yields a 4.7 to 4.9 σ difference with the Standard Model.

889 We should note that the theoretical uncertainties on the dispersion relation in Eq. (2.18),
 890 which assumes analyticity and the optical theorem, are negligible. The cross section that
 891 enters in Eq. (2.18) is the bare cross section, and some of the early experiments were not so
 892 careful in their reporting the data and being clear on what, if any radiative corrections were
 893 applied. All of the modern experiments are well aware of these issues, and their reported
 894 errors include any uncertainties introduced in determining the bare cross section.

895 Hadronic light-by-light contribution

896 The hadronic light-by-light contribution, (Fig. 2.4(e)) cannot at present be determined from
 897 data, but rather must be calculated using hadronic models that correctly reproduce the
 898 properties of QCD. A number of authors have calculated portions of this contribution, and
 899 a synthesis of all contributions has become available from Prades, de Rafael and Vain-
 900 shtein [58]⁵, which has been agreed to by authors from each of the leading groups that were
 901 working in this field. They obtained

$$a_{\mu}^{\text{HLbL}} = (105 \pm 26) \times 10^{-11}. \quad (2.23)$$

902 Additional work on this contribution is underway on a number of fronts, including on the
 903 lattice. A workshop was held in March 2011 at the Institute for Nuclear Theory in Seattle [59]
 904 which brought together almost all of the interested experts.

905 One important point should be made here. The main physics of the hadronic light-by-
 906 light scattering contribution is well understood. In fact, but for the sign error unraveled
 907 in 2002, the theoretical predictions for a_{μ}^{HLbL} have been relatively stable for more than ten
 908 years.

909 There is one newer calculation, which used a Dyson-Schwinger approach, that appeared
 910 to strongly disagree with all of the other model calculations of the hadronic-light-by-light
 911 contribution. However, recently these authors found several sign mistakes that change their
 912 result, moving it closer to other calculations, and have published an erratum [63].

913 At Tau2012, Blum reported that the lattice calculation of the hadronic-light-by-light
 914 contribution had started to see a signal [65]. “Signal may be emerging in the model ballpark”.
 915 Blum also had encouraging words about the precision that the lattice might reach on the
 916 lowest-order hadronic contribution.

917 In addition to the theoretical work on the HLbL, a new facility is being commissioned
 918 at DAΦNE which will provide tagged virtual photons for $\gamma^*\gamma^*$ physics. Both high- and
 919 low-energy taggers are being constructed on both sides of the interaction region to detect
 920 and measure the scattered electron and positron. Thus a coincidence between the scat-
 921 tered electrons and a π^0 would provide information on $\gamma^*\gamma^* \rightarrow \pi^0$, etc. [62], and will pro-
 922 vide experimental constraints on the models used to calculate the hadronic light-by-light
 923 contribution[94].

⁵This compilation is generally referred to as the “Glasgow Consensus” since it grew out of a workshop in Glasgow in 2007.

2.5.4 Summary of the Standard-Model Value and Comparison with Experiment

We determine the SM value using the new QED calculation from Aoyama [67]; the electroweak from Ref. [76], the hadronic light-by-light contribution from the ‘‘Glasgow Consensus’’ [58]; and lowest-order hadronic contribution from Davier, et al., [47], or Hagawara et al., [48], and the higher-order hadronic from Ref. [48] A summary of these values is given in Table 2.3.

Table 2.3: Summary of the Standard-Model contributions to the muon anomaly. Two values are quoted because of the two recent evaluations of the lowest-order hadronic vacuum polarization.

	VALUE ($\times 10^{-11}$) UNITS
QED ($\gamma + \ell$)	$116\,584\,718.951 \pm 0.009 \pm 0.019 \pm 0.007 \pm 0.077_\alpha$
HVP(lo) [47]	$6\,923 \pm 42$
HVP(lo) [48]	$6\,949 \pm 43$
HVP(ho) [48]	-98.4 ± 0.7
HLbL	105 ± 26
EW	154 ± 1
Total SM [47]	$116\,591\,802 \pm 42_{\text{H-LO}} \pm 26_{\text{H-HO}} \pm 2_{\text{other}} (\pm 49_{\text{tot}})$
Total SM [48]	$116\,591\,829 \pm 43_{\text{H-LO}} \pm 26_{\text{H-HO}} \pm 2_{\text{other}} (\pm 45_{\text{tot}})$

This SM value is to be compared with the combined a_μ^+ and a_μ^- values from E821 [6] corrected for the revised value of λ as mentioned above:

$$a_\mu^{\text{E821}} = (116\,592\,089 \pm 63) \times 10^{-11} \quad (0.54 \text{ ppm}), \quad (2.24)$$

which give a difference of

$$\Delta a_\mu(\text{E821} - \text{SM}) = (286 \pm 80) \times 10^{-11} \quad [47] \quad (2.25)$$

$$= (260 \pm 78) \times 10^{-11} \quad [48] \quad (2.26)$$

depending on which evaluation of the lowest-order hadronic contribution that is used [47, 48]. This comparison between the experimental values and the present Standard-Model value is shown graphically in Fig. 2.1.

This difference of 3.3 to 3.6 standard deviations is tantalizing, but we emphasize that whatever the final agreement between the measured and SM value turns out to be, it will have significant implications on the interpretation of new phenomena that might be found at the LHC and elsewhere. This point is discussed in detail below.

The present theoretical error is dominated by the uncertainty on the lowest-order hadronic contribution and uncertainty on the hadronic light-by-light contribution (see Table 2.3). The lowest-order hadronic contribution could be reduced to 25×10^{-11} based on the analysis of existing data and on the data sets expected from future efforts, e.g. VEPP-2000 in Novosibirsk, BES-III and a possible upgrade in energy of DAΦNE [92]. When combined

946 with future theoretical progress on the hadronic light-by-light contribution, the total SM
 947 error could reach 30×10^{-11} .

948 With the proposed experimental error of $\pm 16 \times 10^{-11}$, the combined uncertainty for the
 949 difference between theory and experiment could be as small as $\pm 34 \times 10^{-11}$, which is to be
 950 compared with the $\pm 81 \times 10^{-11}$ in Eq. (2.26).

951 2.5.5 Expected Improvements in the Standard-Model Value

952 Much experimental and theoretical work is going on worldwide to refine the hadronic contri-
 953 bution. The theory of $(g - 2)$, relevant experiments to determine the hadronic contribution,
 954 including work on the lattice, have featured prominently in the series of tau-lepton workshops
 955 and PHIPSI workshops which are held in alternate years.

956 Over the development period of our new experiment, we expect further improvements in
 957 the SM-theory evaluation. This projection is based on the following developments and facts:

- 958 • **Novosibirsk:** The VEPP2M machine has been upgraded to VEPP-2000. The max-
 959 imum energy has been increased from $\sqrt{s} = 1.4$ GeV to 2.0 GeV. Additionally, the
 960 SND detector has been upgraded and the CMD2 detector was replaced by the much-
 961 improved CMD3 detector. The cross section will be measured from threshold to
 962 2.0 GeV using an energy scan, filling in the energy region between 1.4 GeV, where
 963 the previous scan ended, up to 2.0 GeV, the lowest energy point reached by the BES
 964 collaboration in their measurements. See Fig. 2.6 for the present contribution to the
 965 overall error from this region. Engineering runs began in 2009, and data collection
 966 started in 2011. So far two independent energy scans between 1.0 and 2.0 GeV were
 967 performed in 2011 and 2012. The peak luminosity of $3 \times 10^{31} \text{cm}^{-2} \text{s}^{-1}$ was achieved,
 968 which is limited by the positron production rate. The new injection facility, sched-
 969 uled to be commissioned during the 2013-2014 upgrade, should permit the luminosity
 970 to reach $10^{32} \text{cm}^{-2} \text{s}^{-1}$. Data collection had resumed by the end of 2012 with new
 971 energy scan at energies below 1.0 GeV. The goal of experiments at VEPP-2000 is to
 972 achieve a systematic error 0.3-0.5% in $\pi^+\pi^-$ channel with negligible statistical error
 973 in the integral. The high statistics, expected at VEPP-2000, should allow a detailed
 974 comparison of the measured cross-sections with ISR results at BaBar and DAΦNE.
 975 After the upgrade, experiments at VEPP-2000 plan to take a large amount of data at
 976 1.8-2 GeV, around $N\bar{N}$ threshold. This will permit ISR data with the beam energy
 977 of 2 GeV, which is between the PEP2 energy at the $\Upsilon(4s)$ and the 1 GeV ϕ energy
 978 at the DAΦNE facility in Frascati. The dual ISR and scan approach will provide an
 979 important cross check on the two central methods to determine HVP.
- 980 • **KLOE:** The KLOE collaboration has just reported the analysis of their 2008 data set
 981 using the experimental ratio $\pi\pi/\mu\mu$ final states, rather than the luminosity to get the
 982 cross sections [93]. In the future, they will begin the program of two-photon physics will
 983 be ramping up, which will provide experimental input to the hadronic light-by-light
 984 theory.
- 985 • **BaBar:** A significant amount of new data exists from BaBar, which can be used to
 986 provide another ISR measurement from threshold to 3 GeV. It is not at all clear that

the Collaboration will be able to take on the analysis challenge.

- **Belle:** Some work on ISR measurements of $R(s)$ is going on in multi-hadron channels. These studies will complement those completed at BaBar and provide an important check.
- **BES-III:** BES-III can perform a direct measurement of R above 2 GeV with an energy scan. It can use ISR to access the region below it.
- **Calculations on the Lattice for Lowest-Order HVP:** With the increased computer power available for lattice calculations, it may be possible for lattice calculations to contribute to our knowledge of the lowest-order hadronic contribution. Blum and his collaborators are continuing to work on the lowest-order contribution. Several groups, UKQCD (Edinburg), DESY-Zeuthen (Renner and Jansen), and the LSD (lattice strong dynamics) group in the US are all working on the lowest-order contribution.
- **Calculations on the Lattice of Hadronic Light-by-Light:** The hadronic light-by-light contribution has a magnitude of $(105 \pm 26) \times 10^{-11}$, ~ 1 ppm of a_μ . A modest calculation on the lattice would have a large impact. Blum and his collaborators at BNL, RIKEN and Nagoya are working on HLbL, and are beginning to see a signal. See the recent whitepapers [66].

2.6 Physics Beyond the Standard Model

For many years, the muon anomaly has played an important role in constraining physics beyond the SM [45, 46, 76, 99, 100]. The more than 2000 citations to the major E821 papers [6, 5, 22, 21], demonstrates that this role continues. The citations are shown as a function of year in Fig. 2.10. It is apparent that with the LHC results available in 2012, interest in the BNL results has risen significantly. As discussed in the previous section, the present SM value is smaller than the experimental value by $\Delta a_\mu(\text{E821} - \text{SM})$. The discrepancy depends on the SM evaluation, but it is generally in the $> 3\sigma$ region; a representative value is $(286 \pm 80) \times 10^{-11}$, see Eq. (2.26).

In this section, we discuss how the muon anomaly provides a unique window to search for physics beyond the standard model. If such new physics is discovered elsewhere, e.g. at the LHC, then a_μ will play an important role in sorting out the interpretation of those discoveries. We discuss examples of constraints placed on various models that have been proposed as extensions of the standard model. Perhaps the ultimate value of an improved limit on a_μ will come from its ability to constrain the models that have not yet been invented.

Varieties of physics beyond the Standard Model

The LHC era has had its first spectacular success in summer 2012 with the discovery of a new particle compatible with the standard model Higgs boson. With more data, the LHC experiments will continue to shed more light on the nature of electroweak symmetry breaking (EWSB). It is very likely that EWSB is related to new particles, new interactions, or maybe

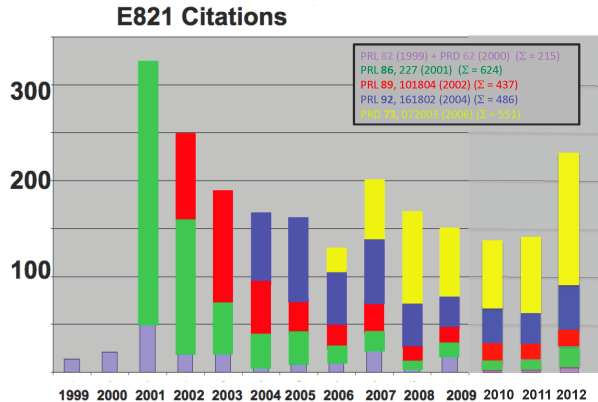


Figure 2.10: Citations by year to the E821 papers reporting physics results as of July 2012: light blue [19] plus [20]; green [21]; red [22]; blue [5]; and yellow the Physical Review article [6].

1024 to new concepts such as supersymmetry, extra dimensions, or compositeness. Further open
 1025 questions in particle physics, related e.g. to the nature of dark matter, the origin of flavor or
 1026 grand unification, indicate that at or even below the TeV scale there could be rich physics
 1027 beyond the standard model.

1028 Unravelling the existence and the properties of such new physics requires experimen-
 1029 tal information complementary to the LHC. The muon ($g-2$), together with searches for
 1030 charged lepton flavor violation, electric dipole moments, and rare decays, belongs to a class
 1031 of complementary low-energy experiments.

1032 In fact, the muon magnetic moment has a special role because it is sensitive to a large
 1033 class of models related and unrelated to EWSB and because it combines several properties
 1034 in a unique way: it is a flavour- and CP-conserving, chirality-flipping and loop-induced
 1035 quantity. In contrast, many high-energy collider observables at the LHC and a future linear
 1036 collider are chirality-conserving, and many other low-energy precision observables are CP-
 1037 or flavour-violating. These unique properties might be the reason why the muon ($g-2$)
 1038 is the only among the mentioned observables which shows a significant deviation between
 1039 the experimental value and the SM prediction, see Eq. (2.26). Furthermore, while $g-2$ is
 1040 sensitive to leptonic couplings, b - or K -physics more naturally probe the hadronic couplings
 1041 of new physics. If charged lepton-flavor violation exists, observables such as $\mu \rightarrow e$ conversion
 1042 can only determine a combination of the strength of lepton-flavor violation and the mass
 1043 scale of new physics. In that case, $g-2$ can help to disentangle the nature of the new physics.

1044 The role of $g-2$ as a discriminator between very different standard model extensions is
 1045 well illustrated by a relation stressed by Czarnecki and Marciano [46]. It holds in a wide
 1046 range of models as a result of the chirality-flipping nature of both $g-2$ and the muon mass:
 1047 If a new physics model with a mass scale Λ contributes to the muon mass $\delta m_\mu(\text{N.P.})$, it also
 1048 contributes to a_μ , and the two contributions are related as

$$a_\mu(\text{N.P.}) = \mathcal{O}(1) \times \left(\frac{m_\mu}{\Lambda}\right)^2 \times \left(\frac{\delta m_\mu(\text{N.P.})}{m_\mu}\right). \quad (2.27)$$

The ratio $C(\text{N.P.}) \equiv \delta m_\mu(\text{N.P.})/m_\mu$ cannot be larger than unity unless there is fine-tuning in the muon mass. Hence a first consequence of this relation is that new physics can explain the currently observed deviation (2.26) only if Λ is at the few-TeV scale or smaller.

In many models, the ratio C arises from one- or even two-loop diagrams, and is then suppressed by factors like $\alpha/4\pi$ or $(\alpha/4\pi)^2$. Hence, even for a given Λ , the contributions to a_μ are highly model dependent.

It is instructive to classify new physics models as follows:

- Models with $C(\text{N.P.}) \simeq 1$: Such models are of interest since the muon mass is essentially generated by radiative effects at some scale Λ . A variety of such models have been discussed in [46], including extended technicolor or generic models with naturally vanishing bare muon mass. For examples of radiative muon mass generation within supersymmetry, see e.g. [101, 102]. In these models the new physics contribution to a_μ can be very large,

$$a_\mu(\Lambda) \simeq \frac{m_\mu^2}{\Lambda^2} \simeq 1100 \times 10^{-11} \left(\frac{1 \text{ TeV}}{\Lambda} \right)^2. \quad (2.28)$$

and the difference Eq. (2.26) can be used to place a lower limit on the new physics mass scale, which is in the few TeV range [103, 102].

- Models with $C(\text{N.P.}) = \mathcal{O}(\alpha/4\pi)$: Such a loop suppression happens in many models with new weakly interacting particles like Z' or W' , little Higgs or certain extra dimension models. As examples, the contributions to a_μ in a model with $\delta = 1$ (or 2) universal extra dimensions (UED) [104] and the Littlest Higgs model with T-parity (LHT) [105] are given by

$$a_\mu(\text{UED}) \simeq -5.8 \times 10^{-11} (1 + 1.2\delta) S_{\text{KK}}, \quad (2.29)$$

$$a_\mu(\text{LHT}) < 12 \times 10^{-11} \quad (2.30)$$

with $|S_{\text{KK}}| \lesssim 1$ [104]. A difference as large as Eq. (2.26) is very hard to accommodate unless the mass scale is very small, of the order of M_Z , which however is often excluded e.g. by LEP measurements. So typically these models predict very small contributions to a_μ and will be disfavored if the current deviation will be confirmed by the new a_μ measurement.

Exceptions are provided by models where new particles interact with muons but are otherwise hidden from searches. An example is the model with a new gauge boson associated to a gauged lepton number $L_\mu - L_\tau$ [106], where a gauge boson mass of $\mathcal{O}(100 \text{ GeV})$ and large a_μ are viable.

- Models with intermediate values for $C(\text{N.P.})$ and mass scales around the weak scale: In such models, contributions to a_μ could be as large as Eq. (2.26) or even larger, or smaller, depending on the details of the model. This implies that a more precise a_μ -measurement will have significant impact on such models and can even be used to measure model parameters. Supersymmetric (SUSY) models are the best known examples, so muon $g-2$ would have substantial sensitivity to SUSY particles. Compared to generic perturbative models, supersymmetry provides an enhancement to

1085 $C(\text{SUSY}) = \mathcal{O}(\tan \beta \times \alpha/4\pi)$ and to $a_\mu(\text{SUSY})$ by a factor $\tan \beta$ (the ratio of the
 1086 vacuum expectation values of the two Higgs fields). Typical SUSY diagrams for the
 1087 magnetic dipole moment, the electric dipole moment, and the lepton-number violating
 1088 conversion process $\mu \rightarrow e$ in the field of a nucleus are shown pictorially in Fig. 2.11.
 1089 The shown diagrams contain the SUSY partners of the muon, electron and the SM
 1090 $U(1)_Y$ gauge boson, $\tilde{\mu}$, \tilde{e} , \tilde{B} . The full SUSY contributions involve also the SUSY part-
 1091 ners to the neutrinos and all SM gauge and Higgs bosons. In a model with SUSY
 1092 masses equal to Λ the SUSY contribution to a_μ is given by [46]

$$a_\mu(\text{SUSY}) \simeq \text{sgn}(\mu) 130 \times 10^{-11} \tan \beta \left(\frac{100 \text{ GeV}}{\Lambda} \right)^2 \quad (2.31)$$

1093 which indicates the dependence on $\tan \beta$, and the SUSY mass scale, as well as the sign
 1094 of the SUSY μ -parameter. The formula still approximately applies even if only the
 1095 smuon and chargino masses are of the order Λ but e.g. squarks and gluinos are much
 1096 heavier. However the SUSY contributions to a_μ depend strongly on the details of mass
 1097 splittings between the weakly interacting SUSY particles. Thus muon $g-2$ is sensitive
 1098 to SUSY models with SUSY masses in the few hundred GeV range, and it will help to
 1099 measure SUSY parameters.

1100 There are also non-supersymmetric models with similar enhancements. For instance,
 1101 lepton flavor mixing can help. An example is provided in Ref. [107] by a model with
 1102 two Higgs doublets and four generations, which can accommodate large Δa_μ without
 1103 violating constraints on lepton flavor violation. In variants of Randall-Sundrum models
 1104 [108, 109, 110] and large extra dimension models [111], large contributions to a_μ might
 1105 be possible from exchange of Kaluza-Klein gravitons, but the theoretical evaluation
 1106 is difficult because of cutoff dependences. A recent evaluation of the non-graviton
 1107 contributions in Randall-Sundrum models, however, obtained a very small result [112].

1108 Further examples include scenarios of unparticle physics [113, 114] (here a more pre-
 1109 cise a_μ -measurement would constrain the unparticle scale dimension and effective cou-
 1110 plings), generic models with a hidden sector at the weak scale [115] or a model with
 1111 the discrete flavor symmetry group T' and Higgs triplets [116] (here a more precise
 1112 a_μ -measurement would constrain hidden sector/Higgs triplet masses and couplings),
 1113 or the model proposed in Ref. [117], which implements the idea that neutrino masses,
 1114 leptogenesis and the deviation in a_μ all originate from dark matter particles. In the
 1115 latter model, new leptons and scalar particles are predicted, and a_μ provides significant
 1116 constraints on the masses and Yukawa couplings of the new particles.

1117 The following types of new physics scenarios are quite different from the ones above:

- 1118 • Models with extended Higgs sector but without the $\tan \beta$ -enhancement of SUSY mod-
 1119 els. Among these models are the usual two-Higgs-doublet models. The one-loop con-
 1120 tribution of the extra Higgs states to a_μ is suppressed by two additional powers of
 1121 the muon Yukawa coupling, corresponding to $a_\mu(\text{N.P.}) \propto m_\mu^4/\Lambda^4$ at the one-loop level.
 1122 Two-loop effects from Barr-Zee diagrams can be larger [118], but typically the contri-
 1123 butions to a_μ are negligible in these models.

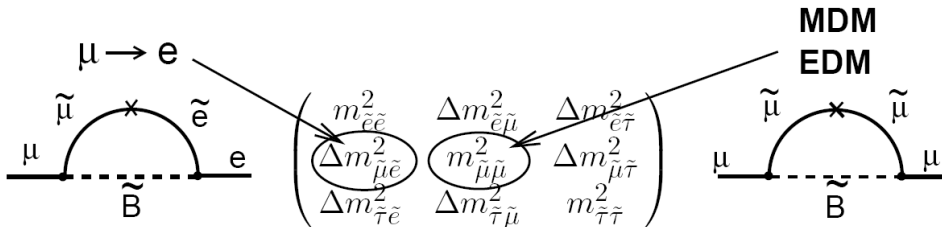


Figure 2.11: The SUSY contributions to the anomaly, and to $\mu \rightarrow e$ conversion, showing the relevant slepton mixing matrix elements. The MDM and EDM give the real and imaginary parts of the matrix element, respectively. The \times indicates a chirality flip.

- Models with additional light particles with masses below the GeV-scale, generically called dark sector models: Examples are provided by the models of Refs. [119, 120], where additional light neutral gauge bosons can affect electromagnetic interactions. Such models are intriguing since they completely decouple $g-2$ from the physics of EWSB, and since they are hidden from collider searches at LEP or LHC (see however Refs. [121, 122] for studies of possible effects at dedicated low-energy colliders and in Higgs decays at the LHC). They can lead to contributions to a_μ which are of the same order as the deviation in Eq. (2.26). Hence the new $g-2$ measurement will provide an important test of such models.

To summarize: many well-motivated models can accommodate larger contributions to a_μ — if any of these are realized $g-2$ can be used to constrain model parameters; many well-motivated new physics models give tiny contributions to a_μ and would be disfavored if the more precise $g-2$ measurement confirms the deviation in Eq. (2.26). There are also examples of models which lead to similar LHC signatures but which can be distinguished using $g-2$.

In the following it is discussed in more detail how a_μ will be useful in understanding TeV-scale physics in the event that the LHC established the existence of physics beyond the standard model [99].

1141 a_μ and supersymmetry

1142 We first focus on the case of supersymmetry, which provides a particularly well-defined and
1143 calculable framework. We illustrate the sensitivity of $g-2$ to the SUSY parameters and the
1144 complementarity to LHC measurements.

1145 As discussed above, supersymmetry with $\tan \beta$ up to 50 and masses in the 100–700 GeV
1146 range can easily explain the currently observed deviation (2.26). Now the SUSY contributions
1147 are discussed in more detail. At the one-loop level, the diagrams of the minimal supersym-
1148 metric standard model (MSSM) involve the SUSY partners the gauge and Higgs bosons and
1149 the muon-neutrino and the muon, the so-called charginos, neutralinos and sneutrinos and
1150 smuons. The relevant parameters are thus the SUSY breaking mass parameters for the 2nd
1151 generation sleptons, the bino and wino masses M_2 , M_1 , and the Higgsino mass parameter μ .
1152 Strongly interacting particles, squarks and gluinos, and their masses are irrelevant on this
1153 level.

1154 If all the relevant mass parameters are equal, the approximation (2.31) is valid, and the
 1155 dominant contribution is from the chargino–sneutrino diagrams. If μ is very large, the bino-
 1156 like neutralino contribution of Fig. 2.11 is approximately linear in μ and can dominate. If
 1157 there is a large mass splitting between the left- and right-handed smuon, even the sign can
 1158 be opposite to Eq. (2.31), see the discussions in [123, 124].

1159 As a result, $a_\mu(\text{SUSY})$ depends not only on the overall SUSY masses but on the indi-
 1160 vidual values of the parameters M_1 , M_2 , and μ . Exchanging these parameters can leave the
 1161 spectrum of SUSY particle masses unchanged but will have an effect on a_μ^{SUSY} . It is shown
 1162 later that this will help to disentangle different possible interpretations of LHC data.

1163 On the two-loop level, further contributions exist which are typically subleading but can
 1164 become important in regions of parameter space. For instance, there are diagrams without
 1165 smuons or sneutrinos but with e.g. a pure chargino or stop loop [125]. Such diagrams can
 1166 even be dominant if first and second generation sfermions are very heavy, a scenario called
 1167 effective SUSY [126].

1168 To date, the LHC experiments have not found indications for SUSY particles but only
 1169 for a Higgs-like particle with mass around 126 GeV. This leads to the following conclusions:

- 1170 • If supersymmetry is the origin of the deviation in a_μ , at least some SUSY particles
 1171 cannot be much heavier than around 700 GeV (for $\tan\beta = 50$ or less), most favorably
 1172 the smuons and charginos/neutralinos.
- 1173 • The negative results of the LHC searches for SUSY particles imply lower limits of
 1174 around 1 TeV on squark and gluino masses. However, the bounds are not model-
 1175 independent but valid in scenarios with particular squark and gluino decay patterns.
- 1176 • The constraint that a SM-like Higgs boson mass is around 126 GeV requires either very
 1177 large loop corrections from large logarithms or non-minimal tree-level contributions
 1178 from additional non-minimal particle content.
- 1179 • The requirement of small fine-tuning between supersymmetry-breaking parameters and
 1180 the Z-boson mass prefers certain particles, in particular stops, gluinos and Higgsinos
 1181 to be rather light.

1182 A tension between these constraints seems to be building up, but the constraints act on
 1183 different aspects of SUSY models. Hence it is in principle no problem to accommodate all
 1184 the experimental data in the general minimal supersymmetric standard model, for recent
 1185 analyses see Refs. [127, 128].

1186 The situation is different in many specific scenarios, based e.g. on particular high-scale
 1187 assumptions or constructed to solve a subset of the issues mentioned above. We will briefly
 1188 review five such cases which exemplify the range of possibilities.

1189 The Constrained MSSM (CMSSM) is one of the best known scenarios. Here, GUT-
 1190 scale universality relates sparticle masses, in particular the masses of colored and uncolored
 1191 sfermions of all generations. For a long time, many analyses have used a_μ as a central
 1192 observable to constrain the CMSSM parameters, see e.g. [129]. The most recent analyses
 1193 show that the LHC determination of the Higgs boson mass turns out to be incompatible
 1194 with an explanation of the current Δa_μ within the CMSSM [130, 131, 132]. Hence, the

1195 CMSSM and similar scenarios is already disfavored now, and it will be excluded if the future
 1196 a_μ measurement confirms the current Δa_μ .

1197 The issue of fine-tuning has led to many proposals for SUSY models in which some or all
 1198 of the experimental constraints are satisfied in a technically natural way. For instance, in the
 1199 so-called natural SUSY scenarios (see e.g. [136, 137]) the spectrum is such that fine-tuning
 1200 is minimized while squarks and gluinos evade LHC bounds. These scenarios can explain
 1201 the Higgs boson mass but completely fail to explain $g-2$ because of the heavy smuons.
 1202 Similarly so-called compressed supersymmetry [138] can be a natural explanation of the
 1203 Higgs mass and the negative LHC SUSY searches but, at least in the version of Ref. [139]
 1204 fails to accommodate a large Δa_μ .

1205 On the other hand, the model of Ref. [133] is an example of a model with the aim to
 1206 reconcile LHC-data, naturalness, and $g-2$. It is based on gauge-mediated SUSY breaking
 1207 and extra vector-like matter, and it is naturally in agreement with FCNC constraints and
 1208 the Higgs boson mass value. In this model the SUSY particles can be light enough to explain
 1209 $g-2$, but in that case it is on the verge of being excluded by LHC data.

1210 The rising tension between the constraints mentioned above, and further recent model-
 1211 building efforts to solve it, are also reviewed in Refs. [134, 135]. In these references, more
 1212 pragmatic approaches are pursued, and parameter regions within the general MSSM are
 1213 suggested which are in agreement with all experimental constraints. All suggested regions
 1214 have in common that they are split, i.e. some sparticles are much heavier than others. Ref.
 1215 [134] suggests to focus on scenarios with light non-colored and heavy colored sparticles; Ref.
 1216 [135] proposes split-family supersymmetry, where only the third family sfermions are very
 1217 heavy. In both scenarios, $g-2$ can be explained, and the parameter space of interest can be
 1218 probed by the next LHC run.

1219 In the general model classification of the previous subsection the possibility of radiative
 1220 muon mass generation was mentioned. This idea can be realized within supersymmetry, and
 1221 it leads to SUSY scenarios quite different from the ones discussed so far. Since the muon mass
 1222 at tree level is given by the product of a Yukawa coupling and the vacuum expectation value
 1223 of the Higgs doublet H_d , there are two kinds of such scenarios. First, one can postulate that
 1224 the muon Yukawa coupling is zero but chiral invariance is broken by soft supersymmetry-
 1225 breaking A -terms. Then, the muon mass, and a_μ^{SUSY} , arise at the one-loop level and there is
 1226 no relative loop suppression of a_μ^{SUSY} [101, 102]. Second, one can postulate that the vacuum
 1227 expectation value $\langle H_d \rangle$ is very small or zero [140, 141]. Then, the muon mass and a_μ^{SUSY}
 1228 arise at the one-loop level from loop-induced couplings to the other Higgs doublet. Both
 1229 scenarios could accommodate large a_μ^{SUSY} and TeV-scale SUSY particle masses.

1230 These examples of the CMSSM, natural SUSY, extended SUSY models, split MSSM
 1231 scenarios, and radiative muon mass generation illustrate the model-dependence of $g-2$ and
 1232 its correlation to the other constraints. Clearly, a definitive knowledge of a_μ^{SUSY} will be very
 1233 beneficial for the interpretation of LHC data in terms of SUSY.

1234 a_μ and model selection and parameter measurement

1235 The LHC is sensitive to virtually all proposed weak-scale extensions of the standard model,
 1236 ranging from supersymmetry, extra dimensions and technicolor to little Higgs models, un-
 1237 particle physics, hidden sector models and others. However, even if the existence of physics

beyond the standard model is established, it will be far from easy for the LHC alone to identify which of these — or not yet thought of — alternatives is realized. Typically LHC data will be consistent with several alternative models.

The previous subsection has given examples of qualitatively different SUSY models which are in agreement with current LHC data. Even worse, even if in the future the LHC finds many new heavy particles which are compatible with SUSY, these new states might allow alternative interpretations in terms of non-SUSY models. In particular universal-extra-dimension models (UED) [142], or the Littlest Higgs model with T-parity (LHT) [143, 144] have been called “bosonic SUSY” since they can mimic SUSY but the partner particles have the opposite spin as the SUSY particles, see e.g. [145]. The muon $g-2$ would especially aid in the selection since UED or Littlest Higgs models predict a tiny effect to a_μ [104, 105], while SUSY effects are often much larger.

On the other hand, a situation where the LHC finds no physics beyond the standard model but the a_μ measurement establishes a deviation, might be a signal for dark sector models such as the secluded U(1) model [119], with new very weakly interacting light particles which are hard to identify at the LHC [121, 120, 122].

Next, if new physics is realized in the form of a non-renormalizable theory, a_μ might not be fully computable but depend on the ultraviolet cutoff. Randall-Sundrum or universal extra dimension models are examples of this situation. In such a case, the a_μ measurement will not only help to constrain model parameters but it will also help to get information on the ultraviolet completion of the theory.

Within the framework of SUSY there are many different well-motivated models as discussed in the previous subsection. Fig. 2.12 illustrates the complementarity between the LHC and $g-2$ in selecting between and analysing such models.

The red points in the left plot in Fig. 2.12 show the values for the so-called SPS benchmark points [149] and new benchmark points E1, E4, NS1. The points E1, E4 are the split scenarios defined in Endo et al, Ref. [134] (cases (a) and (d) with $M_2 = 300$ GeV and $m_L = 500$ GeV), the point NS1 is the natural SUSY scenario defined in Ref. [136]. These points span a wide range and can be positive or negative, due to the factor $\text{sign}(\mu)$ in Eq. (2.31). The discriminating power of the current (yellow band) and an improved (blue band) measurement is evident from Fig. 2.12(a).

Even though several SPS points are actually experimentally excluded, their spread in Fig. 2.12(a) is still a good illustration of possible SUSY contributions to a_μ . E.g. the split scenarios of Refs. [134, 135] are comparable to SPS1b, both in their $g-2$ contribution and in the relevant mass spectrum. Natural SUSY is similar to SPS2, which corresponds to a heavy sfermion scenario. Similarly, the “supersymmetry without prejudice” study of Ref. [150] confirmed that the entire range $a_\mu^{\text{SUSY}} \sim (-100 \dots + 300) \times 10^{-11}$ was populated by a reasonable number of “models” which are in agreement with other experimental constraints. Therefore, a precise measurement of $g-2$ to $\pm 16 \times 10^{-11}$ will be a crucial way to rule out a large fraction of models and thus determine SUSY parameters.

One might think that if SUSY exists, the LHC-experiments will find it and measure its parameters. Above it has been mentioned that SUSY can be mimicked by “bosonic SUSY” models. The green points in Fig. 2.12(a) illustrate that even within SUSY, certain SUSY parameter points can be mimicked by others. The green points correspond to “degenerate solutions” of Ref. [146] — different SUSY parameter points which cannot be distinguished

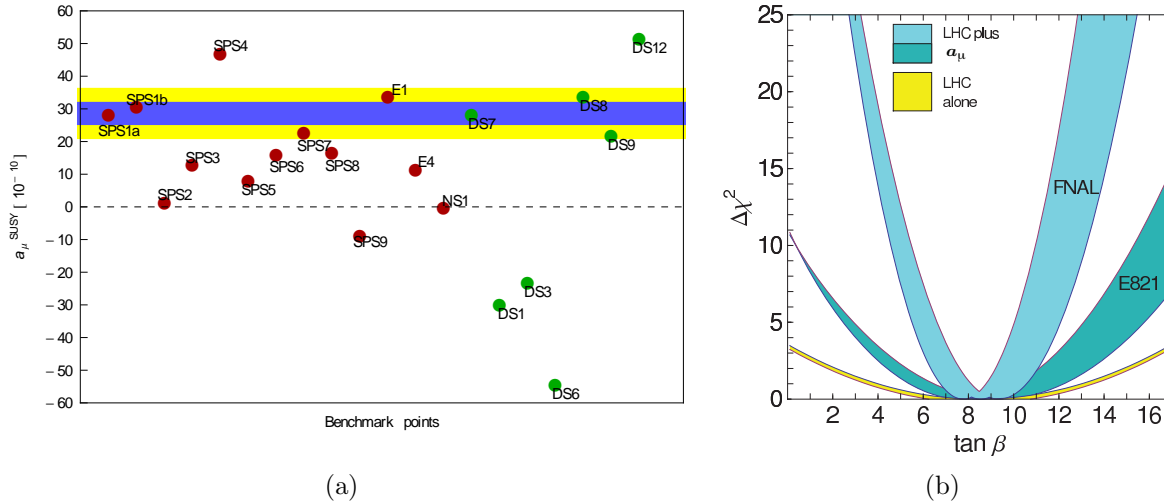


Figure 2.12: (a) SUSY contributions to a_μ for the SPS and other benchmark points (red), and for the “degenerate solutions” from Ref. [146]. The yellow band is the $\pm 1 \sigma$ error from E821, the blue is the projected sensitivity of E989. (b) Possible future $\tan\beta$ determination assuming that a slightly modified MSSM point SPS1a (see text) is realized. The bands show the $\Delta\chi^2$ parabolas from LHC-data alone (yellow) [148], including the a_μ with current precision (dark blue) and with prospective precision (light blue). The width of the blue curves results from the expected LHC-uncertainty of the parameters (mainly smuon and chargino masses) [148].

1283 at the LHC alone (see also Ref. [147] for the LHC inverse problem). Essentially the points
 1284 differ by swapping the values and signs of the SUSY parameters μ , M_1 , M_2 . They have very
 1285 different a_μ predictions, and hence a_μ can resolve such LHC degeneracies.

1286 The right plot of Fig. 2.12 illustrates that the SUSY parameter $\tan\beta$ can be measured
 1287 more precisely by combining LHC-data with a_μ . It is based on the assumption that SUSY
 1288 is realized, found at the LHC and the origin of the observed a_μ deviation (2.26). To fix
 1289 an example, we use a slightly modified SPS1a benchmark point with $\tan\beta$ scaled down to
 1290 $\tan\beta = 8.5$ such that a_μ^{SUSY} is equal to an assumed deviation $\Delta a_\mu = 255 \times 10^{-11}$.⁶ Ref.
 1291 [148] has shown that then mass measurements at the LHC alone are sufficient to determine
 1292 $\tan\beta$ to a precision of ± 4.5 only. The corresponding $\Delta\chi^2$ parabola is shown in yellow in the
 1293 plot. In such a situation one can study the SUSY prediction for a_μ as a function of $\tan\beta$
 1294 (all other parameters are known from the global fit to LHC data) and compare it to the
 1295 measured value, in particular after an improved measurement. The plot compares the LHC
 1296 $\Delta\chi^2$ parabola with the ones obtained from including a_μ , $\Delta\chi^2 = [(a_\mu^{\text{SUSY}}(\tan\beta) - \Delta a_\mu)/\delta a_\mu]^2$
 1297 with the errors $\delta a_\mu = 80 \times 10^{-11}$ (dark blue) and 34×10^{-11} (light blue). As can be seen
 1298 from the Figure, using today’s precision for a_μ would already improve the determination of
 1299 $\tan\beta$, but the improvement will be even more impressive after the future a_μ measurement.

1300 One should note that even if better ways to determine $\tan\beta$ at the LHC alone might

⁶The actual SPS1a point is ruled out by LHC, however for our purposes only the weakly interacting particles are relevant, and these are not excluded. The following conclusions are neither very sensitive to the actual $\tan\beta$ value nor to the actual value of the deviation Δa_μ .

1301 be found, an independent determination using a_μ will still be highly valuable, as $\tan\beta$ is
1302 one of the central MSSM parameters; it appears in all sectors and in almost all observables.
1303 In non-minimal SUSY models the relation between $\tan\beta$ and different observables can be
1304 modified. Therefore, measuring $\tan\beta$ in different ways, e.g. using certain Higgs- or b -decays
1305 at the LHC or at b -factories and using a_μ , would constitute a non-trivial and indispensable
1306 test of the universality of $\tan\beta$ and thus of the structure of the MSSM.

1307 The anomalous magnetic moment of the muon is sensitive to contributions from a wide
1308 range of physics beyond the standard model. It will continue to place stringent restrictions
1309 on all of the models, both present and yet to be written down. If physics beyond the standard
1310 model is discovered at the LHC or other experiments, a_μ will constitute an indispensable
1311 tool to discriminate between very different types of new physics, especially since it is highly
1312 sensitive to parameters which are difficult to measure at the LHC. If no new phenomena
1313 are found elsewhere, then it represents one of the few ways to probe physics beyond the
1314 standard model. In either case, it will play an essential and complementary role in the quest
1315 to understand physics beyond the standard model at the TeV scale.

References

1316

- 1317 [1] O. Stern, Z. Phys. **7**, 249 (1921);
- 1318 [2] W. Gerlach and O. Stern, Z. Phys. **8**, 110 (1922); Z. Phys. **9** and 349(1922), Z. Phys.
1319 **9**, 353 (1924); W. Gerlach and O. Stern, Ann. Phys. **74**, 673 (1924).
- 1320 [3] G.E. Uhlenbeck and S. Goudsmit, Naturwissenschaften **47**, 953 (1925); G.E. Uhlenbeck
1321 and S. Goudsmit, Nature **117** (1926) 264.
- 1322 [4] E. Schrödinger, Ann. Phys. **79** (1926) 361.
- 1323 [5] L.H. Thomas, Nature **117**, (1926) 514 and Phil. Mag. **3** (1927) 1.
- 1324 [6] T.E. Phipps and J.B. Taylor, Phys. Rev. **29**, 309 (1927).
- 1325 [7] P.A.M. Dirac, Proc. R. Soc. (London) **A117**, 610 (1928), and **A118**, 351 (1928). See
1326 also, P.A.M. Dirac, *The Principles of Quantum Mechanics*, 4th edition, Oxford Univer-
1327 sity Press, London, 1958.
- 1328 [8] Sin-itiro Tomonaga, *The Story of Spin*, translated by Takeshi Oka, U. Chicago Press,
1329 1997.
- 1330 [9] R. Frisch and O. Stern, Z. Phys. **85**, 4 (1933), and I. Estermann and O. Stern, Z. Phys.
1331 **85**, 17 (1933).
- 1332 [10] Luis W. Alvarez and F. Bloch, Phys. Rev. **57**, 111 (1940).
- 1333 [11] J.E. Nafe, E.B. Nelson and I.I. Rabi Phys. Rev. **71**, 914(1947).
- 1334 [12] D.E. Nagel, R.S. Julian and J.R. Zacharias, Phys. Rev. **72**, 971 (1947).
- 1335 [13] P. Kusch and H.M Foley, Phys. Rev **72**, 1256 (1947).
- 1336 [14] J. Schwinger, Phys. Rev. **73**, 416L (1948), and Phys. Rev. **76** 790 (1949). The former
1337 paper contains a misprint in the expression for a_e that is corrected in the longer paper.
- 1338 [15] Hans A. Bethe and Edwin E. Salpeter, *Quantum Mechanics of One- and Two-Electron*
1339 *Atoms*, Springer-Verlag, (1957), p. 51.
- 1340 [16] See Figure 5 in Paul Kunze, Z. Phys. **83**, 1 (1933).

- 1341 [17] Carl D. Anderson and Seth H. Neddermeyer, Phys. Rev. **50** (1936) 263, and Seth H.
1342 Neddermeyer and Carl D. Anderson, Phys. Rev. **51** (1937) 844.
- 1343 [18] J.C. Street, E.C. Stevenson, Phys. Rev. **52** (1937) 1003.
- 1344 [19] Y. Nishina, M. Tekeuchi and T. Ichimiya, Phys. Rev. **52** (1937) 1198.
- 1345 [20] M.M. Jean Crussard and L. Leprince-Ringuet, Compt. Rend. **204** (1937) 240.
- 1346 [21] Garwin RL, Lederman LM, Weinrich M, Phys. Rev. 105:1415 (1957)
- 1347 [22] J.I. Friedman and V.L. Telegdi, Phys. Rev. **105**, 1681 (1957).
- 1348 [23] E.J. Konopinski, Ann. Rev. Nucl. Sci. **9** 99, (1959).
- 1349 [24] Garwin RL, Hutchinson DP, Penman S, Shapiro G, Phys. Rev. 118:271 (1960)
- 1350 [25] Charpak G, et al. Phys. Rev. Lett. 6:28 (1961), Nuovo Cimento. 22:1043 (1961), Phys.
1351 Lett. 1:16 (1962), Nuovo Cimento. 37:1241 (1965) and Charpak G. et al. Phys. Lett.
1352 1:16 (1962)
- 1353 [26] Bailey J, et al. Phys. Lett. 28B:287 (1968). Additional details can be found in Bailey J,
1354 et al. Nuovo Cimento. A9:369 (1972) and references therein.
- 1355 [27] Bailey J, et al. Nucl. Phys. B150:1 (1979)
- 1356 [28] E.M. Purcell and N.F. Ramsey, Phys. Rev. **78**, 807 (1950).
- 1357 [29] T.D. Lee and C.N. Yang, Phys. Rev. **104** (1956) 254.
- 1358 [30] J.H. Smith, E.M. Purcell and N.F. Ramsey, Phys. Rev. **108**, 120 (1957).
- 1359 [31] L. Landau, Nucl. Phys. **3**, 127 (1957).
- 1360 [32] N.F. Ramsey Phys. Rev. **109**, 225 (1958).
- 1361 [33] W.C. Griffith, et al., Phys. Rev. Lett. **102**, 101601 (2009).
- 1362 [34] C.A. Baker, et al., Phys. Rev. Lett. **97**, 131801 (2006).
- 1363 [35] J.J. Hudson, et al., Nature **473**, 493 (2011).
- 1364 [36] G.W. Bennett, et al., Phys. Rev. **D 80**, 052008 (2009).
- 1365 [37] Bargmann V, Michel L, Telegdi VL, Phys. Rev. Lett. 2:435 (1959)
- 1366 [38] Bennett GW, et al. (The $g - 2$ Collab.) Phys. Rev. Lett. 92:161802 (2004)
- 1367 [39] Bennett GW, et al.(The $g - 2$ Collab.) Phys. Rev. D, 73:072003 (2006)
- 1368 [40] C.S. Wu, E. Ambler, R.W. Hayward, D.D. Hoppes, R.P. Hudson, Phys. Rev. **105**, 1413
1369 (1957).

- 1370 [41] Mohr PJ, Taylor BN, Newell DB, (CODATA recommended values). *Rev. Mod. Phys.*
1371 80:633 (2008)
- 1372 [42] R. Prigl, *et al.*, Nucl. Inst. Methods Phys. Res. **A374** 118 (1996).
- 1373 [43] W. Liu et al., Phys. Rev. Lett. **82**, 711 (1999).
- 1374 [44] Topical Workshop on The Muon Magnetic Dipole Moment; Oct. 2007
1375 School of Physics and Astronomy, The University of Glasgow. See:
1376 www.ippp.dur.ac.uk/old/MuonMDM/.
- 1377 [45] T. Kinoshita and W.J. Marciano in *Quantum Electrodynamics* (Directions in High En-
1378 ergy Physics, Vol. 7), ed. T. Kinoshita, (World Scientific, Singapore, 1990), p. 419.
- 1379 [46] Andrzej Czarnecki and William J. Marciano, Phys. Rev. **D64** 013014 (2001).
- 1380 [47] Davier M, et al. M. Davier¹, A. Hoecker^{2,a}, B. Malaescu^{1,b}, Z. Zhang¹ Eur. Phys. J. C
1381 71:1515 (2011), erratum Eur. Phys. J. C 72:1874 (2012).
- 1382 [48] Koru Hagiwara, Ruofan Liao, Alan D. Martin, Daisuke Nomura and Thomas Teubner,
1383 J. Phys. **G38**, 085003 (2011).
- 1384 [49] Xu Feng, Karl Jansen, Marcus Perschlies and Dru B. Renner, Phys. Rev. Lett. 107
1385 081802 (2011).
- 1386 [50] A. Czarnecki, B. Krause and W.J. Marciano, Phys. Rev. Lett. **76** (1996) 3267.
- 1387 [51] S. Peris, M. Perrottet and E. de Rafael, Phys. Lett. **B355** (1995) 523.
- 1388 [52] A. Czarnecki, B. Krause and W. Marciano, Phys. Rev. **D52** (1995) R2619.
- 1389 [53] A. Czarnecki, W.J. Marciano and A. Vainshtein, Phys. Rev. **D67** (2003) 073006.
1390 A. Czarnecki, W.J. Marciano and A. Vainshtein, Phys. Rev. **D67** (2003) 073006.
- 1391 [54] James P. Miller, Eduardo de Rafael and B. Lee Roberts, Rept. Prog. Phys. **70**, 795-881,
1392 2007.
- 1393 [55] W.J. Marciano pointed out at the Intensity Frontier Workshop, Argonne, Nat. Lab.
1394 April 2013, that the Higgs' mass measurement from CERN increased the weak contri-
1395 bution by 1×10^{-11} . <https://indico.fnal.gov/conferenceDisplay.py?confId=6248>
- 1396 [56] Andrzej Czarnecki and William J. Marciano in *Lepton Dipole Moments*, ed. B. Lee
1397 Roberts and William J. Marciano, Advanced Series on Directions in High Energy
1398 Physics, Vol. 20, World Scientific, 2010 p. 11 and references therein.
- 1399 [57] Miller JP, Roberts BL, Jungmann K. *Lepton Dipole Moments*, ed Roberts BL, Marciano
1400 WJ, p.333. World Scientific (2010)
- 1401 [58] Prades J, Rafael E. de, Vainshtein A. *Lepton Dipole Moments*, ed Roberts BL, Marciano
1402 WJ, World Scientific (2010), p.303; and arXiv:0901.0306v1 [hep-ph].

- 1403 [59] <http://www.int.washington.edu/PROGRAMS/11-47w/>
- 1404 [60] Stöckinger D. *Lepton Dipole Moments*, ed Roberts BL, Marciano WJ, p.393. World
1405 Scientific (2010)
- 1406 *J. Phys. G* **34**:R45 (2007)
- 1407 [61] Eduardo de Rafael, private communication.
- 1408 [62] G. Amelino-Camelia, et al., (KLOE-2 Collaboration) arXiv:1003.3868v1 [hep-ex] March
1409 2010.
- 1410 [63] Tobias Goecke, Christian S. Fischer, Richard Williams Phys. Rev. **D83**, 094006 (2011),
1411 Erratum-ibid. **D86**, 099901 (2012).
- 1412 [64] C. Fischer, private communication, October 2012.
- 1413 [65] . Tom Blum, The 12th International Workshop on Tau Lepton Physics, 17-21 September
1414 2012, Nagoya University.
- 1415 [66] <http://www.usqcd.org/collaboration.html#2013Whitepapers>
- 1416 [67] Tatsumi Aoyama, Masashi Hayakawa, Toichiro Kinoshita, Makiko Nio. May 2012. May
1417 2012, arXiv:1205.5370 [hep-ph], Phys. Rev. Lett. **109**, 111808 (2012).
- 1418 [68] D. Hanneke, S. Fogwell and G. Gabrielse, Phys. Rev. Lett. **100**, 120801 (2008).
- 1419 [69] rTatsumi Aoyama, Masashi Hayakawa, Toichiro Kinoshita, Makiko Nio. May 2012, e-
1420 Print: arXiv:1205.5368 [hep-ph], Phys. Rev. Lett. **109**, 111807 (2012).
- 1421 [70] R. Bouchendira, P. Clade, S. Guellati-Khelifa, F. Nez, and F. Biraben, Phys. Rev. Lett.
1422 **106**, 080801 (2011).
- 1423 [71] A. Höcker and W.J. Marciano, Particle Data Group, Review *THE MUON ANOMA-*
1424 *LOUS MAGNETIC MOMENT* Updated July 2009, <http://pdg.lbl.gov/>
- 1425 [72] M. Passera, W.J. Marciano and A. Sirlin, Phys. Rev. **D 78**, 013009 (2008).
- 1426 [73] K. Hagiwara, A.D. Martin, D. Nomura and T. Teubner, Phys. Lett. **B649** 173 (2007).
- 1427 [74] M. Davier, hep-ph/0701163v2, Jan. 2007.
- 1428 [75] Fred Jegerlehner and Andreas Nyffeler, Phys.Rept. **477** 1 ((2009)
- 1429 [76] James P. Miller, Eduardo de Rafael, B. Lee Roberts and Dominik Stöckinger, Ann. Rev.
1430 Nucl. Part. Sci. **62**, 237 (2012).
- 1431 [77] R. Alemany, M. Davier and A. Höcker, Eur.Phys.J. **C2** 123 (1998).
- 1432 [78] Fred Jegerlehner, Robert Szafron, Eur.Phys.J. **C71** (2011) 1632.
- 1433 [79] M. Benayoun, P. David, L. DelBuono, F. Jegerlehner, Eur. Phys. J. **C72** (2012) 1848.

- 1434 [80] M. Benayoun, P. David, L. DelBuono, F. Jegerlehner, arXiv:1210.7184v2 [hep-ph] 9 Nov
1435 2012.
- 1436 [81] M. Davier and A. Höcker, Phys. Lett. **B435**, 427 (1998).
- 1437 [82] S. Binner, J.H. Kühn and K. Melnikov, Phys. Lett. **B 459**, 279 (1999).
- 1438 [83] S. Actis, et al., (Working Group on Radiative Corrections and Monte Carlo Generators
1439 for Low Energies), arXiv0912.0749, Dec. 2009, submitted to Eur. Phys. J. **C**.
- 1440 [84] BABAR Collaboration, B. Aubert et al., Phys. Rev. Lett. 103:231801 (2009).
- 1441 [85] <http://tau08.inp.nsk.su/> ; <http://www.hep.manchester.ac.uk/TAU2010> ;
1442 <http://tau2012.hepl.phys.nagoya-u.ac.jp/>
- 1443 [86] <http://phipsi11.inp.nsk.su/>
- 1444 [87] F. Ambrosino et al., (KLOE Collaboration), Phys. Lett. **B 670**, 285 (2009).
- 1445 [88] F. Ambrosino et al., (KLOE Collaboration), Phys. Lett. **B 700**, 102 (2011).
- 1446 [89] Giuseppe Mandaglio, The 12th International Workshop on Tau Lepton Physics, 17-21
1447 September 2012, Nagoya University.
- 1448 [90] Jason Crnkovic, The 12th International Workshop on Tau Lepton Physics, 17-21
1449 September 2012, Nagoya University.
- 1450 [91] G. Venanzoni, Frascati Phys. Ser. **54** (2012) 52 [arXiv:1203.1501 [hep-ex]].
- 1451 [92] D. Babusci, C. Bini, F. Bossi, G. Isidori, D. Moricciani, F. Nguyen, P. Raimondi and
1452 G. Venanzoni *et al.*, collider upgraded in energy,” arXiv:1007.5219 [hep-ex].
- 1453 [93] D. Babusci *et al.* [KLOE Collaboration], Phys. Lett. **B 720** (2013) 336.
- 1454 [94] D. Babusci, H. Czyz, F. Gonnella, S. Ivashyn, M. Mascolo, R. Messi, D. Moricciani
1455 and A. Nyffeler *et al.*, width and the $\gamma^* \gamma to \pi^0$ transition form factor with the KLOE-2
1456 experiment,” Eur. Phys. J. **C 72** (2012) 1917.
- 1457 [95] T. Blum, Phys. Rev. Lett. **91**, 052001-1 (2003).
- 1458 [96] T. Blum, Nucl. Phys. Proc. Suppl. **129**, 904-906, 2004, and arXiv hep-lat/0310064,
- 1459 [97] T. Blum, private communication, February 2012.
- 1460 [98] M. Davier and W.J. Marciano, Ann. Rev. Nucl. Part. Phys. **54**, 115 (2004).
- 1461 [99] D. W. Hertzog, J. P. Miller, E. de Rafael, B. Lee Roberts and D. Stöckinger,
1462 arXiv:0705.4617 [hep-ph].
- 1463 [100] The articles listed in the SPIRES citations to Ref. [21] contain many different models
1464 beyond the standard model.

- 1465 [101] F. Borzumati, G. R. Farrar, N. Polonsky and S. D. Thomas, Nucl. Phys. B **555** (1999)
1466 53 [hep-ph/9902443].
- 1467 [102] A. Crivellin, J. Girrbach and U. Nierste, Phys. Rev. D **83** (2011) 055009
1468 [arXiv:1010.4485 [hep-ph]].
- 1469 [103] E. Eichten, et al., Phys. Rev. Lett. **45**, 225 (1980); K. Lane, arXiv [hep-ph/0102131].
- 1470 [104] T. Appelquist and B. A. Dobrescu, Phys. Lett. B **516** (2001) 85 [arXiv:hep-
1471 ph/0106140].
- 1472 [105] M. Blanke, A. J. Buras, B. Duling, A. Poschenrieder and C. Tarantino, JHEP **0705**
1473 (2007) 013 [arXiv:hep-ph/0702136].
- 1474 [106] S. Baek, N. G. Deshpande, X. G. He and P. Ko, Phys. Rev. D **64**, 055006 (2001)
1475 [hep-ph/0104141]; E. Ma, D. P. Roy and S. Roy, Phys. Lett. B **525** (2002) 101
1476 [hep-ph/0110146]; J. Heeck and W. Rodejohann, Phys. Rev. D **84** (2011) 075007
1477 [arXiv:1107.5238 [hep-ph]].
- 1478 [107] S. Bar-Shalom, S. Nandi and A. Soni, Phys. Lett. B **709**, 207 (2012) [arXiv:1112.3661
1479 [hep-ph]].
- 1480 [108] H. Davoudiasl, J. L. Hewett and T. G. Rizzo, Phys. Lett. B **493** (2000) 135 [arXiv:hep-
1481 ph/0006097].
- 1482 [109] S. C. Park and H. S. Song, Phys. Lett. B **506** (2001) 99 [arXiv:hep-ph/0103072].
- 1483 [110] C. S. Kim, J. D. Kim and J. H. Song, Phys. Lett. B **511** (2001) 251 [arXiv:hep-
1484 ph/0103127].
- 1485 [111] M. L. Graesser, Phys. Rev. D **61** (2000) 074019 [arXiv:hep-ph/9902310].
- 1486 [112] M. Beneke, P. Dey and J. Rohrwild, arXiv:1209.5897 [hep-ph].
- 1487 [113] K. Cheung, W. Y. Keung and T. C. Yuan, Phys. Rev. Lett. **99** (2007) 051803
1488 [arXiv:0704.2588 [hep-ph]].
- 1489 [114] J. A. Conley and J. S. Gainer, arXiv:0811.4168 [hep-ph].
- 1490 [115] D. McKeen, arXiv:0912.1076 [hep-ph].
- 1491 [116] C. M. Ho and T. W. Kephart, Phys. Lett. B **687**, 201 (2010) [arXiv:1001.3696 [hep-
1492 ph]].
- 1493 [117] T. Hambye, K. Kannike, E. Ma and M. Raidal, Phys. Rev. D **75** (2007) 095003
1494 [arXiv:hep-ph/0609228].
- 1495 [118] M. Krawczyk, Acta Phys. Polon. B **33**, 2621 (2002) [hep-ph/0208076].
- 1496 [119] M. Pospelov, Phys. Rev. D **80** (2009) 095002 [arXiv:0811.1030 [hep-ph]].

- 1497 [120] H. Davoudiasl, H. -S. Lee and W. J. Marciano, Phys. Rev. Lett. **109**, 031802 (2012)
1498 [arXiv:1205.2709 [hep-ph]].
- 1499 [121] R. Essig, P. Schuster and N. Toro, Phys. Rev. D **80** (2009) 015003 [arXiv:0903.3941
1500 [hep-ph]].
- 1501 [122] H. Davoudiasl, H. -S. Lee and W. J. Marciano, Phys. Rev. D **86**, 095009 (2012)
1502 [arXiv:1208.2973 [hep-ph]].
- 1503 [123] T. Moroi, Phys. Rev. D **53** (1996) 6565 [Erratum-ibid. **56** (1997) 4424].
- 1504 [124] D. Stöckinger, J. Phys. G **34** (2007) R45 [arXiv:hep-ph/0609168].
- 1505 [125] S. Heinemeyer, D. Stöckinger and G. Weiglein, Nucl. Phys. B **690** (2004) 62 [arXiv:hep-
1506 ph/0312264]; S. Heinemeyer, D. Stöckinger and G. Weiglein, Nucl. Phys. B **699** (2004)
1507 103 [arXiv:hep-ph/0405255].
- 1508 [126] A. Arhrib and S. Baek, Phys. Rev. D **65**, 075002 (2002) [hep-ph/0104225].
- 1509 [127] R. Benbrik, M. Gomez Bock, S. Heinemeyer, O. Stal, G. Weiglein and L. Zeune, Eur.
1510 Phys. J. C **72**, 2171 (2012) [arXiv:1207.1096 [hep-ph]].
- 1511 [128] A. Arbey, M. Battaglia, A. Djouadi and F. Mahmoudi, JHEP **1209**, 107 (2012)
1512 [arXiv:1207.1348 [hep-ph]].
- 1513 [129] R. Ruiz de Austri, R. Trotta and L. Roszkowski, JHEP **0605** (2006) 002 [arXiv:hep-
1514 ph/0602028]; JHEP **0704** (2007) 084 [arXiv:hep-ph/0611173]; JHEP **0707** (2007) 075
1515 [arXiv:0705.2012]; B. C. Allanach, C. G. Lester and A. M. Weber, JHEP **0612** (2006)
1516 065; B. C. Allanach, K. Cranmer, C. G. Lester and A. M. Weber, JHEP **0708**, 023
1517 (2007); J. R. Ellis, S. Heinemeyer, K. A. Olive, A. M. Weber and G. Weiglein, JHEP
1518 **0708** (2007) 083; S. Heinemeyer, X. Miao, S. Su and G. Weiglein, JHEP **0808**, 087
1519 (2008).
- 1520 [130] P. Bechtle, T. Bringmann, K. Desch, H. Dreiner, M. Hamer, C. Hensel, M. Kramer
1521 and N. Nguyen *et al.*, JHEP **1206**, 098 (2012) [arXiv:1204.4199 [hep-ph]].
- 1522 [131] C. Balazs, A. Buckley, D. Carter, B. Farmer and M. White, arXiv:1205.1568 [hep-ph].
- 1523 [132] O. Buchmueller, R. Cavanaugh, M. Citron, A. De Roeck, M. J. Dolan, J. R. Ellis,
1524 H. Flacher and S. Heinemeyer *et al.*, Eur. Phys. J. C **72**, 2243 (2012) [arXiv:1207.7315
1525 [hep-ph]].
- 1526 [133] M. Endo, K. Hamaguchi, S. Iwamoto, K. Nakayama and N. Yokozaki, Phys. Rev. D
1527 **85** (2012) 095006 [arXiv:1112.6412 [hep-ph]].
- 1528 [134] M. Endo, K. Hamaguchi, S. Iwamoto and T. Yoshinaga, arXiv:1303.4256 [hep-ph].
- 1529 [135] M. Ibe, T. T. Yanagida and N. Yokozaki, arXiv:1303.6995 [hep-ph].

- 1530 [136] H. Baer, V. Barger, P. Huang and X. Tata, JHEP **1205** (2012) 109 [arXiv:1203.5539
1531 [hep-ph]].
- 1532 [137] M. Papucci, J. T. Ruderman and A. Weiler, JHEP **1209**, 035 (2012) [arXiv:1110.6926
1533 [hep-ph]].
- 1534 [138] T. J. LeCompte and S. P. Martin, Phys. Rev. D **85**, 035023 (2012) [arXiv:1111.6897
1535 [hep-ph]].
- 1536 [139] H. Murayama, Y. Nomura, S. Shirai and K. Tobioka, Phys. Rev. D **86**, 115014 (2012)
1537 [arXiv:1206.4993 [hep-ph]].
- 1538 [140] B. A. Dobrescu and P. J. Fox, Eur. Phys. J. C **70** (2010) 263 [arXiv:1001.3147 [hep-ph]].
- 1539 [141] W. Altmannshofer and D. M. Straub, JHEP **1009** (2010) 078 [arXiv:1004.1993 [hep-
1540 ph]].
- 1541 [142] T. Appelquist, H. -C. Cheng and B. A. Dobrescu, Phys. Rev. D **64**, 035002 (2001)
1542 [hep-ph/0012100].
- 1543 [143] I. Low, JHEP **0410**, 067 (2004) [hep-ph/0409025].
- 1544 [144] J. Hubisz and P. Meade, Phys. Rev. D **71**, 035016 (2005) [hep-ph/0411264].
- 1545 [145] J. M. Smillie and B. R. Webber, JHEP **0510** (2005) 069 [arXiv:hep-ph/0507170].
- 1546 [146] Adam C, Kneur J -L, Lafaye R, Plehn T, Rauch M, Zerwas D. *Eur. Phys. J. C* 71:1520
1547 (2011) [arXiv:1007.2190 [hep-ph]]
- 1548 [147] N. Arkani-Hamed, G. L. Kane, J. Thaler and L. T. Wang, JHEP **0608**, 070 (2006)
1549 [arXiv:hep-ph/0512190].
- 1550 [148] M. Alexander, S. Kreiss, R. Lafaye, T. Plehn, M. Rauch, and D. Zerwas, Chap-
1551 ter 9 in M. M. Nojiri *et al.*, *Physics Beyond the Standard Model: Supersymmetry*,
1552 arXiv:0802.3672 [hep-ph].
- 1553 [149] B. C. Allanach *et al.*, *Proc. of the APS/DPF/DPB Summer Study on the Future of*
1554 *Particle Physics (Snowmass 2001)* ed. N. Graf, Eur. Phys. J. C **25** (2002) 113 [eConf
1555 **C010630** (2001) P125].
- 1556 [150] C. F. Berger, J. S. Gainer, J. L. Hewett and T. G. Rizzo, JHEP **0902**, 023 (2009)
1557 [arXiv:0812.0980 [hep-ph]].

Chapter 3

Overview of the Experimental Technique

In this chapter we give an overview of how the experiment is done. This is followed by a number of chapters that give the details of the specific hardware being developed for E989. The order of those chapters follows the WBS as closely as possible.

The experiment consists of the following steps:

1. Production of an appropriate pulsed proton beam by an accelerator complex.
2. Production of pions using the proton beam that has been prepared.
3. Collection of polarized muons from pion decay $\pi^+ \rightarrow \mu^+ \nu_\mu$
4. Transporting the muon beam to the $(g - 2)$ storage ring.
5. Injection of the muon beam into the storage ring.
6. Kicking the muon beam onto stored orbits.
7. Measuring the arrival time and energy of positrons from the decay $\mu^+ \rightarrow e^+ \bar{\nu}_\mu \nu_e$

Central to the determination of a_μ is the spin equation¹

$$\vec{\omega}_a = -\frac{Qe}{m} \left[a_\mu \vec{B} + \left(a_\mu - \left(\frac{m}{p} \right)^2 \right) \frac{\vec{\beta} \times \vec{E}}{c} \right], \quad (3.1)$$

that gives the rate at which the spin turns relative the the momentum vector, which turns with the cyclotron frequency. The electric field term is there since we use electrostatic vertical focusing in the ring. At the magic momentum, $p_m = 3.09$ GeV/c, the effect of the motional magnetic field (the $\vec{\beta} \times \vec{E}$ term) vanishes.

Measurement of a_μ requires the determination of the muon spin frequency ω_a and the magnetic field averaged over the muon distribution.

¹See Section 3.3 for the details.

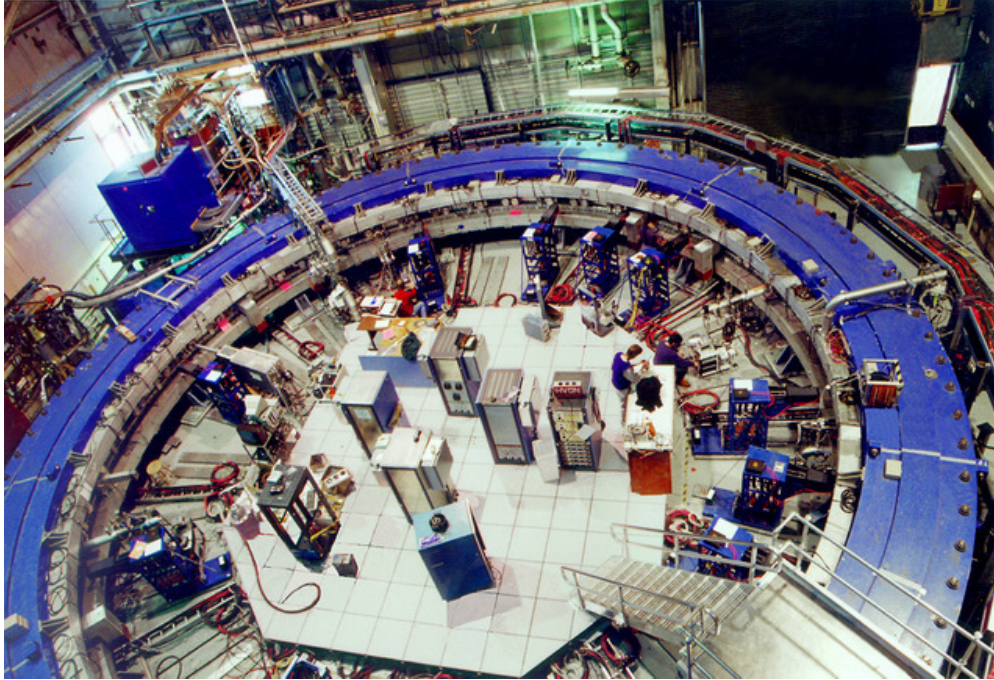


Figure 3.1: The E821 storage-ring magnet at Brookhaven Lab.

1579 3.1 Production and Preparation of the Muon Beam

1580 E989 will bring a bunched beam from the 8 GeV Booster to a pion production target located
 1581 where the antiproton production target was in the Tevatron collider program (see Chapter 7).
 1582 Pions of $3.11 \text{ GeV}/c \pm 5\%$ will be collected and sent into a large-acceptance beamline. Muons
 1583 are produced in the weak pion decay

$$\pi^\mp \rightarrow \mu^\mp + \bar{\nu}_\mu(\nu_\mu). \quad (3.2)$$

1584 The antineutrino (neutrino) is right-handed (left-handed) and the pion is spin zero. Thus the
 1585 muon spin must be antiparallel to the neutrino spin, so it is also right-handed (left-handed).
 1586 A beam of polarized muons can be obtained from a beam of pions by selecting the highest-
 1587 energy muons (a “forward beam”) or by selecting the lowest-energy muons (a “backward
 1588 beam”), where forward or backward refers to whether the decay is forward or backward in
 1589 the center-of-mass frame relative to the pion momentum. Polarizations significantly greater
 1590 than 90% are easily obtained in such beams. The pions and daughter muons will be injected
 1591 into the Delivery Ring (the re-purposed \bar{p} debuncher ring), where after several turns the
 1592 remaining pions decay. The surviving muon beam will be extracted and brought to the
 1593 muon storage ring built for E821 at Brookhaven.

1594 3.2 Injection into the Storage Ring

1595 A photograph of the E821 magnet is shown in Figure 3.1. It is clear from the photo that this
 1596 “storage ring” is very different from the usual one that consists of lumped elements. The

1597 storage ring magnet is energized by three superconducting coils shown in Fig 3.2(b). The
 1598 continuous “C” magnet yoke is built from twelve 30° segments of iron that was designed
 1599 to eliminate the end effects present in lumped magnets. This construction eliminates the
 1600 large gradients that would make the determination of average magnetic field, $\langle B \rangle$, very
 1601 difficult. Furthermore, a small perturbation in the yoke can effect the field halfway around
 1602 the ring at the ppm level. Thus every effort is made to minimize holes in the yoke, and
 1603 other perturbations. The only penetrations through the yoke are to permit the muon beam
 1604 to enter the magnet as shown in Fig 3.2(a), and to connect cryogenic services and power to
 1605 the inflector magnet and to the outer radius coil (see Fig. 3.2(b)). Where a hole in the yoke
 1606 is necessary, extra steel was placed around the hole on the outside of the yoke to compensate
 1607 for the missing material.

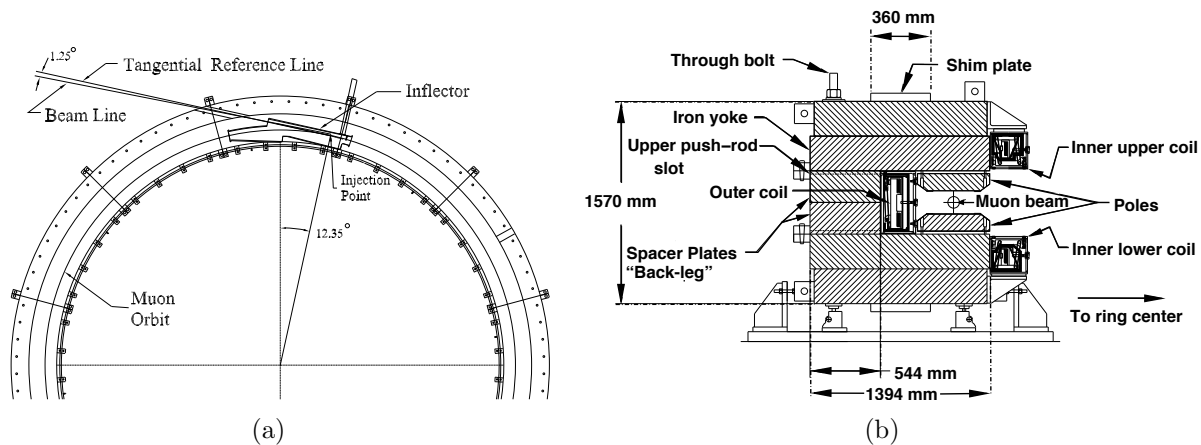


Figure 3.2: (a) Plan view of the beam entering the storage ring. (b) Elevation view of the storage-ring magnet cross section.

1608 The beam enters through a hole in the “back-leg” of the magnet and then crosses into the
 1609 inflector magnet, which provides an almost field free region, delivering the beam to the edge
 1610 of the storage region. The geometry is rather constrained, as can be seen in Fig. 3.3(a). The
 1611 injection geometry is sketched in Fig. 3.3(b). The kick required to put magic momentum
 1612 muons onto a stable orbit centered at magic radius is on the order of 10 mrad.

1613 The requirements on the muon kicker are rather severe:

- 1614 1. Since the magnet is continuous, any kicker device has to be inside of the precision
 1615 magnetic field region.
- 1616 2. The kicker hardware cannot contain magnetic elements such as ferrites, because they
 1617 will spoil the uniform magnetic field.
- 1618 3. Any eddy currents produced in the vacuum chamber, or in the kicker electrodes by the
 1619 kicker pulse must be negligible by 10 to 20 μs after injection, or must be well known
 1620 and corrected for in the measurement.
- 1621 4. Any new kicker hardware must fit within the real estate that was occupied by the E821
 1622 kicker. The available space consists of three consecutive 1.7 m long spaces.

1623

5. The kicker pulse should be shorter than the cyclotron period of 149 ns.

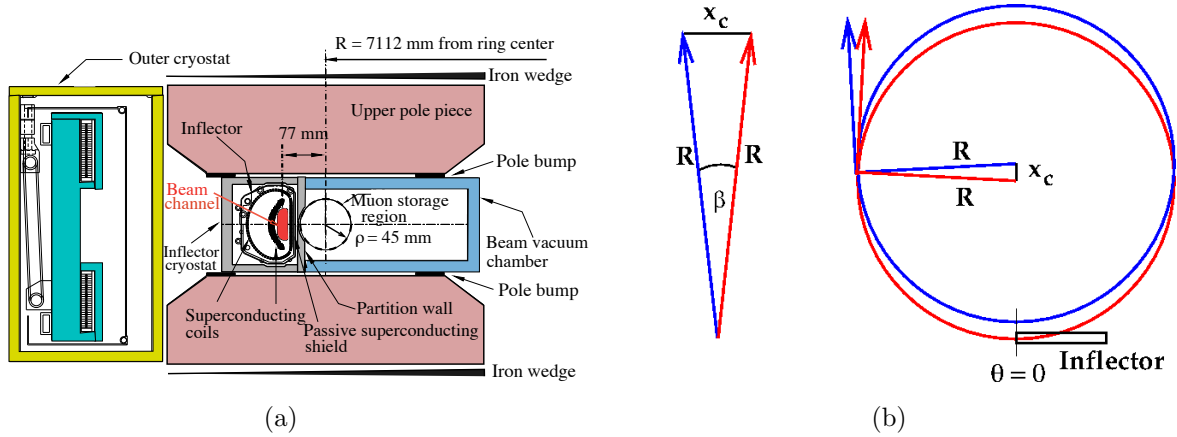


Figure 3.3: (a) The inflector exit showing the incident beam center 77 mm from the center of the storage region. The incident muon beam channel is highlighted in red. (b) The geometry of the necessary kick. The incident beam is the red circle, and the kick effectively moves the red circle over to the blue one.

1624

3.3 The Spin Equations

1625

Measurements of magnetic and electric dipole moments make use of the torque on a dipole in an external field:

1626

$$\vec{\tau} = \vec{\mu} \times \vec{B} + \vec{d} \times \vec{E}, \quad (3.3)$$

1627

where we include the possibility of an electric dipole moment (\vec{d}). Except for the original Nevis spin rotation experiment, the muon magnetic dipole moment experiments inject a beam of polarized muons into a magnetic field and measure the rate at which the spin turns relative to the momentum, $\vec{\omega}_a = \vec{\omega}_S - \vec{\omega}_C$, where S and C stand for spin and cyclotron, respectively. These two frequencies, in the absence of any other external fields, are given by

1628

$$\omega_S = -g \frac{Qe}{2m} B - (1 - \gamma) \frac{Qe}{\gamma m} B; \quad (3.4)$$

1629

$$\omega_C = -\frac{Qe}{m\gamma} B; \quad (3.5)$$

1630

$$\omega_a = \omega_S - \omega_C = -\left(\frac{g-2}{2}\right) \frac{Qe}{m} B = -a_\mu \frac{Qe}{m} B \quad (3.6)$$

1631

1632

(where $e > 0$ and $Q = \pm 1$). There are two important features of ω_a :

1633

- It only depends on the anomaly rather than on the full magnetic moment.

1634

- It depends linearly on the applied magnetic field.

1635 To measure the anomaly, it is necessary to measure ω_a , and to determine the magnetic
 1636 field B . The relevant quantity is $\langle B \rangle$, which is the magnetic field convolved with the muon
 1637 beam distribution, M defined as

$$\langle B \rangle = \int M(r, \theta) B(r, \theta) r dr d\theta, \quad (3.7)$$

1638 where the magnetic field $B(r, \theta)$ is expressed as the multipole expansion

$$B(r, \theta) = \sum_{n=0}^{\infty} r^n [c_n \cos n\theta + s_n \sin n\theta], \quad (3.8)$$

1639 and the muon distribution is expressed in terms of moments

$$M(r, \theta) = \sum_{m=0}^{\infty} [\xi_m(r) \cos m\theta + \sigma_m(r) \sin m\theta]. \quad (3.9)$$

1640 Because the harmonics $\sin n\theta \sin m\theta$, etc., are orthogonal when integrated over one period,
 1641 non-vanishing integrals come from products of the same moment/multipole, in the expression
 1642 for $\langle B \rangle$. To determine $\langle B \rangle$ to sub-part-per-million (ppm) precision, one either needs excellent
 1643 knowledge of the multipole and moment distributions for B and M ; or care must be taken
 1644 to minimize the number of terms, with only the leading term being large, so that only the
 1645 first few multipoles are important. This was achieved in the most recent experiment [6] by
 1646 using a circular beam aperture, and making a very uniform dipole magnetic field.

1647 However there is one important issue to be solved: How can the muon beam be confined
 1648 to a storage ring if significant magnetic gradients cannot be used to provide vertical focusing?
 1649 The answer to this question was discovered by the third CERN collaboration [1], which used
 1650 an electric quadrupole field to provide vertical focusing. Of course, a relativistic particle
 1651 feels a motional magnetic field proportional to $\vec{\beta} \times \vec{E}$, but the full relativistic spin equation
 1652 contains a cancellation as can be seen below. Assuming that the velocity is transverse to the
 1653 magnetic field ($\vec{\beta} \cdot \vec{B} = 0$), one obtains [2, 3]

$$\vec{\omega}_{a\eta} = \vec{\omega}_a + \vec{\omega}_\eta = -\frac{Qe}{m} \left[a_\mu \vec{B} + \left(a_\mu - \left(\frac{m}{p} \right)^2 \right) \frac{\vec{\beta} \times \vec{E}}{c} \right] - \eta \frac{Qe}{2m} \left[\frac{\vec{E}}{c} + \vec{\beta} \times \vec{B} \right]. \quad (3.10)$$

1654 There are both motional magnetic and electric fields in this equation – the terms which
 1655 are proportional to $\vec{\beta} \times \vec{E}$ and $\vec{\beta} \times \vec{B}$, respectively.

1656 The expression for ω_a is

$$\vec{\omega}_a = -\frac{Qe}{m} \left[a_\mu \vec{B} + \left(a_\mu - \left(\frac{m}{p} \right)^2 \right) \frac{\vec{\beta} \times \vec{E}}{c} \right]. \quad (3.11)$$

1657 For the “magic” momentum $p_{\text{magic}} = m/\sqrt{a} \simeq 3.09 \text{ GeV}/c$ ($\gamma_{\text{magic}} = 29.3$), the second
 1658 term vanishes, and the electric field does not contribute to the spin motion relative to the
 1659 momentum.² Note that if $g = 2$, then $a = 0$ and the spin would follow the momentum,
 1660 turning at the cyclotron frequency.

²Small corrections to the measured frequency must be applied since $\vec{\beta} \cdot \vec{B} \simeq 0$ and not all muons are at the magic momentum. These are discussed in Chapter 4.

1661 3.4 Vertical Focusing with Electrostatic Quadrupoles

1662 The storage ring acts as a weak-focusing betatron, with the vertical focusing provided by
 1663 electrostatic quadrupoles. The ring is operated at the magic momentum, so that the electric
 1664 field does not contribute to the spin precession. However there is a second-order correction
 1665 to the spin frequency from the radial electric field, which is discussed below. There is also a
 1666 correction from the vertical betatron motion, since the spin equations in the previous section
 1667 were derived with the assumption that $\vec{\beta} \cdot \vec{B} = 0$.

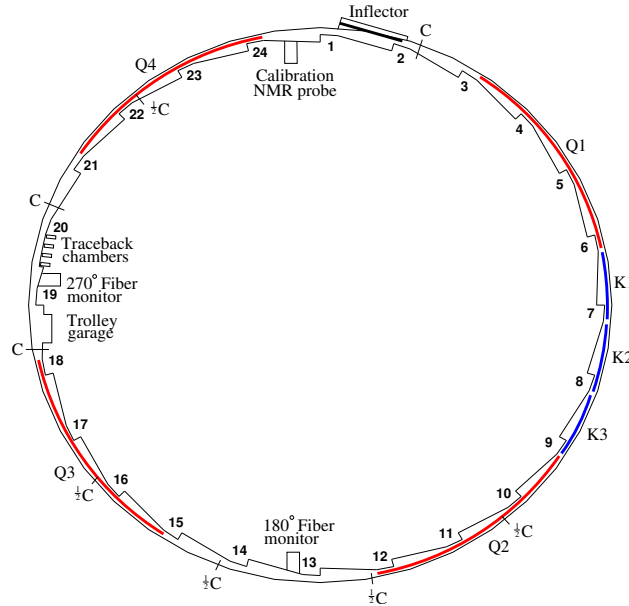


Figure 3.4: The layout of the storage ring, as seen from above, showing the location of the inflector, the kicker sections (labeled K1-K3), and the quadrupoles (labeled Q1-Q4). The beam circulates in a clockwise direction. Also shown are the collimators, which are labeled “C”, or “ $\frac{1}{2}C$ ” indicating whether the Cu collimator covers the full aperture, or half the aperture. The collimators are rings with inner radius: 45 mm, outer radius: 55 mm, thickness: 3 mm. The scalloped vacuum chamber consists of 12 sections joined by bellows. The chambers containing the inflector, the NMR trolley garage, and the trolley drive mechanism are special chambers. The other chambers are standard, with either quadrupole or kicker assemblies installed inside. An electron calorimeter is placed behind each of the radial windows, at the position indicated by the calorimeter number.

1668 3.5 Muon Decay

1669 The dominant muon decay is

$$\mu^\mp \rightarrow e^\mp + \nu_\mu(\bar{\nu}_\mu) + \bar{\nu}_e(\nu_e) \quad (3.12)$$

1670 which also violates parity.

1671 Since the kinematics of muon decay are central to the measurements of a_μ , we discuss
 1672 the general features in this section. Additional details are given in Ref. [17]. From a beam
 1673 of pions traversing a straight beam-channel consisting of focusing and defocusing elements
 1674 (FODO), a beam of polarized, high energy muons can be produced by selecting the "for-
 1675 ward" or "backward" decays. The forward muons are those produced, in the pion rest frame,
 1676 nearly parallel to the pion laboratory momentum and are the decay muons with the highest
 1677 laboratory momenta. The backward muons are those produced nearly anti-parallel to the
 1678 pion momentum and have the lowest laboratory momenta. The forward μ^- (μ^+) are polar-
 1679 ized along (opposite) their lab momenta respectively; the polarization reverses for backward
 1680 muons. The E821 experiment used forward muons, as will E989, the difference being the
 1681 length of the pion decay line, which in E989 will be 1,900 m.

1682 The pure $(V - A)$ three-body weak decay of the muon, $\mu^- \rightarrow e^- + \nu_\mu + \bar{\nu}_e$ or $\mu^+ \rightarrow e^+ +$
 1683 $\bar{\nu}_\mu + \nu_e$, is "self-analyzing", that is, the parity-violating correlation between the directions in
 1684 the muon rest frame (MRF) of the decay electron and the muon spin can provide information
 1685 on the muon spin orientation at the time of the decay. When the decay electron has the
 1686 maximum allowed energy in the MRF, $E'_{\max} \approx (m_\mu c^2)/2 = 53$ MeV. The neutrino and anti-
 1687 neutrino are directed parallel to each other and at 180° relative to the electron direction.
 1688 The $\nu\bar{\nu}$ pair carry zero total angular momentum; the electron carries the muon's angular
 1689 momentum of $1/2$. The electron, being a lepton, is preferentially emitted left-handed in a
 1690 weak decay, and thus has a larger probability to be emitted with its momentum *anti-parallel*
 1691 rather than parallel to the μ^- spin. Similarly, in μ^+ decay, the highest-energy positrons are
 1692 emitted *parallel* to the muon spin in the MRF.

1693 In the other extreme, when the electron kinetic energy is zero in the MRF, the neutrino
 1694 and anti-neutrino are emitted back-to-back and carry a total angular momentum of one. In
 1695 this case, the electron spin is directed opposite to the muon spin in order to conserve angular
 1696 momentum. Again, the electron is preferentially emitted with helicity -1, however in this
 1697 case its momentum will be preferentially directed *parallel* to the μ^- spin. The positron, in
 1698 μ^+ decay, is preferentially emitted with helicity +1, and therefore its momentum will be
 1699 preferentially directed *anti-parallel* to the μ^+ spin.

1700 With the approximation that the energy of the decay electron $E' \gg m_e c^2$, the differential
 1701 decay distribution in the muon rest frame is given by [23],

$$dP(y', \theta') \propto n'(y') [1 \pm \mathcal{A}(y') \cos \theta'] dy' d\Omega' \quad (3.13)$$

1702 where y' is the momentum fraction of the electron, $y' = p'_e/p'_{e \max}$, $d\Omega'$ is the solid angle,
 1703 $\theta' = \cos^{-1}(\hat{p}'_e \cdot \hat{s})$ is the angle between the muon spin and \hat{p}'_e , $p'_{e \max} c \approx E'_{\max}$, and the $(-)$
 1704 sign is for negative muon decay. The number distribution $n(y')$ and the decay asymmetry
 1705 $\mathcal{A}(y')$ are given by

$$n(y') = 2y'^2(3 - 2y') \quad \text{and} \quad \mathcal{A}(y') = \frac{2y' - 1}{3 - 2y'}. \quad (3.14)$$

1706 Note that both the number and asymmetry reach their maxima at $y' = 1$, and the asymmetry
 1707 changes sign at $y' = \frac{1}{2}$, as shown in Figure 3.5(a).

1708 The CERN and Brookhaven based muon $(g - 2)$ experiments stored relativistic muons of
 1709 the magic momentum in a uniform magnetic field, which resulted in the muon spin precessing
 1710 with constant frequency $\vec{\omega}_a$, while the muons traveled in circular orbits. If *all* decay electrons

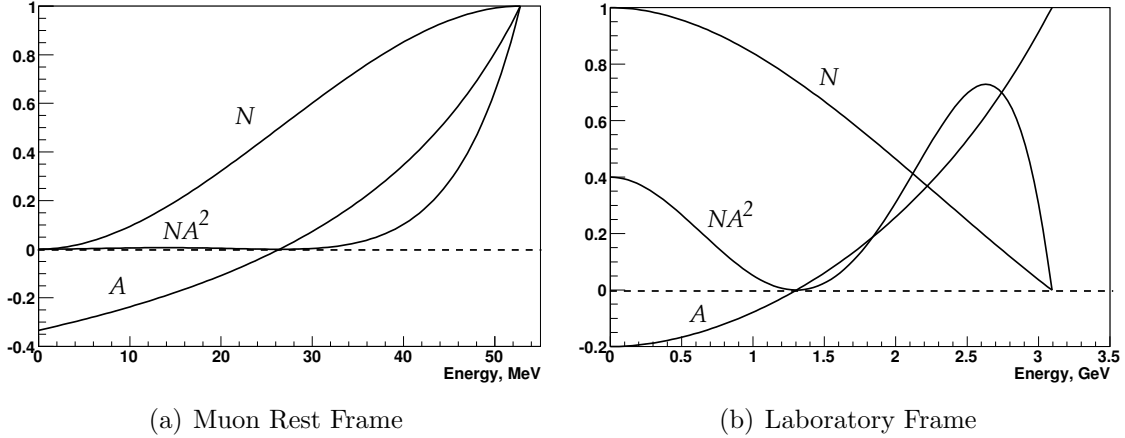


Figure 3.5: Number of decay electrons per unit energy, N (arbitrary units), value of the asymmetry A , and relative figure of merit NA^2 (arbitrary units) as a function of electron energy. Detector acceptance has not been incorporated, and the polarization is unity. For the third CERN experiment and E821, $E_{max} \approx 3.1$ GeV ($p_\mu = 3.094$ GeV/c) in the laboratory frame.

1711 were counted, the number detected as a function of time would be a pure exponential;
 1712 therefore we seek cuts on the laboratory observable to select subsets of decay electrons
 1713 whose numbers oscillate at the precession frequency. The number of decay electrons in
 1714 the MRF varies with the angle between the electron and spin directions, the electrons in
 1715 the subset should have a preferred direction in the MRF when weighted according to their
 1716 asymmetry as given in Equation 3.13. At $p_\mu \approx 3.094$ GeV/c the directions of the electrons
 1717 resulting from muon decay in the laboratory frame are very nearly parallel to the muon
 1718 momentum regardless of their energy or direction in the MRF. The only practical remaining
 1719 cut is on the electron's laboratory energy. An energy subset will have the desired property:
 1720 there will be a net component of electron MRF momentum either parallel or antiparallel
 1721 to the laboratory muon direction. For example, suppose that we only count electrons with
 1722 the highest laboratory energy, around 3.1 GeV. Let \hat{z} indicate the direction of the muon
 1723 laboratory momentum. The highest-energy electrons in the laboratory are those near the
 1724 maximum MRF energy of 53 MeV, and with MRF directions nearly parallel to \hat{z} . There are
 1725 more of these high-energy electrons when the μ^- spins are in the direction opposite to \hat{z} than
 1726 when the spins are parallel to \hat{z} . Thus the number of decay electrons reaches a maximum
 1727 when the muon spin direction is opposite to \hat{z} , and a minimum when they are parallel. As
 1728 the spin precesses the number of high-energy electrons will oscillate with frequency ω_a . More
 1729 generally, at laboratory energies above ~ 1.2 GeV, the electrons have a preferred average
 1730 MRF direction parallel to \hat{z} (see Figure 3.5). In this discussion, it is assumed that the
 1731 spin precession vector, $\vec{\omega}_a$, is independent of time, and therefore the angle between the spin
 1732 component in the orbit plane and the muon momentum direction is given by $\omega_a t + \phi$, where
 1733 ϕ is a constant.

1734 Equations 3.13 and 3.14 can be transformed to the laboratory frame to give the electron

1735 number oscillation with time as a function of electron energy,

$$N_d(t, E) = N_{d0}(E)e^{-t/\gamma\tau}[1 + A_d(E) \cos(\omega_a t + \phi_d(E))], \quad (3.15)$$

1736 or, taking all electrons above threshold energy E_{th} ,

$$N(t, E_{th}) = N_0(E_{th})e^{-t/\gamma\tau}[1 + A(E_{th}) \cos(\omega_a t + \phi(E_{th}))]. \quad (3.16)$$

1737 In Equation 3.15 the differential quantities are,

$$A_d(E) = \mathcal{P} \frac{-8y^2 + y + 1}{4y^2 - 5y - 5}, \quad N_{d0}(E) \propto (y - 1)(4y^2 - 5y - 5), \quad (3.17)$$

1738 and in Equation 3.16,

$$N(E_{th}) \propto (y_{th} - 1)^2(-y_{th}^2 + y_{th} + 3), \quad A(E_{th}) = \mathcal{P} \frac{y_{th}(2y_{th} + 1)}{-y_{th}^2 + y_{th} + 3}. \quad (3.18)$$

1739 In the above equations, $y = E/E_{max}$, $y_{th} = E_{th}/E_{max}$, \mathcal{P} is the polarization of the muon
1740 beam, and E , E_{th} , and $E_{max} = 3.1$ GeV are the electron laboratory energy, threshold energy,
1741 and maximum energy, respectively.

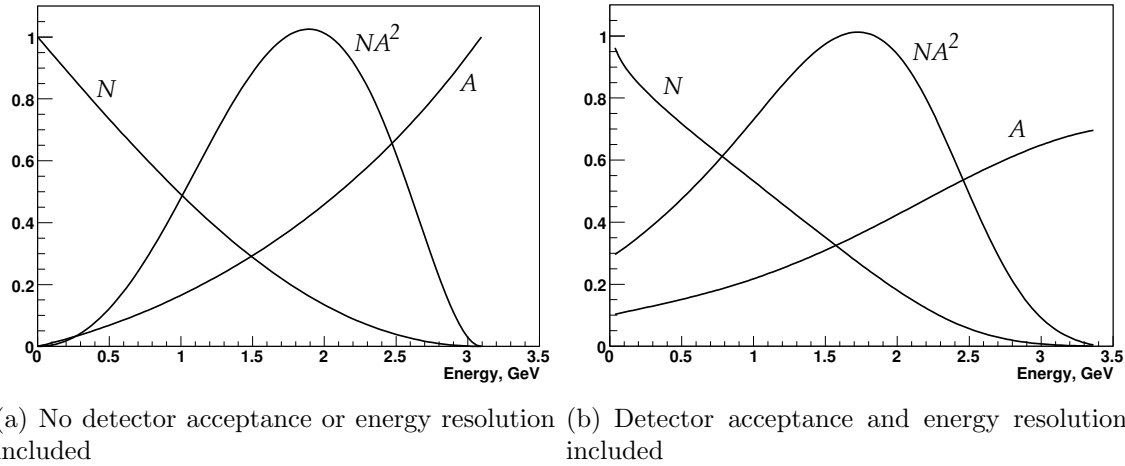


Figure 3.6: The integral N , A , and NA^2 (arbitrary units) for a single energy-threshold as a function of the threshold energy; (a) in the laboratory frame, not including and (b) including the effects of detector acceptance and energy resolution for the E821 calorimeters. For the third CERN experiment and E821, $E_{max} \approx 3.1$ GeV ($p_\mu = 3.094$ GeV/c) in the laboratory frame.

1742 The fractional statistical error on the precession frequency, when fitting data collected
1743 over many muon lifetimes to the five-parameter function (Equation 3.16), is given by

$$\delta\epsilon = \frac{\delta\omega_a}{\omega_a} = \frac{\sqrt{2}}{2\pi f_a \tau_\mu N^{\frac{1}{2}} A}. \quad (3.19)$$

1744 where N is the total number of electrons, and A is the asymmetry, in the given data sample.
 1745 For a fixed magnetic field and muon momentum, the statistical figure of merit is NA^2 , the
 1746 quantity to be maximized in order to minimize the statistical uncertainty.

1747 The energy dependencies of the numbers and asymmetries used in Equations 3.15 and
 1748 3.16, along with the figures of merit NA^2 , are plotted in Figures 3.5 and 3.6 for the case
 1749 of E821. The statistical power is greatest for electrons at 2.6 GeV (Figure 3.5). When a fit
 1750 is made to all electrons above some energy threshold, the optimal threshold energy is about
 1751 1.7-1.8 GeV (Figure 3.6).

1752 The resulting arrival-time spectrum of electrons with energy greater than 1.8 GeV from
 1753 the final E821 data run is shown in Fig. 3.7. While this plot clearly exhibits the expected
 1754 features of the five-parameter function, a least-square fit to these 3.6 billion events gives
 1755 an unacceptably large chi-square. A number of small effects must be taken into account to
 1756 obtain a reasonable fit, which will be discussed in Chapter 5.

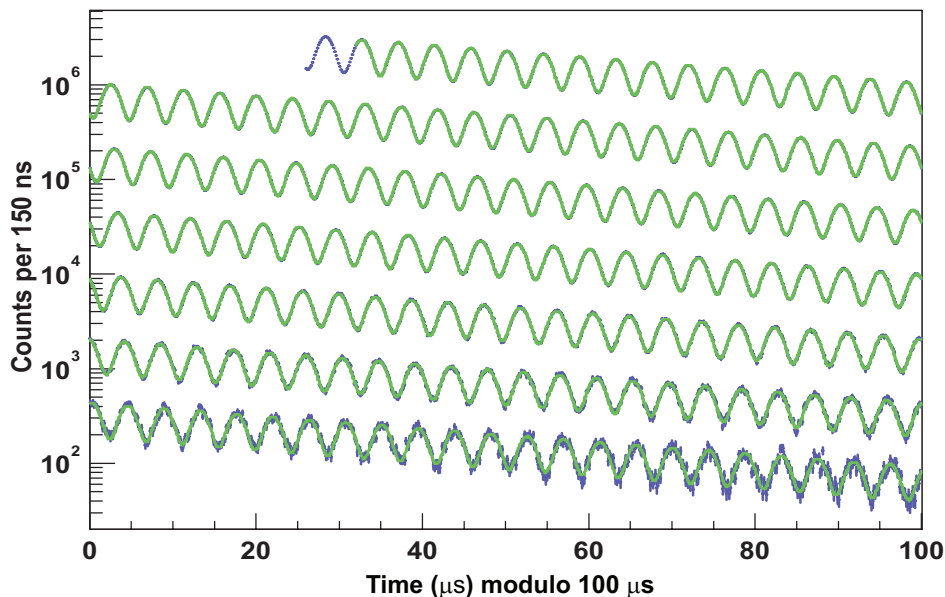


Figure 3.7: Histogram, modulo $100 \mu s$, of the number of detected electrons above 1.8 GeV for the 2001 data set as a function of time, summed over detectors, with a least-squares fit to the spectrum superimposed. Total number of electrons is 3.6×10^9 . The data are in blue, the fit in green.

3.6 The Magnetic Field

The rate at which the muon spin turns relative to its momentum (Eq. 3.11) depends on the anomaly a_μ and on the average magnetic field given by Eq. 3.7. Thus the determination of a_μ to sub-tenths of a ppm requires that both ω_a and $\langle B \rangle$ be determined to this level. The muon beam is confined to a cylindrical region of 9 cm diameter, which is 44.7 m in length. The volume of this region is $\simeq 1.14 \text{ m}^3$ or $\simeq 40 \text{ ft}^3$, which sets the scale for the magnetic field measurement and control. The E989 goal is to know the magnetic field averaged over running time and the muon distribution to an uncertainty of ± 70 parts per billion (ppb).

The problem breaks into several pieces:

1. Producing as uniform magnetic field as possible by shimming the magnet.
2. Stabilizing B in time at the sub-ppm level by feedback, with mechanical and thermal stability.
3. Monitoring B to the 20 ppb level around the storage ring during data collection.
4. Periodically mapping the field throughout the storage region and correlating the field map to the monitoring information without turning off the magnet between data collection and field mapping. It is essential that the magnet not be powered off unless absolutely necessary.
5. Obtaining an absolute calibration of the B -field relative to the Larmor frequency of the free proton.

The only magnetic field measurement technique with the sensitivity needed to measure and control the B -field to the tens of ppb is nuclear magnetic resonance (NMR). Pulsed NMR was used, where a $\pi/2$ RF pulse rotated the spins and the resulting free-induction decay (FID) was detected by a pickup coil around the sample. The E821 baseline design used the NMR of protons in a water sample with a CuSO_4 additive that shortened the relaxation time, with the probes tuned to operate in a 1.45 T field. When the water evaporated from a few of the probes, the water was replaced with petroleum jelly, which the added features of a smaller sensitivity to temperature changes and no evaporation.

Special nuclear magnetic resonance (NMR) probes [42, 6] were used in E821 to measure and monitor the magnetic field during the experimental data collection.³ Three types of probes were used: a spherical water probe that provided the absolute calibration to the free proton; cylindrical probes that were used monitor the field during data collection and in an NMR trolley to map the field; and a smaller spherical probe which could be plunged into the muon storage region by means of a bellows system to transfer the absolute calibration to the trolley probes. A collection of 378 cylindrical probes placed in symmetrically machined grooves on the top and bottom of the muon beam vacuum chamber gave a point-to-point measure of the magnetic field while beam was in the storage ring. Probes at the same azimuthal location but different radii gave information on changes to the quadrupole component of the field at that location.

³The probes are described in Chapter 16

1795 The field mapping trolley contained 17 cylindrical probes arranged in concentric circles
 1796 as shown in Figure 3.8. At several-day intervals during the running periods, the beam
 1797 was turned off, and the field mapping trolley was driven around inside of the evacuated
 1798 beam chamber measuring the magnetic field with each of the 17 trolley probes at 6,000
 1799 locations around the ring. One of the resulting field maps, averaged over azimuth, is shown
 1800 in Figure 3.8(b).

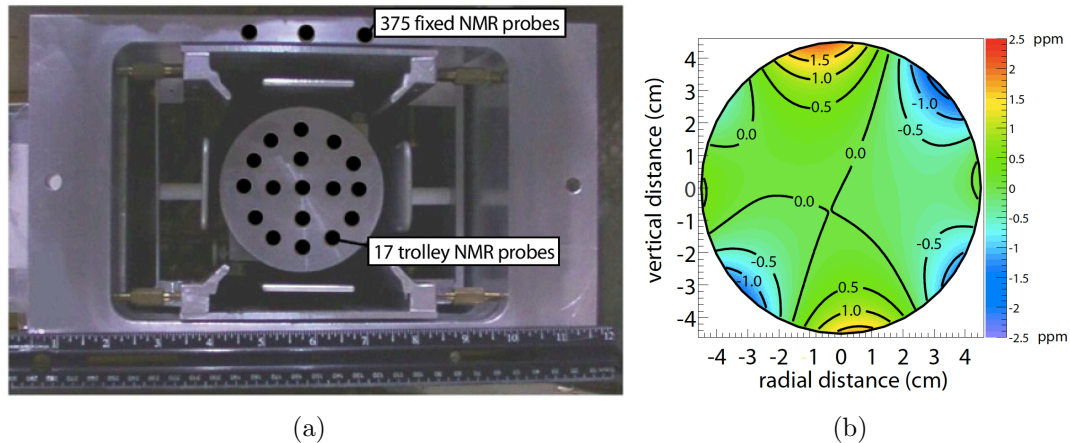


Figure 3.8: (a) The electrostatic quadrupole assembly inside a vacuum chamber showing the NMR trolley sitting on the rails of the cage assembly. Seventeen NMR probes are located just behind the front face in the places indicated by the black circles. The inner (outer) circle of probes has a diameter of 3.5 cm (7 cm) at the probe centers. The storage region has a diameter of 9 cm. The vertical location of three of the 180 upper fixed probes is also shown. An additional 180 probes are located symmetrically below the vacuum chamber. (Reprinted with permission from [6]. Copyright 2006 by the American Physical Society.) (b) A contour plot of the magnetic field averaged over azimuth, 0.5 ppm intervals.

1801 The absolute calibration utilizes a probe with a spherical water sample [7]. The Larmor
 1802 frequency of a proton in a spherical water sample is related to that of the free proton through
 1803 $f_L(\text{sph} - \text{H}_2\text{O}, T) = [1 - \sigma(\text{H}_2\text{O}, T)] f_L(\text{free})$, [8, 9] where $\sigma(\text{H}_2\text{O}, T) = 25.790(14) \times 10^{-6}$ is
 1804 from the diamagnetic shielding of the proton in the water molecule, determined from [10]

$$\sigma(\text{H}_2\text{O}, 34.7^\circ\text{C}) = 1 - \frac{g_p(\text{H}_2\text{O}, 34.7^\circ\text{C})}{g_J(H)} \frac{g_J(H)}{g_p(H)} \frac{g_p(H)}{g_p(\text{free})}. \quad (3.20)$$

1805 The terms are: the ratio of the g -factors of the proton in a spherical water sample to
 1806 that of the electron in the hydrogen ground state ($g_J(H)$) [10]; the ratio of electron to
 1807 proton g -factors in hydrogen [11]; the bound-state correction relating the g -factor of the
 1808 proton bound in hydrogen to the free proton [12, 13]. The temperature dependence is from
 1809 Reference [14]. An alternate absolute calibration would be to use an optically pumped ^3He
 1810 NMR probe [15]. This has several advantages: the sensitivity to the probe shape is negligible,
 1811 and the temperature dependence is also negligible. This option is being explored for E989.

1812 The calibration procedure used above permits the magnetic field to be expressed in terms
 1813 of the Larmor frequency of a free proton, ω_p . The magnetic field is weighted by the muon

1814 distribution, and also averaged over the running time weighed by the number of stored
 1815 muons to determine the value of ω_p which is combined with the average ω_a to determine
 1816 a_μ . The reason for the use of these two frequencies, rather than B measured in tesla can be
 1817 understood from Eq. 3.11. To obtain a_μ from this relationship requires precise knowledge of
 1818 the muon charge to mass ratio.

1819 To determine a_μ from the two frequencies ω_a and ω_p , we use the relationship

$$a_\mu = \frac{\omega_a/\omega_p}{\lambda_+ - \omega_a/\omega_p} = \frac{\mathcal{R}}{\lambda_+ - \mathcal{R}}, \quad (3.21)$$

1820 where the ratio

$$\lambda_+ = \mu_{\mu^+}/\mu_p = 3.183\,345\,137(85) \quad (3.22)$$

1821 is the muon-to-proton magnetic moment ratio [16] measured from muonium (the μ^+e^- atom)
 1822 hyperfine structure[18]. Of course, to use λ_+ to determine a_{μ^-} requires the assumption of
 1823 *CPT* invariance, *viz.* ($a_{\mu^+} = a_{\mu^-}$; $\lambda_+ = \lambda_-$). The comparison of \mathcal{R}_{μ^+} with \mathcal{R}_{μ^-} provides a
 1824 *CPT* test. In E821

$$\Delta\mathcal{R} = \mathcal{R}_{\mu^-} - \mathcal{R}_{\mu^+} = (3.6 \pm 3.7) \times 10^{-9} \quad (3.23)$$

References

- 1825
- 1826 [1] J. Bailey, et al., Nucl. Phys. **B150**, 1 (1979).
- 1827 [2] L.H. Thomas, Nature **117**, (1926) 514 and Phil. Mag. **3** (1927) 1.
- 1828 [3] Bargmann V, Michel L, Telegdi VL, Phys. Rev. Lett. 2:435 (1959)
- 1829 [4] G.W. Bennett, et al., Phys. Rev. **D 80**, 052008 (2009).
- 1830 [5] Bennett GW, et al. (The $g - 2$ Collab.) Phys. Rev. Lett. 92:161802 (2004)
- 1831 [6] Bennett GW, et al.(The $g - 2$ Collab.) Phys. Rev. D, 73:072003 (2006)
- 1832 [7] Fei X, Hughes V, Prigl R, *Nucl. Inst. Methods Phys. Res.* A394:349 (1997)
- 1833 [8] Abragam A. In *Principles of Nuclear Magnetism*, p. 173-178. Oxford U. Press, (1961)
- 1834 [9] Mohr PJ, Taylor BH, *Rev. Mod. Phys.* 77:1 (2005)
- 1835 [10] Phillips WD, et al. *Metrologia* 13:179 (1979)
- 1836 [11] Winkler PF, Kleppner D, Myint T, Walther FG, *Phys. Rev.* A5:83 (1972)
- 1837 [12] Lamb Jr. WE. *Phys. Rev.* 60:817 (1941)
- 1838 [13] Grotch H, Hegstrom RA. *Phys. Rev.* A4:59 (1971)
- 1839 [14] B.W. Petley et al. *Metrologia*.**20**, 81 (1984)
- 1840 [15] J.L. Flowers, B.W. Petley and M.G. Richards, *Metrologia* **30**, 75 (1993).
- 1841 [16] Mohr PJ, Taylor BN, Newell DB, (CODATA recommended values). *Rev. Mod. Phys.*
1842 80:633 (2008)
- 1843 [17] James P. Miller, Eduardo de Rafael and B. Lee Roberts, Rept. Prog. Phys. **70**, 795-881,
1844 2007.
- 1845 [18] W. Liu et al., Phys. Rev. Lett. **82**, 711 (1999).
- 1846 [19] The $g - 2$ Collaboration: R.M. Carey et al., Phys. Rev. Lett. **82**, 1632 (1999).
- 1847 [20] The $g - 2$ Collaboration: H.N. Brown et al., Phys. Rev. D **62**, 091101 (2000).

- 1848 [21] The $g - 2$ Collaboration: H.N. Brown et al., Phys. Rev. Lett. **86**, 2227 (2001).
- 1849 [22] The $g - 2$ Collaboration: G.W. Bennett et al., Phys. Rev. Lett. **89**, 101804 (2002);
1850 Erratum-ibid. **89**, 129903 (2002).
- 1851 [23] F.J.M. Farley, et al., Phys. Rev. Lett. **93** 052001 (2004).
- 1852 [24] J-PARC Letter of Intent xxx, A. Silenko, et al., J. Miller, Y. Semertzidis, spokespersons,
1853 January 2003.

Chapter 4

Beam Dynamics and Beam Related Systematic Errors

4.1 Introduction

In this chapter we discuss the behavior of a beam in a weak-focusing betatron, and the features of the injection of a bunched beam that are important in the determination of ω_a . We also discuss the corrections to the measured frequency ω_a that come from the the vertical betatron motion, and the fact that not all muons are at the magic momentum (central radius) in the storage ring. The final section of this chapter discusses the systematic errors that come from the pion and muon beamlines.

4.2 The Weak Focusing Betatron

The behavior of the beam in the $(g - 2)$ storage ring directly affects the measurement of a_μ . Since the detector acceptance for decay electrons depends on the radial coordinate of the muon at the point where it decays, coherent radial motion of the stored beam can produce an amplitude modulation in the observed electron time spectrum. Resonances in the storage ring can cause particle losses, thus distorting the observed time spectrum, and must be avoided when choosing the operating parameters of the ring. Care is taken in setting the frequency of coherent radial beam motion, the “coherent betatron oscillation” (CBO) frequency, which lies close to the second harmonic of $f_a = \omega_a/(2\pi)$. If f_{CBO} is too close to $2f_a$, the beat frequency, $f_- = f_{\text{CBO}} - f_a$, complicates the extraction of f_a from the data, and can introduce a significant systematic error.

A pure quadrupole electric field provides a linear restoring force in the vertical direction, and the combination of the (defocusing) electric field and the central magnetic field provides a linear restoring force in the radial direction. The $(g - 2)$ ring is a weak focusing ring[1, 2, 3] with the field index

$$n = \frac{\kappa R_0}{\beta B_0}, \quad (4.1)$$

where κ is the electric quadrupole gradient, B_0 is the magnetic field strength, R_0 is the magic radius $\equiv 7112$ mm, and β is the relativistic velocity of the muon beam. For a ring

1881 with a uniform vertical dipole magnetic field and a uniform quadrupole field that provides
 1882 vertical focusing covering the full azimuth, the stored particles undergo simple harmonic
 1883 motion called betatron oscillations, in both the radial and vertical dimensions.

1884 The horizontal and vertical motion are given by

$$x = x_e + A_x \cos(\nu_x \frac{s}{R_0} + \delta_x) \quad \text{and} \quad y = A_y \cos(\nu_y \frac{s}{R_0} + \delta_y), \quad (4.2)$$

1885 where s is the arc length along the trajectory. The horizontal and vertical tunes are given
 1886 by

$$\nu_x = \sqrt{1 - n} \quad \text{and} \quad \nu_y = \sqrt{n}. \quad (4.3)$$

1887 Several n - values were used in E821 for data acquisition: $n = 0.137$, 0.142 and 0.122 . The
 1888 horizontal and vertical betatron frequencies are given by

$$f_x = f_C \sqrt{1 - n} \simeq 0.929 f_C \quad \text{and} \quad f_y = f_C \sqrt{n} \simeq 0.37 f_C, \quad (4.4)$$

1889 where f_C is the cyclotron frequency and the numerical values assume that $n = 0.137$. The
 1890 corresponding betatron wavelengths are $\lambda_{\beta_x} = 1.08(2\pi R_0)$ and $\lambda_{\beta_y} = 2.7(2\pi R_0)$. It is
 1891 important that the betatron wavelengths are not simple multiples of the circumference,
 1892 as this minimizes the ability of ring imperfections and higher multipoles to drive resonances
 1893 that would result in particle losses from the ring.

Table 4.1: Frequencies in the $(g - 2)$ storage ring, assuming that the quadrupole field is uniform in azimuth and that $n = 0.137$.

Quantity	Expression	Frequency [MHz]	Period [μ s]
f_a	$\frac{e}{2\pi mc} a_\mu B$	0.228	4.37
f_C	$\frac{v}{\pi R_0}$	6.7	0.149
f_x	$\sqrt{1 - n} f_c$	6.23	0.160
f_y	$\sqrt{n} f_c$	2.48	0.402
f_{CBO}	$f_c - f_x$	0.477	2.10
f_{VW}	$f_c - 2f_y$	1.74	0.574

1894 As a reminder, the muon frequency, ω_a is determined by the average magnetic field
 1895 weighted by the muon distribution and the magnetic anomaly:

$$\vec{\omega}_a = -\frac{Qe}{m} \left[a_\mu \vec{B} + \left(a_\mu - \left(\frac{m}{p} \right)^2 \right) \frac{\vec{\beta} \times \vec{E}}{c} \right]. \quad (4.5)$$

1896 The field index also determines the angular acceptance of the ring. The maximum hori-
 1897 zontal and vertical angles of the muon momentum are given by

$$\theta_{\text{max}}^x = \frac{x_{\text{max}} \sqrt{1 - n}}{R_0}, \quad \text{and} \quad \theta_{\text{max}}^y = \frac{y_{\text{max}} \sqrt{n}}{R_0}, \quad (4.6)$$

1898 where $x_{\text{max}}, y_{\text{max}} = 45$ mm is the radius of the storage aperture. For a betatron amplitude
 1899 A_x or A_y less than 45 mm, the maximum angle is reduced, as can be seen from the above
 1900 equations.

1901 4.3 Weak Focusing with Discrete Quadrupoles

1902 For a ring with discrete quadrupoles, the focusing strength changes as a function of azimuth,
 1903 and the equation of motion looks like an oscillator whose spring constant changes as a
 1904 function of azimuth s . The motion is described by

$$x(s) = x_e + A\sqrt{\beta(s)} \cos(\psi(s) + \delta), \quad (4.7)$$

1905 where $\beta(s)$ is one of the three Courant-Snyder parameters.[2]

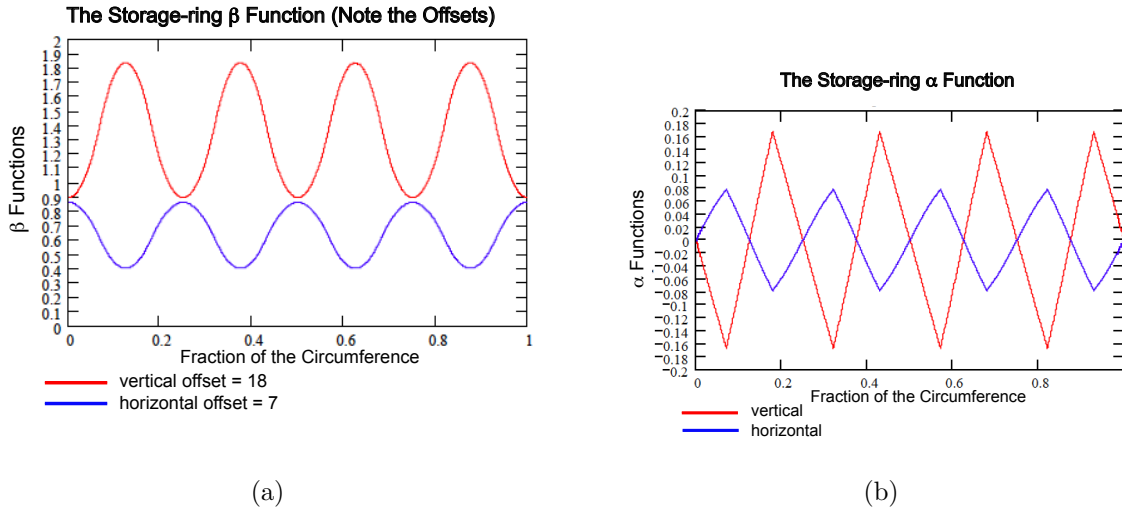


Figure 4.1: (a) The horizontal (radial) and vertical beta functions for the E821 lattice. Note the scale offset. (b) The horizontal (radial) and vertical alpha functions for the E821 lattice. The n -value is 0.134 for both. (From Ref. [9])

1906 The layout of the storage ring is shown in Figure 4.2(a). The four-fold symmetry of the
 1907 quadrupoles was chosen because it provided quadrupole-free regions for the kicker, tracking
 1908 chambers, fiber monitors, and trolley garage; but the most important benefit of four-fold
 1909 symmetry is to reduce the peak-to-peak betatron oscillation amplitudes, with $\sqrt{\beta_{\max}/\beta_{\min}} =$
 1910 1.03. The beta and alpha functions for the $(g - 2)$ storage ring [9] are shown in Fig. 4.1.

1911 Resonances in the storage ring will occur if $L\nu_x + M\nu_y = N$, where L , M and N are
 1912 integers, which must be avoided in choosing the operating value of the field index. These res-
 1913 onances form straight lines on the tune plane shown in Figure 4.2(b), which shows resonance
 1914 lines up to fifth order. The operating point lies on the circle $\nu_x^2 + \nu_y^2 = 1$.

1915 The detector acceptance depends on the radial position of the muon when it decays, so
 1916 that any *coherent* radial beam motion will amplitude modulate the decay e^\pm distribution.
 1917 This can be understood by examining Fig. 4.3. A narrow bunch of muons starts its radial
 1918 betatron oscillation at the point $s = 0$. The circumference of the ring is $2\pi\rho$ so the x -axis
 1919 shows successive revolutions around the ring. The radial betatron wavelength is longer than
 1920 the circumference $2\pi\rho$. The rate at which the muon bunch moves toward and then away
 1921 from the detector is given by $f_{CBO} = f_C - f_x$. The CBO wavelength is slightly over 14
 1922 revolutions of the ring.

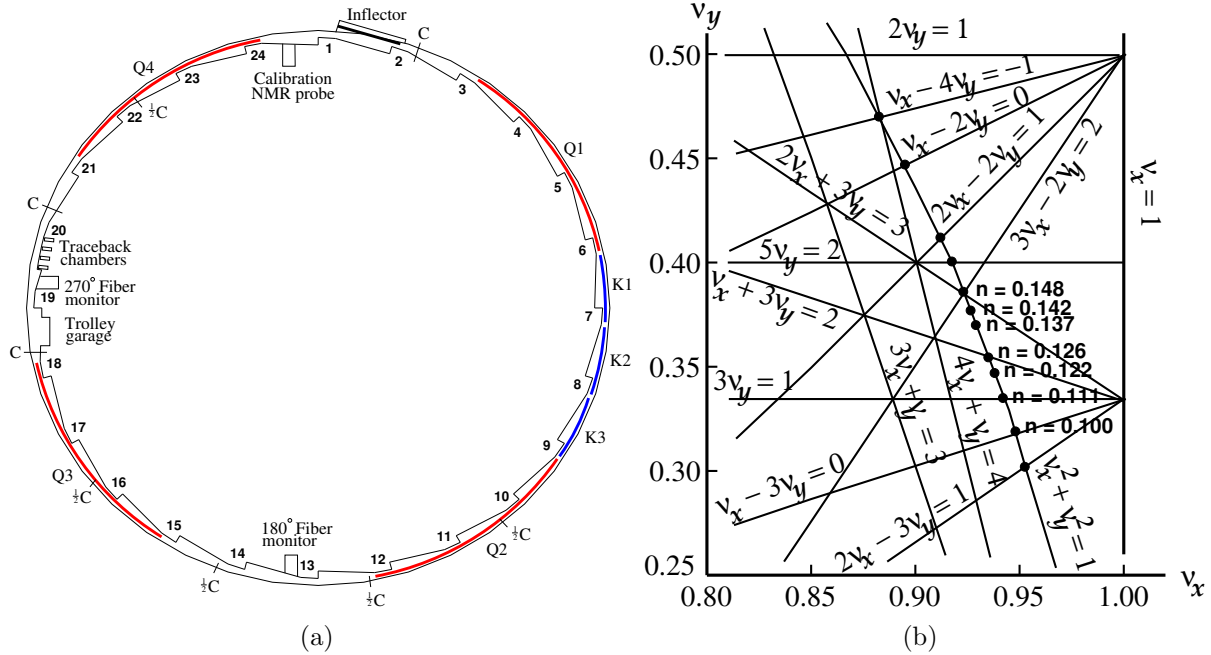


Figure 4.2: (a) The layout of the storage ring. (b) The tune plane, showing the three operating points used during our three years of E821 running.

1923 The presence of the CBO was first discovered in E821 from a plot that showed an az-
 1924 imuthal variation in the value of a_μ shown in Fig. 4.4(a). When the CBO is included, this
 1925 azimuthal dependence disappears. Because the CBO wavelength is only slightly greater
 1926 than the circumference, its effect almost washes out when all detectors are added together.
 1927 Adding all detectors together was one of the techniques used in E821 to eliminate CBO
 1928 effect. However, the four-fold symmetry of the ring was broken by the kicker plates that
 1929 covered one section of the ring, so the cancellation was not perfect, but good enough. This
 1930 will most likely not be true in E989, so it is important to minimize the CBO effects. See
 1931 Chapter 14 for further discussion. Since some detectors saw more injection flash than others,
 1932 this meant that data at times earlier than around $40 \mu\text{s}$ was discarded in those analyses.
 1933 Other analyzers included the CBO and were able to use data from the “quiet” detectors at
 1934 earlier times.

1935 The principal frequency will be the “Coherent Betatron Frequency,”

$$f_{\text{CBO}} = f_C - f_x = (1 - \sqrt{1 - n})f_C \simeq 470 \text{ kHz}, \quad (4.8)$$

1936 which is the frequency at which a single fixed detector sees the beam coherently moving
 1937 back and forth radially. This CBO frequency is close to the second harmonic of the $(g - 2)$
 1938 frequency, $f_a = \omega_a/2\pi \simeq 228 \text{ Hz}$.

1939 An alternative way of thinking about the CBO motion is to view the ring as a spec-
 1940 trometer where the inflector exit is imaged at each successive betatron wavelength, λ_{β_x} . In
 1941 principle, an inverted image appears at half a betatron wavelength; but the radial image is
 1942 spoiled by the $\pm 0.3\%$ momentum dispersion of the ring. A given detector will see the beam
 1943 move radially with the CBO frequency, which is also the frequency at which the horizontal

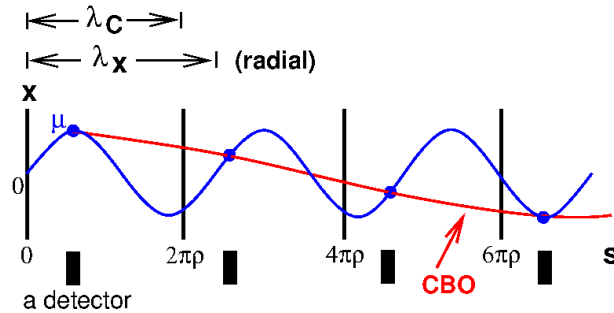


Figure 4.3: A cartoon of the coherent betatron motion (CBO). The radial CBO oscillation is shown in blue for 3 successive betatron wavelengths, the cyclotron wavelength (the circumference) is marked by the black vertical lines. One detector location is shown. Since the radial betatron wavelength is larger than the circumference, the detector sees the bunched beam slowly move closer and then further away. The frequency that the beam appears to move in and out is f_{CBO} .

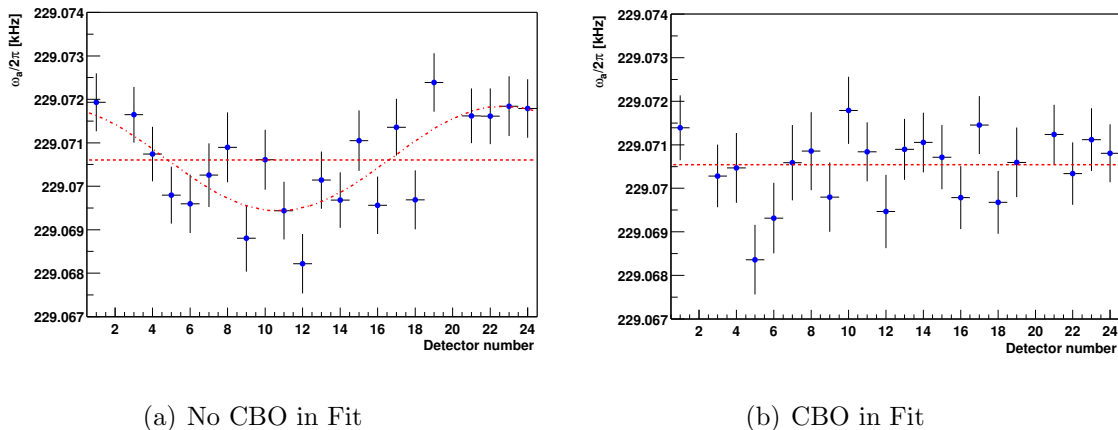


Figure 4.4: The dependence of the extracted value of a_μ vs. detector number. (a) With no CBO in the fit function. (b) With CBO included in the fit function.

1944 waist precesses around the ring. Since there is no dispersion in the vertical dimension, the
 1945 vertical waist (VW) is reformed every half wavelength $\lambda_{\beta_y}/2$. A number of frequencies in
 1946 the ring are tabulated in Table 4.1

1947 The CBO frequency and its sidebands are clearly visible in the Fourier transform to the
 1948 residuals from a fit to the five-parameter fitting function Equation 3.16, and are shown in
 1949 Figure 4.5. The vertical waist frequency is barely visible. In 2000, the quadrupole voltage
 1950 was set such that the CBO frequency was uncomfortably close to the second harmonic of
 1951 f_a , thus placing the difference frequency $f_- = f_{CBO} - f_a$ next to f_a . This nearby sideband
 1952 forced us to work very hard to understand the CBO and how its related phenomena affect
 1953 the value of ω_a obtained from fits to the data. In 2001, we carefully set f_{CBO} at two different
 1954 values, one well above, the other well below $2f_a$, which greatly reduced this problem.

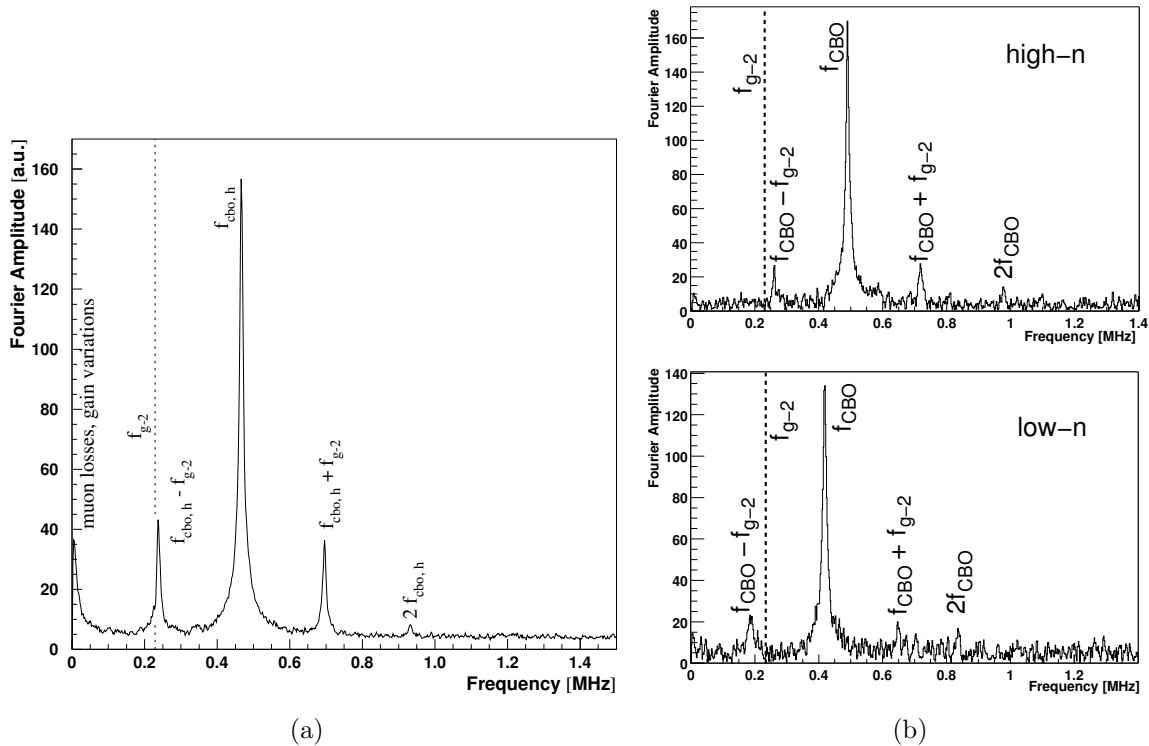


Figure 4.5: The Fourier transform to the residuals from a fit to the five-parameter function, showing clearly the coherent beam frequencies. (a) is from 2000, when the CBO frequency was close to $2\omega_a$, and (b) shows the Fourier transform for the two n -values used in the 2001 run period.

4.3.1 Monitoring the Beam Profile

Two tools are available to us to monitor the muon distribution. Study of the beam de-bunching after injection yields information on the distribution of equilibrium radii in the storage ring. The tracking chambers will provide information on both the vertical and radial distributions of the beam.

The beam bunch that enters the storage ring is expected to have a time spread with of around $\simeq 100$ ns, while the cyclotron period is 149 ns. The momentum distribution of stored muons produces a corresponding distribution in radii of curvature. The distributions depend on the phase-space acceptance of the ring, the phase space of the beam at the injection point, and the kick given to the beam at injection.

With the E821 inflector magnet, the narrow horizontal dimension of the beam at the injection point, about 18 mm, restricts the stored momentum distribution to about $\pm 0.3\%$. As the muons circle the ring, the muons at smaller radius (lower momentum) eventually pass those at larger radius repeatedly after multiple transits around the ring, and the bunch structure largely disappears after $60 \mu s$. This de-bunching can be seen in the E821 data in Figure 4.6 where the signal from a single detector is shown at two different times following injection. The bunched beam is seen very clearly in the left figure, with the 149 ns cyclotron

1972 period being obvious. The slow amplitude modulation comes from the $(g - 2)$ precession.
 1973 By $36 \mu\text{s}$ the beam has largely de-bunched.

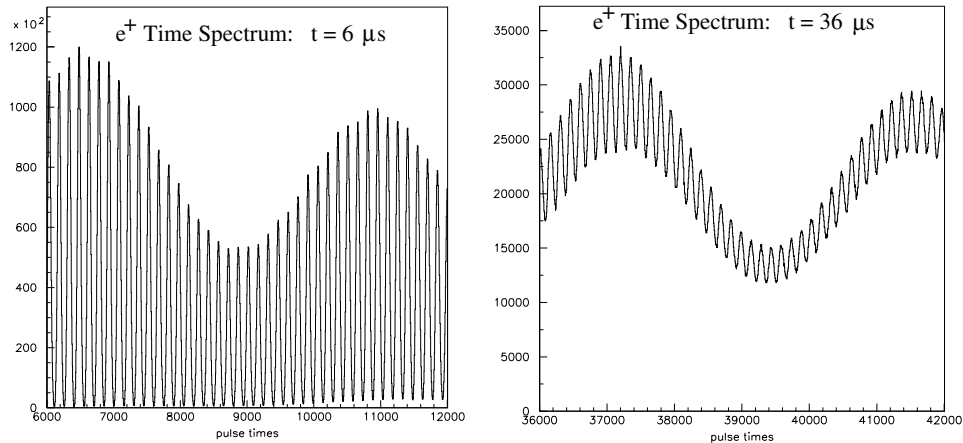


Figure 4.6: The time spectrum of a single calorimeter soon after injection. The spikes are separated by the cyclotron period of 149 ns . The time width of the beam at injection was $\sigma \simeq 23 \text{ ns}$.

1974 Only muons with orbits centered at the central radius have the “magic” momentum,
 1975 so knowledge of the momentum distribution, or equivalently the distribution of equilibrium
 1976 radii, is important in determining the correction to ω_a caused by the radial electric field used
 1977 for vertical focusing. Two methods of obtaining the distribution of equilibrium radii from
 1978 the beam debunching are employed in E821. One method uses a model of the time evolution
 1979 of the bunch structure. A second, alternative procedure uses modified Fourier techniques[8].

1980 The former method was descended from the third CERN experiment, and will also be
 1981 used in E989. The initial bunched beam is modeled as an ensemble of particles having an
 1982 unknown frequency distribution and a narrow time spread. In E821 the beam had an rms
 1983 $\sim 25 \text{ ns}$, occupying ~ 60 degrees of the ring. The model assumes that every time slice of the
 1984 beam has the same frequency profile but the time width is left as a fit parameter, as is the
 1985 exact injection time. The distribution of angular frequencies will cause the bunched beam to
 1986 spread out around the ring over time, in a manner that depends uniquely on the momentum
 1987 distribution. In particular, the time evolution of any finite frequency slice is readily specified.
 1988 A given narrow bin of frequencies contributes linearly to the time spectrum. The total time
 1989 spectrum is a sum over many of these frequency components, with amplitudes that can be
 1990 determined using χ^2 minimization. The momentum distribution is then determined from
 1991 the frequency distribution (or equivalently, from the radial distribution) by

$$\frac{p - p_0}{p_0} = (1 - n) \left(\frac{R - R_0}{R_0} \right). \quad (4.9)$$

1992 The result of the fast-rotation analysis from the R00 period is shown in a plot of the
 1993 beam radius-of-curvature distribution shown in Fig. 4.7. The smooth curve is obtained from
 1994 a modified Fourier transform analysis. The peak of the distribution lies below the nominal

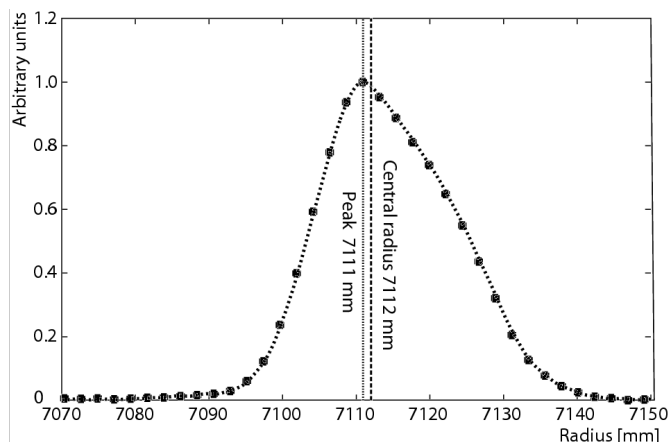


Figure 4.7: The distribution of equilibrium radii obtained from the beam de-bunching. The solid circles are from a de-bunching model fit to the data, and the dotted curve is obtained from a modified Fourier analysis.

1995 magic radius of 7112 mm but the mean is somewhat larger, 7116 ± 1 mm for R00 The rms
 1996 width is about 10 mm. The results from the two methods agree well.

1997 The E989 beam is considerably wider temporally, as is shown in Fig. 7.6. The fast
 1998 rotation analysis was carried out assuming the temporal structure shown in Fig. 4.8(a),
 1999 which was obtained by a preliminary calculation of the beam exiting the Recycler ring. The
 2000 fast rotation spectrum is shown in Fig. 4.8(b) which is very different from that in Fig. 4.6.
 2001 Nevertheless, it was possible to obtain the distribution of equilibrium radii as can be seen in
 2002 Fig. 4.8. Now that we have much better information on the Recycler proton beam structure
 2003 beam we will study this issue in more detail

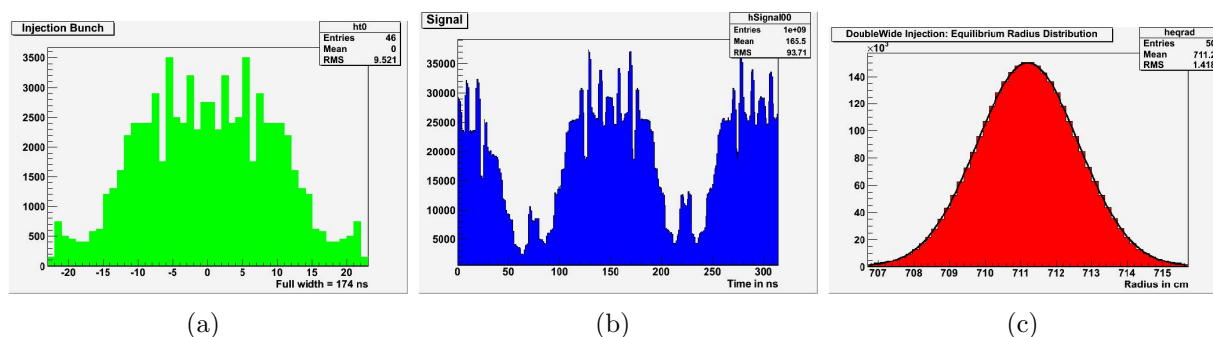


Figure 4.8: Simulations of a temporally wide beam. (a) An early version of the Recycler output beam. (b) The time spectrum shortly after injection, which can be compared with the left-hand E821 calorimeter after injection shown Fig. 4.6. (c) The distribution of equilibrium radii extracted from the debunching in these simulated data.

2004 The measured distribution is used both in determining the average magnetic field seen
 2005 by the muons, and the radial electric field correction discussed below.

2006 The scintillating-fiber monitors show clearly the vertical and horizontal tunes as expected.
 2007 In Figure 4.9, the horizontal beam centroid motion is shown, with the quadrupoles powered

2008 asymmetrically during scraping, and then symmetrically after scraping. A Fourier transform
 2009 of the latter signal shows the expected frequencies, including the cyclotron frequency of
 2010 protons stored in the ring. The traceback system also sees the CBO motion.

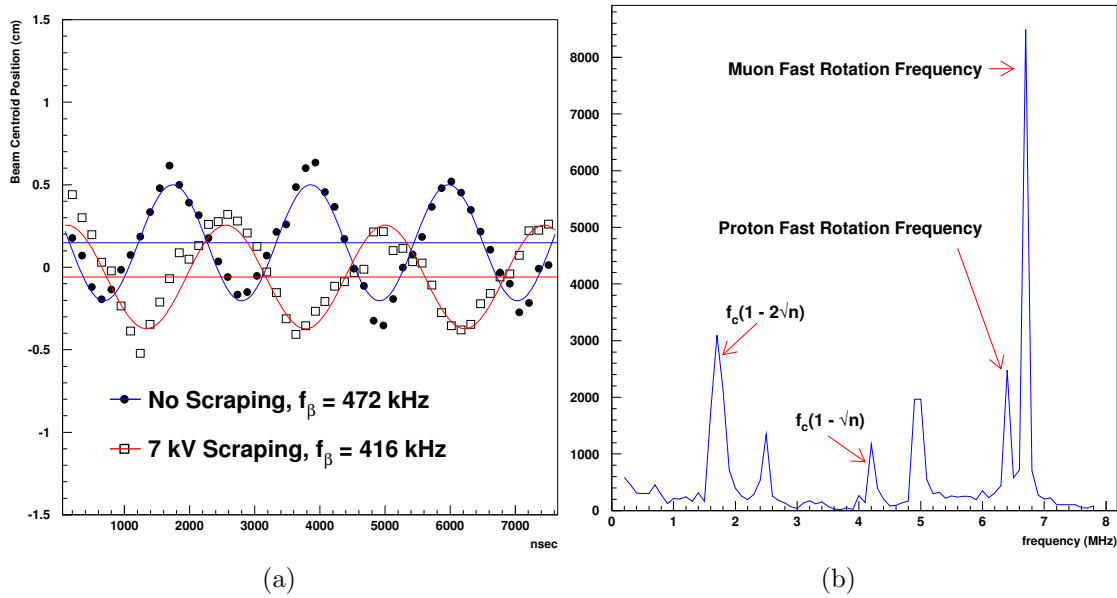


Figure 4.9: (a) The horizontal beam centroid motion with beam scraping and without, using data from the scintillating fiber hodoscopes; note the tune change between the two. (b) A Fourier transform of the pulse from a single horizontal fiber, which shows clearly the vertical waist motion, as well as the vertical tune. The presence of stored protons is clearly seen in this frequency spectrum.

2011 4.4 Corrections to ω_a : Pitch and Radial Electric Field

2012 In the simplest case, the rate at which the spin turns relative to the momentum is given by

$$2013 \omega_a = \omega_S - \omega_C = - \left(\frac{g-2}{2} \right) \frac{Qe}{m} B = -a \frac{Qe}{m} B \quad (4.10)$$

2014 The spin equation modified by the presence of an electric field was introduced earlier, with
 2015 the assumption that the velocity is transverse to the magnetic field. It has also been assumed
 2016 that all muons are at the magic momentum, $\gamma_{\text{magic}} = p_{\text{magic}}/m\beta$. At the current and proposed
 2017 levels of experimental precision, corrections to these approximations must be addressed, since
 2018 the vertical betatron motion must be included, and the momentum acceptance of $\pm 0.5\%$
 2019 means the muon ensemble has a range of momenta. Corrections to the measured value for
 2020 ω_a from these two effects were the only corrections made to the data in E821 after the data
 2021 set was un-blinded. In the 2001 data set, the electric field correction for the low n -value data
 2022 set was $+0.47 \pm 0.05$ ppm. The pitch correction was $+0.27 \pm 0.04$ ppm. These are the only
 2023 corrections made to the ω_a data.

2024 We sketch the derivation for E821 and E989 below[4]. For a general derivation the reader
 is referred to References [6, 7].

2025 Without the assumption that $\vec{\beta} \cdot \vec{B} = 0$ the cyclotron and spin rotation frequencies
2026 become:

$$\vec{\omega}_C = -\frac{Qe}{m} \left[\frac{\vec{B}}{\gamma} - \frac{\gamma}{\gamma^2 - 1} \left(\frac{\vec{\beta} \times \vec{E}}{c} \right) \right], \quad (4.11)$$

2027 and the spin precession frequency becomes[5]

$$\vec{\omega}_S = -\frac{Qe}{m} \left[\left(\frac{g}{2} - 1 + \frac{1}{\gamma} \right) \vec{B} - \left(\frac{g}{2} - 1 \right) \frac{\gamma}{\gamma + 1} (\vec{\beta} \cdot \vec{B}) \vec{\beta} - \left(\frac{g}{2} - \frac{\gamma}{\gamma + 1} \right) \left(\frac{\vec{\beta} \times \vec{E}}{c} \right) \right]. \quad (4.12)$$

2028 Substituting for $a_\mu = (g_\mu - 2)/2$, we find that the spin difference frequency is

$$\vec{\omega}_a = -\frac{QE}{m} \left[a_\mu \vec{B} - a_\mu \left(\frac{\gamma}{\gamma + 1} \right) (\vec{\beta} \cdot \vec{B}) \vec{\beta} - \left(a_\mu - \frac{1}{\gamma^2 - 1} \right) \frac{\vec{\beta} \times \vec{E}}{c} \right]. \quad (4.13)$$

2029 If $\vec{\beta} \cdot \vec{B} = 0$, this reduces to the previously introduced expression

$$\vec{\omega}_a = -\frac{Qe}{m} \left[a_\mu \vec{B} - \left(a_\mu - \frac{1}{\gamma^2 - 1} \right) \frac{\vec{\beta} \times \vec{E}}{c} \right]. \quad (4.14)$$

2030 For $\gamma_{\text{magic}} = 29.3$ ($p_\mu = 3.09 \text{ GeV}/c$), the second term vanishes; and the electric field does
2031 not contribute to the spin precession relative to the momentum. The spin precession is
2032 independent of muon momentum; *all* muons precess at the same rate. Because of the high
2033 uniformity of the B-field, a precision knowledge of the stored beam trajectories in the storage
2034 region is not required.

2035 First we calculate the effect of the electric field, for the moment neglecting the $\vec{\beta} \cdot \vec{B}$ term.
2036 If the muon momentum is different from the magic momentum, the precession frequency is
2037 given by

$$\omega'_a = \omega_a \left[1 - \beta \frac{E_r}{B_y} \left(1 - \frac{1}{a_\mu \beta^2 \gamma^2} \right) \right]. \quad (4.15)$$

2038 Using $p = \beta\gamma m = (p_m + \Delta p)$, after some algebra one finds

$$\frac{\omega'_a - \omega_a}{\omega_a} = \frac{\Delta\omega_a}{\omega_a} = -2 \frac{\beta E_r}{B_y} \left(\frac{\Delta p}{p_m} \right). \quad (4.16)$$

2039 Thus the effect of the radial electric field reduces the observed frequency from the simple
2040 frequency ω_a given in Equation 4.13. Now

$$\frac{\Delta p}{p_m} = (1 - n) \frac{\Delta R}{R_0} = (1 - n) \frac{x_e}{R_0}, \quad (4.17)$$

2041 where x_e is the muon's equilibrium radius of curvature relative to the central orbit. The
2042 electric quadrupole field is

$$E = \kappa x = \frac{n\beta B_y}{R_0} x. \quad (4.18)$$

2043 We obtain

$$\frac{\Delta\omega}{\omega} = -2n(1-n)\beta^2 \frac{xx_e}{R_0^2 B_y}, \quad (4.19)$$

2044 so clearly the effect of muons not at the magic momentum is to lower the observed frequency.
 2045 For a quadrupole focusing field plus a uniform magnetic field, the time average of x is just
 2046 x_e , so the electric field correction is given by

$$C_E = \frac{\Delta\omega}{\omega} = -2n(1-n)\beta^2 \frac{\langle x_e^2 \rangle}{R_0^2 B_y}, \quad (4.20)$$

2047 where $\langle x_e^2 \rangle$ is determined from the fast-rotation analysis (see Figure 4.6). The uncertainty
 2048 on $\langle x_e^2 \rangle$ is added in quadrature with the uncertainty in the placement of the quadrupoles of
 2049 $\delta R = \pm 0.5$ mm (± 0.01 ppm), and with the uncertainty in the mean vertical position of the
 2050 beam, ± 1 mm (± 0.02 ppm). For the low- n 2001 sub-period, $C_E = 0.47 \pm 0.054$ ppm.

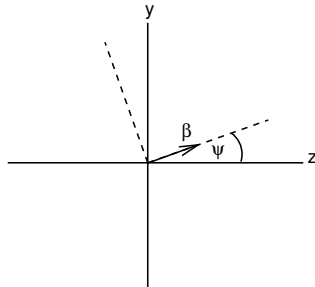


Figure 4.10: The coordinate system of the pitching muon. The angle ψ varies harmonically. The vertical direction is \hat{y} and \hat{z} is the azimuthal (beam) direction.

2051 The betatron oscillations of the stored muons lead to $\vec{\beta} \cdot \vec{B} \neq 0$. Since the $\vec{\beta} \cdot \vec{B}$ term in
 2052 Equation 4.12 is quadratic in the components of $\vec{\beta}$, its contribution to ω_a will not generally
 2053 average to zero. Thus the spin precession frequency has a small dependence on the betatron
 2054 motion of the beam. It turns out that the only significant correction comes from the vertical
 2055 betatron oscillation; therefore it is called the pitch correction (see Equation 4.13). As the
 2056 muons undergo vertical betatron oscillations, the “pitch” angle between the momentum and
 2057 the horizontal (see Figure 4.10) varies harmonically as $\psi = \psi_0 \cos \omega_y t$, where ω_y is the vertical
 2058 betatron frequency $\omega_y = 2\pi f_y$, given in Equation 4.4. In the approximation that all muons
 2059 are at the magic γ , we set $a_\mu - 1/(\gamma^2 - 1) = 0$ in Equation 4.13 and obtain

$$\vec{\omega}'_a = -\frac{Qe}{m} \left[a_\mu \vec{B} - a_\mu \left(\frac{\gamma}{\gamma + 1} \right) (\vec{\beta} \cdot \vec{B}) \vec{\beta} \right], \quad (4.21)$$

2060 where the prime indicates the modified frequency as it did in the discussion of the radial elec-
 2061 tric field given above, and $\vec{\omega}_a = -(Qe/m)a_\mu \vec{B}$. We adopt the (rotating) coordinate system
 2062 shown in Figure 4.10, where $\vec{\beta}$ lies in the yz -plane, z being the direction of propagation, and
 2063 y being vertical in the storage ring. Assuming $\vec{B} = \hat{y}B_y$, $\vec{\beta} = \hat{z}\beta_z + \hat{y}\beta_y = \hat{z}\beta \cos \psi + \hat{y}\beta \sin \psi$,
 2064 we find

$$\vec{\omega}'_a = -\frac{Qe}{m} \left[a_\mu \hat{y} B_y - a_\mu \left(\frac{\gamma}{\gamma + 1} \right) \beta_y B_y (\hat{z}\beta_z + \hat{y}\beta_y) \right]. \quad (4.22)$$

2065 The small-angle approximation $\cos \psi \simeq 1$ and $\sin \psi \simeq \psi$ gives the component equations

$$\omega'_{ay} = \omega_a \left[1 - \left(\frac{\gamma - 1}{\gamma} \right) \psi^2 \right] \quad (4.23)$$

2066 and

$$\omega'_{az} = -\omega_a \left(\frac{\gamma - 1}{\gamma} \right) \psi. \quad (4.24)$$

2067 It is seen that the direction of ω'_a in Figure 4.10 oscillates at the pitch frequency. We are
 2068 interested in the overall precession rate about the y-axis, which can be obtained in terms of
 2069 the period between the times that $\psi = 0$, or the average rate of precession during the pitch
 2070 period. To facilitate obtaining this average, project $\vec{\omega}'_a$ onto axes parallel and perpendicular
 2071 to $\vec{\beta}$, using a standard rotation. Using the small-angle expansions $\cos \psi \simeq 1 - \psi^2/2$, and
 2072 $\sin \psi \simeq \psi$, we find the transverse component of ω'_a is given by

$$\omega_{\perp} = \omega'_{ay} \cos \psi - \omega'_{az} \sin \psi \simeq \omega_a \left[1 - \frac{\psi^2}{2} \right]. \quad (4.25)$$

2073 As can be seen from Table 4.1, the pitching frequency ω_y is more than an order of
 2074 magnitude larger than the frequency ω_a , so that ω_{\parallel} changes sign rapidly, thus averaging out
 2075 its effect on ω'_a . Therefore $\omega'_a \simeq \omega_{\perp}$,

$$\omega'_a \simeq -\frac{Qe}{m} a_{\mu} B_y \left(1 - \frac{\psi^2}{2} \right) = -\frac{q}{m} a_{\mu} B_y \left(1 - \frac{\psi_0^2 \cos^2 \omega_y t}{2} \right). \quad (4.26)$$

2076 Taking the time average yields a pitch correction

$$C_p = -\frac{\langle \psi^2 \rangle}{2} = -\frac{\langle \psi_0^2 \rangle}{4} = -\frac{n \langle y^2 \rangle}{4 R_0^2}, \quad (4.27)$$

2077 where we have used Equation 4.6 $\langle \psi_0^2 \rangle = n \langle y^2 \rangle / R_0^2$. The quantity $\langle y_0^2 \rangle$ was both determined
 2078 experimentally and from simulations. For the 2001 period, $C_p = 0.27 \pm 0.036$ ppm, the
 2079 amount the precession frequency is lowered from that given in Equation 4.5 because $\vec{\beta} \cdot \vec{B} \neq 0$.

2080 We see that both the radial electric field and the vertical pitching motion *lower* the
 2081 observed frequency from the simple difference frequency $\omega_a = (e/m) a_{\mu} B$, which enters into
 2082 our determination of a_{μ} using Equation 3.21. Therefore our observed frequency must be
 2083 *increased* by these corrections to obtain the measured value of the anomaly. Note that if
 2084 $\omega_y \simeq \omega_a$ the situation is more complicated, with a resonance behavior that is discussed in
 2085 References [6, 7].

2086 4.5 Systematic Errors from the Pion and Muon Beam- 2087 lines

2088 Systematic effects on the measurement of ω_a occur when the muon beam injected and stored
 2089 in the ring has a correlation between the muon's spin direction and its momentum. For
 2090 a straight beamline, by symmetry, the averaged muon spin is in the forward direction for

2091 all momenta muons. However, muons born from pion decay in a bending section of the
 2092 beamline will have a spin-momentum correlation, especially when the bend is used to make
 2093 a momentum selection. This is illustrated in Fig. 4.11. For E821 we had a 32 degree bend
 2094 with D1/D2 to select the pion momentum, and a 21 degree bend with D5 to select the muon
 2095 momentum. 57% of the pions were still left at the latter bend. A plot of the simulated muon
 2096 radial spin angle vs. momentum for the E821 beamline is shown in Fig. 4.12. The FNAL
 2097 experiment beamline bends are given in Table 4.2.

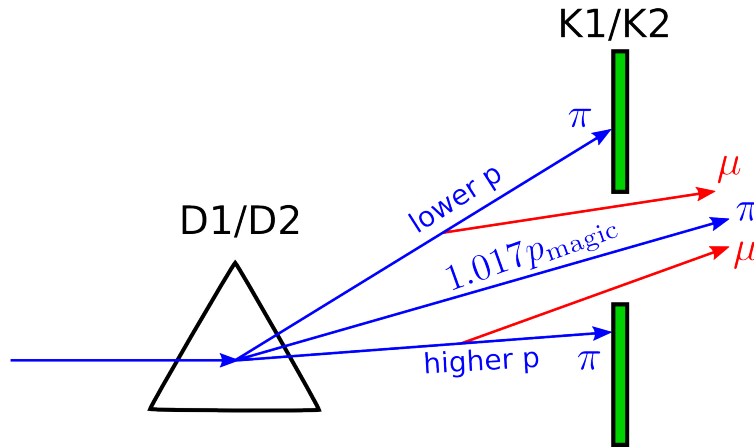


Figure 4.11: Cartoon of the E821 pion/muon beam going through D1/D2. The pions (blue arrows) with momentum (1.017 ± 0.010) times the magic momentum pass through the K1/K2 collimator (green rectangles) slits. Some pions decay after the D1/D2 bend and the decay muons (red arrows) pass through the collimator slit. These muons may have approximately magic momentum, and finally are stored in the muon storage ring. The muon spin direction will then be correlated with it's momentum.

Table 4.2: FNAL beamline horizontal bends.

Bend	Pions left	dp/p	Purpose
3 degree	96%	$\pm 10\%$	Pion momentum selection
19 degree	41%	$\pm 2\%$	M2 to M3
Delivery Ring (DR)	18%	$\pm 2\%$	Remaining pions decay
After DR	$< 10^{-3}$	$\pm 1\%$	Muon momentum selection

2098 The systematic effect is calculated from:

$$\left\langle \frac{d\Theta_{\text{spin}}}{dt} \right\rangle = \left\langle \frac{d\Theta_{\text{spin}}}{dp} \frac{dp}{dt} \right\rangle \quad (4.28)$$

2099 where dp/dt occurs because the muon lifetime in the lab frame is gamma times the rest
 2100 frame lifetime. This gave an E821 beamline “differential decay” systematic effect on the
 2101 measurement of ω_a of 0.05ppm, which was sufficiently small for E821 that we didn't need to

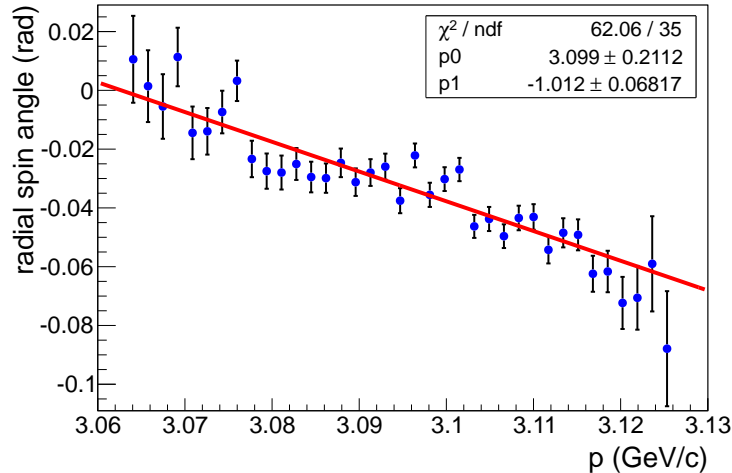


Figure 4.12: Simulation from Hugh Browns BETRAF program of the spin-momentum correlation of muons entering the E821 storage ring, i.e., at the end of the inflector magnet (symbols). The red line is linear fit to data points.

2102 correct for it. We plan to reduce the E821 systematic error from 0.3ppm to 0.1ppm in the
 2103 FNAL experiment.

2104 The design philosophy for the FNAL beamline is significantly different from that of E821.
 2105 For E821 we had a beamline whose length was about the pion $\beta\gamma c\tau$, so to minimize the pion
 2106 “flash” we selected (1.017 ± 0.010) times the magic momentum pions after the target and
 2107 then selected (1.0 ± 0.005) times the magic momentum just before the muon storage ring.
 2108 For the FNAL beamline, effectively all the pions will have decayed before the muon storage
 2109 ring. The pion momentum selection right after the target is only a 3 degree bend and
 2110 selects $\pm 10\%$ in momentum. The capture probability $Y_{\mu\pi}$ for the long straight section of
 2111 the beamline is shown in Fig. 4.13. With $\pm 10\%$ momentum acceptance, the pions which are
 2112 headed for the low momentum side of the beamline acceptance (see Fig. 4.11) can not give
 2113 a magic momentum muon. The pions which are headed for the high momentum side of the
 2114 beamline acceptance will be very inefficient in giving a magic momentum muon. Note that
 2115 this is suggested by Fig. 4.13, but we haven’t yet done the FNAL beamline simulation in the
 2116 bending regions. For later bends, a larger fraction of the pions will have decayed prior to
 2117 the bend compared to E821 (see Table 4.2). We believe this bending section of the beamline
 2118 systematic error will be less or equal the E821 error, but we haven’t properly simulated it
 2119 yet. The timeline for the simulation calculation is given in the next section.

2120 Another systematic effect comes when the muons go around the delivery ring (DR). The
 2121 cyclotron and anomalous magnetic moment frequencies are:

$$\omega_c = \frac{eB}{m\gamma} \quad \omega_a \approx \frac{eaB}{m} \quad (4.29)$$

2122 The former is exact while the latter is good to the sub-ppm level. The “spin tune” is
 2123 then:

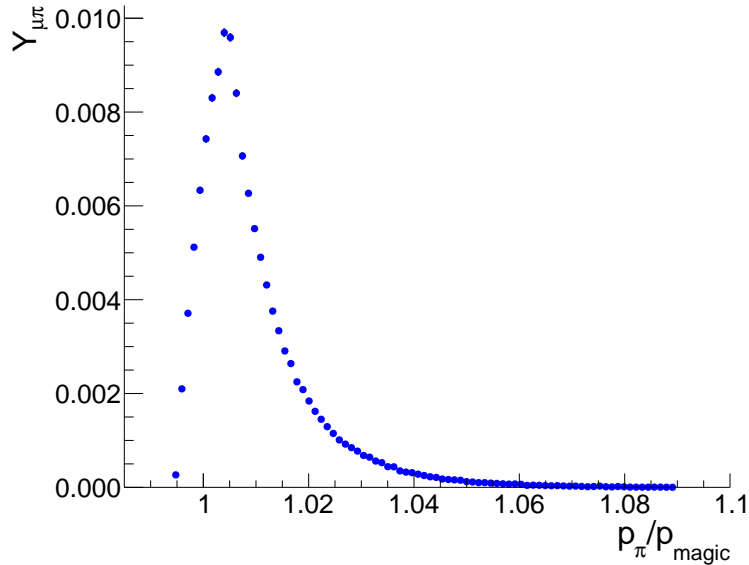


Figure 4.13: Parametric phase space calculation of the π - μ capture probability in the straight section of the FNAL pion decay channel. The muons have the magic momentum $\pm 0.5\%$.

$$Q_{\text{spin}} = \frac{\omega_a}{\omega_c} \approx a\gamma \quad (4.30)$$

2124 The spin-momentum correlation after seven turns in the DR, is shown in Fig. 4.14. The
 2125 slope is less than the slope shown in Fig. 4.12. Of course, Fig. 4.14 is exact, but the energies of
 2126 the muons in the storage ring are different from their energies in the DR due to the material
 2127 the beam passes through between the DR and the storage ring. Once the simulation is
 2128 complete, we will correct our measured value of ω_a for the beamline differential decay effect.

2129 Such correlations also couple to the lost muon systematic error. For E821, the differential
 2130 lost muon rate was about 10^{-3} per lifetime, while the differential decay rate was 1.2×10^{-3}
 2131 per lifetime. As discussed above, the FNAL differential lost muon rate will be less than 10^{-4}
 2132 per lifetime.

2133 4.5.1 Simulation plan and timeline

2134 We are planning to study the beamline systematic errors independently in two ways, us-
 2135 ing phase-space calculations and tracking. The phase-space calculations were first used by
 2136 W.M. Morse for E821 [10]. In E989 the phase-space calculation were used to guide the
 2137 design of the beamline [11] and to estimate the muon capture probability in the straight
 2138 section for this document. While the phase-space method is approximation, it gives quick
 2139 insight into the problem and allows to make studies of an idealized beamline with required
 2140 characteristics without having the actual design of the beamline.

2141 For tracking calculations several off-the-shelf accelerator packages have been considered,
 2142 TRANSPORT, TURTLE, DECAY TURTLE, MAD, TURTLE with MAD input. Suitable tracking pro-
 2143 gram for $(g - 2)$ must be capable of *i*) describing decay of primary particles (pions) into

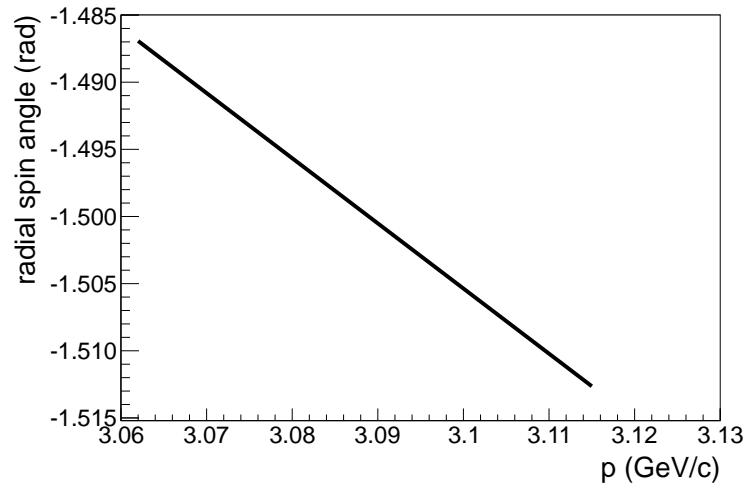


Figure 4.14: Radial spin angle vs. momentum after seven turns in the DR.

2144 secondary particles (muons) and transporting the secondary particles and *ii*) transporting
 2145 spin through the beamline. It turned out that none of the existing programs can be used "as
 2146 is" for the studies of systematic errors in $(g - 2)$. Some modification are needed of any of
 2147 the existing programs. Lack of the source code in some cases (`DECAY TURTLE`) makes imple-
 2148 mentation of the missing features impossible. Our current plan for tracking simulations is to
 2149 use the program `G4Beamline` for the following reason *i*) the program is well-supported and
 2150 is under active development, *ii*) it is based on `Geant4` toolkit which is widely used in physics
 2151 simulations, *iii*) spin tracking has been recently implemented in `Geant4`, *iv*) the accelerator
 2152 team is planning to use `G4Beamline` for beamline simulations, therefore the input configu-
 2153 ration file for the $(g - 2)$ beamline will be provided by the experts, *v*) the common ground
 2154 between `G4Beamline` and the downstream simulation program `g2RingSim` for the $(g - 2)$
 2155 storage ring will simplify the task of combining the two programs together for back-to-back
 2156 simulations.

2157 Recently, a preliminary version of the `G4Beamline` for $(g - 2)$ was released with significant
 2158 boost in performance and bug fixes. The construction of the $(g - 2)$ beamline model for
 2159 `G4Beamline` is in progress. Basing on our experience, we expect to get the results from
 2160 `G4Beamline` simulations in six months.

2161 `G4Beamline` simulations for the straight section will be confronted with the phase space
 2162 simulation to cross-check the two codes. In parallel, we are planning to extend the phase
 2163 space method to the bending sections of the beamline (beamline elements with dispersion).

2164 Finally, the production and collection of pions in the target station was simulated by
 2165 `MARS` (see section 7.4.1). We are planning to confront `MARS` and `G4Beamline` simulations of
 2166 the target station to cross-check the two codes.

2167 References

- 2168 [1] H. Wiedemann, *Particle Accelerator Physics* Vol. 1, Springer-Verlag, (1993) p. 54.
- 2169 [2] D.A. Edwards and M.J. Syphers, *An Introduction to the Physics of High Energy Accel-*
2170 *erators*, John Wiley & Sons, (1993) p. 75.
- 2171 [3] F. Combley and E. Picasso, *Phys. Rept.* **14**, 1 (1974).
- 2172 [4] We follow the approach given by J.M. Paley, Ph.D. Dissertation, Boston University,
2173 2004.
- 2174 [5] L.H. Thomas, *Nature* **117**, (1926) 514 and *Phil. Mag.* **3** (1927) 1, Bargmann V, Michel
2175 L, Telegdi VL, *Phys. Rev. Lett.* 2:435 (1959)
- 2176 [6] F.J.M. Farley and E. Picasso, in *Quantum Electrodynamics*, Adv. Series on Dir. in
2177 H.E.P., V7, T. Kinoshita, ed., World Scientific, 479, (1990).
- 2178 [7] F.J.M. Farley, *Phys.Lett.* **B 42**, 66 (1972), and J.H. Field and G. Fiorentini, *Nuovo*
2179 *Cimento*, **21 A**, 297 (1974).
- 2180 [8] Y. Orlov, et al., *Nucl. Instrum. Meth.* **A482**, 767 (2002).
- 2181 [9] P. Debevec, Ringbeta, DocDB document #762.
- 2182 [10] B. Morse, Phase Space Calculations of Muon Injection, Brookhaven National Labora-
2183 tory, 1998, (g-2) note #303, 1998.
- 2184 [11] V. Tishchenko and W.M. Morse, Phase-Space Calculations of the Muon Acceptance by
2185 the Straight Section of the Fermilab Beamline, Brookhaven National Laboratory, docdb
2186 #487, 2012.

Chapter 5

Statistical and Systematic Errors for E989

E989 must obtain twenty-one times the amount of data collected for E821. Using the T method (see Section 17.1.2) to evaluate the uncertainty, 1.8×10^{11} events are required in the final fitted histogram to realize a 0.10 ppm statistical uncertainty. The systematic errors on the anomalous precession frequency ω_a , and on the magnetic field normalized to the proton Larmor frequency ω_p , must be reduced by a factor of three, down to the ± 0.07 ppm level. E989 will have three main categories of uncertainties:

- **Statistical.** The least-squares or maximum likelihood fits to the histograms describing decay electron events vs. time in the fill will determine ω_a , the anomalous precession frequency. The uncertainty $\delta\omega_a$ from the fits will be purely statistical (assuming a good fit). A discussion of the fitting sensitivity using various weighting schemes is given in Chapter 17, Section 17.2. The final uncertainty depends on the size of the data set used in the fit, which in turn depends on the data accumulation *rate* and the *running time*. These topics are discussed here.
- **ω_a Systematics.** Additional systematic uncertainties that will affect $\delta\omega_a$ might be anything that can cause the extracted value of ω_a from the fit to differ from the true value, beyond statistical fluctuations. Categories of concern include the detection system (e.g., gain stability and pileup immunity discussed in Chapter 17), the incoming beamline (lost muons, spin tracking), and the stored beam (coherent betatron oscillations, differential decay, E and pitch correction uncertainties). These latter topics are discussed in Chapter 4.
- **ω_p Systematics.** The magnetic field is determined from proton NMR in a procedure described in Chapter 16. The uncertainties are related to how well known are the individual steps from absolute calibration to the many stages of relative calibration and time-dependent monitoring. The “statistical” component to these measurements is negligible.

The purpose of this chapter is twofold. First, we summarize the event-rate calculation from initial proton flux to fitted events in the final histograms in order to determine the running

2217 time required to meet the statistical goals of the experiment. We also gather the results of
 2218 many systematic uncertainty discussions that are described in various chapters throughout
 2219 this document and roll up the expected systematic uncertainty tables for E989.

2220 5.1 Event Rate Calculation Methodologies

2221 The E989 Proposal [1] event-rate estimate was made by making a **relative comparison**
 2222 **approach** using like terms with respect to the known situation for rates in the E821 BNL
 2223 experiment. Many factors allow for trivial adjustments (proton fills per second, kinematics
 2224 of the decay line length, kinematics of the decay line capture), while others rely on expected
 2225 improvements in specific hardware components (optimized storage ring kicker pulse shape
 2226 and magnitude, open-ended inflector, thinner or displaced Q1 outer plate and standoffs).
 2227 In E821, the transmission through the closed-ended inflector and subsequently through the
 2228 Q1 outer plates, followed by an imperfect kick, combined to give a sub-optimal storage ring
 2229 efficiency factor, but individually the contributions from each element are not known as
 2230 well as their product. However, we can deduce the realized E821 stored muon fraction with
 2231 some uncertainty compared to the incoming muon beam intensity by knowing the stored
 2232 muon rate as determined from the data rate in the detectors. For E989, each of these beam-
 2233 storage elements is being optimized and detailed simulations have been made to estimate
 2234 the transmission and storage ring efficiency product under a number of scenarios regarding
 2235 proposed upgrades or replacements of components. We choose an intermediate value for the
 2236 purposes of estimating the event rate.

2237 Section 5.1.2 provides a new, **bottom up** calculation of the event rate in which each
 2238 factor from pion production to measured positrons is individually studied or measured to
 2239 obtain the final event rate. Chapter 8 outlines the progress in our end-to-end simulation effort
 2240 of flux and storage rates, essentially the accelerator complex, the inflector, the quadrupoles,
 2241 and the kicker influence. The detector efficiency and response are described in Chapter 17.

2242 5.1.1 Event Rate by a Relative Comparison to E821

2243 Table 5.1 contains a sequential list of factors that affect the event rate from proton on target
 2244 to events in the final histogram. It is modified, where appropriate, compared to the 2010
 2245 Proposal based on new information and studies to date.

2246 A pion production calculation using MARS was made to estimate the number of 3.1 GeV/c
 2247 pions emitted into the accepted phase space of the AP2 line. From this point, a conserva-
 2248 tive approach was to compare known factors between the muon capture and transmission
 2249 at Fermilab to those same factors at BNL. Many of the factors are relatively trivial to com-
 2250 pute, while others rely on our detailed Decay Turtle simulations of the BNL lattice and
 2251 modifications of this lattice for Fermilab. We are in the process of a complete end-to-end
 2252 calculation of the beamline, but this work will take additional time. In the comparison to
 2253 BNL approach, we find the important increase of stored muons per incident proton of 11.5,
 2254 assuming an improved kicker and an open-ended inflector. We require a factor of at least 6
 2255 for an experiment that can be done in less than 2 years. We use the factor of 6 in our beam
 2256 estimates, thus building in $\simeq 100\%$ contingency from the beginning. We expect to require

2257 2 months of setup time with beam to tune various subsystems prior to “good” data taking.
 2258 We expect to use an integrated additional 2 months of beam time, devoted to systematic
 2259 studies. These periods will be distributed throughout the data collection period. We assume
 2260 a 75% uptime factor for the efficiency of data taking during normal running. The down time
 2261 includes the accelerator complex inefficiency (unknown to us for this new operation) and the
 2262 time to be spent mapping the magnet with the trolley (mapping will take place whenever the
 2263 accelerator is down or will interrupt data taking periodically if the uninterrupted machine
 2264 uptime exceeds 2 days. Mapping will take approximately 3 hours. The origin of each factor
 2265 in Table 5.1, is explained in a series of notes following the Table.

Table 5.1: Event rate calculation using known factors and a comparison to the realized stored muon fraction at BNL. This table has been updated compared to the 2010 E989 Proposal.

Item	Value	Rates	Note
Booster cycle (BC) - 15 Hz operation	1.33 s/BC	0.75 BC/s	1
Proton Batches to $g-2$	4/BC	3 batch/s	2
Proton Bunches \rightarrow fill	4/batch	12 fill/s	3
Protons on target	10^{12} p/bunch	1.2×10^{13} p/s	4
BNL realized stored μ/p efficiency	1×10^{-9} μ/p		5
FNAL estimated μ/p improvement factor	6	6000 μ /fill	6
Positrons accepted with $E > 1.8$ GeV	0.15	720 e^+ /fill	7
Positrons with $t > 30$ μ s	0.63	567 e^+ /fill	8
Number of fills for 1.8×10^{11} events	3.17×10^8 fills	–	9
DAQ and experiment production uptime	0.75	–	10
Time to collect statistics	14 months	–	11
Beam-on commissioning	2 months	–	12
Dedicated systematic studies periods	2 months	–	13
Net running time required	18 months	–	14

2266 The following notes explain entries in Table 5.1 and make comparisons to what was
 2267 assumed in the E989 Proposal:

- 2268 1. 15 Hz Booster operation, as described in Section 7.1, remains a valid assumption.
- 2269 2. Neutrino program uses 12 out of 20 batches; 8 out of 20 are in principle available, but
 2270 preparation of the 4 separated bunches of proton in the Recycler requires two Booster
 2271 cycles. Therefore, only 4 of the 8 can be used. This is a change compared to the
 2272 Proposal, which assumed 6/8 were useable.
- 2273 3. Subdivision in Recycler of each batch into 4 “bunches” with roughly equal intensity
 2274 of $\approx 1 \times 10^{12}$ p/bunch. Each is extracted separately with ~ 12 ms spacing and each
 2275 initiates a storage ring “fill.”
- 2276 4. Expected proton intensity per Bunch, or per fill, striking target.
- 2277 5. Measured stored muon fraction per 24-GeV proton on target at BNL per 10^{12} p (Tp).
 2278 This number rolls up individual factors including the FODO line length, the non-
 2279 forward muon acceptance used to minimize the hadronic flash, the transmission through

- 2280 the closed-ended inflector, the losses in the outer Q1 quadrupole plate and standoffs,
2281 and the sub-optimal storage ring kicker efficiency
- 2282 6. Improvement factor estimated by comparing to the known situation at BNL. We arrive
2283 at the following factors: $\times 0.4$ for the reduced pion yield; $\times 1.8$ for the AP2 line with
2284 smaller beta function; $\times 2$ for the longer decay channel; $\times 3$ for the forward decay
2285 optimal muon tune; $\times 1.33$ for opening up the pion momentum acceptance; $\times 2$ for the
2286 open inflector and improved kicker = 11.5. We use a factor of 6 to be conservative,
2287 demonstrating that the experiment can be completed in under two years of net running
2288 time even if one of these projected upgrades is not realized.
- 2289 7. Monte Carlo acceptance of 15% for events with energy above 1.8 GeV and striking the
2290 front face of one of the 24 calorimeter stations.
- 2291 8. Fit starting at $30 \mu\text{s}$; the factor of 0.63 represents those muons that have not yet
2292 decayed, given a $64.6 \mu\text{s}$ muon lifetime in the ring.
- 2293 9. Required number of fills to obtain the full statistical precision.
- 2294 10. Estimate of the uptime for the experiment and accelerator complex during steady-
2295 state data production running. Downtime will occur from accelerator issues related to
2296 the new operational modes and to routine maintenance and servicing; time required
2297 by the experiment to run trolley field mapping program (typically 3 h / 2 days),
2298 and ordinary DAQ and experimental issues requiring intervention. This is a slightly
2299 aggressive number.
- 2300 11. Estimate of 2 months to commission the new experiment and machine operation se-
2301 quence. This is based, in part, on past experience at BNL, and allowing for the new
2302 configuration at FNAL.
- 2303 12. Estimate of periodic dedicated systematic study weeks during data taking periods.
2304 These are crucial to establish uncertainties, but this data typically will not be included
2305 in the final statistics.
- 2306 13. Net data taking in months.

5.1.2 Bottom-Up Event Rate Calculation

Table 5.2 contains a sequential list of factors that affect the event rate based on a bottom-up approach. The beamline momentum bite is set at $dp/p = \pm 2\%$ all the way to the inflector. This is wider than the E821 line and much wider than the acceptance of the storage ring ($\sim \pm 0.15\%$). However, the calculation to date on the muon capture fraction used 0.5% from a wide pion momentum bite. Thus, we include that here. As in the previous section, the last column points to a list of Notes that explain the individual entries. The following notes

Table 5.2: Event rate calculation using a bottom-up approach.

Item	Estimate	Chapter	Note
Protons per fill on target	10^{12} p	7.3	1
Positive-charged secondaries with $dp/p = \pm 2\%$	4.8×10^7	7.4.1	2
π^+ fraction of secondaries	0.48	7.4.1	2
π^+ flux entering FODO decay line	$> 2 \times 10^7$	7.4.1	2
Pion decay to muons in 220 m of M2/M3 line	0.72	–	3
Muon capture fraction with $dp/p < \pm 0.5\%$	0.0036	8	4
Muon survive decay 1800 m to storage ring	0.90	–	5
Muons flux at inflector entrance (per fill)	4.7×10^4	–	5
Transmission and storage using $(dp/p)_\mu = \pm 0.5\%$	0.10 ± 0.04	11.5.1	6
Stored muons per fill	$(4.7 \pm 1.9) \times 10^3$	–	6
Positrons accepted per fill (factors 0.15 x 0.63)	444 ± 180	–	7
Number of fills for 1.8×10^{11} events	$(4.1 \pm 1.7) \times 10^8$ fills	–	8
Time to collect statistics	(13 ± 5) months	–	8
Beam-on commissioning	2 months	–	9
Dedicated systematic studies periods	2 months	–	10
Net running time required	17 ± 5 months	–	11

explain entries in Table 5.2:

1. Same starting point as in Table 5.1.
2. MARS calculation, backed up with 2012 measurement. Assumes improved proton spot size on target to 0.15 mm, which increases the yield by 40 – 60% compared to the measured rates at 0.5 mm spot size. Assumes 40-mm-mr emittance. Measurement verifies yield of positive particles. Simulation shows that 45% of them are pions. The target yield could increase by 14 – 22% if the target geometry were further optimized; see Fig. 7.10 and the text in that section.
3. Pion decay length = 173 m. M2 line = 115.6 m; M3 = 96.7 m; use 220 m total.
4. Preliminary fraction based on a phase Space simulations assuming pion emittance = beam admittance = 40 mm mrad both in x and y ; pions fill the phase space uniformly; muon momentum: $p_{magic} \pm 0.5\%$; These studies are being repeated using full Monte Carlo with G4Beamline. See Tishchenko and Morse, DocDB 895.

- 2327 5. Transmission to storage ring; survive 1800 m; $(c\beta\gamma\tau)_\mu = 19280m$.
- 2328 6. Average results from studies of transmission through the inflector, through the outer
2329 Q1 quadrupole and standoffs, and then kicked onto orbit and stored. The kicker is
2330 assumed to be perfect and that its kick width covers the entire incoming pulse train
2331 (to be determined). The inflector is modeled as having either closed ends, as in the
2332 present E821 inflector that will be used initially, or as open-ended, meaning a material
2333 free version of the same device (see Chapter 11). Additional studies look at not only an
2334 open inflector, but also one with a larger horizontal beam aperture. We do not include
2335 that here. The Q1 and standoff intercept the incoming beam. If they were massless,
2336 a greater fraction of muons is stored. Plans are in place to reduce mass and move the
2337 standoffs. The transmission fraction for a 0.5% dp/p muon beam ranges from 6.5% to
2338 14.5% depending on mass options used for inflector and Q1. We take a central value
2339 of 10% here and propagate the range of uncertainty, which depends on what will be
2340 built. The simulation is described in 8.4.
- 2341 7. Monte Carlo acceptance of 15% for events with energy above 1.8 GeV and striking the
2342 front face of one of the 24 calorimeter stations and assume fit can be started at 30 μ s;
2343 factor 0.63.
- 2344 8. Required number of fills to obtain the full statistical precision.
- 2345 9. Estimate of the uptime for the experiment and accelerator complex during steady-state
2346 data production running. Downtime will occur from accelerator issues related to the
2347 new operational modes and to routine maintenance and servicing; time required by the
2348 experiment to run trolley field mapping program (typically 3 h / 2 days), and ordinary
2349 DAQ and experimental issues requiring intervention. This is a slight aggressive number.
- 2350 10. Estimate of time to commission the new experiment and machine operation sequence.
2351 This is based, in part, on past experience at BNL, and allowing for the new configura-
2352 tion at FNAL.
- 2353 11. Estimate of periodic dedicated systematic study weeks during data taking periods.
2354 These are crucial to establish uncertainties, but this data typically will not be included
2355 in the final statistics.
- 2356 12. Net data taking in months.

2357 5.2 ω_a systematic uncertainty summary

2358 Our plan of data taking and hardware changes addresses the largest systematic uncertainties
 2359 and aims to keep the total combined uncertainty below 0.07 ppm. Experience shows that
 2360 many of the “known” systematic uncertainties can be addressed in advance and minimized,
 2361 while other more subtle uncertainties appear only when the data is being analyzed. Because
 2362 we have devised a method to take more complete and complementary data sets, we antici-
 2363 pate the availability of more tools to diagnose such mysteries should they arise. Table 5.3
 2364 summarizes this section.

Table 5.3: The largest systematic uncertainties for the final E821 ω_a analysis and proposed upgrade actions and projected future uncertainties for data analyzed using the T method. The relevant Chapters and Sections are given where specific topics are discussed in detail.

Category	E821 [ppm]	E989 Improvement Plans	Goal [ppm]	Chapter & Section
Gain changes	0.12	Better laser calibration low-energy threshold	0.02	17.3.1
Pileup	0.08	Low-energy samples recorded calorimeter segmentation	0.04	17.3.2
Lost muons	0.09	Better collimation in ring	0.02	14.4
CBO	0.07	Higher n value (frequency) Better match of beamline to ring	< 0.03	14.3.1
E and pitch	0.05	Improved tracker Precise storage ring simulations	0.03	14.3.2
Total	0.18	Quadrature sum	0.07	

2365 5.3 ω_p systematic uncertainty summary

2366 The magnetic field is mapped by use of NMR probes. A detailed discussion is found in Chap-
 2367 ter 16. In Table 5.4 we provide a compact summary of the expected systematic uncertainties
 2368 in E989 in comparison with the final achieved systematic uncertainties in E821. The main
 2369 concepts of how the improvements will be made are indicated, but the reader is referred to
 2370 the identified text sections for the details.

Table 5.4: Systematic uncertainties estimated for the magnetic field, ω_p , measurement. The final E821 values are given for reference, and the proposed upgrade actions are projected. Note, several items involve ongoing R&D, while others have dependencies on the uniformity of the final shimmed field, which cannot be known accurately at this time. The relevant Chapters and Sections are given where specific topics are discussed in detail.

Category	E821 [ppm]	Main E989 Improvement Plans	Goal [ppm]	Chapter
Absolute field calibration	0.05	Special 1.45 T calibration magnet with thermal enclosure; additional probes; better electronics	0.035	16.4.1
Trolley probe calibrations	0.09	Plunging probes that can cross calibrate off-central probes; better position accuracy by physical stops and/or optical survey; more frequent calibrations	0.03	16.4.1
Trolley measurements of B_0	0.05	Reduced position uncertainty by factor of 2; improved rail irregularities; stabilized magnet field during measurements*	0.03	16.3.1
Fixed probe interpolation	0.07	Better temperature stability of the magnet; more frequent trolley runs	0.03	16.3
Muon distribution	0.03	Additional probes at larger radii; improved field uniformity; improved muon tracking	0.01	16.3
Time-dependent external magnetic fields	–	Direct measurement of external fields; simulations of impact; active feedback	0.005	16.6
Others †	0.10	Improved trolley power supply; trolley probes extended to larger radii; reduced temperature effects on trolley; measure kicker field transients	0.03	16.7
Total systematic error on ω_p	0.17		0.07	16

*Improvements in many of these categories will also follow from a more uniformly shimmed main magnetic field.

†Collective smaller effects in E821 from higher multipoles, trolley temperature uncertainty and its power supply voltage response, and eddy currents from the kicker. See 16.7.

2371 **References**

- 2372 [1] R. M. Carey, K. R. Lynch, J. P. Miller, B. L. Roberts, W. M. Morse, Y. K. Semertzides,
2373 V. P. Druzhinin and B. I. Khazin *et al.*, “The New (g-2) Experiment: A proposal to
2374 measure the muon anomalous magnetic moment to ± 0.14 ppm precision,” FERMILAB-
2375 PROPOSAL-0989.

Chapter 6

Civil Construction Off-Project

The experimental hall is funded as a General Plant Project (GPP), as part of the Muon Campus Program. The beamline and tunnel from the delivery ring to the hall are separate GPP and Accelerator Improvement Projects (AIP). The locations of the buildings on the muon campus is shown in Fig. 6.1.

6.1 The MC1 Building

The muon storage ring will be located in the MC-1 Building on the Muon Campus, which is shown in Fig. 6.2. While it is a general purpose building, the design and features are extremely important to the success of E989. The principal design considerations are a very stable floor, and good temperature stability in the experimental hall. Both of these features were absent at Brookhaven, and presented difficulties to the measurement of the precision field. This design will serve E989, and subsequent experiments well. One portion of the MC1 building will house beamline power supplies and cryo facilities for the two initial experiments on the muon campus: ($g - 2$) and Mu2e.

The floor in the experimental area will be reinforced concrete 2' 9" (84 cm) thick. The floor is 12' below grade. Core samples show that the soil at the location is very compacted, the floor settling is expected to be about 0.25" fully loaded.

This floor will be significantly better than the floor in Building 919 at Brookhaven, where the ring was housed for E821. That floor consisted of three separate pieces: a concrete spine down the middle of the room, with a concrete pad on each side of the spine. Thus the foundation of the ring will be much more mechanically stable than it was at BNL.

Even more important is the temperature stability available in MC-1. The HVAC system will hold the temperature steady to $\pm 2^\circ$ F during magnet operation and data collection. This stability, combined with thermal insulation around the magnet will minimize the changes in the field due to temperature changes in the experimental hall.

A floor plan of MC-1 is shown in Fig. 6.3. The experimental hall is 80' \times 80' with a 30 ton overhead crane. The loading dock in the lower left-hand corner is accessed through the roll-up door labeled in Fig. 6.2 . Unlike in BNL 919, the crane coverage is significantly larger than the storage-ring diameter, simplifying many tasks in assembling the ring.

A detailed MC-1 document is available from FESS, titled "MC-1 Building", dated March



Figure 6.1: The layout of the Muon Campus, which lies between the former Antiproton Rings and the Booster Accelerator. The locations of the $(g - 2)$ and Mu2e experiments are labeled.



Figure 6.2: A rendering of the MC1 building.

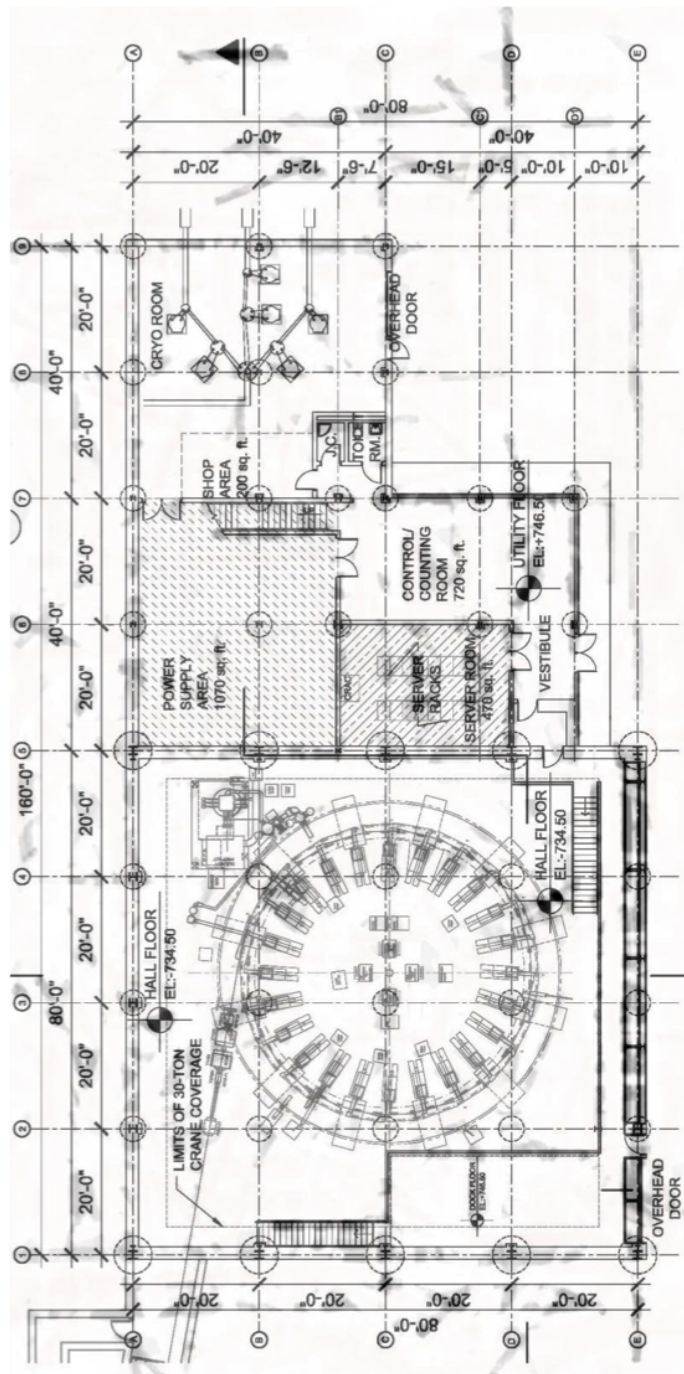


Figure 6.3: The first-floor layout of the MC1 building.

Chapter 7

Accelerator and Muon Delivery

In order to achieve a statistical uncertainty of 0.1 ppm, the total $(g-2)$ data set must contain at least 1.8×10^{11} detected positrons with energy greater than 1.8 GeV, and arrival time greater than $30 \mu\text{s}$ after injection into the storage ring. This is expected to require 4×10^{20} protons on target including commissioning time and systematic studies. For optimal detector performance, the number of protons in a single pulse to the target should be no more than 10^{12} and the number of secondary protons transported into the muon storage ring should be as small as possible. Data acquisition limits the time between pulses to be at least 10 ms. The revolution time of muons around the storage ring is 149 ns, and therefore the experiment requires the bunch length to be no more than ~ 100 ns. Systematic effects on muon polarization limit the momentum spread dp/p of the secondary beam. Requirements and general accelerator parameters are given in Table 7.1.

Parameter	Design Value	Requirement	Unit
Total protons on target	$2.3 \times 10^{20}/\text{year}$	4×10^{20}	protons
Interval between beam pulses	10	≥ 10	ms
Max bunch length (full width)	120 (95%)	< 149	ns
Intensity of single pulse on target	10^{12}	10^{12}	protons
Max Pulse to Pulse intensity variation	± 10	± 50	%
$ dp/p $ of pions accepted in decay line	2-5	2	%
Momentum of muon beam	3.094	3.094	GeV/c
Muons to ring per 10^{12} protons on target	$(0.5 - 1.0) \times 10^5$	≥ 6000 stored	muons

Table 7.1: General beam requirements and design parameters.

7.1 Overall Strategy

The $(g-2)$ experiment at Fermilab is designed to take advantage of the infrastructure of the former Antiproton Source, as well as improvements to the Proton Source and the conversion of the Recycler to a proton-delivery machine. It is also designed to share as much infrastructure as possible with the Mu2e experiment in order to keep overall costs low.

2426 The Antiproton Accumulator will no longer be in use, and many of its components will be
 2427 reused for the new and redesigned Muon beamlines. Stochastic cooling components and other
 2428 infrastructure no longer needed in the Debuncher ring will be removed in order to improve the
 2429 aperture, proton abort functionality will be added, and the ring will be renamed the Delivery
 2430 Ring (DR). The former AP1, AP2, and AP3 beamlines will be modified and renamed M1,
 2431 M2, and M3. The DR Accelerator Improvement Project (AIP) will provide upgrades to the
 2432 Delivery Ring. The Beam Transport AIP will provide aperture improvements to the P1, P2,
 2433 and M1 lines needed for future muon experiments using 8 GeV protons, including ($g - 2$).
 The layout of the beamlines is shown in Fig. 7.1.

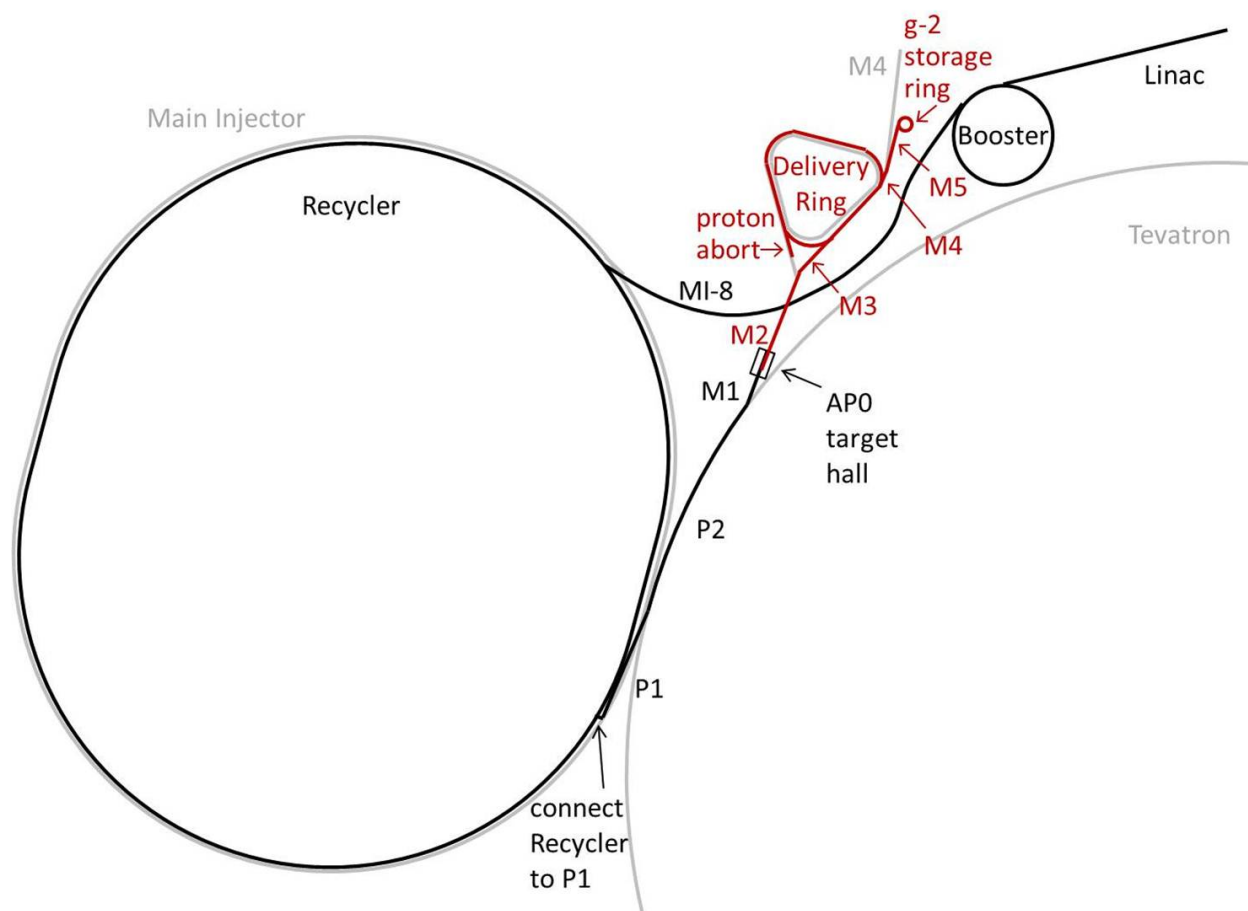


Figure 7.1: Path of the beam to ($g - 2$). Protons (black) are accelerated in the Linac and Booster, are re-bunched in the Recycler, and then travel through the P1, P2, and M1 lines to the AP0 target hall. Secondary beam (red) then travels through the M2 and M3 lines, around the Delivery Ring, and then through the M4 and M5 lines to the muon storage ring.

2434 The Proton Improvement Plan [1], currently underway, will allow the Booster to run at
 2435 15 Hz, at intensities of 4×10^{12} protons per Booster batch. Following the completion of the
 2436 Accelerator and NuMI Upgrades (ANU) subproject at Fermilab to prepare for the $\text{NO}\nu\text{A}$
 2437 experiment [2], the Main Injector (MI) will run with a 1.333 s cycle time for its neutrino
 2438 program, with twelve batches of beam from the Booster being accumulated in the Recycler
 2439

2440 and single-turn injected into the MI at the beginning of the cycle. While the NO ν A beam is
 2441 being accelerated in the MI, eight Booster batches will be available for experimental programs
 2442 such as $(g - 2)$ which use 8 GeV protons. The ANU subproject will also enable injection from
 2443 the Booster into the Recycler. Extraction from the Recycler to the P1 beamline, required
 2444 for $(g - 2)$, will be implemented in the Beam Transport AIP.

2445 Protons from the Booster with 8 GeV kinetic energy will be re-bunched into four smaller
 2446 bunches in the Recycler and transported through the P1, P2, and M1 beamlines to a target
 2447 at AP0. Secondary beam from the target will be collected using a focusing device, and
 2448 positively-charged particles with a momentum of 3.11 GeV/c ($\pm \sim 10\%$) will be selected
 2449 using a bending magnet. Secondary beam leaving the target station will travel through the
 2450 M2 and M3 lines which are designed to capture as many muons with momentum 3.094 GeV/c
 2451 from pion decay as possible. The beam will then be injected into the Delivery Ring. After
 2452 several revolutions around the DR, essentially all of the pions will have decayed into muons,
 2453 and the muons will have separated in time from the heavier protons. A kicker will then be
 2454 used to abort the protons, and the muon beam will be extracted into the new M4 line, and
 2455 finally into the new M5 beamline which leads to the $(g - 2)$ storage ring. Note that the M3
 2456 line, Delivery Ring, and M4 line are also designed to be used for 8 GeV proton transport by
 2457 the Mu2e experiment.

2458 The expected number of muons transported to the storage ring, based on target-yield
 2459 simulations using the antiproton-production target and simple acceptance assumptions, is
 2460 $(0.5 - 1.0) \times 10^5$. Beam tests were conducted using the existing Antiproton-Source config-
 2461 uration with total charged-particle intensities measured at various points in the beamline
 2462 leading to the Debuncher, which confirmed the predicted yields to within a factor of two [3].
 2463 More details are given in Sec. 7.4.1.

2464 7.2 Protons from Booster

2465 During the period when $(g - 2)$ will take data, the Booster is expected to run with present
 2466 intensities of 4×10^{12} protons per batch, and with a repetition rate of 15 Hz. In a 1.333 s
 2467 Main-Injector super cycle, twelve Booster batches are slip-stacked in the Recycler and then
 2468 accelerated in the MI and sent to NO ν A. While the Main Injector is ramping, a time corre-
 2469 sponding to eight Booster cycles, the Recycler is free to send 8 GeV (kinetic energy) protons
 2470 to $(g - 2)$. The RF manipulations of beam for $(g - 2)$ in the Recycler (Sec. 7.3.1) allow
 2471 $(g - 2)$ to take four of the eight available Booster batches. Figure 7.2 shows a possible time
 2472 structure of beam pulses to $(g - 2)$.

2473 The following section describes improvements needed to run the proton source reliably
 2474 at 15 Hz.

2475 7.2.1 Proton Improvement Plan

2476 The Fermilab Accelerator Division has undertaken a Proton Improvement Plan (PIP) [1]
 2477 with the goals of maintaining viable and reliable operation of the Linac and Booster through
 2478 2025, increasing the Booster RF pulse repetition rate, and doubling the proton flux without
 2479 increasing residual activation levels.

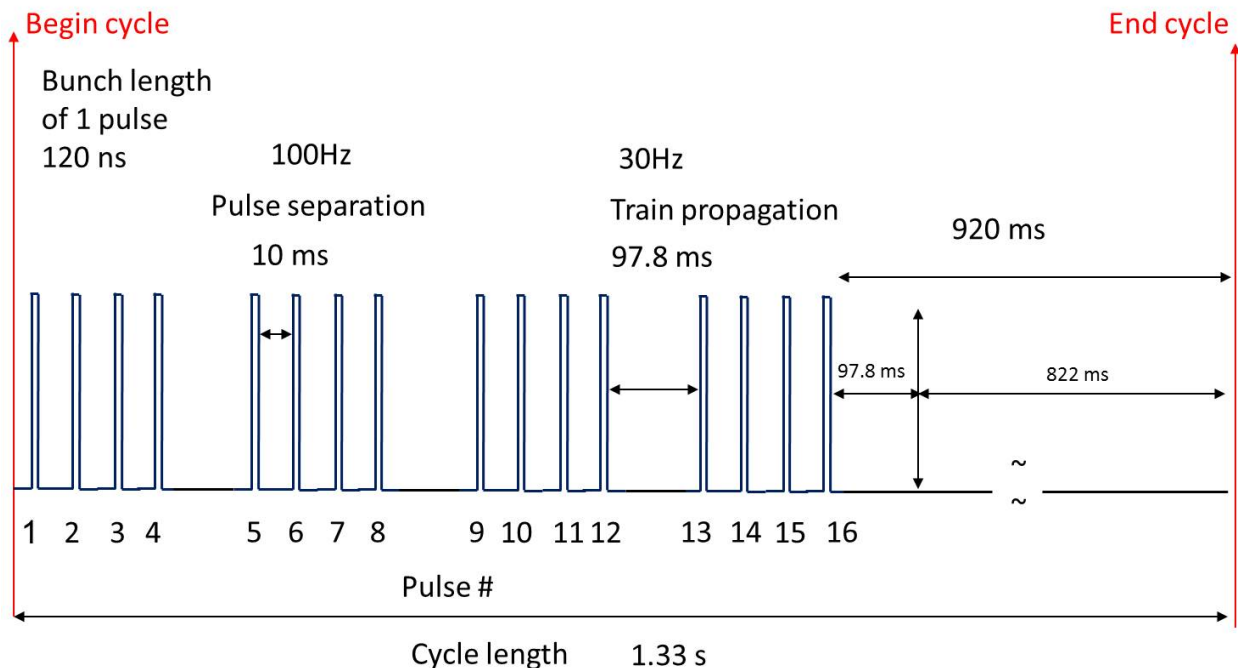


Figure 7.2: Time structure of beam pulses to $(g - 2)$.

2480 The replacement of the Cockroft-Walton pre-accelerator with a radio-frequency quadrupole
 2481 (RFQ) during the 2012 shutdown is expected to increase reliability of the pre-accelerator and
 2482 to improve beam quality.

2483 The Booster RF solid-state upgrade is necessary for reliable 15 Hz RF operations. This
 2484 involves the replacement of 40-year-old electronics that are either obsolete, difficult to find, or
 2485 unable to run at the required higher cycle-rate of 15 Hz, and will allow for easier maintenance,
 2486 shorter repair times, and less radiation exposure to personnel. The solid-state upgrade will
 2487 be completed in 2013.

2488 Refurbishment of the Booster RF cavities and tuners, in particular, cooling, is also nec-
 2489 essary in order to operate at a repetition rate of 15 Hz.

2490 Other upgrades, replacements, and infrastructure improvements are needed for viable
 2491 and reliable operation. Efforts to reduce beam loss and thereby lower radiation activation
 2492 include improved methods for existing processes, and beam studies, e.g., aimed at finding
 2493 and correcting aperture restrictions due to misalignment of components.

2494 The proton flux through the Booster over the past two decades and projected into 2016
 2495 based on expected PIP improvements is shown in Fig. 7.3.

2496 The new PIP flux goal will double recent achievements and needs to be completed within
 2497 five years. Figure 7.4 shows both the increase in flux as well as planned users. The goal
 2498 of doubling the proton flux will be achieved by increasing the number of cycles with beam.
 2499 The intensity per cycle is not planned to increase.

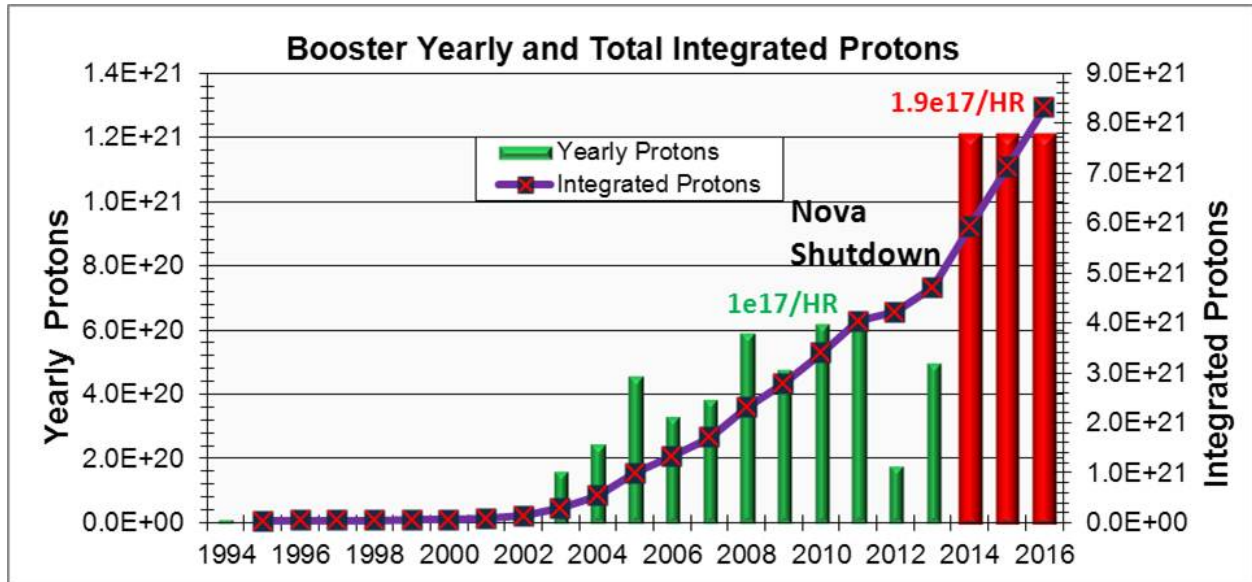


Figure 7.3: Yearly and integrated proton flux (including PIP planned flux increase).

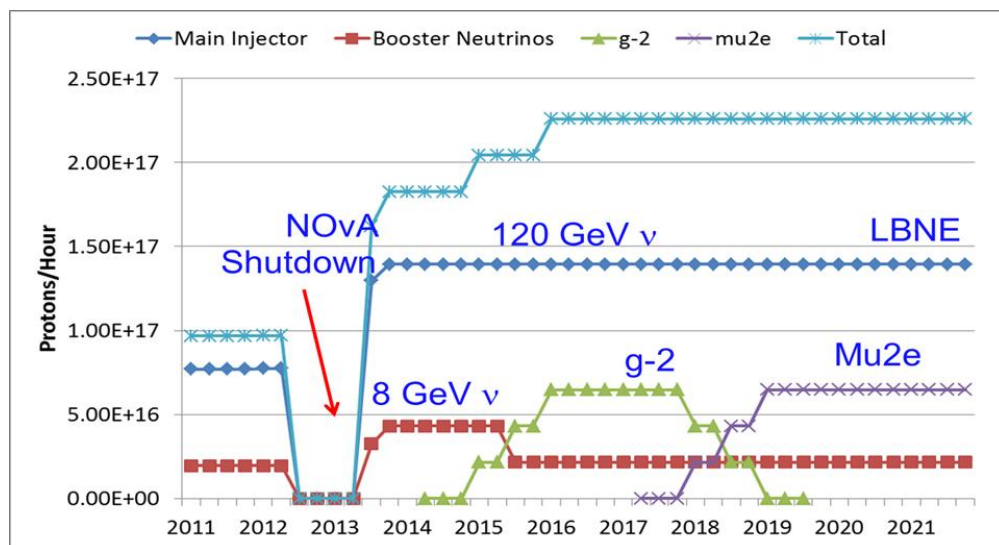


Figure 7.4: Expectations for increases in the proton flux from the Proton Source needed for future experiments.

7.3 Recycler

The $(g - 2)$ experiment requires a low number of decay positrons in a given segment of the detector, and therefore requires that the full-intensity (4×10^{12} protons) bunches be redistributed into four bunches of 1×10^{12} protons. These bunches should be spaced no closer than 10 ns to allow for muon decay and data acquisition in the detector. Because the revolution time of muons in the $(g - 2)$ ring is 149 ns, the longitudinal extent of the bunches should be no more than 120 ns. The Recycler modifications needed to achieve these requirements will be made under the Recycler AIP, and are described below.

7.3.1 Recycler RF

The proposed scheme for $(g - 2)$ bunch formation [4] uses one RF system, 80 kV of 2.5 MHz RF. The design of the RF cavities will be based on that of existing 2.5 MHz cavities which were used in collider running, but utilizing active ferrite cooling. The ferrites of the old cavities and the old power amplifiers will be reused in the new system.

In order to avoid bunch rotations in a mismatched bucket, the 2.5 MHz is ramped “adiabatically” from 3 to 80 kV in 90 ms. Initially the bunches are injected from the Booster into matched 53 MHz buckets (80 kV of 53 MHz RF), then the 53 MHz voltage is turned off and the 2.5 MHz is turned on at 3 kV and then ramped to 80 kV. The first 2.5 MHz bunch is then extracted and the remaining three bunches are extracted sequentially in 10 ms intervals. The formation and extraction of all four bunches takes two Booster ticks or 133 ms. This limits the $(g - 2)$ experiment to using four of the available eight Booster ticks in every Main-Injector super cycle.

Simulated 2.5 MHz bunch profiles are shown in Fig. 7.5. The 53 MHz voltage was ramped down from 80 to 0 kV in 10 ms and then turned off. The 2.5 MHz voltage was snapped to 3 kV and then adiabatically raised to 80 kV in 90 ms. The maximum momentum spread is $dp/p = \pm 0.28\%$. The overall efficiency is 95%, and 95% of the beam captured is contained within 120 ns. Roughly 75% of the beam is contained in the central 90 ns and 60% in 50 ns.

Although the Recycler is not yet configured to do such RF manipulations, by using the 2.5 MHz coalescing cavities in the Main Injector, the proposed bunch-formation scheme was tested with beam. In general, the agreement between simulations and data is very good. For illustration, the comparison between the beam measurements and the simulations for the case in which the 2.5 MHz voltage is ramped adiabatically from 3 to 70 kV in 90 ms is shown in Fig. 7.6.

Extraction from the Recycler and primary proton beam transport will be described in the beamline section, Sec. 7.5.

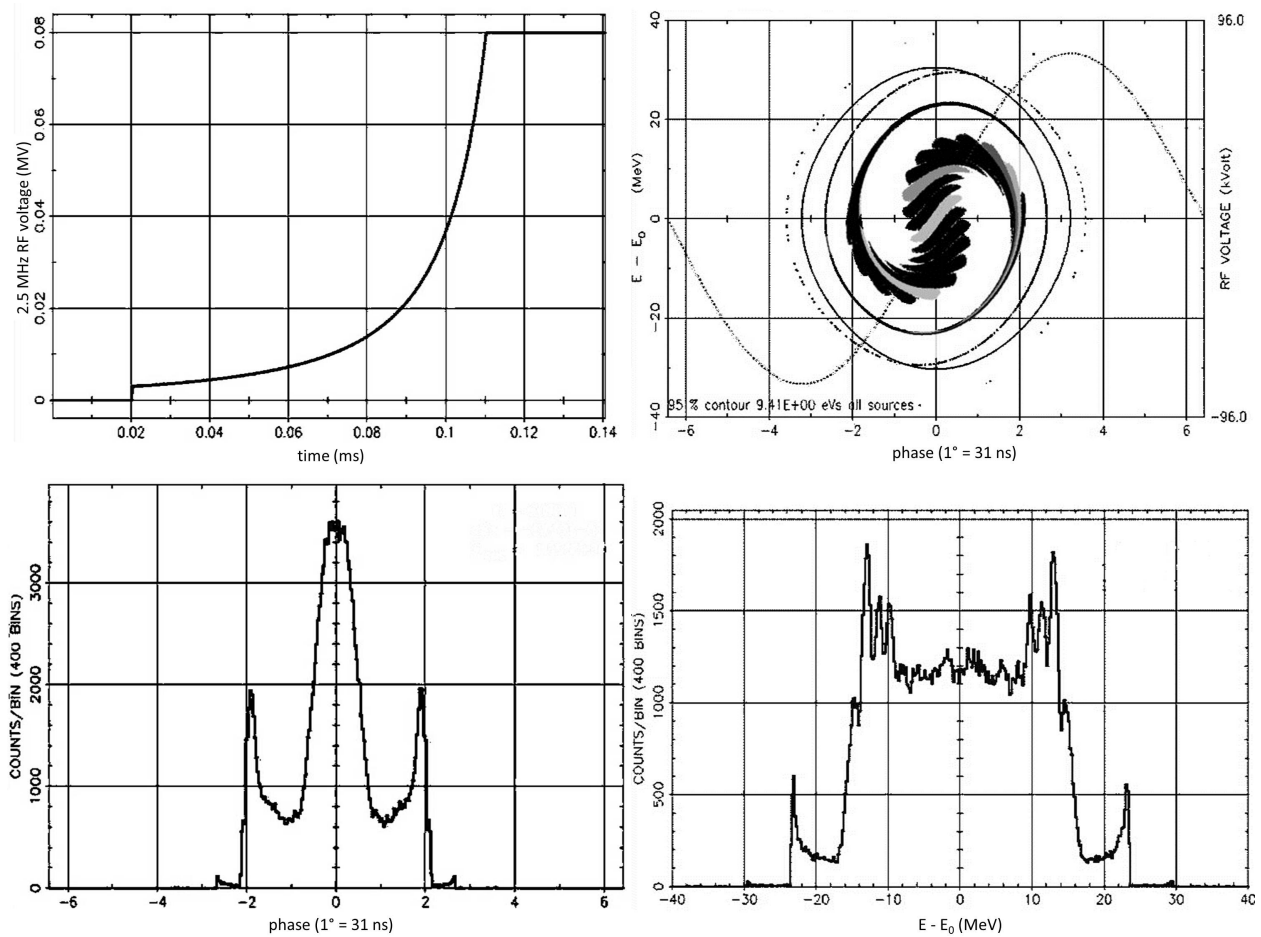


Figure 7.5: Results of RF simulations: 2.5 MHz voltage curve (upper left), phase space distribution (upper right), phase projection (lower left) and momentum projection (lower right).

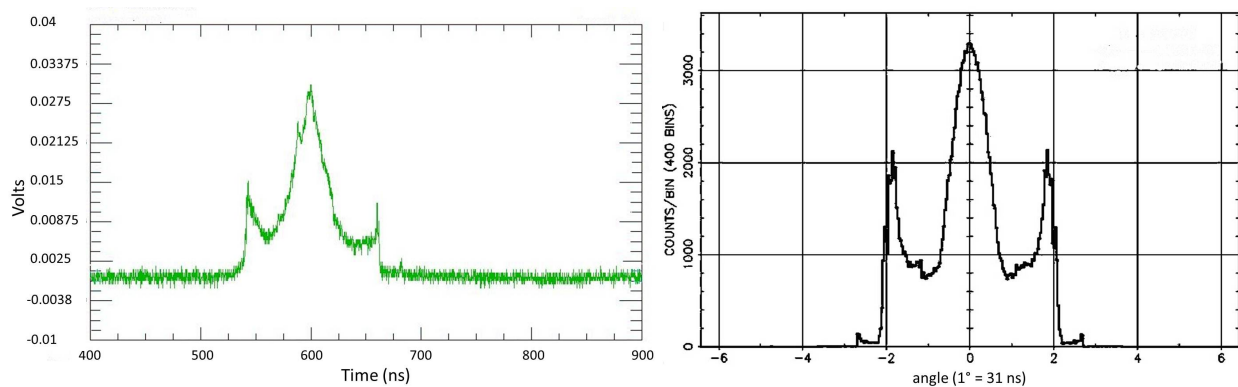


Figure 7.6: Comparison of beam profile (left) with simulation (right) for the case in which the 2.5 MHz voltage is ramped “adiabatically” from 3-70 kV in 90 ms. In both profiles, 95% of the particles captured are contained within 120 ns.

2557 ($g - 2$) target system can be found in Table 7.2.

Parameter	FNAL ($g - 2$) 12 Hz
Intensity per pulse	10^{12} p
Total POT per cycle	16×10^{12} p
Number of pulses per cycle	16
Cycle length	1.33 s
Primary energy	8.89 GeV
Secondary energy	3.1 GeV
Beam power at target	17.2 kW
Beam size σ at target	0.15-0.30 mm
Selected particle	π^+
$ dp/p $ (PMAG selection)	10%

Table 7.2: Beam parameters for the target station.

2558 One significant difference the ($g - 2$) production target station will have from the an-
 2559 tiproton production target station is the pulse rate at which beam will be delivered to the
 2560 target station. The ($g - 2$) production rate will need to accommodate 16 pulses in 1.33 s
 2561 with a beam pulse-width of 120 ns. This is an average pulse rate of 12 Hz. The antiproton
 2562 production pulse rate routinely operated at 1 pulse in 2.2 s or 0.45 Hz. This will be a chal-
 2563 lenging factor that can drive the cost of the design since the lithium lens and pulsed magnet
 2564 will need to pulse at a significantly higher rate. Figure 7.2 shows a possible ($g - 2$) pulse
 2565 scenario for pulsed devices and timing for proton beam impinging on the target.

2566 7.4.1 The ($g - 2$) production target and optimization of production

2567
 2568 The current default target to be used for the ($g - 2$) experiment is the antiproton production
 2569 target used at the end of the Tevatron Collider Run II. This target should be able to produce
 2570 a suitable yield of approximately 10^{-5} π^+ /POT within $|dp/p| < 2\%$. This target design has
 2571 a long history of improvements for optimization and performance during the collider run.
 2572 The target is constructed of a solid Inconel 600 core and has a radius of 5.715 cm with a
 2573 typical chord length of 8.37 cm. The center of the target is bored out to allow for pressurized
 2574 air to pass from top to bottom of the target to provide internal cooling to the Inconel core.
 2575 It also has a cylindrical beryllium outer cover to keep Inconel from being sputtered onto
 2576 the lithium lens from the impinging protons. The target has a motion control system that
 2577 provides three-dimensional positioning with rotational motion capable of 1 turn in 45 s. This
 2578 target and the target motion system need no modifications or enhancements to run for the
 2579 ($g - 2$) experiment. Figure 7.8 shows a drawing and a photo of the current target.

2580 Beam tests were performed to measure the yield from this target in 2012 [3]. The in-
 2581 strumentation measured total number of charged particles and did not differentiate between
 2582 particle species. Plans are in place to repeat the test in 2013 using a Cherenkov counter to
 2583 measure the particle composition of the beam. The yield of positive 3.1-GeV secondaries

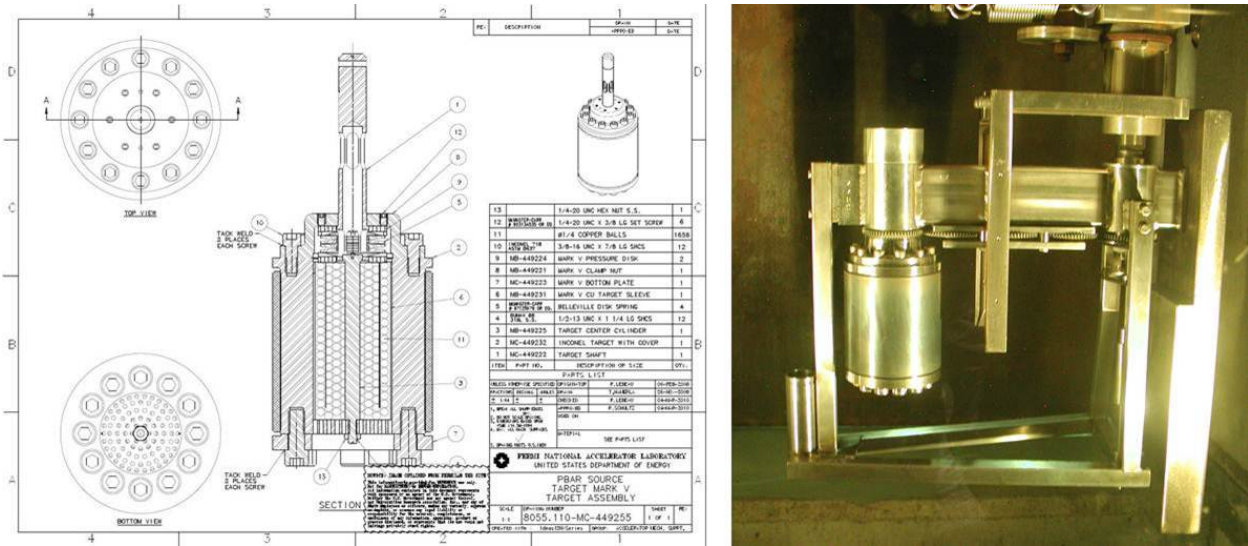


Figure 7.8: Current default target to be used for the $(g - 2)$ target station.

2584 from 10^{12} 8-GeV protons on target measured in the beam test was almost a factor of four
 2585 higher than the 2.2×10^8 particles with $|dp/p| < 10\%$ and 40π mm mr emittance predicted by
 2586 MARS [6] simulations at the beginning of the AP2 line, and was about 60-80% of the number
 2587 predicted at the end of the AP2 line with $|dp/p| < 2\%$ and 35π mm mr. Extrapolated back
 2588 to the start of the AP2 line, that prediction is 4.8×10^7 positive secondaries. The spot size
 2589 of the beam on target was $\sigma_x = \sigma_y = 0.5$ mm. As discussed later in this section and in the
 2590 beamlines section, we plan to reduce the spot size to 0.15 mm, which is expected to increase
 2591 the yield of particles with $|dp/p| < 2\%$ by 40-60%. The expected yield of positive 3.1-GeV
 2592 secondaries with $|dp/p| < 2\%$ exiting the target station will then be at least 4×10^8 , with
 2593 the simulation predicting 48% or 2×10^7 of these to be π^+ 's.

2594 Even though this target is thus expected to produce a reasonable yield of more than 10^{-5}
 2595 π^+/POT for the $(g - 2)$ experiment, considerable effort has been put into investigating a
 2596 cost-effective, practical target design optimized for 3.11 GeV pion production. Simulations
 2597 have been conducted using MARS to determine the optimal parameters, including impinging
 2598 proton spot size at the target, target material, target length and thickness, and target orien-
 2599 tation [7]. A graphical representation of the target system as implemented in the MARS15
 2600 code is shown in Fig. 7.9.

2601 The spot size of the beam on the target is an important parameter in determining the
 2602 pion yield. Initial values for the spot size were simply scaled from the $\sigma_x = \sigma_y = 0.15$ mm
 2603 size of the beam for 120 GeV antiproton production to $\sigma_x = \sigma_y = 0.55$ mm for 8.9 GeV.
 2604 Optimized results from the MARS simulations for the impinging-proton spot size can be seen
 2605 in Fig. 7.10. This plot shows the dependence of pion yield per POT on the beta function β
 2606 at half distance into the target for the current default target. A reasonable range of expected
 2607 β 's which can be achieved is from 2.5 to 3.5 cm. The simulation result demonstrates that
 2608 if the spot size is reduced from the original 0.55 mm to 0.15 mm, a 40-60% increase in pion
 2609 production can be achieved [8] depending on β . These modifications are not directly made
 2610 to the target station or target components but to the beamline just upstream of the target.

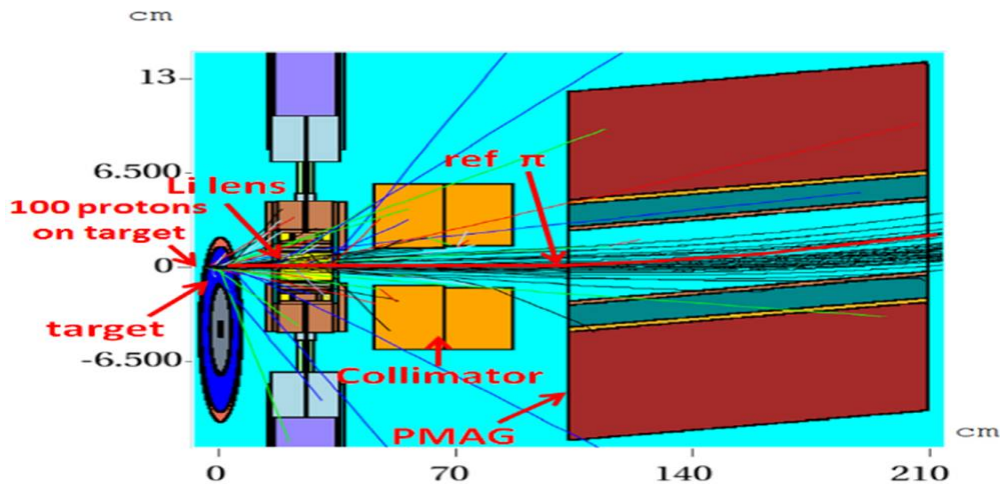


Figure 7.9: Graphical representation of target system used in MARS for simulated yield results.

2611 Details of the beamline optics incorporating this optimization for pion yield can be found in
 2612 Sec 7.5.4.

2613 Also, optimizations concerning parameters for the target material, target length, and
 2614 target width were also considered. First considered were optimizations to the target material.
 2615 Three materials were simulated: Inconel, tantalum and carbon. Figure 7.11 illustrates the
 2616 dependence of yield vs. β at the target for different materials with optimized lengths. Inconel
 2617 and carbon are shown to have higher yields than tantalum. These results, combined with
 2618 Fermilab's long history of building antiproton targets with Inconel, make Inconel the favored
 2619 target material.

2620 Next considering the dimensions of the target, Fig. 7.12a illustrates that a longer target
 2621 will produce higher yields, while Fig. 7.12b demonstrates a weak dependence on the target
 2622 thickness or radius. Therefore, the optimal pion production target may be a cylindrical rod
 2623 with a length of 89 mm and a radius of 0.6 mm. However, to favor a more practical target
 2624 design that will be able to be incorporated into the existing target mechanical and cooling
 2625 systems, horizontal slabs made of Inconel of various heights were simulated. The output of
 2626 the MARS simulation was then placed into G4beamline [9] in order to propagate particles
 2627 through the first four quadrupoles in the M2 beamline. Particles yields were tallied at the
 2628 end of these quadrupoles with appropriate acceptance cuts for the elements. Figure 7.13
 2629 shows the pion yield for two optimized horizontal slab targets one of height 0.60 mm and
 2630 the second of 0.75 mm. They are both approximately 107 mm long. Simulations for these
 2631 slab targets predict that a 22% and 14% gain in pion yield from optimized horizontal slabs
 2632 could be obtained, respectively.

2633 The actual details for the design of the alternate target are currently being worked out.
 2634 However, it is preferred that the simulated horizontal slabs transition into target discs that
 2635 could be mounted on a stacked-disc style target incorporating the simulated dimensions. In
 2636 order to provide cooling to the target material, the target discs would be separated by discs
 2637 of low Z material like beryllium or aluminum. Figure 7.14 is a picture of a proposed design
 2638 of a target incorporating stacked target and cooling discs. The blue material represents discs

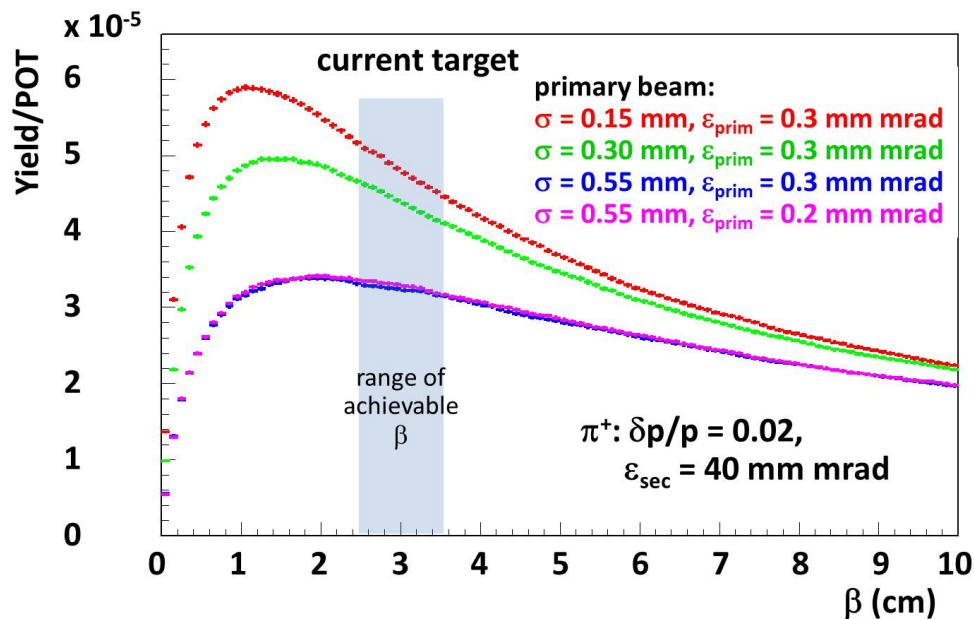


Figure 7.10: MARS simulation result for dependence of pion yield on β for different target spot sizes for a proton beam of emittance ϵ_{prim} and secondary beam momentum spread $|dp/p| = 0.02$ and emittance $\epsilon_{\text{sec}} = 40 \text{ mm mr}$.

2639 of Inconel separated by the grey shaded areas which would be beryllium. One consideration
 2640 for operating with the stacked discs that are very thin, approximately 0.6 mm, is the need for
 2641 beam stability on the target. This may require improvements in upstream trim power sup-
 2642 plies to achieve appropriate stability. A prototype stacked-disc target could be constructed
 2643 and tested with beam to narrow and confirm the design of the alternate target if the default
 2644 target is determined to be inadequate.

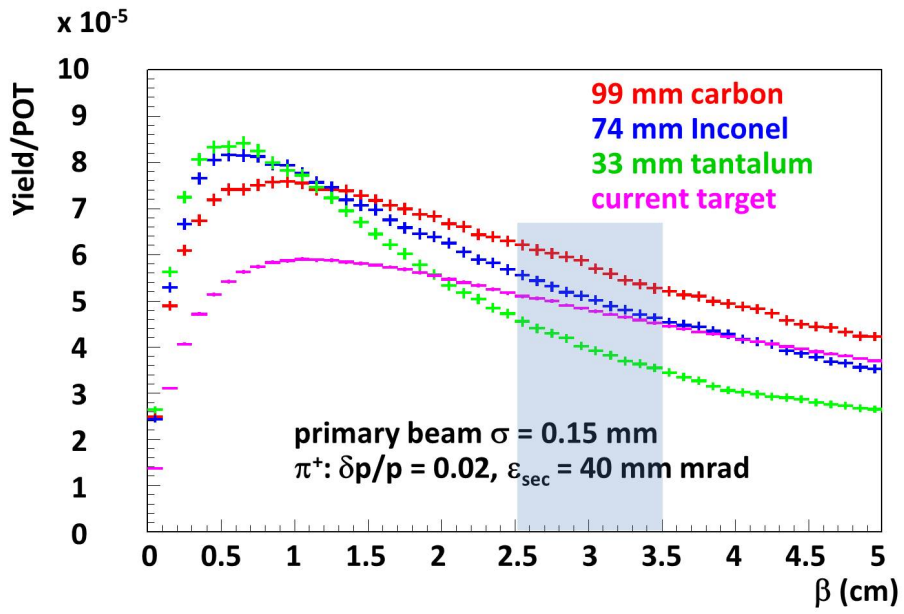


Figure 7.11: MARS simulation result for dependence of pion yield on β for different target materials. The length of the target is proportional to the interaction length of the material.

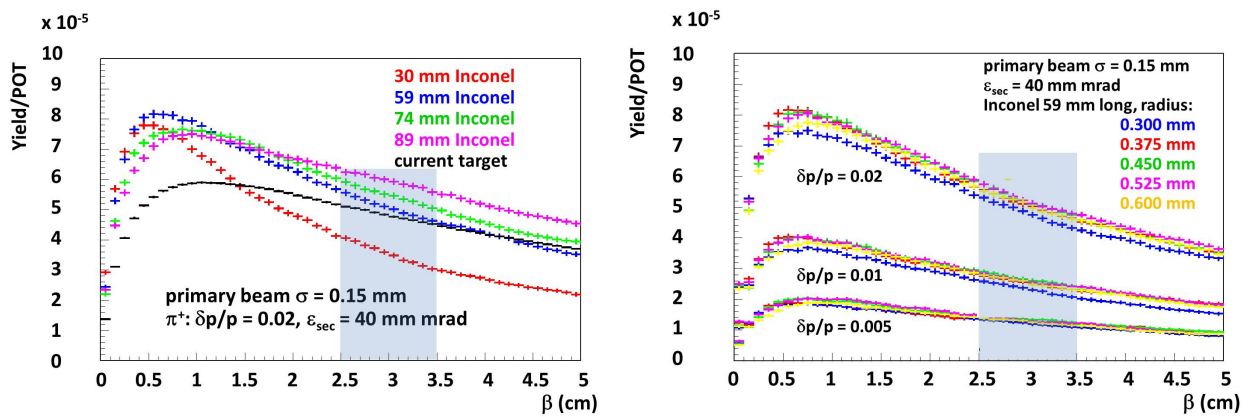


Figure 7.12: MARS simulation result for dependence of pion yield on β for different target lengths (a) and thicknesses (b).

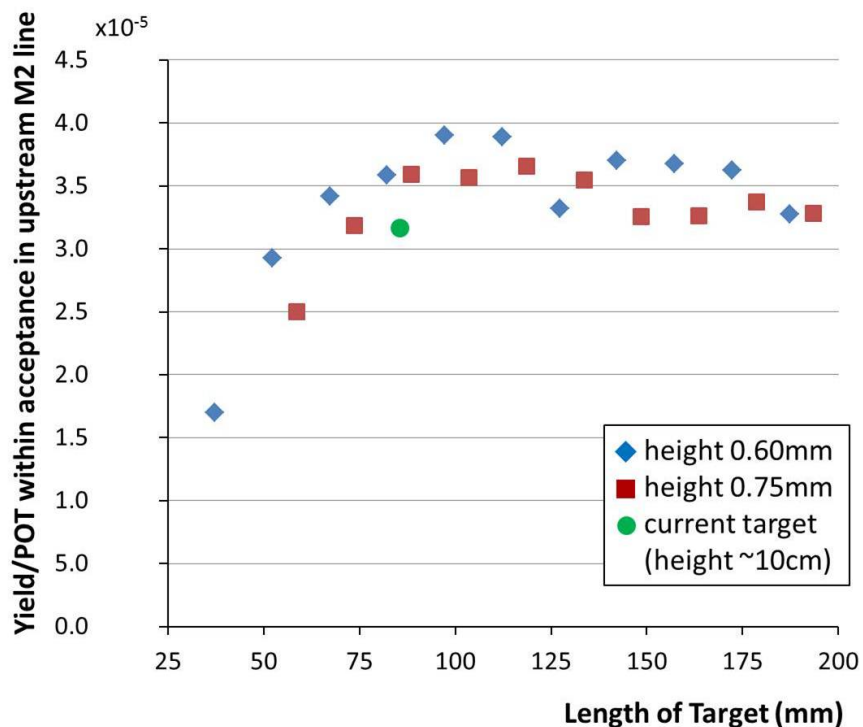


Figure 7.13: MARS/G4beamline predictions for number of pion secondaries from an Inconel target making it to the upstream M2 line as a function of target slab length for a slab of height 0.60 mm (with the upstream end of the target 56 mm from the lens focal point), a slab of height 0.75 mm (with the upstream end of the target 67 mm from the lens focal point), and the current target (assuming a chord length of 75 mm). The location of the target for a given height slab was optimized to give maximum yield. The spot size of beam on the target is taken to be 15 mm and the acceptance 40 mm mr. A thin target of length 107 mm is predicted to give an increase in yield of 14-22% over the existing target.

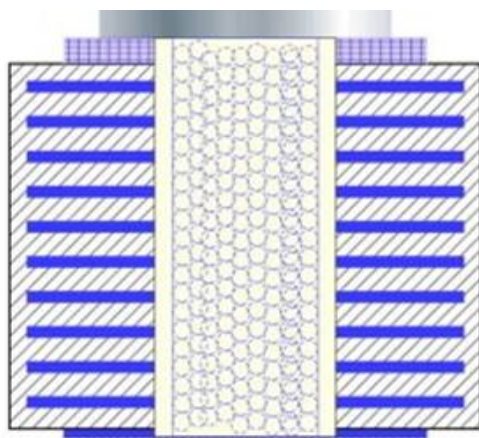


Figure 7.14: Proposal for new ($g - 2$) target design utilizing stacked thin slabs of Inconel (blue) separated by Beryllium (hashed grey). Target material air cooling channels are in the middle of the target.

2645 7.4.2 Focusing of secondaries from the target

2646 The lithium collection lens is a 1 cm radius cylinder of lithium that is 15 cm long and
 2647 carries a large current pulse that provides a strong isotropically focusing effect to divergent
 2648 incoming secondaries after the initial interaction of impinging particles with the target [10].
 2649 The lithium lens cylinder is contained within a toroidal transformer, and both lens and
 2650 transformer are water cooled. Figure 7.15 is a drawing of the lithium lens depicting (a) the
 2651 transformer and lens body, and (b) details of the lithium cylinder.

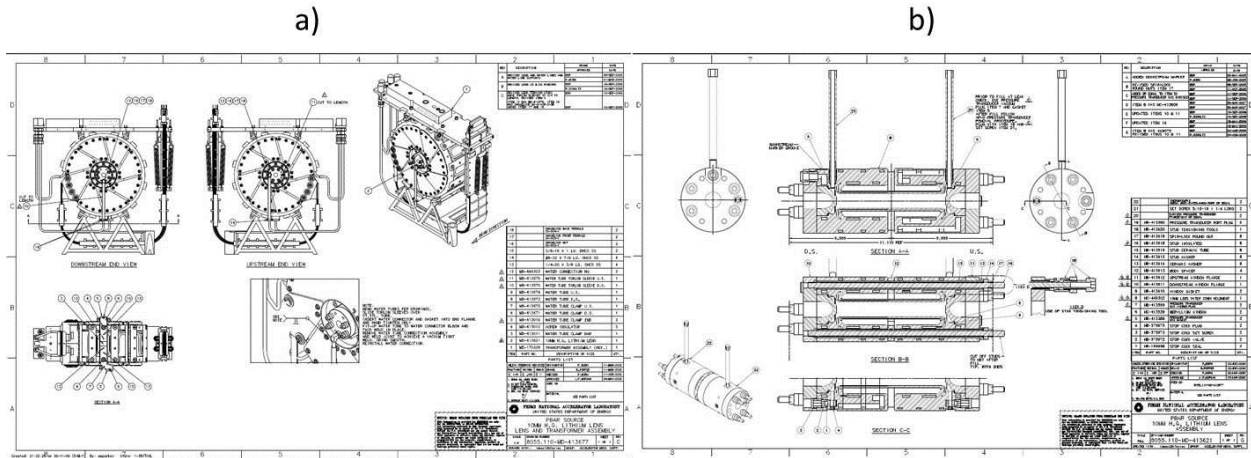


Figure 7.15: Drawing of the lithium lens and transformer (a) and the lithium cylinder body (b).

2652 During antiproton production for the Collider Run II, the lens pulsed at a peak current
 2653 of 62 kA, which is equivalent to a gradient of 670 T/m at 8.9 GeV/c with a base pulse
 2654 width of 400 μ s. Scaling the lens gradient for use at 3.11 GeV/c for $(g - 2)$ and in order
 2655 to accommodate a similar range of focal lengths from the target to the lens of roughly
 2656 28 cm, the gradient required will be 230 T/m at a pulsed peak current of 22 kA with the
 2657 same 400 μ s pulse width. Table 7.3 provides an overview of required operating parameters.
 2658 Accommodating the $(g - 2)$ 12 Hz average pulse rate for the lithium lens is one of the
 2659 biggest challenges and concerns for repurposing the antiproton target station for $(g - 2)$.
 2660 Even though peak current and gradient will be reduced by a factor of about 3, the pulse
 2661 rate will increase by a factor of 24 compared to the operation for antiproton production.
 2662 Resistive and beam heating loads, cooling capacity, and mechanical fatigue are all concerns
 2663 that are warranted for running the lithium lens at the $(g - 2)$ repetition rate.

Lens operation	Pulse width (μ s)	Peak current (kA)	Gradient (T/m)	Pulses per day
Antiproton production	400	62.0	670	38,880
$(g - 2)$ pion production	400	22.6	230	1,036,800

Table 7.3: Lithium lens operation parameters.

2664 Therefore, in order to gain confidence that the lens will be able to run under these
 2665 conditions, a preliminary ANSYS [11] analysis has been conducted. This analysis simulated

2666 thermal and mechanical fatigue for the lens based on the pulse timing scenario in Fig 7.2
 2667 and at a gradient of 230 T/m. These results were compared to results from a similar analysis
 2668 for the lens operating under the antiproton-production mode of a gradient of 670 T/m at a
 2669 pulse rate of 0.5 Hz [12]. Figure 7.16 (left) shows the ANSYS output thermal profile of a
 2670 cutaway of the lens operating at 12 Hz. The lithium body corner is a temperature-sensitive
 2671 location and should avoid lithium melting temperatures of 453.75 K. The corner temperature
 2672 reaches a maximum temperature of 376 K. The plot on the right of Fig. 7.16 is the increase in
 2673 maximum temperature of the lithium over the 16 pulses, depicting a change in temperature
 2674 of 22 K when the operating temperature has come to equilibrium. We conclude from this
 2675 analysis that the lithium lens is adequately cooled to operate at the nominal ($g - 2$) pulse
 2676 rate.

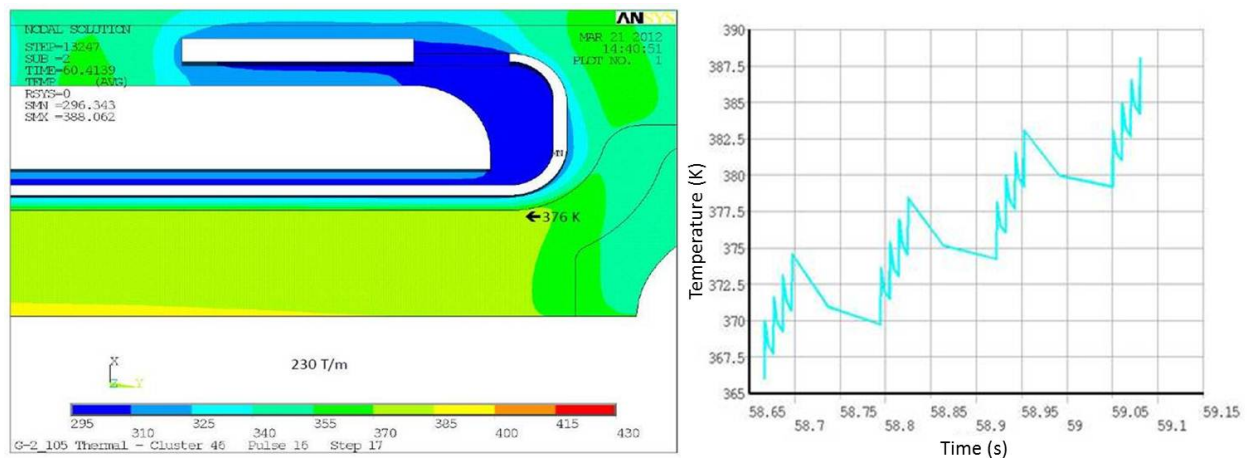


Figure 7.16: Simulated thermal profile from ANSYS for the lens operating at an average pulse rate of 12 Hz (left) depicting little beam heating and a corner temperature of 376 K. (Right) Plots showing lens temperature increase over the 16 pulses.

2677 Mechanical fatigue was also assessed for the lithium lens. Figure 7.17 depicts a constant
 2678 life fatigue plot developed for the lens from the ANSYS analysis. The two red lines represent
 2679 upper and lower estimates of fatigue limits for the lens material. The red data points
 2680 represent fatigues for gradients of 1000 T/m, 670 T/m, and two points at 230 T/m for a
 2681 preload pressure of 3800 and 2200 psi, respectively. For the lens operating in the antiproton
 2682 production conditions of 670 T/m, the mechanical fatigue was a large concern in the lens
 2683 design. It appears that for the ($g - 2$) case, the mechanical fatigue will be a comparatively
 2684 small concern.

2685 This initial assessment of the lithium lens suggests that it should be able to operate at
 2686 the ($g - 2$) repetition rate. However, since the operation of the lithium lens at the average
 2687 12 Hz rate is crucial, testing of the lens at 12 Hz is needed. The lens has been pulsed in a
 2688 test station at a 12 Hz rate in order to confirm that 1M pulses per day can be achieved and
 2689 sustained over many months. The lens has been pulsed 70 million times without problems,
 2690 and data from these tests were used to confirm predictions of the ANSYS model.

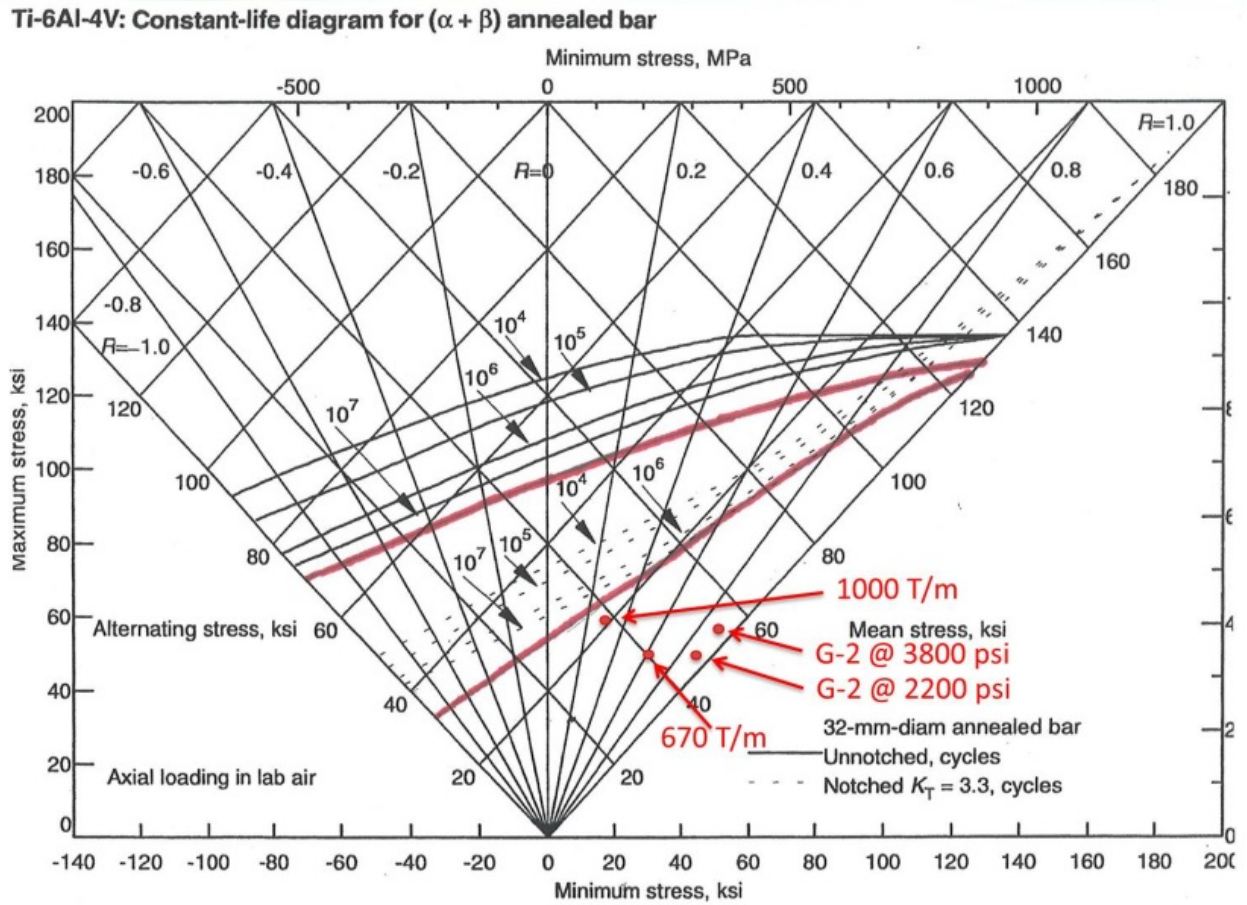


Figure 7.17: Constant-life fatigue plot of the lithium lens for antiproton and ($g - 2$) modes showing that mechanical fatigue for the ($g - 2$) pulse rate is a small concern.

2691 7.4.3 Pulsed magnet (PMAG) and collimator

2692 The pulsed magnet, shown in Fig. 7.18, selects 3.115 GeV/c positive particles and bends
 2693 them 3° into the channel that begins the M2 beamline. The magnet will operate with a
 2694 field of 0.53 T and is a 1.07 m long magnet with an aperture of 5.1 cm horizontally and
 2695 3.5 cm vertically. It is a single-turn magnet that has incorporated radiation-hard hardware
 2696 such as ceramic insulation between the magnet steel and the single conductor bars, as well
 2697 as Torlon-insulated bolts [10]. The pulsed magnet has a typical pulse width of $350 \mu\text{s}$ and
 2698 similarly to the lithium lens, will need to accommodate the $(g - 2)$ pulse rate shown in
 2699 Fig. 7.2. The pulsed magnet is water cooled. In addition to the magnet currently in the
 2700 target vault, there are three spares.

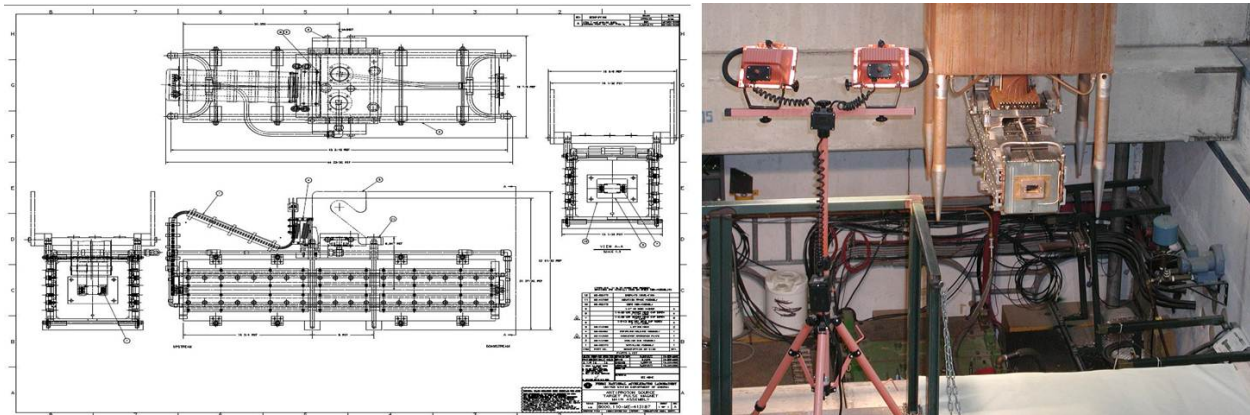


Figure 7.18: Pulsed magnet (PMAG) used for momentum-selection of pions.

2701 One initial concern regarding the pulsed magnet was that while operating in the polarity
 2702 needed to collect positive secondaries, the magnet would have an increase in energy deposited
 2703 in the downstream end of the magnet compared to antiproton production where negative
 2704 secondaries were collected. An increase in energy deposition could potentially lead to magnet
 2705 failures, and therefore running with positive polarity might require a redesign of the magnet.
 2706 A MARS simulation was conducted to look at the energy deposition across the entire pulsed
 2707 magnet compared to the antiproton production case. The simulated magnet was segmented
 2708 in order to highlight sensitive areas. The simulation concluded that although the map of
 2709 energy deposition for the positive particle polarity with 8-GeV protons on target was different
 2710 than for the antiproton production case (120-GeV protons on target), there were no locations
 2711 where the deposited energy was higher, and the total was an order of magnitude lower [13].
 2712 The negative particle polarity case was more than two times lower for 8-GeV primary beam
 2713 than for 120-GeV. Therefore a new pulsed magnet design will not be needed and the default
 2714 plan is to use the device currently installed.

2715 In order to accommodate the $(g - 2)$ pulse rate, the pulsed magnet power supply will
 2716 also need to be modified or replaced with one similar to the new supply for the lithium lens
 2717 with improved charging capability.

2718 The collimator is located directly upstream of the pulsed magnet. The purpose of the
 2719 collimator is to provide radiation shielding to the pulsed magnet to improve its longevity. It
 2720 is a water-cooled copper cylinder 12.7 cm in diameter and 50.8 cm long. The hole through

2721 the center of the cylinder is 2.54 cm diameter at the upstream end, widening to a diameter
 2722 of 2.86 cm at the downstream end. The existing collimator is currently planned to be used
 2723 without modification.

2724 7.4.4 Target station beam dump

2725 The target-station beam dump absorbs particles which are not momentum-selected by the
 2726 pulsed dipole magnet and continue straight ahead. The location of the beam dump can be
 2727 seen in Fig. 7.19. The current beam dump has a graphite and aluminum core which is water
 2728 cooled, surrounded by an outer steel box. The graphite core is 16 cm in diameter and 2 m
 2729 in length, and is designed to handle a beam power of 80 kW [14]. The existing dump has
 2730 a known water leak that developed at the end of the collider run. Therefore, consideration
 2731 for replacing the beam dump will need to be made. The current plan is to replace the beam
 2732 dump with an updated copy of the 80 kW beam dump. The maximum beam energy load
 2733 for $(g - 2)$ would occur if $(g - 2)$ takes advantage of extra cycles, for example if the $\text{NO}\nu\text{A}$
 2734 experiment were not able to run. At a rate of 18 Hz, the beam energy load would be 25 kW,
 2735 which is easily accommodated with the current dump design.

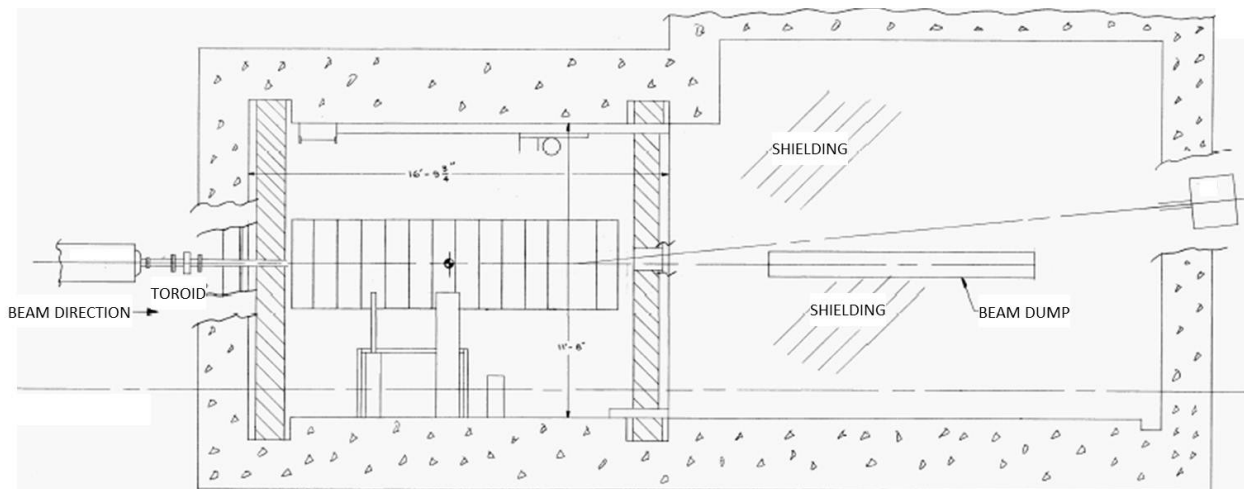


Figure 7.19: Layout of the target-station beam dump.

2736 An alternative, shorter dump was also considered and designed at an operating capacity
 2737 of 25 kW. This design resulted in a copper cylinder 2 ft long and 6 in in diameter, with
 2738 copper cooling tubes vacuum-brazed around the outside of the cylinder. The cost was found
 2739 to be similar to that of replacing the dump with a copy of the current 80-kW one.

2740 7.5 Beam Transport Lines

2741 7.5.1 Overview of $(g - 2)$ beamlines

2742 The existing tunnel enclosures and beamlines connecting the Recycler Ring to the Delivery
 2743 Ring will be largely reused for $(g - 2)$ operation. However, there are fundamental differences
 2744 between the way the Rings and beamlines were operated for Collider Operation and how
 2745 they will be used to support the Muon Campus. A high-intensity, 8 GeV kinetic energy
 2746 proton beam will be transported to the AP0 Target Station in $(g - 2)$ operation and to the
 2747 Delivery Ring for the Mu2e experiment. The increase in intensity from Collider Operation in
 2748 conjunction with the beam size of the 8 GeV beam will present challenges for efficient beam
 2749 transfer. The beamlines downstream of the AP0 Target Station will need to be reconfigured
 2750 to connect to the D30 straight section of the Delivery Ring. New extraction lines will
 2751 be constructed to transport beam from the D30 straight section to the $(g - 2)$ and Mu2e
 2752 experiments. Careful planning is required for the D30 straight section of the Delivery Ring
 2753 due to the presence of both the injection and extraction points. The extraction line will also
 2754 need to support both single-turn extraction for $(g - 2)$ and resonant extraction for Mu2e.

2755 7.5.2 Beamline Changes from Collider Operation

2756 During Pbar operation in Collider Run II, the P1 line connected to the Main Injector at
 2757 the MI 52 location. The P1 line supported operation with three different beam energies,
 2758 150 GeV for protons to the Tevatron, 120 GeV for Pbar production and SY120 operation,
 2759 and 8 GeV for protons and antiprotons to and from the Antiproton Source. (SY120 refers
 2760 to the “Switchyard” of beamlines used for the 120-GeV fixed-target program.) The junction
 2761 between the P1 and P2 lines occurs at F0 in the Tevatron enclosure. The P2 line ran at
 2762 two different beam energies, 120 GeV for antiproton production and SY120 operation and
 2763 8 GeV for protons and antiprotons to and from the Antiproton Source. The P2, P3 (for
 2764 SY120 operation), and AP1 lines join at the F17 location in the Tevatron enclosure. The
 2765 AP1 line also operated at 120 GeV and 8 GeV, but is not used for SY120 operation. The
 2766 AP3 line only runs at a kinetic energy of 8 GeV. The AP3 line connects with the AP1 line
 2767 in the Pre-Vault beam enclosure near the Target Vault and terminates at the Accumulator.

2768 After the conversion from collider to $\text{NO}\nu\text{A}$ and $(g - 2)$ operation, the Recycler will
 2769 become part of the proton transport chain and will connect directly with the Booster. There
 2770 will be a new beamline connection between the Recycler Ring and the P1 line. The P1 line
 2771 will become a dual energy line, with no further need to deliver 150 GeV protons with the
 2772 decommissioning of the Tevatron. The P2 line will continue to operate at both 8 GeV for
 2773 the Muon experiments and 120 GeV for SY120 operation. The AP2 and AP3 lines will need
 2774 to be almost completely dismantled and reconfigured to support both the transport of muon
 2775 secondaries via the Target Station for $(g - 2)$ and protons via the target bypass for Mu2e.
 2776 The $(g - 2)$ 3.1 GeV secondary beamline emanating from the Target Station and the Mu2e
 2777 8 GeV primary beamline bypassing the Target Station will merge and follow a single line
 2778 to the Delivery Ring. The new injection line will connect to the Delivery Ring in the D30
 2779 straight section. The extraction line also originates in the D30 straight section and has to
 2780 be capable of supporting both resonant and single-turn extraction.

2781 The beamlines that made up the Antiproton Source, those that have an “AP” prefix,
 2782 will be modified, reconfigured and renamed prior to $(g - 2)$ operation. The AP1 line will
 2783 only operate at an energy of 8 GeV and will be renamed M1. The AP1 line will be largely
 2784 unchanged, with the exception of the replacement of some magnets to improve aperture. The
 2785 AP2 line will become two separate beamlines and no longer be continuous. The upstream
 2786 end of the line is needed as a pion decay channel for the $(g - 2)$ experiment and will be
 2787 renamed M2. It will provide a connection from the Pbar AP0 Target Station to the M3
 2788 line. The downstream section of AP2 will become the abort and proton removal line from
 2789 the Delivery Ring. The old AP3 line will be required to transport both 8 GeV beam for the
 2790 Mu2e experiment and also a 3.1 GeV secondary beam for the $(g - 2)$ experiment and will be
 2791 renamed M3. The 18.5° right bend will be changed from a two to a three dipole configuration
 2792 in order to avoid higher beta functions in this region. The M3 line will also be modified
 2793 to connect to the Delivery Ring (formerly Debuncher) instead of the Accumulator. The
 2794 extraction line connecting the Delivery Ring to the experiments will be called M4. The M5
 2795 line will branch from the M4 line to the $(g - 2)$ storage ring in the MC-1 Building in the
 2796 “Left Bend” area. Figure 7.20 compares the Pbar beamline configuration with that proposed
 2797 for $(g - 2)$ and Mu2e operation. In general, the AP1, AP2 and AP3 lines will refer to the
 2798 old Pbar beamline configuration and M1, M2, M3, M4 and M5 will refer to the beamline
 2799 configuration for $(g - 2)$ operation.

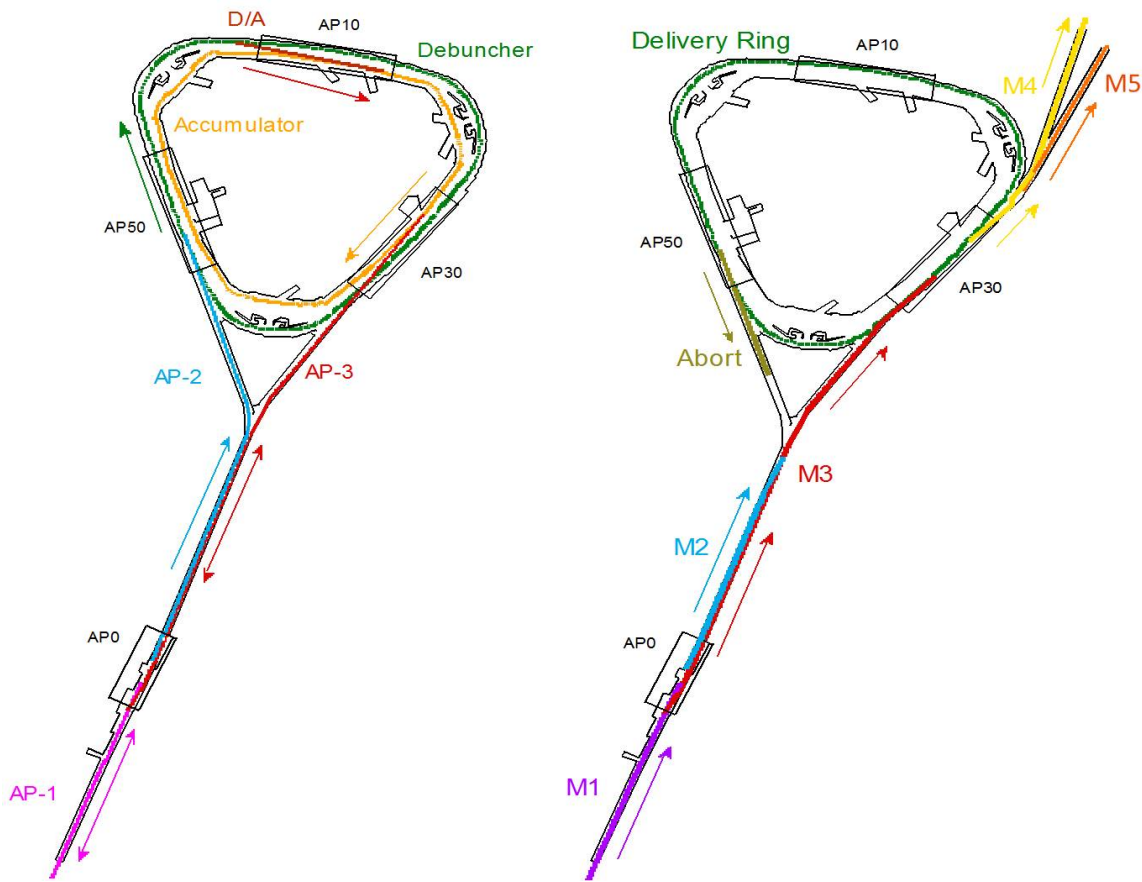


Figure 7.20: Layout of the Antiproton Source beamlines (left) and the reconfigured beamlines for $(g - 2)$ operation (right).

2800 Figure 7.21 shows another view of the Muon Campus beamlines and experimental halls.

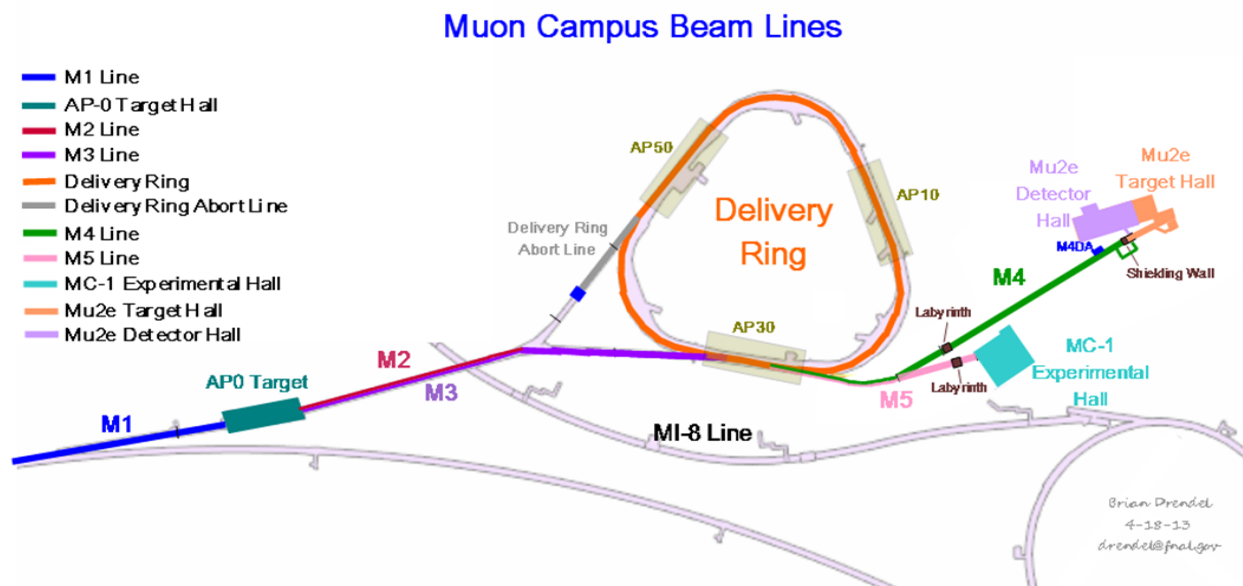


Figure 7.21: The Muon Campus beamlines and experimental halls.

2801 Most of the common improvements to the beamlines and Delivery Ring that benefit Mu2e,
 2802 ($g - 2$), and future experiments will be incorporated into several Accelerator Improvement
 2803 Projects (AIPs). They are the Recycler RF AIP, Cryo AIP, Beam Transport AIP, and
 2804 Delivery Ring AIP. The Cryo AIP provides cryogenics for the ($g - 2$) storage ring and to
 2805 the Mu2e solenoids. Table 7.4 summarizes which improvements are contained in the various
 2806 AIPs, as well as those that will be managed as part of the Mu2e and ($g - 2$) projects. Project
 2807 Managers for the various projects will work closely together to ensure they interface properly.
 2808 Virtually all of the work that is incorporated into the AIPs must be completed prior to beam
 2809 operation to ($g - 2$).

Description	Project	Comment
Cryogenics	CR AIP	
Recycler RF upgrade	RR AIP	
Recycler extraction/P1 stub line	BT AIP	
P1,P2 and M1 aperture upgrade	BT AIP	M1 final focus quadrupoles on $(g - 2)$
Reconfigure AP2 and AP3	$(g - 2)$	New lines are called M2 and M3
Final focus to AP0 Target Station	$(g - 2)$	
AP0 Target Station upgrades	$(g - 2)$	
Beam transport instrumentation	BT AIP	
Beam transport infrastructure	BT AIP	
Delivery Ring injection	DR AIP	
D30 straight section preparation	$(g - 2)$	
Delivery Ring modification	DR AIP	
DR abort/proton removal	DR AIP	
<i>Delivery Ring RF system</i>	<i>Mu2e</i>	
Delivery Ring controls	DR AIP	
Delivery Ring instrumentation	DR AIP	<i>DCCT and Tune measure are Mu2e</i>
<i>Resonant extraction from DR</i>	<i>Mu2e</i>	
Fast extraction from DR	$(g - 2)$	
Delivery Ring infrastructure	DR AIP	
Extraction line to split	$(g - 2)$	Upstream M4 line
<i>Extraction line from split to Mu2e</i>	<i>Mu2e</i>	<i>Downstream M4, including extinction</i>
Extraction line from split to $(g - 2)$	$(g - 2)$	Beamline to MC-1 building

Table 7.4: Beamline, Delivery-Ring, and other upgrades and associated project: $(g - 2)$ project, Mu2e project, Delivery Ring Accelerator Improvement Project (DR AIP), Beam Transport (BT) AIP, Recycler RF (RR) AIP, and Cryo (CR) AIP.

2810 7.5.3 Proton Beam Transport to the Target Station

2811 Beam transport of the 8 GeV primary beam from the Recycler Ring (RR) to the Target
 2812 Station closely resembles the scheme used to transport 120 GeV protons for antiproton
 2813 production in Collider operation. The most notable differences are the change in beam
 2814 energy and the switch from the Main Injector to the RR as the point of origin for the
 2815 P1 line. The beamlines will be modified to 1) provide a connection between the RR and
 2816 P1 line, 2) improve aperture to accommodate the larger beam size and intensity, and 3)
 2817 reconfigure the final focus region in order to reach the desired spot size on the production
 2818 target. Table 7.5 lists the beamlines connecting the RR with the Target Station and their
 2819 respective lengths.

Beam Line	Length (m)
RR to P1	43
P1	182
P2	212
AP1 (M1)	144
RR to Target Total	581

Table 7.5: Recycler Ring to Target beamline lengths.

2820 Recycler Ring to P1 line stub

2821 Operation of ($g - 2$) and Mu2e requires the transport of protons from the RR rather than
 2822 the Main Injector. A new transfer line from the RR to the P1 beamline will be constructed
 2823 to facilitate proton beam transport from the RR to the Delivery Ring. This new beamline
 2824 provides a way to deliver 8 GeV kinetic energy protons to the Delivery Ring, via the RR,
 2825 using existing beam transport lines and without the need for new civil construction.

2826 **Beamline Design** The P1 line is lower in elevation than the RR, thus the beam will be
 2827 extracted downward. This will be accomplished with a horizontal kicker that will displace
 2828 beam into the field region of a Lambertson magnet that will bend beam down. The kickers
 2829 are located immediately downstream of the RR 520 location and the Lambertson will be just
 2830 downstream of the RR 522 location. Due to space limitations, only two vertical bend centers
 2831 made up of the Lambertson and a dipole are used in the new line. An integer multiple of
 2832 360° in betatron phase advance between the two bending centers is required to cancel the
 2833 vertical dispersion from the bends. The new beamline needs to intercept the existing P1 line
 2834 in a location that doesn't disturb the extraction trajectory from the Main Injector, which
 2835 will be retained for SY120 operation. That junction point will be located near quadrupole
 2836 Q703. The angles of both the Lambertson and the vertical bending magnet (VBEND) were
 2837 obtained by matching the site coordinates from the RR to P1 line using TRANSPORT [15]
 2838 code. Figure 7.22 shows the layout of the new line, with the existing P1 line drawn in red.

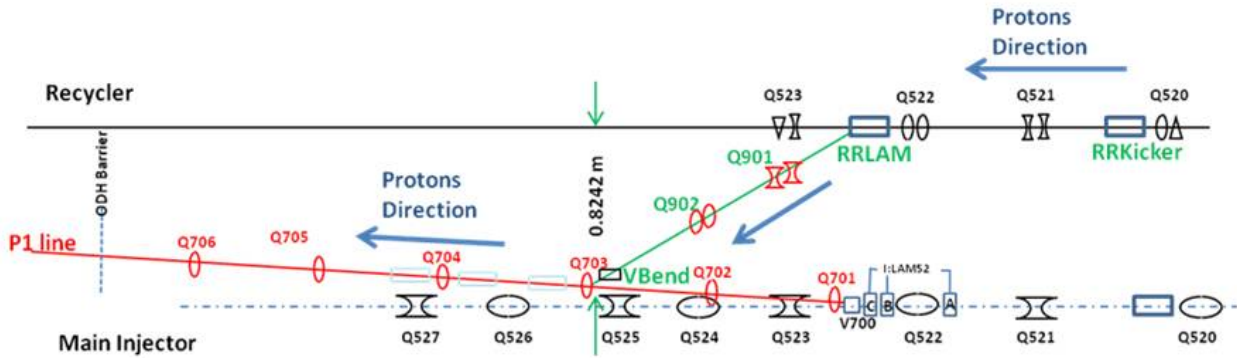


Figure 7.22: The new Recycler Ring to P1 connecting beamline.

2839 **Kickers** The $(g - 2)/\text{Mu}2e$ extraction kicker will be of the same design as the kickers
 2840 used during collider operation, but will be potted instead of using Fluorinert for electrical
 2841 insulation. The physical dimensions and properties of the kickers are listed in Table 7.6. The
 2842 plan is to reuse the ceramic vacuum chamber from old RR kicker magnets, which are slightly
 2843 smaller than the standard RR vacuum chamber. The kicker system will be made up of two
 2844 magnets producing 0.79 mr each for a total kick of 1.58 mr. The new kicker power supplies
 2845 will be located in the MI-52 service building. Power supplies for the new beamline magnets
 2846 will also be located at MI-52. This service building will be expanded to accommodate the
 2847 new power supplies.

Recycler Extraction Kicker RKB-25	
Parameter	Value
Ferrite length	46.6 in
Case length	64.0 in
Insert length	67.78 in
Print number	ME-481284
Maximum strength (each)	0.279 kG m
Maximum kick (each)	0.94 mr @ 8 GeV/c ²
Required kick (each)	0.79 mr @ 8 GeV/c ²
Rise time, 3% - 97%	140 ns

Table 7.6: RR extraction kicker parameters.

2848 **Lambertson** The Lambertson magnet will be rolled 2.7° and the vertical bend magnet
 2849 -4.0° to provide a small horizontal translation in order to create the proper horizontal tra-
 2850 jectory required to match the P1 line. The vertical dipole magnet is a 1.5 m “modified B-1”
 2851 type that will provide a 21 mr bend, matching the bend of the Lambertson. There will be two
 2852 quadrupoles located between the Lambertson and vertical dipole magnets that make up the
 2853 dogleg between the RR and P1 line. Due to space constraints, the quadrupoles are shifted
 2854 downstream from their ideal locations by 0.25 m. A more detailed technical description of

2855 the design features of the new beam line stub can be found in Ref. [16]. Figure 7.23 shows
 2856 the lattice functions for the entire RR to Target Station line.

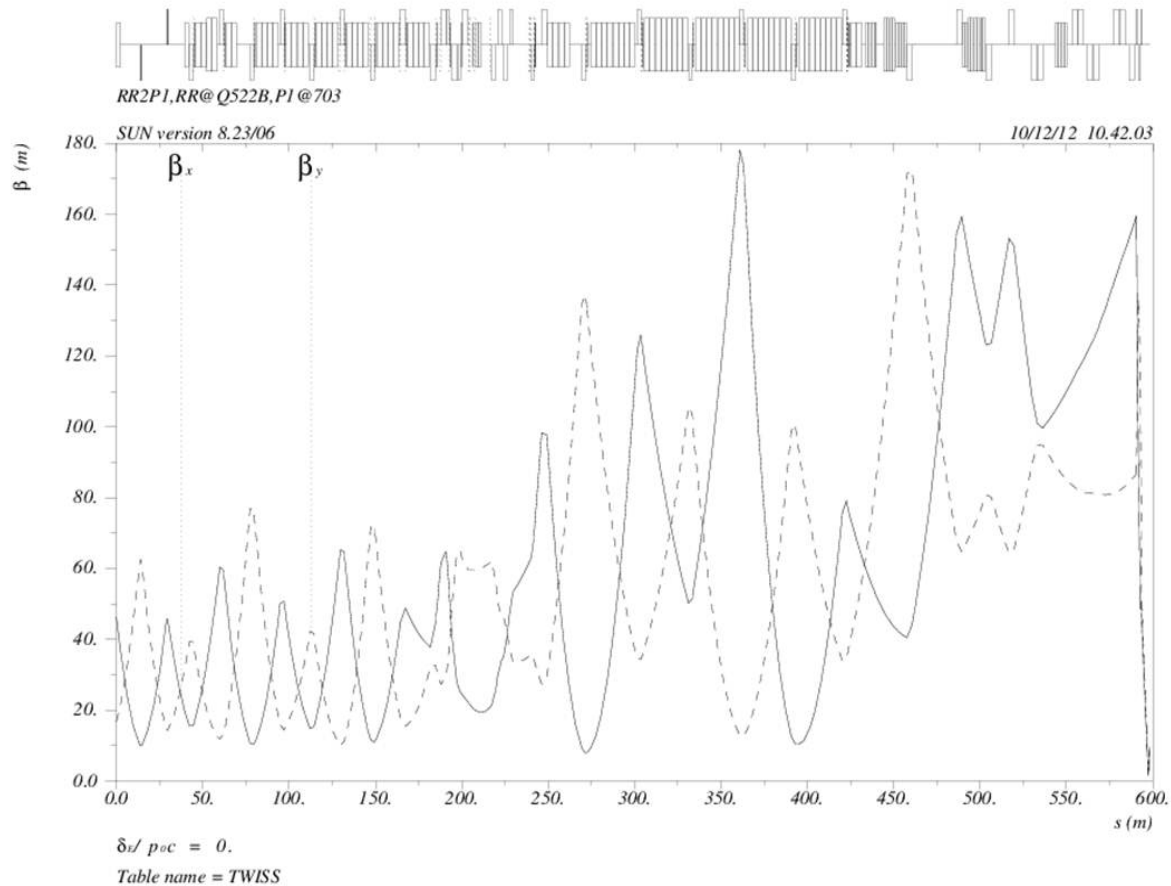


Figure 7.23: Lattice functions for primary beamlines from the Recycler to the Target Station.

2857 **Recycler orbit** The RR extraction scheme incorporates a permanent horizontal 3-bump
 2858 in the RR that displaces the circulating beam outward 25 mm at the upstream end of
 2859 the Lambertson (RLAM). Figure 7.24 shows the trajectories of the circulating and extracted
 2860 beams, including the horizontal bump at the Lambertson. The bump is created by horizontal
 2861 trim dipoles at the 524, 522 and 520 locations. The extraction kickers displace the extracted
 2862 beam inward 25 mm at the same location. This creates a separation of the RR circulating
 2863 beam and extracted beam at the front face of the Lambertson of 50 mm.

2864 **Apertures** Lambertson magnets are typically one of the limiting apertures in a beamline.
 2865 The Recycler extraction Lambertson has an adequate aperture for both the circulating and
 2866 extracted beams. Figure 7.25 shows the footprint of both beams at the Lambertson for both
 2867 a 10σ and 6σ beam size. The vertical bend magnet has a relatively small horizontal aperture,

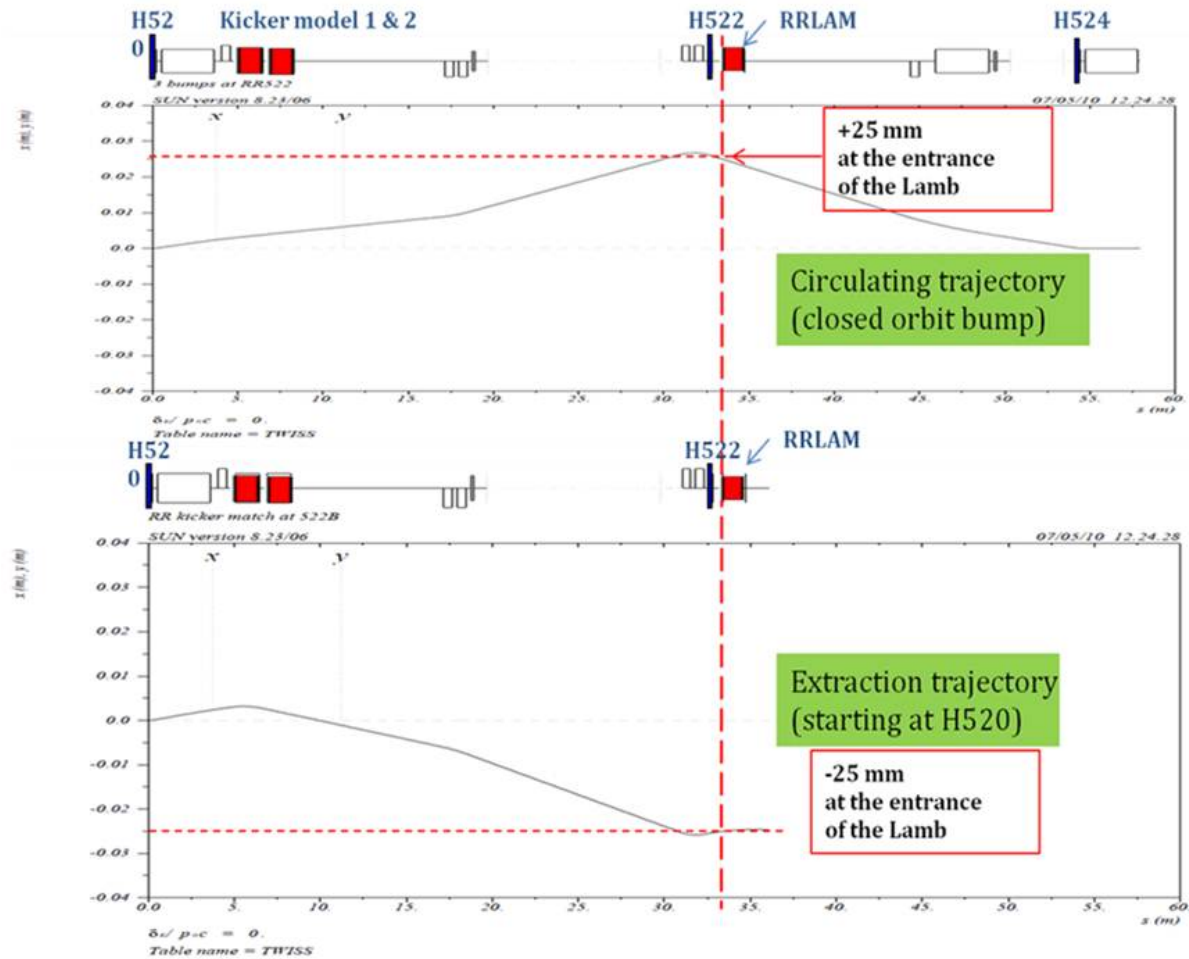


Figure 7.24: Horizontal trajectories for circulating and extracted beam from the Recycler.

2868 but is located where the horizontal beta functions are small. The horizontal acceptance of
 2869 the vertical dipole is actually larger than that of the Lambertson, despite the smaller physical
 2870 aperture. The quadrupole and trim magnets are modeled after those in the Recycler and
 2871 have good apertures.

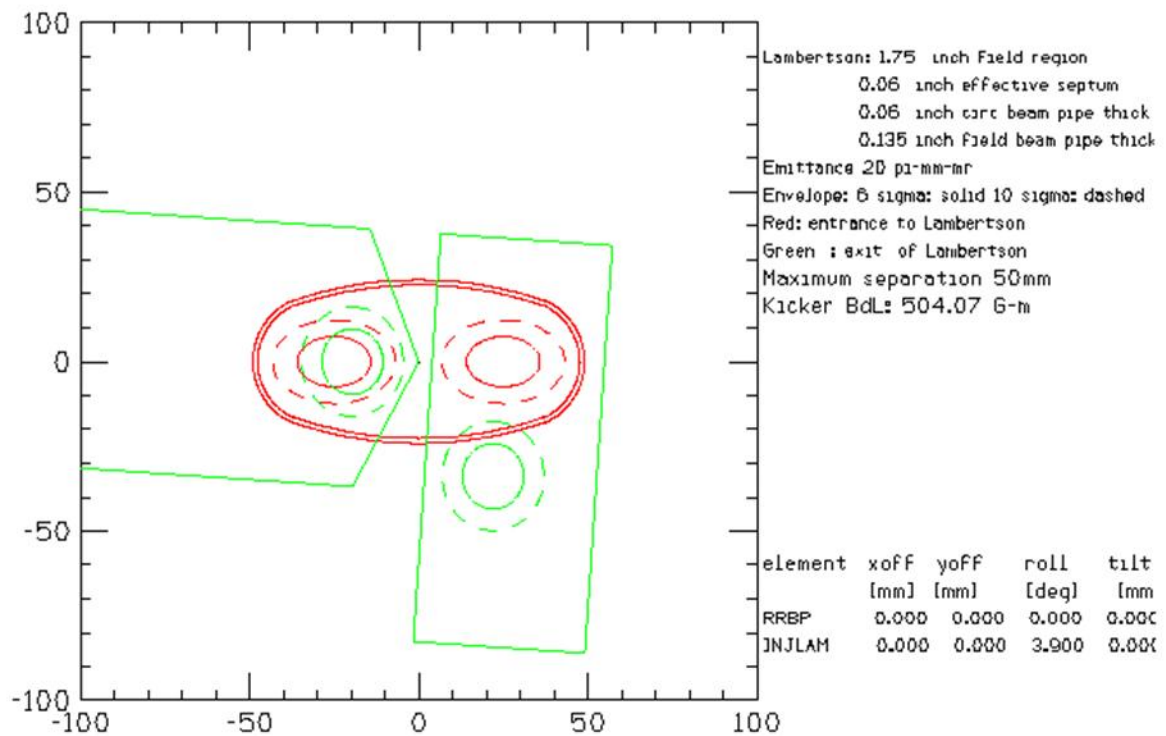


Figure 7.25: Beam sizes at the entrance (red) and exit (green) of the extraction Lambertson. The dashed outline represents 10σ and the solid outline 6σ beam for a normalized emittance of 18π -mm-mr.

2872 7.5.4 P1, P2 and AP1 Aperture Improvements

2873 The increased intensity and beam size planned for muon operation will lead to unaccept-
2874 ably high beam loss unless apertures are improved in the P1, P2 and AP1 lines. Limiting
2875 apertures were identified during Collider Run II when evaluating possible improvements,
2876 simplifying the process of identifying locations. The elimination of AP1 120 GeV opera-
2877 tion for antiproton stacking provides an opportunity to improve the aperture with weaker
2878 magnets that previously were not practical for use as replacements.

2879 The introduction of the P1-line stub has eliminated several aperture restrictions that were
2880 associated with Main Injector extraction. In particular, the vertical C-magnets that follow
2881 the MI-52 Lambertson will be avoided with the new stub line. Most of the P1 line after the
2882 P1-line stub has good aperture, until the former junction area with the Tevatron. The vertical
2883 dipole at the 714 location was installed as a C-magnet because of its proximity with the
2884 Tevatron and has a small horizontal aperture. The decommissioning of the Tevatron allows
2885 the replacement of this magnet with a conventional dipole that will increase the horizontal
2886 acceptance by more than 50%. The new magnet must also be capable of producing enough
2887 field strength to operate at 120 GeV and support SY120 operation. The four Tevatron F0
2888 Lambertsons will no longer be needed to inject protons into the Tevatron and can be removed
2889 to improve the aperture, also in the horizontal plane.

2890 In addition to the improvements to physical aperture, a new quadrupole is proposed in the
2891 region presently occupied by the Tevatron injection Lambertsons at F0. The long drift space
2892 in the P1 and P2 lines required for Tevatron injection results in large excursions in dispersion
2893 throughout the beamlines. Unless the dispersion is reduced, the increased momentum spread
2894 created by RR bunch formation will cause high beam losses. The addition of a quadrupole
2895 (or quadrupoles) in this region will provide the means to improve the optics of the transport
2896 lines.

2897 The P2 line will remain a dual-energy line supporting ($g - 2$) and SY120 operation, so
2898 the junction between the P2, AP1, and P3 beamlines at F17 will remain. The aperture for
2899 both ($g - 2$) and SY120 operation will substantially improve with the proposed replacement
2900 of the F17 C-magnets with a large aperture CDA magnet that both beams will pass through.
2901 The B-3 dipole at the F-17 location will remain.

2902 AP1 will only operate at 8 GeV for ($g - 2$) operation, so the eight EPB magnets that
2903 make up the HV100 and HV102 string can be replaced with larger-aperture, weaker dipoles.
2904 The number of dipoles can be reduced from four to two in each string. The 1.5 m “modified
2905 B-1” magnets (formally known as MDC magnets) have a pole gap that is 2.25 in instead of
2906 1.5 in and provides more than a factor of two increase in acceptance. Several trims will also
2907 be replaced or relocated to complete the aperture upgrade. The final-focus region at the
2908 end of AP1 is described separately in the next section. Table 7.7 summarizes the proposed
2909 improvements to the physical apertures in the RR to Target Station lines. Reference [16]
2910 has a more detailed explanation of the devices used to improve the aperture and how the
2911 improvements will be implemented.

Location	Existing magnet	Proposed improvement
V714	C-magnet	1 B2 magnet
F0 Lambertsons	4 Lambertsons	Remove magnets
F17 (V)	B3 and two C-magnets	1 CDA (retain B3)
HV100	4 EPB dipoles	2 MDC
HV102	4 EPB dipoles	2 MDC

Table 7.7: Proposed aperture improvements for RR to Target Station beamlines.

2912 Final Focus Region

2913 The desired spot size on the production target, a proton beam σ in both planes of 0.15 mm,
 2914 is the same as what was used in antiproton production during collider operation. Because
 2915 the beam momentum is 8.89 GeV/c for ($g - 2$) operation instead of the 120 GeV/c that
 2916 was used for antiproton production, much smaller beta functions are required to achieve this
 2917 spot size (0.068 m vs. 0.878 m, respectively). The existing quadrupole configuration in AP1
 2918 cannot produce the desired spot size and will need to be reconfigured. Figure 7.26 shows
 2919 a modified version of the scheme proposed in Ref. [17], where a quadrupole triplet replaces
 2920 the last quadrupole, PQ9B, in the AP1 line. Figure 7.26 shows the optics in the final 50 m
 2921 of the AP1 line where the final focus occurs. The quadrupoles making up the triplet need to
 2922 be as short as possible while concurrently producing a very strong integrated gradient. The
 2923 PQ8A&B and PQ9A magnets are not powered and can be removed to improve aperture, if
 2924 desired. Larger aperture NDB trim magnets from surplus Pbar inventory will replace HT107
 2925 and VT108 to provide adequate aperture.

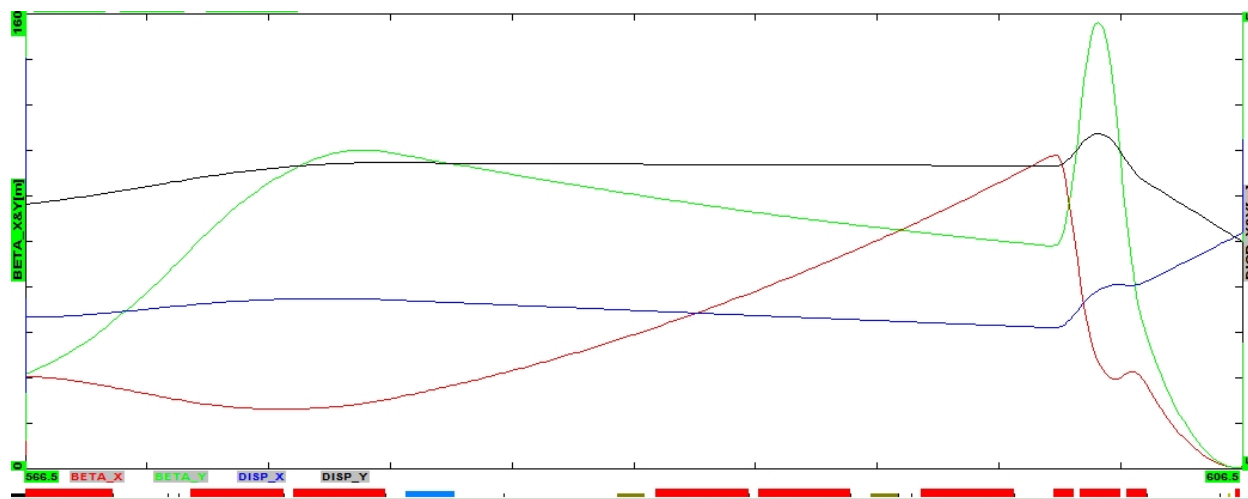


Figure 7.26: Beta functions (horizontal is red, vertical is green) and dispersion functions (horizontal is blue, vertical is black) for final focus region of AP1 line.

2926 The best compromise between maximizing integrated field, minimizing quadrupole length
 2927 and providing adequate aperture, from available magnets, is to use a triplet made of of an
 2928 SQD – SQE – SQD combination. The quadrupoles are required to run between 400 and
 2929 500 Amps in order to achieve the desired 0.15 mm spot size, which equals the highest currents

2930 these types of magnets have ever operated at. The temperature and flow of Low Conductivity
2931 Water (LCW) through these magnets will be particularly critical and may necessitate the
2932 construction of a dedicated closed-loop LCW system to prevent problems from overheating.
2933 The SQE magnet in the middle of the triplet is the strongest Pbar quadrupole available and
2934 operates at the highest current of the triplet quadrupoles (490 Amps).

7.5.5 Pion to muon decay beamlines

The M2 and M3 lines are designed to capture as many magic-momentum muons from pion decay as possible. The M2 line will be rebuilt from the former AP2 line, which transports secondary beam from the target station. The M3 line, rebuilt from the former AP3 line, begins as a target-bypass which will be used by the Mu2e experiment to transport primary 8-GeV protons. For $(g - 2)$, the M2 line crosses over into the M3 line. Focusing of the secondary beam within the target station is limited by available space in the target vault. Immediately following the target station, the M2 line starts with a series of quadrupoles which then match into a regular FODO lattice.

Design layout

With the exception of a few specialized insertions, the M2 and M3 lines track the trajectories of the existing (but now defunct) AP2 and AP3 antiproton lines. The first 115.6 m of M2 downstream of the target-station lithium lens coincides with the AP2 trajectory. Pions collected from the lens are transported to and aligned parallel with the left side of the tunnel via the existing PMAG and IB1 dipoles, each of which bends the beam through 3° (52 mr). From this point, the beam travels a further 96.7 m up to, and including, the existing IQ713 AP2 quadrupole.

Through a two-step horizontal translation, the beam crosses the tunnel to merge with the incoming upstream M3 line (used by the Mu2e experiment). Each of the four horizontal bend centers in this insertion contributes 104 mr. The relatively large bends involved at each stage of this transition are driven by:

- Maintaining tight focusing quad spacing in M2 for $(g - 2)$ to capture as many magic-momentum decay muons as possible;
- Minimizing the distance in which hardware would interfere with transportation / travel down the middle of the tunnel;
- Minimizing the impact of the insertion on maintaining continuous, controlled optical properties, and;
- Providing the flexibility to convert between $(g - 2)$ and Mu2e operations without downtime to reconfigure hardware.

The last two magnets in the transition insertion act as a switch between $(g - 2)$ and Mu2e running. A large-aperture quadrupole, Q733, followed by a modified B1 dipole are both aligned with the M3 trajectory. During $(g - 2)$ operation, the beam enters the quadrupole off-axis and receives a 25 mr dipole kick. The B1 dipole provides an additional 43.6 mr to complete the merger with the M3 line. (For Mu2e operation the beam will enter the quad on-axis, and the B1 dipole is turned off).

Immediately following the transition across the aisle, a specialized insertion created by two SDB dipoles bends the trajectory through 18.5° (323 mr) to the right, aligning with the existing AP3 path in the tunnel. The beam continues for 63.0 m to the beginning of the geometric and optical matching section between the M3 line and the Delivery Ring (DR) injection point in the D30 straight section.

2975 This final injection section satisfies multiple, interleaved design constraints:

- 2976 • Providing the optical match between the lattice functions of the M3 line and those of
2977 the DR;
- 2978 • A 86 mr horizontal right bend to align with the D30 straight section, and;
- 2979 • An overall 4-ft elevation drop from M3 to the DR, performed in two steps.

2980 The first step of the drop in elevation uses two SDC dipoles bending through 85 mr. The
2981 second down-bend is provided by a SDD dipole bending down at 102.7 mr.

2982 Embedded in the level beamline section between the first and second elevation step-
2983 changes, two modified B1 dipoles bend horizontally, each through 43.1 mr to align the
2984 trajectory with the D30 straight section.

2985 The final stages of injection occur entirely in the vertical plane, with the final up-bend
2986 produced by a combination of a C-magnet in the beamline, followed by a large-aperture
2987 focusing quadrupole Q303 and a DC septum in the DR. The C-magnet bends in the upward
2988 direction by 32.2 mr, and steers the beam 11.6-cm high off-axis through Q303, generating
2989 another 29.9 mr of vertical kick. The septum adds 45.0 mr of bend up. Three kicker modules
2990 upstream of quad Q202 close the trajectory onto the orbit of the Delivery Ring.

2991 Total beamline length from the face of the target-station lithium lens to mid-quad Q202
2992 in the Delivery Ring is 296 m. Parameters of the main magnets are listed in Table 7.8.

2993 Optics

2994 Optical properties of the $(g - 2)$ beamline are defined by 65 quadrupoles of the proven
2995 Fermilab SQx and LQx types, and the 4Qx series from Brookhaven. The $(g - 2)$ beamline
2996 design is comprised of distinct optical modules, as illustrated in Fig. 7.27.

- 2997 • A matching section between the lithium lens and the main body of the upstream M2
2998 lattice;
- 2999 • A periodic series of thirteen FODO cells (115.6 m);
- 3000 • An achromatic 18.5° right bend formed using a quadrupole triplet;
- 3001 • A series of six FODO cells in the M3 line, and;
- 3002 • A matching section between the M3 FODO cells and the Delivery Ring in the D30
3003 straight section.

3004 The extreme upstream end of the M2 line is unchanged from the existing AP2 magnet
3005 configuration. Pions from the production target are optically focused by the lithium lens and
3006 the existing Q701 - Q704 quadrupole triplet. The magnet series of PMAG, quad triplet, and
3007 IB1 form a horizontal achromat. The subsequent four quadrupoles are powered individually
3008 in order to perform the optical match to lattice functions of a long section of FODO cells.

3009 In the M2 line, the FODO cells are characterized by their 90° of betatron phase advance
3010 and half-cell length of 4.444 m. The half-cell length is chosen to triple the existing quadrupole

Name (#)	Type	L [m]	B [T]	tilt	G [T/m]
M2 match from lithium lens to FODO section					
	PMAG	1.029	0.05283		
Q701	SQC	0.66675			-5.5725
Q701	SQC	0.66675			+4.7126
Q702	SQC	0.66675			+4.7126
Q704	SQC	0.66675			-5.6254
	MOD B1	1.5065	0.3579		
Q705	SQC	0.66675			+6.5782
Q706	SQC	0.66675			-9.6317
Q707	SQC	0.66675			+5.3884
Q708	SQC	0.4064			+3.3203
90° FODO straight section cells Q709-Q727					
QBNL (13)	4Q24	0.6096			±5.5037
QSQC (6)	SQC	0.66675			±5.1562
M2/M3 merge and 90° FODO cells Q728-Q734					
	SDE	2.500	0.4294		
Q728	4Q24	0.6096			+5.5037
	SDC	1.524	0.3812		
Q729	4Q24	0.6096			-5.5037
	SDC	1.524	0.3232		
Q730	SQC	0.66675			+5.1562
Q731	4Q24	0.6096			-5.5037
	SDE	2.500	0.4294		
Q732	4Q24	0.6096			+5.5037
	CMAG	1.524	0.2393		
Q733	LQC	0.66675			-5.1562
	MOD B1	1.5065	0.2989		
Q734	SQC	0.66675			+5.1562
Q735	SQC	0.66675			-4.4177
Q736	SQC	0.66675			+5.1562
Q737	SQC	0.66675			-3.9445
18.5° triplet achromat					
	SDB	3.048	0.548		
Q738	SQE	1.27635			+3.3814
Q739	SQE	1.27635			-3.1351
Q740	SQE	1.27635			+3.3814
	SDB	3.048	0.548		
M3 72° FODO cells					
Q741-752 (12)	SQC	0.66675			±3.3784
match to Delivery Ring Q202					
Q753	SQC	0.66675			-3.3127
	SDC	1.524	0.576	+90°	
Q754	SQC	0.66675			+3.4055
	SDC	1.524	0.576	-90°	
Q755	SQC	0.66675			-3.2048
	MOD B1	1.5065	0.2952		
Q756	SQE	1.27635			+4.3374
Q757	SQD	0.86995			-3.8292
Q758	SQD	0.86995			-3.8292
Q759	SQE	1.27635			+4.3374
	MOD B1	1.5065	0.2952		
Q760	SQC	0.66675			-3.2856
Q761	SQC	0.66675			+4.0158
	SDD	1.6605	0.638	+90°	
Q762	4Q16	0.4064			-3.3150
Q763	4Q16	0.4064			-3.3150
	CMAG	1.524	0.218	-90°	
Delivery Ring					
Q303	LQD	0.86995			+3.0580
	SEPTUM	1.8796	0.247	-90°	
Q302	SQC	0.66675			-3.9850
Q301	SQC	0.66675			+4.0224
(3)	KICKER	1.0012	0.021	-90°	
Q202	SQC	0.66675			-3.9658

Table 7.8: Main magnet parameters of the M2 and M3 beamlines for $(g - 2)$ operation at 3.094 GeV/c.

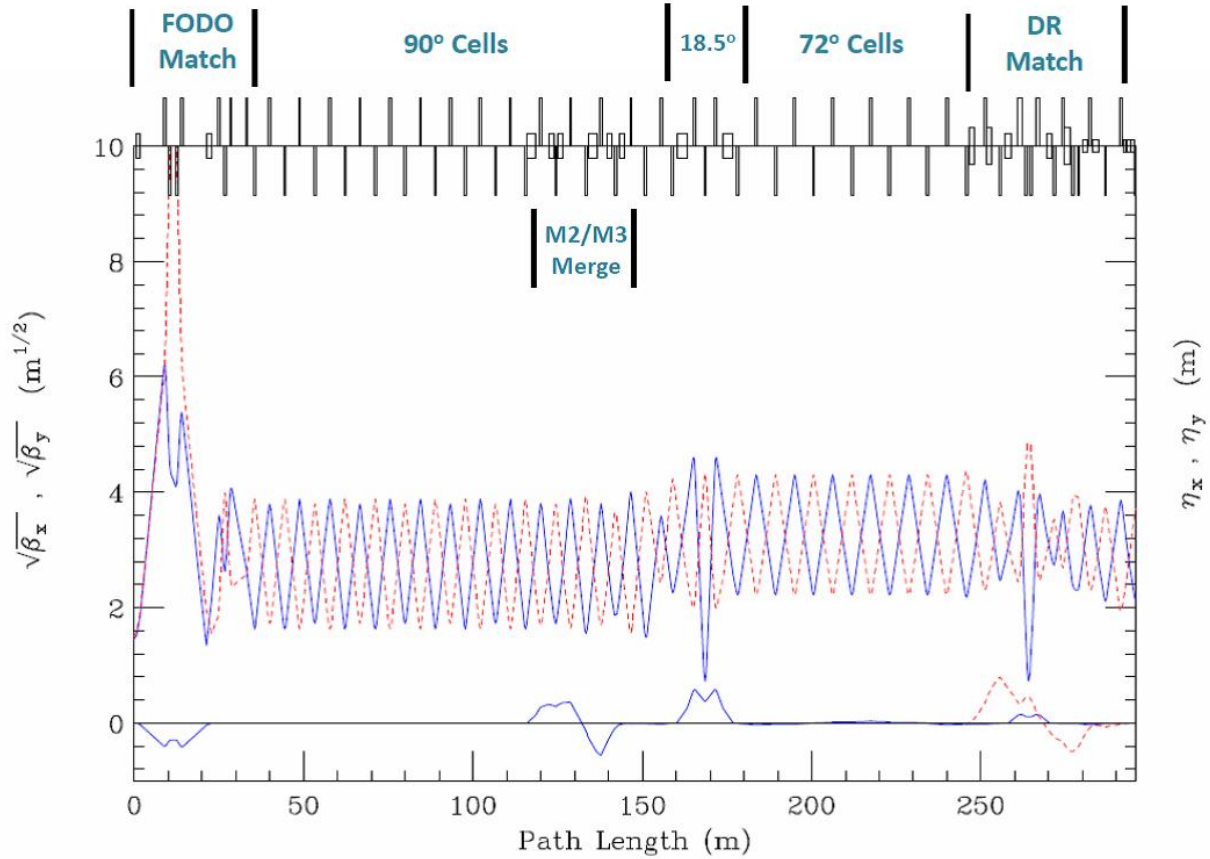


Figure 7.27: Horizontal (solid blue) and vertical (dashed red) lattice functions of the $(g - 2)$ transfer line from the face of the lithium lens to mid quad Q202 in the Delivery Ring. Boxes centered along the top axis indicate dipole locations, while boxes extending up and down are focusing and defocusing quadrupoles.

3011 density in the regularly spaced upstream portion of the M2 line. Embedded in the last four
 3012 of these cells is the two-step horizontal achromat that transitions the M2 line across the
 3013 tunnel to merge onto the M3 line trajectory (Fig. 7.28).

3014 The 18.5° horizontal bend has the two bend centers separated by a quadrupole triplet of
 3015 SQC.s to generate the 180° of betatron phase advance needed to kill the dispersion locally.

3016 M3-line FODO cells are characterized by 72° of phase advance and a half-cell length of
 3017 5.613 m. These parameters are chosen to accommodate Mu2e operation at 8.889 GeV/c.
 3018 The $\sim 25\%$ longer cell length and slightly weaker focusing than in the M2-line FODO section
 3019 relative to M3 allow the SQC quads to operate at approximately their design gradient of
 3020 9.8 T/m.

3021 The final nine quadrupoles in the line perform the optical match between the 72° FODO
 3022 cells and the Delivery Ring. This section contains an achromatic horizontal bend embedded
 3023 in an achromatic vertical descent from the M3 elevation to that of the DR. Lattice functions
 3024 and bend directions are shown in Fig. 7.29.

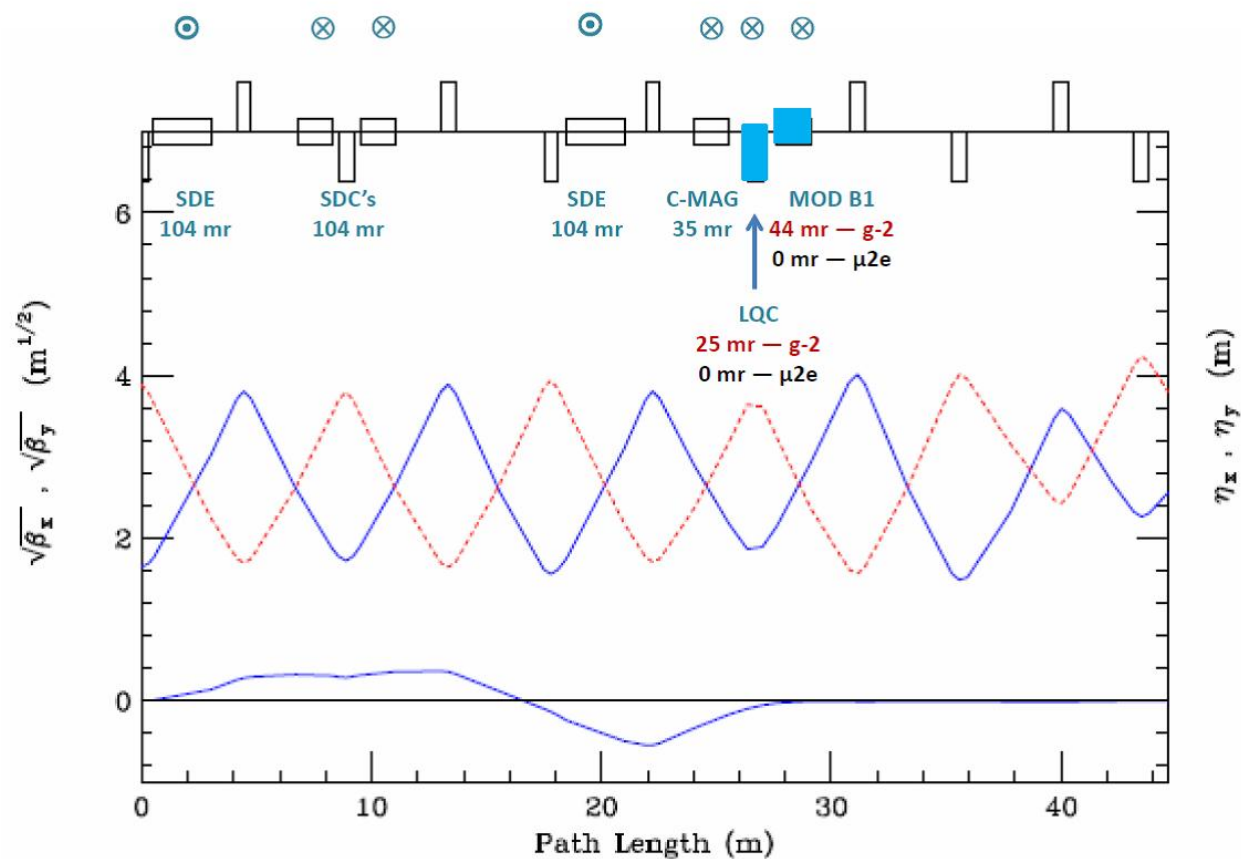


Figure 7.28: Horizontal (solid blue) and vertical (dashed red) lattice functions through the horizontal transition from the M2 line across the tunnel to merge with the M3 line. Circles shown above the upper axis indicate bend directions – those with a cross are bends left, and those with a dot are bends right. The final two (highlighted) magnets create a dipole switch between $(g - 2)$ and Mu2e operations.

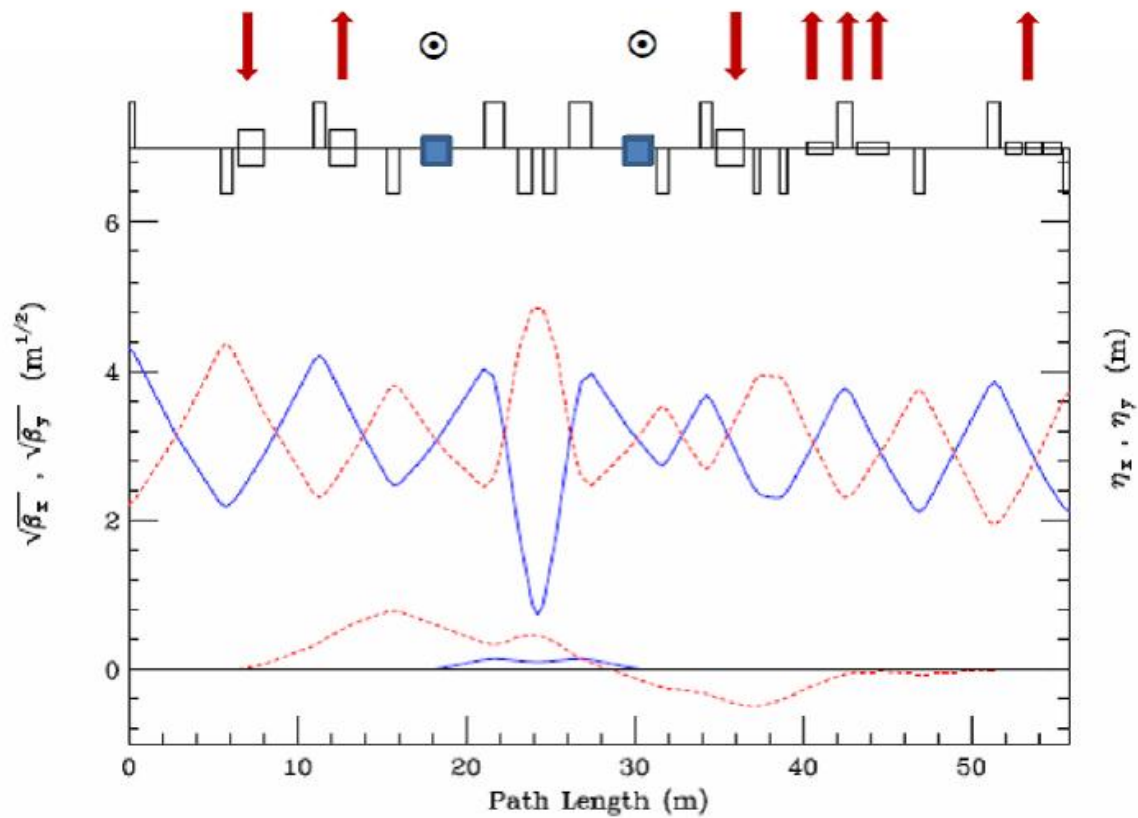


Figure 7.29: Horizontal (solid blue) and vertical (dashed red) lattice functions through the matching section from the M3 FODO cells into the DR straight. Arrows indicate the vertical bend direction in the two steps of the 4-ft drop in elevation.

7.5.6 Delivery Ring

The Pbar Debuncher ring will largely remain intact for $(g-2)$ operation and will be renamed the Delivery Ring for its new role in providing muons to the experiment. A considerable amount of equipment left over from Pbar operation will need to be removed from the Debuncher. Most of the equipment targeted for removal was used for stochastically cooling the antiproton beam during collider operation and is not needed for $(g-2)$. Some of these devices also have small apertures, so the ring acceptance will be improved with their removal. The cooling tanks in the D30 straight section also need to be removed to provide room for the new injection and extraction devices.

The Pbar Accumulator ring will not be needed for $(g-2)$ and Mu2e operation and will become a source of magnets, power supplies and other components for use in the reconfigured beamlines. In particular, the M4 (extraction) line will be largely made up of former Accumulator components. Some larger-aperture magnets will also be needed in the injection and extraction regions and will come from the Accumulator or other surplus sources.

Rings Lattice and Acceptance

The original design lattice for the Debuncher will be used for the Delivery Ring with few modifications. The lattice has a 3-fold symmetry with additional mirror symmetry in each of the three periods, with three zero-dispersion straight sections: D10, D30 and D50. The original lattice parameters were largely dictated by the requirements for Pbar stochastic cooling and the RF systems. The Debuncher was designed with a large transverse and longitudinal momentum acceptance in order to efficiently RF-debunch and stochastically cool antiprotons from the production target. This lattice design is also well suited for $(g-2)$ operation. During Collider Run II, the original lattice was distorted somewhat in order to reduce the beam size in the stochastic cooling tanks that had limiting apertures. Since these tanks will be removed, the lattice that will be used for the $(g-2)$ conceptual-design work will revert back to the original Debuncher design lattice. Figure 7.30 shows the lattice functions for one period of the Debuncher.

It should be noted that the design acceptance of the Debuncher was 20π -mm-mr. During the 25 years of Pbar operation, numerous aperture improvements were undertaken to boost the acceptance of the Debuncher. After the final Collider Run II aperture improvements were put in place in 2007, the measured acceptance of the Debuncher was as high as 33π -mm-mr in both transverse planes. The $(g-2)$ design goal of a 40π -mm-mr acceptance for the Delivery Ring, while reusing as much of the original equipment as possible, presents a difficult challenge.

The transverse acceptances of the Debuncher dipole, quadrupole, sextupole, and trim magnets are quite large. The smallest magnet acceptance is in the vertical plane of the dipoles and is approximately 54π -mm-mr on one end, growing to 79π -mm-mr on the other end. The dipoles have a 90π -mm-mr or larger horizontal acceptance (90π -mm-mr for the $\pm 2\%$ momentum spread and locations with the largest dispersion) and the other magnets have a 100π -mm-mr or larger acceptance in both planes. Since the original Debuncher lattice will not be significantly changed for $(g-2)$ operation, the main Delivery-Ring magnets will not be limiting apertures. In general, devices with a physical aperture of 50 mm or greater

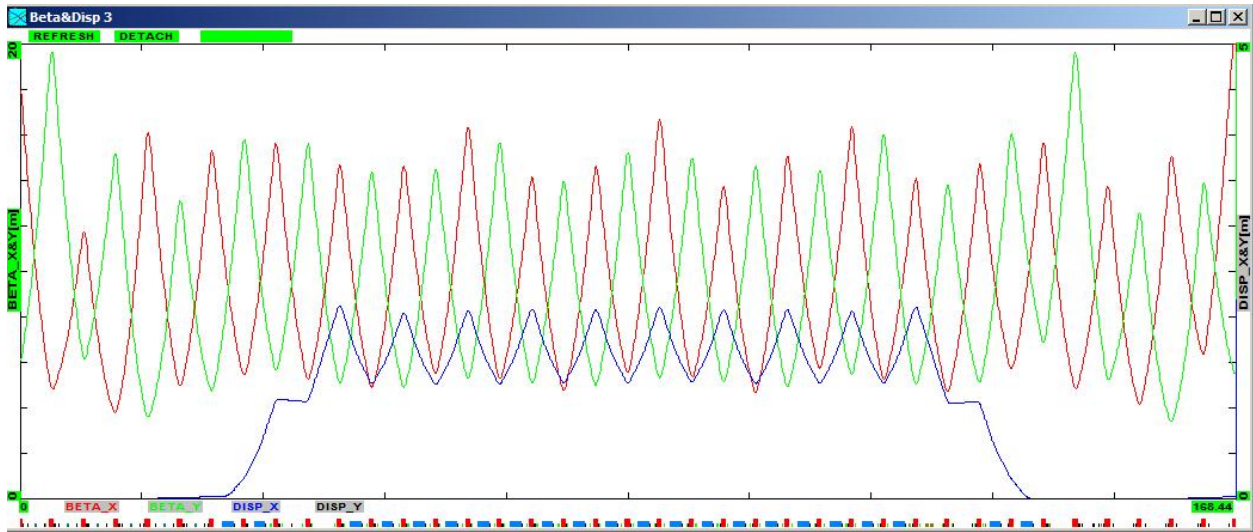


Figure 7.30: Debuncher/Delivery Ring lattice functions through 1/3 of the ring. β_x is in red, β_y in green, and horizontal dispersion in blue.

3067 provide an acceptance of over 40π -mm-mr in the Debuncher, and select locations can provide
 3068 that acceptance for devices that have an aperture of 40 mm, as long as they are relatively
 3069 short.

3070 During Collider operation, the smallest physical apertures in the Debuncher came from
 3071 stochastic cooling tanks, RF cavities, instrumentation, and devices used for injecting and
 3072 extracting beam. Many of these devices will be removed as part of the repurposing of the
 3073 Debuncher for the muon experiments. Some of these devices, most notably the kickers,
 3074 will be retained in the interest of economy and/or complexity and lead-time of manufacture.
 3075 Other devices, such as the injection septa, will be new devices with necessarily small physical
 3076 apertures in order to provide enough bend strength.

3077 During Collider Run II, the Band-4 stochastic cooling tanks were the limiting aperture
 3078 in both planes of the Debuncher. The Band-4 tanks had a 38 mm physical aperture in the
 3079 cooling plane, and there were both horizontal and vertical pick-up and kicker tanks in the
 3080 D10 and D30 straights respectively. All of the stochastic cooling tanks will be removed prior
 3081 to $(g - 2)$ operation.

3082 There is only one RF cavity planned for the Delivery Ring, which is needed to support
 3083 Mu2e operation and will have an aperture similar to the Debuncher rotator cavities. Since
 3084 the rotator cavities had an acceptance that was greater than 100π -mm-mr, the new cavity
 3085 will have ample aperture and need not be removed when switching from operating Mu2e
 3086 to $(g - 2)$. All RF cavities used for antiproton production will be removed prior to $(g - 2)$
 3087 operation.

3088 Many of the beam detectors used during Pbar operation had small physical apertures in
 3089 order to improve sensitivity. Since the beam intensities when running $(g - 2)$ are expected
 3090 to be even smaller than those seen during Pbar operation, designers will need to be mindful
 3091 of the aperture needs of the $(g - 2)$ experiment. Similarly, when instrumentation is being
 3092 considered for reuse in the Delivery Ring, the physical aperture and proposed tunnel location
 3093 should be analyzed for adequate acceptance.

3094 The transverse Schottky detectors used in the Debuncher had apertures that were only
3095 slightly larger than the Band-4 stochastic cooling pick-up. They were removed from the
3096 Debuncher during Run II, but have been reinstalled for use during ($g - 2$) and Mu2e studies.
3097 Although these Schottkys are slated for removal prior to ($g - 2$) operation, the Mu2e exper-
3098 iment may need a new device to monitor tunes during resonant extraction. If a new device
3099 is made, it will need to have adequate aperture for ($g - 2$) or will have to be removed when
3100 switching between the two experiments. The DCCT beam-intensity monitor will also be used
3101 by the Mu2e experiment. It is expected to have adequate aperture as long as it is located
3102 in the middle of a straight section half-cell, where the beam has a circular cross-section.

3103 Both injection from the M3 line and extraction to the M4 line take place in the D30
3104 straight section. Injection will be located in the upstream half of the straight section, and
3105 the pulsed magnetic septum and kicker magnets will have small apertures in order to provide
3106 adequate bending strength. The septum has a small aperture in both planes, while the kicker
3107 is primarily limited in the horizontal plane. The septum is a modified Booster-style (BSE)
3108 magnetic septum magnet. The septum modifications involve increasing the pole gap from
3109 28 mm to 42 mm in order to greatly improve the horizontal acceptance, and reducing the
3110 septum thickness from 14 mm to 9 mm to increase the vertical acceptance. The injection
3111 kicker system will be made up of two surplus Pbar AP4 injection kicker magnets. The
3112 horizontal aperture is only 41 mm and will likely be one of the limiting apertures of the
3113 Delivery Ring. The extraction kicker system will be made up of two Pbar extraction kicker
3114 magnets. They have a vertical aperture of 41 mm and will also be one of the limiting
3115 apertures of the Delivery Ring.

3116 Kickers and Septa

3117 The kickers and septa required for ($g - 2$) operation will need to operate at a much higher
3118 frequency than that used for antiproton production, with peak rates increasing as much
3119 as a factor of 30. In an effort to make the new kicker systems more economical, existing
3120 kicker magnets will be reused. Kickers will be required for injection and extraction from
3121 the Delivery Ring as well as for proton removal. Table 7.9 compares kicker parameters
3122 for existing Pbar systems to the specifications for the ($g - 2$) injection and proton-removal
3123 kickers. The rise and fall time specifications for ($g - 2$) are generally less strict than what
3124 was needed for antiproton production, due to the short bunch length of the muons (and
3125 protons). Decreasing the rise time of the proton removal kicker, however, will reduce the
3126 number of turns required in the Delivery Ring to adequately separate the protons from the
3127 muons. Although the Pbar kicker magnets are suitable for reuse, new power supplies will be
3128 needed to operate at the increased rate. Resistive loads for the kickers will need to be cooled
3129 with Fluorinert. A single Fluorinert distribution system is planned, with piping bridging the
3130 distance between the load resistors from kickers in the D30 and D50 straight sections.

3131 The septa and pulsed power supplies used during Pbar operation are not suitable for
3132 rapid cycling and cannot be used for ($g - 2$). The septa have no internal cooling to handle
3133 the increased heat load from the planned high duty cycle, and the power supplies are not able
3134 to charge quickly enough. The Booster-style septum magnets can be modified to have the
3135 necessary size and field strength required for use in the injection and proton removal systems,
3136 and therefore are the preferred choice. The power supplies used in the Booster to power the

Kicker (modules)	Integrated Field (kG-m)	Kick Angle (mr)	Rise Time 95%/5% (ns)	Fall Time 95%/5% (ns)	Flat Top Time (ns)
Debuncher Extraction (3)	1.34	4.6	150	150	1500
Debuncher Injection (3)	1.81	6.1	185	185	1500
Delivery-Ring Injection (2)	0.64	6.2	n/a	800	300
Delivery-Ring Extraction (2)	0.83	7.0	450	n/a	200
Delivery-Ring Proton Removal (3)	0.52	6.2	180	n/a	270

Table 7.9: Existing Pbar (top) and future ($g - 2$) (bottom) kicker strength and waveform specifications.

septum magnets also appear to be a good fit. Although they are designed to operate at a lower frequency (15 Hz) than the peak needed for ($g - 2$), the lower operating current (for 3.1 GeV/c versus 8.89 GeV/c momentum) should more than compensate for changes to the heat load and mechanical stresses due to the increased pulse rate. The Booster septum magnets are slightly shorter than their Pbar counterparts, so the new septa can comfortably fit between quadrupoles in the injection and proton removal regions.

3143 Delivery Ring D30 straight section

3144 The Delivery-Ring injection and extraction regions will both be located in the D30 straight
 3145 section. In both cases, the tight quadrupole spacing in the Delivery Ring creates physical
 3146 conflicts with existing utilities and ring devices in the areas of elevation change to and
 3147 from ring level. The existing cable trays on the Debuncher side of the ring will need to
 3148 be completely dismantled and relocated towards the middle of the tunnel so that the new
 3149 beamlines can be hung from the ceiling. The extraction line will closely follow the trajectory
 3150 of the decommissioned AP4 (Booster to Debuncher) line. The tunnel in this region has an
 3151 existing stub region that the extraction line will pass through, eliminating the need for civil
 3152 construction to widen and strengthen the tunnel. Figure 7.31 shows the layout of injection
 3153 and extraction devices in the D30 straight section.

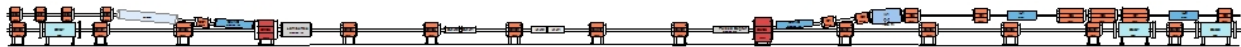


Figure 7.31: D30 straight section, injection on right, extraction on left.

3154 Injection

3155 The M3 line runs above the Delivery Ring in the upstream end of the D30 straight section
 3156 and ends with a vertical translation into the ring. M3 injection will be achieved with a
 3157 combination of a C-magnet, magnetic septum, D3Q3 quadrupole, and kicker magnets, which
 3158 will all provide vertical bends. The septum and C-magnet are both based on existing designs,
 3159 which reduces overall costs, but modified to improve the aperture. Both magnet designs
 3160 required modifications in order to attain the ($g - 2$) acceptance goal of 40π -mm-mr.

3161 The magnetic septum is a modified Booster-style (BSE) magnet, with an increased pole
 3162 gap and a thinner septum to improve aperture. The BSE magnet has a 1.1-in pole gap, which
 3163 will be increased to 1.65 in for the new septum. Similarly, the C-magnet is a larger aperture
 3164 (2.1 in instead of 1.6 in) and shorter (2.0 m instead of 3.0 m) version of the Main-Injector
 3165 ICA magnet. An identical C-magnet is used in the extraction region. The descending beam
 3166 in M3 will pass through the C-magnet first and will be bent upward by 38 mr. The beam
 3167 will continue well above the center of the D3Q3 quadrupole and receive a 30-mr upward
 3168 kick. Since the beam is up to 140 mm above the centerline of the quadrupole, a large-bore
 3169 quadrupole magnet is required in order to provide adequate aperture. The large quadrupole
 3170 at D3Q3 will be the LQE magnet from the D2Q5 location, which will be replaced by an
 3171 8-in quadrupole, as described below. The LQx magnets were designed to have a substantial
 3172 good-field region that extends between the poles. Similar arrangements with LQ magnets
 3173 can be found in Pbar at D4Q5 (former AP2 injection, planned proton removal) and D6Q6
 3174 (former Debuncher extraction). The injected beam then passes through the field region of the
 3175 septum magnet and receives a 37-mr upward bend as required for the necessary trajectory
 3176 entering the injection kicker magnets. The kicker magnets provide a final 6.2-mr vertical
 3177 bend to place the injected beam on the closed orbit of the Delivery Ring.

3178 The two-module kicker system is located between the D30Q and D2Q2 magnets. To min-
 3179 imize the horizontal β function and maximize acceptance, the kickers will be located as close
 3180 to the D2Q2 quadrupole as possible. Spare Pbar injection kicker magnets will be refurbished
 3181 and reused for muon injection. The magnets are already designed to be oriented vertically,
 3182 so little additional effort will be required to convert them to their new application. Kicker
 3183 rise and fall time specifications and power supply information was provided in Table 7.9 and
 3184 the accompanying text. Figure 7.32 shows the injection devices and their location in the
 3185 Delivery Ring, along with their bend angles. Due to the large vertical excursion through the
 3186 top of the D3Q2 magnet, a vertical bump across the injection region will be incorporated
 3187 to lower the beam and improve the aperture. The quadrupole magnets at D2Q2, D30Q and
 3188 D3Q4 will be displaced to create the bump by generating steering due to the beam passing
 3189 off-center through the magnets. To create a 15-mm downward displacement at D3Q2, the
 3190 magnets will be lowered by 8.1, 11.0, and 4.2 mm respectively. It would be beneficial, but
 3191 not necessary for 40 π -mm-mr acceptance, to install an existing “extended star chamber”
 3192 quadrupole at the D3Q2 location. SQD-312, in magnet storage, was previously located at
 3193 D4Q4 in the Pbar AP2 injection area and has an extended top lobe in its star chamber.

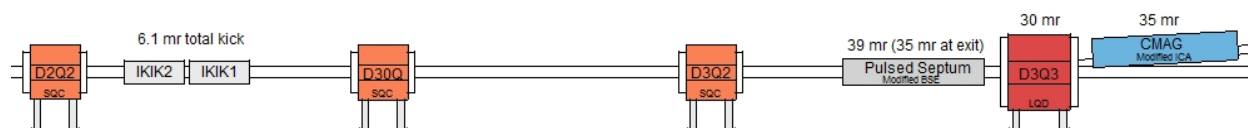


Figure 7.32: Delivery-Ring injection devices.

3194 **Extraction**

3195 Extraction from the Delivery Ring takes place in the downstream half of the D30 straight
 3196 section. The extraction channel and the first 30 m of the M4 line will be used for both
 3197 Mu2e resonant extraction and $(g - 2)$ single-turn extraction. This arrangement avoids the
 3198 complexity and additional expense of dual extraction lines in the limited available space.
 3199 It also eliminates the need to remove potentially highly radioactive objects from the ring
 3200 when switching between experiments. The ideal extraction configuration will provide enough
 3201 aperture for both the Mu2e resonantly-extracted proton beam and the $(g - 2)$ muon beam
 3202 to be transported efficiently through the M4 line.

3203 A Lambertson and C-magnet pair will be used, in conjunction with the intervening D2Q5
 3204 quadrupole, to bend the beam upward out of the Delivery Ring. In the interest of compati-
 3205 bility between $(g - 2)$, Mu2e, and future muon experiments, a Lambertson magnet is required
 3206 for extraction. The resonant-extraction process used for Mu2e is very restrictive on the size,
 3207 strength, and location of the electrostatic septa that are required to split the extracted beam.
 3208 The electrostatic septa must be located on either side of the D2Q3 quadrupole, and are ex-
 3209 pected to be about 1.5 m in length. In order to achieve the goal of a combined extraction
 3210 channel and beamline, the $(g - 2)$ extraction kickers must be located in a lattice location that
 3211 is $\sim n\pi/4$ radians from the Lambertson, where n is an integer, and in an area not already
 3212 occupied by injection or extraction devices.

3213 The $(g - 2)$ extraction kickers will be located between the D2Q2 and D2Q3 quadrupoles.
 3214 There will be two kicker modules of approximately 0.85 m length each. During the dedicated
 3215 period of $(g - 2)$ operation, the kickers will be located as close to the D2Q3 quadrupole as
 3216 possible in order to minimize the vertical β function and maximize acceptance. The kicker
 3217 magnets will be repurposed Pbar extraction kicker magnets that have a vertical aperture of
 3218 41 mm. The kicker magnets will be powered in series from a single power supply. There is also
 3219 an alternative layout planned that would allow $(g - 2)$ to operate after the Mu2e electrostatic
 3220 septa are installed. There is only room for a single kicker near the D2Q2 quadrupole in this
 3221 arrangement, so the kicker magnet would need to be modified in order to provide enough
 3222 bending strength. The relocation of the kicker would also reduce aperture unless the β
 3223 functions in this region could be suppressed by about 20%. Figure 7.33 shows the layout of
 3224 the extraction devices for dedicated $(g - 2)$ operation and 40 π -mm-mr acceptance.

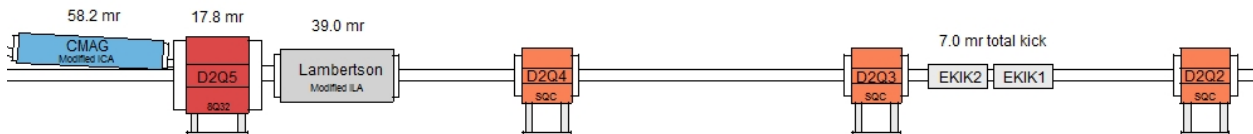


Figure 7.33: Delivery-Ring extraction devices.

3225 **Proton Removal (Abort) System**

3226 The proton removal system is an example of both repurposing an otherwise unneeded part
 3227 of the Antiproton Source and implementing a dual function system that can be used by both

3228 ($g - 2$) and Mu2e. During Mu2e operation, an abort is needed to minimize uncontrolled
 3229 proton beam loss and to “clean up” beam left at the end of resonant extraction. The proton
 3230 beam must be removed quickly, by means of kicker magnets, in order to minimize losses in
 3231 the ring. The ($g - 2$) experiment can benefit from the removal of protons before they reach
 3232 the storage ring. The abort system can serve this purpose, as long as the protons sufficiently
 3233 slip in time to create a gap for the kickers to rise through.

3234 The old Debuncher injection point from the AP2 line in the D50 straight section will
 3235 be used for the abort and proton removal systems. Recall that most of the AP2 line will
 3236 be removed and replaced with the new M2 line that will merge with the M3 line upstream
 3237 of the right bend. The downstream end of AP2, where antiprotons were formerly injected
 3238 into the Debuncher, can now be used to extract protons from the Delivery Ring. This is
 3239 made possible by the change in beam direction (as viewed from above) from clockwise to
 3240 counterclockwise. The existing Pbar injection kicker magnets can be reused, although a new
 3241 power supply will be needed to operate at the frequency needed to support Mu2e and ($g - 2$).
 3242 The septum magnet and power supply will also need to be upgraded for the same reason.
 3243 The new larger-aperture septum magnet will be identical to what was previously described
 3244 for injection into the Delivery Ring. The section of the AP2 beamline being repurposed will
 3245 require the addition of a vertical bending magnet to steer beam into the abort dump located
 3246 in the middle of the Transport tunnel. Figure 7.34 shows the layout of the abort line.

Vertical Profile of the Delivery Ring Abort Line

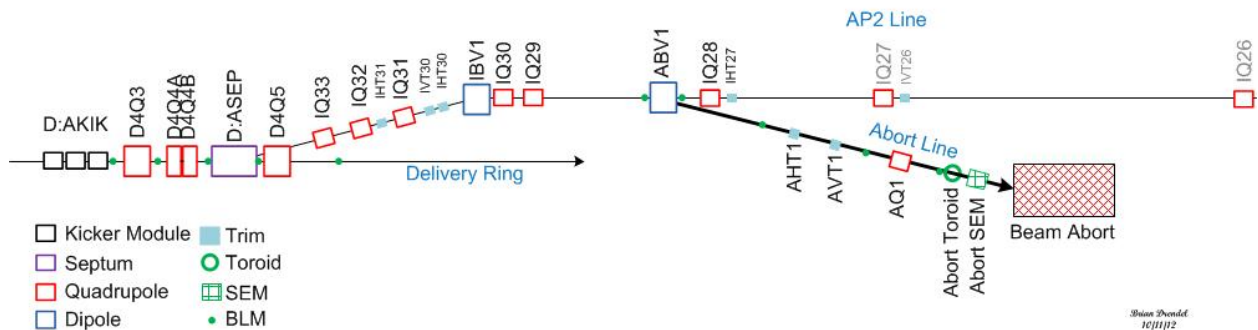


Figure 7.34: Side view of the Delivery Ring Abort/Proton Removal line.

3247 The most economical plan is to only power the first kicker magnet, which provides the
 3248 shortest rise time, a (barely) strong enough kick and requires only a single power supply.
 3249 The rise time of the kickers with this configuration is about 180 ns. The kickers will be
 3250 reconfigured for Mu2e operation, because all three kicker magnets are required to provide
 3251 enough strength due to the higher beam momentum for Mu2e. Mu2e will also need a longer
 3252 flattop to cover the entire proton revolution period of 1695 ns. For ($g - 2$) proton removal,
 3253 the 180-ns rise time requires several revolutions around the Delivery Ring to provide enough
 3254 gap between the muons and protons for the kicker to rise through. Table 7.10 lists the
 3255 separation between the beams and the gap size for different numbers of turns. Four turns
 3256 around the Delivery Ring would be required to cleanly remove all of the protons without
 3257 disturbing the muons. All of the protons could be removed in three turns, but some of the

3258 muons would also be deflected. The table is based on the assumptions already stated: that
 3259 the kicker rise time is 180 ns, the proton and muon bunch lengths are 120 ns and that the
 3260 kicker should not disturb any of the muons.

	Muon vs. Proton		Impact of proton removal kickers
	Centroid time difference (ns)	Gap size (ns)	
Injection	40	None	Unable to kick protons only
1 st turn at Abort	91	None	Unable to kick protons only
2 nd turn at Abort	161	41	25% of protons removed
3 rd turn at Abort	231	111	85% of protons removed
4 th turn at Abort	301	181	Protons cleanly removed
5 th turn at Abort	371	251	Protons cleanly removed

Table 7.10: Efficiency of proton-removal system for different number of turns in the Delivery Ring, based on a 120-ns bunch length and 180-ns kicker rise time.

3261 As the kicker magnets “fill” during the rising current waveform, the kicker magnetic
 3262 field and bending strength increase proportionally. Protons are completely removed from
 3263 the Delivery Ring when the kicker strength is about 85% of what is needed to center beam
 3264 in the abort channel. Between 85% and 100% of the nominal kicker strength, some of the
 3265 protons will be lost on the Abort Septum instead of traveling to the abort. As the kicker
 3266 strength drops below 85%, an increasing number of protons remain in the Delivery Ring. In
 3267 addition to separating the beams to improve removal efficiency, the percentage of protons
 3268 removed can also be increased by firing the kicker earlier and disturbing part of the muons.

3269 A side benefit of the muons taking multiple turns around the Delivery Ring is that
 3270 virtually all of the pions will have decayed before the muons reach the storage ring. The
 3271 primary potential problem with this proton removal concept is due to differential decay
 3272 systematic errors caused by the different muon path lengths as they travel through the
 3273 Delivery Ring. Although a preliminary analysis indicates that this will not be a significant
 3274 problem [18], a more thorough analysis is needed.

3275 Vacuum Systems

3276 The existing vacuum systems in the rings and transport lines have performed very well
 3277 during Pbar operation. Typical vacuum readings in the Debuncher and transport lines were
 3278 approximately 1×10^{-8} Torr. The Debuncher has good ion-pump coverage that should
 3279 generally be adequate for ($g - 2$) operation. Stochastic cooling tanks, kickers and septa that
 3280 will be removed during the conversion have built-in ion pumps, so some of these pumps may
 3281 need to be installed in the vacated spaces. Injection and extraction devices should have ion
 3282 pumps integrated into the design, or there should also be additional pumping capacity added
 3283 to the surrounding area. Vacuum components from the AP2 and AP3 lines should provide
 3284 most of the needs for the reconfigured M2 and M3 lines. The Accumulator has enough
 3285 surplus ion pumps and vacuum pipe available to cover part of the needs for the extraction
 3286 beamlines.

3287 **Infrastructure Improvements**

3288 Electrical power for the Antiproton Source is provided by Feeder 24, which operated with
3289 a power level of about 4.4 MW during Pbar operation. Although the $(g - 2)$ power load
3290 is expected to be considerably less than what was used in Pbar by virtue of the reduced
3291 beam momentum, the Mu2e experiment must also be able to operate the same magnets
3292 at 8.89 GeV/c. For Mu2e, most service buildings are expected to use approximately the
3293 same amount of power as they did in Pbar operation. The exception is the AP-30 service
3294 building, where there will be an increase in power load from the injection- and extraction-
3295 line power supplies. A new transformer may be needed at AP-30 to provide the additional
3296 power. A power test was performed on the individual service building transformers to aid
3297 in predicting the power needs for Mu2e [19]. Also, since the Accumulator will no longer be
3298 used, approximately 1.4 MW will be available for new loads.

3299 Presently, Pbar magnets and power supplies receive their cooling water from the Pbar 95°
3300 Low Conductivity Water (LCW) system. The cooling requirements for $(g - 2)$ are expected
3301 to be lower than for Pbar operation. However, Mu2e will operate at 8.89 GeV/c and create
3302 a substantially larger heat load than $(g - 2)$. Fortunately, the removal of the heat load from
3303 decommissioning the Accumulator and the AP2 line should be enough to offset the increase
3304 from the extraction line and other new loads. The extraction beamlines (M4 and $(g - 2)$ lines)
3305 will have an LCW stub line connecting to the Debuncher header in the D30 straight section.
3306 If necessary, it is also possible to design smaller closed-loop systems that heat-exchange with
3307 the Chilled Water system. The Chilled Water system has adequate capacity and is already
3308 distributed to the Pbar service buildings.

3309 **7.5.7 Muon transport to storage ring**

3310 A three-dimensional drawing of Delivery-Ring injection and extraction and the M4 and M5
3311 lines to the $(g - 2)$ storage ring is shown in Fig. 7.35.

3312 **Considerations**

3313 The $(g - 2)$ 3-GeV muon beam and the Mu2e 8-GeV proton beam must utilize common
3314 D30 extraction magnetic components to complete separation from the Delivery Ring, and
3315 extraction must occur vertically in order to accommodate the existing DR enclosure. The
3316 large differences in beam size and energy place difficult, sometimes conflicting, demands on
3317 the common extraction optics, especially the extraction Lambertson and vertical-bending
3318 dipoles. The civil constraints of the local geography further complicate execution of the two
3319 external beamlines.

3320 The civil constraints of the local geography for what is termed the muon campus can be
3321 deduced from Fig. 7.36. The physical separation from the Delivery Ring through an achro-
3322 matic vertical bend section (which separates and delivers beam into the external beamlines)
3323 must be followed by strong horizontal bends to direct beam to the two experiments. The
3324 length of the Mu2e beamline is limited by wetland avoidance, and the $(g - 2)$ beamline length
3325 by the storage ring / MC-1 building location. The $(g - 2)$ storage ring location is required to
3326 avoid stray magnetic fields from Mu2e components on the west and utility corridors on the

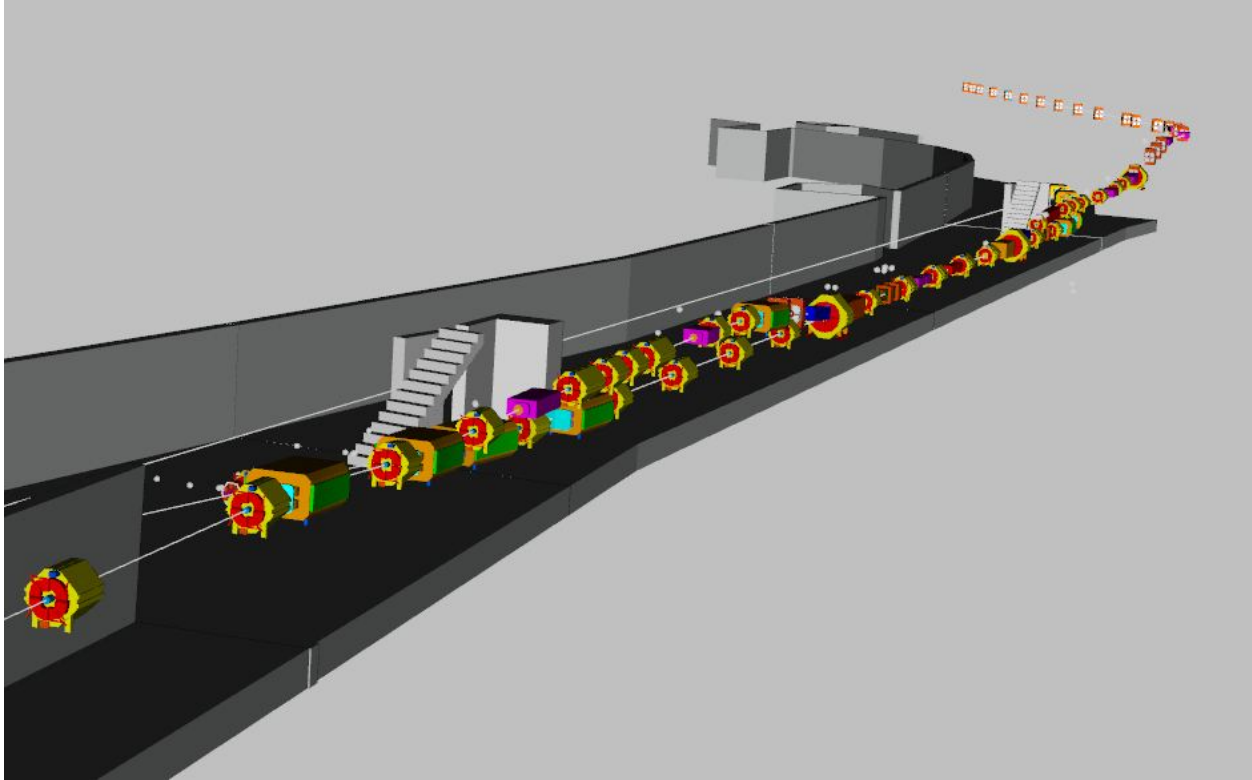


Figure 7.35: Three-dimensional view of Delivery-Ring injection (foreground) and extraction (background) and the M4 and M5 lines to the $(g - 2)$ storage ring.

3327 east. The short distance from the common extraction Lambertson to the $(g - 2)$ ring man-
 3328 dates efficient, space-conserving separation of the two external lines. Separation must first
 3329 occur vertically component-wise and then final separation utilizing a large difference in the
 3330 strengths of the left horizontal bends in the M4 and M5 lines which are vertically indepen-
 3331 dent. With no space available for a second vertical translation (and the required achromatic
 3332 conditions) the first vertical section must take the $(g - 2)$ beamline to the required elevation
 3333 for injection into the $(g - 2)$ storage ring.

3334 To appreciate the complexities of the two beamlines and $(g - 2)$ beam conditions, the
 3335 following criteria that must be addressed are listed under the criteria that dominate the line
 3336 design.

3337 Civil Layout

- 3338 • Horizontal extraction via a kicker in the D30 straight
- 3339 • Vertical separation from the Delivery Ring magnetic components (section common to
 3340 Mu2e/ $(g - 2)$ and takes advantage of existing civil construction)
- 3341 • Vertical separation from Mu2e through a reversed vertical dipole. This section cleanly
 3342 derives a separate beamline for $(g - 2)$ by changing the bend strength and polarity of
 3343 a single dipole between $(g - 2)$ and Mu2e operation. Another dipole is added to the
 3344 M5 line to level the beamline off at the storage ring elevation

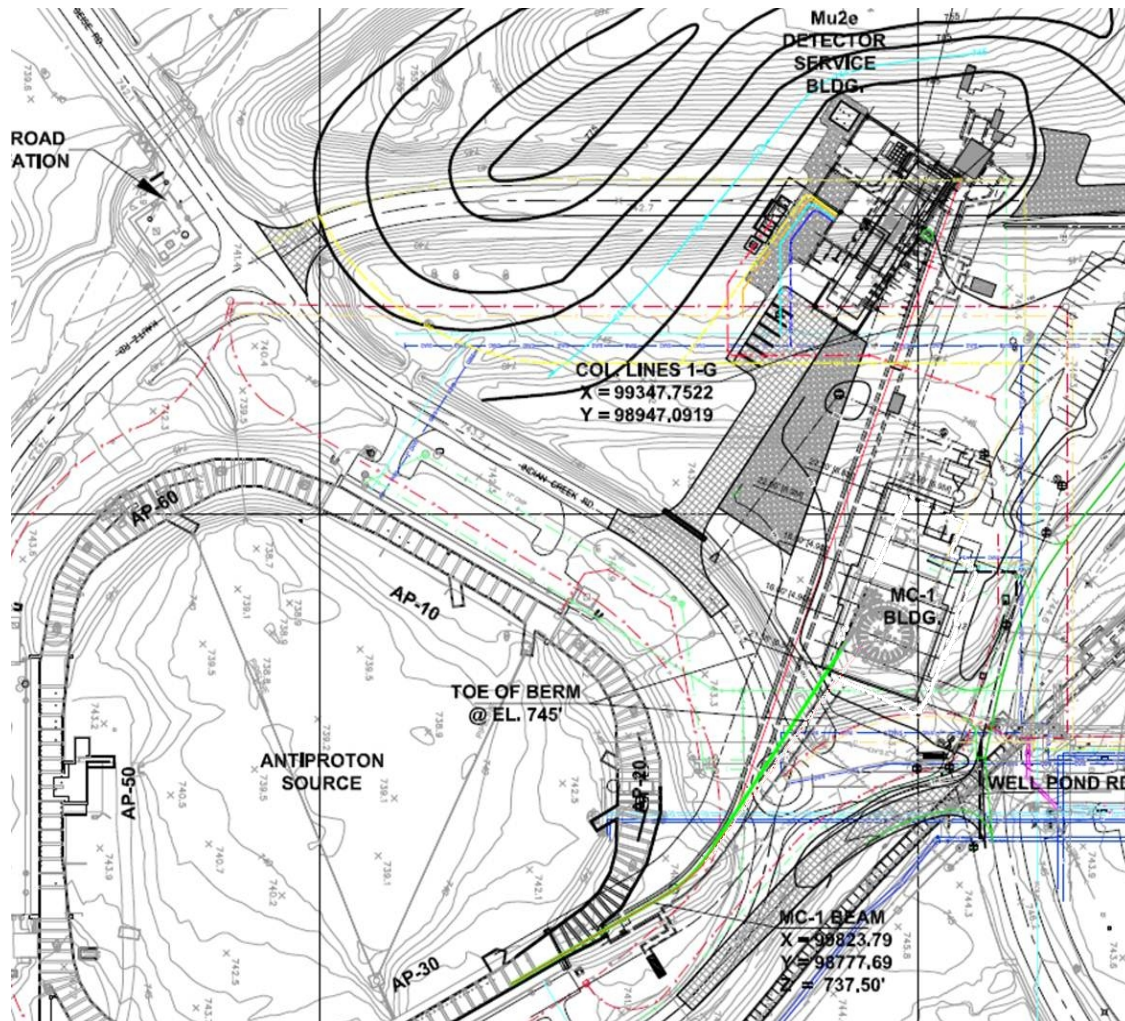


Figure 7.36: Layout of the muon campus showing the M4 and M5 external beamlines and Mu2e and ($g - 2$) experimental halls.

- 3345 • The final elevation is 50' above projected civil elevation of ($g - 2$) ring enclosure floor
- 3346 (@734.5' above sea level) or 225.1460 m and 6.3' above the Mu2e line in this region
- 3347 (@223.2243 m) and 10.3' above the Delivery Ring elevation (@222.005097 m)

- 3348 • A 26.669° horizontal bend string fixes the direction of the beamline from the D30
- 3349 straight towards the geographic location chosen for the ($g - 2$) storage ring. (Mu2e has
- 3350 a 40.5° bend). The change in bend eventually separates the two experimental beamline
- 3351 enclosures.

- 3352 • Tunable dispersion in the horizontal bend string (0-4 m)

- 3353 • A FODO cell periodic section to propagate dispersion to the ring

- 3354 • A final focus section to tune beam through the inflector to injection

3355 **Beam Properties**

- 3356 • Requested geometric acceptance of 40π mm-mr
- 3357 • Limits the beam size or beta functions to ~ 40 m through most of the line, less in some
3358 dipoles
- 3359 • Injection matching into $(g - 2)$ storage ring is strongly influenced by the inflector
3360 aperture

3361 **Beam Optics**

- 3362 • An achromat is required to suppress vertical dispersion from the D30 vertical extrac-
3363 tion to the final beamline elevation. Dispersion must be suppressed upstream of the
3364 horizontal bend string to avoid coupling between the two planes. The M5 vertical
3365 achromat is a complicated 5-bend achromat (if one includes beam passing off-center
3366 through the D2Q5 quadrupole which contributes to vertical dispersion).
- 3367 • An adjustable horizontal dispersion module is required for the 26.669° horizontal di-
3368 rectional bend string. The dispersion can be adjusted to propagate a value between 0
3369 and 4 m to the injection point of the $(g - 2)$ storage ring.
- 3370 • A periodic FODO structure is utilized to propagate either zero dispersion or a dis-
3371 persion wave to the injection point at the ring. Dispersion cannot be matched at the
3372 ring as the line cannot sustain 8 m of dispersion aperture wise. If a new inflector is
3373 built, 4 m is possible. With the existing inflector, however, zero dispersion is the only
3374 solution.
- 3375 • If a new inflector with a significant non-zero field is constructed then the line must
3376 move to the opposite side of the tunnel enclosure to match into the new injection
3377 trajectory. Another dipole would be required to aim correctly to injection.
- 3378 • At this time, momentum collimation would be difficult to incorporate in the external
3379 beamline.

3380 Civil and geographical constraints (avoidance of wetlands, for example) dictate a $\sim 27^\circ$
3381 bend after extraction from D30 to satisfy the location of experimental hall. Only ~ 80 m are
3382 available for the M5 beamline after accomplishing the vertical elevation change.

3383 **Beamline Sections**

3384 As stated above, the M5 beam line is best described in terms of its modular functionality.
 3385 Correspondingly, the following descriptions detail the important sections, and discuss the
 3386 rationale and justify the design approach for each section.

3387 **Extraction from the Delivery Ring** Incorporation of $(g - 2)$ and Mu2e extraction
 3388 systems into the D30 straight has been carefully designed. The extraction part of the straight
 3389 is considered to start at the center of D30Q (the center of the D30 straight). All quadrupoles
 3390 have been carefully and relatively aligned in the optics input deck using the alignment data
 3391 provided in Table 7.11. (This alignment data is considered so critical it has been included
 3392 for future reference.) A number of kicker and septa locations were studied and the final
 3393 location was previously described in Sec. 7.5.6.

3394 The pulsed magnetic kicker provides a +6.1 mr easterly horizontal kick (to the right
 3395 looking downstream). The downstream defocusing quadrupole – D2Q4 – enhances the effect
 3396 of the kicker and maximizes the beam separation at the entrance to a Lambertson. This
 3397 kicked beam is then tracked in coordinate space through the Lambertson and D2Q5 with an
 3398 offset relative to the Delivery Ring central reference orbit. At the entrance to the Lambert-
 3399 son, the horizontal offset generated from circulating Delivery Ring beam is ~ 49 mm. The
 3400 Lambertson is specified to be 1.5 m in length with a 0.8 T maximum field for Mu2e beam,
 3401 and is located just upstream of D2Q5 (0.4 m). It is adjusted to deliver a 40 mr upward bend
 3402 for both Mu2e and $(g - 2)$.

3403 The net bend up requires additional vertical bending which comes from two more sources.
 3404 The next focusing quadrupole (D2Q5) in the Delivery Ring acts like a combined-function
 3405 magnet and adds to the upstream Lambertson kick. (Since D2Q5 is a horizontally focusing
 3406 quadrupole, the offset of the beam vertically generates an upward kick – a kick critical to
 3407 efficient separation of the extracted beam from the Delivery Ring, adding approximately
 3408 17 mr.) Just downstream of D2Q5 a 2 m-long C-magnet with a 58 mr bend angle is planned
 3409 because a Lambertson-type magnet would have a large offset field region, but there is still
 3410 insufficient separation to insert a full dipole. The combined effect of all three vertical bends
 3411 (111.3 mr) allows beam to clear the next magnet – the last horizontally defocusing quadrupole
 3412 in the D30 straight (D2Q6). Beampipe in the extraction line clears D2Q6 by a few inches
 3413 and is 0.524 m, center to center at the upstream end. An SQA quadrupole located just
 3414 downstream of D2Q6 represents the first independent quadrupole in the M4 line.

3415 Once the beam clears the Delivery-Ring components, it can be steered onto a centered
 3416 midplane trajectory in the combined Mu2e/ $(g - 2)$ section of the M4 beamline. Steering
 3417 magnets will be strategically placed to correct for differences between the $(g - 2)$ /Mu2e and
 3418 kicker/septa forms of extraction. The exact extraction orbit depends sensitively on the D30
 3419 quadrupole strengths and these depend on the Delivery-Ring tunes established for resonant
 3420 extraction or muon beam delivery for Mu2e and $(g - 2)$, respectively. It is unlikely these
 3421 will be identical, however for the purposes here, a third-integer resonant extraction tune was
 3422 assumed for Mu2e and a lattice similar to the original Pbar design for $(g - 2)$. The relevant
 3423 quadrupole strength values used are given in Table 7.12 and translated into gradients for the
 3424 $(g - 2)$ 3.1-GeV/c beam.

3425 The initial bend upwards is so strong in order to clear the Delivery Ring, it must be

SpatialAnalyzer SA 2012.07.09			
Points Relative to Coordinate Frame 'A::WORLD:FSCS_XYZ'			
location	x (m)	y (m)	z (m)
D2Q2_CT	30454.057473	30059.297097	222.005099
D2Q2_DN	30454.224153	30059.008397	222.005110
D2Q2_UP	30453.890802	30059.585847	222.005090
D2Q3_CT	30451.839361	30063.137949	222.005506
D2Q3_DN	30452.005882	30062.849149	222.005440
D2Q3_UP	30451.672881	30063.426769	222.005623
D2Q4_CT	30449.625500	30066.971251	222.004893
D2Q4_DN	30449.792071	30066.682481	222.004852
D2Q4_UP	30449.458900	30067.260031	222.004857
D2Q5_CT	30447.409089	30070.809692	222.005368
D2Q5_DN	30447.599539	30070.479722	222.005427
D2Q5_UP	30447.218599	30071.139693	222.005331
D2Q6_CT	30445.185298	30074.661744	222.006067
D2Q6_DN	30445.383758	30074.318054	222.006104
D2Q6_UP	30444.986868	30075.005454	222.006060
D3Q2_CT	30458.488435	30051.624184	222.004533
D3Q2_DN	30458.655185	30051.335484	222.004517
D3Q2_UP	30458.321735	30051.912884	222.004549
D3Q3_CT	30460.706756	30047.782592	222.004346
D3Q3_DN	30460.873366	30047.493822	222.004355
D3Q3_UP	30460.540176	30048.071372	222.004286
D3Q4_CT	30462.920737	30043.948321	222.004030
D3Q4_DN	30463.087337	30043.659580	222.003936
D3Q4_UP	30462.754087	30044.237071	222.004097
D3Q5_CT	30465.137738	30040.108389	222.004650
D3Q5_DN	30465.336018	30039.764599	222.004633
D3Q5_UP	30464.939388	30040.452149	222.004695
D3Q6_CT	30467.357589	30036.264157	222.004381
D3Q6_DN	30467.555989	30035.920447	222.004360
D30Q_CT	30456.274864	30055.456706	222.005097
D30Q_DN	30456.441694	30055.168035	222.004878
D30Q_UP	30456.108074	30055.745346	222.005317
D2Q7_CT	30442.972467	30078.493776	222.005572
D2Q7_DN	30443.139067	30078.205036	222.005532
D2Q7_UP	30442.805817	30078.782526	222.005637
D2Q8_CT	30440.580506	30082.215658	222.004713
D2Q8_DN	30440.774006	30081.944157	222.004801
D2Q8_UP	30440.387026	30082.487128	222.004573

Table 7.11: Alignment coordinates for the D30 straight provided by the Fermilab metrology group.

Device	Magnet Type	Strength	Field	Pitch
D30q	SQC	0.385 m^{-2}	3.98 T/m	0 mr
Kicker	repurposed Debuncher	4 mr	0.028 T	0 mr
d2q2	SQC	-0.388 m^{-2}	4.01 T/m	0 mr
d2q3	SQC	0.378 m^{-2}	3.91 T/m	0 mr
d2q4	SQC	-0.370 m^{-2}	3.82 T/m	0 mr
Lambertson	new design	40 mr	0.28 T (0.79 T / Mu2e)	40 mr
d2q5	8Q32 (replaces SQD)	0.258 m^{-2} (13.3 mr)	2.67 T/m	53.3 mr

Table 7.12: Extraction components and parameters common to the Delivery Ring.

3426 leveled before the final elevation is achieved for Mu2e or ($g - 2$); otherwise it is not possible to implement a vertical achromat, which requires significant phase advance generated
 3427 by quadrupoles. Sufficient space must be allocated for a series of quadrupoles. Therefore, an EDWA dipole is installed after the first quadrupole in the subsequent D30 straight
 3428 with a bend equal and opposite to the combined bends of the Lambertsons and focusing quadrupole. Leveling the line at $\sim 32''$ above the Delivery Ring centerline provides a long
 3429 elevated “straight” (again extracted-beam center to DR-beam center) allowing an independent common extraction beamline to be installed with minimal conflicts with the Delivery
 3430 Ring line below. The only conflicts are with the extended saddle coils of the DR dipoles and these must be avoided. However, now an achromat can be formed using 4 quadrupoles.
 3431 This straight section is followed by two MDC dipoles for Mu2e beam with reverse bends (up/down) that elevate the Mu2e extracted beam to a final elevation of 1.22 m (4') above
 3432 the Delivery Ring. For ($g - 2$), three dipoles are required – the last Mu2e vertical dipole is reversed, sending the beam steeply upward to achieve rapid separation of the M5 line from
 3433 the M4 line. This rapid separation proves critical in order to position the strong horizontal bend section; otherwise the ring location would move eastward into a utility corridor. The
 3434 final elevation of the M5 line is 225.1460 m (738.6') which is 6.3' above the M4 beamline, 10.3' above the M4 beamline enclosure floor and 1.9' from the enclosure ceiling (@740.5' and
 3435 3.9' below the experimental hall ceiling).

3445 Table 7.13 lists the components and strengths for the vertical translation section common to ($g - 2$) and Mu2e, and Table 7.14 in the M5 line, including quadrupoles used to match
 3446 to the horizontal bend string.

3448 Figure 7.37 displays the achromatic optics of Delivery Ring extraction from the center of the first quadrupole upstream of the Lambertsons to the end of the achromat. These
 3449 optical functions are predicated on an assumed matched beam distribution extracted from the Delivery Ring. This is not likely to be the case, and extracted beam properties will differ
 3450 significantly between ($g - 2$) and Mu2e. Therefore it is important that the two vertical achromats have been separated between the M5 line and the M4 line and can be independently
 3451 tuned. The physical layout of this section is shown in Fig. 7.38.

Device	Magnet Type	Strength	Field	Pitch
C-magnet		58 mr	0.3T (0.86 T / Mu2e)	111.3 mr
Q1	4Q24	-0.244 m ⁻²	-2.52 T/m	111.3
D1	EDWA	-111.3 mr	0.377 T (1.08 T / Mu2e)	0 mr
Q2	SQC	0.234 m ⁻²	2.42 T/m	0 mr
Q3	SQD	-0.357 m ⁻²	-3.69 T/m	0 mr
Q4	SQD	0.311 m ⁻²	3.21 T/m	0 mr
Q5	SQD	-0.062 m ⁻²	0.64 T/m	0 mr
D2	MDC	65.5 mr	0.44 T (1.27 T / Mu2e)	65.5 mr
Q6	SQD	-0.132 m ⁻²	-1.36 T/m	65.5 mr
Q7	SQD	0.205 m ⁻²	2.12 T/m	65.5 mr
D3	MDC	94.7 mr	0.64T (-1.27 T / Mu2e)	160.2 mr

Table 7.13: Extraction components and parameters in the vertical translation section common to $(g - 2)$ and Mu2e in the M4 line. Quadrupole strengths are given for $(g - 2)$ only.

Device	Magnet Type	Strength	Field	Pitch
gQ1	4Q24	-0.339 m ⁻²	-3.51 T/m	160.2 mr
gQ2	4Q24	0.229 m ⁻²	2.37 T/m	160.2 mr
gQ3	4Q24	0.01 m ⁻²	0.087 T/m	160.2 mr
gD1	MDC	160.2 mr	1.09 T	0 mr
gQ4	4Q24	0.082 m ⁻²	0.84 T/m	0 mr
gQ5	SQA	0.073 m ⁻²	0.75 T/m	0 mr
gQ6	4Q24	0.056 m ⁻²	0.58 T/m	0 mr

Table 7.14: Components and parameters in the independent $(g - 2)$ vertical translation section in the M5 line including matching quads to the horizontal bend string.

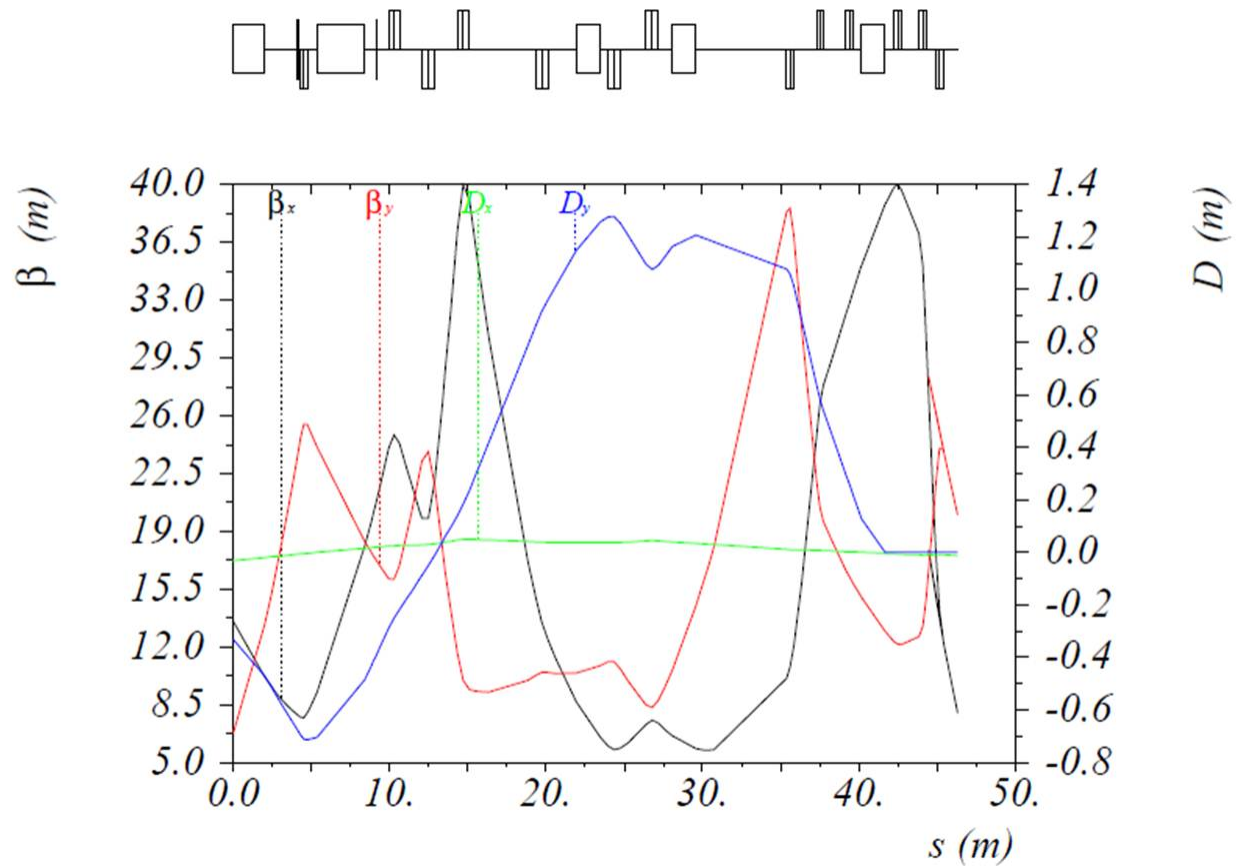


Figure 7.37: The extraction optics showing the two Lambertsons followed by an opposite-sign vertical bend, quadrupoles to form the achromat and a final bend up and then level again to the elevation of the beamline (all EDWA dipoles).

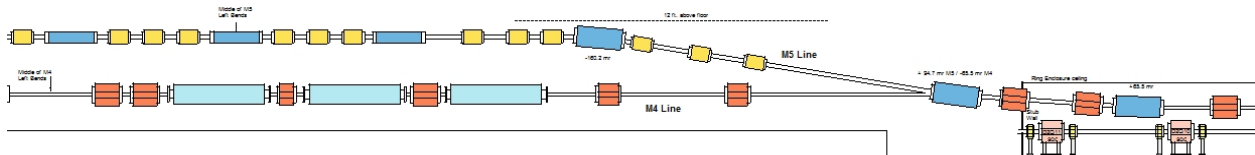


Figure 7.38: Layout of the extraction section showing the MDC bends and the separation of the beamlines to Mu2e and $(g - 2)$.

3455 **Horizontal Bend String** Immediately downstream of the vertical section, a strong west-
 3456 erly bend is required to meet the constraints on the directionality of the beam line and the
 3457 exact location of the $(g - 2)$ ring, particularly the critical bore coordinates through the yoke
 3458 and inflector position relative to the exact ring positioning. The horizontal separation of the
 3459 M4 and M5 lines after the extended vertical separation requires the horizontal bend module
 3460 to be located as close to the end of the vertical section and as compact as possible. The
 3461 bend increases significantly with any further downstream translation and the ring rotates in
 3462 response in order to match to the increased bearing of the beamline – compromising both
 3463 the optics and planning for a new inflector design. (A new inflector design with a significant
 3464 field would require re-locating the beamline to the easterly side of the enclosure to accommo-
 3465 date an additional pair of bend/reverse-bend magnets to realign the trajectory accordingly.)
 3466 Thus, maintaining a bend center of northerly and easterly coordinates, 30420.31542 m and
 3467 30117.58674 m, respectively, is central to an efficient beam transport design.

3468 Final location of the storage ring and MC-1 building moved its location significantly
 3469 which required a re-work of the entire beamline and a ring rotation to properly match the
 3470 injection trajectory to the fixed bend-center with beamline components aligned to within
 3471 a couple of feet of the westerly enclosure wall. Given the civil and beamline work already
 3472 implemented, an exact solution had to be found which met these constraints. The solution, a
 3473 total westerly bend of 26.669° , matched an implementable beamline in the existing enclosure
 3474 design to the injection trajectory of the $(g - 2)$ storage ring when rotated by 2.604° clockwise.
 3475 Figure 7.39 shows the present optimized beamline location in blue as determined by a) the
 3476 ring position, b) the injection alignment requirements, and c) as derived from the bend center
 3477 to upstream inflector-end center coordinates and angular requirements (1.25° relative to the
 3478 ring tangent at the exit of the inflector). The blue circle represents the upstream end of the
 3479 inflector.

3480 The present approach employs a 3-bend module comprised of three MDC dipoles in series
 3481 as shown in Fig. 7.40 with each MDC delivering $1/3$ of the total bend. Quadrupoles in this
 3482 module supply 120° of phase advance between each dipole, with a symmetry point at the
 3483 center ($D'=0$) to cancel horizontal dispersion, fulfilling conditions for a linear achromat. If
 3484 dispersion is required at injection, then the phase advance can be tuned to deliver a net
 3485 dispersion which can be propagated with appropriate optics to the ring. Phase advance and
 3486 dipole placement for dispersion cancellation dictate this section to be restricted to the optics
 3487 as designed. Matching to the optics of this section must occur on either side.

3488 A three-quadrupole matching section connects the optics of the vertical section and the
 3489 horizontal bend module. Table 7.15 lists the components and strengths for the achromatic
 3490 version of this module. The module can be re-tuned to deliver between 0 and 4 m of
 3491 dispersion to the ring. (Dispersion matching is 8 m, but this is too large to be supported in
 3492 the beamline – at $\pm 0.5\%$ dp/p , the offset would be ± 4 cm.)

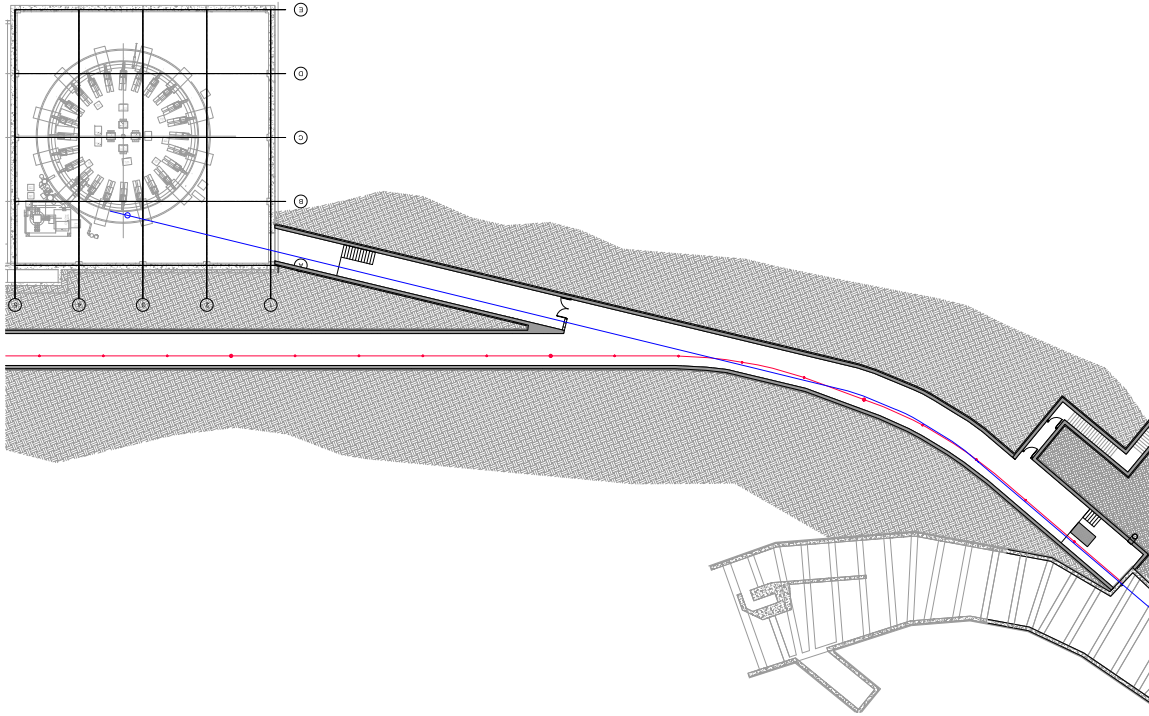


Figure 7.39: Layout of the horizontal bend section showing the horizontal separation of the M4 and M5 lines. The blue line and circle represent the optimized beamline layout and injection point at the upstream end of the inflector. The red line shows the beam trajectory to Mu2e.

Device	Magnet Type	Strength	Field	Bearing
gD2	MDC	155.2 mr	1.05 T	2.25141 rad
gQ7	SQA	0.671 m^{-2}	6.92 T/m	2.25141 rad
gQ8	SQC	-0.991 m^{-2}	-10.22 T/m	2.25141 rad
gQ9	SQB	0.931 m^{-2}	9.60 T/m	2.25141 rad
gD3	MDC	155.2 mr	1.05 T	2.40656 rad
gQ10	SQA	0.931 m^{-2}	960 T/m	2.40656 rad
gQ11	SQC	-0.991 m^{-2}	-10.22 T/m	2.40656 rad
gQ12	SQB	0.671 m^{-2}	6.92 T/m	2.40656 rad
gD3	MDC	155.2 mr	1.05 T	2.56171 rad

Table 7.15: Components and parameters in the horizontal bend section.

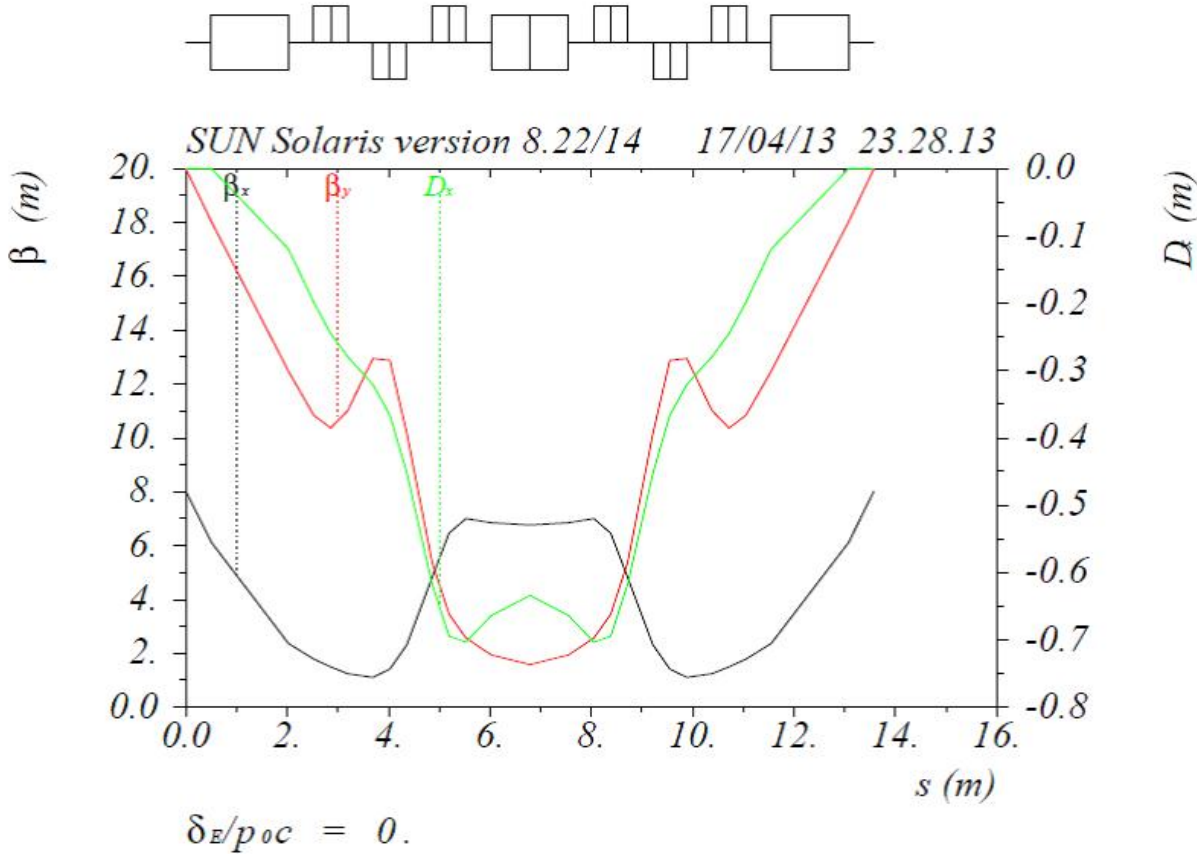


Figure 7.40: The optics of the $(g - 2)$ horizontal bend insert.

3493 **The FODO-cell transport section** Basic FODO-cell optics transport beam most effi-
 3494 ciently with lowest loss and maximum acceptance. (FODO cells are the simplest magnetic
 3495 lens configuration consisting of alternating horizontally- and vertically-focusing quadrupole
 3496 elements.) Therefore this type of module was implemented to transfer beam from the hori-
 3497 zontal bend string to the M5-line final focus quadrupoles. A FODO cell structure with 90°
 3498 of phase advance per cell has been designed, which has not only the smallest beam size when
 3499 both planes are considered, but also the added function of ease of transport for a periodic
 3500 dispersion wave (as generated by the horizontal bend string). This periodicity oscillates
 3501 between peak D and peak D' values (dispersion value and its derivative) every cell, allowing
 3502 simple control of dispersion at injection to the ring.

3503 The current half-cell length is 6.78 m and the peak beta value is 22 m, giving a beam
 3504 size of $\sim \pm 3$ cm through this section of the line. What is convenient about this type
 3505 of interface is that the integrated length of the FODO insertion can be varied by 10-20%
 3506 without significantly impacting the optics or the matching to upstream and downstream
 3507 sections. The optics of a unit FODO cell are shown in Fig. 7.41. Presently, three consecutive
 3508 FODO cells are used. Table 7.16 represents the matching section between the horizontal
 3509 bend and the first FODO cell and the three cells themselves.

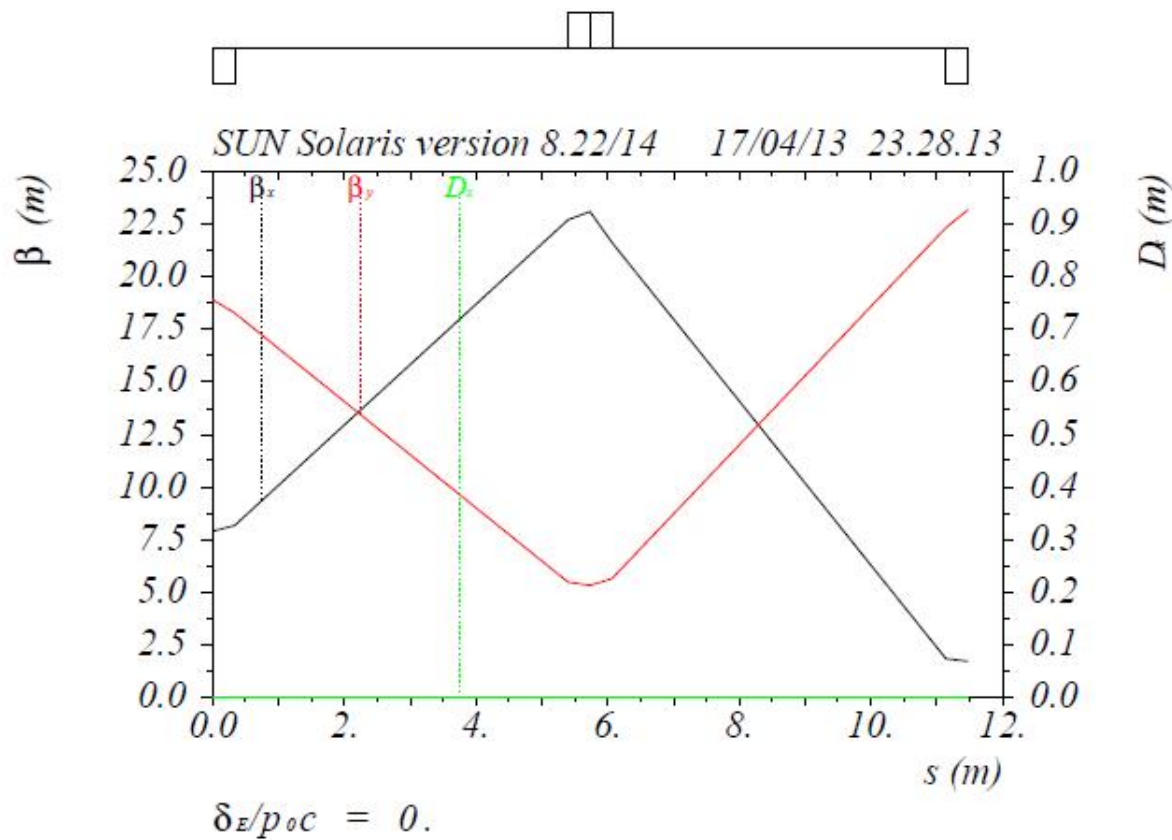


Figure 7.41: The unit FODO cell.

Device	Magnet Type	Strength	Field
gQ13	4Q24	-0.330 m ⁻²	-3.40 T/m
gQ14	SQA	-0.676 m ⁻²	6.97 T/m
gQ15	4Q24	0.362 m ⁻²	3.73 T/m
gQ16	4Q24	0.281 m ⁻²	2.90 T/m
gQ17	4Q24	-0.181 m ⁻²	1.87 T/m
gQ18	4Q24	0.374 m ⁻²	3.86 T/m
gQ19	4Q24	0.314 m ⁻²	3.24 T/m
gQ20	4Q24	0.374 m ⁻²	3.86 T/m
gQ21	4Q24	0.314 m ⁻²	3.24 T/m
gQ22	4Q24	0.374 m ⁻²	3.86 T/m
gQ23	4Q24	0.350 m ⁻²	3.61 T/m

Table 7.16: Matching and FODO-cell components.

3510 **The Final Focus and Injection into the Storage Ring** The final focus is a typical
3511 “collision” type approach which uses a quadruplet of quadrupoles for maximum optical
3512 tuning flexibility at the injection point to the ring. An exact match to storage ring beam
3513 parameters requires a $\beta_x \sim 8$ m, $\beta_y \sim 18$ m, and a large dispersion value of 8 m. However
3514 the present inflector aperture of 18 mm by 56 mm restricts the ability to match properly to
3515 the ring. Although the y plane can be relatively well matched, β_x at the center of the present
3516 inflector, which is 1.7 m long, can only be about 1.7 m for a 40π -mm-mr emittance beam,
3517 and this value translates into a β_x of approximately 2 m at injection rather than 8 m. More
3518 significantly, injected beam is actually diverging rather than converging ($\alpha_x < 0$), creating a
3519 much larger horizontal mismatch in the ring, a quadrupole breathing mode which reaches a
3520 peak β_x value of ~ 70 m, almost an order of magnitude larger than matched beam. Further,
3521 no net dispersion can be transmitted through the present inflector. The dispersion mismatch
3522 results in a dispersion wave around the ring which ranges between 0 and 16 m, reducing the
3523 horizontal momentum acceptance dramatically (particularly when coupled to the large beta
3524 wave). Table 7.17 shows the components and strengths for the final-focus section.

Device	Magnet Type (Status)	Strength	Field
gQ24	4Q24	-0.074 m ⁻²	-0.76 T/m
gQ25	SQA	0.271 m ⁻²	2.79 T/m
gQ26	SQA	0.265 m ⁻²	2.73 T/m
gQ27	4Q24	-0.263 m ⁻²	-2.71 T/m

Table 7.17: Components and strengths for the final focus section.

3525 The design for the final focus using the present inflector is given in Fig. 7.42, showing
3526 a minimum beam size at the center of the inflector. (The injection point is to the right on
3527 the plot.) However, the final focus quadrupoles can be tuned to provide matched beam for a
3528 new inflector design along with varying values of a dispersion function propagated from the
3529 horizontal bend by the FODO section. Two different dispersion values are given in Fig. 7.43
3530 for an exact match to the remaining ring parameters. Figure 7.44 shows the beamline from
3531 the beginning of the horizontal bend section through to the ring injection.

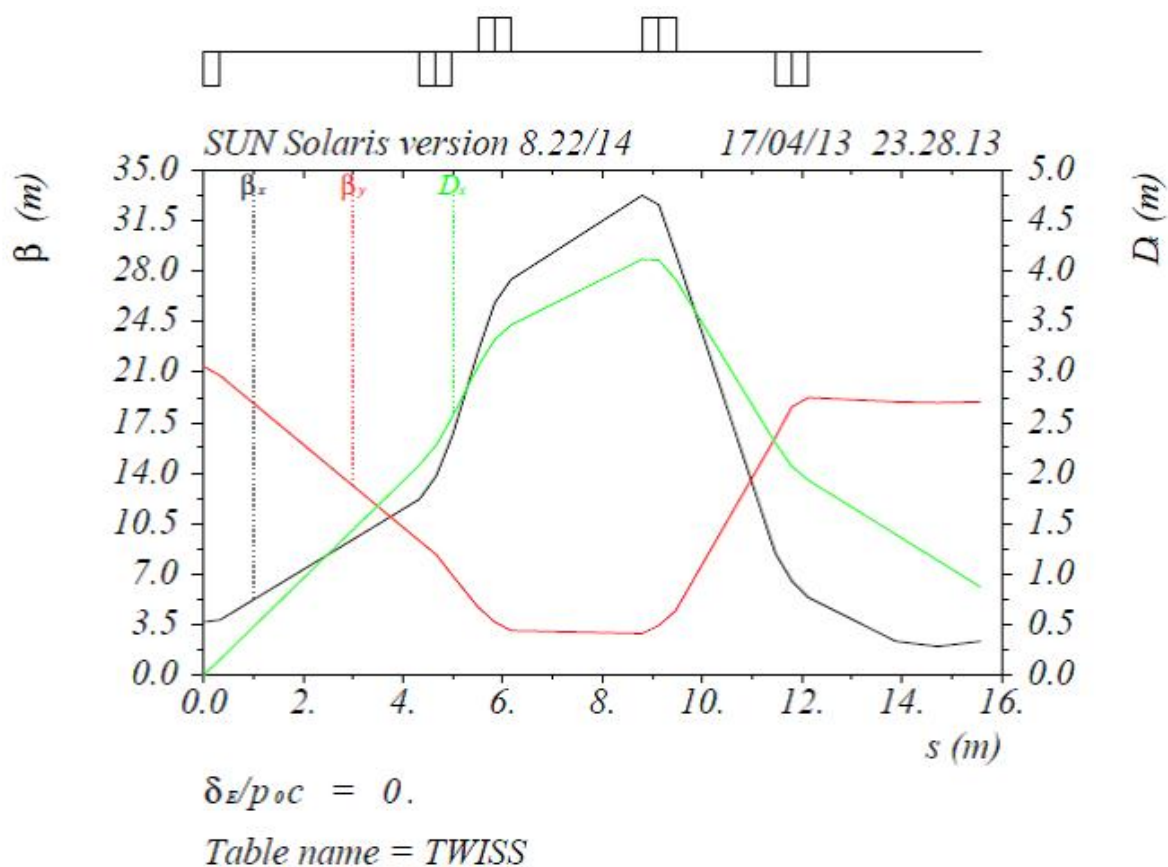


Figure 7.42: One tune of the final focus quadruplet section shows a minimum horizontal beta function at the center of the inflector at about 14 m on the plot. The dispersion function represents one tune of the line.

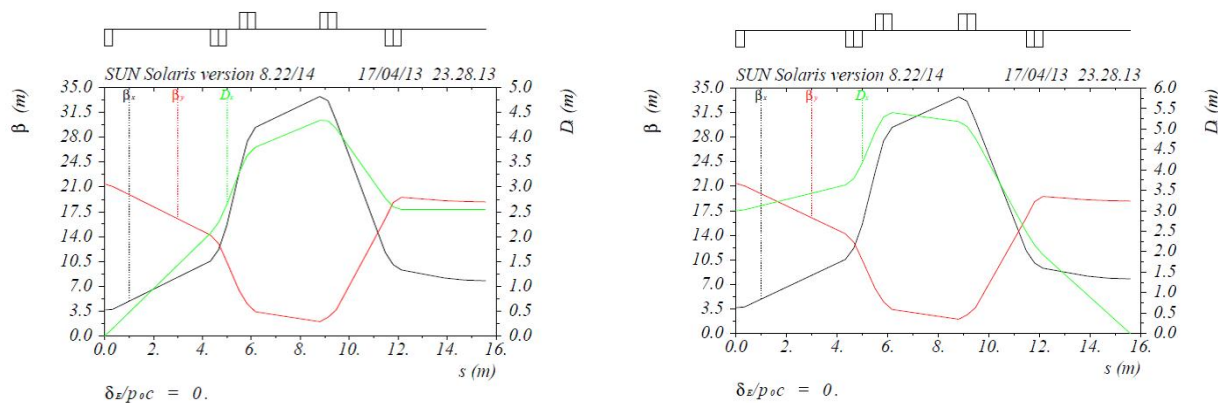


Figure 7.43: The final focus quadruplet showing two different dispersion tunes for a matched beam (assumes a larger-aperture inflector). Injection point at the ring is on the right.

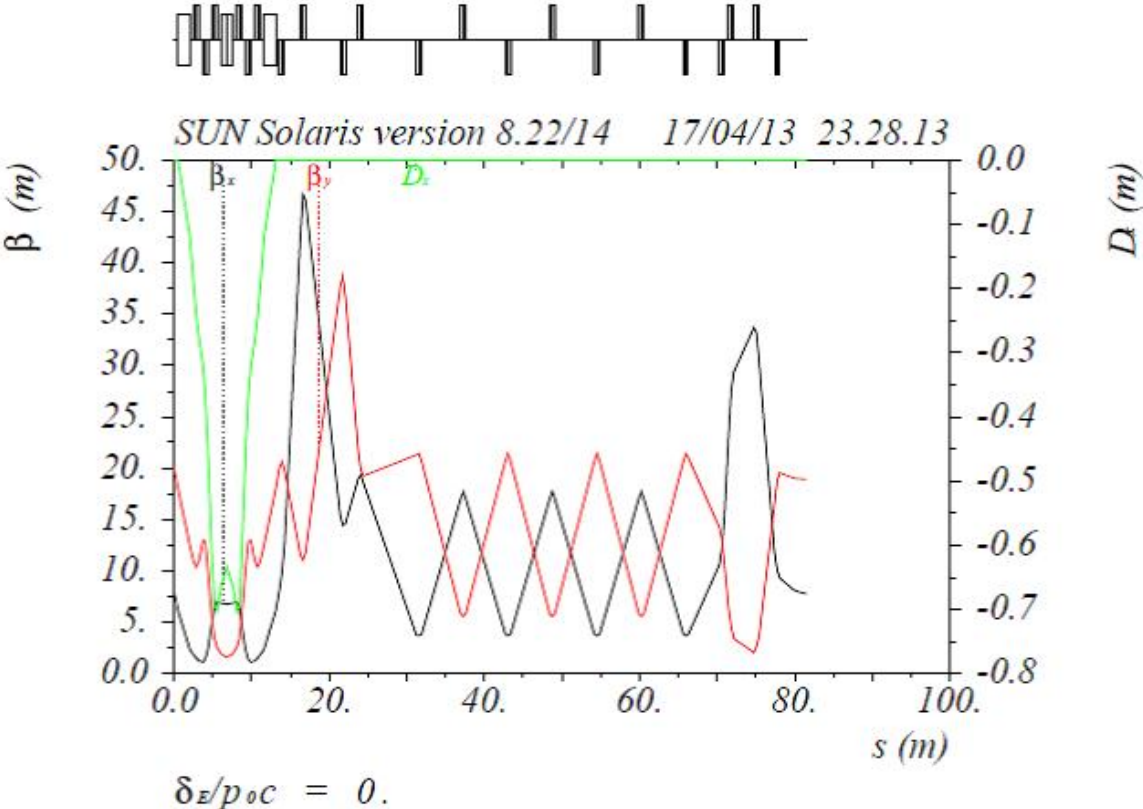


Figure 7.44: The beamline starting at the beginning of the horizontal bend to the point of injection on the right.

7.6 Controls and beam monitoring

7.6.1 Accelerator controls

A well-established controls system allows devices in the former Antiproton-Source (“Pbar”), now Muon, service buildings and tunnel enclosures to receive information such as synchronization signals and to communicate back to other accelerator systems. A map of the service buildings, labeled “AP” for former Antiproton-Source buildings, and “F” for buildings which are part of the F-sector of the Tevatron, is shown in Fig. 7.45. Devices in the new extraction beamlines and MC-1 building will also need to be connected to the controls system.

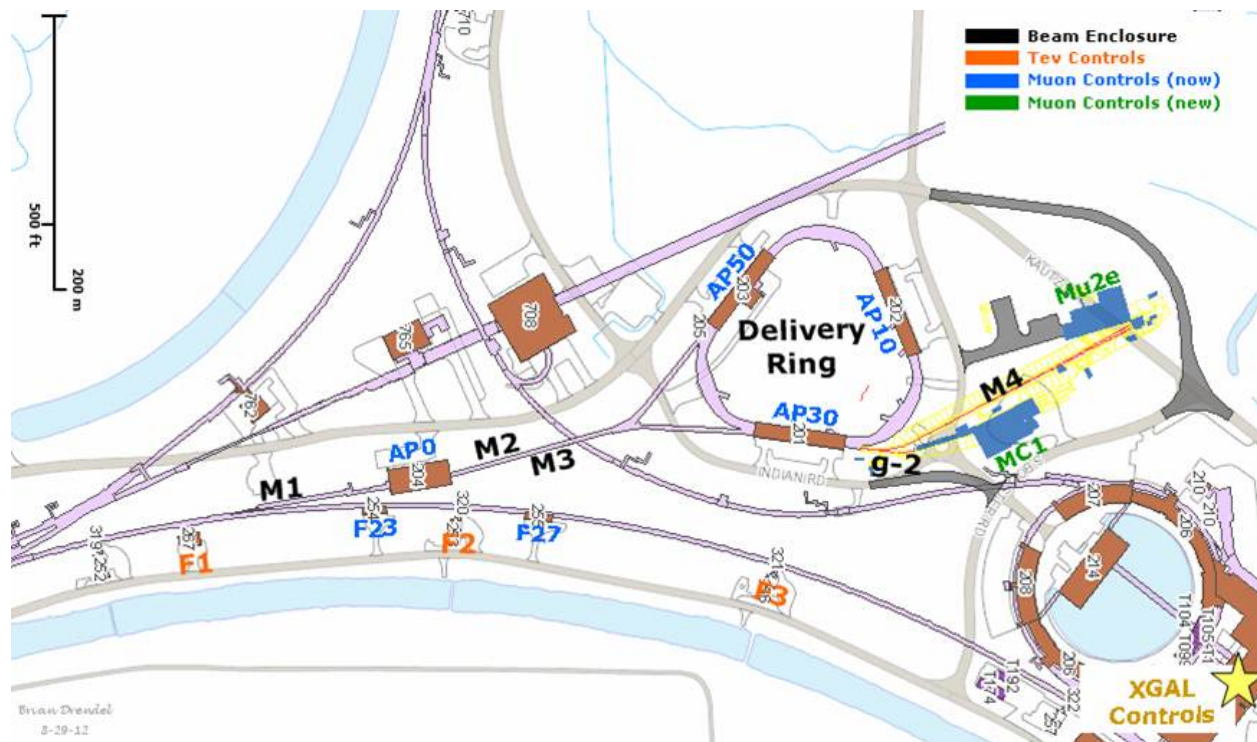


Figure 7.45: Muon Campus service buildings.

CAMAC and links

The existing accelerator service buildings will continue to use the legacy controls infrastructure that is currently in place. These service buildings include all of the Main Injector service buildings, as well as F0, F1, F2, F23, F27, AP0, AP10, AP30 and AP50. Future Muon Campus service buildings, including MC-1 and Mu2e, will be upgraded to a more modern controls infrastructure which will be discussed later in this document. Migration of the existing buildings to the more current controls standard is preferred and is being considered; however, sufficient funding is not available to start the upgrade path and it is believed that the existing infrastructure will be adequate for $(g - 2)$ operations.

Computer Automated Measurement and Control (CAMAC) crates exist in each service building and communicate with the control system through a VME-style front-end computer

3551 over a 10 MHz serial link as shown in Fig. 7.46. Both digital and analog status and control of
 3552 many accelerator devices occur through the CAMAC front ends. There should be no need to
 3553 install additional CAMAC crates, as there is excess capacity in most of the existing crates.
 3554 An inventory of existing CAMAC crates in the Muon service buildings shows that about 25%
 3555 of the slots are unoccupied and could be used for additional CAMAC cards [20]. In addition,
 3556 further slots have become available that were used to interface devices that became obsolete
 3557 with the retirement of Collider Run II operations. It is anticipated that there will be ample
 3558 CAMAC-crate coverage for ($g - 2$) operation in the existing Muon service buildings, and
 3559 very few crates will need to be added or moved.

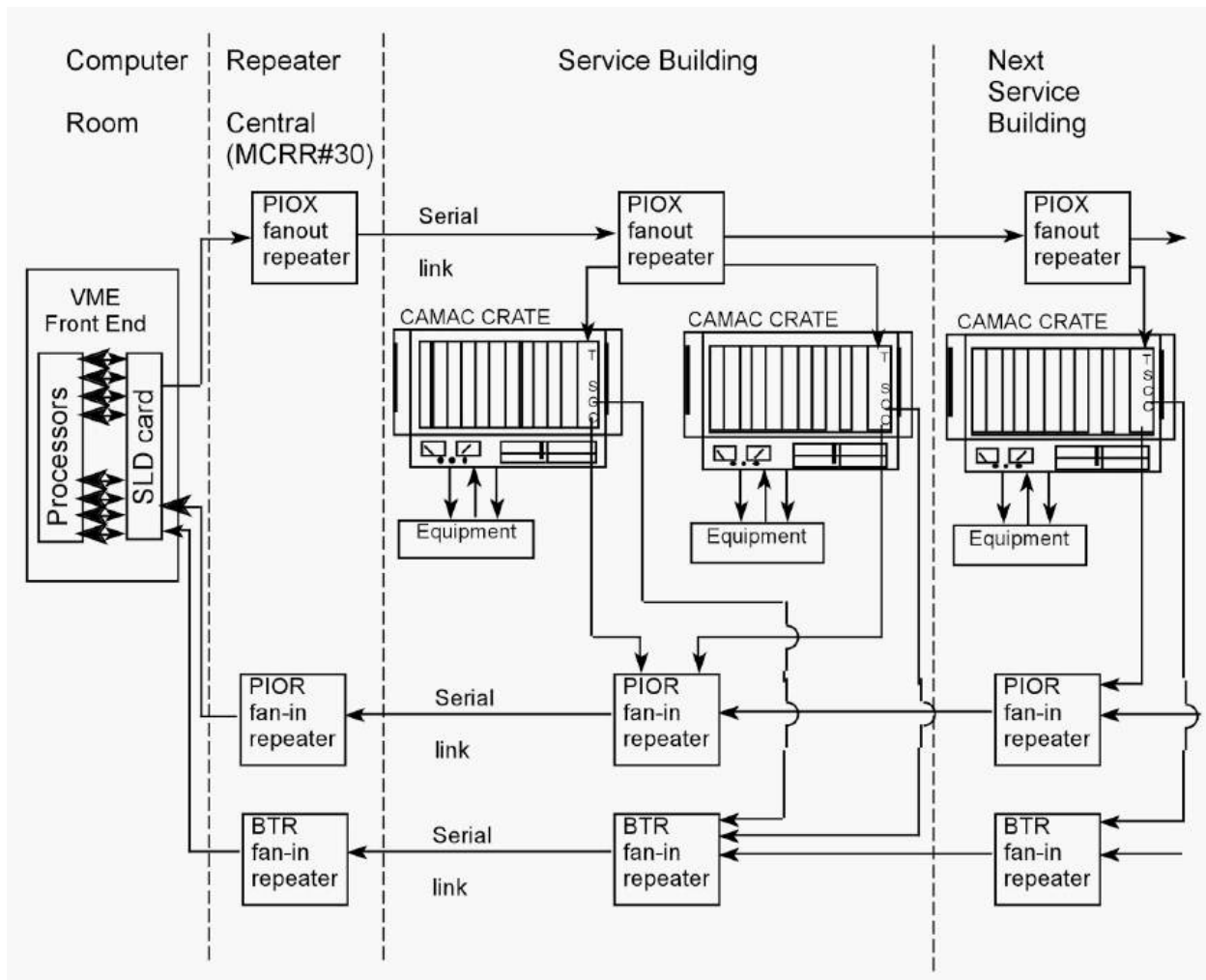


Figure 7.46: Legacy CAMAC crates interfacing VME front ends via serial links provide both analog and digital status and control of accelerator devices, and will continue to be used in existing Muon service buildings.

3560 There are serial links that are distributed through and between the service buildings, via
 3561 the accelerator enclosures, that provide the necessary communications paths for CAMAC
 3562 as well as other necessary signals such as clock signals, the beam permit loop, and the Fire
 3563 and Utilities System (FIRUS). Controls serial links can be run over multimode fiber-optic

3564 cable or copper Heliac cable. Most Muon links that run through accelerator enclosures are
3565 run over Heliac, which should function normally in the radiation environment expected for
3566 ($g - 2$) operations.

3567 Accelerator device timing that does not require synchronization to the RF buckets will
3568 remain on the existing 10 MHz Tevatron Clock (TCLK) system. The existing TCLK in-
3569 frastructure will remain in existing service buildings and new TCLK link feeds will be run
3570 via multimode fiber optic cable from the Mac Room to the new MC-1 and Mu2e service
3571 buildings.

3572 Accelerator device timing for devices that require synchronization to the RF buckets
3573 will continue to be handled through the Beam Synch Clocks; however, a few changes will
3574 be required to maintain functionality. The F0, F1 and F2 service buildings will need both
3575 53 MHz Main Injector beam synch (MIBS) for SY120 operations and 2.5 MHz Recycler
3576 beam synch (RRBS) for ($g - 2$) and Mu2e operations. These buildings already support
3577 multiple beam synch clocks, so the addition of RRBS will require minimal effort. An obsolete
3578 53 MHz Tevatron beam synch (TVBS) feed in the MI60 control room will be replaced with
3579 a 2.5 MHz RRBS feed in order to provide the necessary functionality. The remaining Muon
3580 service buildings currently use 53 MHz MIBS, but will require 2.5 MHz RRBS for ($g - 2$)
3581 and Mu2e operations. This functionality can be obtained by replacing the MIBS feed at F0
3582 with RRBS and using the existing infrastructure. Further upgrades and cable pulls will only
3583 be required if it is later determined that both MIBS and RRBS are required in these service
3584 buildings. New beam synch feeds to the ($g - 2$) and Mu2e service building will be run via
3585 multimode fiber-optic cable from the Mac Room.

3586 The Delivery-Ring permit loop provides a means of inhibiting incoming beam when there
3587 is a problem with the beam delivery system. The Pbar beam permit infrastructure will be
3588 used in the existing buildings. The CAMAC 201 and 479 cards, which provide the 50 MHz
3589 abort loop signal and monitor timing, will need to be moved from the Mac Room to AP50
3590 to accommodate the addition of the abort kicker at AP50. Existing CAMAC 200 modules
3591 in each CAMAC crate can accommodate up to eight abort inputs each. If additional abort
3592 inputs are required, spare CAMAC 200 modules will be repurposed from the Tevatron and
3593 will only require an EPROM or PAL change. The permit loop will be extended to the MC-1
3594 and Mu2e service buildings via multimode fiber-optic cable from the Mac Room. Abort
3595 inputs for these buildings will plug into a Hot-Link Rack Monitor abort card as will be
3596 mentioned below.

3597 Operational and permit scenarios are under development. The capability of running
3598 beam to the Delivery-Ring dump when Mu2e and ($g - 2$) are down will be needed, as well
3599 as the ability to run to either experiment while the other is down.

3600 **Hot-Link Rack Monitor**

3601 New controls installations will use Hot-Link Rack Monitors (HRMs) in place of CAMAC. A
3602 HRM runs on a VME platform that communicates with the control system over Ethernet
3603 as shown in Fig. 7.47. Unlike CAMAC, no external serial link is required, minimizing the
3604 need for cable pulls between buildings. Each HRM installation provides 64 analog input
3605 channels, 8 analog output channels, 8 TCLK timer channels, and 8 bytes of digital I/O.
3606 This incorporates the features of multiple CAMAC cards into a single, compact chassis.

3607 Like CAMAC, when additional functionality or controls channels are needed, additional
 3608 units can be added. As an example, a HRM version of the CAMAC 200 module will be
 3609 constructed to provide inputs into the Delivery-Ring permit system. One or two HRMs
 3610 will be installed in both the MC-1 and Mu2e buildings and should provide ample controls
 3611 coverage for both accelerator and experimental devices.



Figure 7.47: A Hot-Link Rack Monitor is a flexible data acquisition system composed of a remote unit and a PCI Mezzanine card that resides in a VME crate. Each HRM provides sixty-four 16-bit analog input channels, 8 analog output channels, 8 TCLK timer channels and 8 bytes of digital I/O. HRMs will eventually replace all of the functionality of CAMAC [21].

3612 HRMs are expected to eventually replace legacy CAMAC systems in the existing build-
 3613 ings. This migration will start by replacing existing 12-bit MADCs and CAMAC 190 cards
 3614 for analog readings with 16-bit HRM channels. This option was considered for $(g - 2)$ op-
 3615 eration, but was determined to be impractical considering expected funding, limited legacy
 3616 Ethernet connectivity in three of the Muon service buildings, and the determination that
 3617 the existing CAMAC would likely provide adequate performance for $(g - 2)$ operations.

3618 Ethernet

3619 Many modern devices have some form of Ethernet user-interface. In addition, many devices
 3620 and remote front-ends use Ethernet to interface with the control system, instead of using
 3621 the traditional CAMAC. The results are an increasing demand on the Controls Ethernet.
 3622 Figure 7.48 is a map of the Muon Controls network. All of the current Muon Ring service
 3623 buildings have Gigabit fiber-optic connections from the Cross-Gallery computer room to
 3624 Cisco network switches centrally located in each service building. These will provide ample
 3625 network bandwidth and connections after the reconfiguration for $(g - 2)$ and Mu2e. A central
 3626 Ethernet switch that fans out to the other Muon Department buildings is currently located
 3627 in AP10, but will need to be moved to AP30, as will be discussed later in this document.

3628 Ethernet connects between the Muon-Ring service buildings via multimode fiber-optic
 3629 cable paths that traverse the Rings enclosure on the Accumulator side. The multimode fiber
 3630 currently in place will remain functional during $(g - 2)$ operations. However, in the higher-
 3631 radiation environments expected during Mu2e operations, these fiber-optic cables will need

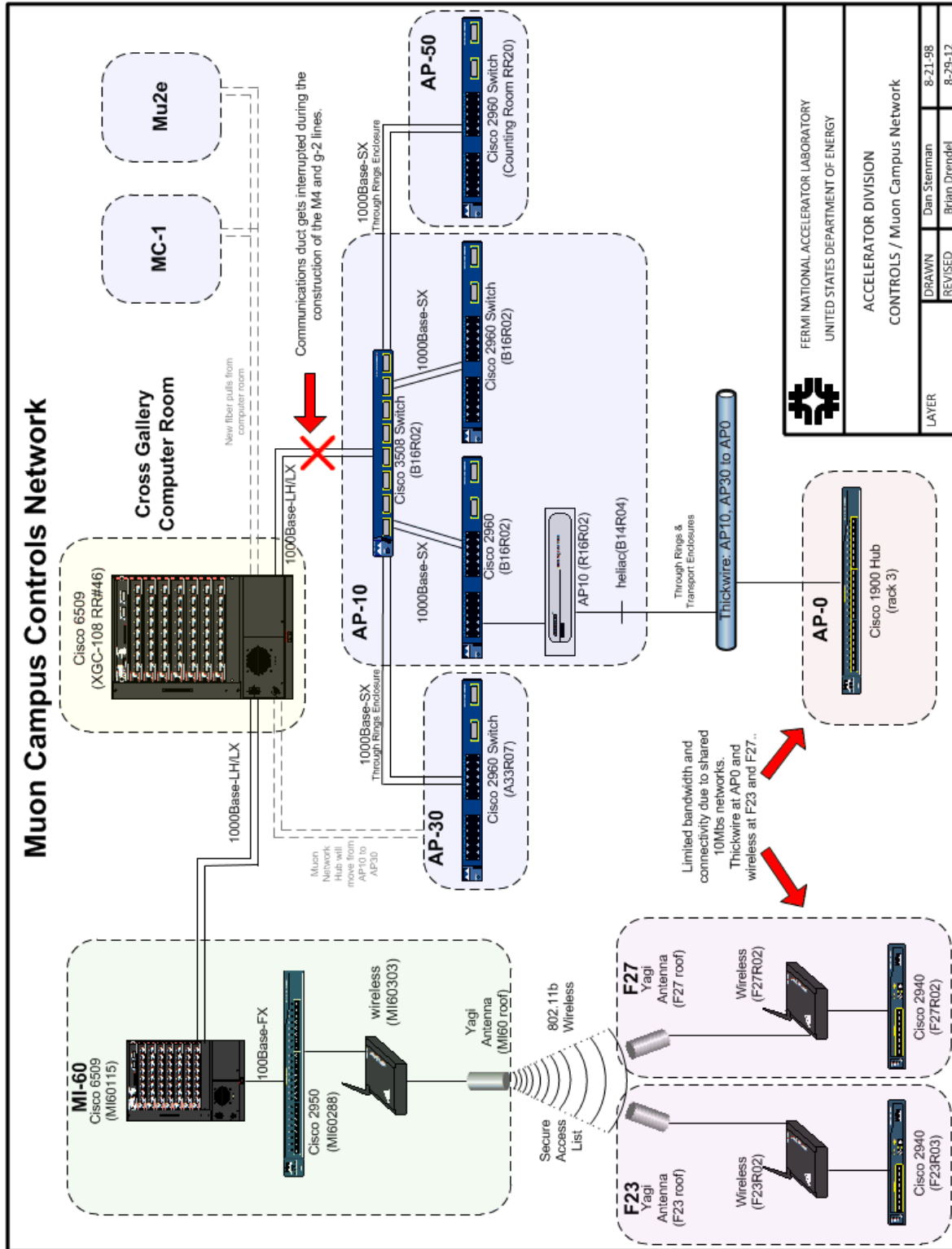


Figure 7.48: Controls Ethernet to the Muon Department service buildings is expected to be adequate for $(g - 2)$ operations. The central switch at AP10 will be moved to AP30. Legacy networks at AP0, F23, and F27 have limited bandwidth and connectivity.

3632 to be upgraded to single-mode fiber at a minimum, or to the more costly radiation-hard fiber
3633 if radiation rates are too high.

3634 Most beamline service buildings have gigabit fiber connected to centrally located network
3635 switches that provide ample network bandwidth and connections. AP0, F23, and F27 are
3636 the only three buildings that do not have this functionality. AP0 runs off a 10 Mbps hub
3637 that connects to 10Base5 “Thicknet” that runs through the Transport and Rings enclosures
3638 back to AP10, while F23 and F27 run off 802.11b wireless from MI60. Both are 10 Mbps
3639 shared networks with limited bandwidth and connectivity. It is anticipated that the network
3640 in these three buildings may be sufficient for $(g - 2)$ operations; however, network upgrade
3641 options are being considered, as will be discussed below.

3642 **Controls connectivity**

3643 Civil construction of the M4 and M5 beamline enclosures will result in the removal of the
3644 underground controls communication duct that provides the connectivity between the Ac-
3645 celerator Controls NETwork (ACNET) and the Muon Campus [22]. Included in this com-
3646 munication duct is the fiber-optic cable that provides Ethernet connectivity, as well as 18
3647 Heliac cables that provide the controls serial links and other signals including FIRUS. These
3648 cables currently connect from this communications duct to the center of the 20 location in
3649 the Rings enclosure, and travel through cable trays on the Delivery Ring side to the AP10
3650 service building. After removal of the communications duct, FESS will construct new com-
3651 munications ducts from the existing manholes as part of a General Plant Project. These
3652 communications ducts will go directly to AP30, MC-1 and Mu2e service buildings without
3653 going through accelerator enclosures. See Fig. 7.49 for drawings of the current and future
3654 controls connectivity paths.

3655 **Restoring connectivity** When the Heliac and fiber-optic cables are cut during the re-
3656 moval of the above-mentioned communications duct, controls connectivity will be lost. The
3657 base plan for restoring both Ethernet and controls-link connectivity is to pull new fiber optic
3658 cable from the cross gallery, through the MI-8 line communications ducts to AP30. As a
3659 result of the new fiber pull, the Ethernet and controls links will fan out from AP30 instead of
3660 AP10. This will require some additional controls hardware configuration and labor. Efforts
3661 will be made to minimize the disruption by pulling the fiber and staging the new hardware at
3662 AP30 before the communication duct is cut. This is especially important for FIRUS which is
3663 necessary for monitoring building protection. This work will be done as part of the Delivery
3664 Ring AIP.

3665 More details regarding the base plan and several alternatives, including cutting and splic-
3666 ing the Heliac cable or attempting to keep the fiber and Heliac intact during construction,
3667 can be found in Ref. [23].

3668 **Establish connectivity to MC-1** New fiber-optic cable will be pulled from the Mac
3669 Room to the MC-1 service building. Single-mode fiber is needed for Ethernet and FIRUS,
3670 and multimode fiber is needed for the timing links and the abort-permit loop. A bundle of
3671 96-count single-mode and a bundle of 36-count multimode fiber-optic cable will be pulled to
3672 MC-1. The fiber bundles will share a common path with the fiber bundles headed toward

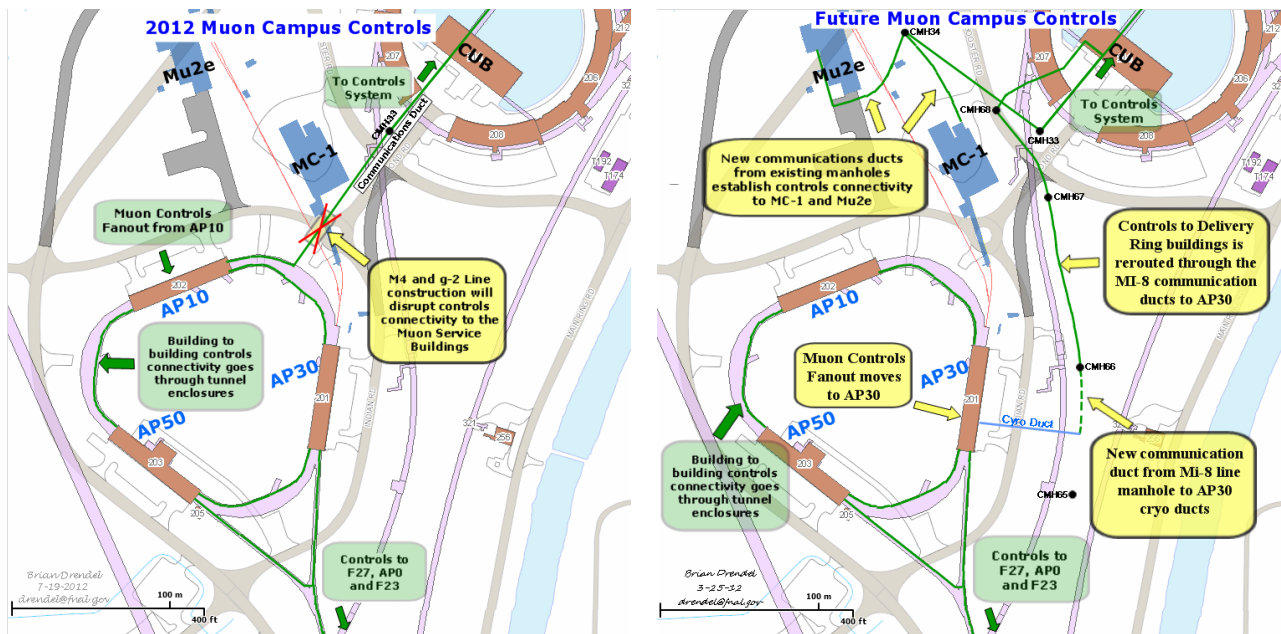


Figure 7.49: Muon campus controls paths. During construction of the M4 and ($g - 2$) beamlines, the communications duct that provides controls connectivity to the Muon Campus will be interrupted. A new communications duct will be built to restore controls connectivity to the Muon service buildings. New controls will need to be established at the MC-1 and Mu2e buildings.

3673 Mu2e from the Cross Gallery to the manhole by Booster West Tower. All three fiber bundles
 3674 will travel through a single inner duct to the manhole. The Mu2e and MC-1 fiber bundles
 3675 will then branch off to a second manhole inside a common inner duct, and then separate into
 3676 the new communication ducts to the Mu2e and MC-1 service buildings. The fiber bundle to
 3677 the MC-1 Building will be pulled by the ($g - 2$) project, and to the Mu2e building by the
 3678 Mu2e project. The fiber pulls will provide ample connectivity for all Ethernet and controls
 3679 signals for both the accelerator and experiment. The ($g - 2$) experiment anticipates requiring
 3680 network rates approaching 100 MB/sec during production data taking which can be handled
 3681 easily with the proposed infrastructure.

3682 One alternate solution considered was to pull the new fiber along the existing communi-
 3683 cations duct until it intersected the extraction-lines enclosure. From there, the fiber could
 3684 be directed along tunnel-enclosure cable trays to the MC-1 service buildings. Though this
 3685 option would provide MC-1 cable-pull lengths of approximately the same length as the base
 3686 option, it was eliminated due to the extra complications of pulling fiber through the tunnel
 3687 enclosures to both Mu2e and AP-30. In both cases, the expected radiation environment
 3688 would require a more expensive radiation-hard single-mode fiber. In addition, the CAMAC
 3689 fiber links only run on multimode fiber, so link and clock repeaters would have to be re-
 3690 designed to run on single-mode fiber, adding additional expense to the project.

3691 **Possible upgrades for legacy networks** If the legacy Ethernet networks at AP0, F23,
 3692 and F27 prove to provide insufficient connectivity or bandwidth for ($g - 2$) operations, they

3693 can be most cost-effectively upgraded by replacing the current 10Base5 “Thicknet” with
 3694 single-mode fiber-optic cable. The path would be from the AP30 service building to the
 3695 Rings enclosure, along the cable trays toward the M3 beamline, and down the Transport
 3696 enclosure. From the Transport enclosure, the fiber-optic cable runs can go to F27 and
 3697 AP0. An additional fiber-optic cable pull from AP0 through the PreVault enclosure provides
 3698 a path to F23. The largest issue with this upgrade is that the single-mode fiber-optic
 3699 cable is susceptible to radiation. If the radiation environment in the accelerator enclosures
 3700 does not allow for single-mode fiber-optic cable, then radiation-hard fiber-optic cable can
 3701 be pulled, but at a higher cost. Standard 96-count single-mode fiber costs approximately
 3702 \$1.50/foot, whereas 96-count radiation-hard fiber costs approximately \$22/foot. Upgrading
 3703 to the radiation-hard cable would add approximately \$50K to the cost of the cable pull.
 3704 Other fiber-optic cable path options have been considered, but prove to be more costly to
 3705 implement.

3706 **Safety system**

3707 The existing safety system enclosure interlock hardware installed in the Pre-Target, Pre-
 3708 Vault, Vault, Transport and Delivery Rings will remain in place. The tunnel egress between
 3709 the Delivery Ring and Transport enclosures on the AP2 side will be blocked as a result of
 3710 the new beam abort dump. A safety system mini loop will be created on each side of the
 3711 abort dump to satisfy ES&H requirements.

3712 The Delivery Ring enclosure is extended to the new extraction line enclosure under AP30.
 3713 New interlocked gates will be installed at the boundary between the Delivery Ring enclosure
 3714 and the extraction enclosure, between the extraction enclosure and the M4 enclosure that
 3715 goes to Mu2e, and between the extraction enclosure and MC-1. Reset boxes for these gates
 3716 will be repurposed from the Tevatron. Enclosure interlocks for the MC-1 experimental hall
 3717 will use the Rack Mounted Safety System (RMSS) chassis mounted in a rack dedicated for
 3718 safety system equipment. The RMSS chassis uses a reset box similar to the Main Injector.

3719 The three Pbar area Critical Device Controllers (CDCs) will be repurposed for $(g - 2)$
 3720 operations, but may need to be relocated to cover the new safety system critical devices that
 3721 will be used during $(g - 2)$ operations. Interlocked radiation detectors may be moved and
 3722 the system may be modified to include Total Loss Monitors (TLMs). The key trees from
 3723 Pre-Vault, Pre-Target, and Transport will remain in the Main Control Room (MCR), while
 3724 the remote AP10 keytree will likely be moved from AP10 to the MCR.

3725 Cryogenics will be used in the MC-1 experimental hall, so an Oxygen Deficiency Hazard
 3726 (ODH) system will be implemented using a safety rated PLC system.

3727 **7.6.2 Accelerator instrumentation**

3728 **Beam types**

3729 Beam monitoring can be divided into distinct zones: primary protons, mixed secondaries,
 3730 proton secondaries, and muon “secondaries” (actually the dominant source of muons should
 3731 be from the decay of the pion secondaries, so are technically “tertiary”). The locations of
 3732 each of these areas are shown in Fig. 7.50. The expected beam properties in each of these
 3733 areas are shown in Table 7.18.

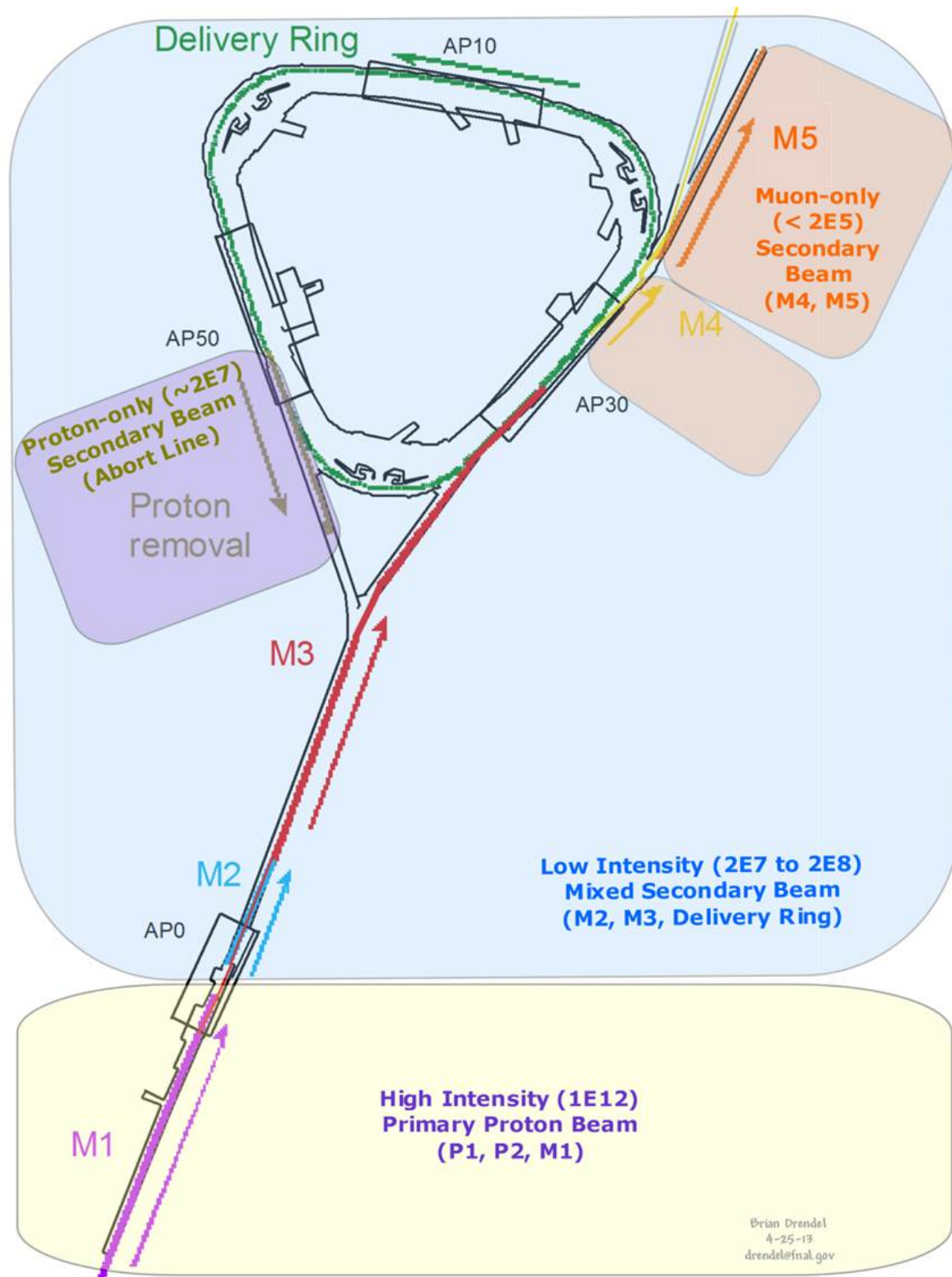


Figure 7.50: Beam monitoring can be divided into four different zones, each with different instrumentation schemes. High-intensity proton beam will be monitored with Toroids, BPMs and BLMs. Low-intensity secondary and proton-only secondary beam will be monitored with Ion Chambers, BPMs and SEMs. Muon-only secondary beam will be monitored with Ion Chambers and SWICs.

Beam Type	Particle Species	Beam Momentum (GeV/c)	Number of Particles	RF Bucket (MHz)	Bunch Length (ns)	Transverse Emittance (mm-mr)
Primary protons	p	8.9	10^{12}	2.515	120	18π
Mixed secondaries	μ^+ , π^+ , p, e^+	3.1	10^7 to 2×10^8	2.515	120	40π
Proton secondaries	p	3.1	10^7	2.515	120	40π
Muons	μ^+	3.1	$< 10^5$	2.515	120	40π

Table 7.18: Expected properties of primary proton beam, secondary beam off the target, and muon beam from pion decay relevant to instrumentation designed to measure beam. Transverse emittances are 95% normalized.

3734 **Primary proton beam** Primary proton beam will traverse the Recycler, P1 stub, P1, P2
 3735 and M1 lines. Much of the instrumentation needed to measure the primary proton beam
 3736 during ($g - 2$) operation already exists, but needs to be modified for use with the faster cycle
 3737 times and 2.5-MHz RF beam structure. The overall beam intensity is similar to that seen in
 3738 Pbar stacking operations, and in many cases requires only small calibration changes be made
 3739 to the instrumentation. Toroids will be used to monitor beam intensity and will be used in
 3740 conjunction with Beam Loss Monitors (BLMs) to maintain good transmission efficiency in the
 3741 beamlines. Multiwires and Secondary Emission Monitors (SEMs) will provide beam profiles
 3742 in both transverse planes. Beam Position Monitors (BPMs) will provide real-time orbit
 3743 information and will be used by auto-steering software to maintain desired beam positions
 3744 in the beamlines.

3745 Toroids are beam transformers that produce a signal that is proportional to the beam
 3746 intensity. There are two toroids in the P1 line, one in the P2 line and two in the M1 line.
 3747 They will continue to be used in ($g - 2$) operation to measure the primary proton beam.
 3748 The electronics for these toroids are comprised of legacy analog processing inside of NIM
 3749 crates. The base plan, due to funding limitations, is to continue to use the legacy electronics.
 3750 If funding becomes available, the electronics would instead be upgraded to a VME-based
 3751 processing environment, repurposing electronics from Collider Run II in order to provide
 3752 cost savings. The existing toroids provide the majority of the required coverage, though the
 3753 addition of a second toroid in the P2 line and a toroid in the P1 stub is desirable. The present
 3754 toroid installation locations will be reviewed and modified as needed to provide adequate
 3755 coverage. One possible change would be to move the upstream P1-line toroid downstream
 3756 of the P1 line and P1 stub merge so that it could measure the beam injected into the P1
 3757 line from the stub. Filters, chokes, and preamps will be added for analog conditioning.
 3758 Electronics will be modified, where necessary, to calibrate the toroids for ($g - 2$) operations.

3759 Beamline BPMs provide single-pass orbit-position information with sub-millimeter res-
 3760 olution, and will continue to be the primary beam-position devices in the P1, P2 and M1
 3761 lines. All BPMs share the Echotek style of electronics which was built as part of the Rapid
 3762 Transfers Run II upgrade [24], and is the current standard for beamline BPMs. A functional
 3763 diagram of the BPM hardware is shown in Fig. 7.51. These BPMs were designed to detect 7
 3764 to 84 consecutive 53-MHz proton bunches and four 2.5-MHz antiproton bunches for Collider
 3765 Run II operations. Minimal electronics modifications will be required to measure the single
 3766 2.5-MHz bunches of 10^{12} particles expected during ($g - 2$) operations. Two additional BPMs
 3767 will be installed in the P1 stub.

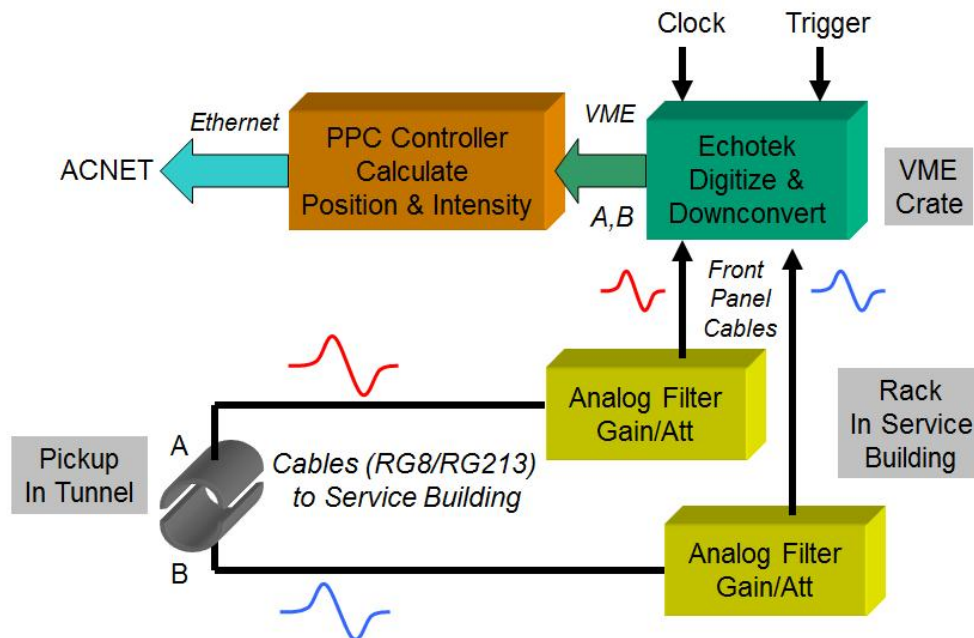


Figure 7.51: BPMs with Echotek processing electronics will be used to measure the transverse beam position of the 2.5-MHz primary proton beam in the P1, P2 and M1 lines for $(g - 2)$ operations. The BPMs are not sensitive enough to see the low intensity secondary beams downstream of the AP0 target [24].

3768 Beam Loss Monitors are already in place in the P1, P2, and M1 beamlines. Existing ion-
 3769 chamber detectors will be utilized for Mu2e operation. BLMs will be upgraded to modern
 3770 BLM log monitor electronics, repurposing unused components from the Tevatron in order to
 3771 minimize cost. An optional upgrade is being considered that would add snapshot capability
 3772 to the BLMs. This feature would allow the loss monitors to distinguish losses from individual
 3773 15-Hz pulses of beam. However, this option adds significant cost to the BLM system. Two
 3774 additional BLMs will be installed in the P1 stub.

3775 There are two types of beam profile monitors in the beamlines: multiwires in the P1
 3776 and P2 lines, and SEMs in the other beamlines. The profile monitors will primarily be used
 3777 for commissioning, studies, and documentation of the beamlines. General maintenance will
 3778 be performed on the hardware and electronics to ensure proper functionality. The current
 3779 location and wire spacing of the monitors will be reviewed and modified accordingly. Two
 3780 additional multiwires will be installed in the P1 stub.

3781 **Mixed secondaries** Mixed-secondary beam will traverse the M2 and M3 lines, as well
 3782 as the Delivery Ring. Changes to existing instrumentation are required in these areas as a
 3783 result of the secondary beam being approximately two orders of magnitude lower in intensity
 3784 than that during the former Antiproton-stacking operations. In addition, 2.515 MHz bunch
 3785 structure and a faster pulse rate must be taken into consideration. Mu2e beam will have
 3786 beam intensities four to five orders of magnitude higher than $(g - 2)$ operations in the
 3787 M3 line and Delivery Ring, so design upgrades must take into account the vastly different

3788 beam intensities required for both experiments. Beam studies have been conducted in order
 3789 to help determine what instrumentation best suits the low-intensity secondaries of $(g - 2)$
 3790 operations [3].

3791 Four toroids are available for use in the secondary beamlines and were the primary
 3792 intensity-measurement device in these lines during Antiproton operations. These will be
 3793 used for Mu2e operations; however, beam studies show that even with high gain and careful
 3794 filtering, we were only able to measure beam intensities at levels one order of magnitude
 3795 higher than $(g - 2)$ operational beam [3], as demonstrated in Fig. 7.52. As a result, toroids
 3796 will likely not be used during normal $(g - 2)$ operations, but may still be used with higher-
 3797 intensity beams during commissioning and studies periods.

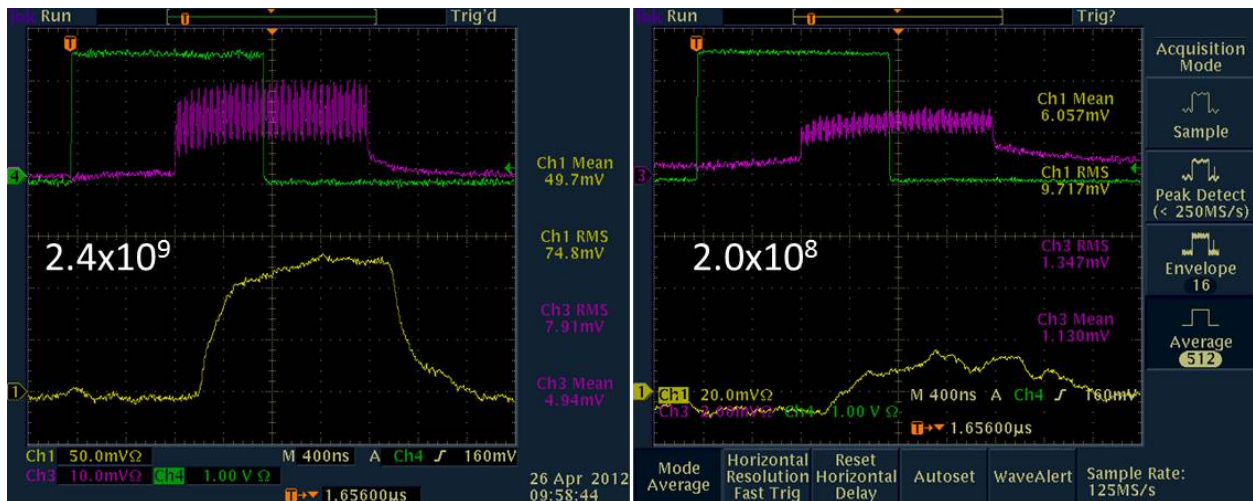


Figure 7.52: The yellow trace on both plots is a calibration test pulse on Toroid 724 in the AP2 line with high-gain preamps and special filtering to look for low-intensity beam. At beam intensities in the low 10^9 s, there is an easily-measurable beam signal. However, when the beam intensities are lowered to the level of 10^7 - 10^8 , the $(g - 2)$ expected secondary beam intensity range, beam intensities can not be measured.

3798 A Direct-Current Current Transformer (DCCT) has been used in the Delivery Ring to
 3799 measure beam intensity. This device will not function at $(g - 2)$ operational intensities and
 3800 cycle time.

3801 Ion chambers will become the primary beam-intensity measurement device for mixed-
 3802 secondary beam. They are relatively inexpensive devices that can measure beam intensities
 3803 with an accuracy of $\pm 5\%$ with as little as 10^5 particles. Ion chambers were used in the AP2
 3804 line in the past, and work was done during beam studies to recommission the ion chamber
 3805 that used to be operational near the end of the AP2 line [3]. For $(g - 2)$ operations, one
 3806 or two ion chambers will be implemented in the M2 line. Ion chambers are also being
 3807 considered for the M3 line and the Delivery Ring; however, these would need to be installed
 3808 in a vacuum can with motor controls to allow them to be pulled out of the beam during the
 3809 higher-intensity Mu2e operations. Figure 7.53 shows an ion chamber installation in the AP2
 3810 line.

3811 Wall Current Monitors (WCMs) are an alternative intensity-measurement device being



Figure 7.53: Fixed-position ion chamber in the AP2 line. The ion chamber is separated from the beam pipe by a vacuum window on each side. Fixed-position ion chambers will only be used in the M2 line. In locations like the M3 line and Delivery Ring that will also see Mu2e beam, the ion chambers will be put inside of vacuum cans and made retractable.

3812 considered for mixed-secondary beam. These devices have the advantage of being completely
 3813 passive, and not requiring a break in the vacuum, which may make them a better fit in the
 3814 M3 line where we need to stay compatible with the higher intensities of Mu2e operations,
 3815 and the Delivery Ring where beam circulates for approximately 56 ms in Mu2e operations.
 3816 New WCM designs are being considered that would provide accurate intensity measurements
 3817 for secondary beam during $(g - 2)$ operations. The design is based on that of a WCM for
 3818 Mu2e extraction. Each slice of the slow-spilled Mu2e beam is approximately 2×10^7 , which is
 3819 consistent with the intensity that we would expect in the M3 line and Delivery Ring during
 3820 $(g - 2)$ operations.

3821 BPMs were a key diagnostic in Antiproton-Source operation providing sub-millimeter
 3822 orbit information in the beamlines and Delivery Ring. BPMs are located at each quadrupole,
 3823 providing ample coverage. There are 34 BPMs in the AP2 line, 28 BPMs in the AP3 line
 3824 and 120 BPMs in the Delivery Ring; however, it is believed that the BPMs in these areas
 3825 will not be able to see the low-intensity 2.515 MHz $(g - 2)$ secondary beam.

3826 SEMs will be used to measure beam profiles in the M2 and M3 lines, as well as the
 3827 Delivery Ring. There are eight SEMs in the AP2 line, seven SEMs in the AP3 line, three
 3828 SEMs in the D/A line, two in the Debuncher, one in the Accumulator and three spares from
 3829 the former AP4 line to draw from. SEM tunnel hardware will require some maintenance, and
 3830 locations where SEMs are moved will require new cable pulls. Beam studies showed that
 3831 special high-gain preamps will be required to measure the low-intensity secondary beam
 3832 during $(g - 2)$ operations [3]. There are only two working high-gain preamps, so additional
 3833 preamps will need to be designed and fabricated. Additional SEMs will need to be added

3834 to the Delivery Ring from the pool of unused SEMs and spares. A photo of a SEM and its
 3835 profile display are shown in Fig. 7.54.

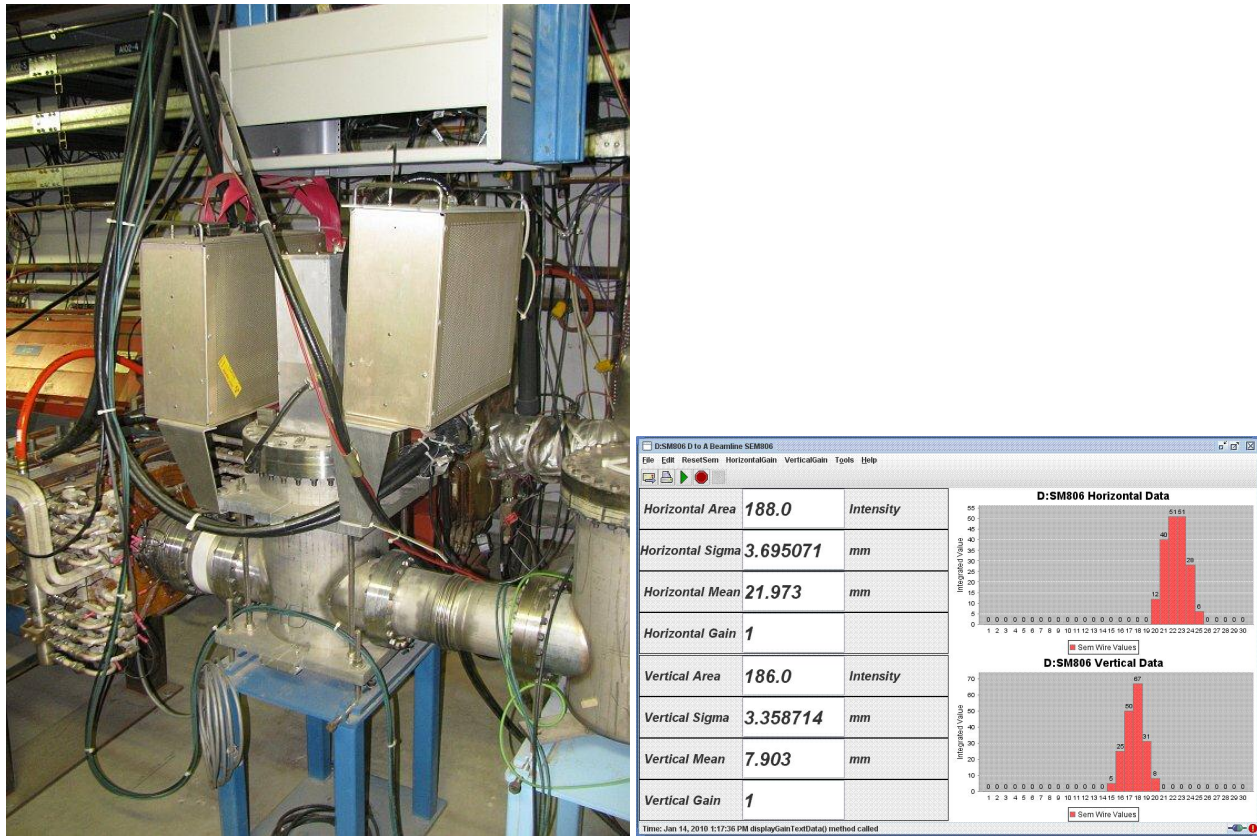


Figure 7.54: SEMs will be used to measure mixed secondary beam profiles. SEM tunnel hardware (left) is pictured. Preamp boxes are mounted next to the vacuum can. The SEM wires can be pulled out of the beam when not in use. SEMs can be used with to measure beam profiles, positions and intensities (right).

3836 BLMs (Fig. 7.55) will be used to help maintain good transmission efficiency through the
 3837 lines. Both Delivery-Ring and AP3 loss monitors will use the existing hardware and elec-
 3838 tronics for $(g - 2)$ operations, but will be replaced for the higher-intensity Mu2e operations.
 3839 Care will need to be taken to make a BLM plan that allows for switching back and forth
 3840 between the two separate BLM systems.

3841 **Proton Secondaries** Proton secondaries will extracted to the DR abort line and will have
 3842 a similar beam intensity to that of the Delivery Ring. Existing instrumentation from the
 3843 downstream AP2 line will be used. A toroid will be used to measure beam intensity for Mu2e
 3844 operations, but will be out of its operational range for $(g - 2)$. If intensity measurement is
 3845 needed, a retractable ion chamber will be added to the line. Ion chambers, SEMs and BLMs
 3846 will be used in the same way they are for the mixed secondary lines.



Figure 7.55: Two styles of BLMs will be used. Tevatron-style ion chamber loss monitors (left) will be used in areas of primary beam, and also in the Delivery Ring for Mu2e operations. The Pbar-style ion chamber, which consists of a plastic scintillator and a long light guide connected to a photomultiplier tube shielded from light in PVC, will be used in the Delivery Ring during $(g - 2)$ operations.

3847 **Muon Secondaries** Muon secondaries will traverse the upstream portion of the M4 line
 3848 and the M5 line. The largest technical challenge will be measuring muon secondary beam,
 3849 which models show should be on the order of 10^5 muons per pulse. This is two or three
 3850 orders of magnitude smaller than the upstream mixed-secondary beam. Most of our standard
 3851 diagnostics will not work at these beam intensities.

3852 Beam intensity will be measured with ion chambers that are designed with three signal
 3853 foils and four bias foils to increase the signal amplification. This design will allow beam
 3854 intensity measurements down to 10^5 particles. The ion chamber in the M4 line will need to be
 3855 retractable in order to be compatible with Mu2e operations, while the M5-line ion chambers
 3856 can be permanently in the beam path. New ion chambers will be designed and built for
 3857 the M4 line because there is not a pool of available spares to populate these beamlines.
 3858 Ion chambers for the M5 line will be provided by the repurposed BNL SWICs as will be
 3859 discussed below. A Wall Current Monitor is another option being considered for beam-
 3860 intensity measurement in the upstream M4 line. Though this device may be able to measure

3861 the Mu2e slow-spill beam intensity, it is not clear if one could be designed that is sensitive
3862 enough to see the lower-intensity muon beam expected for $(g - 2)$ operations.

3863 The base plan for measuring beam profiles in the upstream M4 and M5 lines are to
3864 use Segmented Wire Ion Chambers (SWICs), which are very similar to Multiwires with the
3865 exception that the beam goes through ArCO₂ gas, which is ionized by the charged-particle
3866 beams, creating an amplification that allows measurements of beam intensities down to the
3867 10^4 particle range. In addition, SWICs are robust enough to handle particle beams several
3868 orders of magnitude higher in intensity than are expected during $(g - 2)$ operations. This
3869 will provide the flexibility of running higher-intensity protons through the M4 and M5 lines
3870 for commissioning and beam studies. The SWICs in the upstream M4 line will need to be
3871 retractable since they are a destructive measurement device. Some vacuum cans can be
3872 acquired from other systems in order to minimize the cost; however, the inventory of spare
3873 vacuum cans is not sufficient enough to cover all of the SWICs. The SWICs in the M5 line
3874 will be combination SWIC and Ion Chamber units repurposed from BNL. These devices
3875 have both wires for measuring beam profiles as well as foils for measuring beam intensities,
3876 but are not retractable and require vacuum windows on both sides of the device.

3877 While maintenance is being performed on the BNL SWICs and interfaces to the FNAL
3878 control system are being designed for these devices, three alternate options were or will be
3879 considered for beam profile measurement in the M5 line. The first option is to design and
3880 build new SWICs. This would give us the flexibility of making them retractable and not
3881 require additional vacuum breaks; however, it would also require us to design and build
3882 new Ion Chambers for the line. Similar to the BNL SWICs, newly designed SWICs would
3883 measure beam down to the the 10^4 particle range.

3884 A second option that was considered is the Proportional Wire Chamber (PWC). The
3885 advantage of the PWC is that it can measure beam down to 10^3 particles, and the wire
3886 planes are modular. The major disadvantage is that the wires are easily damaged by higher-
3887 intensity pules, limiting the ability to run higher intensity study beam.

3888 The third option that was considered is to design Scintillator Fiber Profile Monitors
3889 (SFPMs), which can measure down to 100 particles. These devices are similar to SWICs or
3890 PWCs, but the wires are replaced with scintillating fiber. They have been used in the SY120
3891 test-beam lines, and the fibers have been shown to survive long periods of beam operation.
3892 The largest disadvantage is that SFPMs cost significantly more than SWICs.

3893 The upstream M4 line will be made compatible with both Mu2e and $(g - 2)$ operations.
3894 Beam in the M4 line for $(g - 2)$ will be at least two orders of magnitude smaller than the
3895 individual slices of slow-spilled beam that the line will see in Mu2e operations.

3896 If muon beam profile information cannot be accurately measured with the proposed
3897 diagnostics, one option being considered is to develop a tune-up mode. In this mode, protons
3898 in the Delivery Ring would not be sent to the abort, but extracted toward $(g - 2)$ with the
3899 muon beam. This would result in 10^7 particles per pulse in the extraction lines, which is
3900 easily measured by ion chambers and SWICs.

3901 The Cherenkov counter that was used in the BNL experiment is also being prepared for
3902 measurement of particle-type in the M5 line during $(g - 2)$ beam commissioning, as well as
3903 in the AP2 line for beam tests during the preliminary design phase.

3904 **Accelerator instrumentation summary**

3905 A summary of instrumentation devices which will potentially be used for $(g - 2)$ is shown in
 3906 Table 7.19.

Beamline	Beam type	Intensity	Position	Profile	Loss
Primary protons	P1, P2, M1	toroids	BPMs	multiwires, SEMs	BLMs
Mixed secondaries	M2, M3, DR	ion chambers, WCMs	SEMs	SEMs	BLMs
Proton secondaries	DR abort	ion chambers, WCMs	SEMs	SEMs	BLMs
Muons	M4, $(g - 2)$	ion chambers, WCMs	SWICs, PWCs, SFPMs		

Table 7.19: Potential instrumentation to be used in the beamlines for $(g - 2)$ operations.

7.7 ES&H, Quality Assurance, Value Management, Risk

7.7.1 ES&H

The Accelerator Division ES&H Department has the responsibility for providing Environmental, Safety, and Health coordination and oversight of ES&H for all accelerator work on the project. As with all Fermilab projects, attention to ES&H concerns will be part of the project management, and Integrated Safety Management will be incorporated into all processes. Line management responsibility for ES&H will be maintained on this project. Safe coordination of installation activities will be accomplished through the Project Management team, Project ES&H Coordinator, Project Engineer, and Task Manager. During installation, the Subcontractors, T&M Crafts, and all Fermilab personnel will utilize Job Hazard Analyzes to plan all work and to mitigate hazards. The Project Manager and Project ES&H Coordinator will audit compliance with all applicable ES&H requirements.

The handling and installation of magnets, vacuum systems, power supplies, and other accelerator components are common tasks within the Accelerator Division, and standard safety practices will be used. If any work falls outside of common practices, job hazard analyses will be conducted in order to ensure that the tasks are performed safely. Detailed procedures exist for handling components in the radioactive target vault, and the activation will be lower after years of not running beam than it was during antiproton production.

7.7.2 Quality Assurance

All aspects of the accelerator work will be periodically reviewed with regard to Quality Assurance issues from Conceptual Design through completion. The following elements will be included in the design and construction effort: an identification of staff assigned to each task with clear definition of responsibility levels and limit of authority as well as delineated lines of communication for exchange of information; requirements for control of design criteria and criteria changes and recording of standards and codes used in the development of the criteria; periodic review of the design process, drawings, and specifications to insure compliance with accepted design criteria.

7.7.3 Value Management

Significant cost savings have been incorporated into the $(g-2)$ accelerator design by utilizing the existing infrastructure from the Antiproton Source. Existing target station components will be reused: target, lens, collimator, and momentum-selection magnet, as well as maintaining the same target-vault layout. A new target-station dump to replace the current one which has an internal water leak will be constructed using the existing design. As many existing components as possible will be reused for the beamlines, including beamline magnets from the previous $(g-2)$ experiment at BNL. New magnets will be based on existing designs, where practical. Much of the beamline instrumentation will also be recycled, with upgraded readout electronics where necessary in order to see the low-intensity $(g-2)$ secondary and tertiary beam.

3946 7.7.4 Risk

3947 The largest risks to the cost and schedule of the accelerator work are delays of funding and
3948 lack of engineering support when it is needed.

3949 Another large risk depends on Mu2e shielding needs in the Delivery-Ring D30 straight
3950 section, which have not yet been fully determined. Shielding may need to be placed in
3951 areas which would obstruct current plans for reconfiguration of beamlines and cable trays.
3952 Magnets may need to be made radiation-hard.

3953 The external beamline depends on a new tunnel enclosure being built under a General
3954 Plant Project. If that project is delayed or if construction costs rise, there may be a burden
3955 on $(g - 2)$.

3956 Conflicts and difficulty of work in the congested area of the D30 straight section and the
3957 M3 line which joins the DR in that area are a schedule risk on the order of a month or two.

3958 There is also an opportunity that the M2/M3 crossover design may be simplified and be
3959 made to cost up to \$500k less.

3960 Magnets which need to be built new and those which have been taken from the BNL
3961 beamline carry a risk on the order of \$200k.

3962 The possibility that existing accelerator controls infrastructure is not able to support
3963 $(g - 2)$ is low, but carries risks on the order of \$100-200k. The risk that various types of
3964 instrumentation cannot be refurbished or upgraded to see the low-intensity $(g - 2)$ secondary
3965 beam would require new instrumentation to be built at a cost of roughly \$200-400k and a
3966 4-month delay.

3967 The biggest technical risk was that the lithium lens used for focusing secondaries off the
3968 target would not be able to pulse at the $(g - 2)$ rate. However, a lens has been pulsed in a
3969 test stand at the average 12-Hz rate for 70 million pulses without any sign of lens failure,
3970 confirming ANSYS simulations which predicted that mechanical fatigue should be less than
3971 it was during antiproton production.

3972 There is an opportunity to save \$100k if a new transformer will not be required in order
3973 to support the lens power supply.

3974 The risk that the target station does not provide the desired yield may be handled by
3975 running the experiment for a longer period, or additional cooling may be needed for the final
3976 focus system, or a new target may be designed and constructed.

References

3977

- 3978 [1] W. Pellico *et al.*, “Proton Source Task Force Report”, Beams Doc. 3660 (2010); F. G.
3979 Garcia *et al.*, “Fermilab Proton Improvement Plan Design Handbook”, Beams Doc 4053
3980 (2012).
- 3981 [2] D.S. Ayres *et al.*, “NO ν A Technical Design Report”, NO ν A Doc 2678 (2007).
- 3982 [3] D. Still *et al.*, “ $g - 2$ Yield Beam Study Results – April 2012”, $g - 2$ Doc 430 (2012).
- 3983 [4] I. Kourbanis, “Bunch Formation for $g - 2$ experiment”, $g - 2$ Doc 335 (2012).
- 3984 [5] M. Xiao, “Transport from the Recycler Ring to the Antiproton Source Beamlines”,
3985 Beams Doc 4085 (2012).
- 3986 [6] N.V. Mokhov, “The Mars Code System User’s Guide”, Fermilab-FN-628 (1995); O.E.
3987 Krivosheev, N.V. Mokhov, “MARS Code Status”, Proc. Monte Carlo 2000 Conf., p. 943,
3988 Lisbon, October 23-26, 2000; Fermilab-Conf-00/181 (2000); N.V. Mokhov, “Status of
3989 MARS Code”, Fermilab-Conf-03/053 (2003); N.V. Mokhov, K.K. Gudima, C.C. James
3990 *et al.*, “Recent Enhancements to the MARS15 Code”, Fermilab-Conf-04/053 (2004);
3991 <http://www-ap.fnal.gov/MARS/>.
- 3992 [7] C. Yoshikawa *et al.*, “Optimization of the Target Subsystem for the New $g - 2$ Experi-
3993 ment”, IPAC2012.
- 3994 [8] S. Striganov, “Optimization of $g - 2$ Target Parameters”, Fermilab Doc GM2-doc-197.
- 3995 [9] Muons, Inc., <http://www.muonsinc.com/muons3/G4beamline>.
- 3996 [10] B. Drendel *et al.*, “Antiproton Source Rookie Book”, Beams-doc-2872, June 2010.
- 3997 [11] ANSYS® , <http://www.ansys.com>.
- 3998 [12] R. Shultz, “ANSYS Mechanical Simulation for Lithium Lens”, Fermilab Doc GM2-doc-
3999 362.
- 4000 [13] T. Leveling, “An Estimation of Antiproton Source Target Station Performance for Muon
4001 $g - 2$ ”, $g - 2$ Doc 536.
- 4002 [14] C. Hojvat *et al.*, “The Fermilab Tevatron I Project Target Station For Antiproton
4003 Production”, Fermilab TM-1175 (March 1983).

- 4004 [15] D.C. Carey, K.L. Brown, F. Rothacker, FERMILAB-Pub-98/310 (1998).
- 4005 [16] *g* – 2 Doc 484 (2012).
- 4006 [17] V. Lebedev, *g* – 2 Doc 171 (2012).
- 4007 [18] *g* – 2 Doc 252 (2012).
- 4008 [19] J.P. Morgan, “Power tests for Pbar service buildings”, Mu2e Doc 2117 (2012).
- 4009 [20] B. Drendel *et al.*, “Pbar Controls Reference Material”, Mu2e-doc-1161, May 2012.
- 4010 [21] A. R. Franck *et al.*, “HOTLink Rack Monitor”, FERMILAB-Conf-01/342/E.
- 4011 [22] B. Drendel *et al.*, “Controls to Mu2e/g-2/Muon and Communications Duct Issues”,
4012 Mu2e-doc-2069, February, 2012.
- 4013 [23] communications duct details and alternative plans
- 4014 [24] N. Eddy and E. Harms, “Beamline BPM Upgrade”, Beams-doc-1279, September 2004.

Chapter 8

Beam Rate Simulations

The ultimate goal of the beam delivery simulations is a complete “End-to-End” study from pion production on the target to stored muons in the ring. This goal will be achieved by using a sequence of specialized tools. They include a `MARS` calculation for pion production, a combination of phase-space, `Decay Turtle`, and `G4Beamline` calculation of the pion-to-muon decay line, the Delivery Ring, and the final beamline into the storage ring, and a detailed `GEANT4` simulation of the transmission into the ring and the final storage fraction. This is ongoing work by many collaborators. Below we present the status of the individual pieces.

8.1 Pion Production at the Target

The description of the target, lithium lens and initial bending magnet—`PMAG`—are given in Chapter 7. We briefly summarize. Beam tests were performed in 2012 to measure the target yield. The instrumentation was sensitive to the total number of charged particles but it could not differentiate between particle species. Plans are in place to repeat the test in 2013 using a Cherenkov counter to measure the particle composition of the beam. The yield of positive 3.1 GeV/ c secondaries from 10^{12} 8 GeV protons on target measured in the beam test was almost a factor of four higher than the 2.2×10^8 particles with $|dp/p| < 10\%$ and 40π mm mr emittance predicted by `MARS` simulations at the beginning of the AP2 line, and was about 60-80% of the number predicted at the end of the AP2 line with $|dp/p| < 2\%$ and 35π mm mr. Extrapolated back to the start of the AP2 line, that prediction is 4.8×10^7 positive secondaries. The spot size of the beam on target was $\sigma_x = \sigma_y = 0.5$ mm. As discussed in Sec. 7.4.1, we plan to reduce the spot size to 0.15 mm, which is expected to increase the yield of particles with $|dp/p| < 2\%$ by 40-60%. The expected yield of positive 3.1 GeV/ c secondaries with $|dp/p| < 2\%$ exiting the target station will then be at least 4×10^8 , with the simulation predicting 48% or 2×10^7 of these to be π^+ 's. We used this number in our bottom-up rate estimate and for what follows below.

4042 8.2 Muon capture in the straight section of the decay 4043 line

4044 While the G4Beamline code for particle tracking through the $(g - 2)$ beamline is under
4045 development, a valuable insight on the muon collection in a decay line and characteristics
4046 of the muon beam can be obtained with phase space calculations. In Fig. 8.1 we compare
4047 the collection efficiency of muons in the straight section of the E821 and E989 beamlines.
4048 It was obtained by applying the calculated pion momentum cut (see Fig. 8.2) to the muon
4049 capture probability $Y_{\mu\pi}$ and scaling with horizontal (ε_x) and vertical emittance of the beam
4050 (ε_y). For the E821 beamline we used $\varepsilon_x = 42 \text{ mm}\cdot\text{mrad}$, $\varepsilon_y = 56 \text{ mm}\cdot\text{mrad}$; for the E989
4051 beamline we assumed $\varepsilon_x = \varepsilon_y = 40 \text{ mm}\cdot\text{mrad}$.

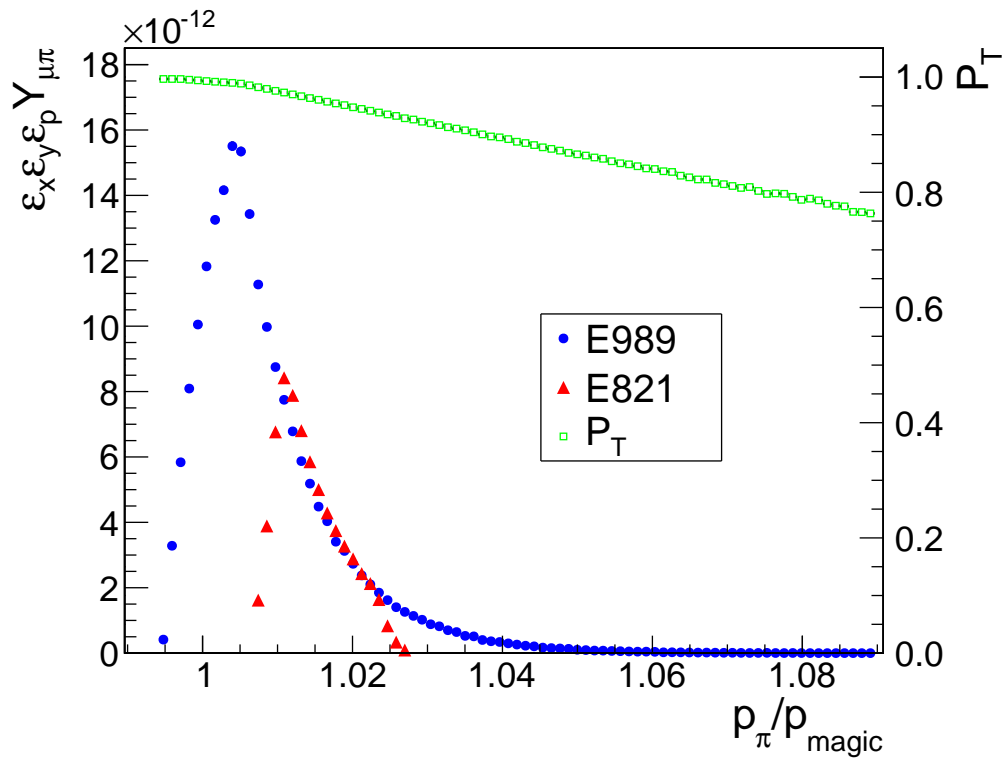


Figure 8.1: Number of muons captured in the straight section of the E821 (red triangles) or E989 beamline (blue circles). Muon polarization is shown by green squares. The muons have the magic momentum $\pm 0.5\%$.

4052 Even though the emittance of the pion beam will be smaller in E989 than in E821, a
4053 higher fraction of the decay muons will be captured by the E989 beamline due to the wider
4054 pion momentum band. An additional factor originates due to the longer decay line in E989,
4055 allowing more pions to decay into muons. The number of decay muons per initial number of
4056 pions is described by (8.1)

$$\frac{N_\mu}{N_\pi} = \left(1 - e^{-L/\beta_\pi \gamma_\pi c \tau_\pi}\right) e^{-L/\beta_\mu \gamma_\mu c \tau_\mu}, \quad (8.1)$$

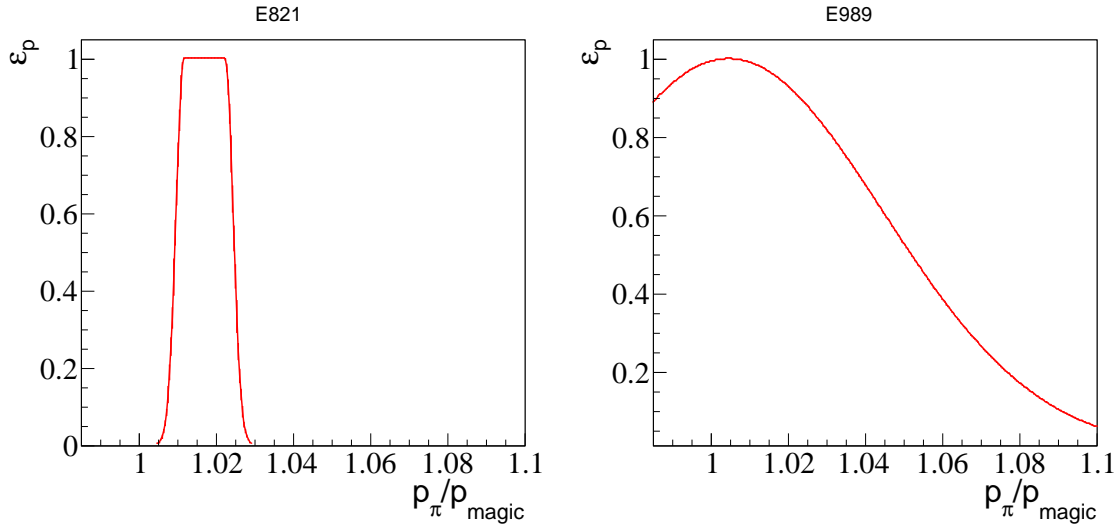


Figure 8.2: Pion momentum bite for E821 (left) or E989 beamline (right).

4057 where L is the length of the decay line. This is illustrated in Fig. 8.3. Thus, the total increase
 4058 in the number of captured muons due to both factors in E989 over E821 is about eight.

4059 The capture fraction for muons in a $|dp/p| < 0.5\%$ momentum bite from the $|dp/p| < 2\%$
 4060 transmitted pion beam is determined to be 0.36% in the M2 (AP2) line, and assuming the
 4061 same efficiency in the M3 line, the number of decay muons entering the Delivery Ring will
 4062 be approximately 5×10^4 . During the 3-4 turns around the 505 m Delivery Ring and then
 4063 through the 128 m M4 and M5 line, the remaining 28% of pions will decay, and approximately
 4064 10% of the muons will also decay. Our studies have not yet accounted for the possible gain
 4065 of additional captured muons in the DR.

4066 Therefore, the number of decay muons with $|dp/p| < 0.5\%$ delivered to the entrance of
 4067 the storage ring in a 120 ns bunch with 10^{12} protons on target is expected to be close to
 4068 5×10^4 .

4069 The calculated polarization component of muons in the spin precession plane is shown
 4070 by green squares in Fig. 8.1. Thus, phase space calculations predict a slightly higher average
 4071 polarization of muons from the straight section in E989 ($P_T = 97.7\%$) over E821 ($P_T =$
 4072 96.3%).

4073 Note that muons from the target station and from bending sections of the beamline
 4074 may have very different characteristics than the muons from the straight section. We are
 4075 planning to extend our calculations to the bending sections. To simulate muons from the
 4076 target station we are planning to use programs MARS and G4Beamline.

4077 8.3 G4Beamline simulations of beam transport and muon 4078 capture

4079 The particle tracking simulation program G4Beamline is based on GEANT4 toolkit. It is
 4080 designed to extend GEANT4 simulations to beamline elements, beam transport lines and decay

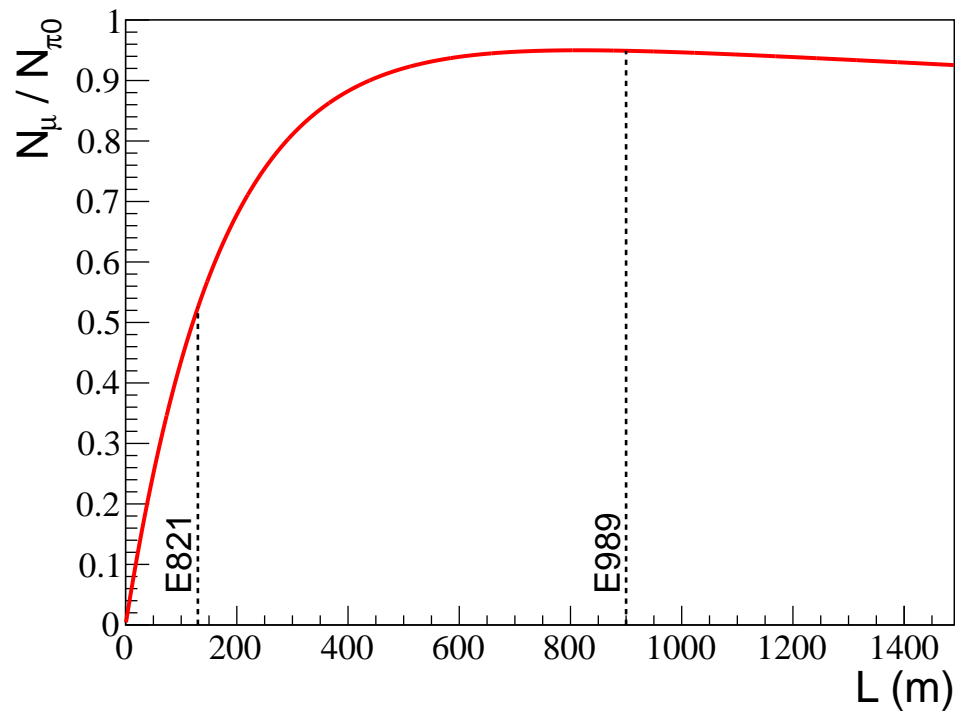


Figure 8.3: Number of muons vs. decay line length.

4081 beam lines. Tracking of particles in `G4Beamline` through a system is as accurate and realistic
 4082 as the `GEANT4` toolkit implements. `G4Beamline` will allow us to simulate various important
 4083 aspects of the $(g - 2)$ experiment on a common ground, including muon production in the
 4084 decay line, and muon capture by the beamline, muon transportation to the $(g - 2)$ ring.
 4085 Most importantly, in combination with the `GEANT4`-based simulation program `gm2RingSim`
 4086 it will allow us to study beam-related systematic errors in $(g - 2)$.

4087 The current `G4Beamline` model of the *M2-M3-delivery ring* section of the $(g - 2)$ beamline
 4088 was obtained directly from lattice in `MAD` format (Fig. 8.4).

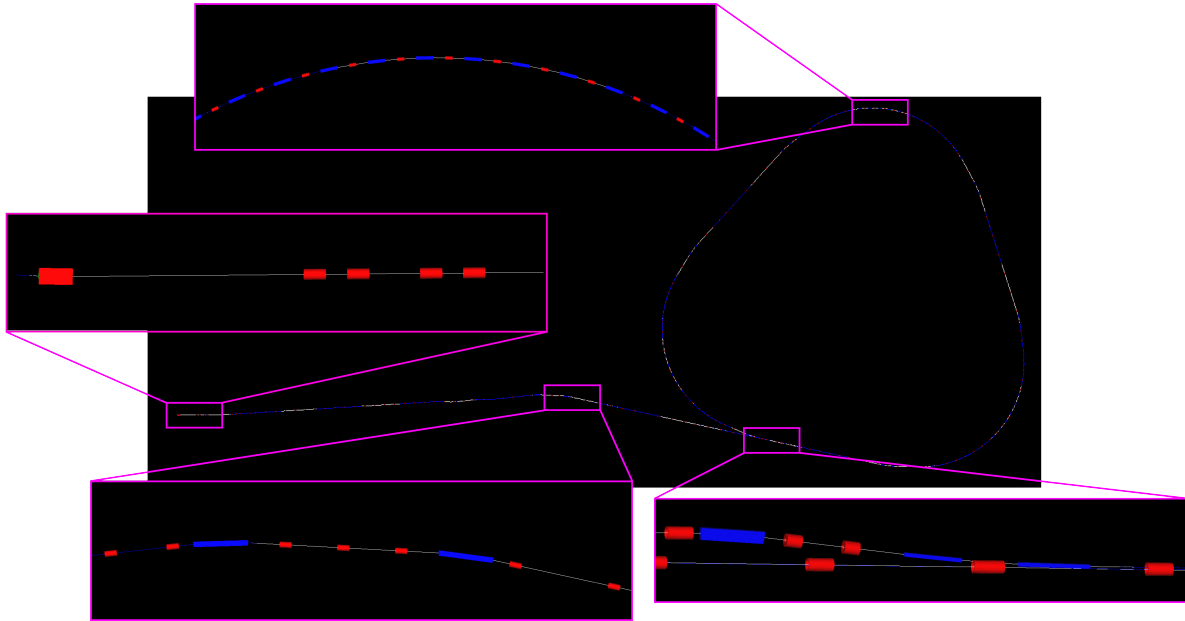


Figure 8.4: `G4Beamline` model of the *M2-M3-delivery ring* section of the $(g - 2)$ beamline.

4089 Our initial attempt to use the `G4Beamline` for $(g - 2)$ beamline flushed out a number
 4090 of important deficiencies in the program. Even though `G4Beamline` has been used with
 4091 success by a number of groups, the code had never been exercised much or at all to model
 4092 non-planar lattices. Thus, when the positions of the `G4Beamline` magnets were compared to
 4093 the 3-dimensional site coordinates produced with the `MAD survey` command, they were rather
 4094 different. We ultimately identified and corrected two problems

- 4095 1. Rectangular bend magnets were effectively rotated in space with respect to a point
 4096 located in the center of the magnet rather than at the upstream end. Aside from
 4097 affecting the position of the downstream elements, this also adversely affected the
 4098 geometric acceptance.
- 4099 2. The beam reference coordinate system was not being transformed properly for all
 4100 rotated bending dipole magnets. This resulted in completely incorrect positions for all
 4101 magnets downstream of any rotated dipole.

4102 Several other identified and fixed problems include *i*) bugs in storing and reading back the
 4103 results of simulations; *ii*) inefficient algorithm was used to determine the position in beam

4104 coordinates leading to $O(N^2)$ scaling of the number of iteration with the number of elements
 4105 N (the updated algorithm has $O(N^2)$ scaling now); The fixes were sent to the code developers
 4106 to be included into the next official release of **G4Beamline**. A few issues still require some
 4107 attention. As of time of this writing, **G4Beamline** still does not correctly handle dipole edge
 4108 focusing. A work on the fix is in progress.

4109 The **G4Beamline** code in its current status allows particle tracking starting from the **PMAG**
 4110 (right after the target station) and up to one turn in the delivery ring. To simulate beam
 4111 extraction from the delivery ring, a time-dependent kicker field needs to be implemented.
 4112 This work is in progress.

4113 Below we show some preliminary results of **G4Beamline** simulations that verify our phase-
 4114 space simulations in a simpler system. The **G4Beamline** program was used successfully to
 4115 simulate muon production and capture in a FODO section of the decay beamline. A FODO
 4116 section is a straight section, it does not contain any dipole magnets. Therefore the simulations
 4117 were not affected by the above described deficiencies of the code. The probability of muon
 4118 production within $\pm 0.5\%$ of magic momentum and capture by a FODO section with 60°
 4119 phase advance is shown in Fig. 8.5 as a function of pion momentum (blue symbols). We
 4120 observe good agreement between the two simulation approaches.

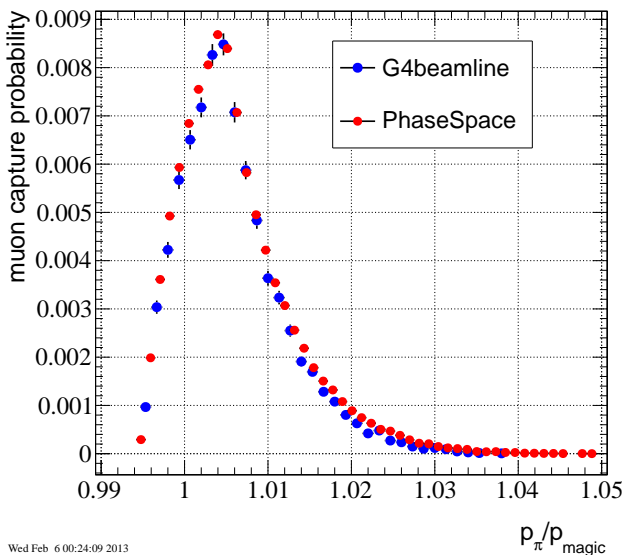


Figure 8.5: Muon production and capture probability in a FODO90 lattice vs. pion momentum, **G4Beamline** (blue symbols) or phase space simulations (red symbols).

4121 8.4 Muon Transmission and Storage Simulations

4122 Muon transmission into the ring and the storage fraction are studied using a detailed
 4123 **GEANT4** simulation of the E821 $g - 2$ experiment, together with substitutions for certain
 4124 elements as proposed in this CDR. The storage rate depends strongly on the amount of

4125 material the muon beam must traverse, as well as the intrinsic momentum spread (dp/p) of
 4126 the muon beam. Common to the studies presented here is the assumption that an ideal
 4127 storage ring kick will be provided to the incoming muon bunch, see Chapter 13. A baseline
 4128 storage rate of 6.5% for a 40π muon beam with $|dp/p| < 0.5\%$ is predicted assuming the
 4129 muon beam must scatter through the two closed ends of the *existing* E821 inflector and the
 4130 *existing* outer Q1 plate and support. Under an ideal setting of a fully open inflector and no
 4131 Q1 scattering, a storage of 22% is expected. A summary of a much larger set of studies is
 4132 presented here.

4133 8.4.1 Simulation Overview

4134 The $g - 2$ muon storage region is a torus with central radius 7112 mm and a ± 45 mm inner
 4135 and outer radius as seen in Fig. 8.6. The $+x$ axis is directed toward the inflector where
 4136 the muons enter the ring, $+z$ is aimed to the right 90° downstream of the x axis, and the
 4137 y axis is oriented in and out of the page with the positive direction defined as outward.
 4138 This coordinate system is useful to describe the ring as a whole (e.g., where is the inflector
 4139 in relation to some other system), but a different beam-centric coordinate is used when
 4140 describing beam dynamics. This coordinate system places the muon beam at the origin
 4141 with the $+x$ direction defined as radially outward, the $+z$ direction aligned with the muon
 4142 momentum direction or more commonly the azimuth direction in a cylindrical coordinate
 4143 system, and the y direction remains unchanged from the previous coordinates. This system is
 4144 shown schematically in Fig. 8.6. The latter coordinate system will be used in this document
 unless otherwise specified.

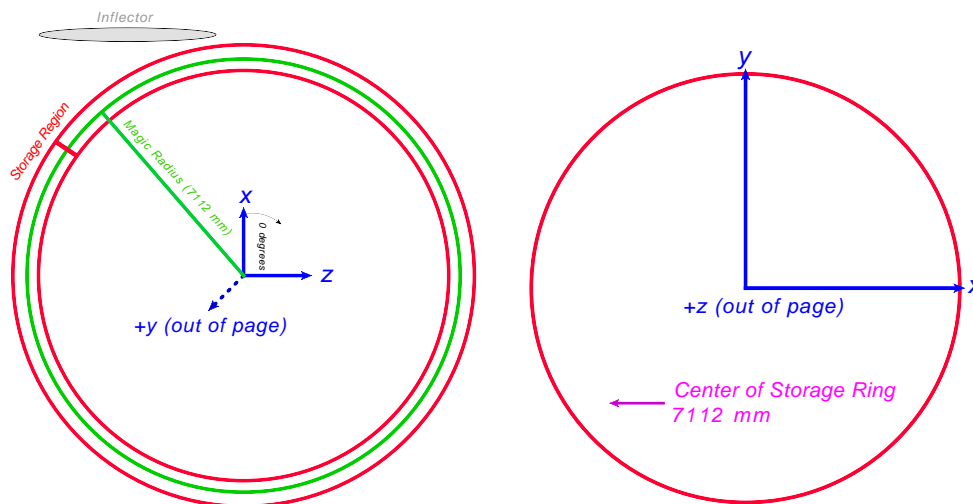


Figure 8.6: Left: Schematic of the $g - 2$ muon storage region viewed from above with the associated coordinate system. The magic radius orbit is shown in green and the inner and outer boundaries of the muon storage region are shown in red. The inflector is shown in grey for orientation. Right: Schematic of the muon beam coordinate system viewed head-on inside the $g - 2$ storage region

4146 The muon beam used at the start of the simulation is created by an “inflexor gun,” a
 4147 GEANT4 particle gun that allows the user to sample a particle phase space $(x, p_x/p_z, y, p_y/p_z)$
 4148 given a set of beam emittances $(\epsilon_{x,y})$ and Twiss parameters $(\alpha_{x,y}, \beta_{x,y}, \gamma_{x,y})$. The beam
 4149 emittance ellipse is defined such that 95% of the beam phase space is contained within the
 4150 bounded region. This is represented by Eq. 8.2 below, with $x' \equiv p_x/p_z$ and $y' \equiv p_y/p_z$.

$$\gamma_x x^2 + 2\alpha_x x x' + \beta_x (x')^2 < \epsilon_x \quad (8.2)$$

$$\gamma_y y^2 + 2\alpha_y y y' + \beta_y (y')^2 < \epsilon_y \quad (8.3)$$

4151 Only two of the three Twiss parameters are required since the third can be computed using
 4152 the Courant-Snyder invariant relationship shown in Eq. 8.4. In practice, γ is the derived
 4153 quantity.

$$\beta\gamma - \alpha^2 = 1 \quad (8.4)$$

4154 Fig. 8.7 is a schematic diagram indicating the relationship between the Twiss parameters
 4155 and physical degrees of freedom (x, x') . It can be seen in this diagram that the maximum
 extent of the beam is given by $\sqrt{\epsilon\beta}$ and the maximum x' is given by $\sqrt{\epsilon\gamma}$.

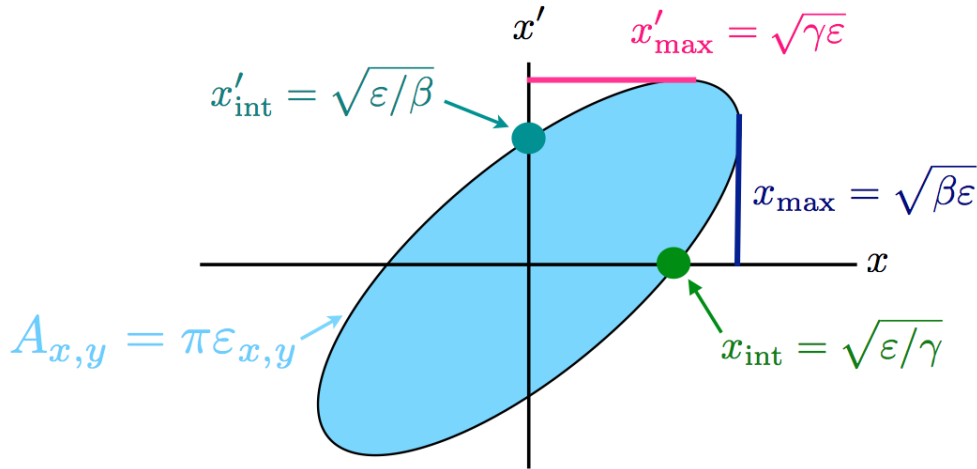


Figure 8.7: Relationship between the Twiss parameters and the physical degrees of freedom x and x' .

4156 The magnitude of the beam momentum is computed by sampling a Gaussian centered
 4157 at the magic momentum ($p_m \equiv m_\mu/a_\mu = 3.094 \text{ GeV}/c$) and a width (dp/p) . Typical values
 4158 for $|dp/p|$ range between 10^{-4} and 10^{-1} for this study.

4159 The beam is generated at a fixed z position either along the inflexor main axis or along
 4160 the azimuthal direction within the $g - 2$ storage region. Typically, the Twiss parameters
 4161 are defined at the “downstream” end of the inflexor one millimeter before the beam must
 4162 traverse inflexor coils. A transport matrix is employed to recompute the Twiss parameters
 4163 when the beam originates at the “upstream” end of the inflexor, which is defined as one
 4164 millimeter before the beam must enter the outer inflexor cryostat. A drift space approx-
 4165 imation is used for the transport matrix. In all studies, the muon storage is computed as
 4166

4167 the ratio of muons remaining in the ring after 100 revolutions vs. the incoming flux, with
 4168 muon decay turned off. The storage ring kicker magnetic field is assumed to be a square
 4169 pulse applied to the first turn only, and at an ideal magnitude (typically 220 G), tuned to
 4170 maximize the storage rate for the given conditions. The E821 LCR pulse was also studied
 4171 for comparison. This non-ideal pulse shape (and magnitude) were not considered for E989.
 4172 Variations studied and optimized in the following include the beam entrance “launch” angle
 4173 into the inflector, the geometrical inflector angle with respect to a tangent to the storage
 4174 ring central radius, and the momentum spread $|dp/p|$ of the incoming beam. Here we report
 4175 only on the storage rate for $|dp/p| < 0.5\%$; the intrinsic momentum acceptance of the ring
 4176 is much smaller.

4177 A number of discrete variations were explored. They include:

- 4178 • **Inflector Field:** *Mapped* means the computed, true inflector magnetic field is loaded
 4179 and vectorially added to the main magnet fringe field. *Vanish* means the field within
 4180 the inflector is identically zero (idealized).
- 4181 • **Inflector Geometry:** *Closed-Closed* represents the existing E821 inflector with the
 4182 magnetic coils covering both the upstream and downstream ends. It also includes the
 4183 aluminum cryostat materials. *Open-Open* is a hypothetical new inflector with both
 4184 upstream and downstream ends open. Intermediate cases have also been studied.
- 4185 • **Quad Geometry:** *Full* is the existing E821 geometry for the outer Q1 quadrupole
 4186 plate and the mechanical Macor standoffs that hold the plate in position. The trajec-
 4187 tory of the incoming muon beam passes through these materials at a small glancing
 4188 angle. The energy loss and multiple scattering have an impact on the storage frac-
 4189 tion. *No Quads* represents the proposed E989 geometry where the Q1 outer plate
 4190 is displaced radially such that no muons pass through these materials. Intermediate
 4191 geometries—e.g., existing Q1 and removed standoffs—were also studied.
- 4192 • **Incoming Beam Tune:** *The E821-match* parameters were determined by minimizing
 4193 the beam amplitude within the inflector volume. *Ideal-match* parameters are derived
 4194 by assuming ideal phase space matching into the storage ring with uniform quadrupole
 4195 coverage.

4196 The generated phase space for an $A = \epsilon\pi = 40\pi$ beam starting in the Downstream
 4197 position with the two beam types, E821-match and Ideal-match, are shown in Fig. 8.8.

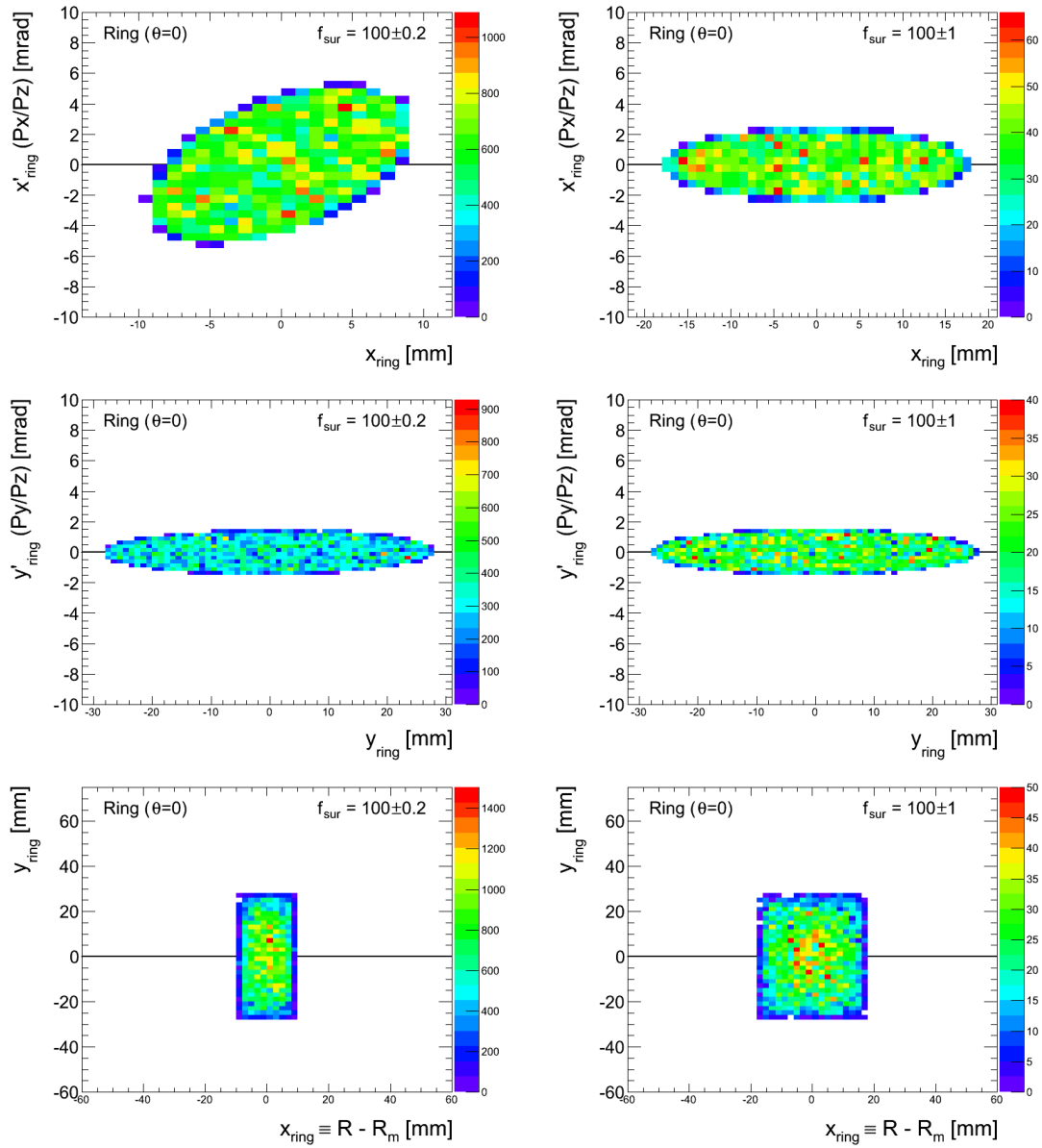


Figure 8.8: Generated Phase Space for the E821-match (left column) and Ideal-match (right column) Beams. The left column shows $x - x'$ and the right column shows $y - y'$. In all plots the origin intersects with the main inflector axis. The most noticeable difference between these two beams is the horizontal width.

4198 8.4.2 Results for Beam Starting at Upstream Entrance of the In- 4199 flector

4200 Here we present the main findings of the studies in which the incoming beam is launched
4201 into the upstream entrance of the inflector. It must cross both ends of the inflector (whether
4202 “open” or “closed,” through the 1.7 m “D”-shaped inflector beam channel physical limi-
4203 tations, and through, if applicable, the outer Q1 plate/support system before entering the
4204 storage region. Fig. 8.9 is a schematic of the magic radius (red line) and the starting location
4205 of the muon momentum vector (blue arrow) and their relationship to other systems in the
4206 ring. The region indicated by “Kicker Plates” provides the idealized horizontal deflection
4207 appropriate to the given situation. There are two degrees of freedom, δ and ℓ , as the beam
4208 enters the storage region. If the inflector is oriented such that it is tangent to the ring,
4209 then the maximum storage rate occurs when $\ell = 0$ and $\delta = -6$ mrad in the case of a fully
4210 vanishing magnetic field within the inflector. In the case of a fully mapped magnetic field,
4211 the optimal inflector angle δ is between $[-2, -4]$ mrad and the optimal launch angle ℓ is
between $[-12, -14]$ mrad.

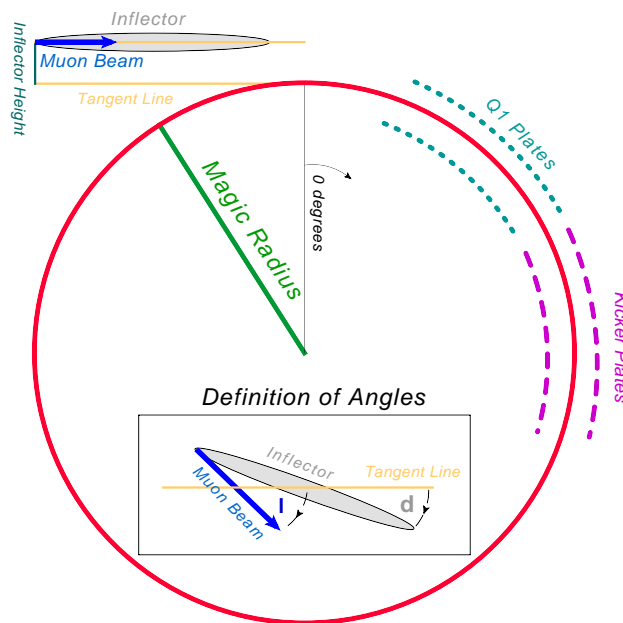


Figure 8.9: Schematic of the $g - 2$ storage ring as viewed from above. The starting location of the muon momentum vector in relation to the magic radius and other detector elements is shown by the blue arrow. The beam originates at the inflector entrance.

4212

4213

4214

4215

4216

4217

4218

4219

The muon storage fraction approaches a maximum when the inflector is fully open and the outer Q1 plate and support are massless only for the E821-match beam tune. The Ideal-match beam storage rates are noticeably lower than the E821-match because more of the beam is lost while traversing the inflector beam channel. Similarly, closing the inflector will drop the storage rate by approximately a factor of two and is nearly equivalent to making the Q1 plate and support massless. Fig. 8.10 shows curves of storage fraction for several benchmark scenarios of inflector and Q1 plate/support geometries. The plots show the

4220 fraction vs. the momentum width of the incoming beam, assuming the beam flux is *common*
 4221 for all scenarios; thus, the fraction is reduced as the beam width increases. It is instructive
 4222 to compare performance at the common $|dp/p| < 0.5\%$ point to tie into the calculation
 4223 of the muon flux described in Section 8.2. Table 8.1 shows the storage rate for the two
 4224 inflector geometry options combined with the two Q1 geometries for the E821-match beam
 4225 with $|dp/p| < 0.5\%$.

Table 8.1: Muon Storage Rates in % for 4 combinations of inflector and Q1 geometries for an E821-match muon beam with $|dp/p| < 0.5\%$. The underlined value for the open inflector and massless quads represents the maximum storage fraction obtainable for an incoming beam having $|dp/p| < 0.5\%$. The bold entry for closed inflector, massless quads represents the best estimate of the starting geometry for E989, prior to installation of a new inflector. All statistical uncertainties are well below 0.1%

Q1 Geometry → Inflector Geometry ↓	Massless Q1 Plate and Support	Massive Q1 Plate and Support
Fully Open	<u>22.0</u>	13.0
Fully Closed	10.0	6.5

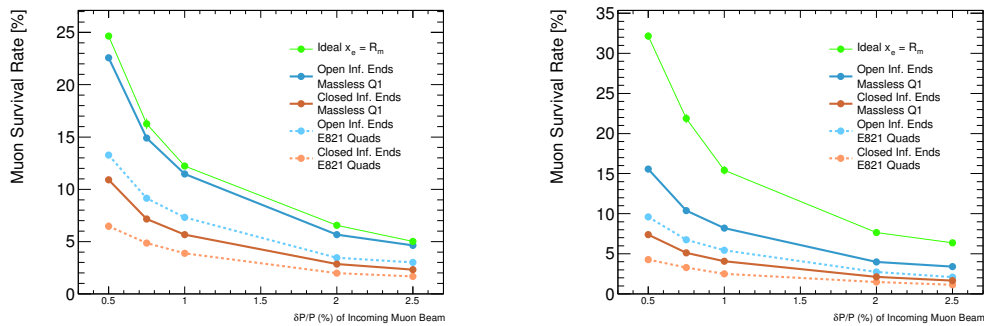


Figure 8.10: Comparison of the muon storage rates for a wide range of dp/p with a variation of inflector and outer Q1 plate/support geometries assuming $A = 40\pi$ beam with the E821-inflector Twiss parameters (left) and the Ideal-match beam parameters (right). The “Ideal” entry represents a pencil beam launched at the magic radius inside the storage ring.

Chapter 9

Relocation of the E821 Storage Ring Magnet

The muon storage ring magnet consists of superconducting coils inside their cryostats and the steel yoke and pole pieces. The steel is easily disassembled and shipped by truck, i.e., the time reversal of the process we used twenty years ago. However, the 15 m-diameter coils were wound in Brookhaven Building 919. In order to maintain the exceptional magnetic field, the coils may not be disassembled to the degree that would allow conventional trucking. Special transportation for the very large load is required. Transporting the coils in their horizontal orientation is highly desired in order to prevent extraordinary forces and stresses on the coils.

The largest portion of the coil transport will occur by barge from Long Island, New York to Illinois via the Mississippi River system to the Illinois Waterway. Along the eastern seaboard the barge will travel through the Intracoastal Waterway keeping the barge near ports and in calm waters as compared to open sea travel. An ocean tug will be used from Long Island to New Orleans. A river tug will be used for the remainder of the trip to Lemont, Illinois. A back up plan could route the barge north via the St. Lawrence Seaway and Great Lakes to the Illinois Waterway.

A feasibility study in 2012 studied the best mode of transportation for the remaining short distance over land between the labs and ports in both Long Island and Illinois. The result of the study indicated that the use of a specialized truck and trailer is the best option. Some vendors in the heavy haul industry are capable of performing the work required with a specialized truck/trailer suitable for moving the $g - 2$ coils. A transportation review based on the feasibility study was held at FNAL in September, 2012. One of the recommendations from this review was to be sure that we document the coil/cryostat system before the move. The documentation is given in Fermilab $g - 2$ doc-db references [1], [2], [3], [4], and [5].

A Request for Proposal (RFP) was written at Fermilab and a meeting for the coil/cryostat transportation was held at BNL in November, 2012. Four companies replied to the RFP and attended the meeting; three of these submitted proposals. Emmert International was chosen to perform the work and the contract was signed.

The present plan is to truck the coil/cryostat from Brookhaven National Laboratory to Smith Point Marina in Suffolk County, Long Island. From this port the barge will travel to the Ozinga port on the Illinois Waterway. From the port in Lemont, the coils will travel via specialized truck/trailer to FNAL this summer.

4259 An analysis has been performed by Emmert International to determine the deflection of
4260 the shipping fixture arms while supporting the coils. This has been determined for various
4261 support conditions that the fixture will undergo during the phases of the shipment. The
4262 results of the Emmert calculations have been verified at Fermilab. The expected forces and
4263 deflections have also been imposed on the coils in a Finite Element Analysis at Fermilab.
4264 The stresses imposed on the coils are seen to be low on the order of a few hundred psi. The
4265 coils and other internal components of the cryostats are not expected to be damaged as a
4266 result.

4267 The shipment of the coils will be performed using a quality assurance plan. The plan
4268 will provide a means of assuring that the coils will not see stresses above those that we plan
4269 for. Severe storms will be avoided. Distant storms that cause higher than normal wave
4270 motion will be monitored. The shipment will be monitored with accelerometers capable of
4271 transmitting a signal. For wave motion approaching our limits, the barge will be called to safe
4272 harbor. A safe harbor plan will be a part of this quality assurance plan. The accelerometer
4273 readings will be recorded for later analysis as well.

4274 9.1 Preparations for Shipping

4275 Figure 9.1 shows a recent picture of the cryostats and the mostly disassembled steel. In this
4276 photo the upper yoke plates have been removed as well as much of the spacer plates. The
4277 coils will be removed for shipment before most of the lower yoke and the remaining spacer
4278 plates will be moved.

4279 The following are the important activities occurring (or in process of occurring) in prepa-
4280 ration for the move:

- 4281 • Replacing all the G10 radial stops with Aluminum stops. The G10 stops do not touch
4282 the mandrel when warm, only when cold. The Aluminum stops are longer and are
4283 designed to touch the mandrel. This prevents the coil from moving side-to-side.
- 4284 • For the outer coil, vertical bolts at the hangar locations will be inserted through the
4285 cryostat's top surface, and engage the mandrel. This is additional protection to prevent
4286 the mandrel from moving side-to-side. FEA simulations of this item and of the first
4287 item, show that these safeguards are sufficient for handling the worse case of 0.7 g side
4288 load.
- 4289 • The exposed (unpainted) surfaces of the yoke steel was coated with Cosmoline to
4290 prevent rusting.
- 4291 • A structure has been designed to support the interconnect and the hardware outside
4292 the outer cryostat (see reference [6]). This is to minimize the stress on both the coils
4293 and cryostat walls.
- 4294 • A shrink wrap will cover the cryostats during the move.
- 4295 • During the move, dry nitrogen will be flowing through the cryostat to keep it dry.



Figure 9.1: Coils/Cryostats at BNL.

4296 9.2 The Coil Shipping Fixture and Transportation

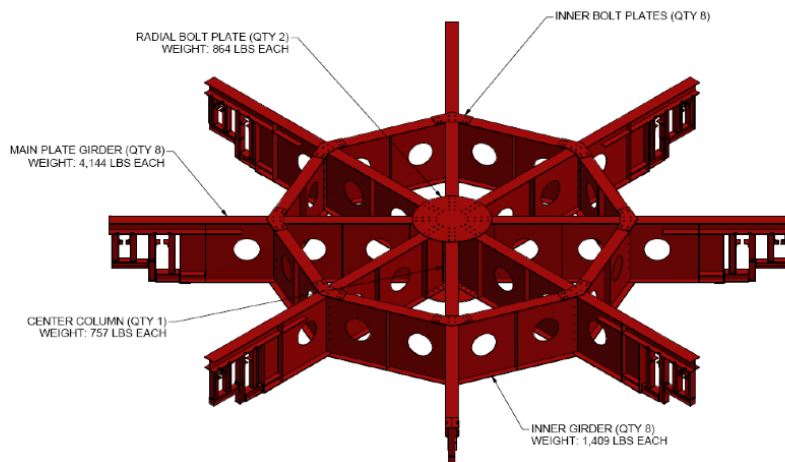


Figure 9.2: The shipping fixture.

4297 Figure 9.2 shows the shipping fixture as specified by Fermilab and designed and built
 4298 by Emmert International per the criteria to carry the coils. The coils will remain very flat
 4299 during the shipment to limit the stress imposed onto the coils.

4300 Figure 9.3 shows an engineering drawing of the mover and support fixture. The overall
 4301 length of this rig is in excess of 117 feet. The trailer has three hydraulic zones to keep the
 4302 load level and to distribute the weight to the wheels evenly. The truck will move slowly
 4303 over the roadways ranging from walking speed to a maximum of 10 mph depending on the
 4304 terrain and the proximity of obstacles along the path. The shipment will move over public
 4305 roadways during night time hours to limit disruption to public traffic.

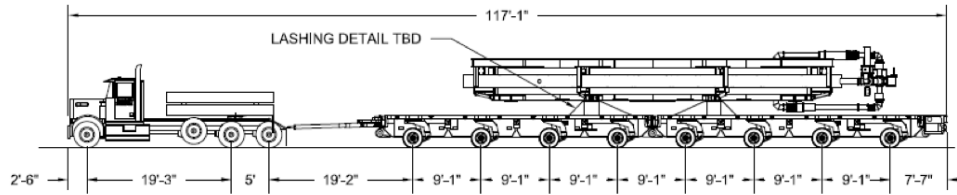


Figure 9.3: Specialized Truck and Trailer for Coil Shipment.



Figure 9.4: Scaled model showing the specialized truck and trailer holding the coils.

4306 Figure 9.4 shows a model of the mover and support fixture. The 50 foot diameter coils
 4307 require roughly the width of four traffic lanes to traverse the roadways in Long Island and
 4308 Illinois.

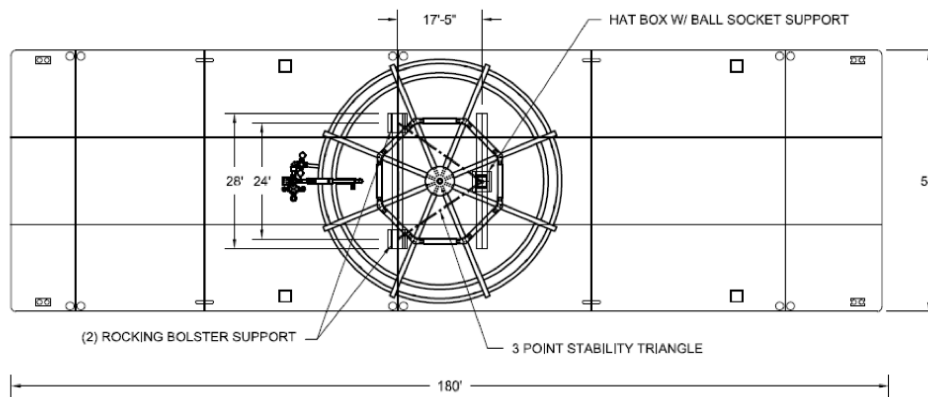


Figure 9.5: Shipping fixture with coils shown secured to the barge.

4309 Figure 9.5 shows a drawing of the shipping fixture with coils secured to the barge. The

4310 barge that we plan to utilize has a 54 foot width by 180 foot length. This barge size is chosen
4311 to limit the maximum roll, pitch, and heave the coils will experience over the water.

4312 **References**

- 4313 [1] E821 Muon Storage Ring Coil Resistance Benchmark. g-2 DocDB note 499-v1.
- 4314 [2] Coil Resistance to Ground Measurements. g-2 DocDB note 352-v1.
- 4315 [3] Cryostat Vacuum System Documentation. g-2 DocDB note 314-v1.
- 4316 [4] E821 Interconnects. g-2 DocDB note 302-v1.
- 4317 [5] Resistance to Ground of the E821 Storage Ring Magnet Coils. g-2 DocDB note 976-v1.
- 4318 [6] Erik Voirin, g-2 Cryostat Interconnect Support for Transportation. g-2 DocDB note
4319 979-v1.

Chapter 10

The Muon Storage Ring Magnet

10.1 Introduction

As emphasized in Chapter 2, the determination of the muon anomaly a_μ requires a precise measurement of the muon spin frequency in a magnetic field ω_a , and an equally precise measurement of the average magnetic field felt by the ensemble of precessing muons, $\langle B \rangle$. We repeat the spin equation given in Eq. 3.11, since it is central to the design of the storage-ring magnet.

$$\vec{\omega}_a = -\frac{Qe}{m} \left[a_\mu \vec{B} + \left(a_\mu - \left(\frac{m}{p} \right)^2 \right) \frac{\vec{\beta} \times \vec{E}}{c} \right]. \quad (10.1)$$

As explained in Chapter 2, the need for vertical focusing and exquisite precision on $\langle B \rangle$ requires that: either the muon trajectories be understood at the tens of parts per billion level, and the magnetic field everywhere be known to the same precision; or the field be as uniform as possible and well-measured, along with “reasonable knowledge” of the muon trajectories. This latter solution was first employed at CERN [1] and significantly improved by E821 at Brookhaven [2]. The uniformity goal at BNL was ± 1 ppm when averaged over azimuth, with local variations limited to ≤ 100 ppm.

Fermilab E989 will use the storage-ring magnet designed and built for Brookhaven E821, with additional shimming to further decrease the local variations in the magnetic field. This requires the relocation of the ring from BNL to Fermilab, which is described in detail in the following chapter. While the magnet steel comes apart and can be moved by conventional trucks, the 14.5 m diameter superconducting coils will need to be moved as a package, on a custom designed fixture that can be pulled by a truck to travel by road, and put on a barge to travel by sea, and then again by road to get it to the Fermilab site.

The storage ring is built as one continuous superferric magnet, an iron magnet excited by superconducting coils. A cross-section of the magnet is shown in Fig. 10.1. The magnet is C-shaped as dictated by the experiment requirement that decay electrons be observed inside the ring. The field, and hence its homogeneity and stability, are determined dominantly by the geometry, characteristics, and construction tolerances of the iron. Although both copper and superconducting coils were considered, the use of superconducting coils offered the following advantages: thermal stability once cold; relatively low power requirements; low voltage, and hence use of a low-voltage power supply; high L/R time constant value

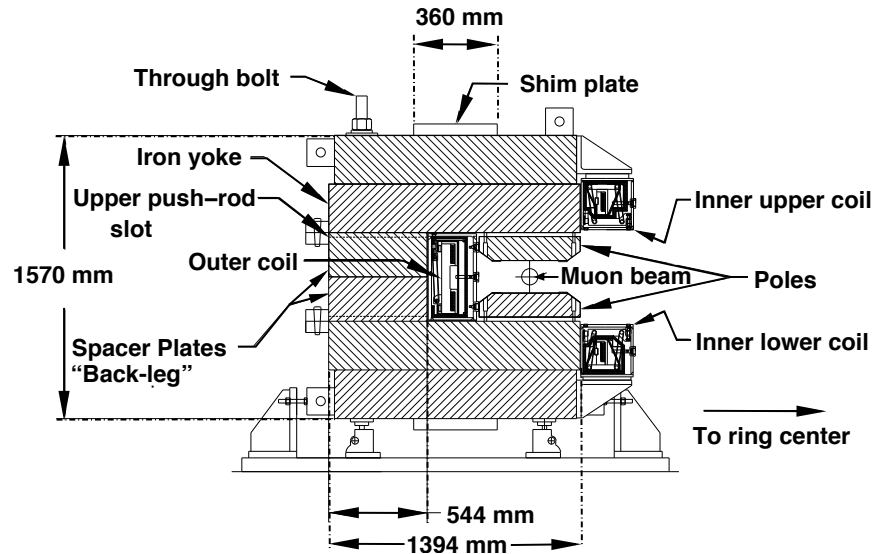


Figure 10.1: Cross section of the E821 storage-ring magnet. The yoke is made up of 12 azimuthal sections, each of which consists of six layers of high quality magnet steel provided by Lukins Steel Corporation. The pole pieces were provided by Nippon Steel Corporation.

4350 and hence low ripple currents; and thermal independence of the coils and the iron. The
 4351 main disadvantage was that the coils would have a much larger diameter and smaller height
 4352 than any previously built superconducting magnet. However, since the E821 magnet team
 4353 could not identify any fundamental problems other than sheer size, they decided to build
 4354 superconducting coils.

4355 To obtain the required precision in such a large diameter magnet with an economical
 4356 design is an enormous challenge. The magnet had to be a mechanical assembly from sub-
 4357 pieces because of its size. With practical tolerances on these pieces, variations up to several
 4358 thousand ppm in the magnetic field could be expected from the assembled magnet. To
 4359 improve this result by the required two to three orders of magnitude required a shimming
 4360 kit.

4361 Because of the dominant cost of the yoke iron, it was an economic necessity to minimize
 4362 the total flux and the yoke cross-section. This led to a narrow pole, which in turn conflicts
 4363 with producing an ultra-uniform field over the 9 cm good field aperture containing the muon
 4364 beam.

4365 A simple tapered pole shape was chosen which minimized variations in the iron perme-
 4366 ability and field throughout the pole. The ratio of pole tip width to gap aperture is only
 4367 2/1. This results in a large dependence of the field shape with the field value B . However,
 4368 since the storage ring is to be used at only one field, $B = 1.45$ T, this is acceptable. Because
 4369 of dimensional and material property tolerance variation, the compact pole piece increases
 4370 the necessity for a simple method of shimming.

4371 Experience with computer codes, in particular with POISSON [4], had demonstrated that,
 4372 with careful use, agreement with experiment could be expected at a level of 10^{-4} accuracy.
 4373 POISSON is a two-dimensional (2D) or cylindrically symmetric code, appropriate for the essen-

4374 tially continuous ring magnet chosen for the ($g - 2$) experiment. Computational limitations,
 4375 finite boundary conditions, and material property variations are all possible limitations on
 4376 the accuracy of paper calculations of the design.

4377 We will briefly discuss the design features that are relevant to E989, especially to moving
 4378 the ring, but not repeat all the details given in Danby et al. [3], and in the E821 Design
 4379 Report [5]. The parameters of the magnet are given in Table 10.1.

Table 10.1: Magnet parameters

Design magnetic field	1.451 T
Design current	5200 A
Equilibrium orbit radius	7112 mm
Muon storage region diameter	90 mm
Inner coil radius - cold	6677 mm
Inner coil radius - warm	6705 mm
Outer coil radius - cold	7512 mm
Outer coil radius - warm	7543 mm
Number of turns	48
Cold mass	6.2 metric tons
Magnet self inductance	0.48 H
Stored energy	6.1 MJ
Helium-cooled lead resistance	$6 \mu\Omega$
Warm lead resistance	0.1 m Ω
Yoke height	157 cm
Yoke width	139 cm
Pole width	56 cm
Iron mass	682 metric tons
Nominal gap between poles	18 cm

4380 10.2 Yoke Steel

4381 E989 will reuse the yoke steel manufactured for the E821 experiment. The yoke pieces have
 4382 been surveyed and disassembled at Brookhaven and are in the process of being shipped to
 4383 Fermilab. The design and construction of the magnet has been documented and published
 4384 in NIM [3] as well as the final report in Phys. Rev. D [2]. We summarize the main design
 4385 features and issues here, with a discussion of potential improvements in Section 10.4.

4386 Ideally, the $g - 2$ magnet would be azimuthally symmetric. To ease the fabrication and
 4387 assembly processes, the magnet was built with twelve 30° sectors. Each sector consists of an
 4388 upper and lower yoke separated by a spacer plate as shown in Fig. 10.1. Due to the large
 4389 thickness of the yoke (54 cm), the individual plates were fabricated separately and welded
 4390 together after machining. The spacer plate is also split at the midplane to allow for the
 4391 installation of beam pipes and other services after the lower section is in place but prior to

4392 the installation of the upper yoke. The yoke plates and spacers in each sector are all fastened
4393 together with eight long high-strength steel bolts that cover the full 1.57 m tall yoke. The
4394 total sector mass is $\approx 57,000$ kg, which results in a total magnet mass of $\approx 680,000$ kg.

4395 Significant quality control efforts were taken during the manufacturing process to ensure
4396 that the magnet had sufficiently uniform permeability and the appropriate geometric shape.
4397 Both of these parameters have strong effects on the uniformity of the magnetic field in the
4398 storage region.

4399 High-quality plates were manufactured by hot-rolling AISI 1006 iron to minimize mag-
4400 netic voids in the material. These plates were manufactured with $< 0.08\%$ of carbon and
4401 other impurities. The finished plates were inspected ultrasonically to detect voids and in-
4402 clusions, and analyzed chemically to understand the composition.

4403 Although the yoke steel is partially magnetically isolated from the storage region by an
4404 air gap near the pole pieces, strict machining specifications are required to minimize non-
4405 uniformities in the storage region field. The surfaces of the yoke plates closest to the storage
4406 region were milled flat within $130\ \mu\text{m}$ and $1.6\ \mu\text{m}$ finish. Similarly, the spacer plate surfaces
4407 were milled flat within $\pm 130\ \mu\text{m}$, with a thickness accurate to $\pm 130\ \mu\text{m}$. These surfaces are
4408 parallel within $180\ \mu\text{m}$. The radial tolerance for each yoke plate and the spacer plates was
4409 $\pm 130\ \mu\text{m}$. When constructed, the vertical yoke gap had an rms deviation of $\pm 90\ \mu\text{m}$, or
4410 500 ppm of the total air gap of 20 cm, and a full-width spread of $\pm 200\ \mu\text{m}$.

4411 Each of the 12 sectors need to be connected smoothly to achieve azimuthal symmetry. To
4412 achieve azimuthal continuity, each sector end has four radial projections for bolts to fasten
4413 adjacent sector ends to each other. When the sectors are fitted to each other, shimmed, and
4414 the bolts tightened, relative motion of adjacent sectors is minimized. The average azimuthal
4415 gap between sectors was 0.8 mm, with an rms deviation of ± 0.2 mm.

4416 When we begin to reconstruct the storage ring, we will clean the yoke steel and remove
4417 any rust that has developed. It will be important to do this in a non-destructive manner
4418 that maintains the high-level of precision achieved during manufacturing.

4419 10.3 Poles and Wedges

4420 E989 will reuse the pole pieces and wedge shims that were manufactured for the E821 exper-
4421 iment. The pole pieces and wedges have been removed from the storage ring at Brookhaven
4422 and have already been shipped to Fermilab where they are awaiting reassembly.

4423 10.3.1 Poles

4424 More stringent quality requirements are placed on the machining of the pole pieces than
4425 the yoke steel. The air gap between the yoke and pole pieces decouples the field region
4426 from non-uniformities in the yoke. Thus, irregularities in the pole pieces dominate the field
4427 aberrations. Ultra-pure continuous vacuum cast steel with $< 0.004\%$ carbon impurities is
4428 used for the pole pieces. The fabrication process greatly minimizes impurities such as ferritic
4429 inclusions or air bubbles.

4430 A dimensioned view of the pole pieces is shown in Figure 10.2. Each 30° yoke sector
4431 contains three pole pieces (azimuthally). The pole pieces are 56 cm wide (radially), with

radius) to close slightly. Thus, during the installation, the poles were aligned with an opening angle of $80 \mu\text{rad}$. A precise bubble level was used to achieve $50 \mu\text{m}$ precision over the length of the pole piece. Pole realignment will be part of the shimming process described in Section 16.8.2.

10.3.2 Wedges

The gaps between the yoke and poles isolate the yoke steel from the poles and provide a region where shims can be inserted to fine-tune the magnetic field. Steel wedges that are sloped radially (see Fig 10.2) are inserted to compensate for the intrinsic quadrupole moment produced by the C-magnet. There are 72 wedges in each 30° yoke sector. The induced quadrupole term depends on the slope of the wedge, which was calculated to be 1.1 cm over the 53 cm width for E821. This wedge angle was verified empirically, and no additional grinding was needed. The radial position of the wedges can be adjusted to change the total material in the gap, affecting only the dipole moment (see Section 16.8.3).

During the ramping of the main coil current, the thick end of the wedge attracts more field lines, leading to a torque. To prevent the wedges from deflecting vertically, an aluminum “anti-wedge” is used to fill the air gap between the wedge and the pole piece.

E989 will reuse the wedge-spacer combination as is. Fine tuning of the quadrupole moment can be achieved with active current shims, as discussed in Section 16.8.3.

10.4 Thermal Effects

Temperature variations in the experimental hall are expected to be controlled within $\pm 1^\circ\text{C}$ during the course of data taking. This will change the shape of the magnet, which will in turn change the magnetic field. We produced thermal simulations with ANSYS to quantify the geometric distortions, which are then input into the OPERA-2D model of the storage ring.

E821 used 3.5” of fiber glass insulation around the bulk of the yoke and 3/8” foam rubber insulation near the poles pieces, as shown in Figure 10.3 (a). Reasonable thermal film coefficients in the range of $5\text{-}25 \text{ W/m}^2\text{C}$ were used at the surfaces of the magnet. Thermal oscillations based on day-night temperature cycles are imposed on the $g - 2$ magnet system and modeled with ANSYS. The air temperature is assumed to be spatially uniform throughout the hall. The model indicates that this will lead to thermal fluctuations at the yoke and pole pieces of a few tenths of a degree, as shown in Figure 10.3 (b). The pole pieces are constrained mechanically to prevent sliding, thus, in response to the thermal variations, they bend.

Figure 10.4 shows the response of the magnet under the 1°C hall fluctuations. The contours show the maximum extent of the deflection for both radial shifts (Figure 10.4 (a)) and vertical shifts (Figure 10.4 (b)). The deflections are on the order of $1 \mu\text{m}$ per degree C change in the hall temperature. The parallelism of the pole faces is known to affect the higher-order multipole components of the magnetic field. Figure 10.5 plots the relative change in the pole gap as a function of radius for the thermal changes described above.

Two different thermal contact resistances of the pole foam rubber insulation were modeled. In both cases, the gap distortion leads to a change of about $1 \mu\text{m}$. The pole gap

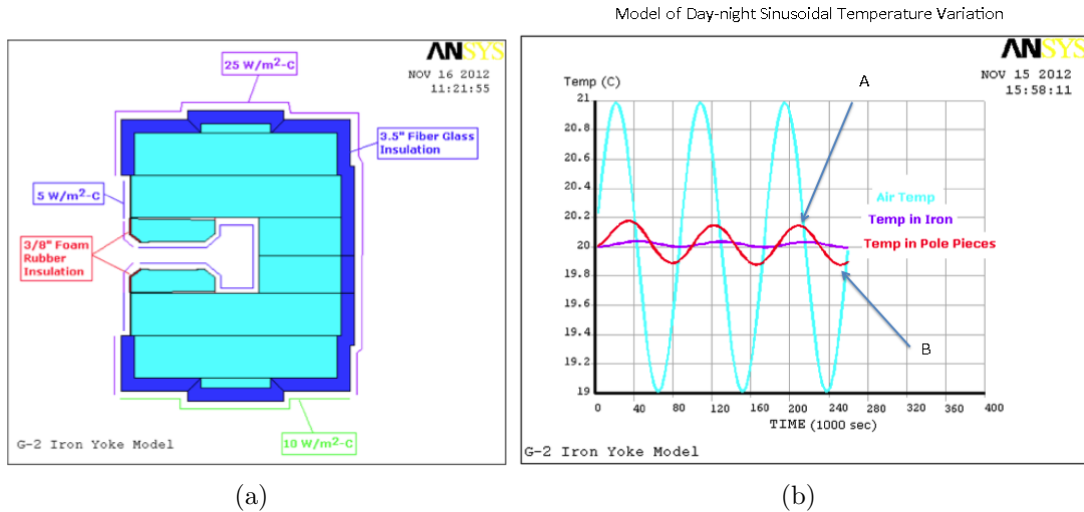


Figure 10.3: (a) An ANSYS model of the $g-2$ storage ring includes the thermal insulation used in E821. (b) Thermal oscillations based on day-night temperature cycles are imposed on the $g-2$ magnet system assuming a $\pm 1^\circ\text{C}$. The temperature variations of the yoke (purple) and pole (red) are overlaid.

4492 distortions were input into the OPERA-2D magnetic field simulation. Distortions on the order
 4493 of a few tenths of a ppm were observed in the sextupole and octupole moment with a change
 4494 of $1\ \mu\text{m}$ in the pole gap. Because the monitoring of the higher order multipole moments is
 4495 done primarily with the trolley runs, extrapolation of the field map from the fixed probes
 4496 during the main data collection will rely on stable magnet geometry.

4497 The ANSYS and OPERA tools nicely complement each other and allow us to understand
 4498 the effects of magnet deflections in E989. We plan to repeat these studies with varied
 4499 insulation thickness and with additional insulation around the inner superconducting coils.
 4500 With a high quality temperature control system stabilizing the experimental hall and better
 4501 thermal isolation of the steel, E989 will have significantly smaller time-dependent magnet
 4502 distortions than E821. This will lead to more stable multipole components.

4503 10.5 The Superconducting Coil System

4504 10.5.1 Overview

4505 The coil design was based on the TOPAZ solenoid at KEK [6]. TOPAZ conductor was used,
 4506 with pure aluminum stabilizer and niobium-titanium superconductor in a copper matrix.
 4507 Conductor characteristics are given in Table 10.5.1. At full field the critical temperature
 4508 of the outer coil is 6.0 K. The magnet typically operates at 5.0 K. This represents 76% of
 4509 the superconductor limit. Each coil block is effectively a very short solenoid with 24 turns,
 4510 and one layer. The coils are wound from the inside of the ring so that, when powered,
 4511 the coils push out radially against a massive aluminum mandrel. Cooling is indirect with
 4512 helium pipes attached to the mandrels. The coil turns, coil stack and insulation are epoxied

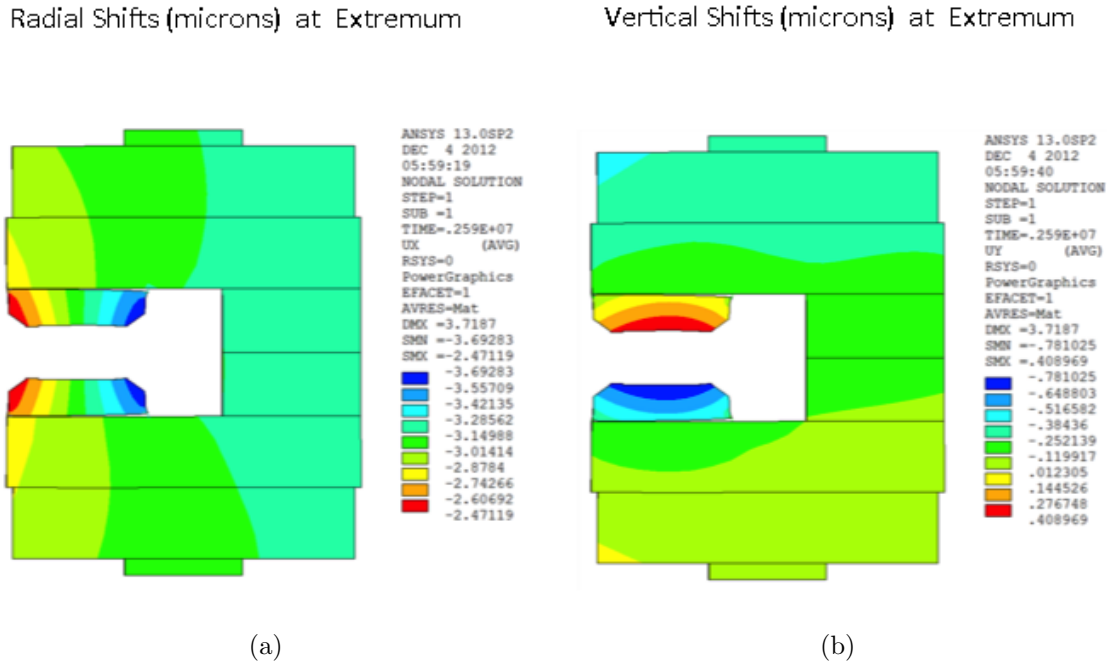


Figure 10.4: The thermal fluctuations depicted in Figure 10.3 are imposed on the magnet, causing distortion of the magnet, as modeled in ANSYS. The deflections are decomposed in (a) the radial and (b) the vertical dimensions for the worst-case scenario.

4513 together, forming a monolithic block. The coils hang from the cryostat with low heat load
 4514 straps, and the shrinkage and expansion of the coils is taken by the straps. The coils are
 4515 located using radial stops on the inner radius. For the outer coil the stops transfer the force
 4516 from the coil to the cryostat box, and push rods from the iron yoke transfer the force from
 4517 the box to the iron (see Fig. 10.7). For the inner coils, pins replace the pushrods.

4518 When the coils are cooled, they contract down onto the radial stops into a scalloped
 4519 shape. When powered, the Lorentz force pushes the coils outward, increasing the force
 4520 against the mandrel, which provides cooling. This feature, the result of winding on the
 4521 inside of the mandrel, reduces the risk of cooling problems even if the coil were to separate
 4522 from the mandrel during transport [7].

4523 A ground plane insulation band of 0.3 mm thickness was built from a sandwich of three
 4524 layers of 50 μm kapton, epoxy coated, between two layers of epoxy-filled fiberglass. The
 4525 insulation assembly was fully cured and placed into the mandrel. A 0.1-mm layer of B-
 4526 stage epoxy film was placed between the mandrel and kapton laminate, and between the
 4527 kapton laminate and the conductor block after winding. A 4.8-mm thick G-10 piece was
 4528 placed on the winding ledge, and on top and on the inner radius of the completed coil block.
 4529 The epoxy-filled fiberglass in the ground plane insulation sandwich improved heat transfer
 4530 between coil and mandrel.

4531 The coil was then wound using a machine that wrapped the superconductor with three
 4532 overlapping layers of 25 μm of kapton and fiberglass filled with B-stage epoxy, 19 mm in
 4533 width, laying the conductor into the mandrel with a compressive load as described in Ref. [3].

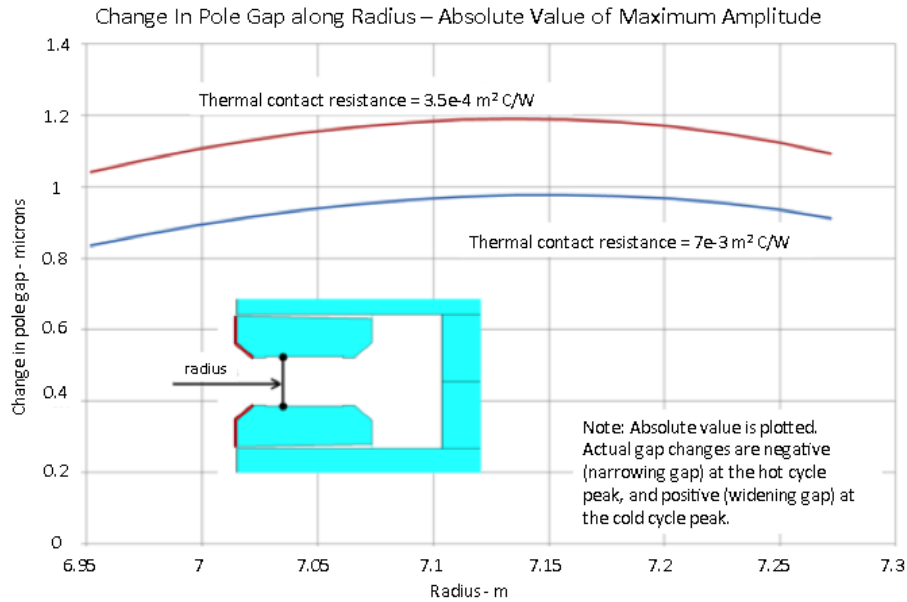


Figure 10.5: The deflections of the pole pieces under thermal variations are quantified in ANSYS simulations as a function of the radial coordinate. Typical fluctuations of 1 °C will produce micron scale distortions. Two different thermal contact resistances are shown.

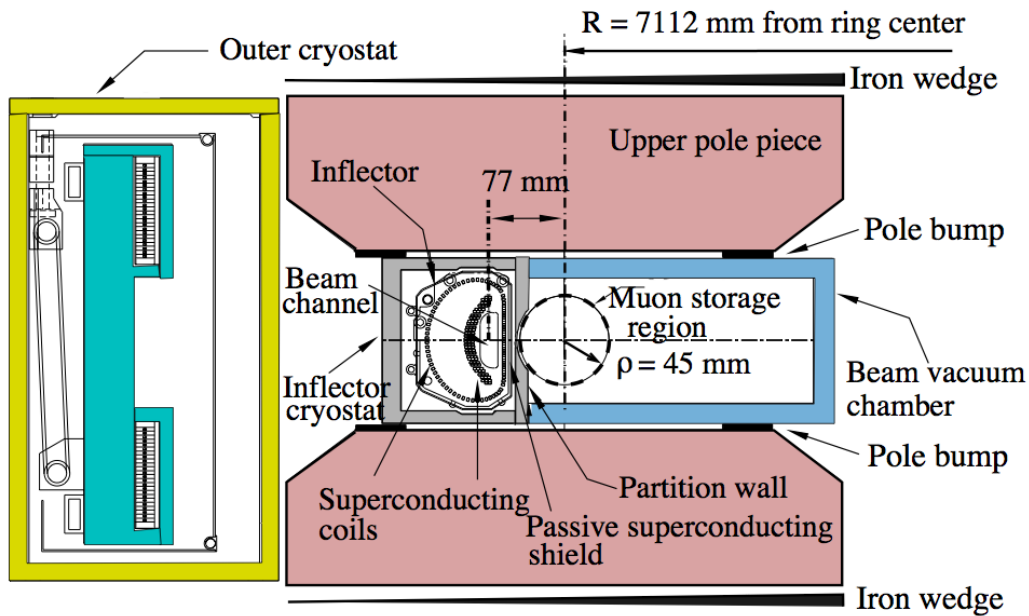


Figure 10.6: The arrangement of the pole pieces, shimming wedges and the inflector cryostat, showing the downstream end of the inflector where the beam exits. The beam is going into the page, and the ring center is to the right.

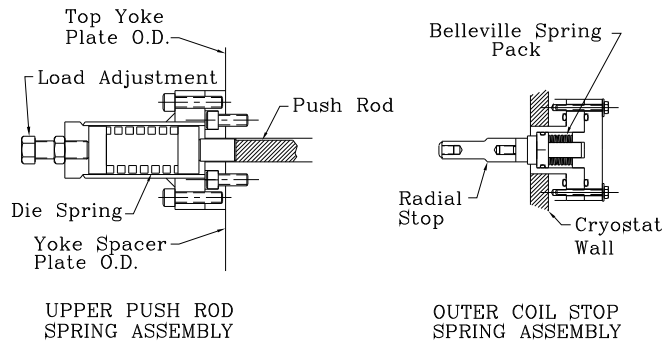


Figure 10.7: The spring-loaded radial stop and push rod. The stops are attached to the cryostat inner wall. The push rods preload the outer cryostat, attaching to the yoke at the outer radius, passing through a radial slot in the yoke to the outer cryostat.

4534 The wrap was tested at 2000 V DC during the wind. Aluminum covers were added after the
 4535 coil was wound, and the entire assembly heated to 125 °C to cure the epoxy. See Fig. 10.8.

4536 The outer coil contains two penetrations, one to permit the beam to enter the ring, and
 4537 one which could have permitted high voltage to be fed to a proposed electrostatic muon
 4538 kicker. It was decided at the time to make this “kicker penetration” in the outer coil, but
 4539 not to make a hole through the magnet yoke until it was shown that this kicker could be
 4540 built (which was not demonstrated).

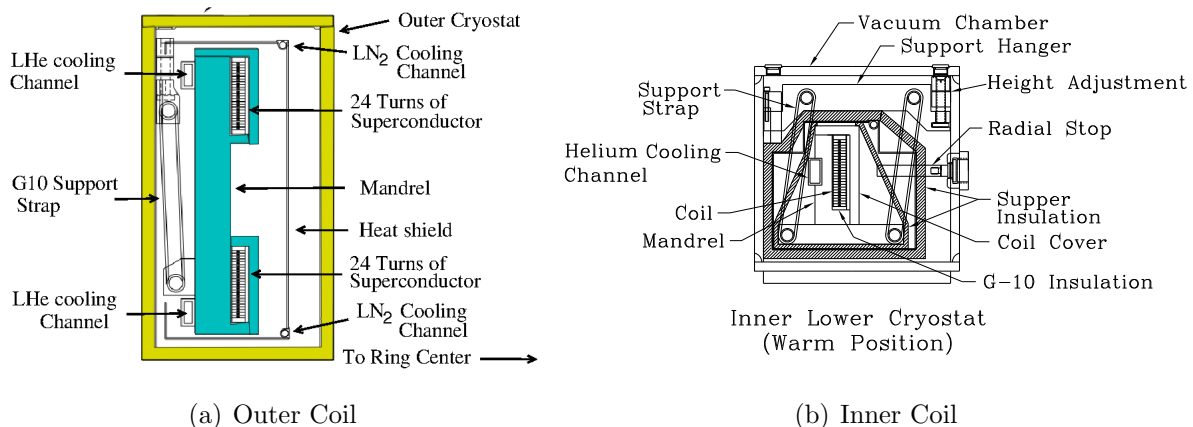


Figure 10.8: The outer and inner coil structures. Both are shown in their warm configuration.

4541 The coils are indirectly cooled with two-phase He flowing through channels attached to
 4542 the mandrel, as shown in Fig. 10.8. The two-phase helium cooling avoids the increase in
 4543 temperature that would occur in a circuit cooled with single-phase helium. The operating

Table 10.2: Superconductor parameters

Superconductor type	NbTi/Cu
Nominal dimensions	1.8 mm \times 3.3 mm
NbTi/Cu ratio	1:1
Filament 50 μ m	
Number of filaments	1400
Twist pitch	27 mm
Aluminum stabilizer type	Al extrusion
Ni/Ti composite dimensions	3.6 mm \times 18 mm
Al/(NbTi + Cu) ratio	10
RRR (Al)	2000-2500
RRR (Cu)	120-140
I_c	8100 A (2.7 T, 4.2 K)

4544 temperature of the coils is within 0.2 K of the coldest temperature in the cooling circuit.
 4545 The advantages of two-phase cooling are: (1) the helium flows in well-defined flow circuits;
 4546 (2) the total amount of helium that can be flashed off during a quench is limited to the mass
 4547 of helium in the magnet cooling tubes; and (3) the location of the helium input and output
 4548 from the cryostat and the location and orientation of the gas cooled leads are not affected
 4549 by the cooling system [8].

4550 The key to the operation of a two-phase helium cooling circuit is a helium dewar (the
 4551 control dewar) that contains a heat exchanger. This heat exchanger sub-cools the helium
 4552 from the J-T circuit before it enters the magnet cooling circuits. This isobaric cooling
 4553 provides a higher ratio of liquid to gas with a higher pressure and lower temperature than
 4554 the refrigerator J-T circuit alone would provide. This feature is important for the long
 4555 cooling channels in the magnet cooling circuits. The use of a heat exchanger in the control
 4556 dewar reduces the helium flow circuit pressure drop by a factor of two or more. The control
 4557 dewar and heat exchanger also have the effect of damping out the oscillations often found in
 4558 two-phase flow circuits. The helium in the control dewar acts as a buffer providing additional
 4559 cooling during times when the heat load exceeds the capacity of the refrigerator.

4560 The ($g-2$) cooling system was originally designed to have three separate cooling circuits:
 4561 a 218 m long cooling circuit that cools all three mandrels in series, the lead and coil inter-
 4562 connect circuits that are 32 m long (the gas-cooled leads are fed off of this circuit), and a
 4563 14 m long cooling circuit for the inflector magnet. Later the cooling system was modified to
 4564 permit each of the mandrels to be cooled separately. Ultimately, the ($g-2$) cooling system
 4565 operates with parallel cooling circuits for the coils, inflector, and lead cooling. Electrically,
 4566 the three coils are connected in series so that the two inner coils are in opposition to the
 4567 outer coil to produce a dipole field between the inner and outer coils. The magnet is powered
 4568 through a pair of tubular gas-cooled leads developed for this application. Each lead consists
 4569 of a bundle of five tubes. Each tube in the bundle consists of three nested copper tubes with
 4570 helium flow between the tubes. The copper tubes used in the leads are made from an alloy
 4571 with a residual resistance ratio of about 64. The lead length is 500 mm. A typical cool down

4572 from 300 to 4.9 K takes about 10 days. Once the control dewar starts to accumulate liquid
 4573 helium, it takes another day to fill the 1000 l dewar. In operation, the pressure drop across
 4574 the magnet system is about 0.02 MPa (3.0 psi). We initiated several test quenches and had
 4575 one unintentional quench when the cooling water was shut off to the compressors. The peak
 4576 measured pressure during a 5200 A quench was 0.82 MPa (105 psi). Other places in the
 4577 cooling circuit could have a pressure that is 40% higher. The quench pressure peak occurs
 4578 11 s after the start of the quench. The quench pressure pulse is about 12 s long compared
 4579 to current discharge time constant at 5200 A of 31 s. The outer coil mandrel temperature
 4580 reaches 38 K after the quench is over. Re-cooling of the magnet can commence within 5 min
 4581 of the start of the quench. After a full current quench, it takes about 2 hours for the outer
 4582 coil to become completely superconducting. The inner coils recover more quickly.

Table 10.3: Estimates of cryogenic heat leaks

		4.9 K load (W)	80 K load (W)
Magnet system heat load	Outer coil cryostat	52	72
	Two inner coils	108	77
	Inflector	8	5
	Interconnects	11	46
	Magnet subtotal	179	200
Distribution	Helium piping	19	
	Control dewar	5	
	Interconnects/valves	33	32
	Nitrogen piping		34
	Distribution subtotal	57	66
Lead gas (1.1 g/s)	Equivalent refrigeration	114	
Total refrigeration		351	266
Contingency		70	51
Cryogenic design	Operating point	421	308

4583 Both persistent mode and power supply excitation were considered. The total flux,
 4584 $\int \vec{B} \cdot d\vec{s}$, is conserved in persistent mode. However, room temperature changes would result
 4585 in changes in the effective area. Thus although the flux, is conserved, the magnetic field in
 4586 the muon storage region is not. Persistent mode would also require a high-current super-
 4587 conducting switch. Power supply excitation with NMR feedback was chosen, although no
 4588 feedback was used for the 1997 run. This method gives excellent control of the magnetic
 4589 field and allows the magnet to be turned off and on easily. The power supply parameters
 4590 are shown in Table 10.5.1.

4591 The quench protection design parameters were determined by the requirements of mag-
 4592 netic field stability and protection of the magnet system in case of a quench. When the
 4593 energy is extracted, eddy currents are set up in the iron which oppose the collapse of the
 4594 field. This can cause a permanent change in the magnetic field distribution [9]. This is
 4595 sometimes called the ‘umbrella effect, since the shape of the change over a pole resembles an

Table 10.4: Power supply parameters

Rating	5 V, 6500 A	
Rectifier	480 VAC input, 12 pulse (Two $\pm 15^\circ$, 6 pulse units in parallel)	
Output filter	0.4 F	
Regulator	Low-level system	0.1 ppm stability with 17 bit resolution
	Power section	Series regulator with 504 pass transistors
Cooling	Closed loop water system with temperature regulation	
Regulation	Current-internal DCCT	± 0.3 ppm over minutes to several hours
	Field-NMR feedback (current vernier)	± 0.1 ppm (limited by the electronics noise floor)
Manufacturer	Bruker, Germany	

4596 umbrella. The eddy currents are minimized if the energy is extracted slowly. There will also
 4597 be eddy currents in the aluminum mandrels supporting the coils. Electrically, this can be
 4598 represented by a one turn shorted transformer. These eddy currents will heat the mandrels
 4599 and can cause the entire coil to become normal. This is called quench-back. This has several
 4600 beneficial effects. The part of the stored energy that is deposited in the coil is deposited uni-
 4601 formly over the entire coil and mandrel assembly. Also, once quench-back occurs, the energy
 4602 extraction process is dominated by the quenchback and not by the specifics of where the
 4603 quench occurred. Therefore, the effects of a quench on the reproducibility of the magnetic
 4604 field should be minimal.

4605 The energy extraction system consists of a switch, resistor, and quench detection elec-
 4606 tronics. An energy extraction resistor of $8 \text{ m}\Omega$ was chosen. Including the resistor leads, the
 4607 room temperature resistance is $8.8 \text{ m}\Omega$. This gives an $1/RC$ time constant of 1 minute. The
 4608 actual time constant varies due to the temperature increase of the coil and dump resistor and
 4609 the effect of eddy currents in the mandrels during the energy extraction (see below). This
 4610 resistance value was calculated to cause quenchback in the outer mandrel within 2 seconds at
 4611 full current. The quench protection circuit is shown in Figure 10.9. The energy extraction
 4612 trigger for a quench which originates in one of the coils is the voltage difference between
 4613 matching coils; for example, $V(\text{outer} - \text{upper}) - V(\text{outer} - \text{lower})$. Since the inductance is
 4614 effectively the same, the voltages should be equal even while charging the magnet, unless a
 4615 quench develops in one coil. This quench threshold is set at 0.1 V. However, the coil inter-
 4616 connects are thermally coupled together with the helium tubes. It is possible that a quench
 4617 in an interconnect could propagate to both coils almost simultaneously. Therefore, a voltage
 4618 threshold of 10 mV was chosen for each interconnect. The outer upper to lower interconnect
 4619 is only 1 m long. This threshold was set to 5 mV. The thresholds were determined by the

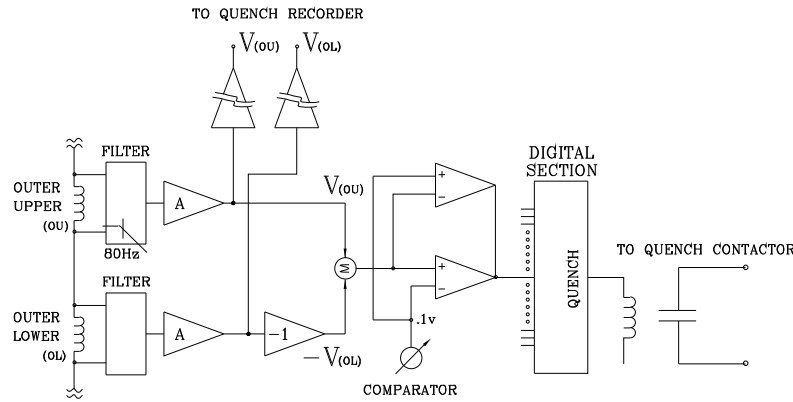


Figure 10.9: Diagram of the quench protection circuit.

4620 requirement that the quench be detected within 0.2 s. The gas-cooled leads develop a voltage
 4621 of typically 15 mV at full current. If the lead voltage exceeds 30 mV, the energy is extracted.

4622 10.5.2 Preparations Prior to Transportation

4623 No significant changes will be made to the design, and nearly all components are reused
 4624 from E821. The WBS sections below describe the steps to reassemble and recommission the
 4625 items above. We will not need to fabricate any parts, other than to replace old components
 4626 or to build spares.

4627 Prior to the coil transportation, room temperature tests were performed to verify as much
 4628 as possible the working state of the system. These were:

- 4629 • Electrical verification of the instruments connected to the coil and/or mandrel. These
 4630 refer to the temperature probes, voltage taps for quench detection, and strain gauges.
 4631 The instruments connected to the cryostat consists of thermometers, voltage taps, and
 4632 strain gauges. These are indicated in figures 10.10 and 10.11. The strain gauges are
 4633 attached to the straps, which counteract the Lorentz forces, and the radial stops, which
 4634 counteract the shrinking of the radial stops due to cooling.
- 4635 • Resistance measurements of the coil at room temperature, which agree with measure-
 4636 ments performed in 1995 (see table 10.5).

Outer Cryostat Thermometer and Strain Gauge Locations

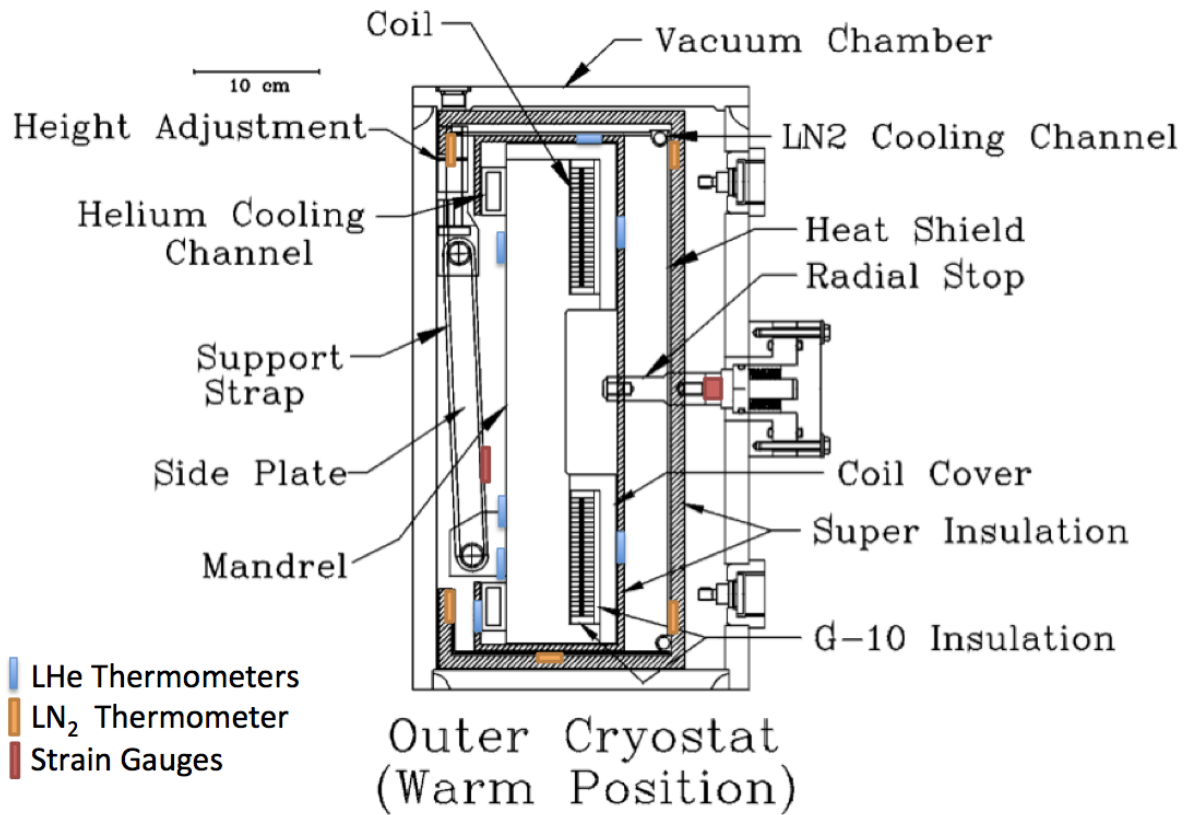


Figure 10.10: Location of outer coil instrumentation, showing the LHe LN₂ thermometers, and strain gauges. There are typically eight thermometers placed at each azimuthal location, with the positions indicated above.

4637
4638
4639
4640
4641
4642
4643

- The resistance between the coil leads and ground was measured to be a few kohms, where as an open resistance was expected. Further tests showed the 'short-to-ground' occurring at the connection between the inner lower coil and the power supply (see figure 10.15), and is a straight-forward repair. There is no short within the coils themselves. This short was likely present during E821 running, and would have contributed a 0.01 mA current-to-ground, out of a total of 5200 A. This is 2 ppb effect and would not have been seen in E821 (see references [11] and [12]).

4644
4645
4646
4647
4648

Following this verification, the interconnections between the three coils (see figure 10.12) were separated by a grinding wheel. The temperature was monitored and kept well below 100 °C during the process to minimize degradation to the Aluminum resistance and the NbTi current-carrying capacity. Figures 10.13 and 10.14 show the details of the welds that were cut in this region.

Inner Cryostat Thermometer and Strain Gauge Locations

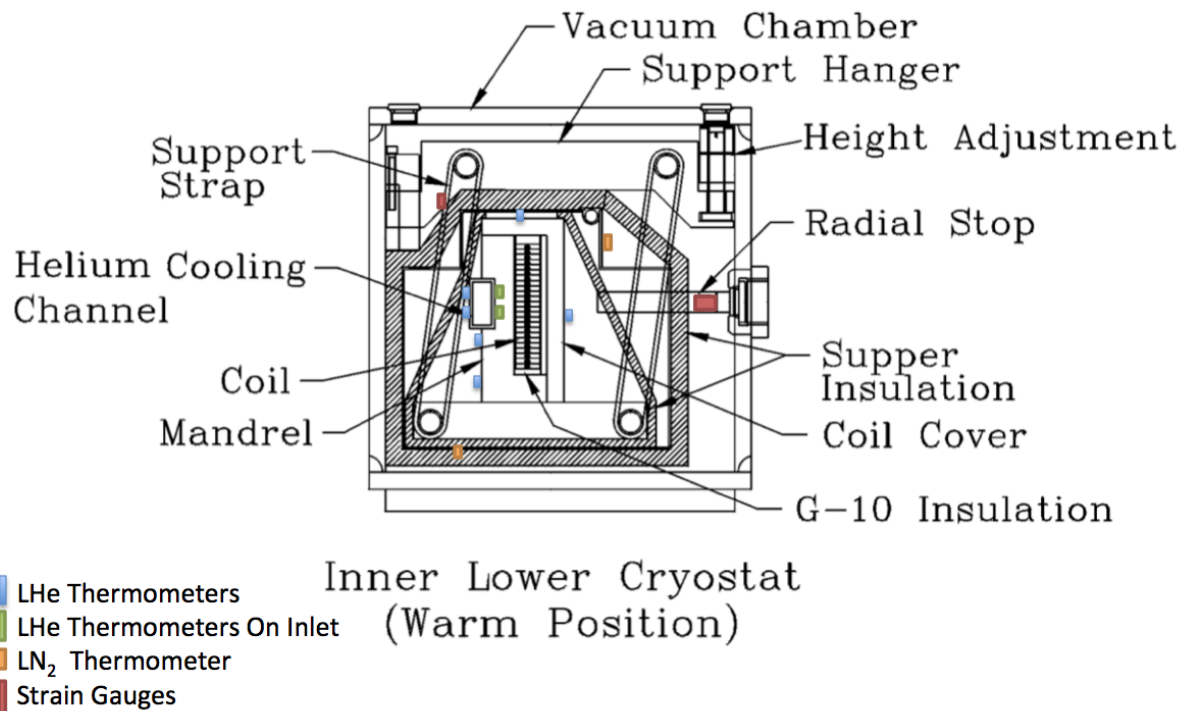


Figure 10.11: Location of the lower inner coil instrumentation, showing the LHe and LN₂ thermometers, and strain gauges. The instrument locations are symmetrically placed for the upper coil instruments. There are typically eight thermometers placed at each azimuthal location, with the positions indicated above.

4649 10.5.3 Cryostat Vacuum Chambers

4650 This WBS consists of the vacuum chambers that provide the thermal insulation for the coils.
4651 After the interconnects have been rewelded (see section 10.5.7), the vacuum flanges enclosing
4652 that region will be reconnected.

4653 For transportation, a vacuum port connected to the outer cryostat will be cut in order
4654 to gain clearance. Therefore, this pipe will be rewelded upon reassembly at Fermilab.

4655 10.5.4 Vacuum Pumps

4656 New or refurbished ‘dry’ vacuum pumps will be used to pump down the cryostat vacuum
4657 chambers. The pumps must remain a few meters away from the storage beam region in order
4658 to not perturb the precision magnetic field. The vacuum quality needed is about 10^{-4} Torr.

4659 E821 implemented a mechanism described below to deal with a potential failure mode
4660 called the “cold cryostat problem.” In the event of loss of cryostat vacuum while the coils are
4661 cold, the cryostat walls will also become cold and therefore will shrink. Such could happen

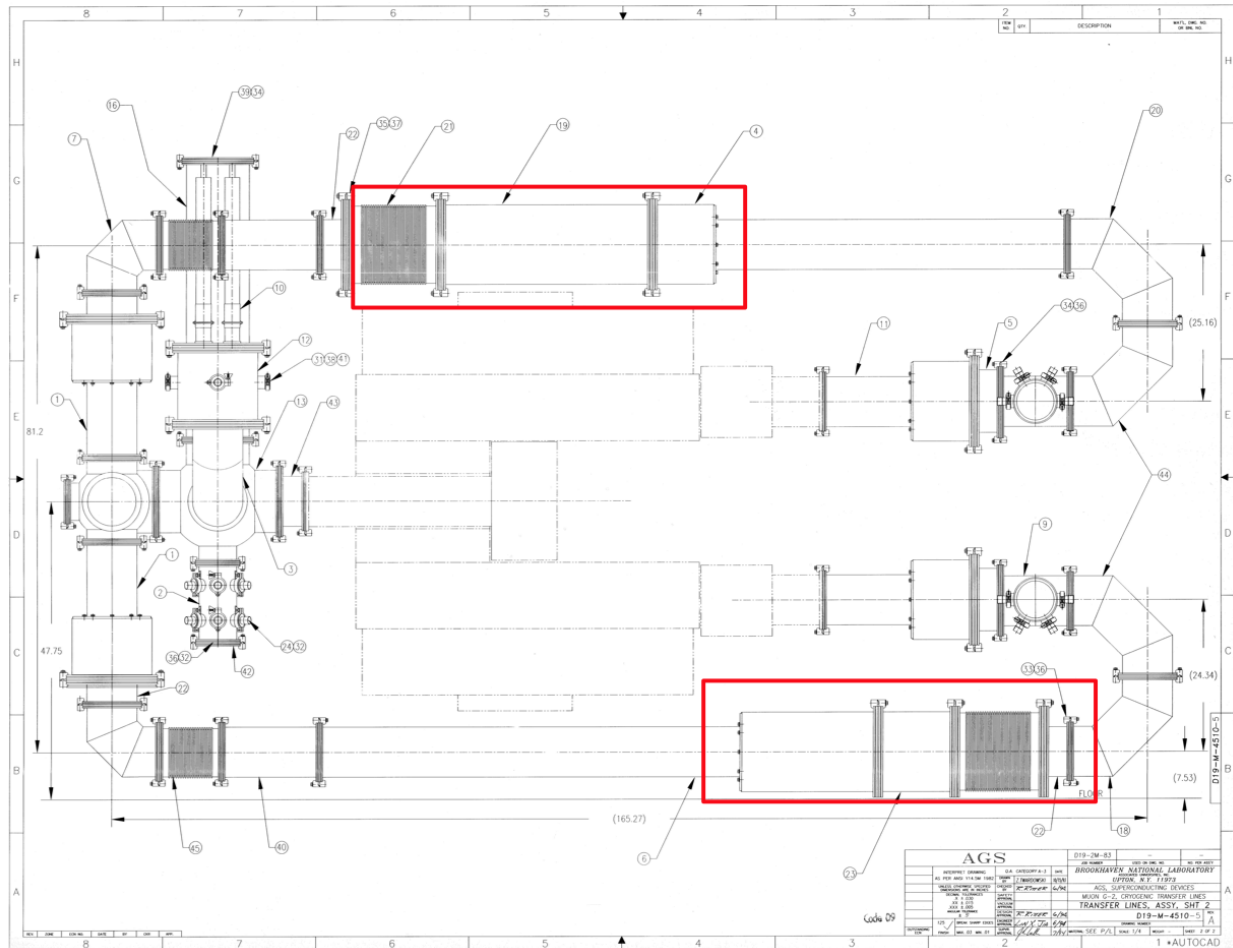


Figure 10.12: The connections between the three coils are indicated. The upper(lower) red box is the connection between the outer-upper (outer-lower) coil and the inner-upper (inner-lower) coil.

4662 if the cryogenic lines leaked cryogenics into the vacuum. However, the cryostat positions are
 4663 firmly attached to the yoke steel in order to have a well-defined coil position. Therefore,
 4664 the cryostat wall at the attachment point would experience stresses exceeding the allowable
 4665 value for Aluminum.

4666 For this potential failure scenario, E821 implemented a scheme to trigger a large Roots
 4667 blower vacuum pump to rapidly evacuate the vacuum chamber.

4668 10.5.5 Power Supply and Quench Protection

4669 The power supply for the main ring will be the same unit used in E821 and as described
 4670 in reference [3]. Therefore the design and specifications will be the same. Once moved to
 4671 Fermilab, the power supply will be refurbished, tested, and then commissioned for installation
 4672 and use. A similar process will be used for the quench protection circuitry and components.
 4673 The voltage taps and quench detection circuitry are located as shown in figures 10.15 and
 4674 10.16.

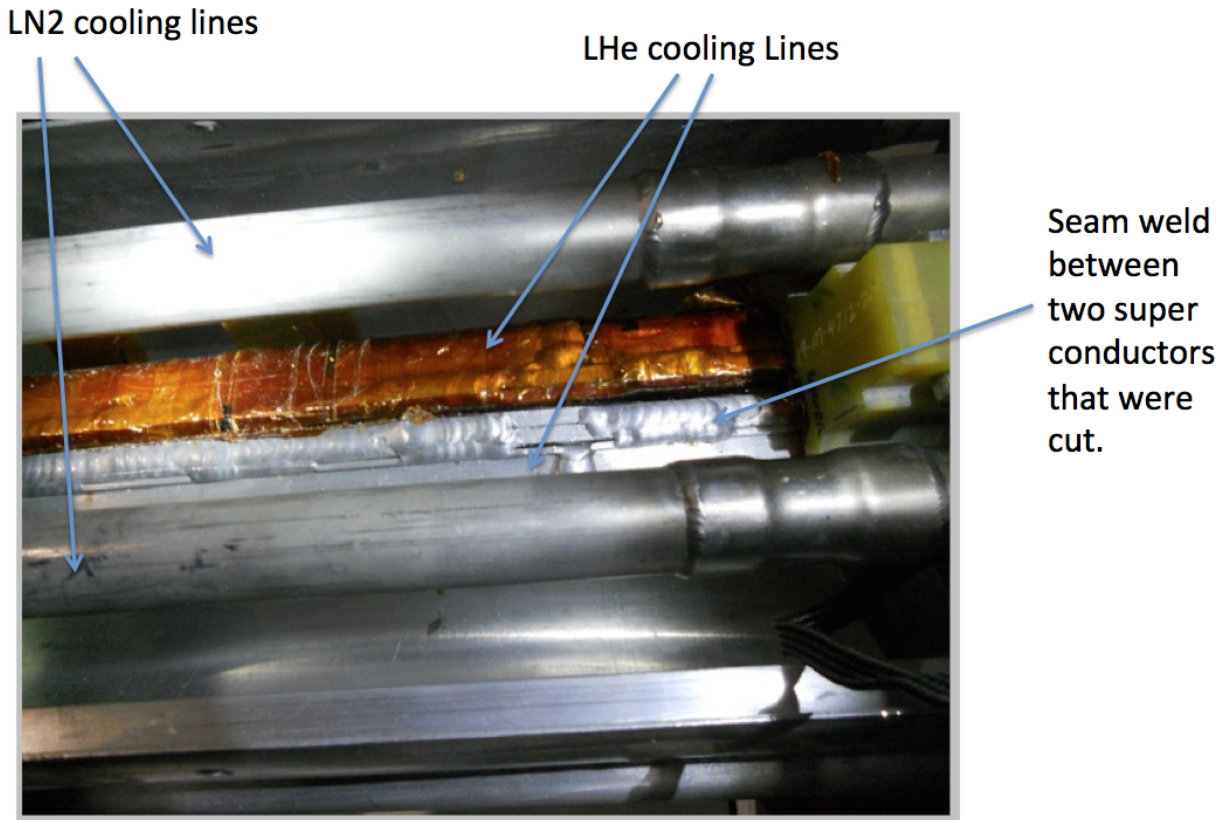


Figure 10.13: Photograph of the region of the interconnection, indicating welds and cooling lines.

4675 Once the hardware examination and the necessary replacement procedures have been
 4676 completed, the power supply unit will be tested in stages. This testing process will be done
 4677 in a staging area and not connected to any other component:

- 4678 • Stage 1: AC power will be applied to the separate modules of the unit. This is to first
 4679 check out operation of readout and controls.
- 4680 • Stage 2: AC power will then be applied to the complete unit with no DC load con-
 4681 nected. This is designed to observe and check out the initial operation and to exercise
 4682 the controls.
- 4683 • Stage 3: Once the controls operation is verified, a partial DC load (10-20%) will be
 4684 applied to exercise the output and to check for stability.
- 4685 • Stage 4: Add parallel DC loads to the output to slowly bring up the power supply to
 4686 full power. Once the initial checkout is done, this step will be repeated.

4687 The quench detection voltage threshold used for E821 was 100 mV across the coils, and 10 mV
 4688 across each interconnect between the outer and inner coils, and 5 mV across the upper and
 4689 lower coils within the outer cryostat. The thresholds were determined by the requirement

Cross Sectional View of An Interconnection

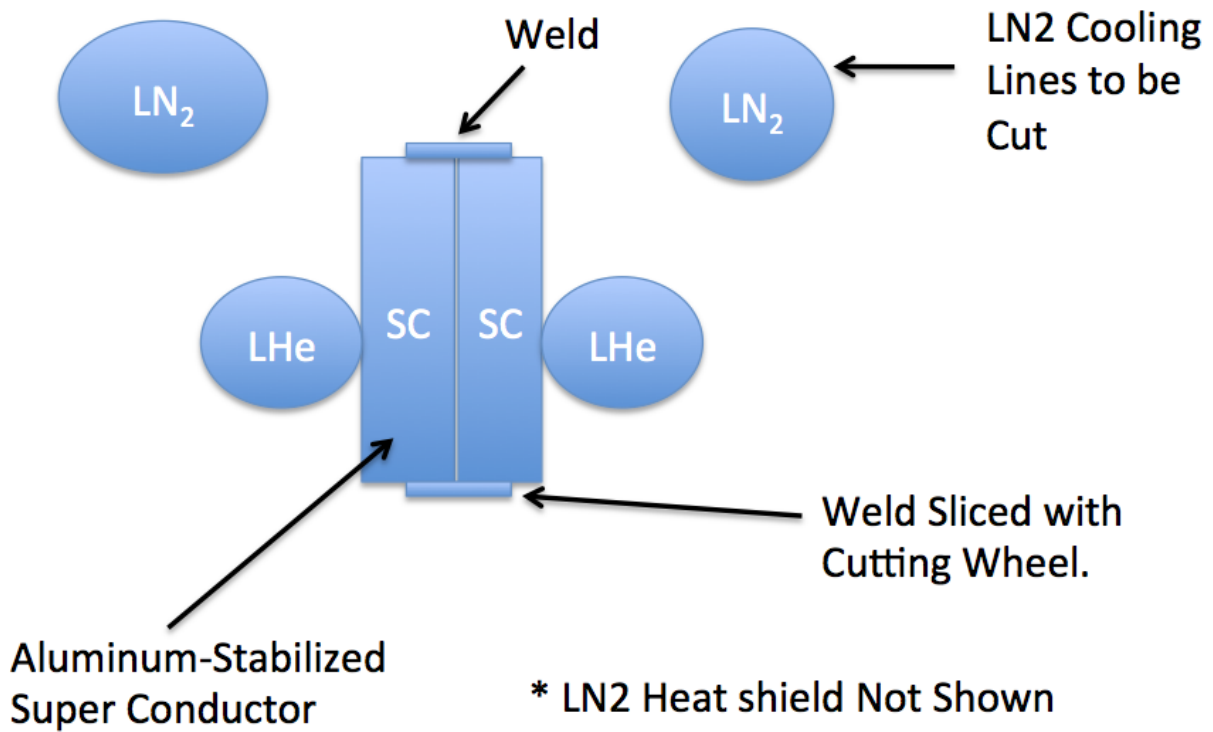


Figure 10.14: Diagram of the region of the interconnection, indicating welds and cooling lines that were cut, in order to facilitate the transportation.

4690 that the quench be detected within 0.2 s. The gas-cooled leads develop a voltage of typically
4691 15 mV at full current. If the lead voltage exceeds 30 mV, the energy is extracted.

4692 In a similar manner to that used for the power supply, the quench protection circuitry
4693 will be examined and refurbished to its original operational state. Testing will also be in
4694 stages until the completed unit, along with the transfer switch and dump resistor, operates
4695 as originally designed. This testing will also be in stages and not connected to any ring
4696 components.

4697 Similar to E821, the dump resistor will be located outdoors. During energy extraction,
4698 approximately 6 MJ of energy will be dissipated into the dump resistor. If the dump resistor
4699 was located indoors, it would raise the air temperature by approximately 2 °C. While that can
4700 be handled by the building HVAC, it would produce unwanted temperature non-uniformity
4701 in the hall.

4702 Once the four main components, power supply, quench protection unit, transfer switch,
4703 and dump resistor have been tested individually, reconnection of these components will be
4704 done in the staging area. At this time, specific procedures will be developed for reconnection.
4705 These procedures will be fully tested and reviewed prior to connection to the main ring coils.
4706 A simulated load will be used to mimic operation of the ring coils. The model will start with

Coil	Resistance (ohms) Sept-1995	Resistance (ohms) Dec-2011
Inner Upper	0.429	0.430
Inner Lower	0.426	0.430
Outer Upper	-	0.483
Outer Lower	-	0.476
Outer Upper + Lower	0.952	0.958

Table 10.5: Room temperature coil resistance (ohms) measurements, showing consistency between Sept-1995 and Dec-2011.

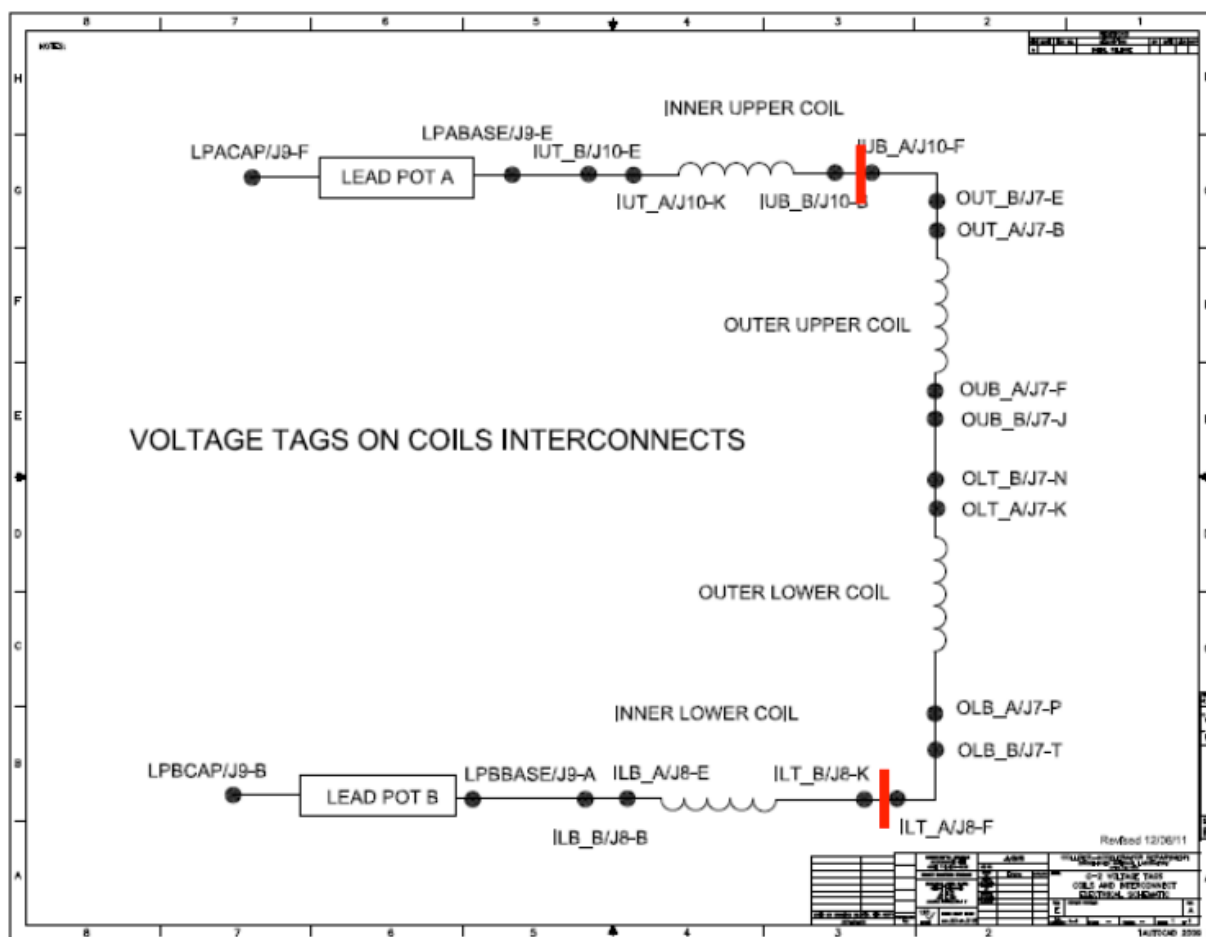


Figure 10.15: Voltage tap locations for quench detection. The red bars indicate the location of the cuts needed for transportation.

4707 resistive or active linear loads. A desired, but not necessary next step would be to use an
 4708 existing magnet coil to test all operation.

4709 After these tests are completed satisfactorily, the components will then be moved to
 4710 the $g - 2$ hall for final assembly and commissioning. The commissioning process will be
 4711 dependent on the assembly of the main ring. Again, this process should be done in stages of

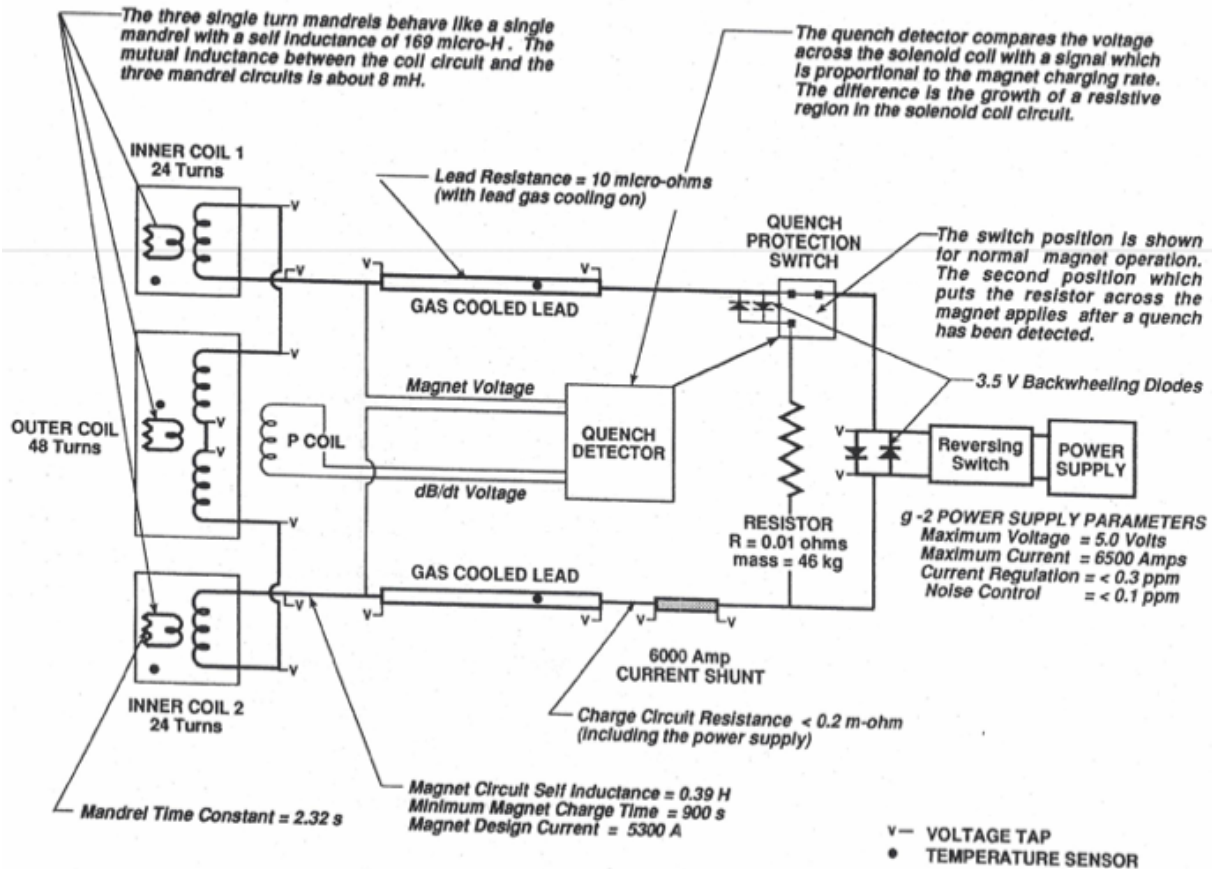


Figure 10.16: Quench detection and power supply diagram.

4712 operation (low to medium power, warm to cold coil operation, including the calibration of
 4713 the voltage threshold levels during power-up procedures) but these stages need to be defined
 4714 once the risk to the main ring connections can be identified and reasonably mitigated.

4715 10.5.6 Cryogenics

4716 This WBS refers to the cryogenics (LHe and LN₂) required to cool the coils to 4.9 K, the
 4717 cooling lines, the heat shields cooled to LN₂ temperatures, and the flow control valves. The
 4718 E821 cryosystem will be reused as much as possible, especially the 1000 liter dewar. The
 4719 E821 cryogenic flow diagram is shown in figure 10.17.

4720 While no design changes will be made, this WBS requires considerable verification, reanal-
 4721 ysis, and documentation due to the significant hazard and stored energy, and the potential
 4722 for the 'cold cryostat' problem as described in the section above.

4723 The documentation were generated for E821, and will be reaccessed for E989. Attention
 4724 will be given to:

- 4725 • Heat load of the system. There will be a slight increase due to the rewelding of the
 4726 coils at the interconnection (see section 10.5.7) and a slightly longer run between the

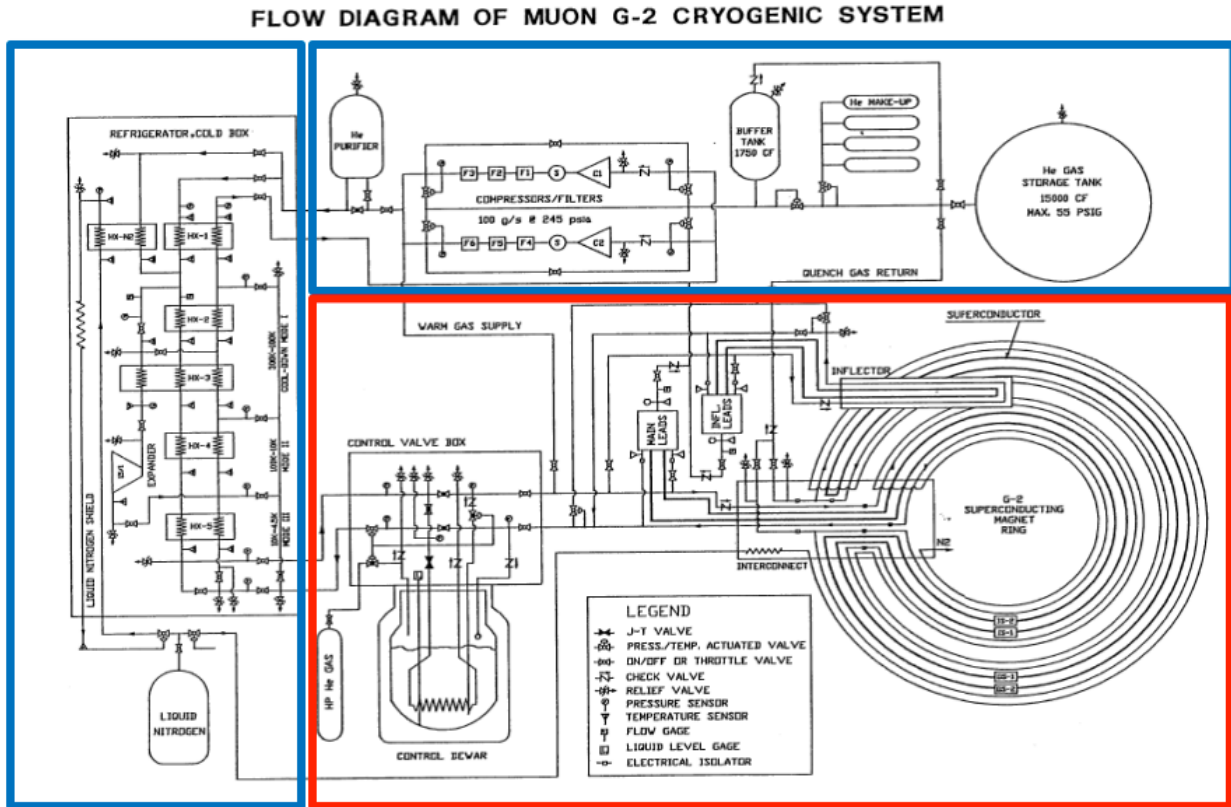


Figure 10.17: The cryogenic plant and its connection with E821 (G-2). The red box outlines the flow within building 919 at BNL. The upper (left) blue box outlines the LHe (LN₂) cryogenic plant.

4727 cryogenic plant and the LHe dewar.

4728 • Flow diagram, pressure drops, and flow rates. These are specified to be identical to
4729 that of E821.

4730 • Cool-down and warm-up procedure.

4731 • Connection to the Controls and Instrumentation WBS.

4732 The Fermilab Accelerator Division (AD) will provide two dedicated refrigeration systems for
4733 E989. An important difference between E821 and E989 is that the latter will share aspects
4734 of the cryogenic plant with the Mu2e experiment[13]. Mu2e and g-2 helium gasses are mixed
4735 together, and therefore share a common compressor. The AD design includes a cryo adsorber
4736 to trap contamination.

4737 10.5.7 Super Conducting Coils

4738 After the steel yoke pieces and coils have been reinstalled into the correct position, the
4739 recommissioning activities can begin. The key recommissioning activities for this WBS
4740 consists of:

- 4741 • Performing electrical continuity tests of the instruments such as thermometers and
4742 strain gauges.
- 4743 • Performing electrical continuity tests on the coils. This also verifies unwanted thermal
4744 shorts.
- 4745 • Rewelding the coil interconnects using pure Aluminum filler using the TiG (Tungsten
4746 inert Gas) welding technique.
- 4747 • Rewelding the LHe and LN₂ cooling lines in the interconnection region.

4748 During the interconnect cutting and the TiG rewelding process, a small amount of degra-
4749 dation to the pure Aluminum stabilizer is to be expected due to work hardening. Work
4750 hardening will cause a resistance increase of the Aluminum, therefore adding to the heat
4751 load at 4.9 K and a small local heating at the interconnection region.

4752 It also reduces the critical current capacity (I_c) before the superconductors become nor-
4753 mal. For the welding that took place during the E821 construction, the SC coil heating due
4754 to welding was modeled. The maximum temperature seen by the SC coils due to welding is
4755 350°C[3]. Degradation of NbTi critical current of < 5% was measured for a 2 T field for an
4756 annealing time of 10s at 400°C[9].

4757 For E821, the coil current and temperature were approximately 5200 A and 4.9 K re-
4758 spectively. The magnetic field at the coil was approximately 2 T. The critical temperature
4759 was estimated to be 6.2 K, giving a safety margin of 1.2 K[10]. However, the magnetic field
4760 at the interconnect is estimated to be < 1 T, and so the safety margin at the interconnect
4761 is even greater.

4762 E821 also welded a test overlap joint, and measured a cold resistance of $16 \cdot 10^{-9} \Omega$ at 2 T.
4763 At the current of 5200 A, the heat load is 0.43 Watts at 4.9 K, as compared to the cooling
4764 capacity of 351 W at 4.9 K (see table 5 of reference [3]).

4765 In summary, the coils were designed with a rather large safety margin. No quenches were
4766 observed to have taken place at the interconnects. To be conservative, we will measure the
4767 resistance properties of an overlap weld, cut it and reweld, and remeasure the resistance
4768 properties. Finally, work hardening of the Aluminum is strongly anti-correlated with yield
4769 strength[14]. Therefore, room temperature tests can be performed to gauge the level of work
4770 hardening.

4771 10.6 ES&H, Quality Assurance, Value Management, 4772 Risks

4773 10.6.1 Yoke, Pole, and Shims

4774 The hazards will be in the stored mechanical energy of these very heavy items during the
4775 use of the crane during installation. While the magnet is powered, the super bolts will be
4776 stressed (stretched) to counteract the magnetic forces' tendency to close the pole gaps. The
4777 stored electro-mechanical energy is approximately 6 MJoules. The storage region magnetic
4778 field of 1.45T is also a hazard.

4779 Mitigation would be to train the collaboration in proper procedures, controlling access to
4780 the area, and implementing a mechanism for detecting high magnetic susceptibility materials
4781 so that they are kept away from the high field area.

4782 Quality assurance, value management, and risks concerns are minimal since these items
4783 have been built and worked to specifications for E821. They are also passive materials and
4784 have high mechanical strength. Since considerable E989 machinery has already developed
4785 to model the magnetic field and temperature, we can simulate all alignment requirements.

4786 **10.6.2 Power Supply and Quench Protection System**

4787 **Hazards**

4788 The hazards during the testing processes will be primarily electrical. There will be an arc-
4789 flash hazard based on the incoming 480 VAC power feed and at 60-amperes. A complete hazard
4790 analysis can be made once the units are received and initially examined. The mitigations
4791 for these hazards are:

- 4792 • In the staging area, a safety disconnect switch will be used to provide emergency shut-
4793 off of power to the power supply.
- 4794 • No operation of any component will be done unattended. There will always be 2
4795 persons minimum present during any operation and testing.
- 4796 • Only properly trained persons, Electrical NFPA-70E and LOTO II at a minimum, will
4797 be allowed to work on the equipment.
- 4798 • Proper PPE and distances will be observed during operation and testing, especially
4799 during initial power up and during full-load operation. The level of PPE will be
4800 determined once the staging area is set up.

4801 **Risks**

4802 Risks to the successful completion of the tasks:

- 4803 • Use of Obsolete Components: Level-Medium. This risk involves the use of relatively
4804 old electronics. Therefore, component failure probability (based on hours of previous
4805 operation and power cycles, will need to be assessed for critical components of the
4806 power supply. Mitigation, at a minimum, will be to list these components and acquire
4807 spares in case of failure. To minimize the effect this risk will have on the schedule, the
4808 component list will be generated in parallel with the other operations. Initial costs will
4809 be incurred to acquire these spare components.
- 4810 • Catastrophic Failure During Testing: Level-Low to Medium. The units have operated
4811 before and they operated as initially designed. Therefore, testing of the components
4812 and of the units in stages should provide early indications of failure and allow replace-
4813 ment before the start of connection and commissioning.

- 4814 • Difficulty in Acquiring the Proper Testing Equipment: Level-Low. At this time, most
4815 equipment needed for testing, is, or should be, readily available on site. Therefore,
4816 purchases of new equipment will be at a minimum.
- 4817 • Catastrophic Failure During Commissioning: Level-Low. The risk here would be the
4818 most critical since failure of any component while connected to the ring coils would also
4819 present risk to the coils themselves. Mitigation here would be the exhaustive testing of
4820 components prior to connection to the ring and the powering up of the ring in stages
4821 of load and cooling. In addition, specific procedures for connection to the rings leads
4822 will be repeatedly and continuously reviewed.

4823 **Quality Assurance**

4824 The assurances that the units will operate as required are two-fold: First, the design is
4825 already done. Redesign should be at a minimum. Second, there will be exhaustive testing of
4826 each component prior to re-assembly. These testing procedures will be continuously reviewed
4827 during and after each stage of testing. Again, the primary process for all this is the initial
4828 examination followed by testing in stages as opposed to a one-time, massive final test. The
4829 staged testing allows deficiencies or problem areas to be identified at the earliest possible
4830 point in the task schedule. This again stresses the importance of the initial examination for
4831 the results of this will determine, in large part, the testing schedule.

4832 **Value Management**

4833 As much reuse of components will be implemented throughout these processes. Also, prelim-
4834 inary examination will serve to spot questionable components. Overall, the refurbishment
4835 process is used to minimize the need to purchase or redesign components and systems. Since
4836 the design is already done and it operated as designed, the risk and extra effort in developing
4837 a new design can be kept to a minimum.

4838 **10.6.3 The Cryogenic and Related Systems**

4839 The hazards are related to the use of LHe and LN₂ cryogenics: thermal energy and ODH.
4840 As described above, if the cooling lines in the vacuum cryostat leak, there is potential for
4841 the ‘cold-cryostat’ scenario (see above). These can be mitigated in the same fashion as
4842 E821. The cooling lines and vacuum chambers can be pressure tested at room temperature,
4843 following delivery from BNL and prior to use.

4844 New quality assurance and value management requirements are minimal since these items
4845 have been built and worked to specifications for E821. Should the items fail during recommissioning,
4846 they can be easily replaced since they are commercially available items of reasonable
4847 cost. These are vacuum parts and cryogenic lines. The only outstanding technical skills re-
4848 quired are Aluminum welding and vacuum leak-testing.

4849 There are inherent risks in nearly all cryogenic systems since these are usually very com-
4850 plex and have long time scales. Even though E821 operated a successful system, significant
4851 engineering is required for recertification. A mitigating factor is that similar systems have
4852 been built at Fermilab, and is inline with the expertise of the project mechanical engineer.

4853 **10.6.4 The Superconducting Coil System**

4854 The coils systems do not present a significant health hazard. Quality assurance and value
4855 management concerns are minimal since these items have been built and worked to specifi-
4856 cations for E821.

4857 The risks are not considerable. The risk of damage to the coils, straps, heat shields,
4858 glue joints are minimal since the stresses expected during transportation are at least 4x
4859 smaller than the maximum allowable stress. The expected stresses and deflections due to
4860 transportation have been simulated by FEA.

4861 However, we itemize them here since the replacement cost of the coils is beyond the scope
4862 of the project:

- 4863 • The coil windings are on the inside radial surface of the mandrel, rather than on the
4864 outside. During power up, the coils push against the mandrel, thereby enhancing the
4865 thermal cooling. Therefore, the system can tolerate failures of the glued interface,
4866 which is designed to enhance thermal conductivity.
- 4867 • Failure of the straps, though unexpected, can be detected as we slowly energize the
4868 coils. If a strap fails, it can be detected as a shift in the coil vertical position. It can
4869 be repaired by cutting an access hole in the vacuum cryostat. The downtime would be
4870 of order 2 weeks.
- 4871 • Failure in the heat shield can be detected as the system taking too long for cool down.
4872 Failure of the cooling lines can be detected as loss of vacuum. These are repaired via
4873 cutting access holes into the vacuum cryostat. However, it will be difficult to locate
4874 the point of failure.
- 4875 • There is a very slight risk of the Aluminum resistance at the interconnection becoming
4876 too high during the reweld. We will prototype the rewelding process and study the
4877 correlation of resistance with yield strength. We can anneal the interconnection to
4878 improve the resistance.

References

- 4879
- 4880 [1] Bailey J, et al. Nucl. Phys. B150:1 (1979).
- 4881 [2] Bennett GW, et al.(The Muon ($g - 2$) Collaboration) Phys. Rev. D, 73:072003 (2006).
- 4882 [3] G.T. Danby, et al., Nucl. Inst and Meth. **A 457**, 151 (2001).
- 4883 [4] Reference Manual for the POISSON/SUPERFISH group of codes, LANL, LA-UR-87-
4884 126.
- 4885 [5] Design Report, BNL E821, A New Precision Measurement of the Muon ($g - 2$) Value at
4886 the level of 0.35 ppm. 3rd edition, D.H. Brown et al. B.L. Roberts Editor, March 1995.
- 4887 [6] A. Yamamoto, H. Inoue, H. Hirabayashi, J. Phys. 45 (1984) C1-337.
- 4888 [7] A. Yamamoto, private communication.
- 4889 [8] M.A. Green et al., Operation of a two-phase cooling system on a large superconduct-
4890 ing magnet, Proceeding of the Eighth International Cryogenic Engineering Conference,
4891 Genoa, Italy, June 1980, IPC Science and Technology Press, 1980, p. 72.
- 4892 [9] Th. Schneider and P. Turowski, Thirteenth International Conference on Magnet Tech-
4893 nology, Victoria, Canada, September 1993, Paper R-J-07.
- 4894 [10] Bill Morse, Characteristic of the E821 Interconnects, GM2-doc-302-v1.
- 4895 [11] Bill Morse, Coil Resistance to Ground Measurements, GM2-doc-352-v1.
- 4896 [12] Bill Morse, Coil Resistance to Ground Measurements, GM2-doc-976-v1.
- 4897 [13] Del Allspach, Vacuum and Cryogenics Presentation at g-2 December 2012 Collaboration
4898 Meeting, GM2-doc-615-v1.
- 4899 [14] T. Tonogi et. al., Aluminum Stabilized Superconductor for the Atlas Central Solenoid
4900 Magnet, Hitachi Cable Review No. 18, V87.

Chapter 11

The Superconducting Inflector Magnet

In this chapter we first introduce the E821 inflector magnet, which is our baseline starting option. We then describe the shortcomings of this magnet, as well as the characteristics and the benefits that an improved inflector would have. Any new design will require significant R&D and OPERA simulations to arrive at a new inflector design.

11.1 Introduction to Inflection Challenges

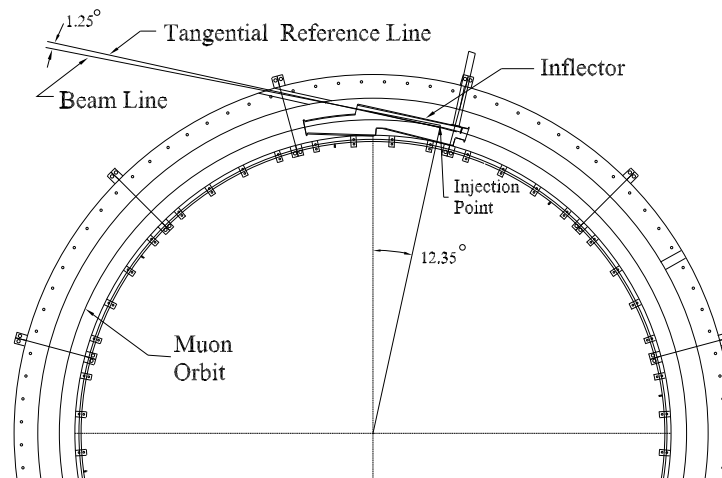


Figure 11.1: Plan view of the beam entering the storage ring.

The typical storage ring is composed of lumped beamline elements such as dipoles, quadrupoles, sextapoles, etc., which leaves space for injection, extraction, and other beam manipulation devices. For the measurement of a_μ , the requirement of ± 1 ppm uniformity on the magnetic field, which in E989 must be known to $\leq \pm 0.07$ ppm, prohibits this usual

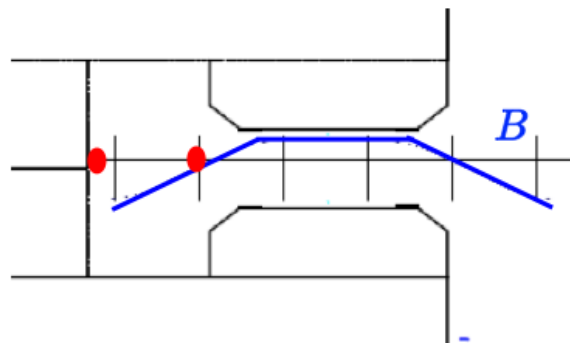


Figure 11.2: The fringe field of the main magnet over the radial range traversed by the beam. The left-hand red dot is where the beam exits hole in the outer coil. The right-hand dot is where the beam enters the inflector. The field inside of the inflector is not constant until part way down.

4913 design. Instead, as described in Chapter 10 the $(g - 2)$ storage ring is designed as a mono-
 4914 lithic magnet with no end effects. The “C”-magnet construction shown in Fig 10.1 presents
 4915 several obstacles to transporting a beam into the storage ring: There must be holes through
 4916 the back-leg of the magnet and through the outer coil cryostat and mandrel for the beam
 4917 to enter the experiment. These holes must come through at an angle, rather than radially,
 4918 which complicates the design, especially of the outer-coil cryostat.

4919 A plan view of the beam path entering the storage ring is given in Fig. 11.1. Since
 4920 the beam enters through the fringe field of the magnet, and then into the main 1.5 T
 4921 field, it will be strongly deflected unless some magnetic device is present that cancels this
 4922 field. This device is called the inflector magnet. In reality, there is a fringe field that grows
 4923 approximately linearly as the beam moves radially inward from the hole in the outer cryostat
 4924 to the location of the inflector entrance. This is sketched in Fig. 11.2.

4925 The injection beam line is set to a 1.25° angle from the tangential reference line (Fig. 11.1).
 4926 The inflector is aligned along this reference line and its downstream end is positioned at the
 4927 injection point, which is tangent to the ring. The point where the reference line is tangent
 4928 to the storage ring circumference is offset 77 mm radially outward from the muon central
 4929 orbit. The main magnet fringe field, upstream of the inflector, bends the incoming beam by
 4930 about 1.25° , so that the beam enters the inflector nearly parallel to the inflector axis.

4931 The requirements on the inflector magnet are very restrictive:

- 4932 1. To a good approximation it should null the storage ring field such that the muons are
 4933 not deflected by the main 1.5 T field.
- 4934 2. It should be a static device *to prevent time-varying magnetic fields correlated with*
 4935 *injection*, which could affect $\int \vec{B} \cdot d\vec{\ell}$ seen by the stored muons and produce an “early
 4936 to late” systematic effect.
- 4937 3. It cannot “leak” magnetic flux into the precision shimmed storage-ring field that affects
 4938 $\int \vec{B} \cdot d\vec{\ell}$ at the sub-ppm level.

- 4939 4. It cannot contain any ferromagnetic material, which would distort the uniform mag-
 4940 netic field.
- 4941 5. The inflector should have a "reasonable" aperture to match the beamline to the ring
 4942 acceptance.
- 4943 6. The inflector angle in the cryostat should be variable over the full range permitted by
 4944 the constraints of the space available.

4945 11.2 The E821 Inflector Design and Operation

4946 Three possible solutions were considered in E821: A pulsed inflector, a superconducting
 4947 flux exclusion tube, and a modified double $\cos\theta$ magnet. The pulsed inflector proved to
 4948 be technically impossible at the repetition rate necessary at BNL. Furthermore it violates
 4949 item 2 above. Naively one could imagine that a superconducting flux exclusion tube would
 4950 work for this application. However, an examination of Fig. 11.3 shows that in the vicinity
 4951 of the tube, the magnetic field is perturbed on the order of 10%, or 100,000 ppm [1], an
 4952 unacceptable level. Attempts to figure out how to mitigate this problem were unsuccessful.
 4953 This is because the large eddy currents needed to shield the 1.45 T field are large enough to
 4954 affect the uniformity of the field seen by the muons contained in the red semicircle. However,
 4955 this principle will re-appear in the discussion of how to shield the 200 G (20 mT) residual
 4956 magnetic field from the truncated double $\cos\theta$ design employed in the E821 inflector. The
 4957 properties of the E821 Inflector are summarized in Table 11.1

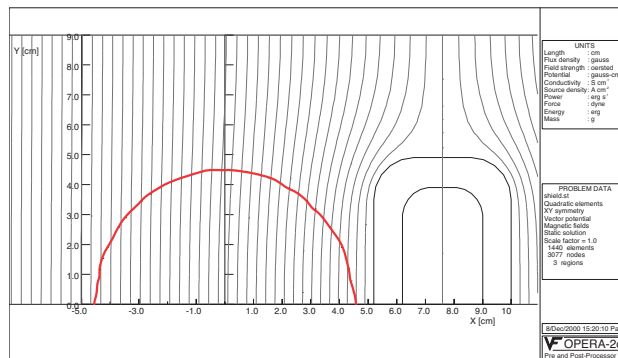


Figure 11.3: The calculated magnetic field outside of a superconducting flux exclusion tube placed in a 1.45 T magnetic field. The red circle is the muon beam storage region. (From Ref. [1])

4958 11.2.1 Magnetic Design of the E821 Inflector

4959 Only the double $\cos\theta$ design[2] satisfied the three criteria listed above. The double $\cos\theta$
 4960 design has two concentric $\cos\theta$ magnets with equal and opposite currents, which outside has
 4961 negligible field from Ampère's law. A double $\cos\theta$ design provides a 1.5 T field close to the

Table 11.1: Properties of the E821 Inflector.

Overall dimension	110(W)×150(W)×2025(L) mm ³
Magnetic length	1700 mm
Beam aperture	18 mm (W) × 56 mm (H)
Design current	2850 A (with 1.45 T main field)
Number of turns	88
Channel field	1.5 T (without main field)
Peak field	3.5 T (at design current, with main dipole field)
Inductance	2.0 mH
Resistance	1.4 Ω (at 300 K)
Cold mass	60 kg
Stored energy	9 kJ (at design current)

Table 11.2: Properties of the inflector superconductor.

Configuration (NbTi:Cu:Al)	1:0.9:3.7
Stabilizer	Al (99.997% RRR = 750)
Process	Co-extrusion
NbTi/Cu composite	Diameter 1.6 mm monolith
NbTi filament	Diameter 0.02 mm
Number of filaments	3050
Twist pitch	31 mm
Conductor dimension	2 × 3 mm ²
Insulated conductor dimension	2.3 × 3.3 mm ²

4962 storage region, and traps its own fringe field, with a small residual fringe field remaining.
 4963 However, what is needed for the $(g - 2)$ beam channel is a septum magnet. This is achieved
 4964 by truncating the two $\cos \theta$ distributions along a line of constant vector potential A [2]. The
 4965 truncation method is shown in Fig. 11.4, taken from Ref. [2], which should be consulted for
 4966 additional details.

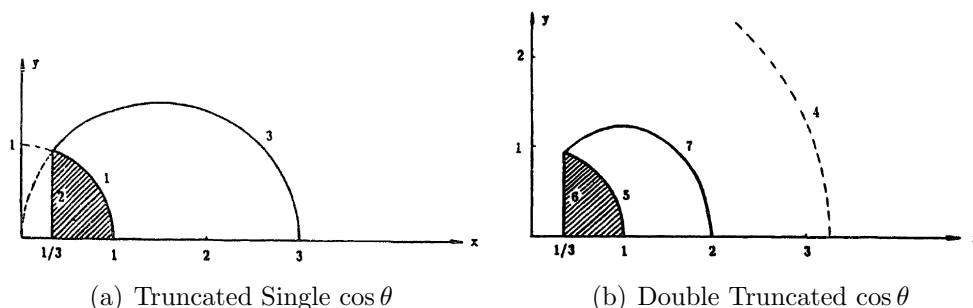


Figure 11.4: (a) The principle of the truncated single $\cos \theta$ magnet. (b) The principle of the truncated double $\cos \theta$ magnet.

4967 Aluminum-stabilized superconductor was chosen for the BNL $(g - 2)$ inflector: (a) to
 4968 minimize the interactions of the incoming pion/muon beam at both upstream and down-
 4969 stream ends of the coil with no open apertures for the beam, and (b) to make the coils and
 4970 cryostat design compact, so that the conductive cooling (without liquid helium containers
 4971 surrounding the coils) can be achieved effectively. An existing Al-stabilized superconductor
 4972 was supplied by Japan KEK (fabricated by Furukawa Co.). This conductor was developed
 4973 for ASTROMAG (Particle Astrophysics Magnet Facility) [3, 4]. Fig. 11.5 shows the cross-
 4974 section of this conductor. The basic parameters are listed in Table 11.2. From computer
 4975 calculations, which include the self-field effect [5], show that the peak field seen by the inflec-
 4976 tor conductor filaments reaches 3.5 T. This is due to the superposition of the return flux and
 4977 the main field. Short sample tests showed that the critical current of this superconductor is
 4978 about 3890 A at 4.6 K and 3.5 T. In the $(g - 2)$ storage ring, the inflector sees 1.45 T field
 4979 (from the main magnet) even at zero operating current. From the conductor characteristics,
 4980 the inflector operates at around 73% of the full load (at 4.6 K). The short sample test data

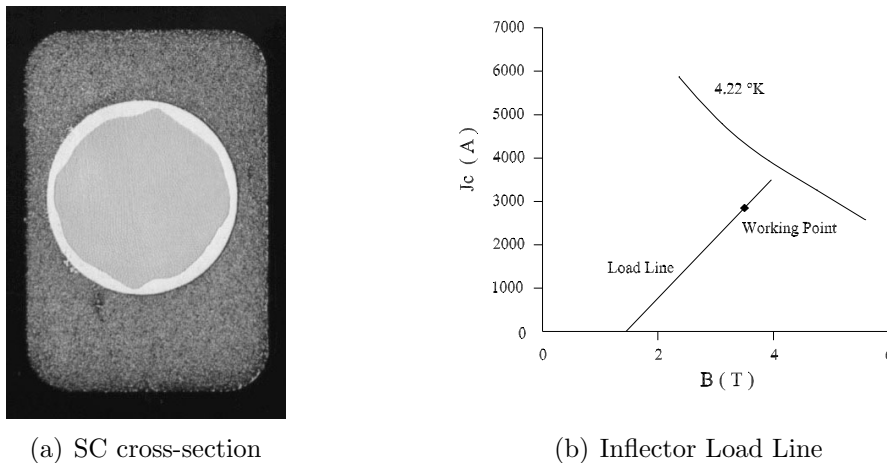


Figure 11.5: (a) The inflector superconductor cross-section. (b) Superconductor characteristics and the inflector load line in the environment of 1.45 T magnetic field.

4981 and the inflector load line (in the storage ring field environment) are shown in Fig. 11.5(b).

4982 The result is a magnet with conductors arranged as shown in Fig. 11.6(a). The conductors
 4983 are connected in series, with an equal number with current into and out of the page. In
 4984 Fig. 11.6(a) the current is flowing out of the page in the backward “D” shaped pattern of
 4985 conductors, and into the page in the “C” shaped arrangement of conductors. The field from
 4986 the inflector magnet is vertical up in the beam channel and downward in the return area,
 4987 as shown in Fig 11.6(a). With the main storage ring field vertical, there is no field in the
 4988 beam channel and $\simeq 3 \text{ T}$ field in the return area. With this design and the ASTROMAG
 4989 conductor, it is difficult to enlarge the beam channel very much because moving the “C”
 4990 arrangement of conductors to the left would quickly exceed their critical current.

4991 There are two sources of magnetic flux from the inflector that can leak into the storage
 4992 region. Because the field is produced by discrete conductors, rather than a continuous current
 4993 distribution, some flux does leak out of this arrangement of conductors, see Fig. 11.6(b). The
 4994 inflector lead configuration is also important, and when it was necessary to produce a second
 4995 inflector, the lead configuration was changed to reduce this effect.

4996 The coil was wound in two different pieces indicated by “inner” and “outer” coils in
 4997 Fig. 11.6(a). One end of the coil is shown in Fig. 11.7(a) The choice was made to wind the
 4998 coil over the beam channel, because this configuration would have less flux leakage, and was
 4999 thought to be more stable from quenches. However, a 0.5 m prototype was constructed with
 5000 one open and one closed end, which are shown in Fig. 11.7. This prototype inflector was
 5001 operated in the earth’s field, and then in an external 1.45 T field without incident.

5002 The inner coil and the outer coil are connected in series. The joint is located inside the
 5003 downstream end of the coils; and is made by soldering the superconductors without removing
 5004 the aluminum stabilizer. The joined leads were placed inside a U-shaped groove, as shown
 5005 in Fig. 11.8, attached to the coil end structure. Cooling tubes run through the extender
 5006 (aluminum block). One temperature sensor was mounted near the joint to monitor the local

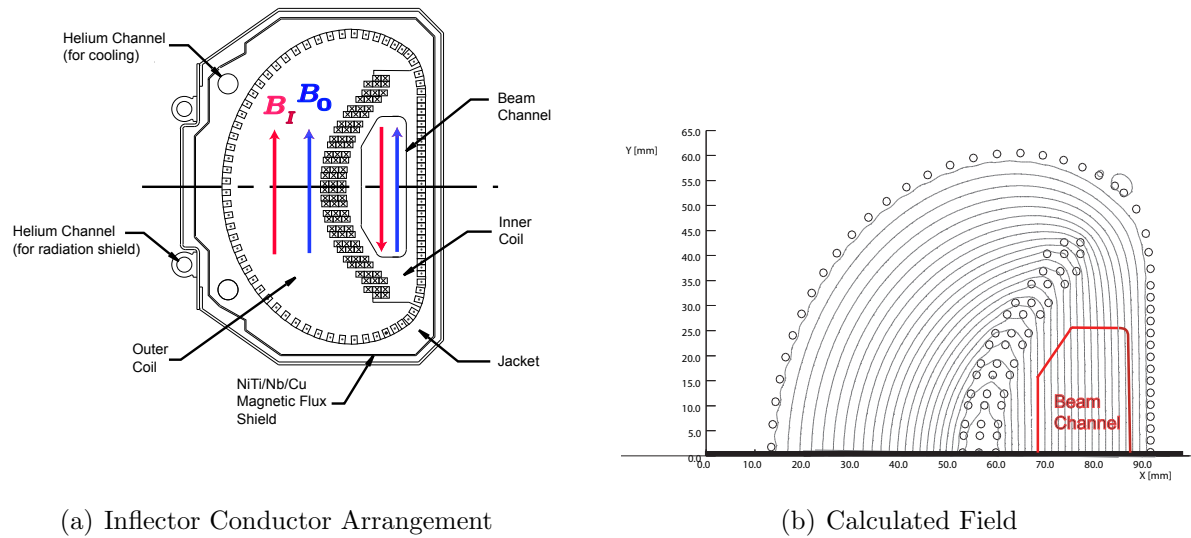


Figure 11.6: (a) The arrangement of conductors in the inflector magnet, showing the direction of the inflector field B_I and the main field B_0 for a beam of positive muons going into the page. The current in the inner “C” is into the page and is out of the page in the backward “D”. (b) Magnetic field lines generated by this arrangement of conductors. The beam aperture is $18 \times 56 \text{ mm}^2$.

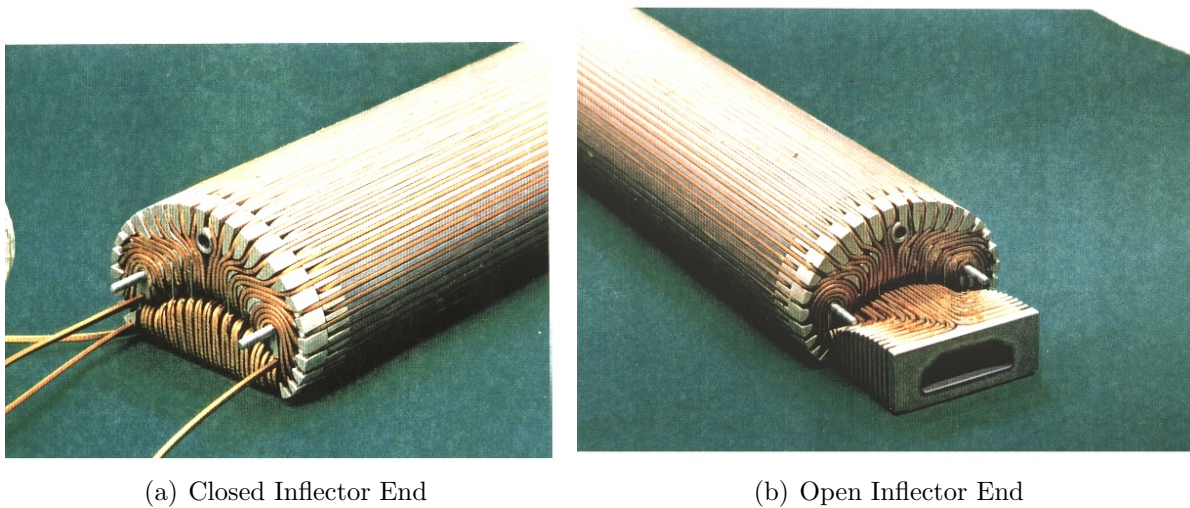
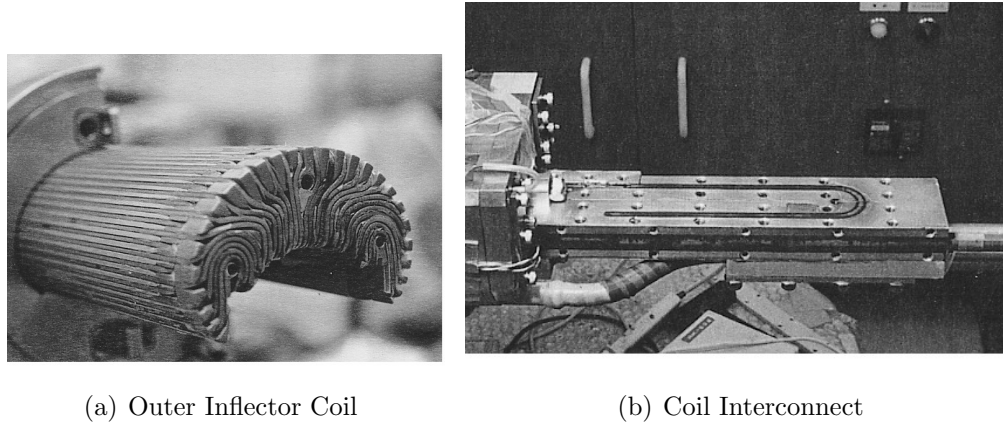


Figure 11.7: (a) The prototype closed inflector end. (b) The prototype open inflector end.

5007 ohmic heating.

5008 The geometry of the inflector cryostat is complicated by the proximity of the outer-coil
 5009 cryostat, the pole pieces and the muon beam. A sketch of the beam path through the outer
 5010 coil is shown in Fig. 11.9(a). The complicated arrangement where the inflector entrance

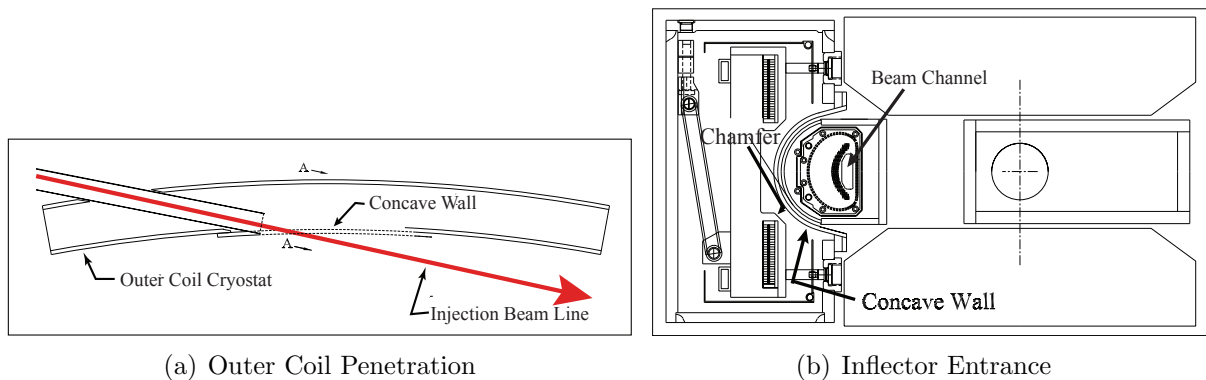


(a) Outer Inflector Coil

(b) Coil Interconnect

Figure 11.8: (a) The arrangement of conductors in the inflector magnet.(b) The joint and lead holder for the interconnect.

5011 nests into the concave wall of the inflector cryostat is shown in Fig. 11.9(b). Fig. 11.10
 5012 shows the combined inflector cryostat and beam vacuum chamber. The cryostat region and
 5013 beam region have different vacuums, so the inflector can be cooled, independent of whether
 5014 the beam vacuum chamber is evacuated.



(a) Outer Coil Penetration

(b) Inflector Entrance

Figure 11.9: (a) A plan view of the beam penetration through the outer coil and cryostat.
 (b) An elevation view of the inflector entrance showing the concave wall of the outer-coil
 cryostat where the beam exits the outer coil-cryostat.

5015 The exit of the inflector magnet is shown in Fig. 11.11, which clearly indicates the accel-
 5016 erator physics issue. The incident beam is contained in the red 18 mm × 56 mm “D”-shaped
 5017 channel, while the stored beam is confined to a 45 mm diameter circular aperture. Thus
 5018 it is impossible to match the β or α functions between the ring and the muon beamline
 5019 without unacceptable losses in the injection channel. The result is a “ β wave” that reduces
 5020 the acceptance of the ring.

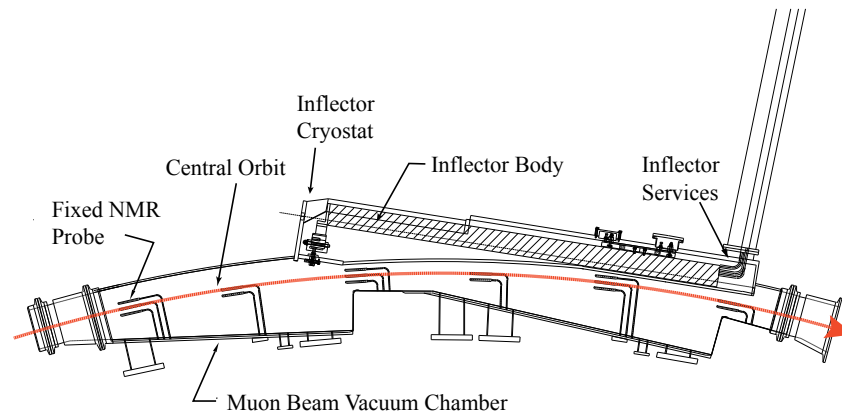


Figure 11.10: Plan view of the combined inflector cryostat-beam vacuum chamber arrangement. The inflector services (power, LHe and sensor wires) go through a radial hole in the back-leg outside of the storage-ring magnet. The NMR fixed probes are in grooves on the outside of the vacuum chambers, above and below the storage region. The red arrow shows the muon beam central orbit.

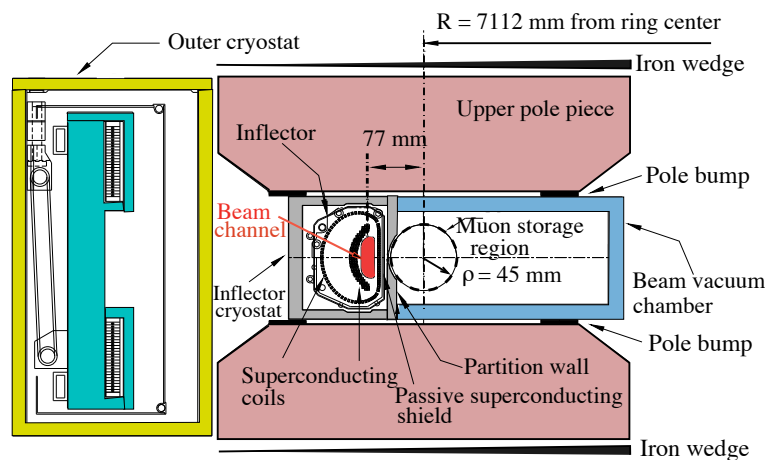


Figure 11.11: The inflector exit showing the incident beam center 77 mm from the center of the storage region. The incident muon beam channel is highlighted in red. (Modified from Fig. 10.6)

5021 11.2.2 Shielding the residual fringe field

5022 At the design current, the maximal fringe field within the muon storage region was calculated
 5023 to be about 200 G (1.4%) near the outer edge. The fringe field behaves in such a way that
 5024 it is a rapidly varying function along the transverse direction, i.e. the radial direction of the
 5025 storage ring, and essentially gives a negative disturbance. The fringe field of the inflector

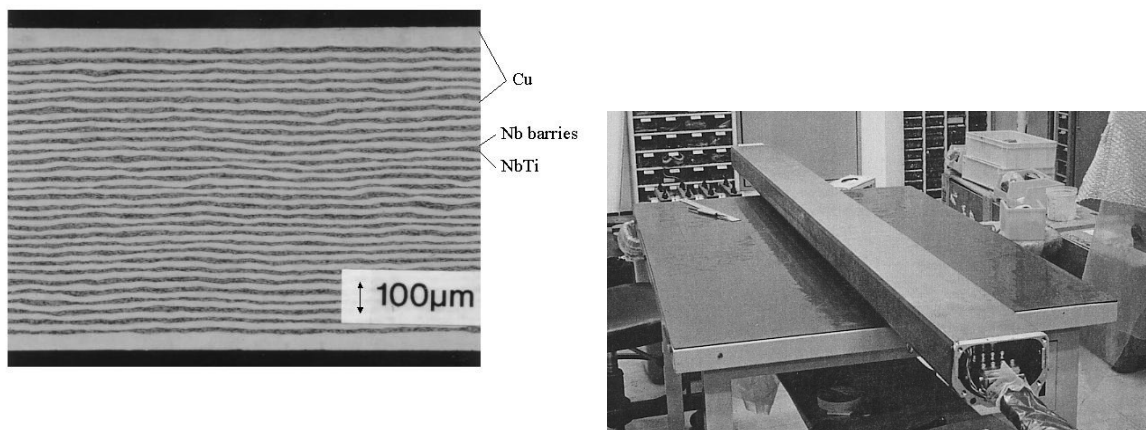
5026 is opposite to the main field at the outer radius of the storage ring, and changes sign while
5027 crossing the central orbit.

5028 The consequence of such a fringe field is severe. The high gradient of the field is beyond
5029 the working range of the NMR probes, so that the magnetic field map of the storage region
5030 would be incomplete, directly impacting the error of the measurement precision of the muon
5031 magnetic moment.

5032 Conventional magneto-static shimming studies to reduce this fringe field using computer
5033 simulations were carried out. The iron compensation must be located outside the muon
5034 storage region, far from the disturbance it is trying to shield. Thus its contribution to the
5035 central field would be a slowly varying function in this space (long wavelength), which is not
5036 able to cancel the larger gradient fringe field to an acceptable level [10].

5037 The best way to eliminate a multipole fringe field is to create an opposite multipole
5038 current source with the same magnitude. The best such current source is the super-current
5039 generated inside a superconducting material due to the variation of the surrounding field.
5040 A method of using SC material to shield the inflector residual fringe field was studied and
5041 developed. The fringe field specification was then satisfied.

5042 A test sheet of a superconducting shield was developed that contained 30 layers NbTi, 60
5043 layers Nb, and 31 layers Cu. The Cu layers greatly improved the dynamic stability against
5044 flux jumping [7]. The Nb layers act as barriers, which prevent the diffusion of Ti into Cu. The
5045 diffusion could form hard inter-metallic layers and create difficulties for the rolling process.
5046 Fig. 11.12 shows the typical cross section of the sheet. Based on successful tests, Nippon
5047 Steel Corp. developed large, thin pieces of sheet especially for the $(g - 2)$ inflector, to cover
5048 its $2 \times 0.5 \text{ m}^2$ surface and to fit into the limited space between the storage region and main
5049 magnet coil. The shielding result was extremely satisfactory.



(a) SC shield X-section

(b) SC shield installed

Figure 11.12: (a)Cross section of the multi-layer superconducting shield sheet. (b)The superconducting shield installed around the body of the inflector.

5050 The steps in using the shield are as follows:

- 5051 1. With the inflector warm (~ 20 K) the storage ring magnet is powered and allowed to
5052 reach equilibrium.
- 5053 2. The inflector is then cooled to superconducting temperatures. The shield material is a
5054 Type-II super conductor, where $H_{C1} = 0.009$ T for NbTi is the maximum field for the
5055 Meissner effect to occur. Therefore, as it is cooled down to the superconducting state,
5056 the shield is not able to expel the external field. Rather, the external field will fully
5057 penetrate the shield. and the shield traps the main field.
- 5058 3. The inflector is then powered. In this superconducting state, the shield will exhibit
5059 perfect diamagnetism, and will resist any change in the flux penetration through its
5060 surface.

5061 11.2.3 Performance of the E821 Inflector

5062 Two full-size inflectors were produced. To emphasize the importance of the superconducting
5063 shield, we relate what happened when the shield on the first inflector was damaged. In
5064 the testing of the first inflector, an accident occurred, where the interconnect shown in
5065 Fig. 11.8(b) was melted, leaving a few centimeters of undamaged cable outside of the inflector
5066 body. In order to repair it, the superconducting shield was cut to give access to the damaged
5067 superconductor. After the repair, an attempt was made to apply a patch to the shield.
5068 Unfortunately this attempt was not completely successful. The resulting fringe field reduced
5069 the storage-ring field by 600 ppm (8.7 G) over a 1° azimuthal angle, resulting in unacceptable
5070 magnetic-field gradients for the NMR trolley probes closest to the inflector body. It was also
5071 realized that a significant fringe field came from the inflector leads. An average field map
5072 from the 1999 run using the damaged inflector, and from the 2001 run using the new inflector
5073 are shown in Fig. 11.13. The field in the region with large gradients had to be mapped by
5074 a special procedure following data taking. This large fringe field introduced an additional
5075 uncertainty into the average field of ± 0.20 ppm in the result [12]. The 1999 result had a total
5076 error of ± 1.3 ppm, so the additional 0.2 ppm uncertainty introduced by the damaged shield
5077 was small compared to the statistical error of ± 1.2 ppm. Had this error not be eliminated,
5078 its effect would have been quite serious for the 2000 and 2001 results, both of which had a
5079 total error of ± 0.7 ppm.

5080 The damaged inflector was replaced in mid 1999, well before the 2000 running period.
5081 Two modifications were made to the new inflector design: The superconducting shield was
5082 extended further beyond the downstream end; The lead geometry was changed to reduce
5083 the fringe field due to the inflector leads. Both of these improvements were essential to the
5084 excellent shielding obtained from the second inflector. For both the 2000 and 2001 running
5085 periods, the fringe field of the inflector was immeasurably small [15, 16].

5086 11.3 Lessons for E989 from the E821 Inflector

5087 The most important single lesson from the E821 inflector came from the flux leakage from
5088 the damaged inflector, and the realization that the first design of the inflector leads also

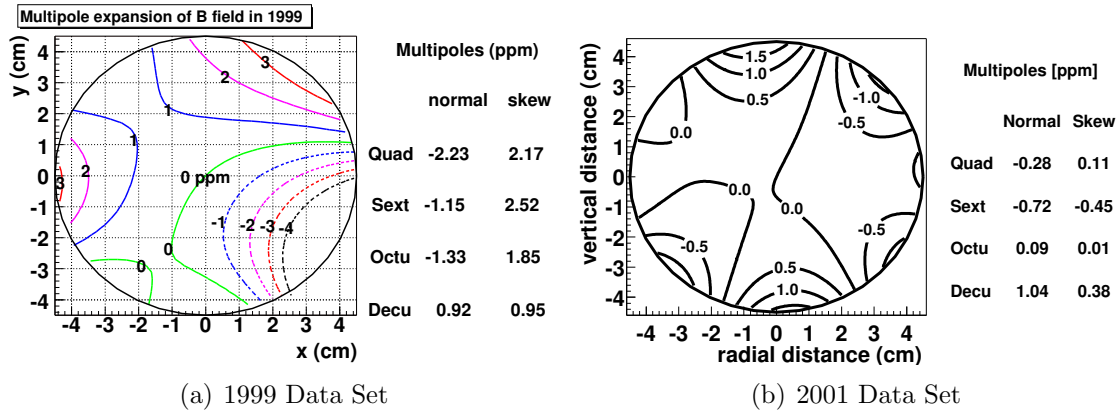


Figure 11.13: The average magnetic field $\langle B \rangle_{azimuth}$ (a) with the damaged inflector (1 ppm contours) (b) and with the second inflector (0.5 ppm contours). Note that the large disturbance in the average field was from a 600 ppm disturbance in the field over 1° in azimuth.

5089 contributed to this problem (see Fig.11.13). The ± 0.2 ppm systematic error from this prob-
 5090 lem is three times the E989 magnetic field error budget of ± 0.07 ppm. The highly localized
 5091 600 ppm perturbation at the location of the “repaired” superconducting shield could not
 5092 be shimmed away. The second issue that must be addressed is the mismatch of the E821
 5093 inflector aperture and the storage ring acceptance. The third issue is to open the ends.

5094 The guiding principles going forward are:

- 5095 • *The flux inside of the inflector must be confined inside of the inflector and not permitted*
 5096 *to leak into the storage region.*
- 5097 • *Any new inflector design must have a horizontal (radial) aperture significantly larger*
 5098 *than 18 mm; as close to 40 mm as possible.*
- 5099 • *The ends of the inflector need to be open, rather than have coil windings across them.*

5100 The latter two conditions could increase the number of stored muons by almost a factor of
 5101 four.

5102 The muon injection efficiency achieved in E821 was around 2%. Early simulations pre-
 5103 dicted that it should be 5 - 7%. Opening the ends of the inflector would have doubled the
 5104 number of stored muons. So it becomes clear that a new open-ended inflector with a larger
 5105 aperture, perhaps as large as 30 to 40 mm diameter is desirable. It is a high priority to
 5106 determine what aperture is possible. Given the time that will be needed to develop a new
 5107 inflector, it is difficult to have a new inflector ready by mid-2015 when the shimming program
 5108 would be ready to install vacuum chambers and the inflector. Because of the potential of
 5109 a new inflector to increase significantly the number of stored muons, understanding what is
 5110 possible will be a high priority.

5111 Going forward, we need: (i) To open both ends of the inflector; (i) A larger aperture than
 5112 the E821 inflector; Careful lead design to minimize stray field; A passive superconducting
 5113 shield that prevents flux leaking from the inflector into the precision magnetic field.

5114 11.4 A New Inflector

5115 Several concepts have been considered to replace the existing inflector. Any new design is
 5116 constrained by the injection geometry shown in Figs. 11.1, 11.9 11.10 and 11.11. A passive
 5117 superconducting shield to remove any leakage flux from the new inflector will be essential.

5118 The small aperture of the E821 inflector, and the coil windings over the beam channel
 5119 make matching the beamline to the storage ring impossible. Since E989 plans to accumulate
 5120 21 times the data of E821, it is necessary to revisit the inflector aperture issue. Opening the
 5121 radial aperture to a 30 to 40 mm would come close to matching with the incoming beam,
 5122 and permit many more muons to be stored. The trade-off as the aperture gets larger and the
 5123 centroid of the injected beam is displaced radially outward, a larger kick is needed to place
 5124 the beam on orbit. Shielding the flux leakage from a larger open end will also be challenging.

5125 In E989 the knowledge of the average magnetic field needs to be improved by a factor of
 5126 three over E821. While the plan to improve the magnetic field measurement and control is
 5127 discussed in Chapter 16, this plan is meaningless if any device in the experiment spoils the
 5128 field by introducing extraneous magnetic flux into the storage region. The damaged inflector
 5129 in E821 demonstrated how a 0.2 ppm problem can easily be introduced.

5130 Two possible suggestions have been proposed for a new inflector:

- 5131 • A double coil structure that is either the double-cosine θ design, or another double
 5132 magnet that cancels the storage ring field.
- 5133 • An elliptical double dipole magnet

5134 Any of the powered magnet solutions would need a passive superconducting shield that
 5135 traps whatever flux might leak from the magnets, preventing this leakage flux from changing
 5136 the magnetic field seen by the muons while they are stored in the ring.

5137 11.4.1 A New Double Cosine Theta Magnet

5138 This option needs study. The truncated double cosine theta design encased in a multi-layer
 5139 superconducting shield worked well in E821, albeit with the limitations discussed above.
 5140 Certainly any new design must have open ends, since the multiple scattering makes it im-
 5141 possible to correctly match the incoming beam to the ring. The open ends will certainly
 5142 produce issues for shielding the fringe field, which are common to the other wound magnets
 5143 discussed below.

5144 Fortunately our UK colleagues at the Rutherford-Appleton Laboratory (RAL) have sug-
 5145 gested studying how to make such a double-cosine theta magnet using modern supercon-
 5146 ductor, with an increased aperture. A target would be going from the $18 \times 56 \text{ mm}^2$ E821
 5147 aperture to $40 \times 56 \text{ mm}^2$.

5148 11.4.2 Double magnet, using the serpentine winding technique

5149 Brett Parker at Brookhaven has developed a new technique to wind superconducting mag-
 5150 nets, using CNC techniques [17], which permits multi-layer coils of rather complicated current
 5151 distributions to be fabricated. An example of a quadrupole magnet is shown in Fig. 11.14.

5152 A visit to his lab at BNL was very informative, and he has confirmed that he could wind
 5153 elliptical dipoles, as well as circular ones.



Figure 11.14: Coil for a superconducting quadrupole

5154 An examination of Fig. 11.11 shows the problem. A circular cross section moves the
 5155 beam center further away from the center of the storage region, thus requiring a much
 5156 stronger kick. An elliptical cross section would significantly open the radial beam aperture,
 5157 while reducing the extra kick needed to store the beam. The cross section of such a coil
 5158 is shown in Fig. 11.15. Parker says that to achieve the fields needed in E989, it would be
 5159 necessary to have four layers. There would also have to be the canceling magnet outside,
 5160 and a superconducting shield to remove any residual flux.

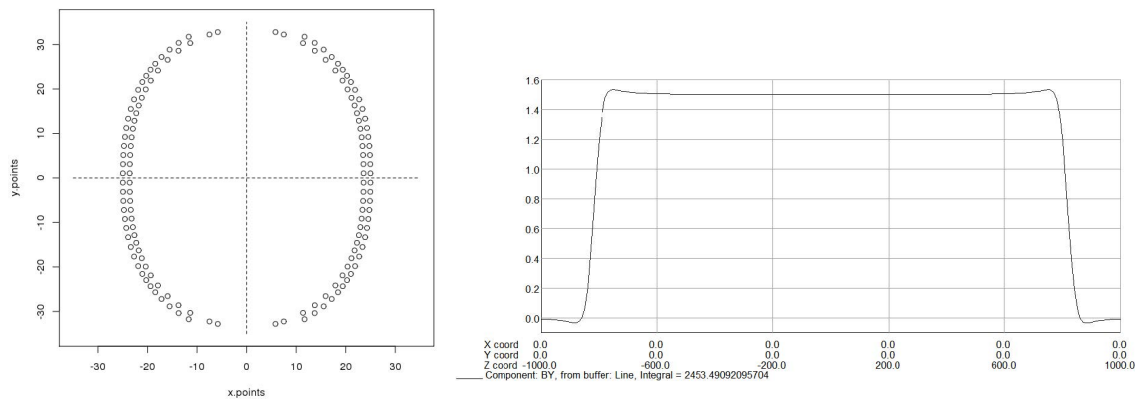


Figure 11.15: (a) An elliptical coil arrangement. (b) The calculated longitudinal magnetic field from this coil arrangement.

5161 11.4.3 Inflector Superconducting Passive Shield

5162 While the exact fringe field will be modeled by computer simulations, and made as small
 5163 as practically possible, our baseline goal for the shield is that it should be able to cancel a
 5164 fringe field < 1 kG.

5165 The shield will surround the inflector coils. The shield should be as large and as long
 5166 as possible, while still fitting within the inflector cryostat. The open end of a new inflector

5167 will present additional challenges for the shield, and will need to be studied in simulations.
 5168 From this constraint, the shield diameter will be approximately 12 cm. It extends 26 cm
 5169 downstream of the inflector coils. Upstream, it is flush with the coils due to space limitations.

5170 We have several options for shield material supply: (1) reuse the shield from existing
 5171 working shield, (2) reuse the shield from spare (but broken) inflector, and (3) contact industry
 5172 to fabricate a new shield.

5173 Option (1) is not preferred, since we need to preserve a working inflector. Option (2) is
 5174 a possibility. The shield was epoxied to the inflector mandrel. We should be able to melt
 5175 the epoxy to remove the shield.

5176 For option (3), we have contacted and are in discussion with MTI Metal Technology[20]
 5177 and ATI Wah Chang[21]. We have not been able to contact Nippon Steel, the original maker
 5178 of the shield.

5179 In principle, a shield can be fabricated from smaller overlapping pieces. However, care
 5180 must be taken to provide sufficient cooling. We should prototype, test, and verify that the
 5181 overlapping region functions properly as a shield. Given the issues with the attempt to repair
 5182 the damaged shield on the original inflector, overlapping shields, rather than one continuous
 5183 one, may not be a viable option.

5184 Luvata Waterbury Incorporated of CT, is willing to supply 7 meter x 25 cm x 100 microns
 5185 of NbTi. A purchase requisition has been made. This quantity is sufficient to fabricate a
 5186 2 m long, 100 μ m thick shield.

5187 The shield would be formed by overlapping three 2.3 m long, 0.25 m wide NbTi pieces
 5188 to surround the new inflector coils.

5189 This material is monolithic NbTi and so is not the multi-layer NbTi-Cu structure used
 5190 in E821, which is more robust against flux-jumping. We will test and measure the shielding
 5191 and critical current properties of this NbTi sheet.

5192 We will also test the shielding properties of the overlapping region of the individual NbTi
 5193 pieces.

5194 If this monolithic NbTi material is used in the new inflector, and flux-jumping occurs
 5195 during data-taking, it would require us to turn off the inflector current, warm up and re-cool
 5196 the NbTi passive shield.

5197 **11.5 Muon Storage Simulations Using a New Inflector**

5198 Several aspects of a new superconducting inflector magnet are simulated¹ to study their
 5199 impact on the fraction of muons transmitted into the storage region. The options studied are
 5200 the following with the E821 setting shown in parentheses: *a*) open-end vs closed-end (E821)
 5201 geometry, *b*) 40 mm vs 18 mm (E821) horizontal aperture, *c*) sensitivity to beam phase-
 5202 space matching. Results of the simulation are presented as improvement factors defined as
 5203 the fraction of stored muons with the new inflector divided by the baseline E821 inflector.
 5204 The baseline E821 storage rate is also presented. Assuming all improvements add coherently,
 5205 a new open-ended inflector with a 40 mm horizontal aperture is expected to increase the
 5206 fraction of stored muons by a factor of 3.8 compared to the E821 inflector.

¹This material complements the discussion in Section 8.4

5207 11.5.1 E821 Inflector Simulation

5208 The E821 inflector magnet is simulated using a **GEANT**-based software, which allows particle
 5209 tracking beginning at the upstream end of the inflector. Within this framework, the closed
 5210 ends of the inflector are constructed using distinct volumes of aluminum (1.58 mm), copper
 5211 (0.39 mm), and niobium-titanium (0.43 mm). An additional 4 mm of aluminum is added to
 5212 each end to model the window, flange, and cryostat. Between the end-caps, a “D”-shaped
 5213 vacuum beam channel is constructed to approximate the double cosine theta geometry. The
 5214 magnetic field within the beam channel is the vector sum of the main magnet fringe field
 5215 and the 1.45 T field ($\int \vec{B} \cdot d\vec{\ell} = 2.55 \text{ Tm}$) produced by the inflector magnet.

5216 The E821 muon beam is simulated by uniformly populating a 40π phase space ellipse.
 5217 The phase space axes are determined by the beam TWISS parameters, α and β in both
 5218 horizontal (x) and vertical (y) directions. The nominal TWISS parameters are determined
 5219 by maximizing the transmission rate through the inflector and shown in Table 11.3 when the
 5220 beam is localized at the “downstream”-end of the inflector (*i.e.* nearest to the ring). The
 5221 beam momentum, $|P|$, is generated by sampling a Gaussian distribution with mean equal to
 5222 the magic momentum P_{magic} and width $\delta P/P = 0.5\%$. The longitudinal width of the beam,
 5223 or equivalently the width in time, is 25 ns.

Table 11.3: Nominal muon beam Twiss parameters.

Direction	Emittance (ε)	α	β
Horizontal (x)	40	-0.544	2.03
Vertical (y)	40	-0.0434	19.6

5224 All muons passing into the storage region are given a “perfect kick” to place them onto
 5225 a stable orbit. This kick is modeled by applying a 220 Gauss magnetic field throughout the
 5226 kicker volume for the first revolution. Finally, the storage rate is defined as the fraction of
 5227 muons surviving 100 revolutions around the storage ring. No muons are allowed to decay in
 5228 this simulation.

5229 11.5.2 Open-ended vs. Closed-ended Inflector Geometry

5230 The E821 inflector magnet was constructed with a closed end (*i.e.* the superconducting coils
 5231 wrapped around the end of the magnet) because this greatly reduced magnetic flux leakage
 5232 into the muon storage region. The impact of the closed end on the horizontal and vertical
 5233 emittance was studied analytically and with the **GEANT** tracking software. In the analytic
 5234 approach, the fraction of muons traversing the inflector ends is studied by comparing the
 5235 horizontal and vertical beam widths (σ_x, σ_y) after multiple scattering in the material. In
 5236 this study, a beam filling the horizontal aperture of 18 mm grows to a size of ≈ 35 mm,
 5237 suggesting that approximately half ($18/35 = 51\%$) of the beam will fail to exit the inflector
 5238 aperture. With two closed ends the net effect is to lose between 50 – 75% of the incoming
 5239 beam.

The tracking simulation approach removes the end coils, flange, and window from the GEANT inflector material without altering the magnetic fields. Table 11.4 summarizes the muon storage rates assuming an open and a closed inflector magnet. The beam parameters and inflector aperture are identical in both simulations. Values in parentheses show the results of an incoming beam with a momentum spread of 2% instead of the nominal 0.5%.

Table 11.4: Summary of E821 Inflector Simulations.

Inflector Geometry (Upstream-Downstream)	Muons Generated	Muons Surviving	Storage Fraction
Open-Open	5000 (20000)	664 (691)	13.2±0.3 (3.4±0.1)
Closed-Open	5000 (20000)	522 (593)	10.4±0.3 (2.8±0.1)
Closed-Closed	5000 (20000)	323 (395)	6.5±0.3 (1.9±0.1)
Improvement Factor \equiv Open-Open/Closed-Closed			
	5000 (20000)	-	2.1× (1.7×)
Improvement Factor \equiv Closed-Open/Closed-Closed			
	5000 (20000)	-	1.6× (1.5×)

11.5.3 Sensitivity to Beam Phase-space Matching

A consequence of the limited inflector aperture is gross phase space mismatching into the storage region. This is seen by studying the amplitude of the muon beam (A), which is defined as $A = \sqrt{\beta\varepsilon}$. The maximum horizontal size of a beam clearing the inflector is ± 9 mm, thus, a beam with $\varepsilon = 40$ mm-mrad must have $\beta_x < 2.5$ m and $\beta_y < 19.6$ m. As this beam propagates into the storage region the horizontal β -function subsequently undergoes large oscillations with $\beta^{\max} = 28$ m and $\beta^{\min} = 2.5$ m. This corresponds to a modulation of the horizontal beam amplitude (A) of $r = \sqrt{\frac{\beta^{\max}}{\beta^{\min}}} = 3.4$. This oscillation causes significant beam to be lost on the collimators in the ring.

An alternative to these large oscillations is to perfectly match the β -functions into the storage ring. Assuming a drift space within the inflector ($\vec{B} = 0$), then the β -function at the inflector is defined as $\beta^{\text{inf}} = \beta^{\text{ring}} + s^2/\beta^{\text{ring}}$. The resulting β -functions ($\beta_x^{\text{inf}} = 7.6$ m and $\beta_y^{\text{inf}} = 19.2$ m) requires the incoming beam to be 2.38 times larger than the inflector aperture. Thus, only $1/2.38 = 42\%$ of the beam will clear the inflector. This conclusion follows the GEANT-based tracking result, which shows 53% of the beam clearing the inflector aperture.

11.5.4 Increased Horizontal Aperture

The E821 inflector was constructed with a ± 9 mm horizontal aperture in part due to the double cosine theta magnet geometry and the limited space between the outer main magnet cryostat and the muon storage region. The horizontal aperture also constricts the available phase space in the muon storage region, whose aperture is ± 45 mm.

5266 An augmented inflector “D”-shaped aperture of $\pm 20 \times \pm 28 \text{ mm}^2$ is modeled in the
 5267 **GEANT** tracking software. In this study, the main magnet fringe field is assumed to be
 5268 identically canceled within the inflector beam channel for simplicity. The horizontal beam
 5269 size is increased allowing for ideal matching to the storage ring β -function, corresponding to
 5270 $\beta_x = 7.6 \text{ m}$. The horizontal and vertical α Twiss parameters are set to zero in this scenario.

5271 Table 11.5 summarizes the muon storage rates for the two apertures (18 vs 40 mm) and
 5272 the two end coil inflector geometries (open vs closed) ².

Table 11.5: Summary of E821 Inflector Simulations. The “D”-shaped aperture shown in Fig. 11.6(a) was used. The vertical aperture was 56 mm, the horizontal (radial) aperture was 18 mm, or 40 mm.

Inflector Aperture (Open or Closed ends)	Muons Generated	Muons Surviving	Storage Rate
18 mm Aperture ($A_{\pm 9}$)			
(open ends)	120000	11444	9.5 ± 0.1
(closed ends)	120000	5117	4.2 ± 0.1
40 mm Aperture ($A_{\pm 20}$)			
(open ends)	120000	19161	15.9 ± 0.1
(closed ends)	120000	8706	7.2 ± 0.1
Improvement Factor $\equiv A_{\pm 20} / A_{\pm 9}$			
(open ends)	-	-	$1.7 \times$
(closed ends)	-	-	$1.7 \times$
Improvement Factor $\equiv A^{\text{Open}} / A^{\text{Closed}}$			
(18 mm Aperture)	-	-	$2.2 \times$
(40 mm Aperture)	-	-	$2.2 \times$
Improvement Factor $\equiv A_{\pm 20}^{\text{Open}} / A_{\pm 9}^{\text{Closed}}$			
	-	-	$3.8 \times$

5273 11.5.5 Future Simulations

5274 It is clear that we need a full tracking simulation to replace the phase-space models used
 5275 thus far. The incoming beam to the inflector needs to be optimized for the 18 mm inflector
 5276 opening, and for 40 mm new inflector. The inflector team will work with the beamline
 5277 experts to make sure that these essential calculations are high priority.

5278 11.6 ES&H

5279 The superconducting inflector is in a cryostat that includes one section of muon beam tube.
 5280 The cryostat vacuum is separate from the beam vacuum chamber, so that the inflector

²Note that these storage rates are computed with a different muon beam and therefore can not be compared directly to the rates in the previous sections.

5281 can be operated independently of whether the muon beam chamber is evacuated. The
5282 cryogenic system, and its operation will follow all Fermilab safety standards for cryogenic
5283 and vacuum system operations. This includes, but is not limited to Extreme Cold Hazard,
5284 Oxygen Deficiency Hazards. The cryogenics involved are liquid helium and liquid nitrogen.
5285 No flammable liquids or gases will be employed. The existing E821 inflector was operated
5286 at Brookhaven National Laboratory where similar safety requirements were in place.

5287 **11.7 Risks**

5288 **11.7.1 Relocation Risk**

5289 There is a small risk that in the de-installation at Brookhaven and shipping to Fermilab of the
5290 E821 Inflector that some problem is introduced that compromises the inflector performance.
5291 We will seek to minimize this risk by careful disassembly and shipping. As soon as cryogenic
5292 capability is available in MC-1, we will set up a test stand in the experimental area outside
5293 of the ring to cool and power the inflector.

5294 **11.7.2 Other Risks**

5295 There is the possibility that some mechanical aspect of the E821 inflector has deteriorated
5296 in the 12 years since it was operational, causing the magnet to quench repeatedly before
5297 reaching full current. This risk is probably small, since it was tested at KEK, shipped to
5298 BNL, installed, and was brought to full current with only a few training quenches. It was
5299 very robust in subsequent operation at BNL. The plan to test it as soon as possible at
5300 Fermilab will clarify this risk.

5301 A helium leak in the valve box or lead-pot will need to be located and repaired. There is
5302 a small risk that the leak was in the magnet itself, but this is viewed as extremely unlikely
5303 by Akira Yamamoto, who supervised the engineering design and construction, and Wuzheng
5304 Meng, who did the magnetic design and was responsible for its operation at BNL.

5305 The most sensitive part of the re-installation is reconnecting the inflector leads. Our
5306 technician Kelly Hardin was involved in the disassembly at BNL, and understands the issues
5307 involved in the reconnection very well.

5308 **11.8 Quality Assurance**

5309 Proper quality assurance is essential in the transport and reassembly of the inflector magnet.
5310 The mechanical aspects, heat shield, etc. will be carefully examined for issues, once the
5311 inflector arrive at Fermilab. It will be determined as quickly as possible whether the inflector
5312 meets the Muon g-2 requirements for performance and reliable operation. Quality Assurance
5313 will be integrated into all phases of the transport and reassembly work. including design,
5314 procurement, fabrication, and installation.

5315 **11.9 Value Engineering**

5316 The baseline is to begin the experiment by re-using the existing E821 Inflector. A new
5317 inflector with a much larger horizontal aperture could permit three to four times as many
5318 muons to be stored. A gain of this factor would significantly improve the statistical reach of
5319 the experiment, and permit more beam time to be used for systematic studies. This presents
5320 a significant opportunity to improve the experiment and to use running time more effectively.
5321 At present we plan that our UK collaborators at the Rutherford-Appleton Laboratory will
5322 produce a new inflector. If they are unable to obtain funding, we will explore the possibility
5323 that a larger-aperture inflector can be produced in collaboration with Brett Parker at BNL.

References

- 5324
- 5325 [1] A. Yamamoto, et al., Nucl. Inst. Meth. **A 491**, 23 (2002).
- 5326 [2] Frank Krienen, Dinesh Loomba and Wuzheng Meng, Nucl. Inst. Meth. **A238**, 5 (1989).
- 5327 [3] A. Yamamoto, Nucl. Instr. and Meth. A 453 (2000) 445.
- 5328 [4] Y. Makida, et al., IEEE Trans. Magn. 27(2) (1991) 1944.
- 5329 [5] M. Garber, A. Ghosh, W. Samson, IEEE Trans. Magn. 25 (2) (1989) 1940.
- 5330 [6] Y. Saito, et al., Development of beam inflection superconducting magnet evaluation of
5331 prototype, Tokin Technical Review, No. 20.
- 5332 [7] M.N. Wilson, Superconducting Magnets, Oxford Science Publications, Oxford, 1983.
- 5333 [8] A. Yamamoto, Status of the inflector, Internal Meeting Minutes, 1992; W. Meng, K.
5334 Woodle, Superconducting shield test on ($g - 2$) inflector magnet, ($g - 2$) Note, No. 210,
5335 1994.
- 5336 [9] M.A. Green, W. Meng, IEEE Trans. Appl. Supercond. 5 (2) (1995) 667.
- 5337 [10] G.T. Danby, W. Meng, W. Sampson, K. Woodle, IEEE Trans. Magn. 30 (4) (1994)
5338 1766.
- 5339 [11] I. Itoh, T. Sasaki, IEEE Trans. Appl. Supercond. 3 (1993) 177.
- 5340 [12] H.N. Brown, et al, Phys. Rev. Lett. **86** 2227 (2001).
- 5341 [13] F. Krienen, et al., IEEE Trans. Appl. Supercond. **5** (2) (1995) 671.
- 5342 [14] W. Meng, K. Woodle, Superconducting shield test on g-2 inflector prototype, g-2 Note,
5343 No. 210, 1994.
- 5344 [15] The $g - 2$ Collaboration: G.W. Bennett et al., Phys. Rev. Lett. **89**, 101804 (2002);
5345 Erratum-ibid. **89**, 129903 (2002).
- 5346 [16] Bennett GW, et al. (The $g - 2$ Collab.) Phys. Rev. Lett. 92:161802 (2004)
- 5347 [17] <http://www.bnl.gov/magnets/Staff/Parker/>
- 5348 [18] Brett Parker, private communication, March 2013.

- 5349 [19] Lance Cooley, Fermilab. Private Communication.
- 5350 [20] Steve Smith at MTI Metal Technology. <http://www.mtialbany.com/>
- 5351 [21] Tony Nelson at ATI Wah Chang. <http://www.atimetals.com/>

Chapter 12

Beam Vacuum Chambers

The muon storage volume, which lies within the 1.45 T magnetic field, is evacuated in order to minimize multiple scattering of muons and positrons. This is accomplished by a set of aluminum vacuum chambers, which also provides mechanical support for:

- the beam manipulation systems: the electrostatic plates of the quadrupole system, the collimators, and plates of the magnetic kicker system.
- the positron detection systems: the trace-back straw trackers and auxiliary detectors such as the fiber harp.
- the magnetic field measurement systems: ~ 400 fixed NMR probes surrounding the storage volume, a set of rails for the trolley NMR system, and the plunge probe system.

The chambers from BNL E821 will be reused for E989, and we will make changes as described in the section below. The chamber design is detailed in the BNL E821 design report[1], and so only a brief discussion is given here. Figure 12.1 shows the layout. The system comprises mainly 12 large vacuum chambers, separated by 12 short bellows adapter sections.

A simplified FEA model of a large vacuum chamber is shown in figure 12.2, depicting the top plate the contains 15 grooves for mounting the NMR probes. The 15 grooves on the bottom and flange ports are not shown. The FEA model predicts that the top and bottom surfaces deflect by 0.453 mm under vacuum load[2]. This is agreement with the measurement of 0.45 mm[4]. The FEA model reconfirms that the chamber has a safety factor of 2.9, and the wall stresses are below 12000 psi, as required by the ASME Pressure Vessel Code for pressure vessels for Aluminum 6061-T6.

The 12 vacuum chambers and 12 bellow adapter sections are bolted together and placed in between the upper and lower pole pieces. The average radius of this structure is mechanically fixed and cannot be adjusted. There are thin dielectric sheets in between vacuum sections to prevent low frequency eddy currents from traveling in between the sections. Finally, all chamber materials including bolting hardware are non-magnetic.

Figures 12.3 and 12.4 show the cage system and how it resides inside a vacuum chamber. The cage system holds the quadrupole plates, kicker plates, and the rails used by the trolley. Screws allow for adjusting the position of the cage within the vacuum chamber system. The position of the cage system plays an important role, and has the following requirements. (1)

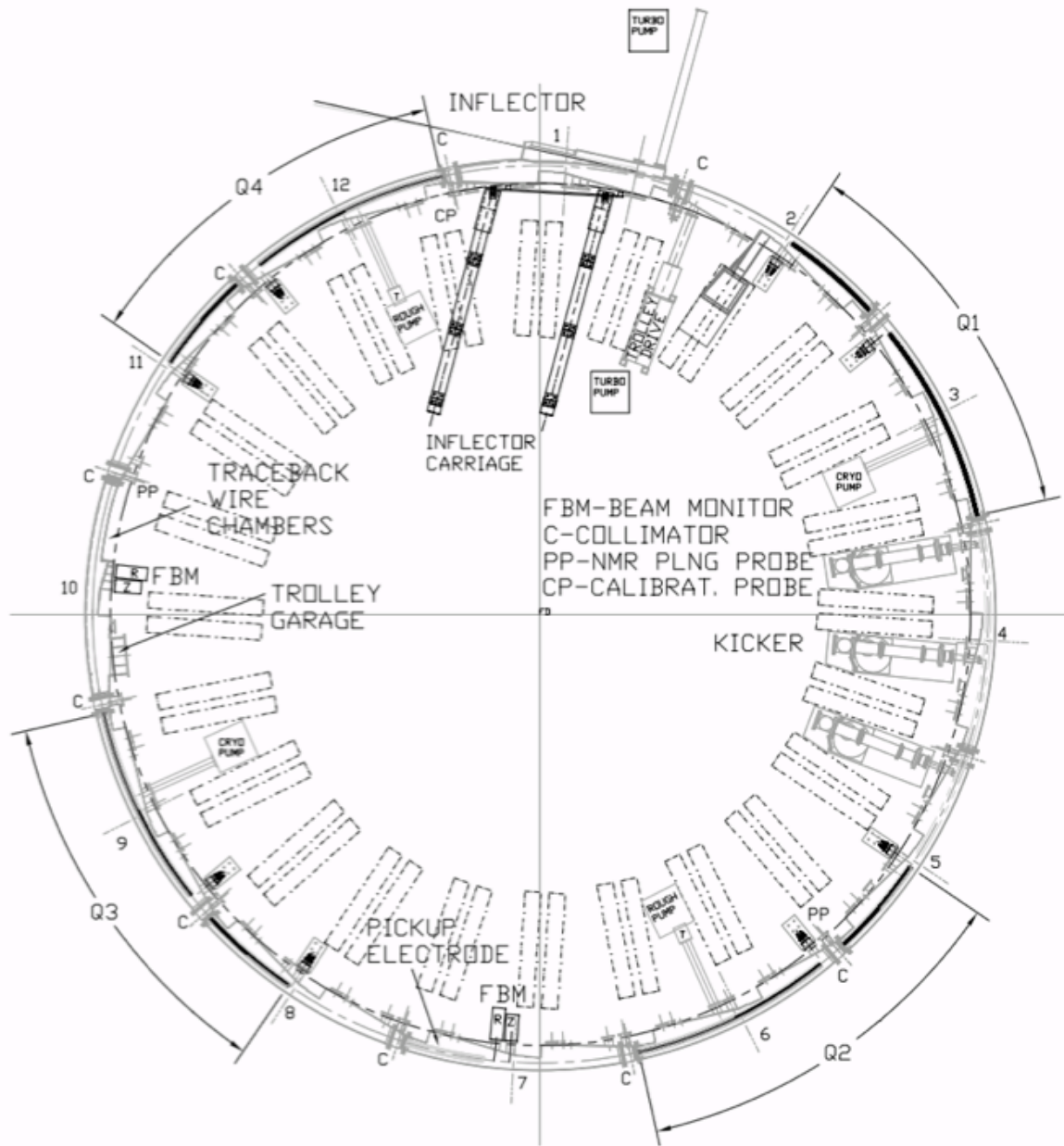


Figure 12.1: Layout of the BNL E821 beam vacuum chamber system.

5383 The rail system from neighboring vacuum sections must line up to allow smooth motion of
 5384 the trolley as it travels between sections. And (2), since the quadrupole plates and kicker
 5385 plates positions define the beam storage region, these devices should place the beam in the
 5386 most uniform portion of the magnetic field. The beam center should be at the geometrical
 5387 center between upper and lower pole faces. A critical period occurs after installing the
 5388 chambers and before vacuum pump down. During this time, the vacuum flanges are open
 5389 which allows access to the adjustment screws. The precise adjustment of these screws will
 5390 ensure that the rails are aligned well enough to allow the trolley to move smoothly between

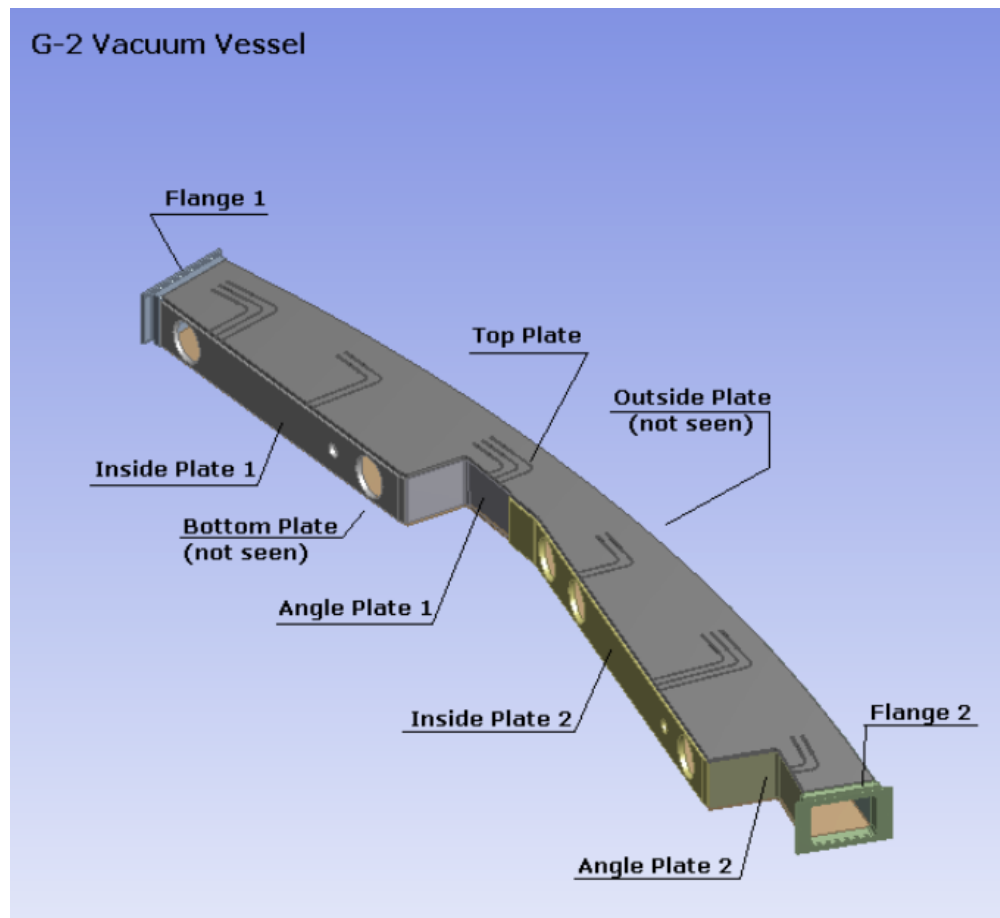


Figure 12.2: Simplified mechanical model for stress and strain analysis.

5391 adjacent sectors.

5392 12.1 Changes to the E821 Design

5393 For E989, we are proposing to make the following changes. We will add fixed NMR probes to
 5394 the mid plane ('mid plane probes') of the beam storage region. A concept is shown in figures
 5395 12.5 and 12.6, showing the probes mounted to the cage system. The mid plane probes will
 5396 have the long axis aligned in azimuth, and should lie as close as possible to the edge of the
 5397 beam region. However, they must remain sufficiently far from the quadrupole and kicker
 5398 plates in order to prevent sparking and signal pickup. The probes will be in vacuum, and the
 5399 probe coax cables attach to commercially-available vacuum SMA electrical feed throughs.
 5400 As shown from simulations, the magnetic field values should be within the mid plane probe
 5401 operating range ($\sim \pm 200$ ppm).

5402 For E821, a small fraction of the upper and lower fixed probes were too close (in azimuth)
 5403 to the boundary between two pole pieces. In this region, the magnetic field gradient is
 5404 generally larger due to gaps and steps (of order < 25 microns) between two pole pieces, and
 5405 therefore degrades the probe's S/N. For E989, we will either lengthen or cut new grooves to

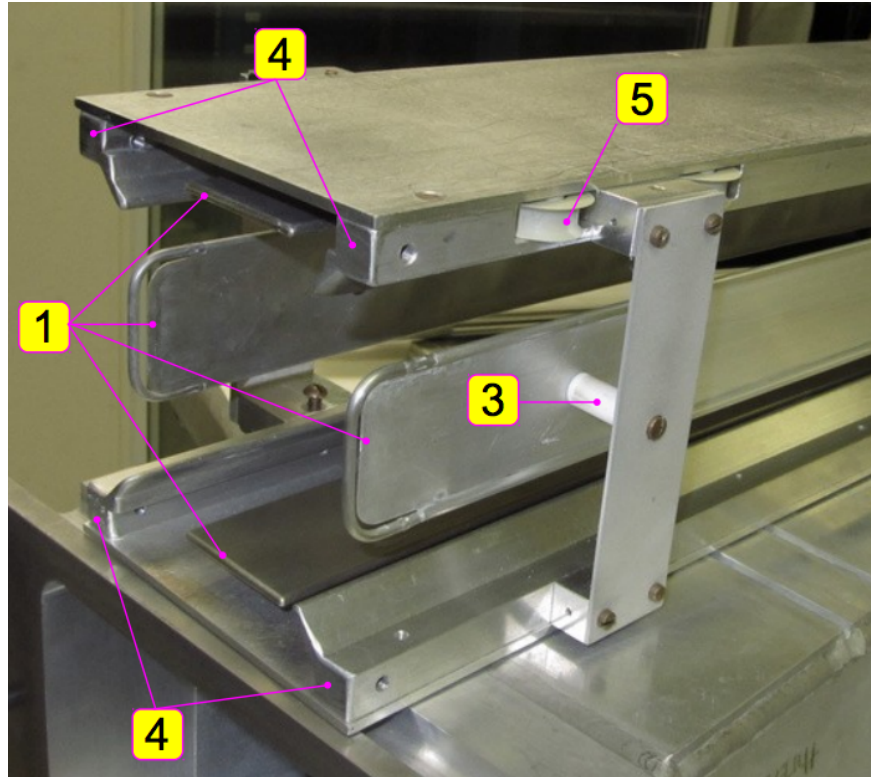


Figure 12.3: Picture of a cage system showing the (1) quadrupole plates, (3) macor (insulator) supports, (4) trolley rails, and (5) a wheel for guiding the cable that pulls the trolley

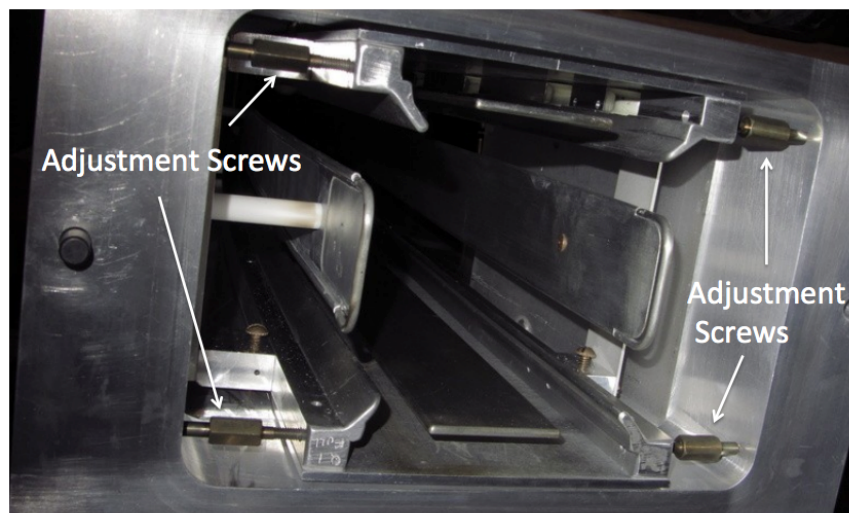


Figure 12.4: Picture of a cage system inside a vacuum chamber showing the adjustment screws to center the quadrupole plates with the geometrical center of the pole pieces.

5406 optimize probe placement.

5407 In E821, the trace back system operated in air and was located in vacuum chamber sector
5408 10, which was modified to be without a 'scallop'. For E989, the straw trace back system

5409 will be in vacuum, and vacuum chamber sector 10 will have its scallop shape reinstalled.
 5410 A second straw station will be placed in sector 8. The inner radius vertical side walls of
 5411 sectors 8 and 10 will be modified to accept the straw chamber flange. Figure 12.8 shows the
 5412 locations of the proposed changes.

5413 The kicker occupies chamber sectors 4 and 5. The magnetic kicker firing will cause eddy
 5414 currents, which compromises physics data at beginning of injection and reduces the kicker
 5415 field strength. OPERA-3D simulations are being done to see whether the top and bottom
 5416 surface of the vacuum chamber can be redesigned to reduced eddy currents. A concept for
 5417 this modification is shown in figure 12.7. Finally, the vertical inner radius surface of the
 5418 vacuum chamber will be lined with insulation. This will improve the thermal stability of the
 magnet iron, which is critical for the field uniformity as discussed in Section 10.4.

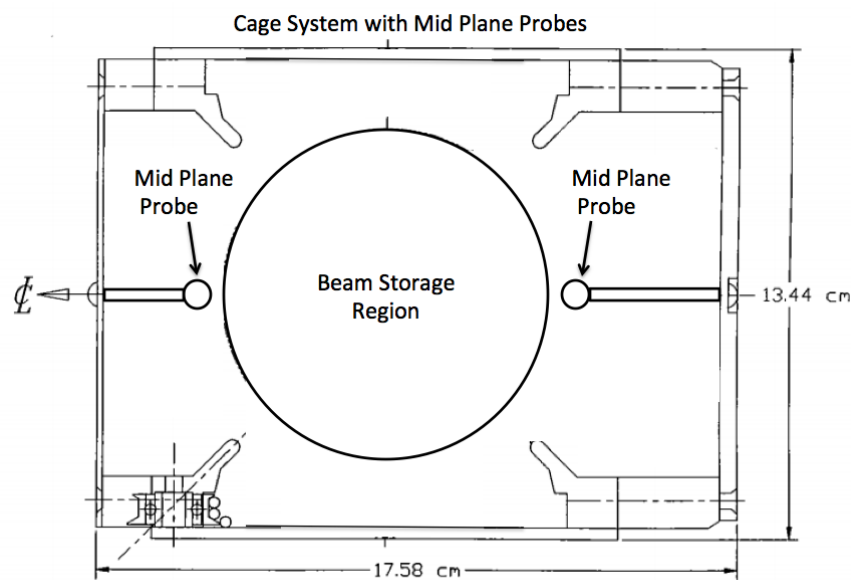


Figure 12.5: Concept for placement and attachment of mid plane probes within the cage systems that do not contain quadrupole and kicker plates. Signal coax cables attach to commercially available vacuum SMA electrical feed throughs. The main axis of each probe is oriented out of the page, parallel to the muon beam direction.

5419

5420 12.2 Vacuum Chambers

5421 This WBS refers to the actual chambers, the small bellows, the piping to the pumps, and
 5422 the bolting hardware. We are exploring major modifications to sectors 8, 10, 4, and 5. This
 5423 WBS also covers the reassembly labor effort.

5424 Chamber sectors 8 and 10 would be re-machined to accept the new in-vacuum straw trace
 5425 back chambers. For sector 10, the 'scallop' portion must be reinstalled. Chamber sectors 4
 5426 and 5 would have the top and bottom plates modified to install transverse grooves to reduce
 5427 eddy currents.

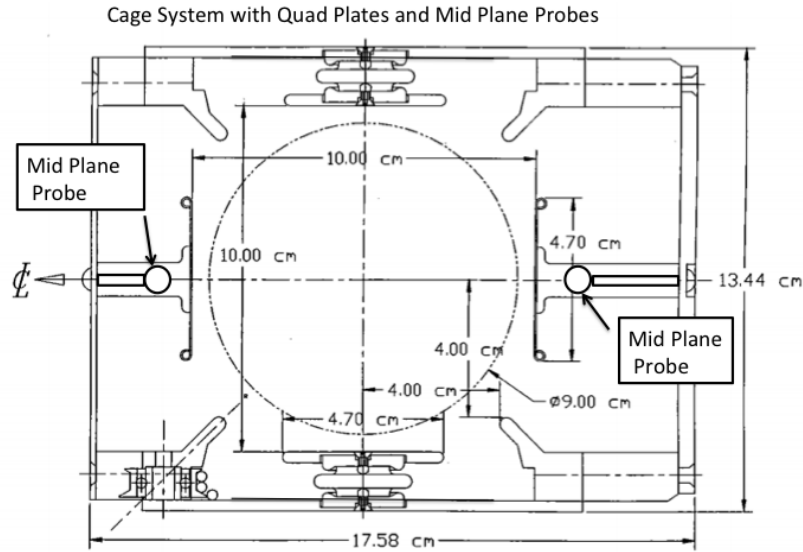


Figure 12.6: Concept for placement and attachment of mid plane probes within the cage system in the quadrupole plate region. The mid plane probes are farther from the beam center. They are offset and do not interfere with the macor quadrupole plate support stands. Signal coax cables attach to commercially available vacuum SMA electrical feed throughs.

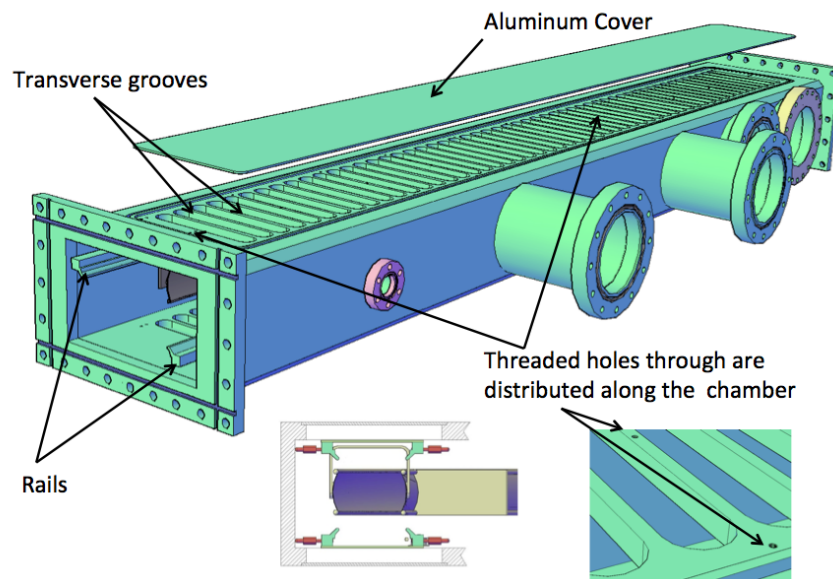


Figure 12.7: Concept for modifying chamber sectors 4 and 5 to reduce eddy currents induced by the kicker system.

5428

12.3 Vacuum Pumps

5429

The vacuum level must be less than 10^{-6} Torr in the region of the quadrupoles. This is to minimize the trapping of ionized electrons due to the residual gas. However, there is a

5430

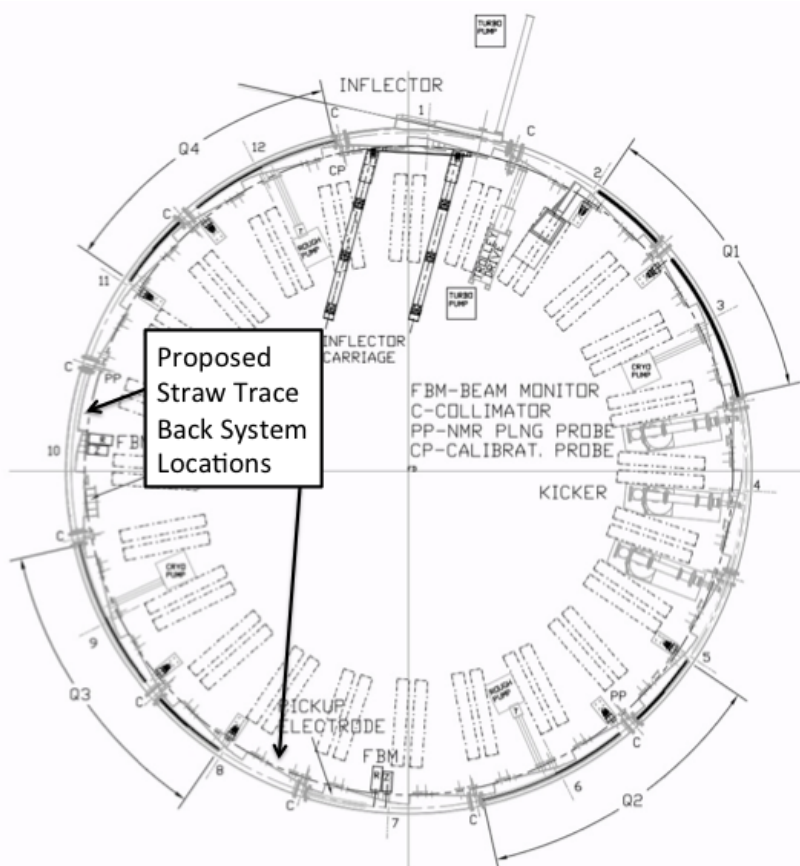


Figure 12.8: Proposed locations for in-vacuum straw trace back chambers.

5431 vacuum load of $\sim 2.1 \times 10^{-5}$ Torr l/s from each of the two straw tracker trace back system
 5432 [3]. From this requirement alone, the minimum pumping speed is 21 liters/sec at 10^{-6} Torr.
 5433 However, each pump is attached to the vacuum chamber through a large pipe. As the
 5434 pumps will likely contain ferromagnetic material and generate transients that would affect
 5435 the magnetic field uniformity, they must remain sufficiently far from the vacuum volume.
 5436 For E821, this distance was 1-2 meters. Therefore, extra piping will increase slightly the
 5437 pumping speed requirement. The exact minimum pumping speed will be determined by
 5438 engineering calculations. For E821, the pumping speed was 2000 liters/sec at 10^{-6} Torr,
 5439 accomplished by 3 pumps spaced uniformly over the ring.

5440 Finally, the vacuum chamber system should remain clean, as the quadrupole and kicker
 5441 plates carry high voltage and the high current, respectively. We will ensure this by utilizing
 5442 dry (oil-free) roughing and turbo pumps.

5443 12.4 Mechanical Interface

5444 As mentioned above, the vacuum chambers must provide the mechanical interface for several
 5445 systems. This WBS covers the following activities needed for the NMR system:

- 5446 • Modifications to the upper and lower grooves to improve the S/N of fixed probes near

5447 the boundary between pole pieces.

- 5448 • Adding additional commercially available vacuum SMA connections to readout the in-
5449 vacuum mid plane probes. The exact number and location will be estimated by OPERA
5450 simulations.
- 5451 • Calibration of the trolley position in absolute space: for a given motor or position
5452 encoder reading, what is the actual position of fiducial marks on the trolley in absolute
5453 space.
- 5454 • Calibration and operation of the positions of the plunge probe motors. Calibration
5455 refers to converting a given motor encoder reading to an actual position (in absolute
5456 space) of the probe head.

5457 The mechanism to move the plunge probe is shown in Figure 12.9. This mechanism bolts
5458 to vacuum flanges at positions shown in figure 12.1. The probe itself is in air. There is
5459 a vacuum bellows in which the probe is inserted. The probe is moved radially by piezo
5460 electric motors. We expect no changes are needed for the plunge probe mechanism, other
than connection to a different computer.

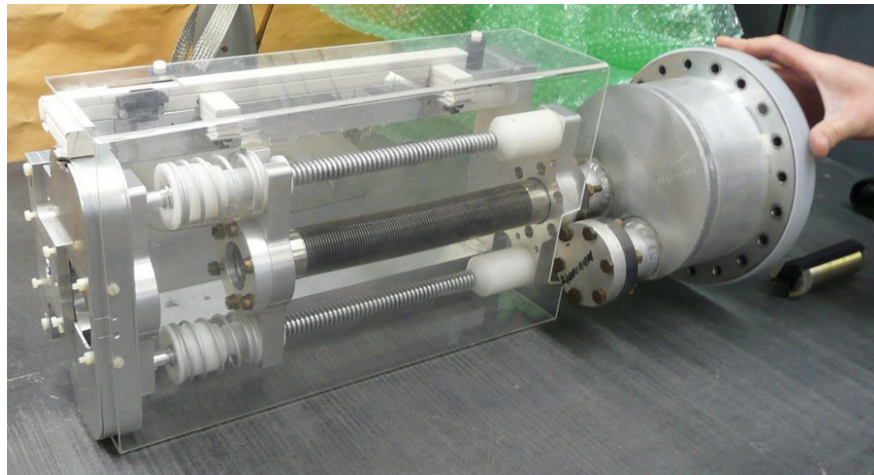


Figure 12.9: The plunge probe mechanism.

5461

5462 12.5 ES&H, Quality Assurance, Value Management, 5463 Risk

5464 The vacuum chamber system should pose no health hazard, since the chambers, when evacu-
5465 ated, have a 2.9 safety factor for stress before yield. Quality assurance and value management
5466 concerns are minimal since we are reusing or modifying a few E821 chambers.

5467 There is a risk that the new in-vacuum straw traceback chambers provide too much gas
5468 load to the vacuum. In that event, a corrective action could be to add additional pumping.
5469 This risk is addressed in the straw trace back discussion of this document.

5470 **References**

- 5471 [1] Design Report, BNL E821, A New Precision Measurement of the Muon ($g - 2$) Value at
5472 the level of 0.35 ppm. 3rd edition, D.H. Brown et al. B.L. Roberts Editor, March 1995.
- 5473 [2] G-2 Vacuum Chamber FEA. g-2 DocDB note 417-v1.
- 5474 [3] Tracker Requirements. g-2 DocDB note 514-v1.
- 5475 [4] H.C. Hseuh et al, E821 Muon $g - 2$ Internal Note No. 248, 1(1995).

5476 Chapter 13

5477 The Fast Muon Kicker

Injected muons exit the downstream end of the inflector magnet, and enter the good field region of the main dipole. The trajectory of the muons exiting the inflector is a circle displaced 77 mm radially outward the closed orbit of the storage ring. The path of the muons that emerge without having been scattered in the coil end of the inflector will be tangential to that displaced circle. On exiting the inflector, muons are within the full 1.41 T field of the ring dipole. The muons cross the closed orbit of the storage ring, that is the orbit at the magic radius, about 90° azimuthally around the ring from the end of the inflector. The circular trajectory of the muons intersects that closed orbit at an angle of $\theta_0 = 10.8\text{mrad}$. Indeed the minimum crossing angle, namely $\theta_0 = 10.8\text{mrad}$ obtains for trajectories that are tangential at the inflector exit. Any angle, positive or negative, with respect to the tangent line results in crossing angle greater than the minimum. Therefore muons that scatter in the inflector coil end will necessarily cross the closed orbit with a larger angle. The crossing angle is related to the scattering angle α according to

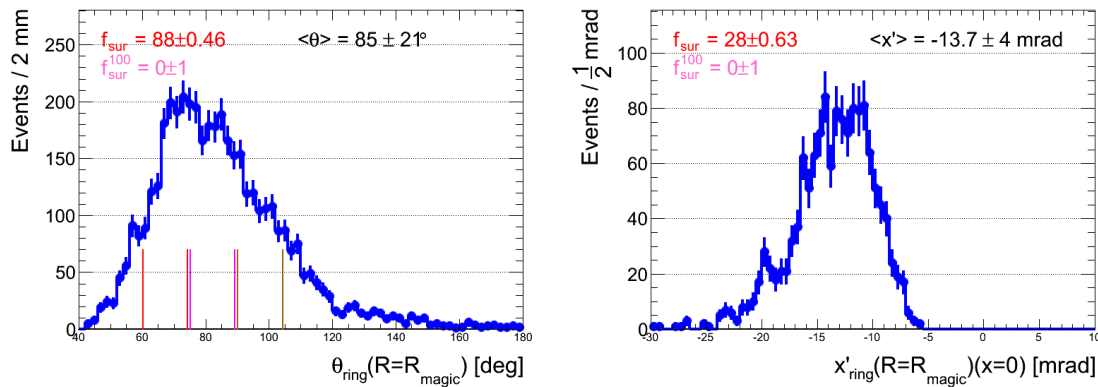
$$\theta \sim (\theta_0^2 + \alpha^2)^{\frac{1}{2}}.$$

5478 The contribution to beam divergence angle due to multiple scattering in the coil end is
5479 estimated to be about 4.6 mrad. Divergence due to the finite emittance of 40 mm-mrad is
5480 about 4 mrad. The result is that the mean angle at which muons cross the closed orbit is
5481 $\theta \sim 12.4$ mrad. Simulation that includes energy spread of the injected muons and scattering
5482 in the quadrupole plate indicates that the mean angle is nearly 14 mrad. Our specification
5483 for the system is a 14 mrad kick.

5484 The azimuthal angle at which the muons cross the closed orbit, and the crossing angle are
5485 computed using a **GEANT4** simulation of the E821 experiment. This result, however, assumes
5486 three properties of the muon beam which are not realized in the experiment. First, the beam
5487 must have zero emittance (i.e., $|p| = p_z$), momentum localized around the magic momentum
5488 (i.e., $\delta p/p \ll 1$), and no multiple scattering as it traverses the outer quadrupole plates and
5489 standoffs. Varying each of these properties changes the azimuthal position and the crossing
5490 angle as seen in Table 13.1. Assuming a realistic beam with 40π emittance, $\delta p/p = 0.5\%$, and
5491 allowing for multiple scattering through the quadrupoles plates, the required kick increases
5492 from 10.8 mrad to 13.7 ± 3.9 mrad. Distributions of the azimuthal crossing point and crossing
5493 angle θ under these assumptions are shown in Fig. 13.1.

Table 13.1: Summary of Kicker Requirements for Different Beam and Ring Properties.

Beam $\delta p/p$ (%)	Emittance [mm · mrad]	Multiple Scattering	Azimuthal Crossing Point [degrees]	Crossing Angle [mrad]
0	0	OFF	89 ± 0	10.8 ± 0
0.5	0	OFF	88 ± 17	12.4 ± 2.7
0	40	OFF	86 ± 10	11.3 ± 3.3
0	0	ON	76 ± 7.8	15.1 ± 1.8
0.5	40	ON	85 ± 21	13.7 ± 3.9

Figure 13.1: (a) Azimuthal crossing angle in degrees (b) Required kick x' in milliradians.

5494 The fast kicker is a pulsed magnet with vertical field that directs the muons, onto the
5495 ideal orbit by compensating the crossing angle. Ideally, the centroid of the injected bunch,
5496 on exiting the field of the kicker plates will coincide with the closed orbit of the storage
5497 ring, thus ensuring maximal capture efficiency and minimum residual coherent betatron
5498 oscillation. The 10 - 14 mrad kick requires an integrated vertical field of 1.1 - 1.4 kG-m.
5499 The kicker is comprised of three independent 1.7m long magnets, each with dedicated pulse
5500 forming network. Muons are delivered to the storage ring in pulses with transverse emittance
5501 near 40π mm-mrad, pulse length of about 120ns and at a repetition rate of up to 100Hz. The
5502 ideal kicker field maintains a flat top at about 220 - 280 Gauss, for the full 120ns, and then
5503 returns to zero before the lead muons complete a single revolution and re-enter the kicker
5504 aperture 149ns later.

5505 The injection of muons into the storage ring is complicated by several requirements:

- 5506 1. Since the magnet is continuous, any kicker device has to be inside of the precision
5507 magnetic field region.
- 5508 2. The kicker hardware cannot contain magnetic elements such as ferrites, since they will
5509 spoil the uniform magnetic field.
- 5510 3. Any eddy currents produced in the vacuum chamber, or in the kicker electrodes, must

- 5511 be negligible by 10 to 20 μs after injection, or must be well known and corrected for
 5512 in the measurement.
- 5513 4. Any kicker hardware must fit within the real estate occupied by the E821 kicker, which
 5514 employed three 1.7 m long devices.
- 5515 5. The kicker pulse should be shorter than the cyclotron period of 149 ns

5516 13.1 Requirements for the E989 Kicker

5517 The need for a fast muon kicker was introduced in Section 3.2. Direct muon injection was
 5518 the key factor that enabled E821 to accumulate 200 times the data as the preceding CERN
 5519 experiment. Since E989 needs more than twenty times as much data as E821, it is critical
 5520 that the limitations of the E821 kicker be eliminated. The layout of the E821 storage ring is
 5521 repeated in Fig 13.2. The three kickers magnets are located approximately 1/4 of a betatron
 5522 wavelength around from the inflector exit.

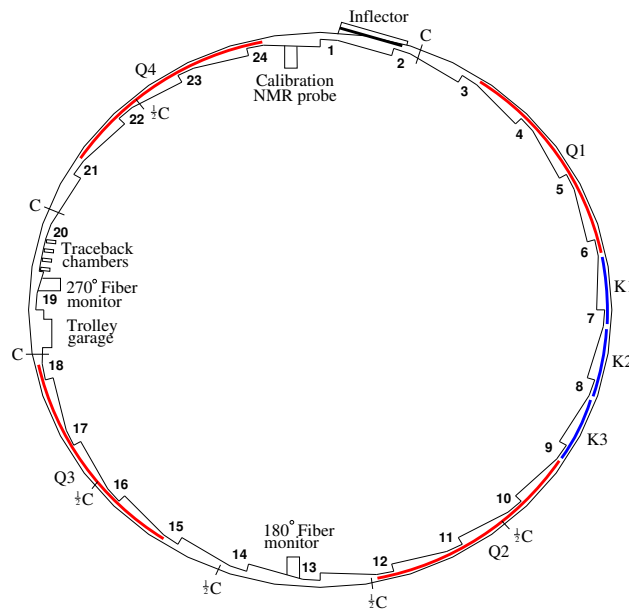


Figure 13.2: The layout of the storage ring, as seen from above, showing the location of the inflector, the kicker sections (labeled K1-K3), and the quadrupoles (labeled Q1-Q4) (Fig. reffg:ring repeated here for convenience).

5523 13.1.1 The E821 Kicker and its Limitations

5524 The E821 kicker [1] consisted of three identical sectors with 1.7 m long parallel plates carrying
 5525 current in opposite directions, located as shown in Fig. 13.2. Each section was powered by a
 5526 pulse forming network where a HV capacitor was resonantly charged to $\simeq 95$ kV, and then
 5527 shorted to ground by a deuterium thyratron, giving a characteristic damped LCR oscillating

5528 current and magnetic field. The resulting LCR pulse is shown in Fig. 13.3. Unfortunately
 5529 the LRC pulse was much wider than the beam width, in fact significantly longer than the
 5530 cyclotron period of 149 ns. This is emphasized by the series of red gaussians which are
 5531 separated by the 149 ns revolution period. Thus the beam is kicked several times before the
 5532 LCR pulse dies away.

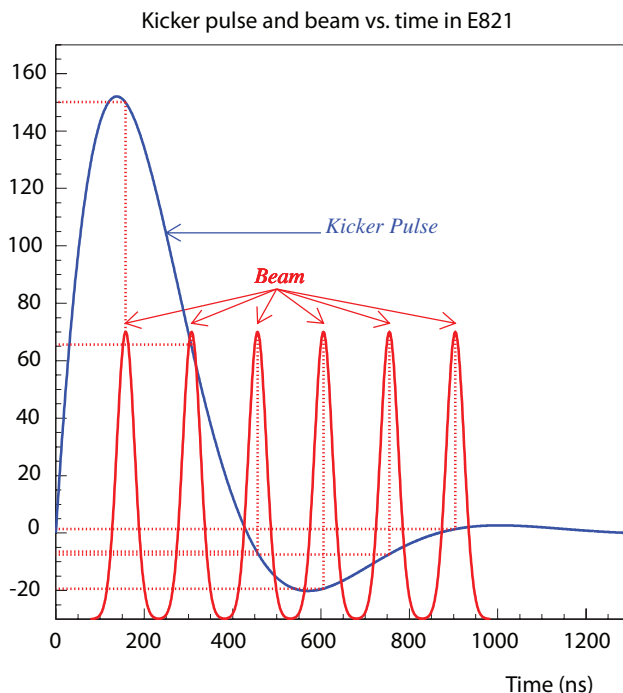


Figure 13.3: The E821 kicker LCR waveform (blue). The red pulses represent the injected beam, which has a cyclotron period of 149 ns.

5533 The kicker units began sparking around 95 kV, and each section had a different volt-
 5534 age defined as 100%. The number of muons stored vs. kicker high voltage is shown in
 5535 Fig. fg:stored-v-HV. Unfortunately, at the maximum voltage possible, the number of stored
 5536 muons did not turn over. It is not clear how many muons might have been stored if it
 5537 had been possible to increase the voltage until the maximum number of stored muons was
 5538 reached.

5539 13.2 New Kicker Design

5540 The design of the kicker for E989 attempts to address the shortcomings of the E821 kicker,
 5541 specifically, the pulse shape and pulse amplitude. We are developing a pulse forming network
 5542 based on a Blumlein triaxial transmission line as an alternative to the E821 LCR PFN. The
 5543 kicker plates are redesigned to yield a spatially more uniform field and with somewhat higher
 5544 efficiency in terms of gauss per unit current through the plates. The kickers consist of 1.7m
 5545 long plates as shown in Figure 13.5

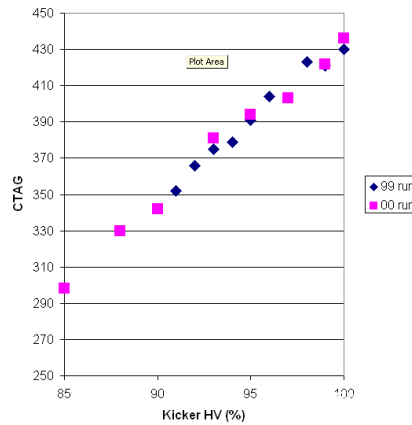


Figure 13.4: The number of stored muons versus kicker high voltage (arbitrary units).

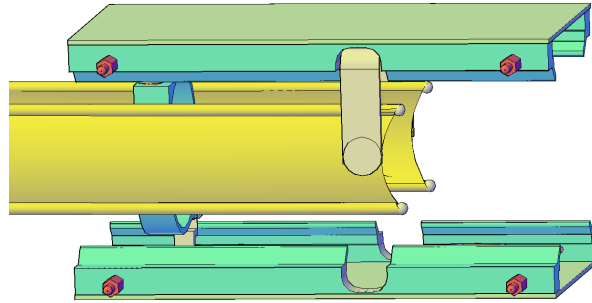


Figure 13.5: The kicker plates for E989. The current pulse is fed to the 1.7m long plates at the far end to the left of the plot. A jumper connecting the plates at the near end that closes the circuit is shown.

5546 The proposed implementation is a variation on a transmission line PFN driving a matched
 5547 load. We consider each 1.7 m long pair of kicker plates a load (each pair of plates is a
 5548 transmission line in its own right) with impedance Z_L , and imagine, at least conceptually,
 5549 that each kicker is terminated with a resistive load $R = Z_L$. If the impedance of the PFN
 5550 transmission line matches the impedance of kicker plates and load, then we anticipate
 5551 a rectangular current pulse with width $\tau = 2L/c$ where L and c are the length and group
 5552 velocity of the PFN, and current $I = V/Z$, where V and Z are the peak charging voltage
 5553 and the impedance of the line respectively. With such a configuration we expect that the
 5554 rise and fall time of the pulse will be limited by the turn on/off time of the thyatron switch
 5555 of about 20-30ns.

5556 We estimate the impedance of the kicker plates to be nearly 600Ω . The current required
 5557 to achieve the requisite ~ 250 G field is about 3kA corresponding to the impractically high
 5558 charging voltage of 1.8MV if the impedance of the PFN is matched to the impedance of
 5559 the kicker plates. Furthermore it would be awkward to terminate the kicker plates with

5560 a resistor. We propose alternatively to place a load resistor with resistance of only 25 Ω .
 5561 between the pulse forming network and the kicker plates. The PFN transmission line is then
 5562 matched to the load resistor. The reflections that will inevitably arise from the imperfect
 5563 match at the junction of load resistor and kicker plates, will be confined to the plates, and
 5564 dissipated on the timescale of the plate transit time of about 6ns. We thus deliver the
 5565 desired current with $\sim 87\text{kV}$ charging voltage. At the transition through the load resistor to
 the kicker, the transmission line is tapered to mitigate the mismatch.

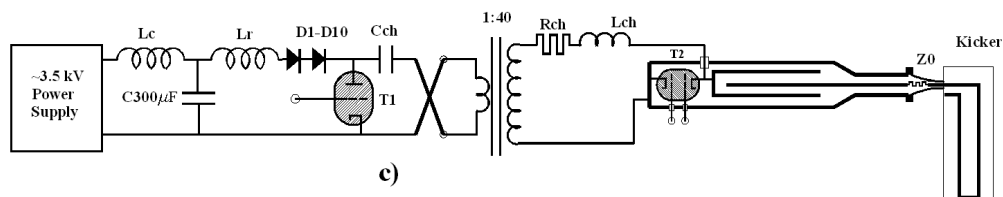


Figure 13.6: Schematic of the kicker, pulse forming network and charging circuit. The Blumlein, resistive load (Z_0) and kicker are in series to the right of the figure. In the final installation the load resistor is mounted near the vacuum chamber coupling directly to the kicker plates. The blumlein connects to the resistor via high voltage coax.

5566

5567 13.3 New Pulseforming Network

5568 The pulse forming network that we are developing for the kicker is a Blumlein triaxial
 5569 transmission line. The Blumlein is shown schematically in Figure 13.7. The LCR circuit
 5570 used in E821, and a coaxial transmission line are included in the Figure for comparison. The
 5571 equivalent circuit for a Blumlein is a pair of series bi-axial lines with a shared conductor and
 5572 it is so rendered blumlein in Figure 13.8.

The width of the pulse

$$\tau = \frac{2L}{v} = 2L \frac{\sqrt{\mu\epsilon}}{c}.$$

5573 For the bi-axial line the voltage at a matched load is half the charging voltage. For the
 5574 Blumlein, output voltage and charging voltage are one and the same[2]. Another advantage
 5575 of the Blumlein as compared to a bi-axial transmission line is that the base of the thyatron
 5576 can be fixed at ground potential. A bi-axial pulse forming network would require that the
 5577 base of the tube float to high voltage when the thyatron is switched. The Blumlein
 5578 PFN under development at Cornell is shown in cross section in Figure 13.9. The middle
 5579 conductor is connected through a large resistance and inductance to the high voltage power
 5580 supply. Current flows through the load Z_L off of the central conductor during the charging
 5581 cycle. The thyatron (T) shorts the middle conductor to the outer conductor and after a
 5582 delay of $T/2$, where T is the width of the current pulse generated by the line, the current
 5583 flows through the resistive load and into the kicker.

5584 Some details of our implementation of the Blumlein are shown in Figure 13.10. The
 5585 left and right drawings correspond to configurations with characteristic impedance of 25 Ω

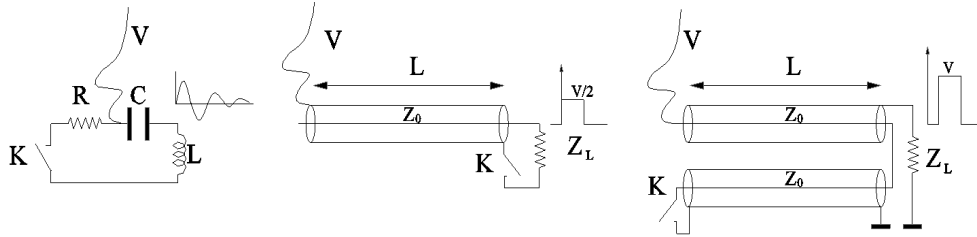


Figure 13.7: The overdamped LCR circuit at left was use in E821. The line labeled “V” indicates the charging voltage and K the thyatron switch. At center is a coaxial transmission line PFN. The Blumlein equivalent circuit is at the right. The corresponding pulse shape is shown for each of the configurations. Note that for both coaxial and triaxial lines, pulse width is proportional to twice the line length. Voltage across a matched load for the blumlein is twice that of the coax. The Blumlein pulse is delayed by half of the pulse width.

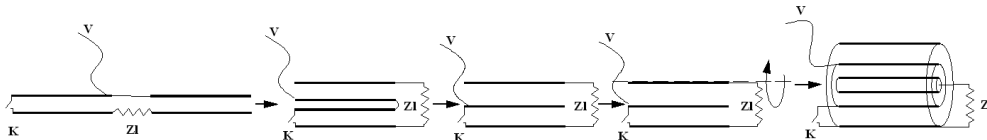


Figure 13.8: Topological modification of series coaxial lines into a tri-axial blumlein transmission line. (One can choose the rotation axis coinciding with the lower plate).

5586 and 12.5Ω respectively, (assuming 561 silicon oil with $\epsilon = 2.7$). We have modeled the
 5587 basic electrical properties of the pulser with an equivalent circuit using SPICE. Each of the
 5588 two series coaxial lines are modeled with discrete elements as shown in Figure 13.11. The
 5589 kicker load is represented with characteristic capacitance and inductance. The current pulse
 5590 through the kicker when the switch is closed, as computed with SPICE, is shown in Figure
 5591 13.12.

5592 The impedance of the triaxial line is equivalent to the sum of the impedances of the
 5593 series bi-axial lines. The middle conductor in Figure 13.9 that is charged to high voltage
 5594 serves as the inner conductor for one bi-axial line and the outer conductor for the other. The
 5595 impedance of each of these bi-axial components is 12.5Ω . The output of the PFN is coupled
 5596 to the load with a pair of parallel 50Ω high voltage coaxial cables, with combined impedance
 5597 of 25Ω . The transition hardware is shown in Figures 13.13 and in an exploded view in 13.14.

5598

5599 A schematic of the Blumlein pulser connected via high voltage coax to the kicker inside
 5600 the muon ring vacuum chamber is shown in Figure 13.15. Also shown is the electronics rack
 5601 with 1500 V power supply, thyatron driver, and thyatron trigger pulser. The cylindrical
 5602 container sitting on the floor beside the rack is the oil tank with high voltage transformer.
 5603 The single high voltage transformer will charge the three Blumleins for each of the three
 5604 kickers. Figure 13.16 is a rendering of the 5m long Blumlein with coupling to charging
 5605 transformer at the right and transition to a pair of coaxial cables at the left. The thyatron

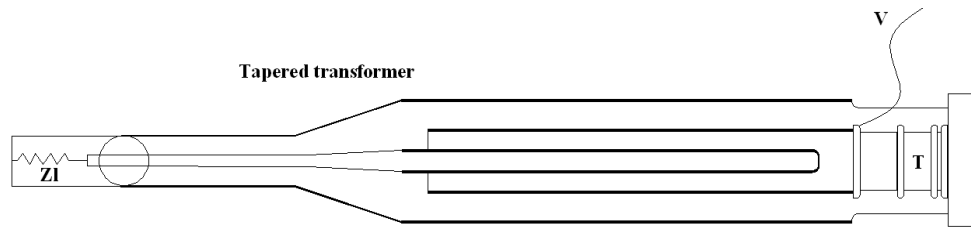


Figure 13.9: Middle conductor is charged to high voltage via the line labeled “V”. The centermost conductor is coupled via a high voltage coaxial cable to the resistive load that is mounted directly to the input of the kicker. (The kicker is not shown here.) The thyatron (T) shorts the middle conductor to ground. The volumes between conductors, around the thyatron and load are all filled with transformer oil.

5606 is housed in the section at the extreme right.

5607 13.4 New Kicker Plate Design

5608 The geometry of the kicker plates will be optimized for better uniformity over the storage
 5609 volume and higher efficiency. We show the field profile for the proposed plate geometry in
 5610 Figure 13.17(Left) as compared to the E821 geometry in Figure 13.17(Right). A proper
 5611 calculation of the magnetic field generated by the time dependent current pulse has not yet
 5612 been completed. But in the limit of steady state current and neglecting the effect of eddy
 5613 current in the vacuum chamber and plates themselves, the new plate geometry provides at
 5614 least 33% more magnetic field per unit current than the old design. Distancing the kicker
 5615 plates from the vacuum chamber also mitigates the effect of induced field in the aluminum.
 5616 We estimate that a current of 3500A will be required to achieve a 14mrad kick, corresponding
 5617 to a charging voltage of 87.5 kV, (~ 10 kV below the breakdown voltage of the E821 kicker
 5618 system).

5619 Whereas in the E821 configuration, the kicker plates served as rails for the NMR trolley,
 5620 those functions will be separated in the new implementation as can be seen in Figure 13.18.
 5621 The kicker plates will be suspended from the top of the vacuum chamber as shown in Figure
 5622 13.19. Care must be taken to ensure the stability of the plates with respect to the time
 5623 dependent forces associated with the current pulse. At the same time it is desirable to
 5624 minimize the thickness of the plates and scattering of decay electrons.

5625 13.5 Kicker R&D at Cornell

5626 A laboratory has been outfitted at Cornell to build and test a prototype Blumlein pulse
 5627 forming network and fast kicker magnet. The electronics that has been recovered from the
 5628 E821 experiment and re-assembled includes: high voltage power supply, high voltage charging
 5629 transformer, thyatron driver, trigger pulser and thyatron. We have fabricated a prototype
 5630 5 meter Blumlein and tests with a resistive load are in progress. Figure 13.20 shows two

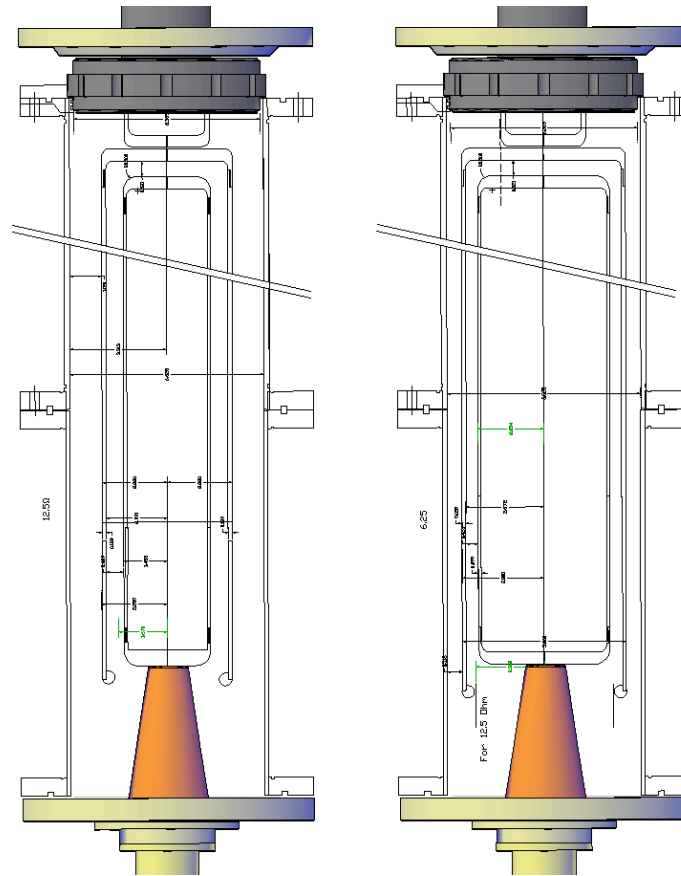


Figure 13.10: Cross section of 25Ω (left) and 12.5Ω (right) Blumlein. The central conductor couples through the orange transition at the bottom of the figure to the load resistor and kicker. The middle conductor connects through the U bracket near to the top to the thyatron (not shown). The penetration of the high voltage charging line through the outer conductor to the middle conductor is not shown.

5631 views of the prototype Blumlein. The downstream, business end of the Blumlein is shown
 5632 in Figure 13.21. For the test in progress, the line is terminated in a 25Ω resistive load. The
 5633 Figure also shows the current pulse through the load as measured with both E-field antenna
 5634 and B-field current monitor. The rise and fall time of the E-field pulse is dominated by the
 5635 thyatron turn on and off time. The limited bandwidth of the B-field further degrades the
 5636 apparent rise time. The base width of the E-field pulse is about 100 ns and the rise time is
 5637 30ns, not atypical for a 10 year old, 4-gap tube. (We plan to experiment with other 4-gap
 5638 thyatron and are investigating the possibility of a 2-gap tube. The required standoff voltage
 5639 is somewhat less than 100kV, and we have identified a two-gap tube that at least according
 5640 to its specifications is a viable alternative.

5641 The prototype vacuum chamber is shown in Figure 13.22. Ports have been added to the
 5642 top and bottom of the chamber to provide a path for the laser light for the Faraday effect
 5643 field measurement. Macor high voltage standoffs are mounted to the ceiling of the chamber.
 5644 The new plates will hang from the standoffs. (The laser light ports and macor standoffs are

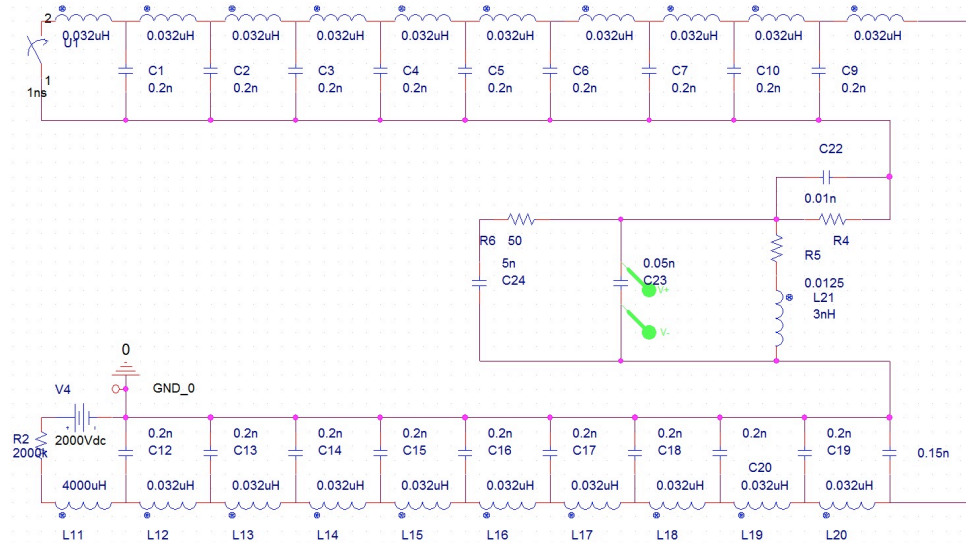


Figure 13.11: Discrete circuit element of the Blumlein that is shown as the right hand schematic in 13.7. Each of the two transmission lines is assembled with lumped inductance and capacitance. The kicker load is represented as inductance with small capacitance.

5645 not visible in the Figure)

5646 The coaxial coupling of the Blumlein to the prototyp vacuum chamber is shown in Figure
5647 13.23.

5648 The kicker lab is equipped to test and modify and test again the PFN and the kicker
5649 plate assembly as required to meet the design specifications.

5650 13.6 Kicker Field Measurement

5651 Measurement of the time dependent field of the kicker will ultimately determine the effec-
5652 tiveness of the design choices. Furthermore, it is essential to measure, and ideally eliminate,
5653 fields due to the eddy currents in the vacuum chamber and kicker plates, that are generated
5654 by the kicker pulse. If the eddy currents have a long decay time, any persistent field will
5655 introduce a systematic shift in a_μ .

5656 We plan to implement a Faraday rotator to measure the time dependence of the kicker
5657 field and associated persistent fields modeled on the device used in E821. We have machined
5658 ports into the prototype vacuum chamber for transmitting polarized laser light through a
5659 birefringent crystal that will be mounted between the plates in the laboratory. It is desirable
5660 to repeat field measurements in-situ during the course of the experiment and we are exploring
5661 the possibility of implementing a Faraday rotator for that purpose.



Figure 13.12: Pulse generated by blumlein equivalent circuit in Figure 13.11. Width of the “flat” top is about 70 ns. (Major ticmarks (solid lines) along time axis are every 50 ns.)

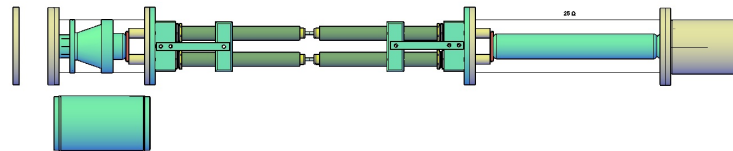


Figure 13.13: Transition from Blumlein to load. The green cylinder at the right couples to the centermost conductor of the Blumlein. With the outer conductor in place (not shown in this view), this short coax will have an impedance of 25Ω . The 25Ω coax couples to a pair of 50Ω high voltage coax cables. At the load end of the cables, there is a transition back to a single 25Ω coax and to the load resistor through the exponential impedance transformer.

5662 13.7 Risks

5663 13.7.1 Performance Risk

5664 The kicker system will be designed to provide an integrated field of 1447 G-m for the duration
 5665 of the length of the injected muon pulse ($\sim 120\text{ns}$), and then drop to zero field, 149ns after the
 5666 first muons entered the ring. Failure to achieve the specified field value will result in reduced
 5667 muon capture efficiency and increased coherent betatron oscillation of the muons that are
 5668 captured. Failure to turn off after 149 ns will likewise compromise capture efficiency and
 5669 contribute to coherent betatron motion. The risk of less than optimal system performance are
 5670 increase in statistical error (fewer muons) and additional systematic error (increased coherent
 5671 betatron motion). The risk will be mitigated by extensive system testing and optimization
 5672 prior to installation.

5673 A failure of the thyatron tube, a breakdown internal to the Blumlein-PFN, or a break-



Figure 13.14: Exploded view of the impedance transformer in Figure 13.13 is shown at left. Two possible implementations of the load resistor, that is located on the axis of the transformer, are shown at right.

5674 down of the plates inside the vacuum chamber would have more catastrophic consequences,
 5675 as very few muons will store without an operational kicker. We plan to operate the system
 5676 continuously at the design repetition rate before installation into the muon ring to establish
 5677 reliability. We note that the system is designed to operate at 87 kV, approximately 10 kV
 5678 below the level at which the E821 system was limited by breakdown.

5679 There is some risk that the kicker will excite a long lived eddy current in the vacuum
 5680 chamber that will in turn generate a lingering magnetic field that will alter the muon pre-
 5681 cession frequency. We plan to calculate and more importantly measure the parasitic fields
 5682 generated by the kicker pulse and if we are unable to eliminate them entirely, to account for
 5683 them in the analysis. We are developing instrumentation for an in-situ monitor of the long
 5684 lived field.

5685 13.8 Quality Assurance

5686 The quality of the kicker system will be assured by extensive testing in advance of installation
 5687 into the ring.

5688 13.9 ES& H

5689 The kicker system will operate at high voltage $\sim 90\text{kV}$, however there will be no exposed
 5690 high voltage. All external surfaces of the Blumlein will be fixed at ground potential. As
 5691 there are no diodes in the charging circuit, the time constant for dissipation of stored charge

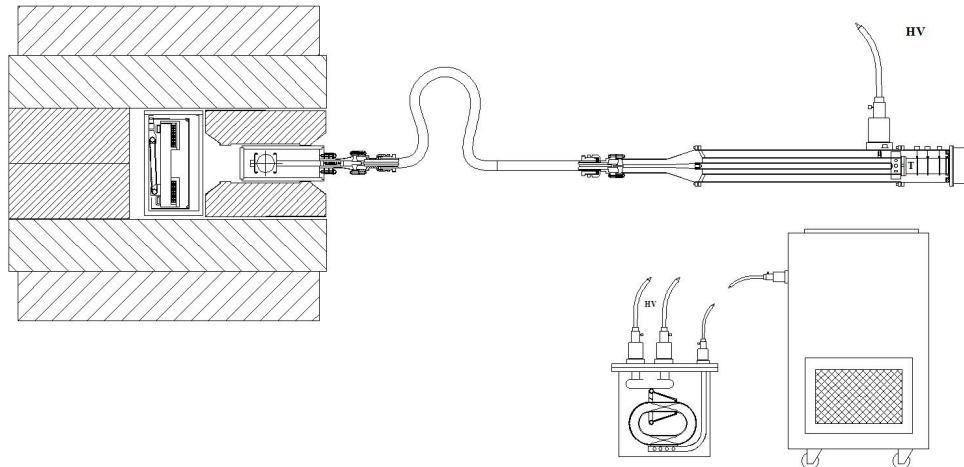


Figure 13.15: Blumlein is coupled through a pair of 25Ω high voltage coaxial cables to the kicker magnet inside the ring vacuum chamber. (Only a single coax is shown). High voltage power supply and thyatron driver are in the electronics rack at right. The 1:84 high voltage transformer that provides charging voltage to the PFN is in the oil tank to the left of the electronics rack.

5692 is a few seconds. A procedure for de-energizing in the event that disassembly is required will
 5693 be established. Each of the three Blumlein tri-axial lines will be filled with non-flammable
 5694 and nontoxic 561 silicon transformer oil. While there is the danger of a spill, (75 liters/line),
 5695 the oil itself is not hazardous.

5696 13.10 Value management

5697 We are reusing as much as possible, components from E821, in particular, the thyatron
 5698 tubes.

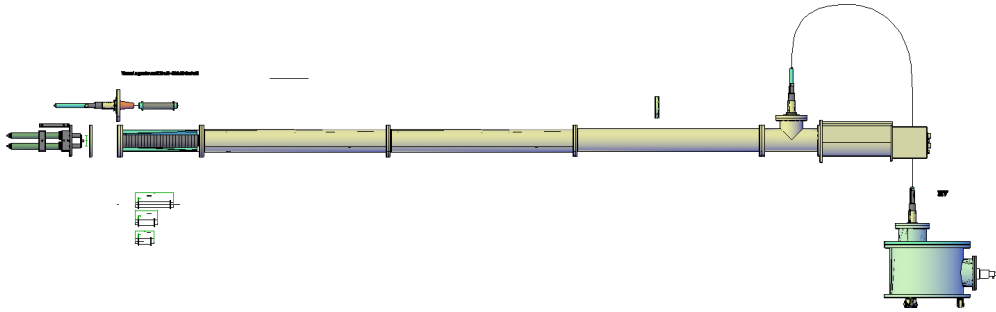


Figure 13.16: Blumlein connected to high high voltage charging transformer. Transition to dual coaxial lines is at the left.

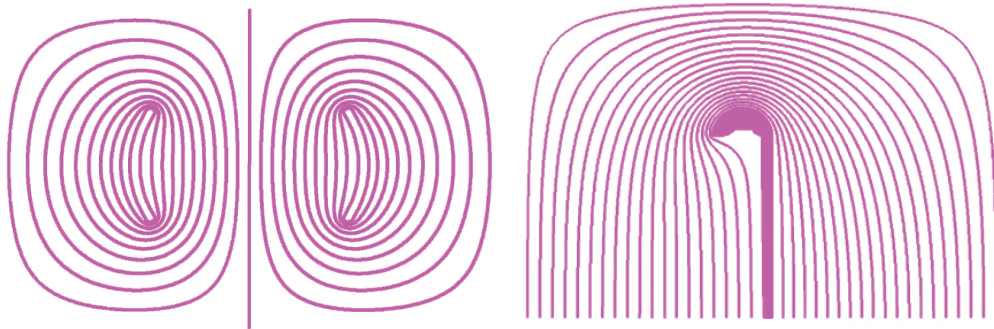


Figure 13.17: (Left) Proposed kicker plate geometry and magnetic field lines computed with MERMAID. (Right) One quadrant of the E821 kicker plate geometry and field lines. The boundary condition at the vacuum chamber surface is set to mimic effect of induced currents due to fast rise time. Note high density of field lines at the edge of the plate that also serves as the trolley rail.

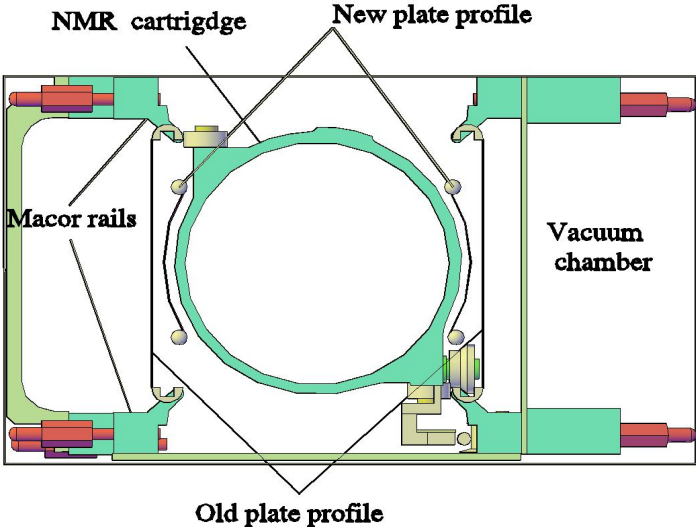


Figure 13.18: E821 kicker plates, new plates, NMR trolley, and new rails are shown in the vacuum.

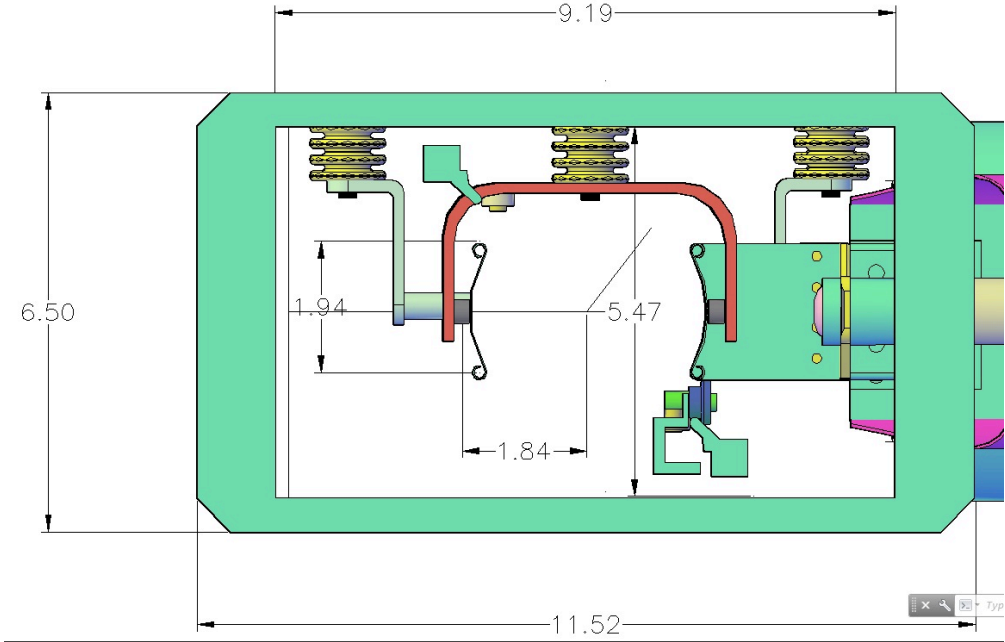


Figure 13.19: The new kicker plates hang from macor standoffs mounted on the top of the vacuum chamber. The crossover from inner to outer plate at the far end of the kicker is also shown.



Figure 13.20: (Left) Upstream end of Blumlein. The black cable attached at the top of the transition delivers the charging current. The thyatron is mounted horizontally in the far right module with the red High Voltage warning label. The space between the conductors of the Blumlein and the volume around the thyatron is filled with transformer oil. (Right) Looking from the business end of the Blumlein upstream towards the thyatron.

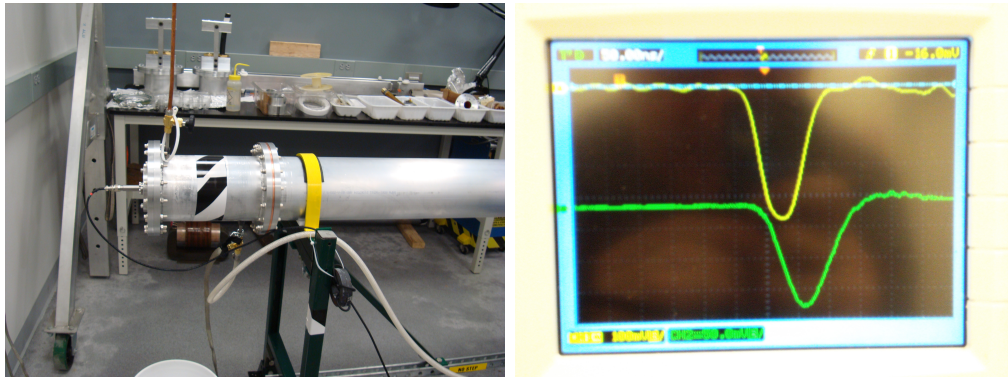


Figure 13.21: (Right) Pulse generated with Blumlein, discharged through a resistive load that is in the end section of the Blumlein (Left). The horizontal scale (hard to see) is 50 ns/division. The base of the yellow pulse is about 100 ns and the rise time 30 ns. The nominal pulse width, for the 5 m line and ideal switch is 50 ns. The width of this pulse is dominated by the thyatron switching time. The yellow signal is from an antenna probe and the green from a somewhat slower current monitor. With 561 oil, $\epsilon = 2.7$ the pulse width ~ 50 nsec, with Castor oil, $\epsilon = 4.7$, the pulse width ~ 66 nsec. and with addition of Ferrofluid, $\mu_{eff} \sim 3$, the pulse width ~ 112 nsec.

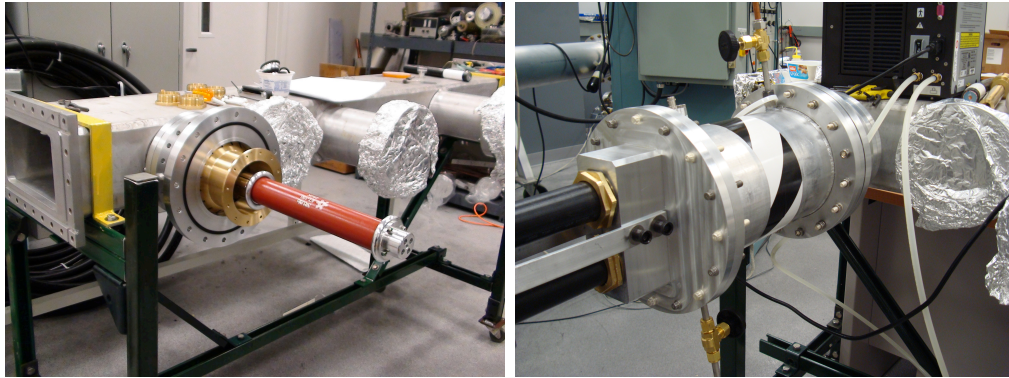


Figure 13.22: (Left) Load resistor at vacuum chamber port. (Right) The pair of coaxial cables links the Blumlein output to the load resistor (located inside the chamber with the black and white tape) and then to the kicker plates inside the vacuum chamber.



Figure 13.23: A pair of 50Ω coaxial cables couples Blumlein (background) to input to vacuum chamber (foreground)

5699 **References**

- 5700 [1] Efstathiadis E, et al. *Nucl. Inst. and Methods Phys. Res.* A496:8-25 (2002)
- 5701 [2] A.D. Blumlein, Apparatus for Generating Electrical Impulses, U.S. Patent No. 2,496,979
5702 Feb 7(1950).

Chapter 14

The Electrostatic Quadrupoles

14.1 Introduction

One of the ways to be able to store a significant number of muons in the storage ring is to use electric focusing quadrupoles (ESQ) and muons at their magic momentum of about 3.09 GeV/c. At that momentum the radial E -field precesses the muon momentum and the muon spin vectors at exactly the same rate and thus it does not influence the $(g - 2)$ precession frequency. The method was first used in the final muon $(g - 2)$ experiment at CERN [1], and in E821, the muon $(g - 2)$ experiment at BNL [2]. We have also decided to use it for E989, the FNAL experiment, after we have carefully considered alternatives, e.g., weak magnetic focusing, and alternating skew electrostatic quad focusing. However, we found the present scheme, used in E821, to be preferable.

The principal characteristics of the design are similar to the E821 ESQ described in [3]. In the present document we describe them and include the main points that aim to improve the muon ring acceptance and reduce muon losses as well as certain systematic errors associated with the coherent betatron oscillation frequencies. Fig. 14.1 shows a schematic of the top view of the muon $(g - 2)$ ring and the vacuum chambers indicating the azimuthal coverage of the quadrupoles in E821. The total azimuthal coverage is 43%, keeping a four-fold symmetry with segment names of Q1, Q2, Q3, and Q4. Each quad segment consists of a “short” quad of 13° and a long one of 26° , (see Fig. 14.2), for two reasons: 1) to make every quadrupole chamber independent of others, facilitating their development, testing, etc., and 2) to reduce the extent of low energy electron trapping. Therefore there are two high voltage vacuum-to-air interfaces for each quadrupole segment.

The maximum voltage we used during the muon runs on the ESQ of E821 was 25.4 kV, resulting in a field focusing index of 0.144. We now plan to raise the maximum voltage to 32 kV for a field focusing index of $n = 0.18$. At $n = 0.18$, we expect the following things to happen:

1. Increase the ring admittance and most likely the muon storage efficiency.
2. Reduce the muon losses during storage.
3. Reduce the coherent betatron oscillation (CBO) systematic error.

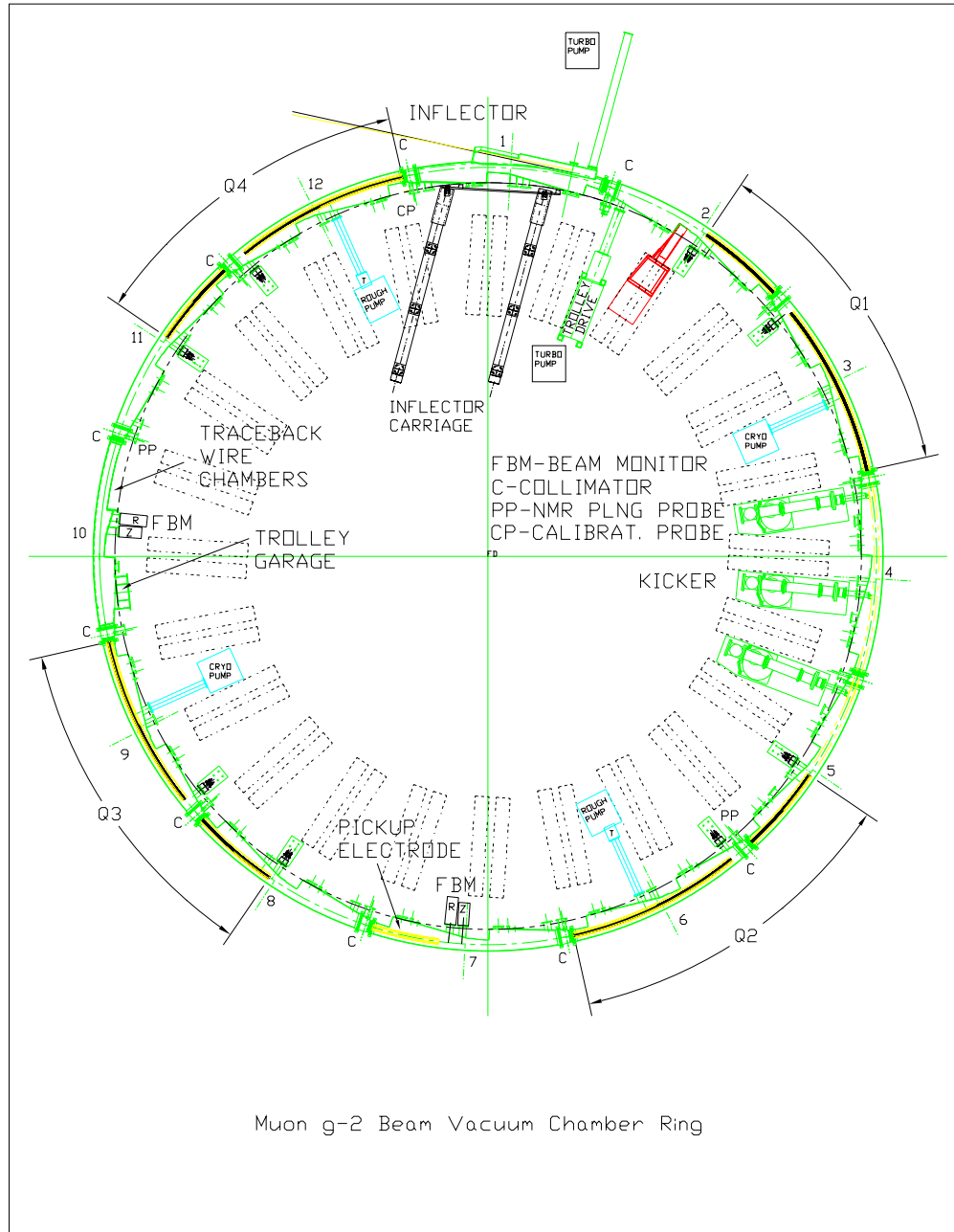


Figure 14.1: A schematic of the muon ($g-2$) ring as well as the location of Q1, Q2, Q3, and Q4, the four-fold symmetric electrostatic focusing system.

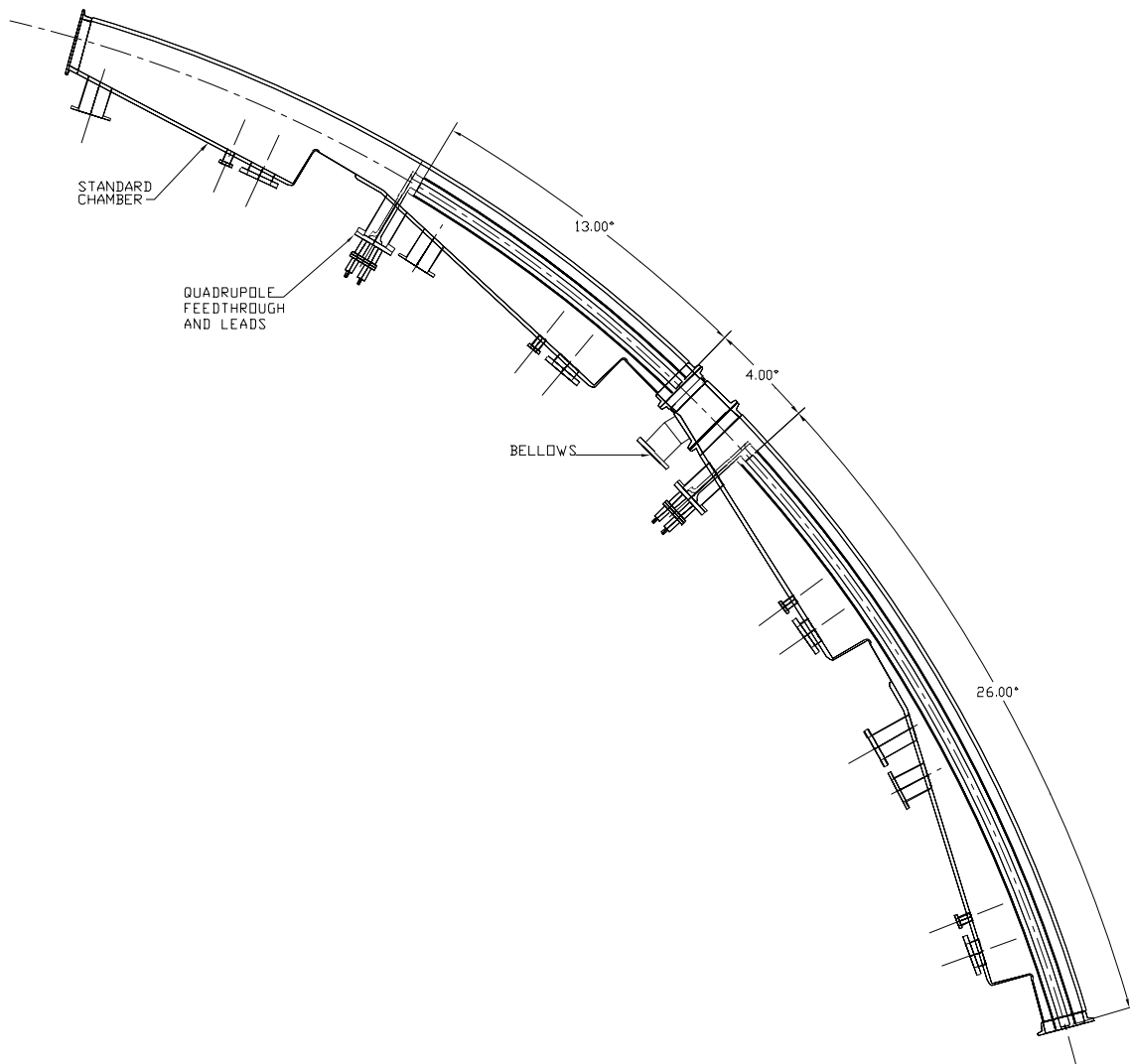
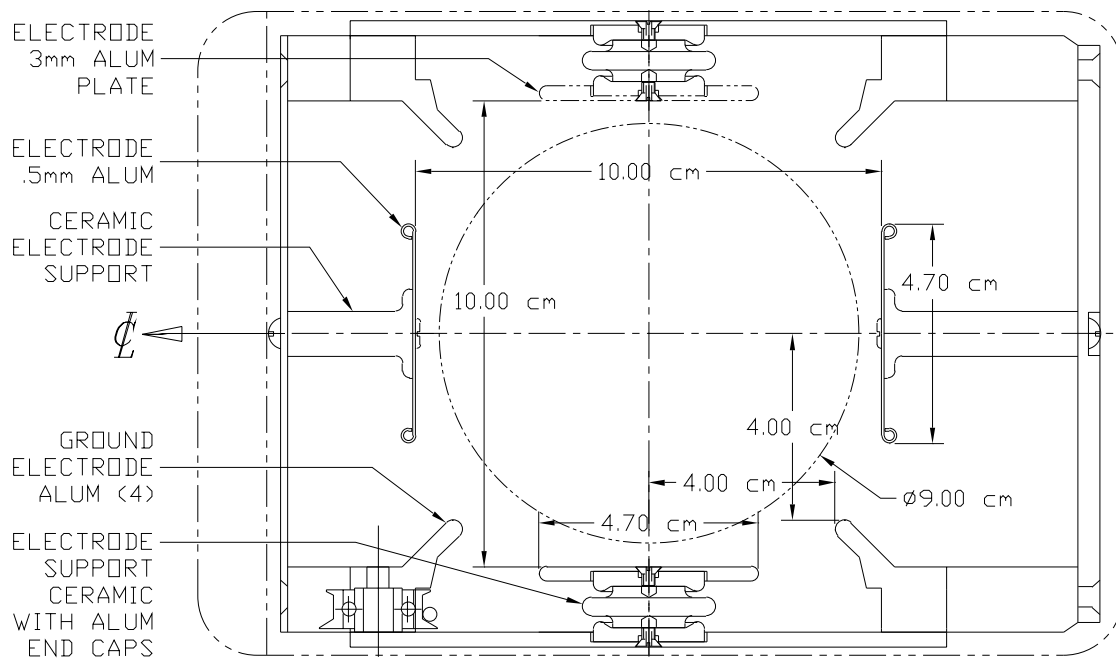


Figure 14.2: A schematic of a short quad of 13° , and the adjacent long one of 26° is shown here. The high voltage feeding leads break the quad symmetry at the upstream end of the plates to quench the low energy electron trapping and guide them outside the magnetic field region, where they can be released. Some of the bellows were equipped with collimators where the muon beam was scraped immediately after injection.

5733 We will test the quads up to 35 kV, about 10% higher voltage than the anticipated
 5734 nominal voltage level. A large number of improvements will be implemented to the new
 5735 system based on the experience we accumulated running the quadrupole system for E821.
 5736 They are discussed later on in this chapter.

5737 14.2 E821 Design and Limitations

5738 The cross-section of the quadrupoles is shown in Fig. 14.3 with the various dimensions
 5739 indicated in the figure. The ESQ consist of four aluminum plates symmetrically placed
 5740 around the muon storage region. The placement accuracy was 0.5 mm for the horizontal
 5741 (top/bottom) quad plates, and 0.75 mm for the vertical (side) quad electrodes. When
 5742 measured by the surveyors they were found to be well within those values.



ELECTRODE AND SUPPORT FRAME - END VIEW

Figure 14.3: A schematic of the quadrupole cross-section. The rails in the corners are kept at ground potential. Most of the support insulators are replaced with uniform diameter insulators of 0.5 cm.

5743 Fig. 14.4 shows a picture of the quadrupoles at the downstream end of one chamber.
 5744 The main issue in E821 was to be able to hold the high voltage without sparking for about
 5745 1 ms. This is a very demanding task, especially for storing negative polarity muons, due

5746 to low energy electron trapping in the quad region. We were able to achieve this task by
5747 designing the HV feeding leads in a way to quench the low energy electron trapping, see
5748 Figs. 14.5, 14.6, 14.7.

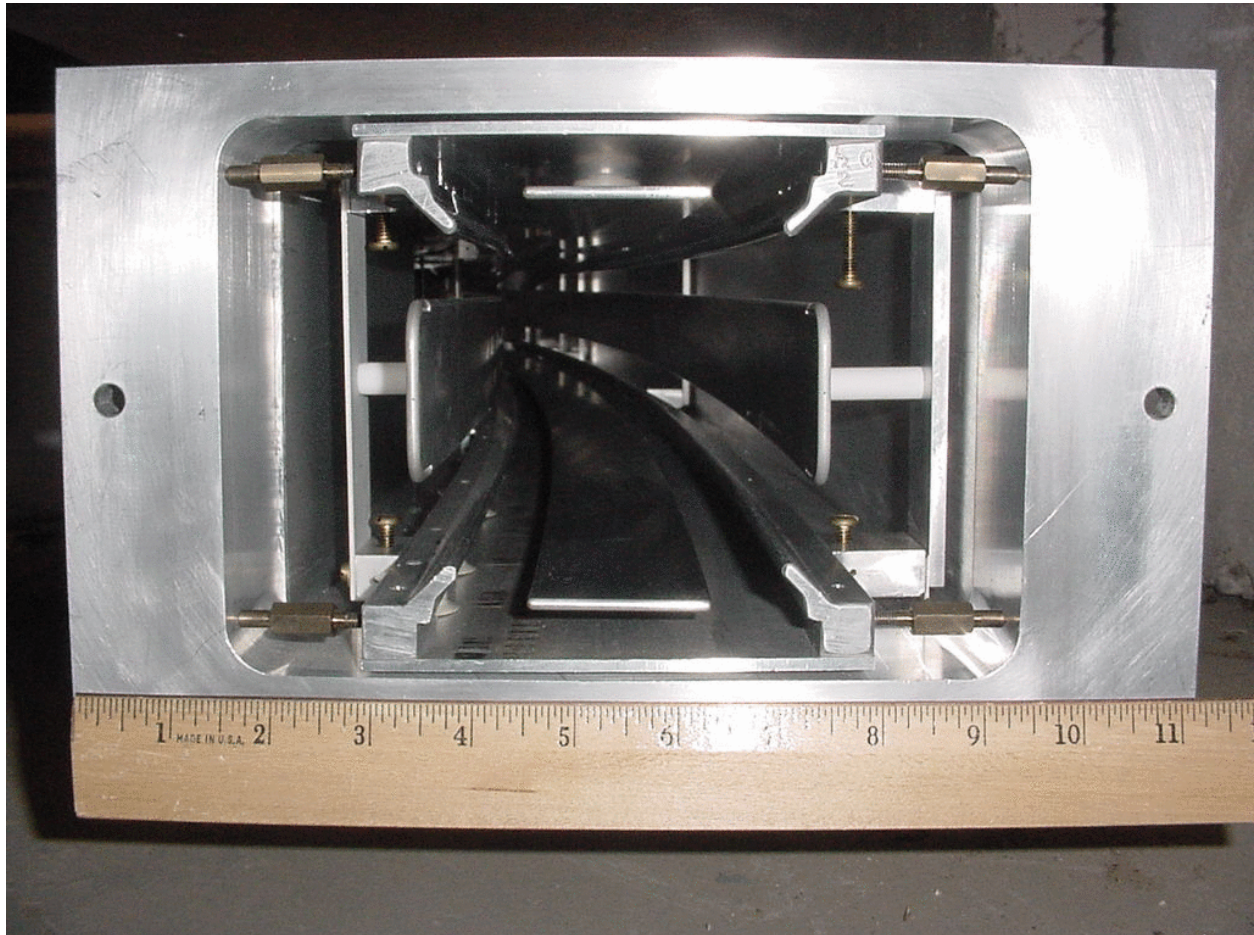


Figure 14.4: A photograph of the downstream end of a vacuum chamber with the cage and quads showing.

5749 Fig. 14.8 shows the schematic of the HV pulsing system. Two of the quadrupoles were
5750 used to scrape the injected beam horizontally, by moving the beam sideways [3], while all the
5751 quadrupoles were used to scrape the beam vertically [3]. The HV monitor location is also
5752 indicated. Fig. 14.9 shows the (home-made) HV monitors output waveforms as recorded by
5753 an oscilloscope.

5754 The great success of the quadrupole system is based on the fact that it allowed the storage
5755 of positive and negative muons for more than 0.75 ms in the storage ring, even though
5756 the azimuthal quad coverage was almost half that of the last muon ($g - 2$) experiment at
5757 CERN. The vacuum requirements were in the low 10^{-6} Torr for the positive muons and
5758 low 10^{-7} Torr for the negative muons. Higher vacuum pressures were tolerated for limited
5759 operation periods. Those requirements allowed a speedy recovery after any unavoidable
5760 opening up of the vacuum chambers during the initial stages of the runs, related mostly to
5761 issues other than the quadrupole operations.

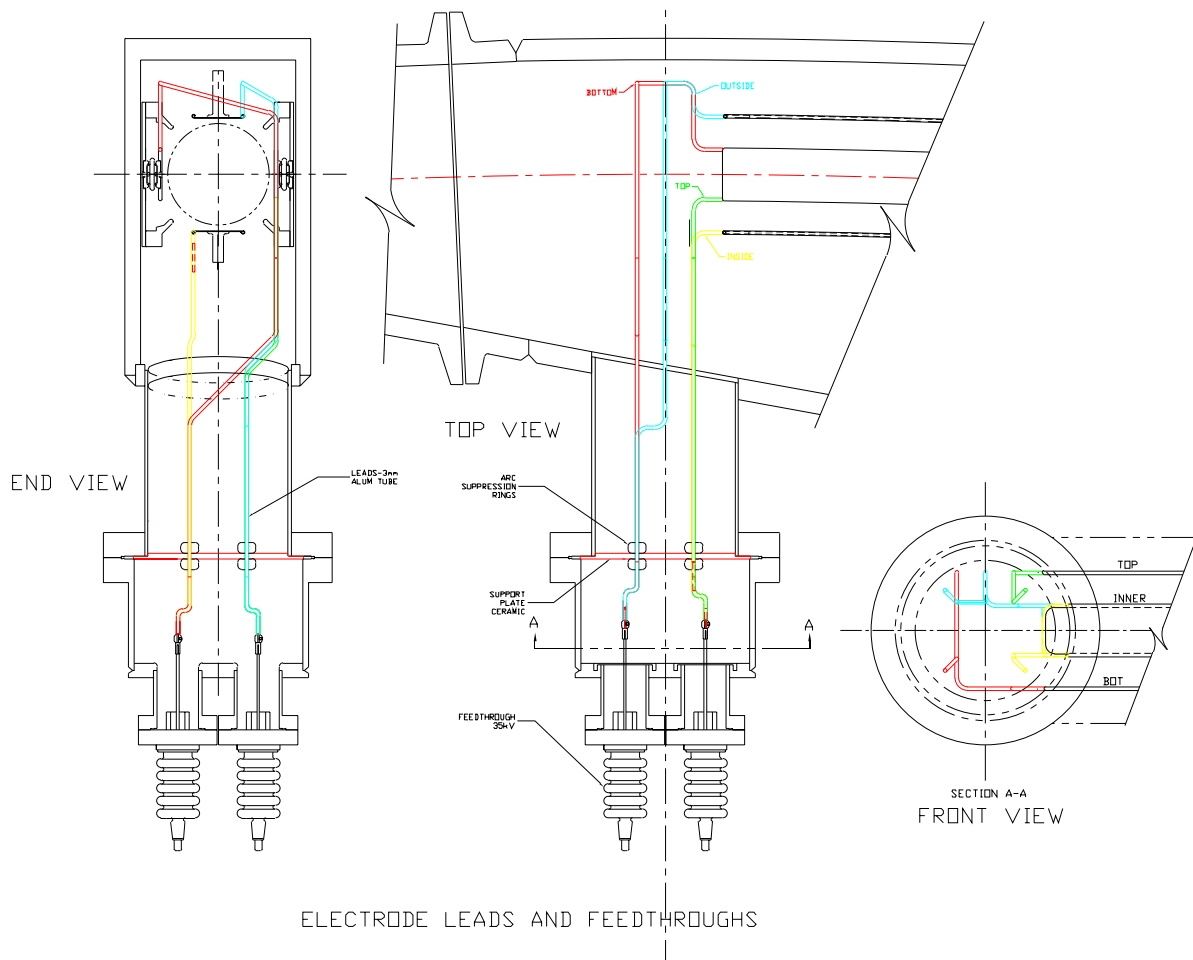


Figure 14.5: Various aspects of the quadrupole high voltage feeding lead geometry, designed to minimize low energy electron trapping.

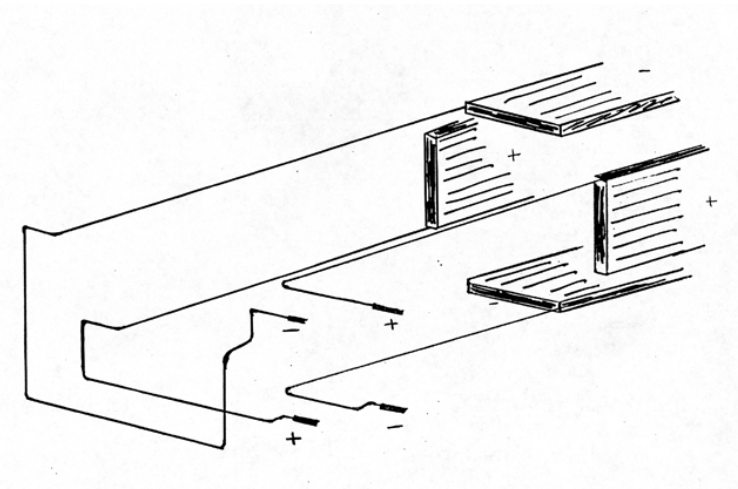


Figure 14.6: Early stages of a hand drawing indicating the high voltage feeding lead geometry.

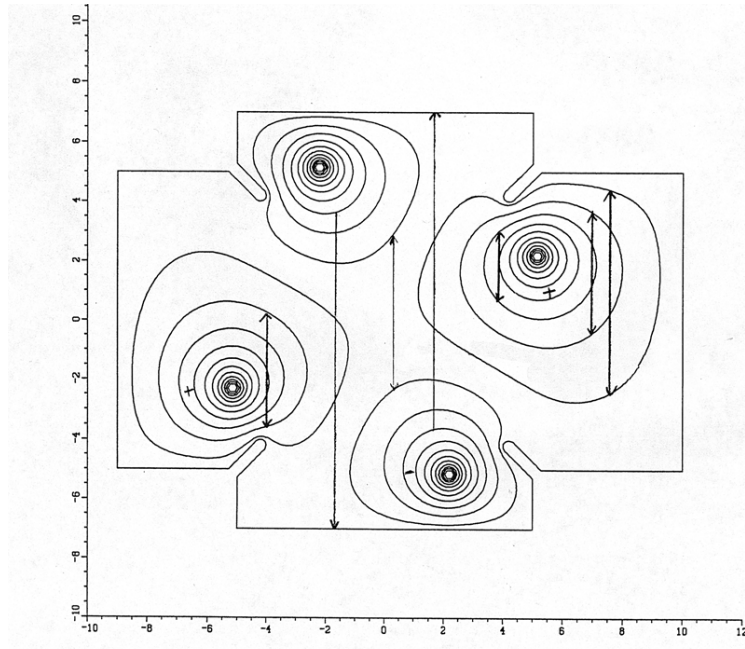


Figure 14.7: A cross section of the lead geometry (vertical [cm] vs. horizontal [cm]). The schematic shows the equipotential lines from an OPERA calculation as well as the low energy electron trapping regions derived from energy conservation. The lead-geometry was designed to optimize the quenching of the electron trapping for the negative muon storage polarity.

5762 For E989 we focus on positive muon storage only, due to the following advantages:

- 5763 • It allows us to improve the E -field quality by restoring the normal quadrupole field in
5764 the lead region. The plan is now to connect the leads at the center of the plates, expose
5765 the E -field from the leads for a couple of centimeters, and then hide them behind a
5766 ground shield. The aim is to shield the muon storage region from the E -field generated
5767 by the leads. Space is very tight at this location, so we will work very carefully to
5768 avoid sparking.
- 5769 • Due to the relaxed vacuum requirements associated with μ^+ running, we will be able
5770 to raise the high voltage and keep it there for longer times. This may have an impact
5771 on the muon lifetime measurement or other systematic error measurements.
- 5772 • For E821, the quadrupoles required a lengthy conditioning period (a couple of hours,
5773 depending on pressure) after every trolley run. For positive muon storage, plus an
5774 automated conditioning system, we expect to minimize this recovery time by a factor
5775 of two to three. Quadrupole conditioning is much more straight forward in the positive
5776 polarity than in the negative polarity. The main reason is that in the negative polarity
5777 the support insulators are intercepting the low energy trapped electrons, which, de-
5778 pending on the trapping rate, could cause sparking. The conditioning process in the
5779 negative polarity was very delicate and lengthy. One of the possible models for why it
5780 worked was that the slow conditioning creates a thin conducting layer on the insulator

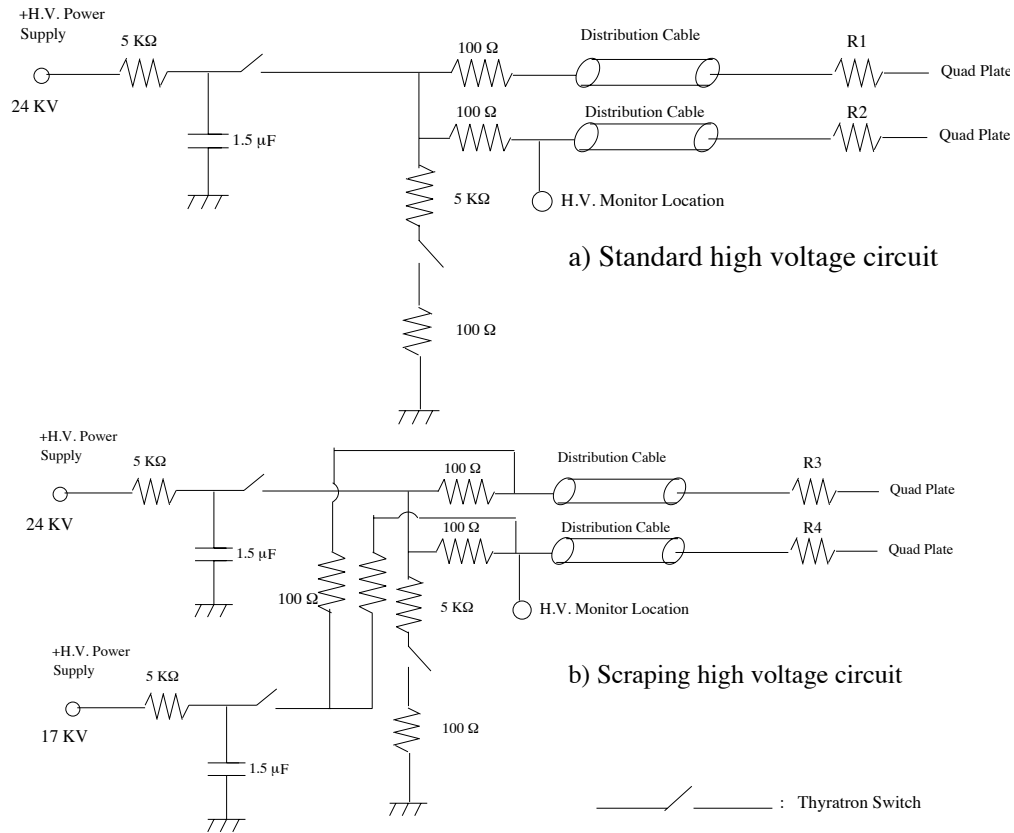


Figure 14.8: A schematic of the scraping and normal HV pulsing systems. The Thyatron switch model used in E821 was the CX1585A produced by English Electric Valve, good to 40 kV.

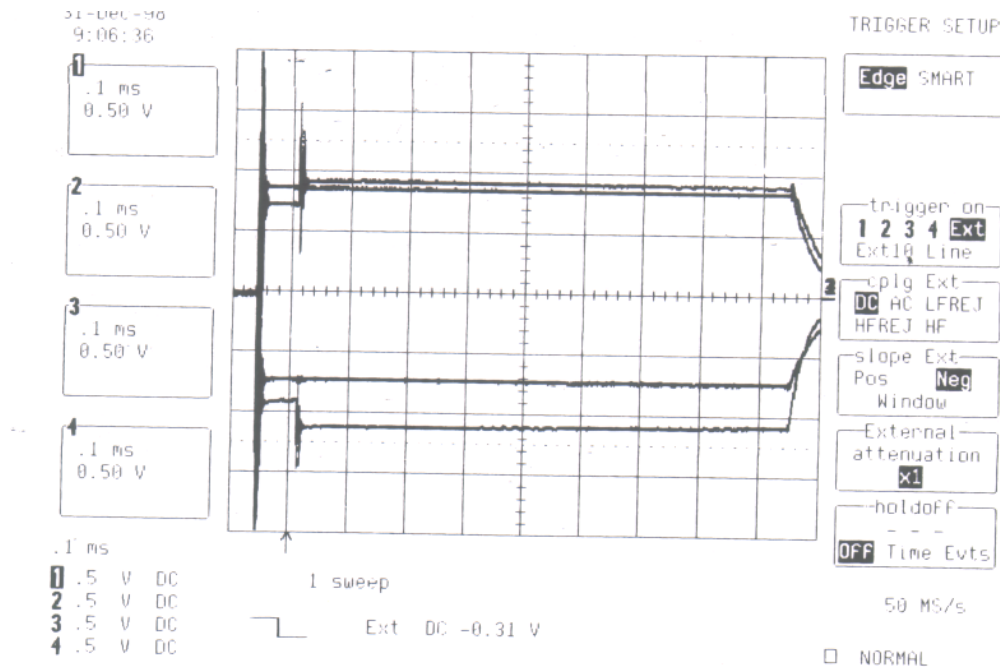


Figure 14.9: The output of the HV monitors as recorded by the oscilloscope.

5781 surface, allowing them to slowly move and thus avoid accumulating a critical level. For
 5782 the positive polarity there are no insulators in the way of the trapped electrons. We
 5783 will write a computer software program that will be able to condition the quadrupoles
 5784 taking into account the vacuum pressures and sparking history.

- 5785 • For positive muon storage we expect the voltage on the plates to be more stable as a
 5786 function of time and from pulse to pulse.

Table 14.1: Comparison of high- n and very high- n values.

Parameter	n=0.142	n=0.18
horizontal tune, ν_x	0.926	0.906
vertical tune, ν_y	0.377	0.425
f_{CBO}	495 kHz	634 kHz
f_{CBO}/f_a	2.15	2.76
$1/(f_{\text{CBO}} - 2f_a)$	$27\mu\text{s}$	$5.7\mu\text{s}$
HV	25 kV	32 kV

5787 For E989 we require improvements in a number of areas:

- 5788 1. Operate the quadrupoles at a higher n -value to primarily change the horizontal co-
 5789 herent betatron oscillations (CBO) frequency away from near twice the muon ($g - 2$)
 5790 frequency. The CBO frequency, being very close to twice the ($g - 2$) frequency, see
 5791 Table 14.1, pulled the ($g - 2$) phase and was a significant systematic error that required
 5792 special attention during data analysis. We aim to operate at $n = 0.18$ to reduce it by
 5793 more than a factor of three. Other improvements, e.g., properly matching the beam-
 5794 line to the storage ring (requiring a proper inflector channel) is expected to reduce it
 5795 by at least another factor of three. Overall the CBO systematic error can be reduced
 5796 to the level required by E989.
- 5797 2. Reduce the muon losses by more than an order of magnitude to reduce the muon losses
 5798 systematic error. We will achieve this goal by moving the operating point to $n = 0.18$,
 5799 beam scraping by 2 mm in the horizontal and vertical directions after injection, and by
 5800 keeping the radial B -field below 50 ppm (this level of radial B -field displaces the average
 5801 vertical position by about 2 mm). The region around $n = 0.18$ is more resonance free
 5802 than the previous n -values we ran with, see Fig. 14.10. We will refine the quadrupole
 5803 operating mode by running precision beam dynamics tracking simulations to more
 5804 accurately predict the muon population phase-space after scraping.
- 5805 3. Shield the muon storage region from the modified quadrupole field due to the HV
 5806 feeding lead geometry. This region is less than 5% of the good quad coverage around
 5807 the ring, but it can still influence the muon loss rate.
- 5808 4. The quadrupole voltage monitors were home-made with limited success in achieving
 5809 an adequate frequency compensation. We now plan to equip every quad plate (32 in
 5810 total) with a commercially available frequency compensated HV monitor. This will

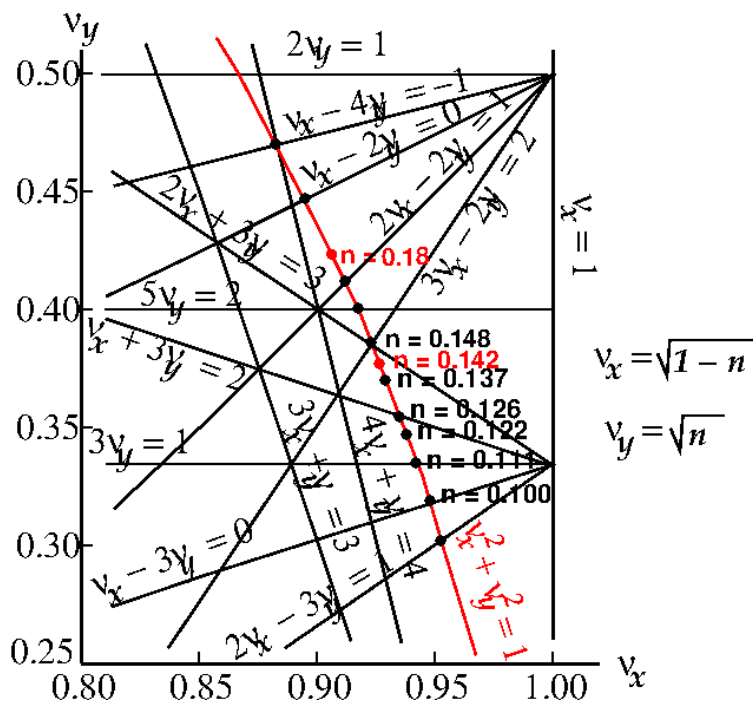


Figure 14.10: The vertical vs. horizontal tune plane together with a number of potential resonance points. The n -values $n = 0.142$; 0.18 are indicated in red. $n = 0.18$ lies between the resonance lines $\nu_x - 2\nu_y = 0$ and $2\nu_x - 2\nu_y = 1$.

5811 improve the voltage stability readout by an order of magnitude. In addition, we will
 5812 cross-calibrate the frequency compensation of each monitor with the electric field in
 5813 the quad region measured using the Kerr effect.

5814 5. Improve the reliability of the HV-vacuum interface regions with a goal of reducing
 5815 sparking by at least an order of magnitude. The base design is to cover the interface
 5816 in oil capable of holding high electric fields. Alternative design calls for increasing the
 5817 spacing between positive and negative leads in the air side of the interface.

5818 6. The outer Q1 plate and support insulators are estimated to have reduced the stored
 5819 muon population by about 40%. We now plan to address the muon loss issue by a
 5820 number of alternative modifications. Currently the baseline is to relocate the outer Q1
 5821 from $x = -5$ cm to $x = -7$ cm to allow for the uninhibited injection of the muon beam.
 5822 Fig. 14.11 shows the OPERA model of the quadrupole plates in a quadrupole cage. The
 5823 plate width is adjusted so that only the normal quadrupole field is dominant, and the
 5824 20-pole is kept at the 2% level. Every other multipole is below 0.1%, including the
 5825 sextupole, octupole, etc. Fig. 14.12 shows the current plan for providing a “massless”
 5826 outer Q1 plate, by placing it outside the muon path. In order to restore an acceptable
 5827 field quality, the plate voltage also needs to be raised by about a factor of two, see
 5828 Fig. 14.13. Another parameter we can use to improve the field quality is to work with
 5829 the plate geometry (width, shape, etc.). The requirement of increasing the voltage by
 5830 a factor of about two we believe we can achieve in the positive muon polarity and we

5831

will test it with the setup planned at BNL.

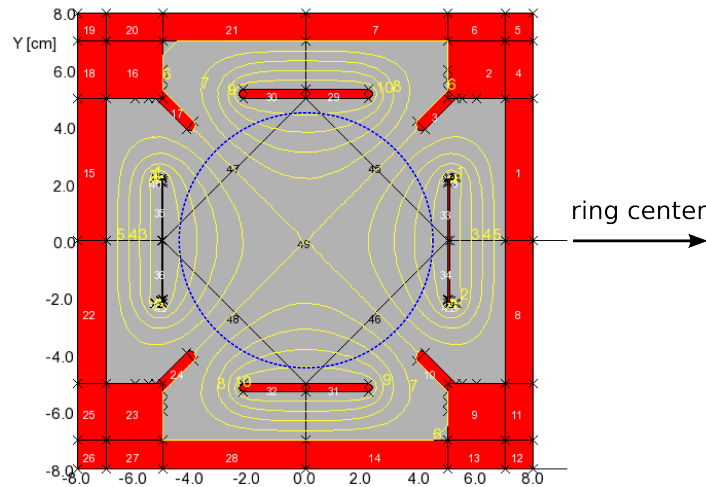


Figure 14.11: An OPERA model of the (normal: Q2, Q3, and Q4) electrostatic quadrupole plates. The top/bottom plates are at a positive voltage and the side electrodes are at (the same) negative voltage. The yellow curves represent the equipotential lines. The 90-mm-diameter muon storage region is indicated by the blue dashed circle.

5832

7. Measure the plate vibration during pulsing and stiffen the plate support as needed.

5833

14.3 Improvements that Permit Higher n -Value Operation

5834

5835 Quad upgrade and testing aims to produce an ESQ focusing system that maximizes muon
 5836 statistics and minimizes potential systematic errors. Fig. 14.14 shows one segment of the
 5837 muon ($g - 2$) electrostatic quadrupoles at BNL outside its vacuum chamber.

5838 Vladimir Tishchenko is the L3 manager for the ESQ system and Yannis Semertzidis
 5839 was the former L3 manager for the same system. The ESQ system currently consists of
 5840 8-chambers, 4-pulsers systems, 6-HV-power supplies, and a HV monitoring system:

5841

- Refurbish the HV pulsers to operate at a maximum voltage of ± 35 kV, from the present ± 25 kV used in E821. The side insulators are all varnished due to the negative muon operation at BNL, see Fig. 14.15. The insulators will be either cleaned or will be replaced by new ones.

5842

5843

5844

5845

- Utilize a C-magnet at BNL to imitate the conditions of running the ESQ in the muon ($g - 2$) magnet as closely as possible. For practical reasons we can only test the half-scale quadrupoles, as the (straight) C-magnet under consideration could not accommodate the full scale quads, see Fig. 14.16. We will be able, however, to extrapolate to the full quads by placing stricter requirements on the vacuum pressure.

5846

5847

5848

5849

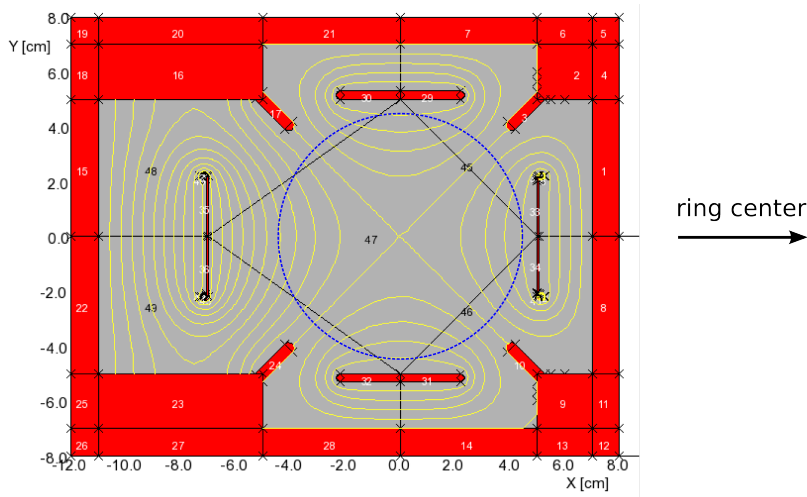


Figure 14.12: An OPERA model of the electrostatic quadrupole plates for Q1. The left plate is displaced to the outside by 2 cm to allow the muons to enter the storage region without having to cross the plates or the support insulators. In order to restore a good field quality (indicated by the symmetric equipotential lines in the center region), the voltage on the left plate is about twice that on the right plate. The 90-mm-diameter muon storage region is indicated by the blue dashed circle.

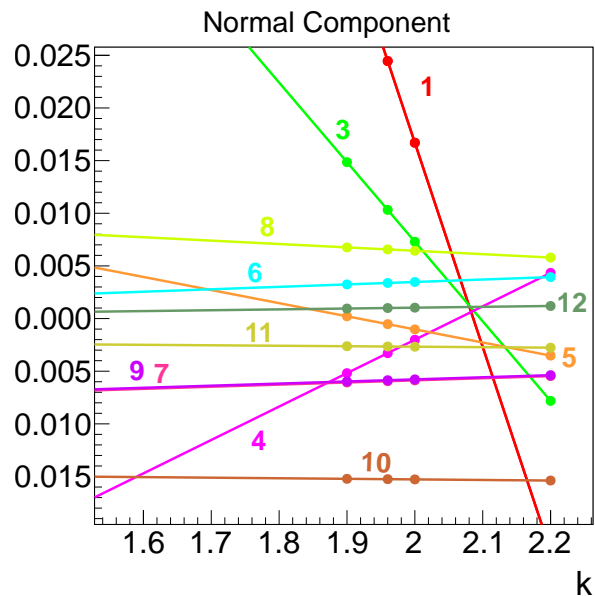


Figure 14.13: Results from OPERA as a function of the voltage multiplication factor for the displaced (outer Q1) plate. Most of the multipoles are below 0.5% but not all. Next we will study the effect of the plate shape on the multipoles.



Figure 14.14: One cage (placed here up-side-down) that holds the plates of the electrostatic quadrupoles of the muon ($g - 2$) experiment.

- 5850 • Optimize the ESQ for positive polarity muon storage. The leads will be re-configured
5851 to quench the low energy electron trapping more efficiently aiming to achieve higher
5852 electric field gradient by 30% compared to E821. Achieving this goal will help eliminate
5853 the CBO systematic error as well as substantially reduce muon losses.
- 5854 • Expand the HV vacuum chamber/air interface tube aiming to significantly reduce the
5855 sparking in the vacuum side of the leads.
- 5856 • Modify the geometry of the HV-vacuum interface to reduce sparking in the air side
5857 of the HV lead system or immerse it in oil that can withstand the E -field strength.
5858 The later is applied routinely in HV applications but it is harder to gain access to it.
5859 The sparking rate in the positive polarity in E821 was dominated by sparks at those
5860 locations (approximately one spark per 0.5-1 million pulses).
- 5861 • Shield the electric field generated by the leads from the muon storage region.
- 5862 • Measure or place strict limits on the magnetic field generated by the trapped electrons.
- 5863 • Calibrate the pulse shape output of the commercial HV monitors by measuring the
5864 electric field generated by the plates using the Kerr effect. The bandwidth (BW) of
5865 the Kerr effect measurement is in the GHz range and therefore it is not limited by
5866 the level of frequency compensation due to the large capacitance of the components
5867 involved.



Figure 14.15: The side support insulators are varnished due to trapped electron obstruction during negative muon operations at BNL (darkened appearance close to the plate).

- 5868 • Measure the vibration parameters of the quadrupole plates when pulsed using a laser
5869 light and a split diode detector. The quad plates can flex under the electromagnetic
5870 forces when pulsed. This flexing is (crudely) estimated that it can be of order 10 mm
5871 if the pulse duration is of order 1 s. However, for 1 ms the plates can only move by
5872 about $10\ \mu\text{m}$, much below our specs. We will setup a laser system to measure the plate
5873 motion due to the impulse of the electrostatic pulse.

5874 14.3.1 Coherent Betatron Oscillations

5875 The average position and width of the stored beam can vary as a function of time as the
5876 beam alternately focuses and defocuses in the ring. This is the result of a mismatched
5877 injection from the beam-line into the $(g - 2)$ ring via a narrow line, the so-called inflector
5878 magnet. This imposes an additional time structure on the decay time spectrum because the
5879 acceptance of the detectors depends on the position and width of the stored muon ensemble.

5880 The CBO frequency in E821 was close to the second harmonic of ω_a , so the difference
5881 frequency $\omega_{\text{CBO}} - \omega_a$ was quite close to ω_a , causing interference with the data fitting procedure
5882 and thereby causing a significant systematic error (see Chapter 4). This was recognized
5883 in analyzing the E821 data set from 2000. In the 2001 running period the electrostatic
5884 focusing field index, n , was adjusted to minimize this problem. This greatly reduced the
5885 CBO systematic uncertainty. We will follow this strategy again but this time we will increase
5886 the quad voltage by another 30% to decrease the CBO systematic error by more than a factor

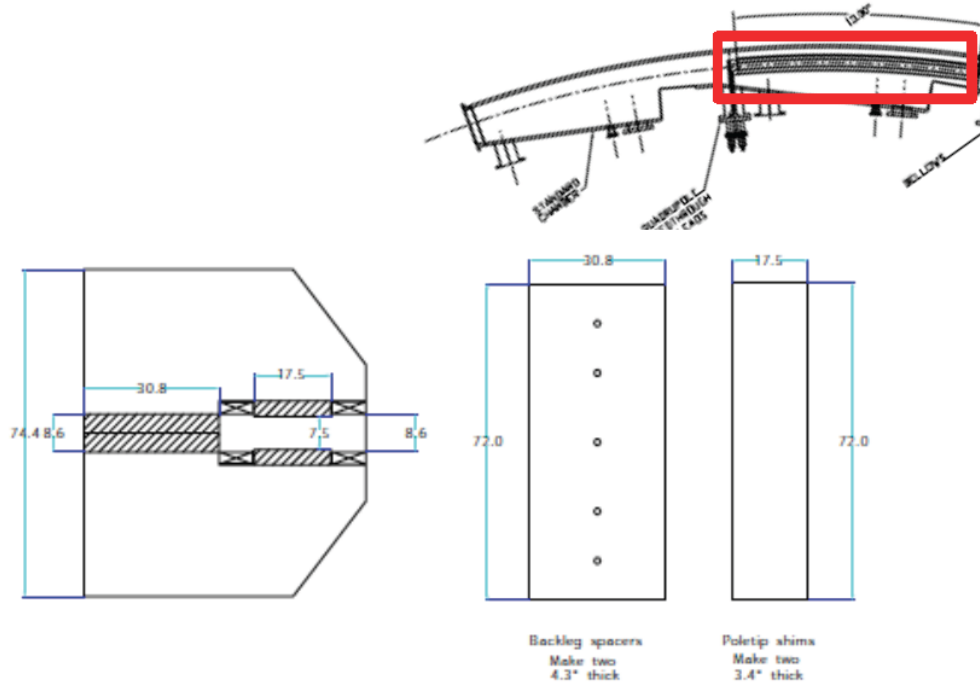


Figure 14.16: A C-magnet is being prepared at BNL for testing the quad upgrades. The magnet can fit the short quads but it requires shortening the plates by about 20 cm (for testing purposes only).

5887 of three, see Fig. 14.17.

5888 In addition, the anticipated new kicker pulse shape will better center the beam on orbit.
 5889 On the detector side, we plan to increase the vertical size of the detectors compared to E821
 5890 (from 14 to 15 cm). This reduces the fraction of lost electrons passing above or below the
 5891 detector, and therefore the sensitivity of the detector acceptance to beam position and width.

5892 In an ideal world, where the detector resolution is uniform around the ring, the CBO
 5893 systematic error averages to zero when all the detected positron pulses are summed up.
 5894 However, for E821 the kicker plate geometry broke significantly the detector resolution sym-
 5895 metry around the ring resulting to a non-zero average. With the new design we expect to
 5896 significantly restore this symmetry.

5897 The combined efforts should reduce the CBO uncertainty by at least a factor of four to
 5898 well below 0.02 ppm. If a new inflector with wider horizontal aperture is used, then it is
 5899 feasible to eliminate the CBO systematic error to well below our sensitivity level.

5900 14.3.2 Electric Field and Pitch Correction

5901 With a vertical magnetic field B_y and radial electric field E_r , the precession frequency is
 5902 given by

$$\omega_a = -\frac{Qe}{m} \left[a_\mu B - \left(a_\mu - \frac{1}{\gamma^2 - 1} \right) \beta E_r \right]. \quad (14.1)$$

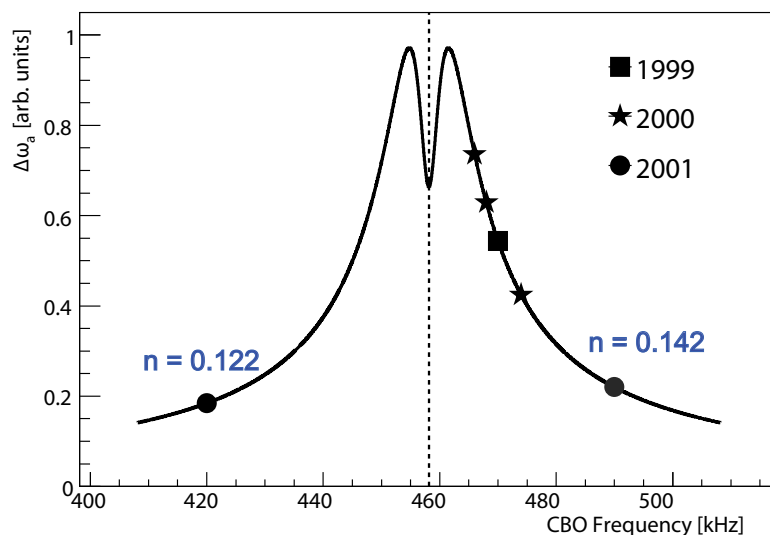


Figure 14.17: The CBO systematic raw error (arbitrary units) as a function of CBO frequency. The year notation indicates the frequencies ran with in E821. For E989 we plan to use much higher field focusing index (see quad section) with a projected CBO frequency of 634 kHz. This frequency will significantly reduce the CBO systematic error.

If B_y and E_r vary with position, the time averages $\langle B_y \rangle$ and $\langle E_r \rangle$ should be used. At exactly the magic momentum the effect from E_r is zero. Muons of slightly higher momentum δp have an equilibrium orbit

$$x_e = \frac{R_o}{1 - n} \cdot \frac{\delta p}{p}.$$

5903 As they oscillate about this equilibrium orbit they experience a mean radial electric field
 5904 $\langle E_r \rangle = n (\beta B_y / R_o) x_e$ and their deviation from the magic momentum is proportional to x_e .
 5905 This leads to a correction to ω_a proportional to x_e^2 . In this experiment n is measured from
 5906 the observed horizontal betatron frequency, and the distribution of muons with respect to x_e
 5907 is found from the modulation of counting rate by the rotation frequency of the muon bunch.
 5908 The observed value of $\langle x_e^2 \rangle$ was confirmed by simulation. The correction is +0.46 ppm.

5909 With electric focusing, the plane in which the muon spin is precessing oscillates vertically,
 5910 exactly following the oscillation of the muon momentum. When the orbit is inclined at angle
 5911 ψ to the horizontal, ω_a is reduced by the factor $(1 - \frac{1}{2}\psi^2)$. If ψ_m is the angular amplitude
 5912 of the vertical oscillation, the average over the ensemble of muons is $(1 - \frac{1}{4}\langle \psi_m^2 \rangle)$ where the
 5913 brackets indicate an average over the muon population, $\langle \psi_m^2 \rangle = n \langle y_m^2 \rangle / r_o^2$ where y_m is the
 5914 amplitude of the vertical oscillation.

5915 Information on $\langle \psi^2 \rangle$ is obtained by simulation in which a representative set of muons is
 5916 tracked around the ring from the inflector exit, via the kicker magnet, for many turns. The
 5917 discrete quadrupole structure and aperture defining collimators are included as well as the
 5918 calculated deviations from a pure quadrupole field. The pitch correction is +0.29 ppm.

5919 A combined (correlated) electric field and pitch correction uncertainty of 0.05 ppm was
 5920 used in E821. We expect to improve on our knowledge of the electric field and pitch cor-

5921 rections by use of a new muon traceback system that can better image the beam motion
 5922 versus time at a number of azimuthal positions around the ring. Furthermore, our simulation
 5923 effort has improved, which is essential to some of these corrections. It is expected to reduce
 5924 the uncertainty on these important corrections and we estimate a final combined error of
 5925 less than 0.03 ppm. Precision tracking simulation using Runge-Kutta integration provides
 5926 enough accuracy to check the size of the pitch effect. Figure 14.18 shows the $(g - 2$
 5927 $- \text{ideal})/(\text{ideal})$ for a single particle with an initial vertical angle of 0.5 mrad, as a func-
 5928 tion of time. The estimated shift converges very quickly to the value estimated analytically
 5929 $(-0.25\theta_0^2 = -6.25 \times 10^{-8})$ to better than sub-ppb, much better than needed for E989.

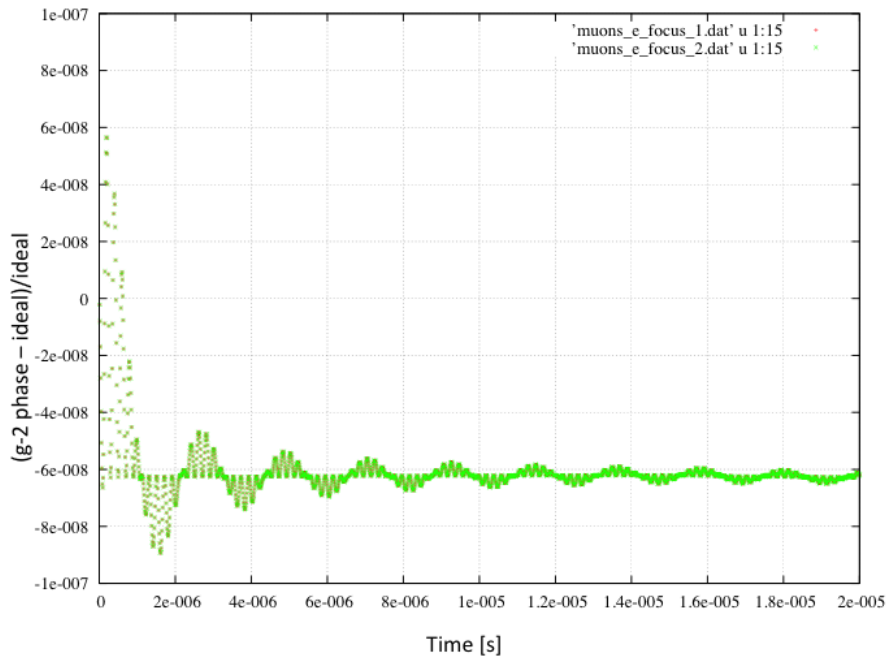


Figure 14.18: Tracking simulation of temporal evolution of relative deviation of $(g - 2)$ phase of a single particle with an initial vertical angle of 0.5 mrad.

5930 14.4 Collimators and Lost Muon Systematic Error

5931 The E821 lost muon systematic error was 0.09 ppm. In this section we discuss how we
 5932 will decrease the lost muon rate with an improved storage ring/collimator system. The
 5933 distortions of the vertical (y) and horizontal (x) closed orbits (CO) due to radial (B_r) and
 5934 vertical B_y multipole magnetic field distortions are:

$$\Delta y_{\text{CO}} = \sum_{N=0}^{\infty} \frac{R_0}{B_0} \frac{B_{rN} \cos(N\Theta + \phi_{yN})}{N^2 - \nu_y^2} \quad (14.2)$$

$$\Delta x_{\text{CO}} = \sum_{N=0}^{\infty} \frac{R_0}{B_0} \frac{B_{yN} \cos(N\Theta + \phi_{xN})}{N^2 - \nu_x^2}, \quad (14.3)$$

Table 14.2: Distortion of the closed orbits for E821 (FNAL) tune values and B_{rN}/B_0 and $B_{yN}/B_0 = 10$ ppm.

N	y_{CO} (mm)	x_{CO} (mm)
0	0.53 (0.40)	0.08 (0.09)
1	0.08 (0.09)	0.53 (0.40)
2	0.02 (0.02)	0.02 (0.02)
3	0.01 (0.01)	0.01 (0.01)

5935 where N is multipole component, $R_0 = 7112$ mm is equilibrium radius, $B_0 = 1.45$ T is central
 5936 value of the dipole magnetic field, ν_x and ν_y are horizontal and vertical tunes, respectively.

5937 For E821, the average radial magnetic field B_{r0} drifted by typically 40 ppm per month,
 5938 which was correlated with temperature changes. About once a month B_{r0} was adjusted with
 5939 the current shims to maximize the number of stored muons, i.e., centering the beam vertically
 5940 in the collimators. From equ. (14.2) $B_{r0}/B_0 = 40$ ppm changes the vertical closed orbit by
 5941 2 mm. At FNAL we plan much better temperature control compared to E821. B_{y1}/B_0 was
 5942 shimmed to < 20 ppm, which distorted the horizontal closed orbit by < 1 mm. For the
 5943 FNAL experiment, we want both of these components < 10 ppm. Other components are
 5944 less important since $\nu_y^2 \approx 0.18$ and $\nu_x^2 \approx 0.82$ are closest to the integers 0 and 1, respectively
 5945 (see Table 14.2). For E821 we used $\nu_y^2 \approx 0.13$ and $\nu_x^2 \approx 0.87$.

5946 The E821 collimators were circular with radius 45 mm. The E821 beta functions vs. ring
 5947 azimuth are shown in Fig. 14.19. The FNAL experiment collimators will be oval with the
 5948 x and y axes modulated by the square root of the beta functions, i.e., ± 0.8 mm in x and
 5949 ± 0.7 mm in y .

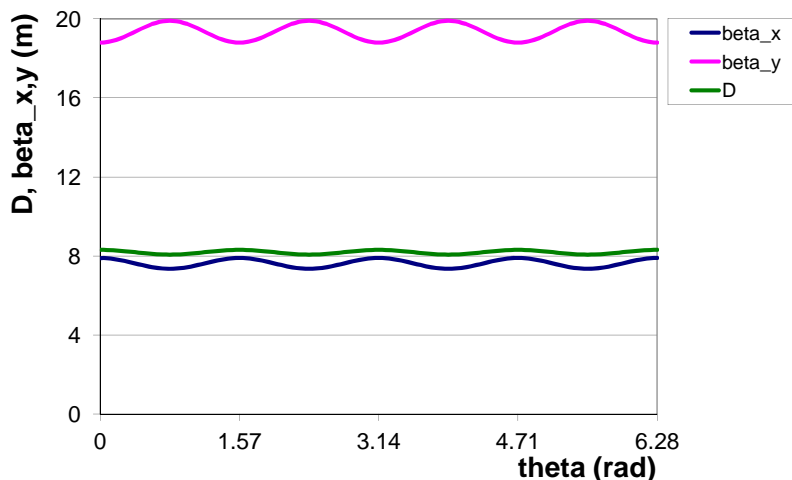


Figure 14.19: E821 horizontal and vertical beta functions.

5950 Fig. 14.20 shows the E821 collimator ring placement. Since the E821 kick extended over
 5951 many turns, we needed “half” collimators just after the kicker and at π radial betatron

5952 phase advance, so that the muons would survive enough turns to get the full kick. The
5953 FNAL kicker is being designed to give the full kick on the first turn. Thus we can go from
5954 3 full collimators and 5 half-collimators to eight full collimators.

5955 We purposely distorted the vertical and horizontal closed orbits by 2.6 mm during scrap-
5956 ing for the first 10^2 turns, but 2.6 mm was not large compared to the above effects. Indeed,
5957 when there were large temperature variations, we sometimes observed that the lost muon
5958 rate went *up* after scraping ended! With better control over the horizontal and vertical orbit
5959 distortions due to B_{r0} and B_{y1} , oval collimators to match the ring beta functions, and eight
5960 full collimators, we anticipate a lost muon rate at FNAL which will be about ten times lower
5961 than E821. The exact lost muon rates will be calculated with tracking simulation. The
5962 collimator positions should be surveyed to better than 0.2 mm. The coefficient of expansion
5963 of steel is $1.3 \times 10^{-5}/\text{C}$; multiplying times the radius of 7.1 m gives 0.1 mm/C.

5964 The collimators are able to be put into the “beam position”, or into the “trolley position”.
5965 The latter is required to run the NMR trolley. We will put one collimator into the beam
5966 position and record the lost muon rate with the lost muon detector. This takes about ten
5967 minutes of data collection. Then we put a second collimator into the beam position. We
5968 will have from simulation how much the lost muon rate should decrease with two collimators
5969 perfectly aligned with respect to the closed orbit. If we dont observe this decrease, we will
5970 remotely position the second collimator in x and y until we achieve the desired result. Then
5971 we put in the third collimator, etc.

5972 14.5 ES&H

5973 Potential hazards of the ESQ system are power system and X-rays.

5974 The system contains both low voltage, high voltage (up to 75 kV) and high current
5975 circuits. There are no exposed electrical terminals. All electrical connections are bolted
5976 and enclosed. Cables will either be run along the floor in cable tray or in double-grounded
5977 conduit. The power supplies and the thyratrons are fused. We will use lock out/tag out
5978 when servicing the unit. When the power supplies are disabled, the storage capacitors will
5979 also be shorted to ground with a safety relay. We do not anticipate that we will need to work
5980 on the unit hot. There are no requirements for emergency power. There will be a remote
5981 control unit in the control room. The operation of ESQ will be limited to system experts
5982 and trained personnel.

5983 Soft X-rays can be produced in the system in spark discharges. Even though the ESQ
5984 system is designed to have no sparks during normal running conditions, sparks are most
5985 likely to occur during conditioning of the system. Aluminum vacuum chambers with 1-cm-
5986 thick walls provided adequate shielding against X-rays in E821. Due to higher operating
5987 voltage in E989 the shielding by vacuum chambers may not be sufficient. We are planning
5988 to develop an integrated X-ray safety plan together with the kicker group.

5989 One of the alternative designs of the outer plate of Q1 quadrupole includes beryllium foil.
5990 Beryllium is ideal material for such purpose due to its mechanical, electrical and magnetic
5991 characteristics. Most importantly, muon scattering in beryllium will be significantly reduced
5992 in comparison with aluminum plate due to lower Z of beryllium. However, beryllium is
5993 a significant health hazard. We are not planning to machine beryllium. The foil will be

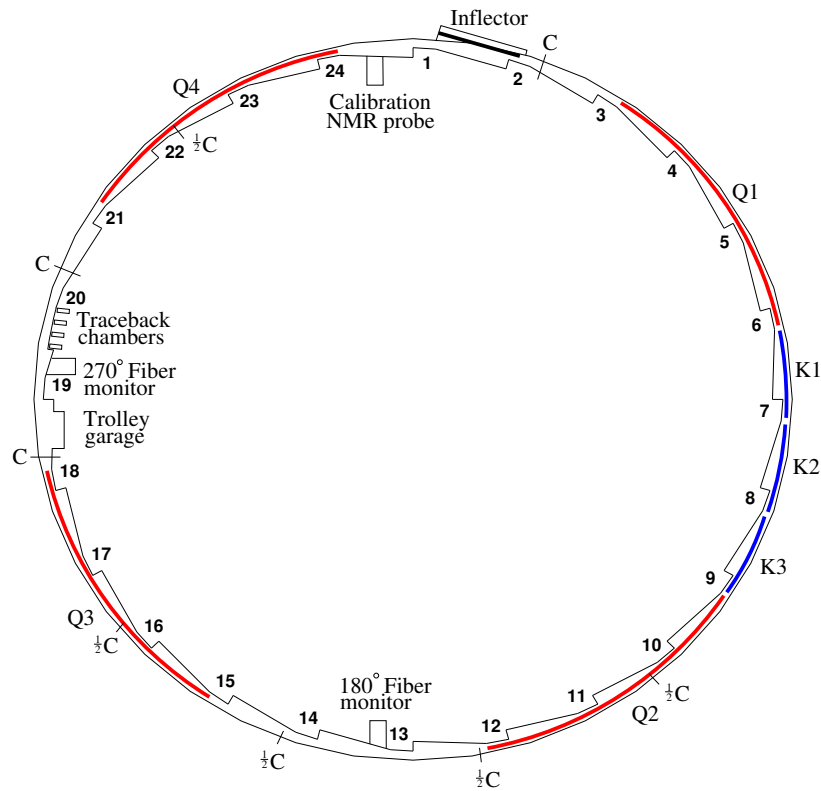


Figure 14.20: Schematic diagram of the E821 ring showing the location of the half and full collimators. For the FNAL experiment, there will only be full collimators.

5994 produced and, presumably, assembled by a certified commercial company. During running
5995 the beryllium plate will be enclosed in vacuum chamber inaccessible to regular personnel.
5996 Only certified personnel will be allowed to perform work on a modified ESQ Q1.

5997 The ESQ design will be reviewed by the (PPD or AD) electrical safety committee. Proper
5998 Operational Readiness Clearance will be obtained before unattended operation of the sys-
5999 tems. Job Hazard Analyses will be performed for any work tasks that involve working on
6000 the high voltage systems.

6001 14.6 Risks

6002 The baseline design is to displace the Q1 outer plate by about 2 cm (the needed displacement
6003 will be determined more accurately by R&D studies). If the baseline design cannot be
6004 achieved for various reasons, we will consider the following alternatives for Q1 outer plate, *i*)
6005 a plate made from a thin beryllium foil, *ii*) a plate made from a thin wire mesh, *iii*) a plate
6006 made from a thinner aluminum foil, *iv*) a plate from other alternative materials (e.g. fiber
6007 carbon). This will lead to the following consequences to the Project

- 6008 • More effort will be needed for R&D studies of alternatives.
- 6009 • Muon scattering in any material will reduce the fraction of stored muons and hence
6010 increase the time required to reach the statistical goal of the experiment. The preferable
6011 material is beryllium.
- 6012 • Beryllium foil will increase the cost of the Project. The cost of the beryllium material
6013 for the plate is about \$16 k per meter. Thus, to cover a 5-m-long quadrupole plate at
6014 least \$90 k in addition will be required not including the manufacturing and assembling
6015 expenses.
- 6016 • Beryllium is a hazardous material. Special handling requirements will complicate ESQ
6017 plate installation and adjustment procedure.

6018 The baseline design is to increase the operating voltage of ESQ to ± 35 kV. The CBO
6019 systematic error will be more challenging to address if this goal is not reached. This will
6020 also increase muon losses.

6021 The ESQ system requires good vacuum to operate properly (10^{-6} Torr or better). Bad
6022 vacuum conditions may lead to inability of ESQ to operate at nominal voltage. One potential
6023 source of vacuum leak is the tracker system. If the leak is too large, additional vacuum
6024 pumps may be needed to pump the vacuum chambers equipped by the tracker system. If
6025 high vacuum conditions are not met with installation of additional vacuum pumps, we may
6026 consider taking production data without tracker system and taking special runs with the
6027 tracker system to measure the distribution of muons in the storage ring. The disadvantage
6028 of such a mode of operation is that the tracker runs will be excluded from the production
6029 dataset.

6030 14.7 Quality Assurance

6031 Reliable operation of the quadrupole system is necessary to achieve the experiment's goals.
6032 We have planned a testing program that includes computer simulations and extensive hard-
6033 ware testing of the ESQ system in advance to installation into the experiment to insure
6034 reliability, and this is accounted for in the cost and schedule estimation.

6035 BNL is establishing a test stand to assess performance of the ESQ system. The test
6036 stand will include C-magnet, vacuum system, high voltage electrical system, high voltage
6037 monitors, electrooptic high-voltage system and the data acquisition system. It will be used
6038 to

- 6039 1. Study the stability of the high voltage with and without magnetic field by pulsing the
6040 plates 10% above nominal voltage.
- 6041 2. Study the mechanical stability of the quadrupole plates under high voltage stress.
- 6042 3. Perform R&D studies of the Q1 outer plate.
- 6043 4. Perform R&D studies of high voltage leads.
- 6044 5. Test the procedure of conditioning the ESQ system.
- 6045 6. Measure the X-rays exposure level due to sparking.
- 6046 7. Develop and test the data acquisition system.

6047 We are planning to install the ESQ system a year in advance of the start of the ex-
6048 periment. This will allow us to test the system in real experimental environment and will
6049 give us sufficient time to make alternation if necessary without delaying the schedule of the
6050 experiment.

6051 To assure the quality of the future experimental data and to identify potential problems
6052 we will continue doing precision computer simulations of two types, OPERA simulations of
6053 the electric field produced by both quadrupole plates and high voltage leads, and tracking
6054 simulations of muons in the electric and magnetic field using **Geant4** and/or independent
6055 dedicated tracking program developed by Y. Semertzidis for E821. The computer simulations
6056 will be backed up by analytic calculations where possible.

6057 14.8 Value Management

6058 The reference design is lower cost than other alternatives we have considered (see discussion
6059 above) and this is the design we will use, provided it meets the requirements. The design
6060 process has benefitted from the experience gained in E821.

6061 The baseline design is to re-use the existing E821 electrostatic focusing quadrupoles.
6062 Some components require cleaning and refurbishing. To meet the statistics goal of the E989
6063 experiment and maximize the number of stored muons we are planning to upgrade the outer
6064 plate of the quadrupole Q1. To meet the systematics goals of E989 we are planning to
6065 modify some components of the EQS system (improve rigidity of ESQ cages to meet new

6066 requirements on alignment precision, redesign high voltage leads to provide the electrostatic
6067 field of better quality, upgrade some components of the high voltage power system to enable
6068 operation at higher field focusing index, etc.). Where possible, the upgrade will reuse the
6069 existing components from E821.

6070 We are planning to re-use the existing Boston waveform digitizer electronics used in muon
6071 lifetime measurements by the MuLan collaboration [4]. The digitizers will be used to record
6072 HV traces from each quadrupole plate (32 channels total).

6073 We are also planning to re-use the existing C-magnet 18C72 for the test stand at BNL
6074 (Fig. 14.21). The magnet requires refurbishing and upgrade to accommodate the $(g - 2)$
6075 vacuum chamber.



Figure 14.21: Photograph of the magnet 18C72 for the test stand at BNL.

6076 14.9 R&D

6077 Work is well underway on R&D studies of quadrupole Q1. The **Geant4** simulations conducted
6078 independently by N.S. Froemming [5] and T. Gadfort [6] were important in guiding the choice
6079 of material for the outer plate of Q1. The preliminary **OPERA** simulations were important
6080 in making the choice of the baseline design of quadrupole Q1 (Fig. 14.12). The tracking
6081 simulations were important in understanding the muon beam dynamics in $(g - 2)$ storage
6082 ring with skew and upright quadrupoles [7, 8]. More precision computer simulations will be
6083 conducted to finalize required tolerances and to quantify systematic uncertainties related to
6084 ESQ system. Extensive tests of a prototype of quadrupole Q1 will be conducted in a test
6085 stand at BNL.

6086 References

- 6087 [1] J. Bailey, et al. Nucl. Phys. B150:1 (1979)
- 6088 [2] G.W. Bennett, et al., Phys. Rev. D 73, 072003 (2006)
- 6089 [3] Y.K. Semertzidis et al., Nucl. Instr. Meth. Phys. Res., A 503 (2003) 458-484
- 6090 [4] V. Tishchenko *et al.* [MuLan Collaboration], Phys. Rev. D 87, 052003 (2013)
6091 arXiv:1211.0960 [hep-ex].
- 6092 [5] N.S. Froemming, “Scattering Through Q1 outer”, g-2 note #567,
6093 <http://gm2-docdb.fnal.gov:8080/cgi-bin/ShowDocument?docid=567>
- 6094 [6] T. Gadfort, “Muon Storage Rate Study”, g-2 note #920,
6095 <http://gm2-docdb.fnal.gov:8080/cgi-bin/ShowDocument?docid=920>
- 6096 [7] Y.K. Semertzidis, “Quadrupoles: Focusing on positive muons”, g-2 note #914,
6097 <http://gm2-docdb.fnal.gov:8080/cgi-bin/ShowDocument?docid=914>
- 6098 [8] V. Tishchenko *et al.*, “Electrostatic Focusing Quadrupoles: Recent studies”, g-2 note
6099 #911, <http://gm2-docdb.fnal.gov:8080/cgi-bin/ShowDocument?docid=911>

Chapter 15

Ring Instrumentation and Controls

This chapter gives a preliminary description of the g-2 cryogenic and vacuum control system. This control system will be a copy of the typical Siemens S7-400 PLC (Programmable Logic Controller) control system as deployed by the Fermilab mechanical department.

The g-2 cryogenic and vacuum system will be located on the Muon campus in the MC1 building, Muon g-2 experimental hall. This area is classified as ODH class 0 area and has several large cryogenic and gas components. Cryogenics include liquid Helium and Liquid Nitrogen.

This cryogenic system has approximately 300 electronic input sensing devices and 50 output devices. Input devices include temperature sensors, pressure transmitters, vacuum gages, level probes, and strain gages. Output devices include solenoid valves, control valves, and vacuum valves and pumps.

All electronic and electrical control system equipment is air cooled and does not require any forced air cooling or water cooling. Cabinet air vents are provided for certain devices where appropriate.

The control system equipment components are all commercially available products which are UL listed. The cryogenic control system has been designed and will be built following all the required rules and standards such as the NEC and NFPA 70E. All premises wiring is to be installed by Fermi Electrical contractors and licensed electricians.

15.1 Cryogenic/Vacuum Control System

15.1.1 Programmable Logic Controller

The g-2 cryogenic/vacuum system will be controlled by a Siemens S7-400 PLC with S7-300 associated I/O modules (or equivalent industrial controls system) networked on a Profibus network. This PLC system will be programmed using the Siemens S7 engineering programming software (or equivalent software meeting IEC 61131-3 standard). Siemens S7-400 PLC systems are currently in use at several Fermilab projects: LAPD, LBNE 35 Ton, Super CDMS, and NML/CMTF. A diagram of the typical PLC in use at Fermilab is given in figure 15.1

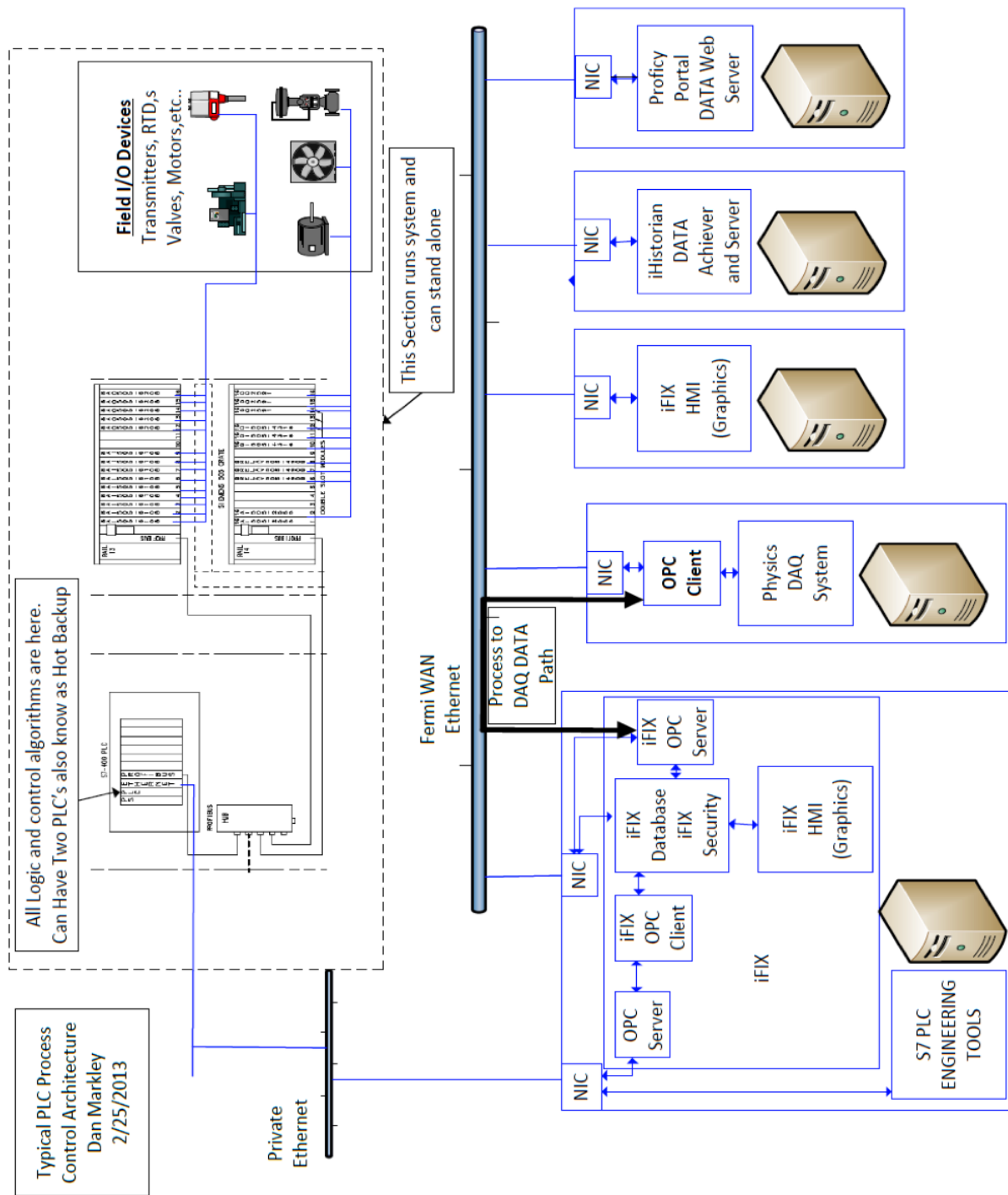


Figure 15.1: Diagram of a typical PLC in use at Fermilab.

6129 **15.1.2 Human Machine Interface**

6130 Human Machine Interface (HMI) controls will be provided through GEFANUCs iFIX soft-
 6131 ware. iFIX connects to the S7-400 through Private Ethernet using an OPC driver purchased

6132 from Kepware. iFIX will handle all operator security, computer alarming, and remote op-
 6133 erator controls via the PPD-iFIX server. iFIX will also provide historical data through the
 6134 PPD-iFIX historian. This historical data will be viewable in iFIX picture displays or on the
 6135 web through the iFIX Proficiency portal server. An example of a HMI for the LAPD experiment
 6136 is shown in figure 15.2.

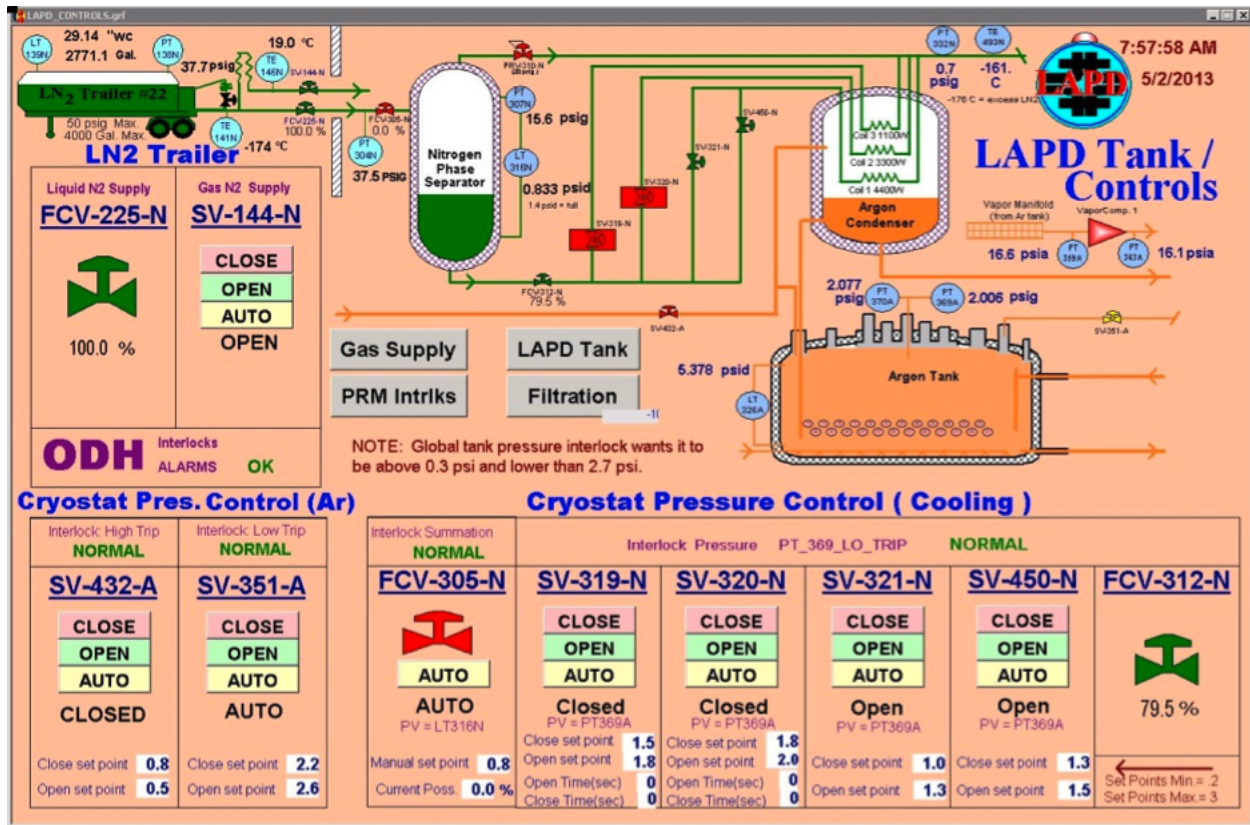


Figure 15.2: Human Machine Interface for the LAPD experiment.

15.2 Life Safety and System Reliability

ODH Control System

6137 The ODH system will utilize four MSA O2 heads. Two O2 heads will be located near the
 6138 ceiling of the g-2 experimental hall, with another two O2 sensors located near the floor of
 6139 the hall. There will be an ODH warning horn and strobe lamp. These will be centrally
 6140 located in the hall. There will be two ventilation fans used to maintain the ODH risk class
 6141 zero status in the g-2 hall. One fan will exhaust air out of the g-2 hall at the ceiling venting
 6142 it outside. The second fan will supply fresh air to the building near the floor outside of the
 6143 rings. These fans are controlled by the S7 PLC and can also be run locally using a switch
 6144 mounted at the fan controls. The ODH system is hardwired to both fans such that during
 6145 an ODH alarm both fans run.
 6146
 6147

6148 The O2 Sensors are MSA model A-UltimaX-PL-A-14-03D2-0000-100 and have a span of
6149 0-25%. Each O2 sensor is to be wired to an MSA electronic controller which provides an
6150 analog output signal wired to the S7 PLC. This MSA electronic unit also provides relays
6151 which have three O2 level alarms thresholds, 18.5%, 18%, and 17.5%. The relay output
6152 that is set at 18.5% is wired directly to the ODH warning horns and strobe lamps located
6153 in MC1 and FIRUS. The MSA electronic unit also provides a trouble relay output which is
6154 also wired to the PLC and FIRUS. The trouble output is wired in a failsafe manner, such
6155 that loss of power or blown fuse to the ODH controls will generate a trouble alarm.

6156 The MSA equipment is wired directly to its own self-contained control circuitry in its
6157 own enclosure. This self contained enclosure has its own power supply which is independent
6158 of the PLC control system, allowing the ODH system to function independently of the PLC
6159 control system. The power for this ODH system comes from a U.P.S.

6160 **15.2.1 Uninterruptible Power Supply (U.P.S.)**

6161 The control system U.P.S. is to be a commercial unit such as those manufactured by Best
6162 power. The U.P.S. input power is fed from a premises powered outlet using the U.P.S. input
6163 line cord. This U.P.S. system will be diesel generator backed. The diesel generator will be
6164 auto start with auto switchover on commercial power loss. There may be other loads on this
6165 generator as well.

6166 The U.P.S. has standard outlets located on the rear of the cabinet. An APC surge
6167 protector is located on the U.P.S. and its input power cord is plugged into the U.P.S output
6168 outlets. All relevant control system loads are plugged into the APC surge protector output
6169 outlets.

6170 **15.2.2 PLC Reliability and Redundancy**

6171 Siemens SIMATIC (S7 PLC and ET200M I/O modules) components meet all relevant in-
6172 ternational standards and are certified accordingly. Temperature and shock resistance are
6173 defined in the SIMATIC quality guidelines, as are vibration resistance or electromagnetic
6174 compatibility. The Siemens S7 PLC system equipment can be redundant at many different
6175 levels, from the PLC CPU (Hot Backup) to the module and instrument level. The level of
6176 redundancy, if any, has not yet been determined for the g-2 control system.

6177 **References**

- 6178 [1] Electrical Design Standards for Electronics to be used in Experiment Apparatus at
6179 Fermilab.
- 6180 [2] EED/Infrastructure Doc. No:H011228A.

Chapter 16

The Precision Magnetic Field: ω_p

In this chapter we present the requirements on the storage ring magnetic field and field measurement, with a conceptual design for fulfilling these requirements. We first consider the field measurement requirements and the recommended design. The requirements on the storage ring magnetic field and recommended design are then discussed.

16.1 Precision Magnetic Field Measurement

16.1.1 Relation between a_μ and ω_p

In an idealized experiment, the anomaly a_μ could be extracted by measuring the difference frequency ω_a between the muon spin ω_s and cyclotron frequencies ω_c for a muon in a storage ring with a perfectly homogeneous magnetic field \vec{B} with no focusing (see Eqn. 3.11):

$$\vec{\omega}_a = -\frac{Qe}{m_\mu} a_\mu \vec{B}. \quad (16.1)$$

The magnetic flux density $|\vec{B}|$ could be determined through proton nuclear magnetic resonance (NMR) measurements via $\omega_p = \gamma_p |\vec{B}|$, where ω_p is the free proton precession frequency and $|\vec{B}|$ is the lab-frame magnetic field which governs muon motion in the storage ring. The free proton gyromagnetic moment ratio γ_p is currently known to 24 ppb [1]. The muon charge to mass ratio appearing in Eq. 16.1 can be expressed in terms of (m_e/m_μ) known to 25 ppb and (e/m_e) known to 22 ppb [1]. Even with measurements of ω_a and ω_p at the ppb level of precision, a_μ could only be extracted to 41 ppb due to uncertainties on these auxiliary ratios. Fortunately the anomaly a_μ is dimensionless and can instead be extracted from the same measurements in terms of a ratio of frequencies and a dimensionless ratio of magnetic moments :

$$a_\mu = \frac{\omega_a/\omega_p}{\mu_{\mu^+}/\mu_p - \omega_a/\omega_p}. \quad (16.2)$$

This is derived from Eq. 16.1 based on relations between fundamental constants, with the requirement that ω_p refers to the free proton precession frequency in the same flux

density \vec{B} seen by the muons. The additional input, $\mu_{\mu^+}/\mu_p = 3.183\,345\,24(37)$ (120 ppb) is determined from the E1054 LAMPF measurement of Zeeman ground state hyperfine transitions in muonium (Mu) [1, 2]. The result is based solely on measured quantities, the validity of the Breit-Rabi Hamiltonian to describe the experiment, and a small (17.6 ppm) bound-state QED correction to the g factor for a muon in muonium (where the uncertainty on the correction is sub-ppb). Alternatively, the same experiment measured the ground state hyperfine interval in muonium, $\Delta\nu_{\text{Mu}}(\text{E1054}) = 4\,463\,302\,765(53)$ Hz (12 ppb), where the theoretical prediction is given by [1]:

$$\Delta\nu_{\text{Mu}}(\text{Th}) = \frac{16}{3} cR_\infty \alpha^2 \frac{m_e}{m_\mu} \left(1 + \frac{m_e}{m_\mu}\right)^{-3} + \text{higher order terms} \quad (16.3)$$

$$= 4\,463\,302\,891(272) \text{ Hz (61 ppb)}. \quad (16.4)$$

The theory uncertainty has a 101 Hz (23 ppb) contribution from uncertainty/incompleteness in the theory calculation, but is dominated by the uncertainty in the mass ratio m_e/m_μ which appears as a parameter in the prediction. The uncertainties on the Rydberg R_∞ and fine structure constant α are negligible in comparison. The hyperfine interval is dominated by QED contributions, but there is a weak contribution $\Delta\nu_{\text{Weak}} = -65$ Hz from Z^0 exchange, a hadronic contribution $\Delta\nu_{\text{Had}} = 236(4)$ Hz, and a hadronic light-by-light contribution of 0.0065 Hz (see references in [1]). Setting $\Delta\nu_{\text{Mu}}(\text{E1054}) = \Delta\nu_{\text{Mu}}(\text{Th})$ can determine the mass ratio (m_μ/m_e) to 25 ppb, which in turn can determine $\mu_\mu/\mu_p = 3.183\,345\,107(84)$ to 26 ppb since

$$\frac{\mu_\mu}{\mu_p} = \frac{m_e}{m_\mu} \frac{\mu_e}{\mu_p} \frac{g_\mu}{g_e}, \quad (16.5)$$

where the uncertainty on μ_e/μ_p is 8.1 ppb and the uncertainty on g_μ/g_e is less than 1 ppb [1].

This determination, which is nearly 5 times more precise than μ_μ/μ_p extracted directly from measurement, requires that the Standard Model fully describes $\Delta\nu_{\text{Mu}}$. However, theories predicting new contributions to the muon anomaly might also lead to new contributions to $\Delta\nu$ that should be considered for consistency.

Given that the difference between a_μ^{E821} and a_μ^{SM} is roughly twice the weak contribution to a_μ , a comparable contribution to $\Delta\nu$ would imply the current theory uncertainty might be underestimated, as would be the 26 ppb uncertainty assigned to μ_μ/μ_p . A more precise, independent measurement of μ_μ/μ_p , planned at J-PARC, would be very helpful. Note however, that even in the absence of a new measurement, any BSM theory can be tested against E989 at the 0.14 ppm level as long the BSM contributions to $\Delta\nu$ are considered simultaneously and the uncertainties on the contributions are less than 25 ppb.

Finally, we note that the appearance of g_μ in Eqn. 16.5 entails that it appears indirectly in Eqn. 16.2 when the value of μ_μ/μ_p is used which depends on muonium hyperfine theory. This redundancy can be eliminated by using:

$$a_\mu = \frac{g_e}{2} \frac{\omega_a}{\omega_p} \frac{m_\mu}{m_e} \frac{\mu_p}{\mu_e}. \quad (16.6)$$

6236 16.1.2 Physics Requirements on ω_p

6237 Based on the above approach for a_μ , our goal for the total uncertainty on ω_p in E989 is
6238 $\delta\omega_p \leq 0.07$ ppm, roughly a factor of three smaller than was achieved in E821. Here ω_p refers

6239 to the free proton precession frequency weighted by the muon distribution in the storage
6240 ring.

6241 16.1.3 Error budget for the ω_p measurement

6242 The systematic errors on the field measurement from E821 are listed below in Table 16.1. The
6243 sources of these uncertainties are discussed in the rest of this chapter. The final column lists
6244 the uncertainties currently anticipated for E989. The recommended hardware and procedures
6245 to achieve these uncertainties are the main content of this chapter.

Source of errors	R99 [ppm]	R00 [ppm]	R01 [ppm]	E989 [ppm]
Absolute calibration of standard probe	0.05	0.05	0.05	0.035
Calibration of trolley probes	0.20	0.15	0.09	0.03
Trolley measurements of B_0	0.10	0.10	0.05	0.03
Interpolation with fixed probes	0.15	0.10	0.07	0.03
Uncertainty from muon distribution	0.12	0.03	0.03	0.01
Inflector fringe field uncertainty	0.20	–	–	–
Time dependent external B fields	–	–	–	0.005
Others †	0.15	0.10	0.10	0.03
Total systematic error on ω_p	0.4	0.24	0.17	0.070
Muon-averaged field [Hz]: $\tilde{\omega}_p/2\pi$	61 791 256	61 791 595	61 791 400	–

Table 16.1: Systematic errors for the magnetic field for the different run periods in E821. R99 refers to data taken in 1999, R00 to 2000, R01 to 2001. †Higher multipoles, trolley temperature and its power supply voltage response, and eddy currents from the kicker.

6246 It is important to note the steady reduction in uncertainties achieved in E821. The goal
6247 of 0.070 ppm uncertainty on ω_p for E989 in Table 16.1 reflects the current estimates of what
6248 can be achieved based on the experience in E821 and following the approach outlined below.

6249 16.2 Recommended Design

6250 E989 will largely use the principles and field measurement hardware originally developed at
6251 the University of Heidelberg and Yale that were employed successfully in E821 at BNL [5]
6252 and E1054 at LANL [2]. The E821 field measurement electronics and the underlying physics
6253 are described in [3]. The calibration of the field measurements in terms of the equivalent free
6254 proton precession frequency using an absolute calibration probe is described in [4]. Details
6255 of the E821 field analysis, systematics, and of the hardware are described in the final E821
6256 paper [5], and in several theses [6, 7, 8].

6257 While E821 achieved an uncertainty $\delta\omega_p \approx 0.17$ ppm, E989 will have to implement
6258 specific changes to the hardware and techniques to reduce the systematic errors to a final
6259 goal of $\delta\omega_p \approx 0.07$ ppm. The recommended E989 hardware, techniques, and changes from
6260 E821 will be discussed in the rest of this chapter.

16.2.1 Overview of field measurement using NMR

Pulsed Nuclear Magnetic Resonance (NMR) is at the heart of the magnetic field shimming, measurement and control systems, since it can measure magnetic fields to absolute accuracies of tens of parts per billion (ppb).

The pulsed NMR hardware developed for E821, which produced and detected the free induction decay (FID) signals from protons in water has already demonstrated single shot accuracy at the level of 10 ppb [3], and absolute calibration in terms of the free proton precession frequency at the level of 35 ppb [4]. The challenge of the field measurement is to effectively transfer this absolute calibration to the many NMR probes required to monitor the field in the large volume and over the long periods of time in which muons are stored.

There are four major tasks required from the NMR system:

- (1) Monitoring the field when muon data are being collected;
- (2) Mapping the storage ring field when the beam is off;
- (3) Providing an absolute calibration relating field measurements to the Larmor frequency of a free proton;
- (4) Providing feedback to the storage ring power supply when muon data are collected.

We start with a brief description of NMR, explain the field measurement tasks in more detail, then describe the required hardware.

Field measurement with NMR

Precision measurements of the magnetic field are made by inducing and detecting the free induction decay (FID) signal of protons in water using NMR [9, 10, 3]. The water samples are located in small volumes (typically $<1 \text{ cm}^3$) surrounded by a coil L_s and the rest of the body of an NMR probe. The probes used for these purposes are shown in Figs. 16.1 and 16.2. Several hundred fixed probes are located around the azimuth of the ring, just above and below the muon storage volume. Other sets of probes are pulled through the storage volume in a trolley used to determine the field seen by the muons. A final set of probes is used for calibration.

In a typical measurement, an RF pulse at $f_{\text{ref}}=61.74 \text{ MHz}$, is used to produce a linearly polarized rf magnetic field in the coil L_s , orthogonal to the storage ring dipole field. This rotates the magnetization of the protons in the sample so it is perpendicular to the main field of 1.45 T. After the pulse, the proton spins precess coherently in the external field at the proton magnetic resonance (Larmor) frequency $f_{\text{NMR}} \approx 61.79 \text{ MHz}$. The magnetic field from the rotating magnetization induces an electromotive force in the coil L_s which is called the NMR signal. This signal typically decays exponentially with a time constant of approximately 1 ms. The coil (which is used for both excitation and detection) is part of a circuit with a capacitor C_s in series to form a resonant circuit at the NMR frequency f_{NMR} with a quality factor Q typically between 30 and 100. An additional coil in parallel, L_p is used to match the impedance of the probe at f_{NMR} to the 50Ω impedance of the cable. The NMR signal propagates through a cable to a duplexer which directs the signal to a low-noise preamplifier. The amplified signal is mixed with the synthesizer frequency f_{ref} , and the

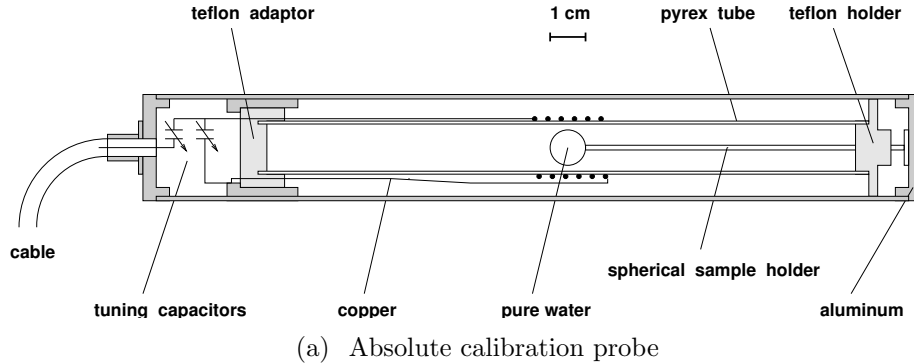


Figure 16.1: (a) Absolute calibration probe featuring a spherical sample of water. This probe and its driving and readout electronics are the very same devices employed in reference [2] to determine λ , the muon-to-proton magnetic-moment ratio. (b) The spherical Pyrex container for the absolute probe.

6303 difference frequency $f_{\text{NMR}} - f_{\text{ref}} \equiv f_{\text{FID}}$ goes through a low pass filter and is amplified. This
 6304 signal is referred to as the FID (free induction decay). The frequency of the FID, f_{FID} , is
 6305 sensitive to the local field value and is of order 50 ± 5 kHz. The exact frequency is determined
 6306 by counting zero crossings of the FID and those of a 20 MHz clock in a counter until the
 6307 signal has decayed to about $1/e$ of its peak value, which takes of order 1 ms. The local
 6308 magnetic field is then characterized by the frequency $f_{\text{NMR}} = f_{\text{ref}} + f_{\text{FID}}$ with a resolution
 6309 approaching 20 ppb.

6310 As discussed below, the reference frequency $f_{\text{ref}} = 61.74$ MHz is chosen such that $f_{\text{ref}} <$
 6311 f_{NMR} , and is obtained from a frequency synthesizer phase locked to a Rb frequency standard
 6312 stabilized by GPS. The same Rb standard will provide the time base for the ω_a measurement.

6313 16.2.2 The Fixed Probe NMR system

6314 The purpose of the fixed probe system is to accomplish the first task of monitoring the field
 6315 continuously while muon data are being collected. The fixed probe system consists of the
 6316 fixed NMR probes and the accompanying VME system, DAQ, pulser, mixer, multiplexers,
 6317 and digitizers. A block diagram of the recommended system is shown in Fig. 16.3.

6318 The recommended design consists of a set of 378 NMR probes at 72 locations in azimuth
 6319 around the ring. The number of probes at each azimuthal position alternates between two
 6320 probes at radii of 7112 and 7142 mm, or three probes at radial positions of 7082, 7112, and
 6321 7142 mm, where the probes are placed in matching grooves on the upper and lower surfaces
 6322 of the storage ring vacuum chambers. From this geometry the fixed probes provide a good
 6323 monitor of the dipole field around the ring, with some sensitivity to changes in the skew and
 6324 normal quadrupole components.

6325 Groups of 20 probes are connected to a single analog multiplexer. Twenty multiplexers
 6326 are required to handle all of the fixed probes. The plunging probe and the absolute cali-

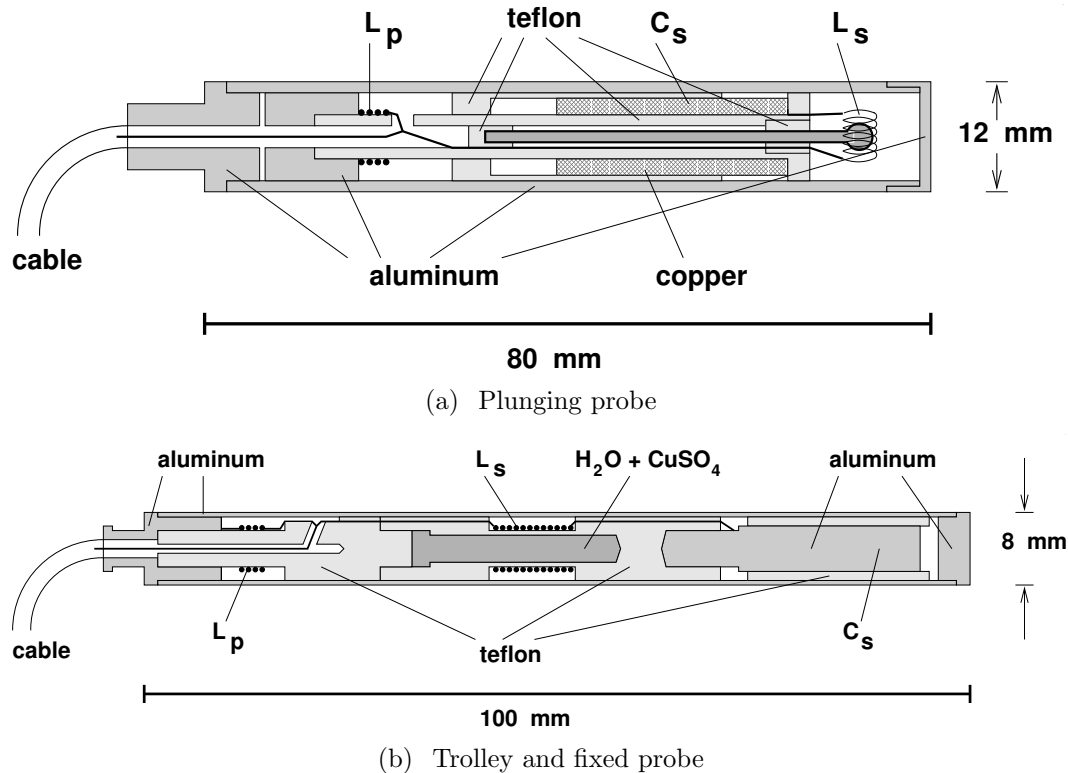


Figure 16.2: (a) Plunging probe, which can be inserted into the vacuum at a specially shimmed region of the storage ring to transfer the calibration to the trolley probes. (b) Schematic of the probes used in the trolley and as fixed probes. The resonant circuit is formed by the two coils with inductances L_s and L_p and a capacitance C_s made by the Al-housing and a metal electrode. The active water volume has a diameter of 2.5 mm and a length determined by the coil L_s of 15 mm.

6327 bration probe (see below) are also connected to one of the multiplexer inputs. In a typical
 6328 measurement sequence, one probe from each multiplexer will be excited and its FID passed
 6329 to a frequency counting module (there are 20 of these). Roughly 0.2 s later, a second probe
 6330 is selected, excited, and read out. Given this 5 Hz rate per multiplexer and 20 multiplexers,
 6331 100 probes are read out per second, and all fixed probes are read out every 4 seconds while
 6332 muons are stored.

6333 In E821, roughly half of these fixed probes were used to monitor the storage ring field.
 6334 Of the remainder, some probes were noisy, and a significant number of fixed probes were
 6335 located in regions near the pole-piece boundaries, where the local magnetic field gradients
 6336 were sufficiently large to reduce the free induction decay time in the probe. This limited the
 6337 precision of the frequency measurement.

6338 In E989 several steps will be taken to increase the number of useful probes. First, finite
 6339 element analysis of the vacuum chambers indicates that the grooves containing the probes can
 6340 be extended without significantly increasing the deflection of the chambers under vacuum.
 6341 This will allow probes to be moved farther from pole boundaries, increasing the number of

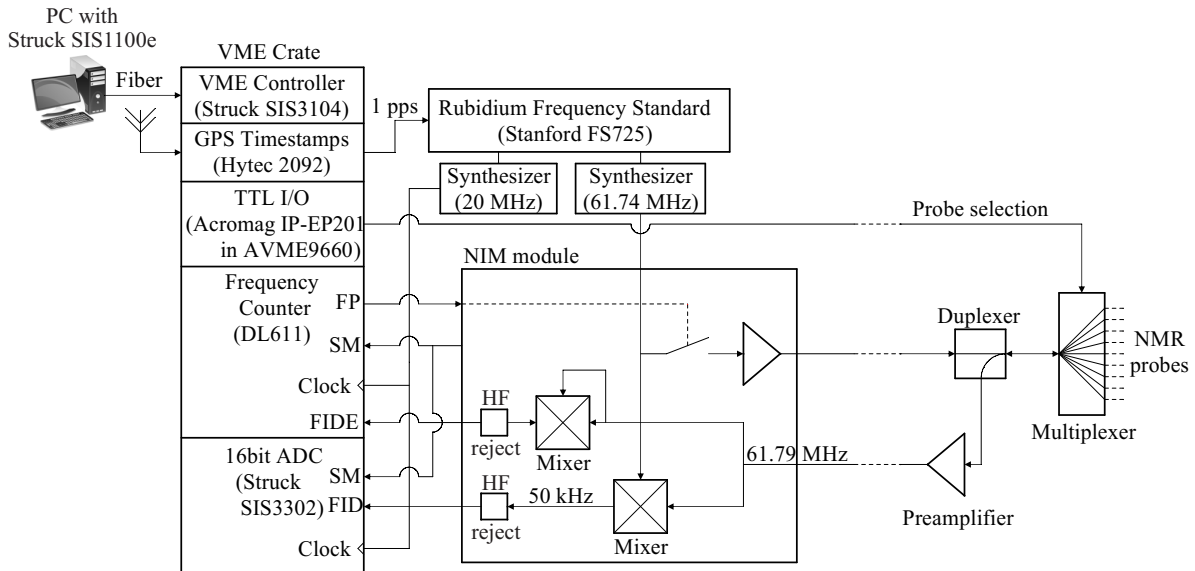


Figure 16.3: A schematic of the fixed probe system. The system consists of a set of NMR probes close to the muon storage volume connected to multiplexer boxes that sit on the storage ring magnet. The multiplexers, which contain the duplexers and preamplifiers, are connected to NIM modules and a VME system and DAQ that sit in the counting house. The functions of each element are described in the text.

6342 useful probes. Second, in E821 the majority of the NMR samples in the fixed probes were
 6343 cylinders of water. Over the course of the experiment, the water samples could evaporate. In
 6344 E989, the possibility of replacing the water samples with petrolatum (CAS 8009-03-8) will
 6345 be explored. Petroleum jelly was observed in E821 to have several advantages over water:
 6346 low evaporation, a proton NMR signal comparable in magnitude and frequency to water.
 6347 Further, the temperature coefficient of its chemical shift is smaller than that of water, which
 6348 provides greater immunity from temperature changes for our experiment. In addition, it has
 6349 favorable relaxation times; preliminary measurements at U. Michigan indicate T_2 of order 40
 6350 ms. Third, during the refurbishment of the E821 probes (see below), any defective electrical
 6351 contacts which led to poor signal quality will be improved. Finally, the NMR electronics of
 6352 E821, which extracted precession frequencies by counting zero-crossings of FIDs mixed down
 6353 to the 50 kHz range, will be supplemented with a high-performance set of digitizers. The 16
 6354 bit (13 bits effective), 20 MS/sec digitizers (Struck SIS 3302) will allow useful information
 6355 to be extracted from probes with short signals. In addition, higher resolution is possible by
 6356 interpolating the positions of zero-crossings. Fitting the signals around zero crossings can
 6357 help when dealing with probes with poor signal to noise. Digitizers will allow the lineshape
 6358 (and changes in the lineshape) to be extracted from the Fourier transform of the signals.
 6359 This may allow a more robust extraction of the average field compared to counting zero
 6360 crossing when the digitization noise is comparable or less than the signal to noise of the FID,
 6361 since the zero-crossing rate itself is time-dependent when the lineshape is asymmetric.

6362 16.2.3 Fixed Probes for E989

6363 The same basic probe design from E821 is recommended for E989 (see Fig.16.2(b)). Materials
6364 used to construct the probes, mostly aluminum and teflon (PTFE), have low susceptibility
6365 and the coax cable has copper conductors instead of the more common copper-plated steel.
6366 Each probe's outer aluminum shell has a diameter of 8 mm, which fits in grooves machined
6367 into the outside surface of the top and bottom plates of the vacuum chamber. The probe's
6368 outer shell and the inner body form the capacitor C_s , which in series with L_s makes a
6369 resonant circuit. C_s is adjusted by moving a PTFE sleeve in and out to tune the circuit to
6370 the frequency ω_p . The circuit quality factor $Q \approx 30$ corresponds to a bandwidth of 3% which
6371 is the range over which the magnetic field can be measured without retuning the probes.
6372 A coil in parallel, L_p , allows for tuning the impedance of the probe to 50Ω for optimal
6373 transmission.

6374 Resurrecting the existing E821 measurement system requires a complete working set of
6375 probes provided either by refurbishing existing ones or constructing new ones.

6376 Refurbishing existing probes:

6377 In E821 the sample volume was filled with water doped with CuSO_4 . This dopant is para-
6378 magnetic and is used to shorten the magnetization recovery time T_1 so measurements can
6379 be made more frequently. For pure H_2O , $T_1 \approx 3.5\text{s}$, so consistent free-induction-decay NMR
6380 measurements could only be taken every 10-15 seconds. However, paramagnetic impurities
6381 also shift the measured frequency, and changes in the CuSO_4 concentration, for example due
6382 to slow evaporation of the water, will affect the stability of the measurement. An examina-
6383 tion of probes from E821 indicated that in some probes water had leaked and corroded part
6384 of the probe. These probes need to be rebuilt. To prevent similar difficulties in E989, we are
6385 investigating the use of petroleum jelly in place of the CuSO_4 -doped water. This idea was
6386 implemented in some fixed probes of E821 by R. Prigl. We have recently measured the NMR
6387 relaxation times of a sample of petrolatum at 0.4 T using saturation-recovery (for T_1) and a
6388 standard spin-echo sequence (for T_2) at Michigan. We find $T_2 \approx T_1 \approx 40$ ms, which is long
6389 enough for very high resolution frequency determination, and will not restrict T_2^* which is
6390 typically limited to a few milliseconds by local field gradients. The temperature dependence
6391 of the diamagnetic shielding is also crucial. Preliminary work in E821 indicated the temper-
6392 ature coefficient of the chemical shift is smaller than in water, providing greater stability. (A
6393 measurement of the temperature dependence at 1.5 T using a warm-bore superconducting
6394 solenoid magnet is under preparation at Michigan. A temperature controlled plug containing
6395 a fixed probe with a petrolatum will be placed in the bore, which is thermally isolated from
6396 the superconducting coil to measure the temperature dependence.)

6397 The scale of the refurbishing effort can be estimated from tests on about 40 fixed probes
6398 from E821. The results indicated that about 1/4 of the probes had water leaks and corrosion,
6399 and will need to be rebuilt. Another area of some concern occurs where the coil wire and
6400 coax cable shield are bonded to the aluminum parts with low temperature solder. These
6401 connections require inspection and all broken connections will require re-soldering. Once a
6402 decision regarding the use of petroleum jelly has been made, all probes will be refilled, tuned
6403 and checked for correct functioning.

6404 An existing dipole magnet at University of Washington (UW) has been re-purposed to
6405 provide the 1.45 Tesla field required for testing the probes. Its field is uniform to 100 ppm/cm
6406 but will be shimmed to 10 ppm uniformity over the active volume of the probe to increase
6407 the duration of the NMR signal. A Metrolab PT 2025 Teslameter with 10 ppm accuracy is
6408 used to independently map the field in the magnet. A test facility to provide the $\pi/2$ pulse,
6409 send/receive duplexer switch and preamplifier that does not require the E821 electronics has
6410 been set up at UW.

6411 **Constructing new probes:**

6412 Any new probes constructed must meet the above geometry and materials requirements
6413 including any solders used to bond the wires. The probes will be reverse engineered and
6414 CAD drawings produced. In consideration of the quantity, new parts will be produced using
6415 computer numerically controlled mills and lathes at the UW machine shop. Metric sized
6416 aluminum tubing 8 mm \times 0.5 mm and 7 mm PTFE rods are available in the European
6417 market. After the parts are completed the coils will be wound and the same procedure as
6418 for refurbishing will be followed.

6419 **Testing the probes:**

6420 For each probe, the resonant circuits are tuned to 61.79 MHz and 50 Ω impedance using a
6421 vector impedance meter. The resonance is then excited in the probe and if the free induction
6422 decay (FID) is observed with sufficient signal to noise ratio SNR, the probe passes the test.
6423 In the E821 system the SNR at the beginning of the FID was \approx 300:1.

6424 **16.2.4 Multiplexers**

6425 Groups of up to 20 fixed probes are connected to a single multiplexer a few meters away,
6426 which sits on top of the magnet. The multiplexer design is described in [3, 6]. It is a self-
6427 contained electronic module that selects one of 20 NMR probes based on the bit pattern of
6428 5 TTL-levels which are set in the counting house, and which arrive on a DB-9 connector.
6429 The TTL signals control PIN diodes in the multiplexer that direct an RF $\pi/2$ pulse, coming
6430 from the NIM modules in the counting house, to tip the spins in the selected NMR probe.
6431 To improve the isolation of open switches, effective- $\lambda/4$ lines are incorporated. A duplexer
6432 (basically a transmit/receive switch) in the multiplexer directs the output of the RF pulse
6433 towards the NMR probe, while isolating the pulse from a sensitive low-noise preamplifier.
6434 After the RF pulse, the duplexer directs the low-level FID precession signal to the low-noise
6435 preamplifier, which has a gain of approximately 60 dB. The multiplexer requires an external
6436 source of power, +15 Volts at 0.3 Amperes. The switches, duplexer, and TTL integrated
6437 circuits are fabricated with discrete surface mount components, and replacements are readily
6438 available.

6439 In E821 the preamplifier consisted of two RF amplifier modules, UTO-101 and GPD-
6440 201 made by AvanteK, a company no longer in existence. An important characteristic of
6441 these amplifiers is their rapid recovery from an overload condition as experienced when
6442 the probe is excited. While some AvanteK products are still sourced at Teledyne-Cougar,

6443 future supplies are not guaranteed. For existing modules we will procure spare Avantek
 6444 products. In constructing new multiplexer modules for E989, a new preamplifier design will
 6445 be considered.

6446 16.2.5 Pulser and Mixer

6447 Each of the 20 multiplexers is connected to a single width NIM module located in the counting
 6448 house. These function as the receiver and transmitter (pulse generator) for the NMR fixed
 6449 probes. The pulse generator creates the $4 \mu\text{s}$ $\pi/2$ pulse at $\nu_{\text{ref}} = 61.74$ MHz and sends it
 6450 through a custom made 10-watt class C amplifier to the multiplexer. In the receiver part of
 6451 the module, the amplified NMR signal from the multiplexer, which is at the Larmor frequency
 6452 $\nu_L \approx 61.79$ MHz, is mixed with the frequency synthesizer output in a double balanced mixer.
 6453 The intermediate frequency output at the difference frequency $\nu_L - \nu_{\text{ref}}$ is selected by a low
 6454 pass filter and further amplified. This signal (at roughly 50 kHz) is referred to as the FID
 6455 (free induction decay) of the NMR probe. In a second branch of the receiver, the envelope
 6456 of the NMR signal, called FIDE, is constructed by multiplying the preamplifier output by
 6457 itself and filtering out the $2\nu_L$ component. A TTL SM (signal measure) pulse is generated in
 6458 the NIM module roughly $10 \mu\text{s}$ after the end of the RF pulse. This pulse goes to the custom
 6459 Heidelberg DL611 frequency counter module in the NMR VME crate (discussed below) to
 6460 start the zero crossing counter. The delay accomodates dead time in the preamplifier located
 6461 in the multiplexer as well as transients such as those from ringdown of the L_s coil and decay
 6462 of the transient response in the low-pass filter after the mixer.

6463 The inputs and outputs of the NIM modules are shown in Fig. 16.3. The inputs are the
 6464 TTL FP (fire pulse) which starts the RF pulse generator. The FP signal is generated in
 6465 the DL611 frequency counter modules in the VME crate. A second input is the synthesizer
 6466 reference at 61.74 MHz, and the NMR probe signal from the multiplexer preamplifier. The
 6467 outputs are the $\pi/2$ pulse, a TTL signal whose width is the dead time of the receiver (the
 6468 SM signal), the FIDE and two channels of the FID (one for the zero-crossing counter and
 6469 one for a digitizer in the VME crate).

6470 This module contains mostly surface mount and integrated circuit components and re-
 6471 placements are readily available. The exceptions are 5 amplifiers GPD-201, GPD-202, and
 6472 3 GPD-462 made by Avantek, which no longer exists. The most likely point of failure in
 6473 the 10 watt class C amplifier is a DU2820S MOSFET, which is still available and could be
 6474 replaced if necessary with little difficulty. Replacement amplifiers exist but they tend to
 6475 be wide band class A amplifiers which are less efficient. In constructing new pulser/mixer
 6476 modules, using a class A or class AB amplifier would require that it be mounted external
 6477 to the NIM module to dissipate the additional heat. Modular high performance commercial
 6478 RF amplifiers are available from Amplifier Research and other vendors.

6479 16.2.6 Frequency Reference

6480 The $(g - 2)$ experiment is essentially a measurement of the ratio ω_a/ω_p . Its goal is to achieve
 6481 relative uncertainties of 0.07 ppm for both of these frequencies. Frequency references are
 6482 necessary for both of these measurements, and the contribution to the uncertainty budget
 6483 from uncertainties in the reference should be made negligible.

6484 The NMR system requires a frequency synthesizer at 61.74 MHz which is amplified and
 6485 pulsed for manipulating the proton spins in the NMR probes. The FID at the Larmor
 6486 frequency (typically 61.79 MHz) is mixed down by subtracting the 61.74 MHz reference.
 6487 The frequency of the resulting 50 kHz signal is determined by counting zero crossings with
 6488 respect to a 20 MHz clock for the fixed probes or the 61.74 MHz reference clock for the probes
 6489 in the trolley. The accuracy goal for the ω_p determination requires that the 61.74 MHz and
 6490 20 MHz clocks be accurate at the ppb level. Since the NMR clocks and the clock used by
 6491 the waveform digitizers to determine the muon spin precession frequency are phase-locked to
 6492 the same master clock, the variations in the master clock frequency drop out to first order,
 6493 and the ppb-level accuracy requirement is reduced to be less than about 10^{-5} . Nevertheless,
 6494 to simplify the study of systematic uncertainties in the magnetic field, our goal is to have
 6495 relative uncertainties in the reference clock frequencies be less than 1 ppb. This uncertainty
 6496 must be achieved for short times, that is, for a single NMR measurement that takes about a
 6497 few milliseconds where phase noise is the limiting factor. The long-time drift over the course
 6498 of the experiment, that is, several years, should also be less than 1 ppb.

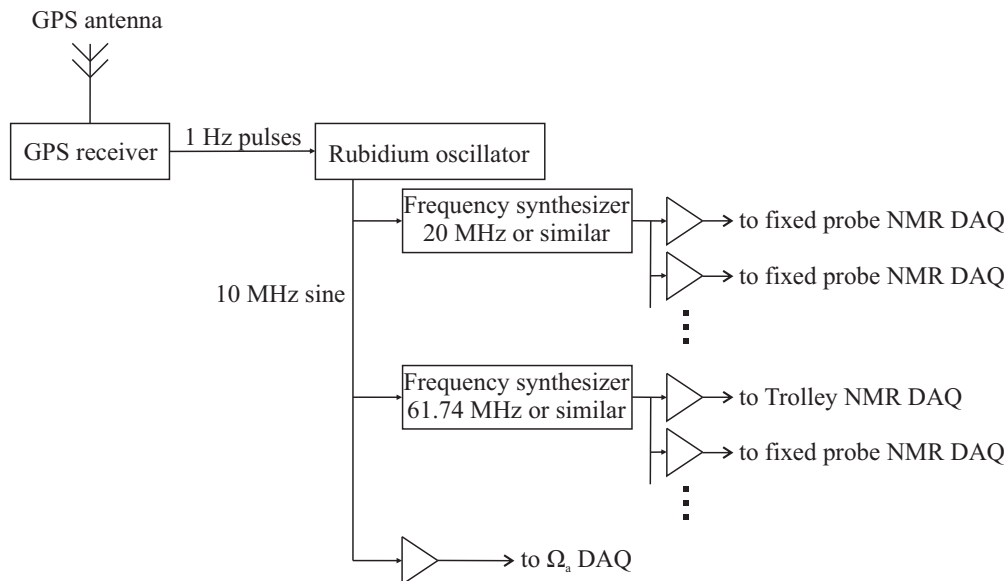


Figure 16.4: Scheme for common master-clock.

6499 Figure 16.4 shows how the reference frequencies are generated. The master clock is
 6500 planned to be an atomic rubidium oscillator that is disciplined by GPS for better long-term
 6501 stability. It generates a master frequency that is a sine wave, usually at 10 MHz. The master
 6502 frequency is distributed to the data acquisition system for ω_a , where frequency synthesizers
 6503 are used to transfer the master clock frequency to the clock frequency needed by the waveform
 6504 digitizers. It is also used as input for the frequency synthesizer responsible for the reference
 6505 frequency ω_{ref} , and for another synthesizer responsible for the fixed 20 MHz frequency signal.
 6506 Frequency synthesizers in both systems should have resolutions of about 1 ppb, to allow for
 6507 some variability in the frequency that can be used for blinding schemes and for tests of
 6508 systematics. It is the synthesized frequencies that must fulfill the accuracy requirement

6509 discussed above. Master clock and synthesizers that fulfill the requirements given above are
6510 available from vendors including EndRun Technologies (vendors for Meridian Precision GPS
6511 Frequency Standard), Precision Test Systems, Symmetricon, Agilent, and Stanford Research
6512 Systems. Distribution amplifiers from vendors including Stanford Research Systems and
6513 Mini-Circuits can distribute the master clock and the needed reference frequencies to the
6514 places where they are needed. There is experience in the collaboration in the specification
6515 and use of these systems from E821 and, more recently, from the clock system used for the
6516 MuLan experiment at PSI in Switzerland.

6517 **16.2.7 NMR VME System and DAQ**

6518 The fixed probe NMR system will be controlled by a VME crate in the counting house,
6519 performing similar functions as in E821 but with updated hardware for E989.

6520 The NMR VME system (see Fig. 16.3) is required to perform the following tasks: (1)
6521 Send a bit pattern to each multiplexer that encodes which NMR fixed probe to use (2) Send
6522 FP (fire pulse) signals to the NIM modules in an adjacent crate, (which send the RF $\pi/2$
6523 pulses to the fixed probes) (3) Count zero crossings of the FIDs from the NIM modules (4)
6524 Send the zero crossing data and a timestamp to a PC to be recorded.

6525 The Eltec 9 VME crate controller used in E821, which ran the realtime operating system
6526 OS9, no longer works and must be replaced. The original E821 NMR VME crate, which was
6527 customized with the addition of -5V power supply to run the Heidelberg DL611 frequency
6528 counter modules, is still operational.

6529 For E989 the recommended design replaces the Eltec controller with a Struck SIS1100
6530 VME crate controller which connects via a fiber optic cable to a Struck SIS3104 PCIe card
6531 on a PC running Scientific Linux. The new controller is compatible with the VMEbus
6532 IEEE-1014 standard E821 crate, and with the faster 2eVME bus cycles of VME64x systems.

6533 To accomplish task (1) above, a 5-bit pattern using TTL levels must be set in each of
6534 the 20 multiplexers, and is used to select which of the 20 fixed NMR probes is to be used.
6535 In E821 these levels were set by two custom VME modules made at Heidelberg (module
6536 number DL620). These modules still work, but a commercial solution will be sought as
6537 replacement in case of failure and to allow more multiplexers to be added easily. Possible
6538 solutions include an Acromag AVME9660 VME carrier card for up to 4 IP-EP201 FPGA
6539 Digital I/O modules with 48 TTL lines each. FPGA I/O modules using high-speed USB
6540 or PCIe interfaces are also possible but a VME-based solution is preferred. The latter is
6541 more portable (modules reside in a single crate) and flexible (allows the VME crate to placed
6542 in the experimental hall and controlled by the PC over a single fiber optic cable), and the
6543 software should be easier with just a single interface to deal with.

6544 To accomplish task (2), the fire pulse (FP) TTL signal can be issued by the Heidel-
6545 berg DL611 frequency counter modules. There are 5 DL611 modules, and each one can
6546 issue 4 independent FPs, allowing 20 NIM modules to be controlled. These DL611 modules
6547 still function and will be used as is in E989. New modules acting as spares based on the
6548 DL611 design will be made at the Center for Experimental Nuclear Physics and Astrophysics
6549 (CENPA) at the University of Washington. These additional modules will allow more multi-
6550 plexers to be controlled if more fixed probes are added. Note that the new digital I/O cards
6551 could also be used to issue the FP signals.

6552 Task (3) which involves counting the FID zero crossings will be accomplished with the
6553 existing DL611 modules and with the spares that are constructed. The DL611 modules,
6554 which are described in [3], count the zero crossings, k , of the FID till the FIDE signal
6555 falls below an adjustable threshold or until a maximum time has elapsed. Over the same
6556 interval the ticks, N , of an external clock at $\nu_{\text{clock}}=20$ MHz are counted. This 20 MHz clock
6557 signal is an input on the front panel of each DL611, and comes from a stabilized frequency
6558 synthesizer. For both counters the start and stop coincide with a positive zero crossing of
6559 the FID. The frequency of the FID is $\nu_{\text{FID}} = k \times \nu_{\text{clock}}/N$. For FID signals exceeding 1 ms,
6560 the uncertainty on the frequency due to the discretization of the clock counts is roughly 8
6561 ppb or less. The uncertainty on the frequency due to the finite signal-to-noise of the FID
6562 (typically $S/N \approx 100$ when FIDE falls below threshold) is given roughly by $\sigma_s/(S/N)$ where
6563 σ_s is the signal linewidth, and S/N is the signal-to-noise ratio. This is typically of order 25
6564 ppb on a single NMR FID above threshold for a millisecond or more [3]. Any new design
6565 for the multiplexer preamps, NIM module electronics, and DL611 modules will need to meet
6566 or exceed these specifications. The option of performing the frequency determination with
6567 fast, high-accuracy digitizers will be investigated (see section 16.2.8).

6568 Recording the results of the frequency measurement, task (4), is accomplished by reading
6569 the contents of the DL611 VME addresses containing the zero-crossing and clock counts, and
6570 writing them to disk on the DAQ PC. In E821, roughly 100 fixed NMR probes were read per
6571 second, and data rates were much less than 100 kB/second. Another custom VME module
6572 from Heidelberg provided a timestamp to be recorded with the measurements. For E989
6573 the preliminary design replaces the Heidelberg timestamp module with a Hytec 2092 VME
6574 module. This module has an antenna input to receive GPS timing signals and provides a
6575 timestamp with an absolute accuracy better than 100 ns with respect to UTC (Co-ordinated
6576 Universal Time). This is more than adequate for NMR signals which are typically 1 ms in
6577 length or longer. The advantage of this scheme is that by providing all NMR signals with
6578 a reliable, high-resolution absolute time stamp, potential external influences on the storage
6579 ring field from booster operations at 15 Hz, and pickup from power lines at 60 Hz and
6580 harmonics, can be investigated (see section 16.6). Field measurements in coincidence with
6581 muon fills of the storage ring (which are typically asynchronous with the NMR readings)
6582 and other external events can be investigated. Finally, the Hytec module produces a GPS-
6583 derived 1 pps TTL output which will be used to stabilize a rubidium frequency reference
6584 producing a 10 MHz reference for the NMR and ω_a frequency synthesizers. There is other
6585 hardware for obtaining a GPS-derived 1 pulse-per-second reference and reliable computer
6586 timestamps - the Hytec module is recommended as part of the conceptual design since it
6587 accomplishes several goals in a single module. We will also investigate the Meridian Precision
6588 GPS Frequency Standard with a built-in high stability rubidium frequency reference.

6589 Finally we note that low level software for the Struck controller has been developed to
6590 control the original Heidelberg clock, DL620 probe selector, and DL611 frequency counter
6591 modules. It can be recommended for use in E989 over alternative controllers because it has
6592 already been shown to work.

16.2.8 Digitizer

The Larmor frequency of precessing proton spins can be determined by counting zero-crossings of the FID and ticks of a clock over the same interval, to a single-shot precision approaching 10 ppb [3]. This requires FIDs which are several ms long and S/N greater than 100:1. Many fixed probes will be near pole boundaries where field inhomogeneities can be large, resulting in short (sub-ms) FIDs with poor frequency resolution. In E821, some fixed probes were not used to track the storage ring magnetic field because of these issues.

To increase the number of useful fixed probes in E989, the vacuum chamber grooves of probes close to pole boundaries will be extended so these probes can be placed in more homogeneous field regions. This should result in longer FIDs and better frequency resolution. A second improvement is to supplement the zero-crossing counters with a fast, low-noise digitizer, such as the Struck SIS3302. Each SIS3302 can digitize 8 channels with a 16-bit ADC (13 effective bits). The module would get its signals from the second FID outputs of the NMR NIM modules and digitize at 20 MHz for roughly 5 ms. This will allow field measurements to be recovered from probes with very short signals since the FIDE thresholds for counting zero-crossings (which are fixed in the NIM modules) can be tailored for individual probes in software when analyzing digitized FIDs. Second, the occasional problem of electronics noise causing additional clock counts in the zero-crossing counter can be eliminated in software which analyzes the FIDs. Third, more advanced techniques for analyzing the FIDs can be used. Zero-padding and Fourier-transforming signals would yield high-resolution lineshapes from which the line center can be extracted. Similarly, the frequency resolution can be improved by fitting or interpolating the FID near the first and last zero-crossings. This will yield resolution finer than a single clock tick and will effectively improve the S/N since it amounts to averaging the signal near the crossings. Finally, it is well known that signals with asymmetric lineshapes yield zero-crossing rates that vary with time during the FID, and the line center is best represented by the FID frequency at $t=0$, at the start of the FID [38]. Such effects can be accounted for by Fourier-transforming the signal or extrapolating the zero-crossing rate to the start of the signal. Zero-crossing counters are insufficient to perform this analysis.

The digitizer will only provide these benefits if the digitization noise is comparable or less than the noise on the signal. For E821, FID signals were of the order of a volt. When the FID envelope (FIDE) dropped below threshold at ≈ 100 mV, the S/N of 100 implies signal noise was of order 1 mV. For the SIS3302, with a -1V to 1V full scale range, and minimum 13 effective bits, the digitization noise is predicted to be 0.24 mV, safely below the signal noise.

With a sampling frequency of 20×10^6 samples/s, 16-bit resolution, and a period of 5×10^{-3} s, a single probe will probe ≈ 200 kB/sample. Measuring 100 fixed probes per second yields total data rate of 20 MB/s. This is near the limit for IEEE-1014 VME backplanes, but easily handled by VME64 or VME64x crates. There would be no need to store all digitized signals. After the frequency information has been extracted, a small subset of fully digitized FIDs could be retained. The computing power required to Fourier analyze the signals in real-time can be handled by any state-of-the-art PC

We also note that a high performance digitizer is necessary for analyzing the lineshapes of the calibration probes. The lineshapes contain information about perturbations due to

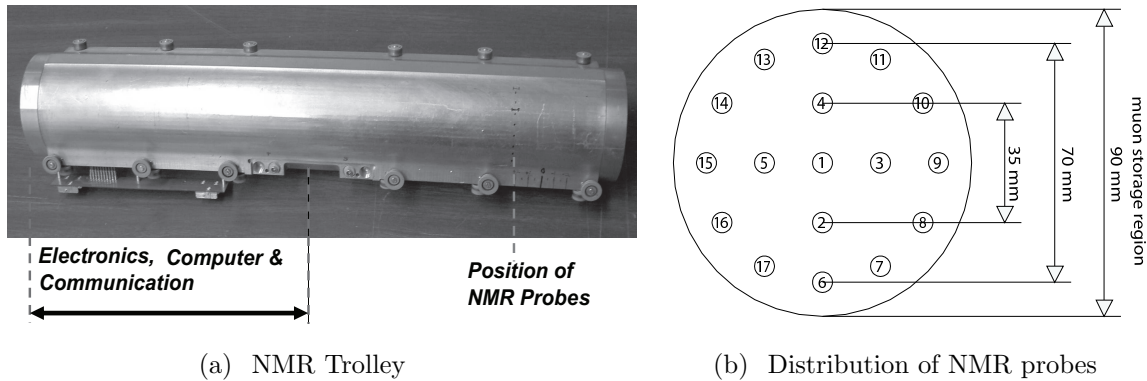


Figure 16.5: (a) Photograph of the NMR trolley, which measures the magnetic field in the storage ring. The array of 17 NMR probes, which are located inside the trolley housing, are 82(1) mm behind the front of the trolley. Electronics occupies one end of the device. At the other end where the probes are located, the field perturbation from the electronics is less than 2 ppm and is accounted for as part of the calibration procedure. (b) The probe numbers and placement are given by the schematic.

6637 probe materials, the amount of water in the thin neck of the spherical water sample and other
 6638 effects. This information can be used to reduce the uncertainties in the absolute calibration.

6639 16.3 Trolley

6640 The trolley performs the second major task of the field measurement system: it determines
 6641 the magnetic field distribution over the muon storage volume around the ring intermittently
 6642 when the beam is off. It uses an in-vacuum NMR trolley system developed for E821 at the
 6643 University of Heidelberg [7], shown in Fig. 16.5(a). This trolley contains 17 NMR probes
 6644 arranged in concentric circles as shown in Fig. 16.5(b). Each probe measures the field at
 6645 several thousand points around the ring. The trolley is built from non-magnetic materials
 6646 and has a fully functional CPU on-board which controls the FID excitation and FID zero
 6647 crossing counter. Additional sensors connected to the microcontroller are used to measure
 6648 position, pressure, and temperature. The trolley is pulled around the storage ring by two
 6649 cables, one from each direction circling the ring. One of these cables is a thin co-axial cable
 6650 with only copper conductors and Teflon dielectric and outside protective coating (Suhner
 6651 2232-08). It carries simultaneously the dc supply voltage, the reference frequency f_{ref} and
 6652 two-way communication with the spectrometer via RS232 standard. The other cable is non-
 6653 conducting nylon (fishing line) to eliminate pickup from the pulsed high voltage on the kicker
 6654 electrodes.

6655 Magnetic Field Maps

6656 From the trolley field measurements, the multipole composition of the field averaged over the
 6657 ring azimuth is extracted, then folded with the multipole expansion of the measured stored

6658 muon beam profile. Because muons can not be stored while the trolley is in the storage
6659 volume, trolley field maps must alternate with periods in which muon spin precession data
6660 are taken. Over the duration of E989, trolley runs will be scheduled at irregular intervals such
6661 that the overall distribution of trolley runs versus time is uniform. This reduces correlations
6662 between trolley runs and possible biases from day/night or other potential periodic changes
6663 in the storage ring field.

6664 During mapping, the trolley is moved into the storage ring and pulled continuously
6665 clockwise or counterclockwise through the entire storage volume over the course of roughly
6666 2 hours. The field is sampled at roughly 6000 locations in azimuth by each of the 17 probes
6667 (which are cycled though continuously) for a total of 100,000 field points. During these runs, a
6668 cross-calibration of the field observed by the fixed probes and the field measured by the trolley
6669 probes is performed. This is required to determine the magnetic field encountered by the
6670 stored muons in the storage volume from the measurements of the surrounding fixed probes
6671 taken at the same time. Because this cross-calibration between the trolley measurements
6672 and fixed probes will be slightly different each time the magnet is powered up or down
6673 (because the field shape changes slightly), trolley runs must be taken every time the magnet is
6674 changed. This cross-calibration is sensitive to magnet temperature and current, both of which
6675 also change the field shape slightly. Improved insulation of the magnet and experimental
6676 hall floor, as well as the more uniform thermal environment in the E989 experimental hall
6677 versus E821 should keep the magnet temperature more stable and uniform. This will also
6678 reduce the magnitude of changes to the current required to stabilize the field. Reductions in
6679 both factors should reduce changes in the cross-calibration and allow better tracking of the
6680 storage ring field between trolley runs. Note that these changes in cross-calibration can be
6681 determined in advance of data-taking by measuring the difference in fixed probe and trolley
6682 probe measurements as the current in the magnet is changed deliberately, and as a function
6683 of the experimental hall/magnet temperature. Finally, the frequency of trolley runs will be
6684 adjusted and additional insulation can be used to ensure that the uncertainty on the field
6685 tracking goals will be met.

6686 The performance of the system can be gauged from E821. The magnitude of the field
6687 measured by the central trolley probe is shown as a function of azimuth in Fig. 16.6 for one
6688 of the trolley runs in E821. The insert shows that the fluctuations in this map that appear
6689 quite sharp are in fact quite smooth, and that the noise is small in comparison.

6690 Since the NMR frequency is only sensitive to the magnitude of B and not to its direction,
6691 in addition to the main vertical field B_y , in principle there could be significant radial fields
6692 and fields in the azimuthal direction. In practice, the magnitude of radial field will be
6693 measured (see section 16.8.2), pole tilts will be measured with a precision electrolytic tilt
6694 sensor and adjusted, and surface correction coils will be used to ensure the radial field is less
6695 than 50 ppm. In E821 the average radial field achieved was 20 ± 10 ppm [39]. Longitudinal
6696 components of the field will be similarly restricted, especially by improved shimming. This
6697 sequence of measurements and corrective actions should ensure the difference between $|\vec{B}|$
6698 and $|B_y|$ is less than 0.01 ppm.

6699 Since the storage ring has weak focusing, the average over azimuth is the important
6700 quantity in the analysis. This is achieved using the trolley field maps by averaging the
6701 trolley probe measurements over azimuth. A contour plot for an azimuthally-averaged field
6702 map from E821 is shown in Fig. 16.7(b). Such azimuthally-averaged field maps are then

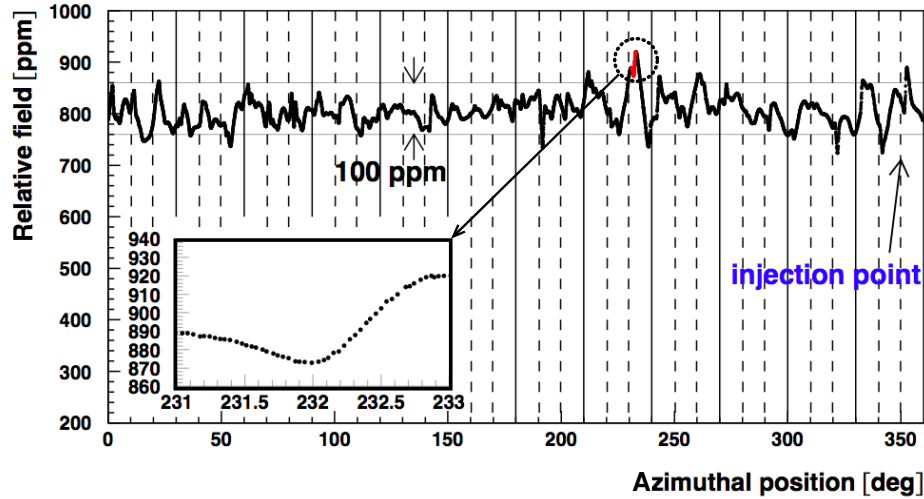


Figure 16.6: The magnetic field measured at the center of the storage region vs. azimuthal position. Note that while the sharp fluctuations appear to be noise, when the scale is expanded the variations are quite smooth and represent true variations in the field.

6703 expressed in a two-dimensional multipole distribution over the radial and vertical directions,
 6704 x and y . It is more natural to use cylindrical coordinates (r, θ) where $r = 0$ is the center of
 6705 the storage region and $\theta = 0$ points radially outward from the center of the ring. This yields
 6706 the field expansion:

$$B(r, \theta) = \sum_{n=0}^{n=\infty} \left(\frac{r}{r_0}\right)^n [a_n \cos n\theta + b_n \sin n\theta], \quad (16.7)$$

6707 where the normal multipoles, a_i , and skew multipoles, b_i are normalized at $r_0 = 45$ mm. In
 6708 practice the series is limited to $n \leq 4$. An example of the multipole decomposition is shown
 6709 in Table. 16.2.

Table 16.2: Multipoles at the outer edge of the storage volume (radius = 4.5 cm). The left-hand set are for the plunging station where the plunging probe and the absolute calibration probe are inserted. The right-hand set are the multipoles obtained by averaging over azimuth for a representative trolley run during the 2000 period.

Multipole [ppm]	Calibration Station		Azimuthal Average	
	Normal	Skew	Normal	Skew
Quadrupole	-0.71	-1.04	0.24	0.29
Sextupole	-1.24	-0.29	-0.53	-1.06
Octupole	-0.03	1.06	-0.10	-0.15
Decupole	0.27	0.40	0.82	0.54

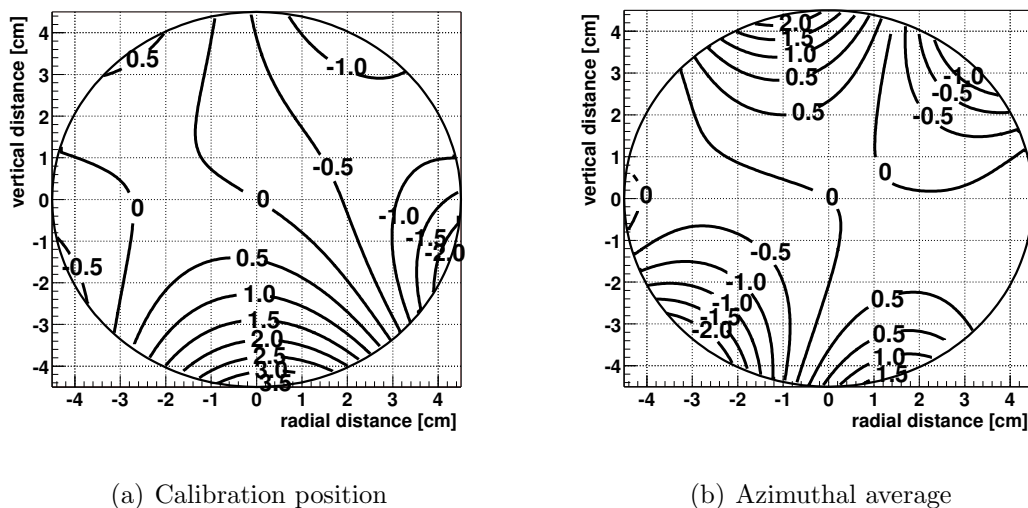


Figure 16.7: Homogeneity of the field (a) at the calibration position and (b) for the azimuthal average for one trolley run during the 2000 period. In both figures, the contour spacing is 0.5 ppm.

6710 Fixed probe tracking of the magnetic field

6711 During data-collection periods the field is monitored with the fixed probes. To determine
 6712 how well the fixed probes permitted us to monitor the field in the storage ring acting on the
 6713 muons, the field average determined by the trolley, and that predicted by the fixed probes is
 6714 compared for each trolley run. The results of this analysis for the E821 2001 running period
 6715 is shown in Fig. 16.8. The rms distribution of these differences is 0.10 ppm.

6716 The uncertainty in interpolating the storage ring field between trolley runs, by using
 6717 the fixed probes, will be reduced from 0.07 ppm achieved in E821 to 0.03 ppm in E989
 6718 (see Table 16.1). The improvements are the result of several changes. First, the E989
 6719 experimental hall floor will be monolithic and much more mechanically stable than the
 6720 E821 floor which was composed of three concrete sections. Second, the E821 experimental
 6721 hall had very poor temperature control (day-night changes of nearly 4°C were common),
 6722 essentially no insulation, and large changing temperature gradients across the magnet. In
 6723 E989, temperature stability and uniformity in the hall is a high priority. The HVAC system
 6724 will hold the hall stable and uniform to $\pm 1^\circ$ C during data collection periods. This is at least
 6725 a factor two more stable than E821. Also, the thermal insulation around the magnet will
 6726 be improved, and heat flow from gaps around the magnet coil cryostats will be eliminated.
 6727 These major improvements should reduce the temperature-induced changes in the field by a
 6728 factor of two.

6729 The RMS difference in field average predicted from the fixed probes and that measured by
 6730 the trolley was roughly 0.1 ppm in E821, where trolley runs were taken approximately every
 6731 3 days. For the same time interval between trolley runs in E989, this RMS difference should
 6732 be reduced by a factor 2 given the improvements in the hall floor, HVAC, and insulation.

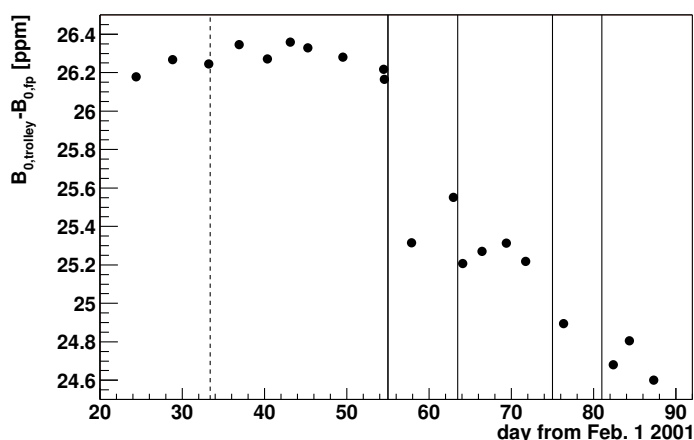


Figure 16.8: The difference between the average magnetic field measured by the trolley and that inferred from tracking the magnetic field with the fixed probes between trolley runs. The vertical lines show when the magnet was powered down and then back up. After each powering of the magnet, the field does not come back exactly to its previous value due to hysteresis, so that only trolley runs taken between magnet powerings can be compared directly.

6733 Assuming the improvements only reduce the RMS difference to 0.07 ppm, the goal of 0.03
6734 ppm on field interpolation with the fixed probes can be achieved by more frequent trolley
6735 runs. In E821 the interval between trolley runs was roughly 3 days, and did not need to
6736 be more frequent since the experiment was statistics limited. For E989, this interpolation
6737 uncertainty must be reduced significantly compared to E821. Trolley runs which are 3 times
6738 more frequent should reduce the interpolation uncertainty by another factor between $\sqrt{3}$
6739 and 3. Finally, we anticipate having more fixed probes available for field tracking and we are
6740 exploring the possibility of adding more fixed probes in the midplane of the magnet, located
6741 inside the vacuum chambers at radii just inside or outside the quadrupole plates. Also, the
6742 use of petroleum jelly with its reduced temperature coefficient of chemical shift and the more
6743 stable probe temperatures should reduce the 0.1 ppm interpolation uncertainty in E821 due
6744 to greater immunity of the fixed probes to temperature effects. Finally, OPERA studies of
6745 the magnet indicate a small sensitivity of the difference between the fixed probes and trolley
6746 probes to small changes in the magnet current. This is due to nonlinearity in the $B - H$
6747 curves of the yoke and pole pieces, leading to slight changes in the field shape. In E821,
6748 the current in the magnet was adjusted based on feedback from the NMR. In E989, the
6749 magnetic field should be much more stable passively, so the feedback corrections (changes to
6750 the current) should be smaller. Also, the effect of slight changes in the magnet current on
6751 the difference between trolley probes and fixed probes can be measured and compared with
6752 the OPERA model. The results of these studies and changes to the field due to temperature
6753 changes, should allow corrections to be made to the fixed probe readings that incorporate
6754 both magnet temperature changes and changes in magnet coil current. These efforts should

6755 further reduce the 0.1 ppm RMS uncertainty in E821 to achieve an interpolation uncertainty
6756 of 0.03 ppm in E989.

6757 **Uncertainty from the muon distribution**

6758 The value of ω_p entering into the determination of a_μ is the field profile weighted by the muon
6759 distribution. The multipoles of the field, Eq. (16.7), are folded with the muon distribution,

$$M(r, \theta) = \sum [\gamma_m(r) \cos m\theta + \sigma_m(r) \sin m\theta], \quad (16.8)$$

6760 to produce the average field,

$$\langle B \rangle_{\mu\text{-dist}} = \int M(r, \theta) B(r, \theta) r dr d\theta, \quad (16.9)$$

6761 where the moments in the muon distribution couple moment-by-moment to the multipoles
6762 of B (expressed in terms of the free proton precession frequency). The determination of $\langle B \rangle$
6763 is more accurate if the field is quite uniform (with small higher multipoles) so the number of
6764 terms is limited, and the muons are stored in a circular aperture, thus reducing the higher
6765 moments of $M(r, \theta)$.

6766 In E821 the weighted average was determined using two techniques. One used a muon
6767 tracking calculation and a field map to determine the field seen by each muon. The second
6768 determined the average field from the dipole and quadrupole components of the magnetic field
6769 coupled with the beam center determined from a fast-rotation analysis. These two agreed
6770 extremely well, validating the choice of a circular aperture and the ± 1 ppm specification on
6771 the field uniformity that were set in the design stage of the experiment. Part of the E821
6772 muon distribution uncertainty came from radial and vertical offsets of the beam. These offsets
6773 couple with normal and skew quadrupole moments of the field. For E821, these corrections
6774 were of order 0.012 ppm for the skew quadrupole (limited by the RMS scatter of the skew
6775 quadrupole), and 0.022 ppm for the normal quadrupole. The latter was limited primarily
6776 by a lack of knowledge of the muon beam radial position on a run by run basis. Sextupole
6777 and higher skew multipoles of the beam were less than 10^{-3} in E821 and did not require
6778 correction. No correction was made for the 11 ppb normal sextupole field contribution in
6779 E821. These techniques worked quite well in E821, and the uncertainty on $\langle B \rangle$ weighted by
6780 the muon distribution was conservatively estimated as ± 0.03 ppm [5].

6781 In E989 we anticipate several improvements. First, the muon beam distribution will
6782 be monitored every fill with higher precision by the fast rotation analysis and new muon
6783 trackers. Second, improved field uniformity and improved magnet stability (so the multipole
6784 decomposition is more stable) will couple with the improved knowledge of the beam. The
6785 combined improvements will reduce the normal and skew quadrupole uncertainties, which
6786 were 0.012 ppm and 0.022 ppm in E821, to below 0.01 ppm for E989. By measuring and
6787 correcting the normal sextupole contribution to 20% or better of its value (which was left
6788 as a 0.011 ppm uncertainty for E821), that contribution can be made negligible. The effects
6789 due to these higher multipoles should also be reduced due to higher field uniformity and
6790 stability, and by moving the trolley probes to slight larger radius. Finally, if necessary,
6791 we could make another shell for the trolley (but use the same electronics) to map the full
6792 storage volume by introducing some openings. The openings would allow the trolley probes

6793 to be moved out to the radial limits of the storage aperture. The field measurement might
6794 require letting the storage ring up to air (since the trolley electronics are normally cooled
6795 in part by convection, and opening up the trolley shell and running the system in vacuum
6796 might cause overheating). Based on the E821 experience we think such measures should not
6797 be necessary. Measurements of the higher multipoles can also be made before the vacuum
6798 chambers are installed with the shimming trolley (discussed below), and the influence of the
6799 vacuum chambers on the field can be measured.

6800 To summarize, improved field homogeneity and stability, and improvements in muon
6801 tracking should allow E989 to achieve 0.01 ppm uncertainty on the muon distribution con-
6802 tribution to the determination of ω_p .

6803 16.3.1 General trolley requirements

6804 In the following sections, we will first specify the requirements on the trolley for E989 based
6805 on the field mapping tasks outlined above, then discuss the conceptual design of future
6806 upgrades and efforts related to the trolley system in detail.

6807 As can be seen from Table 16.1, trolley related systematic errors in the BNL E821 ex-
6808 periment were significant and require improvement to meet the physics goals in E989. The
6809 two main sources of uncertainty stem from the calibration procedure of the trolley probes to
6810 the plunging probe (0.09 ppm) and errors related to position uncertainties during the actual
6811 trolley runs (0.05 ppm). Additional smaller effects (like temperature or voltage drifts) were
6812 grouped into one systematic error (Others) together with non-trolley related systematics in
6813 the field measurement. For the new E989 experiment, the trolley system will be used in
6814 a very similar fashion to E821. Given the required improvements in the overall systematic
6815 errors for the field measurement, we will need some changes for the new system.

6816 Trolley measurement of B_0

6817 In E821, the uncertainty on the trolley measurement of B_0 was 0.05 ppm (see Table. 16.1),
6818 due primarily to nonlinearities in the trolley position readout. This 0.05 ppm uncertainty
6819 will be reduced to 0.03 ppm in E989 by reducing the trolley position uncertainty to 5 mm,
6820 which is more than a factor two better than E821. Second, uncertainties due to trolley
6821 rail irregularities will be reduced, as discussed below. Third, a more sophisticated feedback
6822 algorithm to stabilize the magnet during trolley runs will be developed (E821 turned off the
6823 feedback, requiring a correction for field drift). Fourth, the uncertainty on the field integral
6824 in azimuth depends on position uncertainty coupled with field gradients. In E989 we aim
6825 to reduce the field gradients in azimuth by a factor two compared to E821. Finally, we will
6826 use a slightly more sophisticated numerical integration technique (Simpson's) to extract the
6827 field integral from discretized data. These steps should reduce the uncertainty on the trolley
6828 measurement of B_0 to 0.03 ppm in E989, as discussed in detail below.

6829 The requirements for the actual measurement during a single trolley run remain the
6830 same. An individual NMR frequency measurement will have a precision at least as good as
6831 20 ppb as was achieved in E821. The field will be measured at 6000 points around the ring
6832 for each probe. A single trolley run should be accomplished in at most two hours. While
6833 about 1 hour is required for the mapping of the 6000 data points for each probe, the return

6834 trip can be sped up to reduce the interruption of the spin frequency measurement. Trolley
6835 runs should be repeated more frequently than in E821 where an interval of 2-3 days was
6836 typical. Increased frequency of trolley measurements will reduce the error associated with
6837 the fixed probe interpolation and reduce uncertainties associated with temperature changes
6838 in the storage ring.

6839 As mentioned above, transverse and longitudinal position uncertainties coupled with
6840 field gradients are a major systematic error category in the measurement. While we plan
6841 on having improved overall shimming in E989 and hence reduced gradients, we will also
6842 put effort into reducing the position uncertainties. In E821 the longitudinal position of the
6843 trolley during field mapping was inferred from two sources. First, the unwinding of the trolley
6844 cable was measured by optical rotary encoders in the drums (see Fig. 16.10). Second, the
6845 observed change in the NMR frequency in the fixed probes due to the small but measurable
6846 changes in the magnetic field induced by the trolley (maximally in the vicinity of the onboard
6847 electronics). The overall longitudinal position knowledge was estimated to be on the order of
6848 1 cm corresponding to a 50 ppb systematic error. Together with the better shimming in the
6849 azimuthal direction (see section 16.8), we aim to reduce the position uncertainty to 5 mm to
6850 significantly reduce this error.

6851 During its movement, the trolley rides on two rails, which determine its transverse posi-
6852 tion with respect to the center of the muon distribution. The requirements on the precision
6853 alignment of the trolley rails remain the same as in E821. A maximal deviation from the
6854 ideal position of ± 0.5 mm will keep the associated systematic error below 10 ppb. The rails
6855 were not continuous at the junctions between adjacent vacuum chambers. Slight misalign-
6856 ment of neighboring rails at these gaps led to possible transverse deviations of the trolley's
6857 center introducing an estimated systematic error of 10 ppb. In E989, we will reduce these
6858 misalignments and precisely verify the deviation of the rails from their nominal position
6859 around the full azimuth. Here, we will employ two methods, namely (1) optical survey with
6860 laser systems or other precision metrology observation equipment and (2) the introduction of
6861 known (measured), transverse gradients by means of the pole surface coils during dedicated
6862 special trolley runs.

6863 During the calibration, relative position uncertainties between the plunging and trolley
6864 probes contribute to the overall systematic error. In E821, the transverse reproducibility was
6865 estimated to be 1 mm, whereas the relative position uncertainty in azimuth was determined
6866 to 3 mm. This resulted in systematic error contributions of 20 ppb and 30 ppb, respectively.
6867 For E989, we aim to cut these contributions in half (at least in the azimuthal direction) by
6868 more precise alignment of the probes in a repeatable way. For this, we plan to (1) introduce a
6869 mechanical stop for the trolley in the calibration region, (2) allow positioning of the plunging
6870 probe in all three directions and (3) by carefully testing the calibration transfer from the
6871 absolute calibration probe to the trolley in a homogeneous solenoid test magnet before data
6872 taking.

6873 Other effects contributed to the E821 result with a summed contribution of 50 ppb.
6874 These included the temperature and trolley power supply voltage dependence of the NMR
6875 measurement and an estimate of the influence of higher multipoles. The dependence of
6876 the FID frequency measurement on the supply voltage of the trolley was measured to be
6877 0.27 ppm/V and a voltage stability of 50 mV was achieved. In the new experiment, a modern
6878 power supply will significantly reduce the voltage drift and make this contribution totally

negligible. We will also reduce the effects of external temperature changes on the extracted NMR frequency. One possibility is to use petroleum jelly instead of water for the NMR probes due to the reduced temperature coefficient of the jelly. In addition, an increase in the heat dissipation of the trolley would reduce the change of its temperature during the measurement. Overall, temperature-related effects should be much smaller in E989, and we can carefully study them in the solenoid test magnet under controlled temperature conditions.

The 30 ppb systematic error in E821 stemming from the folding of higher multipoles with the muon distribution can be improved by a modification of the current trolley probe arrangement shown in figure 16.5(b). There is room to further move the probes to an outer position closer to the 4.5 cm aperture of the muon storage region. In addition, a reconfiguration of the overall probe distribution can help to get a better handle on the measurement of the sextupoles and higher multipoles.

It should be noted that any additional modifications should respect the strict requirement that the field at the trolley NMR probes is disturbed as minimally as possible. The maximal distortion of the field caused by the trolley electronics in E821 was about 2 ppm and future changes cannot introduce any major additional magnetic contribution compared to this level.

In the following sections, we will detail our specific conceptual design for future upgrades and activities that are aimed to meet the above outlined requirements for the E989 experiment.

16.3.2 Garage

When not in use, the trolley is parked in a garage (see Fig. 3.4) in a special vacuum chamber. The trolley garage shown in Fig. 16.9 serves the purpose of storing the trolley inside the vacuum outside the muon storage aperture during the main periods of muon spin precession measurement. A set of three rods driven by a non-magnetic piezo motor provides the mechanism to move cut-outs of the rails into the muon storage region and retract them. The in-vacuum requirements and a lack of motion stops have possibly put stress on these mechanics over the course of the E821 operation. The overall integrity of the system will need inspection to understand if the system is suited for operation over several years of data taking in E989. Future improvements might include the replacement of the rods, the addition of non-magnetic limit switches to smoothly stop the movement of the cut-out rails when finally in place, or even a re-design of the garage with a switchyard solution. While ideally the garage could be operated as is in E989, the changes required to improve this system will be decided after detailed inspection in the near future at Brookhaven and later at Argonne.

As can be seen in Figure 3.4, the trolley garage is attached to one of the twelve vacuum chambers. Since the upgrades to other systems (such as the alignment of the trolley rails) will require work on the vacuum chambers, upgrades to the garage will have to be coordinated with these other activities over the next two years.

16.3.3 Drive

The trolley drive mechanism shown in Figure 16.10 is located about 120° away from the garage. It is connected to one of the vacuum chambers and sits on the inner side of the

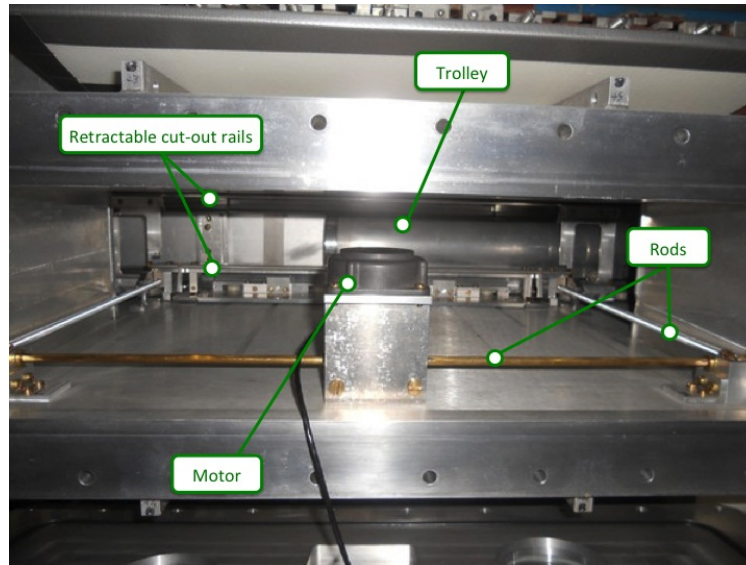


Figure 16.9: Trolley garage with the piezo motor, the driving rods, the rails and the trolley partially in the parking position where it can be retracted from the storage region.

6920 storage ring (see the 1 o'clock position in Fig. 12.1). The cable drums together with the
 6921 driving piezo motors are outside the vacuum. Two 1.5 m-long tubes guide the two cables
 6922 from the drive to the vacuum chamber and provide the vacuum feedthrough. Two cables are
 6923 required to pull the trolley a full 360 degrees in each direction during its NMR measurement
 6924 and its return trip. Since the cables remain attached to the trolley during the storage in
 6925 the garage, one of the two cables runs through the kicker region. To prevent any damage to
 6926 the onboard trolley electronics from electronic pickup on the cable from the kicker pulses,
 6927 this cable is a non-conducting fishing line. The other cable is an all-copper double-shielded
 6928 cable with an outer coating suitable for in-vacuum operation. This cable allows the feeding
 6929 of the power and reference frequency signal as well as the communication with the trolley
 6930 microcontroller.

6931 The cable drive mechanism will need refurbishment and inspection of its functional in-
 6932 tegrity. In general, we expect it to be used mainly as is since the overall wear in E821 was
 6933 small and the mechanical parts should survive several more years of operation during the
 6934 E989 experiment. In order to speed up the return trip of the trolley to improve the duty
 6935 cycle of muon spin precession measurements, an upgrade of at least one of the motors is an-
 6936 ticipated. We also plan to relocate two optical rotary encoders that monitor the unwinding
 6937 of the cables to minimize some non-linearities in their readback values with respect to the
 6938 actual cable unwinding length. For full operation of the drive, the motor controller needs to
 6939 be brought back into operation. Its central component is an Infineon SAB80C535 microcon-
 6940 troller that facilitates the communication with the remote DAQ. Its refurbishment should
 6941 mainly require compilation and uploading of the Pascal software code which we have from
 6942 E821.

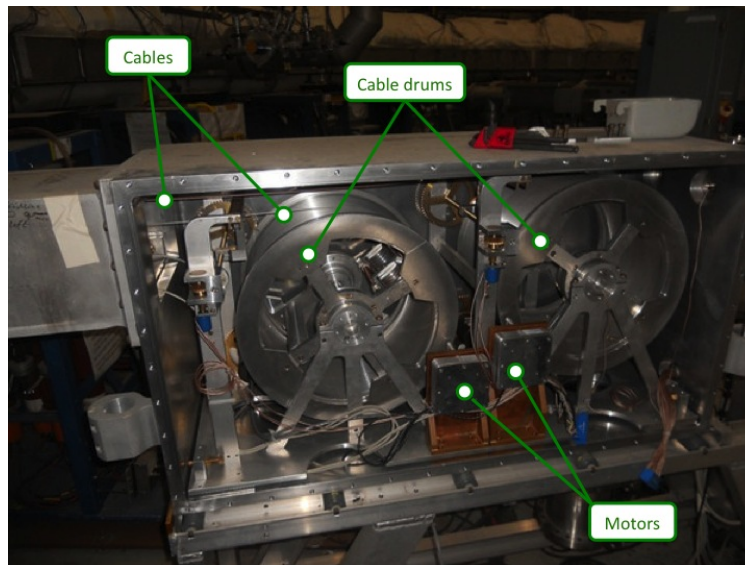


Figure 16.10: Trolley drive with the cable drums, motors and cables.

16.3.4 Position Measurement

The measurements of the trolley's position in both the longitudinal and transverse directions relative to its motion plays an important role in the evaluation of several systematic error sources. Uncertainties in the trolley's position convoluted with the local field gradients give rise to uncertainty in determining the average B field over the ring. The same effects introduce uncertainty in the cross-calibration with the plunging probe.

As stated in the requirements section 16.3.1 above, some improvements in the determination of the trolley's position compared to the E821 experiment are necessary. Together with the better shimming of the magnet (see section 16.8) and hence reduced field gradients, this will significantly reduce position related systematic errors for E989.

During the calibration procedure of the trolley probes in a specially shimmed region in the ring, the plunging probe and the trolley probes need to be positioned repeatedly at the same position. The uncertainty in E821 for the relative azimuthal alignment was estimated to be 3 mm. As the trolley was positioned by eye, we foresee improvements by means of a well-defined stop mechanism or an external laser survey system viewing a fine positioning grid through the viewing port. The plunging probe from E821 had motion limited to the vertical and radial directions. Adding motion in the azimuthal direction inside the vacuum chamber should also help in reducing position uncertainties in calibration.

While the trolley moves on the rails around the ring, the transverse position of the 17 NMR probes relative to the central muon orbit is mainly defined by the precision alignment of the rails. An average radial and vertical deviation of the rails of less than ± 0.5 mm will be sufficient to keep the associated systematic error negligible. After mechanical improvements of the rail fixture, curvature, and positioning inside the vacuum chambers are performed in conjunction with other work on the cages, these stringent alignment requirements must be verified. We anticipate a combination of two measurements to have a consistent cross-check

6968 of the trolley's transverse movement. The first verification will be based on optical (or other
6969 suitable) survey techniques with the trolley riding on the rails. This technique should work
6970 on individual vacuum chambers in air. Once all chambers are mounted in the storage ring
6971 and it is evacuated, optical inspection of the trolley's movement could only happen via ports
6972 on the inner radius of the chambers (see Figure 3.4). However, the sole inspection of the
6973 trolley's movement inside a non-evacuated chamber might be sufficient since FEA modeling
6974 and measurements show that the deflection of the chamber walls is small. A second technique
6975 involves imposing radial and vertical gradients using the surface coils to observe the changes
6976 in the NMR probe readings around the ring.

6977 In E821 the longitudinal position measurement of the trolley was achieved with a com-
6978 bination of optical rotary encoders and potentiometers monitoring the cable unwinding as
6979 well as the response spikes in the NMR frequency of the fixed probes due to the passing
6980 electronics of the trolley. The overall estimate of the longitudinal uncertainty was on the
6981 order of one centimeter. We aim to reduce this uncertainty to 5 mm or better by refurbishing
6982 an onboard barcode reader that was mostly unused in E821 due to its overheating in the vac-
6983 uum environment. As can be seen in Figure 16.11, the vacuum chambers are equipped with
6984 marks around the ring. The continuously spaced marks have a spacing of 2.5 mm while the
6985 larger spaced irregular codes serve as absolute reference marks. A reduction of the power con-
6986 sumption by using more efficient LEDs and light sensitive detectors or by increasing the heat
6987 dissipation capabilities of the reader head will then give a direct longitudinal measurement
6988 of the trolley at the required precision level.

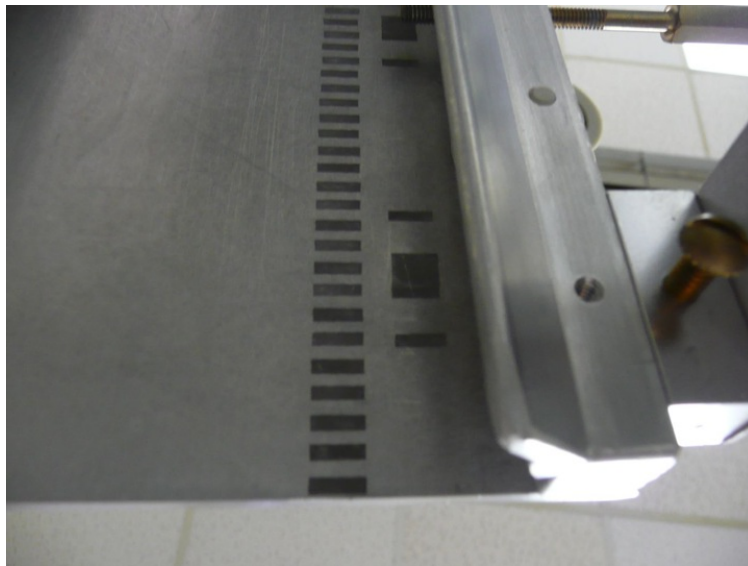


Figure 16.11: Trolley bar code marks on vacuum chamber plate.

6989 **16.3.5 Probes**

6990 The 17 trolley NMR probes (see Figure 16.2(b)) are identical to the fixed probes. No major
6991 work should be necessary for future use in E989 except for a standard refurbishment pro-

cedure performed by collaborators from the University of Washington. These activities (see section 16.2.3) will include the refilling with the NMR substance (either water or petroleum jelly), resoldering of broken wire connections, tuning of the probes Q-value and impedance matching to the $50\ \Omega$ cable as well as testing of a normal NMR response at 1.45 T. Replacement of parts of the probe would also be handled in these steps. To reduce the uncertainties in the absolute calibration of these probes, minor changes to the coil windings and sample may be made so the active volume of the probes is better defined and so the centers of the active volumes are the same at the millimeter level. This can be achieved by restricting the sample to the most homogeneous part of the field produced by the coil L_s , and by ensuring the number of windings and their positions in the 17 probes are identical.

As can be seen in Figure 16.5(b), the outermost radius covered by the trolley probes is 3.5 cm. While it would be preferable to have information over the full 90-mm aperture, space limitations inside the vacuum chamber, which can be understood by examining Figs. 3.8, prevent a larger diameter trolley. The folding of the muon distribution with the magnetic field multipole expansion is performed over the entire muon storage aperture with radius 4.5 cm. In E821, the estimate of the contribution from the sextupole and higher multipoles was obtained from data with a special shimming trolley, which mapped the field before the vacuum chambers were installed, and amounted to a systematic error contribution of 0.03 ppm. Since a different arrangement of the 17 NMR probes especially moving some out to a larger radius, could be beneficial to reduce this contribution. The implementation would require two new teflon holder plates inside the trolley with a new hole configuration for the probe placement.

16.3.6 Frequency Measurement

The NMR frequency measurement for the 17 NMR trolley probes is currently all integrated into the onboard electronics. At its heart sits the Motorola 68332 μ C microcontroller with a multitude of functionality. Power, RS232 communication, and the NMR reference frequency are brought in over a single double-shielded cable. The remaining NMR components (RF pulse amplifier, multi- and duplexer, signal preamplifier and frequency counter) are all integrated into the trolley housing. Additional temperature and pressure sensors and the barcode reader are also available. The development of this minimally magnetic, low power and noise system was a major effort in E821. As future changes to the internal electronics come at the risk of a failure and require significant engineering resources, we will avoid such activities as much as possible.

Even the low electric power of less than 1 W leads to changes in the temperature of the trolley electronics and the probes of a few degrees $^{\circ}$ C over the course of a trolley run. As the measured NMR frequency is temperature dependent, minimization of the temperature changes will help to reduce the associated systematic error. While we will also study the temperature dependence carefully in a test solenoid, we will investigate whether more heat can be dissipated via radiation to the vacuum chamber walls by increasing the surface emissivity of the trolley, or if an additional heat sink could improve the temperature stability.

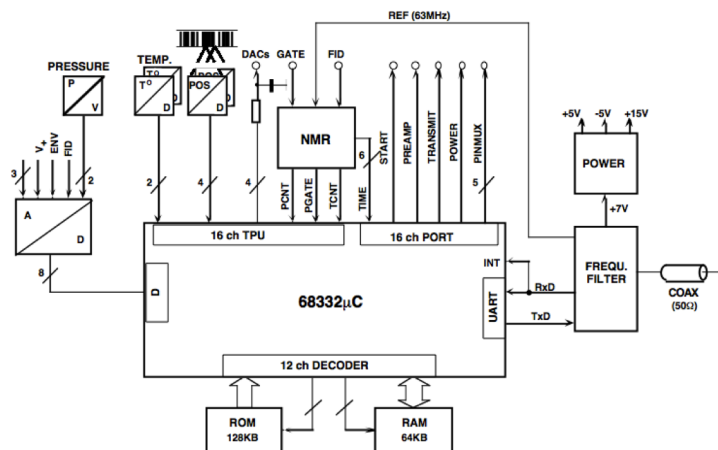


Figure 16.12: Schematics of central electronics on board of the trolley.

16.3.7 DAQ

The DAQ computer communicates with the onboard microcontroller using the RS232 protocol over the single coaxial cable connected to the trolley. A new DAQ computer will perform this function in E989 and will provide all necessary user interfaces to execute commands on the trolley microcontroller. The same DAQ infrastructure will be used to communicate with the trolley drive, which is similarly interfaced via a microcontroller. The plunging probe actuator mechanism shares the same microcontroller concept and could be operated from this computer, too. If possible, we will also operate the garage retraction mechanism from the same computer.

16.4 Absolute calibration of the trolley probes

16.4.1 Principles of calibration

Our technique for measuring a_μ requires that we determine the storage ring magnetic field, during the times the muons are stored, in terms of the Larmor precession frequency free protons would exhibit ω_p . Given a cyclotron period of 150 ns, in a typical lab-frame lifetime of 64 μ s the average muon goes around the ring more than 400 times and samples the field in a toroidal volume. The relevant field average is constructed by averaging a toroidal field map over azimuth, then weighting by the muon distribution in the storage ring. The muon distribution is determined by the fast rotation analysis and straw trackers.

The Larmor frequency of free protons in the storage volume at the time muons are stored obviously can not be measured directly; several intermediate steps are required. The field measurements of the trolley sample the field in the storage volume, but at different times than when muons are stored. The fixed probes measure the field at the same time that muons are stored, but outside the storage volume. The fixed probes are cross-calibrated by the trolley so they can be used to determine the field in the storage volume when the muons are stored.

7056 In E821 the difference between the predicted field average from the fixed probes and that
 7057 actually measured by the trolley had an RMS difference of roughly 0.1 ppm. As discussed
 7058 earlier, this will be reduced by (i) having more fixed probes available to track the field; (ii)
 7059 having greater thermal stability of the magnet and probes so the storage ring dipole field
 7060 and higher multipoles are more stable, leading to greater stability in the cross-calibration
 7061 between trolley probes and fixed probes; (iii) calibrating the changes to the cross-calibration
 7062 due to changes in magnet or probe temperature and from changes in the magnet current;
 7063 (iv) possibly using midplane fixed probes to improve tracking of the normal multipoles; (v)
 7064 having much more frequent trolley runs (this alone should reduce the tracking uncertainty
 7065 significantly - in E821 trolley runs were performed every 2-3 days).

7066 From the fixed probe readings and the values of the cross-calibration of these probes,
 7067 the azimuthal field average that each trolley probe would see can be predicted. The final
 7068 step is to calibrate the predicted trolley probe reading in terms of the equivalent free proton
 7069 precession frequency. This absolute calibration of the trolley probes is done with two special
 7070 NMR probes; the plunging probe and absolute calibration probe.

7071 The absolute calibration probe has a spherical water sample (see Figs. 16.2(a), 16.2(b)) [4].
 7072 The Larmor frequency of a proton in a spherical water sample is related to that of the free
 7073 proton through [9, 1]

$$f_L(\text{sph} - \text{H}_2\text{O}, T) = [1 - \sigma(\text{H}_2\text{O}, T)] f_L(\text{free}), \quad (16.10)$$

7074 where $\sigma(\text{H}_2\text{O}, T)$ is from the diamagnetic shielding of the proton in the water molecule,
 7075 determined from [11]

$$\sigma(\text{H}_2\text{O}, T) = 1 - \frac{g_p(\text{H}_2\text{O}, T) g_J(H) g_p(H)}{g_J(H) g_p(H) g_p(\text{free})} \quad (16.11)$$

$$= 1 - [25.790(14) + 0.01036(30) \times (T - 34.7^\circ\text{C})] \times 10^{-6}. \quad (16.12)$$

7076 The g -factor ratio of the proton in a spherical water sample to the electron in the hy-
 7077 drogen ground state ($g_J(H)$) is measured to 10 parts per billion (ppb) [11]. The ratio of
 7078 electron to proton g -factors in hydrogen is known to 9 ppb [14]. The bound-state correc-
 7079 tion relating the g -factor of the proton bound in hydrogen to the free proton are calcu-
 7080 lated in references [15, 16]. The temperature dependence of σ is included above by using
 7081 $d\sigma(\text{H}_2\text{O}, T)/dT = 10.36(30) \times 10^{-9}/^\circ\text{C}$ [17].

7082 Absolute calibration probe

7083 The absolute calibration probe does not consist solely of a perfect sphere of water. Param-
 7084 agnetism and diamagnetism of the materials used in the probe construction leads to pertur-
 7085 bations in the field at the water sample, and small departures from sphericity of the sample
 7086 also require correction. The magnetic field acting on a proton in the water sample B_p is
 7087 related to the field in the absence of the probe, B , by a total correction factor δ_t ,

$$B_p = (1 - \delta_t)B, \text{ where} \quad (16.13)$$

$$\delta_t = \sigma(\text{H}_2\text{O}, T) + \delta_b + \delta_p + \delta_s. \quad (16.14)$$

7088 Contributions to δ_i come from the temperature-dependent diamagnetic shielding of protons
 7089 in a water molecule $\sigma(\text{H}_2\text{O}, T)$ discussed above, the shape-dependent bulk diamagnetism of
 7090 the water sample δ_b , paramagnetic impurities in the water sample δ_p , and the magnetic field
 7091 from the magnetization of paramagnetic and diamagnetic materials in the probe structure,
 7092 δ_s [4]. The bulk correction is given by $\delta_b = \left(\epsilon - \frac{4\pi}{3}\right) \chi$, where ϵ is a sample-shape dependent
 7093 factor and χ is the susceptibility of water $\chi(\text{H}_2\text{O}) = 0.720(2) \times 10^{-6}$ [18]. For a sphere
 7094 $\epsilon = 4\pi/3$ so $\delta_b = 0$ (for an infinitely long cylinder $\epsilon = 2\pi$ when the axis is perpendicular
 7095 to \vec{B}). The sphericity of the glass bulb containing the water sample can be measured with
 7096 an optical comparator, and corrections to δ_b can be made for asphericity, bubbles or excess
 7097 water in the neck of the sample, and other imperfections. Using pure, deionized, multiply-
 7098 distilled water in the absolute calibration probe reduces δ_p . The presence of impurities can be
 7099 monitored by measuring the magnetization time-constants T_1 and T_2 using appropriate pulse
 7100 sequences. The perturbation due to probe materials δ_p can be minimized by using material
 7101 with low susceptibility and testing them for magnetic impurities. The residual influences
 7102 must be measured so δ_p is known at the 10 ppb level or better. Tight mechanical tolerances
 7103 can ensure symmetry about the cylindrical axis of the probe and reduce the sensitivity to
 7104 the orientation of the probe. Symmetry about the midplane can help make the lineshape
 7105 symmetric (reducing time-dependence in the FID zero-crossing rate).

7106 The properties of the absolute calibration probe developed for LANL E1054 and E821
 7107 were measured carefully at LANL at 1.7 T so the absolute field in terms of the free proton
 7108 precession frequency was determined by the probe to an accuracy of 34 ppb [4]. Measure-
 7109 ments made by the absolute calibration probe were expressed in terms of the equivalent free
 7110 proton frequency at 1.45 T to an accuracy of 0.05 ppm in E821.

7111 The very same absolute calibration probe was used in E1054 to determine μ_μ/μ_p [2]. An
 7112 additional shift of the calibration in E989 versus those in the solenoid at LANL arises due to
 7113 the presence of magnetic images of the magnetized sample and probe materials in the high- μ
 7114 iron of the pole pieces. These effects are at the level of a few ppb and were insignificant
 7115 for E821, but they will be determined as part of the calibration procedure in E989. By
 7116 using the same absolute calibration probe as E1054, there is a direct robust link of our E989
 7117 magnetic field to the muon magneton; proton NMR has only the role of a intermediate fly
 7118 wheel. This link is independent of possible future changes in fundamental constants in the
 7119 regular adjustment procedures [1], unless the muon magneton will be remeasured better
 7120 experimentally or the theory-dependent value of μ_μ/μ_p is used to extract a_μ . In these case
 7121 μ_μ/μ_p is largely independent of the properties of the probe.

7122 Based on the discussion above, the same very well studied absolute calibration probe
 7123 is recommended for use in E989. The uncertainties on its properties will be reduced from
 7124 0.05 ppm in E821 to 0.035 ppm in E989 as follows. First, the measurements of the absolute
 7125 calibration probe which were determined in the E1054 solenoid at 1.7 T in terms of the
 7126 free proton precession frequency to an accuracy of 0.034 ppm [4] will be repeated through
 7127 extensive testing in a solenoid at FNAL at 1.45 T. By constructing a thermal enclosure for
 7128 use in the solenoid with 0.1 °C stability, and with a higher performance ADC for the FID,
 7129 the properties of the absolute probe should be determined at least as well as E1054, but
 7130 now at the correct field for E989 and with greater control over the temperature. Another
 7131 improvement is that construction of a new calibration platform will allow a few additional

7132 probes to be used to track the changes of the solenoid field during these calibration studies.
7133 The perturbation due to magnetic images in the pole pieces can be determined by comparing
7134 the influence of the same materials in both the solenoid and the storage ring and cross-checked
7135 with predictions. Finally, the absolute calibration probe will be used for calibration at times
7136 of the day when the experimental hall temperature and magnet are most stable. The probe
7137 temperature will be monitored and determined with less than 0.5 °C uncertainty in the
7138 absolute temperature so the associated uncertainty in the diamagnetic shielding is less than
7139 0.005 ppm. Calibrations performed at different temperatures should be consistent once the
7140 known temperature-dependent changes in shielding are accounted for.

7141 These procedures should improve the accuracy of the absolute calibration probe to 0.035
7142 ppm in E989. In addition, one or two other auxiliary absolute calibration probes will be
7143 constructed for comparison. These probes will use slightly different designs, such as glass
7144 water samples made by slumping glass on machined spheres [13], and probe bodies made
7145 of a combination of paramagnetic and diamagnetic metals for zero net susceptibility and
7146 magnetization. These probes might also be made smaller and less massive to reduce the sen-
7147 sitivity to magnetization of probe materials and from field inhomogeneities, and for possible
7148 use in the calibration of trolley probes. Such efforts should provide redundant checks on the
7149 accuracy of the main absolute calibration probe.

7150 **Cross-calibration of the trolley with the plunging probe**

7151 The next stage of calibration involves shimming a section of the storage magnetic field to
7152 be as uniform as possible. This can be done by tailoring the surface correction coil currents
7153 temporarily to reduce the multipoles locally. Additional sets of coils (on the other side of the
7154 surface coil PCBs and/or on coils between the pole pieces and yoke) will be used to remove
7155 gradients in the azimuthal direction. This shimming needs to be done only over a restricted
7156 volume that encompasses the active volumes of the trolley probes.

7157 Ideally, the field in the homogeneous field region is measured by the trolley probes; then
7158 the trolley is moved away and the absolute probe determines the field at the locations just
7159 measured by the active volumes of the 17 trolley probes. The magnet is stabilized during this
7160 procedure, which is repeated many times. Since the absolute probe is too large to reach all of
7161 the locations measured by the trolley probes, an intermediate probe called the plunging probe
7162 is used (see Fig. 16.2). The plunging probe must be calibrated by the absolute calibration
7163 probe.

7164 To cross calibrate the trolley probes with the plunging probe during E821, the field
7165 was measured by the 17 trolley probes at the calibration location. The trolley was moved
7166 away, and the plunging probe was moved in the radial and vertical directions to measure
7167 the field at the locations formerly occupied by the trolley probes. The difference between
7168 the measurements calibrates each trolley probe with respect to the plunging probe (after
7169 correcting for drifts in the field at the level of 0.1 ppm, which were measured by fixed probes
7170 $\approx 10^\circ$ away from the calibration location).

7171 Errors in the E821 calibration procedure arose both from uncertainties on the positions
7172 of the centers of the active volumes inside the trolley (unknown at the level of a few mm
7173 in azimuthal direction) and of the trolley itself. The position uncertainty on the location
7174 of the active volumes of the calibration probes was also at the 1 mm level. Coupled with

7175 field gradients in the azimuthal direction gave a 0.03 ppm contribution to the uncertainty in
7176 the relative calibration. In the transverse plane, the trolley probes are fixed with respect to
7177 the frame inside the trolley that holds them, and the trolley transverse position is restricted
7178 below a mm by the rail system on which it rides. The vertical and radial positions of the
7179 trolley probes with respect to the plunging probe are determined by applying a sextupole
7180 field with the surface coils and comparing the change of field measured by the two probes.
7181 Magnetic field inhomogeneities of order 0.02 ppm/mm in the calibration region used in E821
7182 (see Fig. 16.7(b) and Table 16.2) coupled with radial and vertical position uncertainties of
7183 order 1 mm to give a 0.02 ppm uncertainty.

7184 Additional uncertainties arise from field drifts and uncertainty in water sample temper-
7185 ature. Each trolley probes was calibrated against the plunging probe approximately 6 times
7186 in the 2001 run of E821. The RMS scatter of these 6 measurements of the relative calibra-
7187 tions of each probe versus the center trolley probe, averaged about 0.14 ppm. The resulting
7188 uncertainty on the relative calibration was estimated as 0.07 ppm.

7189 The calibration of the center trolley probe with respect to the absolute calibration probe
7190 had an uncertainty of 0.05 ppm, so the total trolley probe calibration uncertainty was 0.09
7191 ppm.

7192 Small changes to this procedure can reduce the uncertainties to 0.05 ppm for E989. For
7193 E821, the plunging probe could only be translated along a vertical axis and radial axis. Since
7194 the trolley could not be positioned with high precision in the azimuthal direction, there were
7195 uncertainties at the mm level between the plunging probe azimuthal position and the those
7196 of the active volumes of the trolley probes (which were not visible from the exterior). To
7197 reduce these uncertainties we envision modifying the plunging probe to provide 3-dimensional
7198 positioning. The trolley position during calibration will be controlled and measured more
7199 precisely than E821 by using physical stops and/or optical survey or other high accuracy
7200 position readout of the trolley and plunging probe positions. In addition, the locations of
7201 the active volumes of all the trolley probes will be made more uniform by adjustments to
7202 the coil windings and sample position. The active volumes will be determined beforehand
7203 in the solenoid to sub-mm accuracy ¹, and precision fiducial marks on the exterior of the
7204 trolley will be added. Finally, we anticipate automating these procedures with a closed
7205 loop positioning system so each trolley probe can be calibrated dozens or even hundreds of
7206 times. By reducing the position uncertainties on the trolley probe active volumes to a mm
7207 or less in azimuth, vertical and radial, and by positioning the trolley and plunging probe
7208 more accurately during calibration, the position uncertainties will be reduced by a factor
7209 two compared to E821. The RMS scatter of relative calibration measurements should be
7210 reduced from 0.14 ppm achieved in E821 to 0.1 ppm or below assuming no improvement in
7211 the field shimming. Using petroleum jelly in the trolley probes, which has greater immunity
7212 to evaporation than water and a chemical shift with a smaller temperature dependence,
7213 might reduce this RMS scatter even further. In addition to these steps, significant attention
7214 will be paid to monitoring the probe temperatures, and additional coils might be used to
7215 further reduce local field gradients and changes during calibration. By automating the trolley
7216 probe calibration and taking dozens of measurements, field drifts can be averaged out and

¹By superimposing gradient fields in azimuth, the location where the line center does not shift determines the effective center. The linewidth will be broadened however.

7217 the error on the mean can be brought down significantly. In a similar way, the RMS scatter of
 7218 0.05 ppm in E821 on the absolute calibration of the center trolley probe should be reduced,
 7219 and by automating and repeating the calibration many times, the goal of calibrating the
 7220 center trolley probe with respect to the absolute calibration probe to an accuracy of 0.05
 7221 ppm should be achievable.

7222 We note that the calibration with the plunging probe can be done with the ring under
 7223 vacuum as many times as is necessary during E989. If necessary, calibration with the absolute
 7224 calibration probe can be done with the ring backfilled with nitrogen to reduce effects due to
 7225 the paramagnetism of O₂ which appear at the level of 30 ppb. Calibration with the absolute
 7226 probe will be done before and after muon data-taking, and any time the ring is let up to
 7227 air. More frequent absolute calibration will be performed if necessary to achieve the trolley
 7228 calibration uncertainty of 0.05 ppm.

7229 16.4.2 ³He Magnetometry

7230 A second absolute calibration probe being considered will use the NMR signal from polarized
 7231 ³He. There are several potential advantages to using hyperpolarized ³He in place of distilled
 7232 water in the calibration/field-mapping probes, which will lead to reduced systematic un-
 7233 certainties. First, the diamagnetic shielding factor (see equation 16.14) for ³He has been
 7234 calculated to be $\sigma_{^3\text{He}} = 59.967\,43(10) \times 10^{-6}$ [1]. This shielding is larger than for H₂ and
 7235 H₂O, but the uncertainty is much smaller, and the temperature coefficient is about 100 times
 7236 smaller [18, 27].

7237 A second advantage is that the susceptibility of ³He is negligible, so the NMR frequency
 7238 does not depend on the shape of the ³He volume, unlike the water sample which has to
 7239 be spherical. In addition, motional narrowing eliminates line-shape distortion and the FID
 7240 produces a Lorentzian line shape whose center is well defined. For H₂O the line shape must
 7241 be analyzed in the same way as reference [11] in order to accurately transfer the calibration.

7242 Our experience with hyperpolarized xenon suggests that that signal-to-noise is compara-
 7243 ble to the E821 H₂O calibration sample. NMR with hyperpolarized ³He produced by laser
 7244 optical pumping is also practical because the NMR signal per atom is of order 10⁵ times
 7245 larger than that from protons at 1.5 T, compensating for the much lower concentration in
 7246 the gas phase.

7247 Another advantage is that samples can be made smaller, e.g. 5 mm diameter and thus
 7248 average the field over a smaller volume. However cell-shape effects, discussed in the next
 7249 paragraph, are more difficult to deal with in smaller cells.

7250 Given the advantages above, the field can be determined in terms of the bound (or free) ³He
 7251 precession frequency with smaller systematic uncertainties than water. To get an absolute
 7252 calibration in terms of ω_p would require knowledge of $\mu_{^3\text{He}}/\mu_p$, the ratio of magnetic moments
 7253 of a free ³He to a free proton. However, the most precisely measured related quantity is
 7254 $\mu'_{^3\text{He}}/\mu'_p = -0.761\,786\,1313(33)$ (4.3 ppb), the magnetic moment ratio of a bound ³He to
 7255 that of proton in a spherical water sample [13, 1]. Still, since this ratio is known to 4.3
 7256 ppb, measurements with the water-based absolute calibration probe should agree with a ³He
 7257 based probe to 4.3 ppb. Performing this cross-check would be quite valuable. Further work
 7258 to measure $\mu_{^3\text{He}}/\mu_p$ or $\mu_{^3\text{He}}/\mu_B$, would also be very valuable.

7259 Hyperpolarized ^3He can be provided from a spin-exchange (SEOP)[29, 28] or metastability-
7260 exchange (MEOP)[30, 31] set up. We have extensive experience with SEOP and have worked
7261 closely with MEOP systems and will cooperate with expert groups at Ecole Normal Supérieur
7262 and Simon Fraser to develop an effective system. The MEOP approach has advantages for
7263 the calibration because it can be applied at room temperature and therefore in-situ in the
7264 probe. In the MEOP scenario, a turnkey 1083 nm laser light from a fiber laser (*e.g.* Keopsys
7265 CYFL-GIGA series) is distributed to each of the probe cells by a fiber. A discharge is struck
7266 in the cell to produce the excited state. Polarization of 10% or more is expected in a few
7267 minutes. A second option is hyperpolarized ^3He produced in a separate cell and transferred
7268 to the calibration cells through PFE tubing similar to the polarizers we have used for med-
7269 ical imaging work [32]. In either scenario, the dominant corrections, which are small, will
7270 arise due to cell-shape effects (δ_b in equation 16.14), i.e non-sphericity of the cell, but more
7271 importantly the polarized gas residing in any tubing or pull off left over from the cell filling
7272 procedure.

7273 High-field hyperpolarization magnetometry using the MEOP technique will be developed
7274 at Michigan working with long-term collaborators on a search for the electric dipole moment
7275 of Xe atoms [33] and medical-imaging work [34]. One of the challenges is producing high
7276 magnetization at high field (signal-to-noise is proportional to magnetization, i.e. the prod-
7277 uct of polarization and gas density). High-field MEOP polarization of ^3He has been recently
7278 studied by the ENS group [35, 36], who show that, due to higher polarization rates, nuclear
7279 polarization, of 80% at 1.33 mbar and 25% at 67 mbar, have been achieved. The magnetiza-
7280 tion at 67 mbar is essentially identical to protons in H_2O at 1.5 T, though the signals may
7281 be slightly smaller due to the difference of gyromagnetic ratios (32.4 MHz/T for ^3He and
7282 42.6 MHz/T for protons).

7283 The development work at Michigan will make use of our 1.45 T magnet and will enable
7284 probe development, polarization, and studies of temperature dependence similar to those
7285 planned for petroleum jelly. SEOP polarized samples are also under consideration, and we
7286 have significant experience in these techniques and equipment.

7287 16.5 Feedback to the magnet power supply

7288 A feedback system similar to E821 will be used to stabilize the storage ring magnetic field
7289 at the 1 ppm level or below.

7290 Field measurements from a subset of fixed probes determine an error signal from the set
7291 field value. The error signal (and integrals and possibly derivatives of the error signal) are
7292 operated on by a digital PID or other feedback controller scheme implemented in software
7293 on the NMR DAQ PC. The optimal feedback loop scheme and loop coefficients will be
7294 determined before data-taking through Zeigler-Nichols or other established tuning schemes.
7295 Field perturbations for tuning schemes can be introduced through a single coil winding on
7296 the inner radius of the vacuum chamber of the outer cryostat. A coil in this location produces
7297 a field similar to that from the outer coils, and ppm scale perturbations can be introduced
7298 with currents of a few hundred mA in a single winding.

7299 During data-taking, trolley runs, and probe calibration, the controller will update the
7300 output of a stable 16-bit current output DAC board in the NMR VME crate or a separate

7301 PCI or USB board on the NMR PC. The analog output signal is sent to an additional winding
7302 on the Danfysik DCCT used to monitor and provide precision feedback to the Bruker magnet
7303 power supply.

7304 Required updates rates are low due to long magnet time constants, and were much
7305 less than 1 Hz in E821 where a 12-bit Jorway Model 31 (voltage output) DAC residing in a
7306 CAMAC crate was used. This scheme achieved ppm level stability or better in E821. With a
7307 more stable thermal and mechanical environment for the magnet, and an optimized feedback
7308 loop, we anticipate similar or better magnetic field stability in E989.

7309 16.6 Time-dependent perturbations to the B field

7310 In E821, the ramping of the AGS magnets changed the field at the center of the storage
7311 ring by ≈ 0.5 mG over each cycle. The proton beam was extracted and muons were stored
7312 at the flattop of the cycle and there was little effect on the $g-2$ measurement. However,
7313 during the ramp up or down, the field in the storage volume changed by roughly 10-15 ppb
7314 as measured by the fixed probe NMR system [8]. The main effect is thought to be due
7315 to fields produced by currents induced in the outer mandrel [24]. Calculations which treat
7316 the magnet as coupled transformers formed by the mandrels and coils, but ignore any other
7317 effects (such as skin effects), predict field perturbations of order 25 ppb. The effects of these
7318 time-dependent external fields in the storage volume are thought to be understood within a
7319 factor of 2-3.

7320 For E989, time-dependent magnetic fields from sources such as the booster and power
7321 lines will perturb the field in the storage ring. These were measured during booster operation
7322 in 2012 at the future site of the $g-2$ ring. The main components observed were roughly 30
7323 μG at 15 Hz, 45 μG at 30 Hz, and between 80-220 μG at 60 Hz depending on the location.
7324 Using these fields as input to the calculations outlined above predicts perturbations of order
7325 ± 4 ppb in the storage ring field.

7326 The effect of these external fields in E989 can be monitored in several ways. First, the
7327 readings of the fixed probes will be timestamped with an absolute accuracy better than a ms.
7328 Since the FIDs have time constants of just a few ms, shorter than the perturbations, the fixed
7329 probe readings can be Fourier-analysed to determine the magnitudes and phases of external
7330 field effects up to frequencies of a few hundred Hz. If necessary, corrections can be applied
7331 to ω_p based on these measurements. Second, the external fields will be monitored in E989
7332 by a few high-bandwidth devices such as flux-gate magnetometers positioned at the center
7333 and around the ring (but not in the storage volume). Knowledge of these fields, coupled
7334 with detailed OPERA modeling of the effects of time-dependent external fields in progress,
7335 will lead to independent estimates of the perturbation inside the storage volume. The effects
7336 of perturbation can also be studied in a controlled manner by introducing time-dependent
7337 fields with large diameter coils and measuring the response with the fixed probes.

7338 If necessary, an active feedback system will be developed to nullify the influence of these
7339 field in the storage volume below the 10 ppb level. Several schemes are possible. Least
7340 effective might be a simple frame around the magnet with bucking coils. Currents of a few
7341 amps can be used to actively buck out external field changes of a few hundred μG detected
7342 by fluxgate magnetometers. A second approach, which is recommended, is adding a coil

winding to the inner radius of the outer cryostat and possibly the inner cryostats. Such coils can effectively oppose the currents induced in the outer and inner mandrels, and cancel the perturbations in the storage volume. These options will be explored while the magnet is shimmed, before taking data. These counter-measures should reduce the uncertainties on ω_p due to time-dependent external fields below the 10 ppb level.

Other possible time-dependent field sources include those from pulsed currents in the calorimeters and trackers, and currents drawn as filtering capacitors in electronics close to the storage ring are recharged. These effects will be measured with high bandwidth field detectors such as small pickup loops, Hall probes, or measurements based on the Faraday effect. Eddy-current or other shielding of these fields will be explored if necessary.

Transient fields from the kicker are discussed below.

16.7 Other effects on the field determination

Other contributions to the E821 systematic uncertainty on ω_p came from neglecting higher multipoles (beyond the quadrupole) in the field convolution with the muon distribution, from uncertainties in the trolley temperature (which affects the diamagnetic shielding of water and the trolley electronics), fluctuations in the trolley supply voltage (which can lead to FID baseline shifts and uncertainties in counting zero-crossings), and from uncertainty in the magnitude of magnetic field transients from the kicker (from kicker-induced eddy currents). The total of these effects was estimated to be 0.1 ppm in E821 (see [5] and Table 16.1).

These uncertainties will be reduced to 0.03 ppm in E989. First, higher field uniformity and stability and better monitoring of the muon distribution will reduce the effects of higher multipoles below 0.01 ppm. The normal sextupole contribution will be corrected for, rather than left as an uncertainty. Moving the trolley probes to larger radius will also reduce these uncertainties, as will efforts to map the field over the full aperture before and during vacuum chamber installation.

Changes in the trolley temperature lead to observed fluctuations in trolley probe readings of order 0.05 ppm/°C. These effects will be extensively studied in a thermal enclosure and ultra-stable solenoid so temperature effects can be corrected rather than left as an uncertainty. The temperature sensors in the trolley will be calibrated to 0.1°C. Also, the possibility of using petrolatum in the trolley probes will be investigated. This would reduce the temperature sensitivity. Finally, applying a high-emissivity coating to the trolley could lead to a reduction in the temperature rise of the trolley (perhaps by a factor of two or more). The efforts should reduce temperature-related uncertainties by a factor of 2 or more.

The trolley 9.9 V power supply will be replaced with a modern, stable linear supply. The E821 supply drifted around 50 mV which coupled with a voltage sensitivity of roughly 0.4 ppm/V observed in the probe readings. Stability and monitoring at the level of 10 mV or below is sufficient to eliminate this uncertainty, and should be achievable.

To reduce the effects of the kicker field transients we will measure the kicker field in the storage volume before data-taking using the Faraday effect, as was done in E821 [40]. In E989 we will take additional steps. First we will use the Faraday measurements in the storage volume to calibrate an additional system just outside the storage volume. This will

7385 be monitored during data-taking in E989 and used to correct the field average. The kicker
7386 pulses might be recorded as a redundant check on the Faraday measurements.

7387 These efforts should reduce the systematics observed in E821 to 0.03 ppm in E989.

7388 16.8 Magnet Shimming

7389 16.8.1 Overview

7390 The main technical objective of the $g - 2$ storage ring shimming is to produce a field that
7391 is extremely uniform when averaged over azimuth. Both the muon distribution and the
7392 average field can be described by multipole expansions (see Sec 16.3). Care should be taken
7393 to minimize higher-order multipoles in the field. Improved field uniformity at any local
7394 azimuthal position is also desirable since the performance of the NMR probes relies on
7395 keeping the field gradients as small as possible in order to optimize the measurement of the
7396 free induction decay (FID) signal (see Sec 16.2.3). Furthermore, small field gradients reduce
7397 the uncertainty contribution from the position uncertainty of the probes. Since the probes
7398 sample the field over a non-negligible volume, the requirements on knowledge of the position
7399 are relaxed if the field gradients are minimized.

7400 Before shimming, the magnet was designed to produce a field uniformity in the muon
7401 storage region of better than a few parts in 10^4 . This was achieved by using high-quality
7402 steel for the magnet yoke, and ultra-low carbon steel (ULCS) for the pole pieces. Upon
7403 assembly, the field uniformity is improved by more than two orders of magnitude through
7404 a shimming sequence. The general shimming strategy implemented in E821 was two-fold:
7405 passive shimming via precision alignment of ferromagnetic materials and active shimming
7406 utilizing current distributions. We will base our general shimming procedure on that of
7407 E821 and the experience gained therein. The $g - 2$ superconducting coils, yoke, pole pieces,
7408 and shims has been simulated with OPERA-2D as well as OPERA-3D. The results of these
7409 simulations are compared both with POISSON simulations and results obtained during the
7410 development of E821 [19, 20, 21, 22, 23, 25, 26]. One critical aspect of the simulation is
7411 the use of realistic B-H magnetization curves. Although the steel is not fully saturated
7412 at 1.45 T, the response is not perfectly linear. This non-linearity is partially responsible
7413 for generating higher-order multipole moments in the shimming simulations, and must be
7414 recognized during the actual shimming procedure. Our OPERA simulations will allow for a
7415 sophisticated shimming plan that improves the overall uniformity of the field in E989. The
7416 shimming consists of the following elements: (1) Passive shimming using precise positioning
7417 of materials, and (2) Active correction coils.

7418 16.8.2 Passive Shims

7419 Passive shimming refers to the set of mechanical adjustments that are performed during the
7420 assembly of the ring and remain fixed during a long running period. The general strategy is
7421 to begin with adjustments far from the muon storage region and work towards it with finer
7422 and finer adjustments. The principle passive shimming controls consist of the following:

- 7423 1. Iron pieces on the yoke

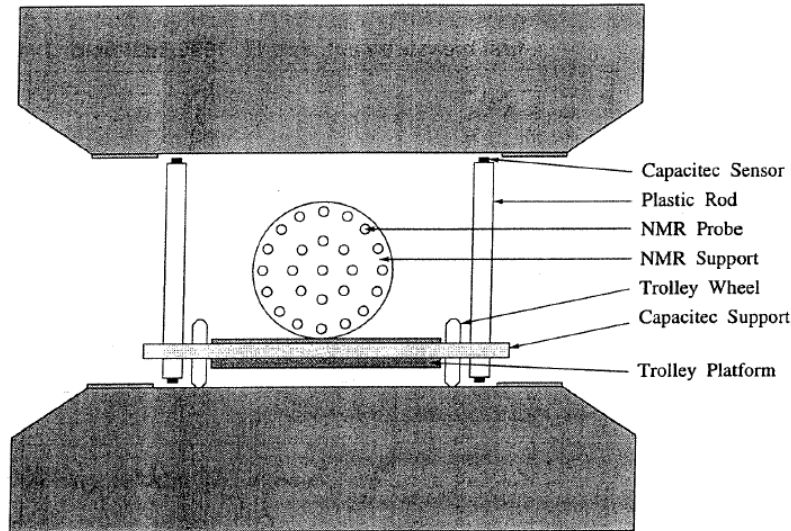


Figure 16.13: Schematic depiction of the NMR shimming trolley situated on a platform. Capacitive sensors on plastic rods help measure the pole piece alignment.

- 7424 2. Alignment of the pole faces
- 7425 3. Wedge shims in the air gap between the pole piece and yoke
- 7426 4. Edge shims in the gap between upper and lower pole faces
- 7427 5. Iron pieces in the azimuthal gaps between adjacent pole faces

7428 Throughout the physics measurement, the NMR trolley described in Section 16.3 will
 7429 travel around the ring to map out the magnetic field. However, prior to the installation of
 7430 the vacuum chambers, more space is available between the pole pieces and a larger trolley
 7431 will be used. This shimming trolley (see Figure 16.13) consists of 25 NMR probes; one is
 7432 at the center of the muon storage region, eight are at a radius of 2.25 cm, and 16 are at
 7433 a radius of 4.5 cm. This allows a mapping that extends to the outer radius of the muon
 7434 storage region. The shimming trolley was positioned on the end of a ≈ 7 meter turntable
 7435 arm positioned about the center of the storage ring. Rotating the turntable allowed the
 7436 shimming trolley to map the field at various azimuthal positions.

7437 The platform on which the shimming trolley rests also allows for a precision measurement
 7438 of the vertical gap between the upper and lower pole faces. Plastic rods with capacitive
 7439 sensors (model Capacitec HPB-150A-A-L2-10-B-D) on each end allowed for a determination
 7440 of the relative parallelism between the poles [26]. By rotating the assembly by 180° about the
 7441 vertical axis, any systematic error due to the relative length of the rods can be eliminated.
 7442 The shimming trolley provides data that is analyzed and used for the next stage of the
 7443 shimming procedure.

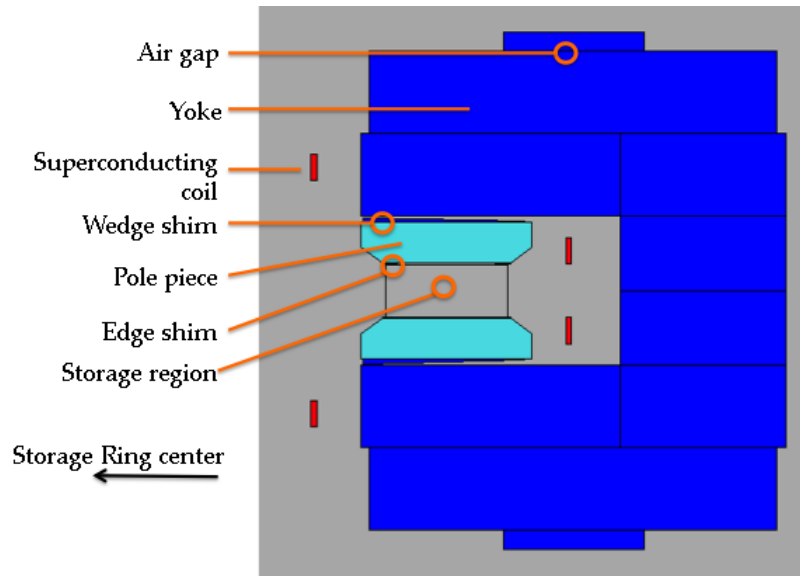


Figure 16.14: OPERA-2D model of the $g - 2$ magnet. The yoke and wedge shims are steel and shown in blue. The yoke (cyan) is made from ultra-low carbon steel (ULCS). The current in the superconductor coils is into the page for the inner coils and out of the page for outer coils.

7444 Procedure

7445 A two-dimensional slice of the $g - 2$ magnet simulated in OPERA-2D is shown in Figure 16.14
7446 fore reference.

7447 **Yoke Iron** The yoke is subdivided into twelve 30° sectors, as described in Section 10.2.
7448 Long wavelength azimuthal variations in the field uniformity can be addressed by adjusting
7449 the positioning of pieces of iron on the outer surface of the yoke. In particular, an increase
7450 in the air gap between the top piece of steel and the upper yoke plate (see Figure 16.14)
7451 leads to an increase the overall reluctance of the magnetic circuit. In this manner, rough
7452 adjustments to the dipole field can be achieved on a sector-by-sector basis. In other regions
7453 of the ring, steel shims will be added to the outside of the yoke in order to compensate for
7454 holes that are required for items like vacuum feedthroughs, the inflector, etc.

7455 **Pole Piece Alignment** The Capacitec sensors mounted to the shimming trolley apparatus
7456 will measure the gap to a precision of $< 0.25 \mu\text{m}$. An increase in the gap size of $25 \mu\text{m}$
7457 corresponds to a 100 ppm decrease of the dipole field. A $50 \mu\text{m}$ tilt over the length of the
7458 pole corresponds to a change in the quadrupole moment of 120 ppm. Thus the information
7459 from the shimming trolley will be used to properly align the pole pieces.

7460 **Wedge Shims** Wedge shims are inserted into the 2-cm air gap between the pole piece
7461 and the yoke, as depicted in Figure 16.15. The gap is designed to isolate the high-quality
7462 precision pole pieces from the yoke steel, which contains some magnetic inhomogeneities.

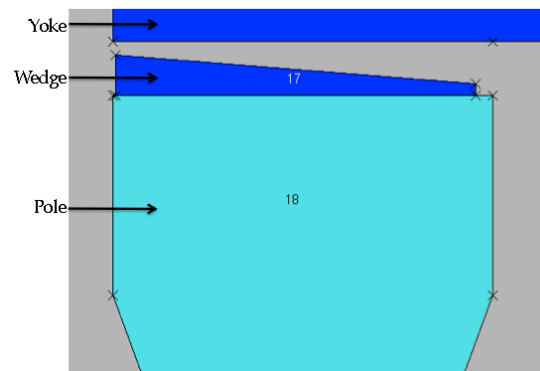


Figure 16.15: OPERA-2D model of the $g - 2$ magnet, zoomed in on the air gap between the yoke and pole pieces. The wedge shims are radially adjustable.

7463 Each 30° sector contains 72 wedge shims, which are 9.86 cm wide (azimuthally) and 53 cm-
 7464 long (radially)[37]. This is shorter than the 56 cm-long pole pieces (radially), to accommodate
 7465 radial adjustments. At the inner radius, the wedge shims are 1.65 cm thick, while at the
 7466 outer radius, they are 0.5 cm thick. Viewed from above, each wedge shim is rectangular.
 7467 Thus the space between adjacent wedge shims increases as the radial coordinate increases.

7468 The angle of the wedge shims was calculated to be 20 milliradian in order compensate for
 7469 the intrinsic quadrupole moment produced by the C-shaped magnet. Due to the asymmetry
 7470 in the C-magnet, the field lines tend to concentrate in the gap near the return yoke. The
 7471 dipole field is determined by the average thickness in the air gap above the storage region.
 7472 The average wedge thickness is adjusted by translating the radial position of the wedge
 7473 shims. Because of the shallow angle of 20 mrad, a radial movement by $50 \mu\text{m}$ changes the
 7474 gap by $1 \mu\text{m}$, allowing fine control for the dipole field. OPERA-2D simulations show that
 7475 inserting the wedges into the air gap (towards the return yoke) radially by $50 \mu\text{m}$ produces
 7476 a 5.4 ppm increase in the dipole field. The quadrupole and higher-order multipoles are each
 7477 affected by less than 0.1 ppm for this adjustment.

7478 **Edge Shims** Each of the 36 pole pieces has four removable edge shims mounted on the
 7479 surface closest to the muon storage region, as shown in Figure 16.16. Each shim is 5 cm
 7480 wide (radially), spans one pole piece (10° azimuthally), and is positioned at either the inner
 7481 or outer edge of the pole faces. Variation of the thickness of the edge shims can produce
 7482 predictable multipole corrections.

7483 In E821, the shims were ordered oversized (3.2 mm for the outer shims and 4.4 mm for
 7484 the inner shims) and then ground down to tune the quadrupole through octupole moments.
 7485 A first pass was performed to uniformly grind the shims as a function of azimuth. A final
 7486 pass optimized the thickness of the edge shims pole-piece-by-pole-piece.

7487 We have studied the effect of systematic shim thickness variations in OPERA-2D. Since the
 7488 2D model assumes vertical symmetry, the upper and lower edge shims are always adjusted
 7489 simultaneously. Symmetrically increasing the thickness of both the inner and outer edge
 7490 shims primarily affect the sextupole moment. OPERA-2D simulations found that a $100 \mu\text{m}$

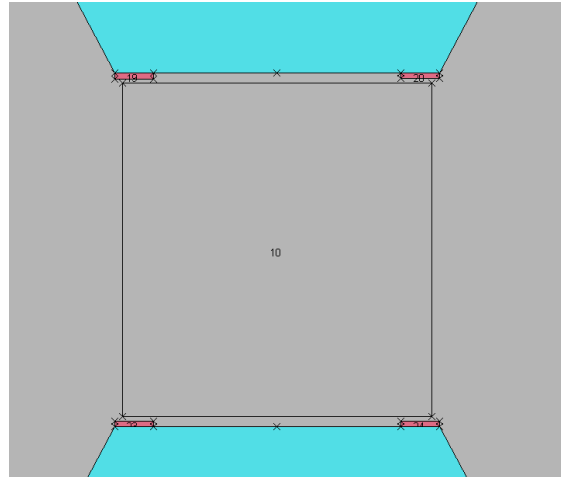


Figure 16.16: OPERA-2D model of the $g - 2$ magnet, zoomed in on the storage region. Edge shims are mounted on the pole pieces. “Inner” refers the shim at smaller radius (closest to the center of the ring), while “outer” refers to the shim at the larger radius (closest to the return yoke).

7491 increase in the edge shim thickness in all four corners increases the sextupole moment by
 7492 10.8 ppm. Asymmetric thickness adjustment leaves the sextupole moment unchanged and
 7493 allows fine tuning of the quadrupole and octupole moments. Increasing the outer shim
 7494 thickness by $100\mu\text{m}$ while decreasing the inner edge shim thickness by the same amount
 7495 increases the quadrupole and octupole moments by 13.2 ppm and 5.6 ppm, respectively.
 7496 Although the simulation utilized vertical symmetry, this model can be extended to up-down
 7497 and diagonal (skew) asymmetries.

7498 We plan to use a similar shimming strategy in E989. We will order oversized edge shims,
 7499 map the field, grind the shims, and iterate. Based on the experience of E821 and the extensive
 7500 OPERAsimulations, we believe this phase of the shimming will require only two iterations.

7501 **Gap shims** Significant variations in the magnetic field occur at the azimuthal boundaries
 7502 between adjacent pole pieces, as shown in figure 16.17. The effect is even more pronounced at
 7503 the pole piece surface than in the storage region, jeopardizing the effectiveness of the fixed
 7504 probes located near the inter pole piece gaps. In E989, we plan to reduce the azimuthal
 7505 variations in the field by shimming the gaps with thin iron plates. The basic concept would
 7506 be to span the surface of adjacent pole pieces with high quality steel plates varying from 10
 7507 to $100\mu\text{m}$. Simulations show that a local change of $10\mu\text{m}$ in the air gap between the pole
 7508 pieces results in a 40 ppm shift in the dipole field. This should be a fairly short wavelength
 7509 affect that will reduce the local field gradients and improve the performance of the fixed
 7510 NMR probes mounted in the vacuum chambers.

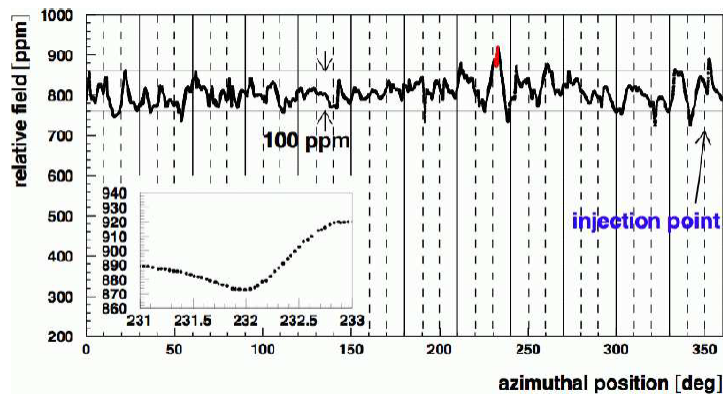


Figure 16.17: The magnetic field determined by the center NMR trolley probe versus azimuthal position in the storage ring during one trolley pass (reproduced from Ref [5]). The solid vertical lines denote boundaries between the 12 yoke sectors. The dashed vertical lines denote the pole piece boundaries.

7511 Radial Field

7512 For E821, an auxiliary measurement of the radial component of the magnetic field was per-
 7513 formed during the passive shimming phase prior to the installation of the vacuum chambers.
 7514 In the storage region, the direction of magnetic field is principally vertical. The presence of a
 7515 radial field component has a significant impact on the muon storage beam dynamics, affect-
 7516 ing both the mean vertical position and the vertical betatron oscillations. Quantitatively,
 7517 the radial field component needs to be measured to ≈ 10 ppm. However, the NMR probes
 7518 only measure the total magnitude of the magnetic field without providing information about
 7519 the separate vertical and radial components. In E821 an auxiliary measurement using Hall
 7520 probes was implemented to quantify the radial component of the field. We plan to repeat
 7521 this procedure.

7522 Figure 16.18 shows a schematic representation of the E821 setup used to measure the
 7523 radial field. Two Hall probes (BH-206, F.W. Bell) were vertically aligned to measure the
 7524 radial magnetic field, with the Hall currents running in the z and y directions. To ensure
 7525 alignment of the setup with respect to the gravitational vertical direction, electrolytic tilt
 7526 sensors (RG33A, Spectron Systems Technology, Inc.) were mounted to the support structure.
 7527 Finally to account for potential misalignment of the Hall probes with respect to the support
 7528 structure, the measurements were repeated after rotating the entire structure by 180° about
 7529 the vertical axis and taking the difference of the Hall voltages.

7530 Figure 16.19 shows the data from the Hall probes overlaid on the expected radial field
 7531 as determined from the multipole expansion of the absolute field measurement. The overall
 7532 precision of the radial field measurement was significantly better than the required 10 ppm.
 7533 Figure 16.20 shows the radial field measurement (dots) from the Hall probe as a function
 7534 of the azimuthal position around the ring. The line in this plot represents the measured
 7535 pole tilt derived from the capacitive sensor data described above. The tracking of these two
 7536 curves demonstrates the dependence of the radial field on the pole alignment.

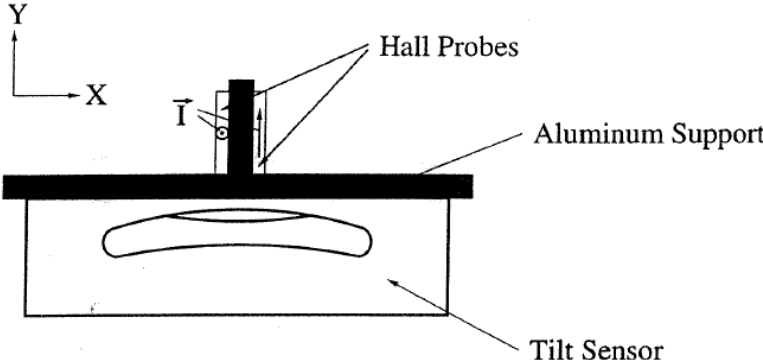


Figure 16.18: (a) A schematic representation of the radial field measurement configuration. Two Hall probes are mounted to measure the radial component of the field (x) with Hall currents oriented in the z and y directions. The rigid configuration is equipped with a tilt sensor. Rotating the entire setup 180° about the y -axis isolates the radial component.

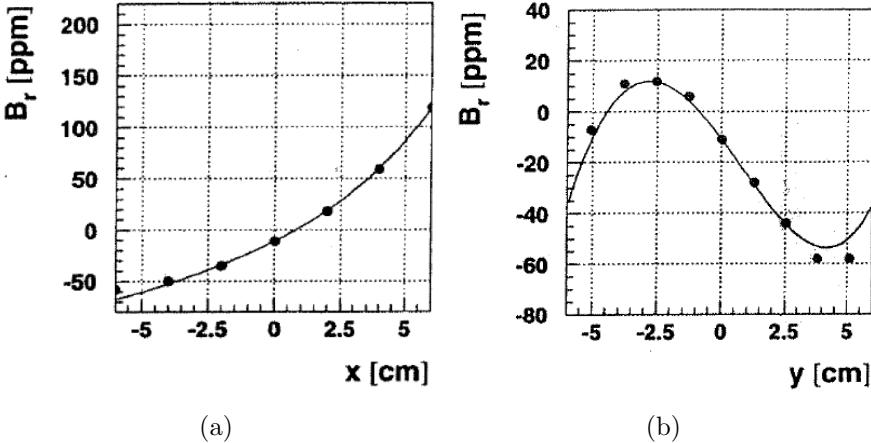


Figure 16.19: Radial component of the magnetic field in ppm as a function of (a) radial position x and (b) vertical position y . The dots show the data from the Hall probe, while the solid lines represent the field variation expected from the multipole coefficients calculated from the absolute field measurement.

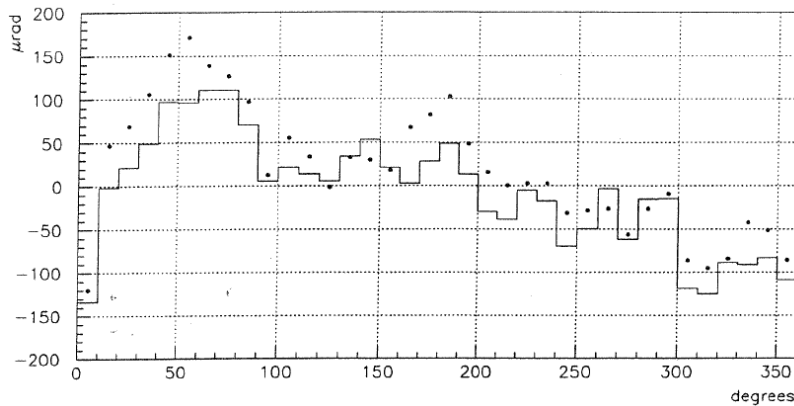


Figure 16.20: (a) The radial field measurement (dots) from the Hall probe and the average pole tilt (line) from the tilt sensor are shown as a function of the azimuthal position around the ring.

16.8.3 Active Shims

Active shimming refers to the adjustment of current distributions to eliminate any residual field non-uniformities that remain after the passive shimming is complete.

The principle active shimming controls consist of the following:

1. Control of the main superconductor current
2. Surface correction coils on printed circuit boards mounted between the pole face and the vacuum chamber
3. Dipole correction loops placed in the gap between the wedge shim and the yoke
4. Gap correction loops located in the azimuthal gaps between adjacent pole faces

Main Current

The central value of the dipole field is determined primarily by the current in the main superconducting coils. The nominal current is 5200 Amp per turn. OPERA simulations show that an increase of 1 A increases the field in the storage region by about XX ppm. During beam-on data collection periods, the field is monitored by the fixed NMR probes. The shape of the magnet gets distorted due to temperature variations, so a feedback loop is utilized to stable the dipole field.

Surface Correction coils

Correction coils on the surface of the poles permit fine control of static, and slowly varying errors. The surface coils can be used to correct lowest multipoles to tens of ppm, thus providing significant overlap between the iron shimming and the dynamic shimming. These coils have been constructed to generate moments over the entire 360° azimuth. The coils

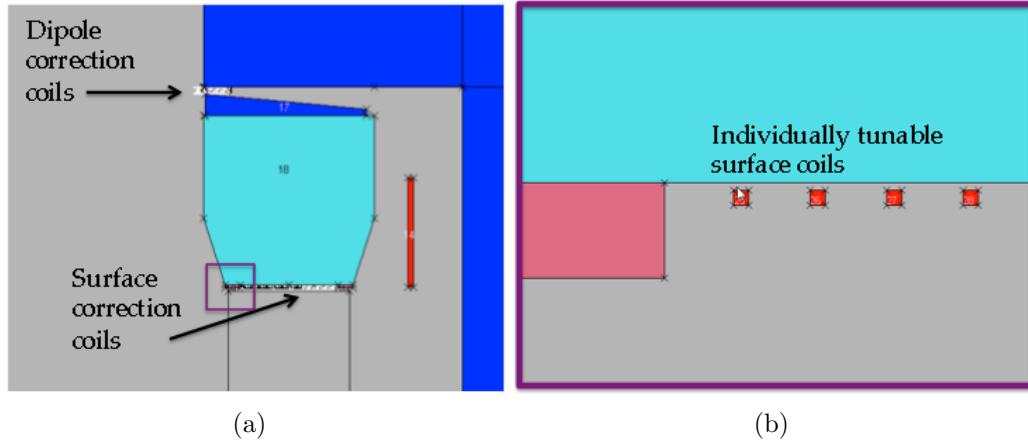


Figure 16.21: OPERA-2D depiction of the dipole correction coils and the surface correction coils. (a) Schematic overview showing the positions of the current traces on the printed circuit boards. The purple box is zoomed in and displayed in panel (b). Individual traces are adjusted to tune various multipole contributions.

7558 were designed with printed circuit boards, with 120 wires running azimuthally around the
 7559 ring on the top and bottom pole surfaces facing the storage ring gap, and spaced radially
 7560 2.5 mm apart, to avoid lumpy effects which generate higher multipoles. The boards must
 7561 be thin enough to fit between the pole faces and the vacuum chamber. We have studied the
 7562 surface correction coils in OPERA-2D (see Figure 16.21) and verified that the various multipole
 7563 contributions can be compensated with the appropriately applied current distributions. A
 7564 summary of the principle current distributions is shown in Table 16.8.3. E821 used these
 7565 coils successfully to shim out the final few ppm for the higher order multipoles.

Table 16.3: Current distributions needed to correct for various multipole components, and the maximum range that can be corrected with less than 1 Amp. The currents are calculated at the fixed vertical position of the boards ($y=a=9$ cm).

Multipole	$K(x)$ ($y = a$)	Maximum range (ppm)
Quadrupole	a	20
Sextupole	$2ax$	10
Octupole	$3ax^2 - a^3$	8
Decupole	$4ax(x^2 - a^2)$	6
Duodecupole	$5a(x^4 - 2x^2a^2 + a^4/5)$	4
Quattuordecupole	$2ax(3x^4 - 10x^2a^2 + 3a^4)$	2

7566 For E989, we plan to fabricate 12 new printed circuit boards at Fermilab that extend over
 7567 each sector. Because these coils extend azimuthally around the entire ring, interconnects
 7568 between adjacent boards must be designed. We will study the trace spacing and radial
 7569 range to ensure our solution provides fine enough tuning without drawing too much power.
 7570 Currents are expected to be limited to about 1 Amp. Finally, we will explore the option of

7571 using the bottom of the boards for active current shims in the gaps between pole pieces.

7572 **Dipole correction loops**

7573 The “continuous” ring was built with 10° pole sections, 36 of which form an almost continuous
7574 ring. Dipole correction coils are located in the air gaps of each 10° pole, as depicted in Figure
7575 16.21 (a). These coils consist of 50 turns of copper wire wound in a rectangular shape. The
7576 dipole correction coils will be capable of tuning each pole section independently. E821 used
7577 active NMR feedback loops to stabilize the field by adjust the main superconductor current.
7578 It is possible that the field could be stabled in each pole piece separately by using the local
7579 NMR feedback to adjust the dipole correction currents. This would be particularly useful
7580 if temperature gradients over the 14 m diameter ring lead to different field distortions in
7581 different locations.

7582 **Gap correction loops**

7583 We want to minimize the azimuthal variation of the magnetic field, as explained in Section
7584 16.8.2. Thus, E989 will use OPERA-3D to study the possibility of adding small loops to the
7585 bottom of the surface correction coil boards at the azimuthal positions between adjacent
7586 poles. We would primarily have control over the dipole moment, with limited ability to
7587 modify the higher order multipoles.

7588 **16.8.4 E821 results**

7589 E821 successfully implemented many of the passive and active shimming techniques described
7590 above. Table 16.8.4 shows the historical progression of the uniformity of the field as a
7591 function of time during the commissioning phase of the experiment. As they adjusted shims
7592 closer to the storage region, the higher order multipoles became more controlled. The final
7593 column shows the principle changes that were implemented at that step. We plan to use this
7594 experience to compress the shimming schedule for E989.

7595 **16.9 Alternatives**

7596 The determination a_μ in terms of ω_a/ω_p and μ_μ/μ_P requires the storage ring magnetic field be
7597 measured in terms of the muon distribution weighted free proton precession frequency, ω_P . In
7598 principle this could be done by injecting a 3.1 GeV/c polarized proton beam into the storage
7599 ring with a proton spin analyzer (polarimeter) in the ring based on the spin dependence of
7600 p -carbon elastic scattering. The anomalous precession frequency would be close to 40 MHz,
7601 and the phase space of the protons and muons would have to be matched or measured to mm
7602 precision. Proton beam measurements of the field distribution would have to alternate with
7603 muon injection. Developing a polarized proton source, 3.1 GeV/c accelerator, polarimeter,
7604 proton beam position monitoring hardware etc. would add significant cost and technical
7605 challenge to the experiment, and it’s not clear that the field determination could be made
7606 to 70 ppb. Further, during periods of muon injection, an NMR-based system of fixed probes
7607 outside the storage volume would still be required to monitor the field and provide feedback

Table 16.4: Quadrupole (Q), Sextupole (S), Octupole (O), and Decupole (D) multipoles, broken down into normal(n) and skew(s) components, in ppm, evaluated at the storage radius ($r = 4.5$ cm).

Date	Q_n	S_n	O_n	D_n	Q_s	S_s	O_s	D_s	Action
Jun 1996	-169.12	112.03	-34.16	23.71	27.06	5.82	3.12	0.46	Initial configuration
Nov 1996	5.52	3.19	-1.11	1.95	9.13	5.32	0.85	0.45	Edge shims ground uniformly
Jul 1997	5.26	2.94	-1.03	1.45	12.26	2.78	0.36	0.25	Edge shims ground in each pole piece+ pole alignment
Aug 1998	7.73	-5.29	-2.79	0.38	-2.07	-0.02	-0.25	0.71	Final passive shimming
Sep 1998	-2.54	-1.25	-2.70	0.34	-2.39	-0.18	-0.28	0.42	Active shimming commissioned
PRD	0.24	-0.53	-0.10	0.82	0.29	-1.06	-0.15	0.54	Publication

7608 to the power supply to stabilize the field. A similar NMR system would be required to shim
7609 the magnet.

7610 Other field measurement technologies such as Hall probes have been considered. One
7611 advantage is that a 3-axis device could make measurements of B_x , B_y , B_z . However, Hall
7612 probes have a significant temperature dependence ($\leq 10\text{ppm}/^\circ\text{C}$), resolutions at the 1 ppm
7613 level (versus 20 ppb for NMR), and fluctuating offsets. Commercial technology is currently
7614 inadequate for the level of accuracy sought in E989. Further, they would require frequent
7615 calibration in terms of an equivalent free proton precession frequency, so an NMR-based
7616 absolute calibration probe would still have to be developed and tested.

7617 Finally we note that pulsed NMR is preferred over CW techniques since the latter typ-
7618 ically requires a small field modulation coil that perturbs the local field, introduces image
7619 fields in the iron poles and yokes, and is potentially difficult to calibrate at the precision
7620 sought in E989. In addition, the lineshape analysis required in CW techniques to achieve
7621 ppb levels of precision is substantially more difficult than the analysis methods required for
7622 analyzing pulsed NMR FIDs. Newer approaches replace the field modulation with frequency
7623 modulation, but still must deal with the time constants of the probes and of the samples,
7624 and still need a sophisticated signal analysis to determine the resonance frequency precisely
7625 from the time domain response.

7626 For the trolley garage, an alternative redesign has been considered by changing to a
7627 switch-yard solution. This could possibly increase durability due to reduced mechanical
7628 movement and improve the handling and operability. In addition, except for the trolley
7629 itself, the rails remain completely in the same position during the trolley measurement
7630 and the muon injection. In the current garage, this is not the case and hence the slightly

7631 changed configuration during trolley operation and standby introduces a small distortion
7632 to the magnetic field measurement. A switch yard design would eliminate this to the most
7633 extent possible since the rails barely move.

7634 We will also investigate improvements with respect to systematic uncertainties by chang-
7635 ing the size and shape of the trolley probes. Smaller probes could allow positioning of the
7636 probes to even larger radii and hence improving on the determination of higher multipoles.
7637 However, the expected gains need to be understood to verify such change as the current
7638 probes are certainly already close to optimal.

7639 A major alternative could be the design of a new trolley system with much reduced
7640 onboard functionality. Given the crucial role of this system in the g-2 experiment, a replace-
7641 ment of the existing trolley would eliminate such single point of failure. In this alternative
7642 version, the onboard electronics would ideally be reduced to only host the multi- and du-
7643 plexer, a preamplifier, and a small control unit including some of the sensor functionality
7644 (temperature, pressure, position measurement). This scheme requires that the NMR analog
7645 signal can propagate with minimal distortion over the 45 m long co-axial cable to the outside
7646 of the vacuum where electronics for frequency determination would be located. Similarly,
7647 the RF pulse would be sent to the trolley from the outside eliminating the need of the RF
7648 amplifier onboard. The processing of the NMR signal could then happen analogously to
7649 the fixed probes in the proposed new readout system with full digitization. However, such
7650 an alternative development would require major cost and labor resources and the actual
7651 implementation has to be based on a more detailed cost-benefit-analyses.

7652 **16.10 ES&H**

7653 The trolley garage, which is part of the field monitoring system, is a vacuum vessel. Lasers
7654 are used during survey/alignment activities and calibration activities. The storage ring
7655 magnetic field is at 1.45 T and has a strong fringe field in the interior of the ring. The
7656 hazards encountered in the field monitoring operation are therefore Laser Hazards, Vacuum
7657 Vessel Hazards, and High Magnetic Field Hazards. Engineering review will determine the
7658 necessary requirements on the vacuum vessels. Job Hazard Analysis will be performed for
7659 any testing, installation, or operational task that involves personnel working in the high field
7660 environment or using lasers.

7661 In addition there will be three or four 19" racks of field measurement electronics. These
7662 will typically draw a few kW of power each, and do not produce high voltages or large
7663 currents. All personnel working on this equipment will be trained to ensure safe operation.

7664 **16.11 Risks**

7665 **Fixed Probe System**

7666 The fixed probe system is essential for field monitoring during data taking. The technology
7667 required to monitor the field at the required level already exists so the risks are primarily in
7668 two other categories; (1) the risk that the refurbishment of the fixed probe system can not
7669 be completed on time, (2) the magnet stability is worse than anticipated.

7670 The refurbishment of the fixed probe electronics requires that new preamplifiers for the
7671 NMR signal and a new RF pulse amplifier must be found since the vendors for the E821
7672 components are not in business. These risks are minor or non-existent as new candidate
7673 components (with higher performance in some cases) have been identified and will be tested.
7674 The risks to the schedule come primarily from the time and effort required to refurbish the
7675 roughly 400 fixed probes and the NIM crate and multiplexer electronics. The mechanical
7676 work on the fixed probes can be distributed to additional university or laboratory machine
7677 shops so it may be done in parallel. Filling the samples and tuning the probes can also be
7678 done in parallel by any group with a vector impedance meter or network analyzer. In E821
7679 such work was done by undergraduates. If the electronics work falls behind schedule, it can
7680 also be done in parallel at the Electronic Design Facility at Boston University, at Argonne,
7681 or Fermilab once new boards have been designed.

7682 The second risk regarding magnet stability is more serious but unlikely as the new build-
7683 ing is designed specifically for magnet stability. If the anticipated gains in magnet stability
7684 do not materialize, additional insulation can be applied around the magnet and on the ex-
7685 perimental hall floor. If necessary, an inexpensive, easily installed and removed thermal
7686 enclosure from 80/20 aluminum framing and foam board insulation can be constructed.

7687 **Absolute Calibration System**

7688 The calibration of the trolley probes requires that the absolute calibration probe and plunging
7689 probe and their positioning systems have been extensively tested. The risks here are that
7690 the probes are damaged, and that the system doesn't perform to specifications.

7691 If the calibration probes are damaged, they can be remade. The most delicate part is
7692 the highly-spherical glass bulb used in the absolute calibration probe. This part has survived
7693 nearly 20 years already, and the vendor, Wilmad LabGlass has already been contacted
7694 regarding making replacements. Spare absolute calibration probes will be prepared for E989,
7695 and ready for use long before data-taking.

7696 The risk that the new calibration system does not perform to specifications are small.
7697 The changes from E821 are relatively minor but should be effective (primarily adding motion
7698 in the azimuthal direction for the plunging probe, adding a closed loop positioning system,
7699 and precise location of trolley probe active volumes). These systems involve little technical
7700 risk and their performance can be tested thoroughly before the experiment takes data. The
7701 worst schedule risk is losing roughly 2-3 weeks of muon data. If the calibration system is
7702 not ready when the experiment starts, muon data can still be taken while the calibration
7703 system is being prepared. When the system is ready, roughly 2-3 weeks of muon data would
7704 be lost for installation as it would involve letting the vacuum chambers up to air, installing
7705 the system, testing it, and pumping back down.

7706 **Trolley**

7707 The trolley and its associated mechanics are a central piece in the measurement of the
7708 magnetic field of the storage ring. A major risk would be the partial or complete failure of
7709 the onboard electronics. Depending on the severity of the failure mode, the consequences
7710 could range from a replacement of the broken component, a redesign of parts of the electronics

7711 up to the need of a complete redesign of the trolley electronics. While the probability is low
7712 for this to happen, a realization of this risk could have both significant cost and schedule
7713 impact. Mitigation of the risk is hence important. It involves careful refurbishment of the
7714 system with guidance from former experts as well as the refurbishment of both existing
7715 trolleys so that both are fully operational.

7716 Other major devices associated with the trolley, namely the garage and drive, could be
7717 damaged during the shipping process or due to mishandling in the refurbishment work. This
7718 would cause additional required efforts to repair beyond the current anticipated upgrade
7719 plans. Good packing for the shipping, immediate inspection of the functionality after the
7720 transport and careful handling following the instructions of former experts will help to mit-
7721 igate this risk. During the refurbishment, we might find that portions of the motor control
7722 systems in the garage and the drive might have failed due to the age of the electronics. While
7723 low in probability, the main mitigation is in testing these components as early as possible to
7724 verify that they still operate as needed. Otherwise, a replacement was needed adding some
7725 additional costs and labor efforts. Similarly, the trolley garage mechanics might be diagnosed
7726 to be too low in reliability requiring more effort beyond the planned upgrade to establish a
7727 well working system for the full data taking period. This risk will either be realized or retired
7728 after a thorough inspection of the garage mechanism once shipped to Argonne National Lab.
7729 The probability of this risk is expected to be low.

7730 Another risk is associated with the position measurement upgrades to determine the
7731 longitudinal position of the trolley during its data taking. There is a small possibility that the
7732 anticipated upgrade of the barcode reader does not succeed because of remaining overheating
7733 or other unforeseen issues. In the case of this event, alternative solutions must be sought to
7734 meet the requirements. Additionally, general upgrades to the barcode reader or to increase
7735 the heat dissipation could end up in the need to extend the trolley's length. While unlikely,
7736 this would require adaption of the trolley garage's dimensions and the associated vacuum
7737 chamber layout.

7738 Other Performance Risks

7739 Many of the risks that we don't achieve the uncertainties outlined in Table 16.1 can be
7740 mitigated by spending enough time on trolley runs and trolley calibration so the goals are
7741 met. These activities will often conflict with data-taking which reduces the statistical un-
7742 certainties on ω_a . A balance between these activities will be established that brings the
7743 uncertainties down on a_μ most efficiently. This will depend on actual event rates and mag-
7744 net stability. If the storage ring dipole and quadrupole fields are at least a factor of two
7745 more stable than E821, and if the field measurement hardware and shimming performance
7746 goals outlined above are met, the target on ω_p should be achievable without major risks to
7747 the schedule.

7748 Shimming

7749 The shimming procedure used in E821 has been examined and provides the basis for shim-
7750 ming the field in E989. Careful review of past safety procedures will be necessary to ensure
7751 the successful, safe shimming of the field. An examination of associated risks reveals two

7752 main categories of risks associated with the shimming procedure: damage to equipment and
7753 delay of the experiment. To mitigate each category, we will begin as early as possible with
7754 a well-formulated plan.

7755 Damage during shipping is a risk for the yoke, poles, wedge shims, edge shims and dipole
7756 correction coils. To address this risk, we have shipped most of the steel well in advance of
7757 the installation in the experimental hall at Fermilab. If there were any unexpected accidents
7758 in transit, this would allow us the necessary time to order replacements for these parts.
7759 Additionally, there are ongoing risks to the materials during both the shimming procedure
7760 and the subsequent running due to the enormous energy stored by the $g-2$ magnet. The stray
7761 fields are significant enough to loose ferromagnetic materials in the experimental hall towards
7762 the steel. These pieces could potentially impact and damage the precisely manufactured
7763 surfaces of the shims and poles, causing major distortions to the field and posing a significant
7764 risk to human safety. To address these issues, we will follow safety procedures to ensure that
7765 no loose magnetic materials are left in the hall when the ring is powered. We will check that
7766 the shims are securely fastened to the pole and yoke pieces. We will continue to examine the
7767 forces on the various screws and bolts in simulations to ensure that sufficient safety factors
7768 are utilized. In all cases, following disciplined safety procedures will prevent potentially
7769 damage to both people and equipment.

7770 The shimming procedure calls for ordering oversized edge shims and then grinding them
7771 down to the appropriate thickness. There is a schedule risk associated with grinding off too
7772 much material. We would then need to reorder the shims and recommence the grinding step
7773 of the shimming, which would delay meeting our shimming goals. To mitigate this we will
7774 continue to compare our simulation results with past experience to get a solid understanding
7775 of the dependence of the multipole moments on the shim thickness. We will proceed with
7776 a conservative plan to grind in a couple of iterations, so as to prevent “overshooting” the
7777 required thickness.

7778 A schedule risk would be realized if the shimming procedure fails to achieve the required
7779 uniformity. This could occur in a variety of ways, for example if detector systems introduce
7780 large, non-symmetric distortions to the field or if the finite-size effects of surface coils limit
7781 our fine tuning ability. If we do not achieve our uniformity goals, we would have to make
7782 improvements in other areas - namely, better knowledge of the probe positioning, better
7783 absolute calibration and better temperature control. To address these issues, we will continue
7784 to study the magnet in OPERA and advance the simulation plans. We will get an early start
7785 on the fabrication of the printed circuit boards, and understand their requirements and
7786 technical capabilities. We will also remain involved with the other teams to ensure their
7787 systems do not introduce unmanageable distortions to the field, due to either materials or
7788 currents. A test stand with an ≈ 1.45 T field will be available to test proposed systems
7789 before hand. These steps will help ensure that the uniformity goals are achieved.

7790 16.12 Quality Assurance

7791 It is necessary to test the NMR hardware before shimming and installation in the $g-2$ stor-
7792 age ring. This requires the development of independent test-stands that include a set of
7793 NMR probes, NMR electronics, DAQ, and a magnet. We have located at least 4 magnets

7794 suitable for these purposes, where the requirements on the magnet depend on the hardware
7795 component being tested.

7796 To test the fixed probes requires a vector impedance meter or network analyzer and a
7797 magnet at 1.45 T with field gradients less than 20 ppm/cm. The latter is sufficient to ensure
7798 an FID of ms duration, sufficient to confirm the probe works. An electromagnet suitable for
7799 testing fixed probes and basic functioning of the NMR hardware is being prepared spring
7800 2013 at the University of Washington.

7801 Precision tests of the NMR hardware - such as single shot frequency resolution, temper-
7802 ature dependence of NMR signals, reference frequency dependence of the electronics, aging
7803 effects, measurements of T_2 , etc. require magnets with stability of 0.01-0.1 ppm per hour
7804 and field gradients of <0.2 ppm/cm. Such a magnet is available to the group at University of
7805 Michigan (with access to a large bore persistent mode MRI magnet). The University of Mas-
7806 sachusetts group has unrestricted access for several years to a small bore (89 mm) peristent
7807 mode superconducting magnet from Cryomagnetics, with better than 0.01 ppm/hr stability
7808 and a shim set to achieve sub-ppm/cm homogeneity over an 8 cm³ volume. The small bore
7809 cannot accommodate the E989 NMR probes (it can only accomodate the plunging probe),
7810 but many sensitive tests of the NMR electronics and behavior of the NMR probe samples
7811 (temperature effects etc.) can be measured at the 10 ppb level using custom probes.

7812 Finally, we require a large bore superconducting persistent mode magnet at Fermilab for
7813 local tests of the hardware. The LANL Biological and Quantum Physics group agreed to
7814 transfer to FNAL the Oxford Magnet Technology Unistat 41443 MRI solenoid used by E1054
7815 at Los Alamos. This solenoid has measured stability of better than 0.1 ppm/hour, a shim
7816 set for ppm-level homogeneity over a 10 cm diameter volume, and a 910 mm bore diameter,
7817 essential for extensive performance tests of the NMR trolley in advance of installation in
7818 the g-2 storage ring. This will also be essential for determining the magnet influence of the
7819 calorimeter and tracker hardware on the storage ring field. (Early tests of basic performance
7820 of the trolley will be made with a large gap electromagnet at BNL).

7821 Extensive early testing of the NMR hardware should allow identification of problems
7822 and the implementation of solutions in advance of installation in the g-2 ring. By having
7823 several absolute calibration probes, repeated calibration of the trolley probes, and extensive
7824 investigations of potential systematics, we intend to produce a robust result on ω_p .

7825 **16.13 Value Management**

7826 We are realizing significant savings in the magnetic field measurement system by refurbishing
7827 as much of the E821 hardware as possible, rather than building a completely new system.
7828 At the same time, we are making improvements (such as the change to the NMR sample
7829 material, improved shimming and magnet temperature control, improved calibration appa-
7830 ratus, ...) that improve operational characteristics and reliability and which are necessary
7831 to reach our goal of an uncertainty on $\omega_p \leq 70$ ppb.

References

- 7832
- 7833 [1] P. J. Mohr, B. N. Taylor, and D. B. Newell, Rev. Mod. Phys. **84**(4), 1527 (2012).
- 7834 [2] W. Liu *et al.*, Phys. Rev. Lett. **82**, 711 (1999);
- 7835 [3] R. Prigl, *et al.*, Nucl. Inst. Methods Phys. Res. **A374** 118 (1996).
- 7836 [4] X. Fei, V. Hughes and R. Prigl, Nucl. Inst. Methods Phys. Res. **A394**, 349 (1997).
- 7837 [5] G. Bennett, *et al.*, (Muon ($g - 2$) Collaboration), Phys. Rev. **D73**, 072003 (2006).
- 7838 [6] Ralf Prigl, doctoral thesis, University of Heidelberg (1994).
- 7839 [7] Alex Grossmann, doctoral thesis, University of Heidelberg (1998).
- 7840 [8] Huaizhang Deng, doctoral thesis, Yale University (2002).
- 7841 [9] A. Abragam, *Principles of Nuclear Magnetism* (Oxford Univ. Press, New York, 1961).
- 7842 [10] C.P. Slichter, *Principle of Magnetic Resonance* (Springer-Verlag, New York, 1989).
- 7843 [11] W.D. Phillips *et al.*, Metrologia **13**, 179 (1977).
- 7844 [12] B.W. Petley *et al.*, Metrologia **20**, 81 (1984).
- 7845 [13] J.L. Flowers *et al.*, Metrologia **30**, 75 (1993).
- 7846 [14] P.F. Winkler, D. Kleppner, T. Myint, and F.G. Walther, Phys. Rev. **A5**, 83 (1972).
- 7847 [15] W.E. Lamb Jr., Phys. Rev. **60**, 817 (1941).
- 7848 [16] H. Grotch and R.A. Hegstrom, Phys. Rev. **A4**, 59 (1971).
- 7849 [17] B.W. Petley *et al.*, Metrologia **20**, 81 (1984).
- 7850 [18] Y.I. Neronov and A.E. Barzakh, Sov. Phys. JETP **48**, 769 (1978).
- 7851 [19] G.T. Danby and J.W. Jackson, E821 Muon $g - 2$ Internal Note No.1, 1(1987).
- 7852 [20] K. Woodle, E821 Muon $g - 2$ Internal Note No.44, 1(1990).
- 7853 [21] S. Redin, E821 Muon $g - 2$ Internal Note No.51, 1(1990).

- 7854 [22] X. Fei and V.W. Hughes, E821 Muon $g - 2$ Internal Note No. 86 (R), 1(1991).
- 7855 [23] M.J. Fischer, E821 Muon $g - 2$ Internal Note No. 114, 1(1992).
- 7856 [24] Y.K. Semertzidis, C.S. Lin, and W.M. Morse, E821 Muon $g - 2$ Internal Note No.155,
7857 1(1993).
- 7858 [25] G.T. Danby and J.W. Jackson, E821 Muon $g - 2$ Internal Note No.180, 1(1993).
- 7859 [26] R. Prigl, Internal Note.
- 7860 [27] R. V. Reid, Phys. Rev. A, **11**, 403 (1975).
- 7861 [28] M. A. Bouchiat, T. R. Carver, and C. M. Varnum, Phys. Rev. Lett. **5**, 373 (1960).
- 7862 [29] T.E. Chupp, K.P. Coulter, Phys. Rev. Lett. **55**, 1074 (1985); M. E. Wagshul and T. E.
7863 Chupp, Phys. Rev. A **40**, 4447 (1989).
- 7864 [30] F.D. Colgrove, L.D. Schaerer, G.K. Walters, Phys. Rev. **8** 439 (1962).
- 7865 [31] ENS MEOP
- 7866 [32] M. S. Rosen, T. E. Chupp, K. P. Coulter, R. C. Welsh, S. Swanson, Rev. Sci. Instrum.
7867 **70**, 1546 (1999).
- 7868 [33] S.R. Nuss-Warren et al., Nucl. Inst. Meth. A **533**, 275 (2004).
- 7869 [34] S. D. Swanson, M. S. Rosen, B. W. Agranoff, K. P. Coulter, R. C. Welsh, T. E. Chupp,
7870 Magn. Reson. Med. **38**, 695 (1997).
- 7871 [35] M. Abboud, A. Sinatra, X. Maitre, G. Tastevin, P.-J. Nacher, Europhys. Lett., **68**, 480
7872 (2004).
- 7873 [36] M. Abboud, PhD thesis, "Pompage optique de lithium-3 forte pression dans un champ
7874 magnétique de 1.5 Tesla", University of Paris VI (2005).
- 7875 [37] G.T. Danby *et al.*, Nucl. Inst. Meth. A **457**, 151 (2001).
- 7876 [38] B. Cowan, Meas. Sci. Technol. **7**, 690 (1996).
- 7877 [39] S.I. Redin *et al.*, Nucl. Inst. Meth. A **473**, 260 (2001).
- 7878 [40] E. Efstathiadis *et al.*, Nucl. Inst. Meth. A **496**, 8 (2003).

Chapter 17

The ω_a Measurement

The anomalous spin precession frequency ω_a is one of the two observables required to obtain the muon anomalous magnetic moment, a_μ . In order to reach the experiment's proposed goal of 0.14 ppm precision in a_μ , the targeted error budget allows for a 0.1 ppm statistical uncertainty combined with equal 0.07 ppm systematic uncertainties from the ω_a and ω_p analyses. This chapter summarizes the procedure for the ω_a measurement, with subsequent Chapters 18-23 elaborating upon the design of each subsystem. First the decay kinematics are reviewed and the encoding of the muon spin information into the data set is explained (Section 17.1). From that basis several complementary methods are explained (17.1.2). Then a review of uncertainties is presented, first the statistical (Section 17.2) and then the systematic uncertainties intrinsic to the detector (Section 17.3). Finally the detector system organization is outlined and broken down into subsystems (Section 17.4). These subsystems include: stored muon monitoring, decay positron tracking, electromagnetic calorimeter, signal digitization, data acquisition, and slow control systems.

17.1 Measurement Overview

The anomalous precession frequency, ω_a , is the difference between the ensemble-averaged muon spin precession and the cyclotron frequency. The weak decay of the muon is parity violating, with the consequence that the emitted positron energy is correlated—on average—with the muon spin direction. Therefore by measuring the decay positrons and analyzing their energy, a measurement of the muon spin is possible. The angle between the boost from the muon center-of-mass frame (CM) to the lab frame and the muon spin acts as an analyzer. As the spin rotates relative to the boost direction the rate observed modulates at the frequency ω_a . That modulation is observed over several boosted muon lifetimes and fit to extract ω_a .

17.1.1 Muon Decay and Boost Kinematics

For a thorough discussion of the kinematics of muon decay, see 3.5. Here, we summarize the most important aspects with respect to the detector design. The angular distribution of emitted positrons from an ensemble of polarized muons at rest is

$$dn/d\Omega = 1 + a(E) (\hat{S}_\mu \cdot \hat{P}_e), \quad (17.1)$$

7908 where \hat{S}_μ is the muon spin direction and \hat{P}_e is the positron momentum direction. The
 7909 asymmetry a depends on positron energy (E) and is such that the higher-energy positrons
 7910 are emitted parallel to the muon spin.

7911 The decay positron energies in the laboratory frame are related to the CM energy by

$$E_{e,lab} = \gamma(E_e^* + \beta P_e^* \cos \theta^*). \quad (17.2)$$

7912 The starred quantities indicate CM frame, $\gamma = 29.3$, and θ^* is the angle between the rest
 7913 frame positron momentum and the boost direction. The maximum energy in the lab frame
 7914 occurs when the positron momentum is aligned with the boost direction and the decay
 7915 energy is the maximum. Therefore by applying a threshold to the lab frame positron energy,
 7916 only the highest energy muon rest frame decay positrons are observed. This captures the
 7917 important relationship that the positron *energy* in the lab frame is correlated to the emitted
 7918 *angle* and therefore muon spin in the CM frame.

7919 17.1.2 Analysis Methods Summary

7920 The standard analysis procedure is to identify individual decay positrons and plot the rate
 7921 of their arrival versus time using only events having a measured energy above a threshold.
 7922 This is dubbed the T (time) method; it was the dominant analysis technique used in the
 7923 Brookhaven experiment and it is fairly robust against systematic uncertainties.

7924 The rate of detected positrons above a single energy threshold E_{th} is

$$\frac{dN(t; E_{th})}{dt} = N_0 e^{-t/\gamma\tau_\mu} [1 + A \cos(\omega_a t + \phi)]. \quad (17.3)$$

7925 Here the normalization, N_0 , average asymmetry, A , and initial phase, ϕ , are all dependent
 7926 on the threshold energy.

7927 The T Method is sufficient to reach the experimental goal and it is tested. Additional
 7928 analysis techniques can also be employed. Weighting the events by the asymmetry associated
 7929 with their energy, or directly by their energy, increases the statistical power for the same
 7930 data set at the cost of more stringent systematic requirements. As in the T method, the
 7931 data stream from the calorimeters must be first deconstructed into individual events, which
 7932 are then processed into histograms. The systematic uncertainties are largely based on the
 7933 stability of the deconstruction process vs. time in the storage ring fill. The Q method does
 7934 not require event by event reconstruction. Instead, it simply integrates the detector current
 7935 (energy for a linear device) vs. time in fill.

7936 The two methods we plan to use have the following features:

- 7937 • **T Method:** Events are individually identified and sorted. The events vs. Time-in-
 7938 Fill histogram is built from all events with reconstructed energy above a threshold. All
 7939 events in the histogram are given equal weight. The figure-of-merit (FOM) is optimized
 7940 for a positron energy threshold of 1.8 GeV, as discussed below. The quantity ω_a is
 7941 obtained from a fit to a pileup-subtracted histogram. This is the standard method used

7942 in E821 and the benchmark for determining the statistical and systematic requirements
7943 for the E989 experiment.

7944 • **Q Method:** Detector current is integrated as a function of time; that is, events *are not*
7945 individually identified. This procedure leads to a histogram of Energy vs. Time-in-Fill,
7946 which is built by summing the response of all digitized waveform samples vs. time for
7947 an entire calorimeter station. No attempt to correct for pileup is necessary here and
7948 a very low threshold is desired. The acceptance-corrected FOM is nearly identical to
7949 the standard T method.

7950 17.2 Statistical Uncertainty

7951 The T and Q methods lead to similar histograms (see Figure 17.3 below) with different bin
7952 weights and asymmetries. A fit is performed using Equation 17.3 and the relevant parameter
7953 ω_a is obtained. The optimization of the experimental system follows from minimizing the
7954 uncertainty on that parameter, namely $\delta\omega_a$. A detailed study [1] of the statistical methods
7955 gives guidance to the statistical power of any data set built using various weighting methods.
7956 The uncertainty on ω_a can be parameterized by

$$\delta\omega_a = \sqrt{\frac{2}{N(\gamma\tau_\mu)^2} \cdot \frac{\langle p^2 \rangle_y}{\langle pA \rangle_y^2}}, \quad (17.4)$$

7957 where N is the integrated number of decay positrons in the analysis, p is the weight function
7958 and therefore is method dependent, and $\langle f \rangle_y$ is the value of f averaged over all detected
7959 positron energies above threshold. The parameter y is the fractional decay positron energy
7960 with respect to a maximum value; therefore y ranges from 0 to 1, where $y = 1$ corresponding
7961 to approximately 3.1 GeV.

7962 In the following, care must be paid to whether distributions shown vs. y are differential or
7963 whether they represent the integrated value from threshold y . For example, Fig. 17.1 shows
7964 *differential* plots of N , A and NA^2 vs. energy for a uniform acceptance detector. The plots
7965 illustrate the importance of the higher-energy positrons that have the greatest asymmetry.
7966 The asymmetry is negative for lower-energy positrons; thus, a single low threshold can be
7967 expected to dilute the average asymmetry. Importantly, the modification of the ideal curves
7968 owing to finite detector acceptance is non-negligible, as the detector placement has been
7969 designed to greatly favor the higher-energy events. Low-energy positrons can curl between
7970 detectors and be missed. The acceptance impacts the values of N and A , which are functions
7971 of the energy-dependent detector acceptance. In the T method, each event carries the same
7972 weight ($p = 1$) and the uncertainty $\delta\omega_a$ following Eq. 17.4 reduces to

$$\delta\omega_a = \frac{1}{\gamma\tau_\mu} \sqrt{\frac{2}{NA^2}}. \quad (17.5)$$

7973 The boost factor $\gamma = 29.3$ is fixed by the magic momentum requirement. The figure of merit
7974 (FOM) that should be maximized to minimize $(\delta\omega_a)^2$ is NA^2 . The value of the threshold

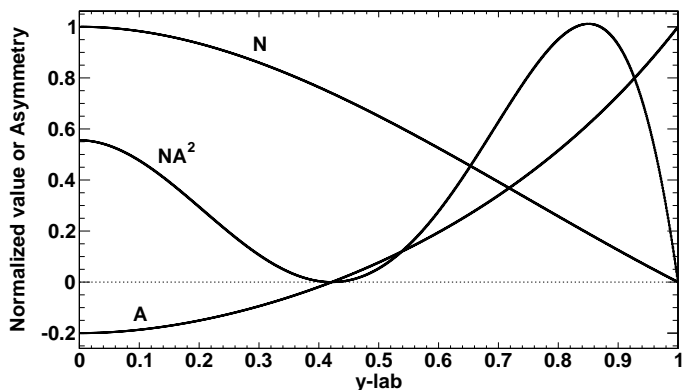


Figure 17.1: The differential distributions: normalized number of events (N/N_{total}), asymmetry (A), and the figure of merit (NA^2). Note, this plot assumes uniform detector acceptance across the full energy spectrum.

7975 that maximizes the FOM corresponds to $A \approx 0.4$ and an energy of 1.8 GeV. Therefore the
 7976 relative uncertainty in ω_a is

$$\frac{\delta\omega_a}{\omega_a} = \frac{1}{\omega_a} \cdot \frac{\sqrt{2}}{\gamma\tau_\mu A} \cdot \frac{1}{\sqrt{N}} \approx \frac{0.0385}{\sqrt{N}}. \quad (17.6)$$

7977 For a statistical uncertainty on $\delta\omega_a/\omega_a$ of 0.10 ppm, $N = 1.5 \cdot 10^{11}$ fitted events would be
 7978 required, stemming from a 100% polarized stored muon beam.

7979 The Q method is essentially an energy-weighted ($p = y$) analysis with a single very
 7980 low threshold, since events do not need to be individually identified. The current in the
 7981 detectors is simply summed vs. time. The computation of $\langle p^2 \rangle_y / \langle pA \rangle_y^2$ in Eq. 17.4 is non-
 7982 trivial. We conducted a simulation that included the finite detector acceptance to determine
 7983 a realistic FOM for the T and energy-weighted (Q) technique. Figure. 17.2 shows the results
 7984 vs. threshold energy; albeit, the Q threshold is by definition at the lowest value of y . The
 7985 FOM for the energy (Q) at near-zero threshold is to be compared to the T method at its
 7986 peak. They are comparable.

7987 A tacit assumption in the T method is that the energy and arrival time at the detector
 7988 are known accurately. The events are sorted and placed into histograms with uniform weight.
 7989 When the rate is high events can overlap in time and space such that some fraction of them
 7990 cannot be resolved into individual occurrences. A pileup subtraction procedure is required
 7991 prior to fitting for ω_a . In contrast, the Q method involves integrating the light yield from the
 7992 calorimeters as a function of time with near-zero threshold. We have studied this method
 7993 using Monte Carlo simulations to determine the proper weighting to place on the bins in
 7994 the fit; they vary over the $g - 2$ cycle, but can be easily determined using a sample of
 7995 late-time data. Figure 17.3 shows a fit to Monte-Carlo data generated with the full ring
 7996 simulation in terms of muon spin and time dependence and folding in the finite acceptance
 7997 of the detectors. Here, the beam polarization is assumed to be unity and an event is accepted
 7998 at its Monte-Carlo energy if the positron hits anywhere on the front face of a calorimeter.
 7999 The variable R parameterizes the difference, in part-per-million, between the true simulated

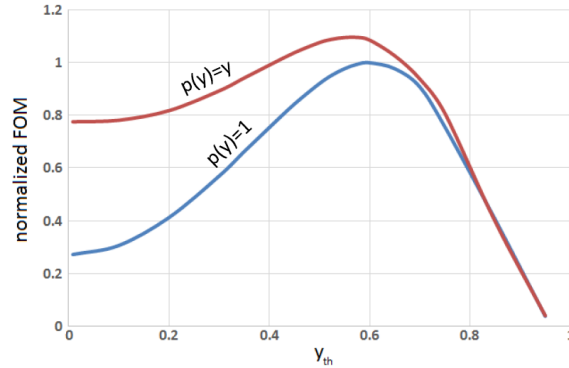


Figure 17.2: The figure-of-merit for the T ($p(y) = 1$) and energy-weighted ($p(y) = y$) distributions produced as the output of a detailed analysis using simulated data and finite detector acceptance. Of particular interest is the low-threshold value for the energy-weighted distribution, which corresponds to the Q method analysis and the maximum of the T distribution, which corresponds to the typical threshold of approximately 1.8 GeV used in the event-based analysis.

8000 frequency for ω_a and the value returned by the fit; thus $R = 0$ corresponds to the desired
 8001 input and the reported error on R is the uncertainty in ppm. Both T and Q methods give
 8002 similar statistical precision.

8003 The Q method was not possible in E821 owing to the high energy threshold and lack
 8004 of memory in the digitizers or, alternatively, the transfer rate to the DAQ. These technical
 8005 limitations are easily overcome with today's large memories in such devices and faster bus
 8006 speeds. Note that the data sets in the T and Q method are not identical, but substantial
 8007 overlap exists. For example, in the T method, all events below ~ 1.8 GeV do not contribute
 8008 and all events above are weighted with $p = 1$. The Q method includes all events that strike
 8009 the detector and weights each by its energy, $p = y$. Therefore, a combination of the results
 8010 of the two methods will enable an overall reduction in the final uncertainty of ω_a ; but more
 8011 importantly, the two methods will serve as important cross checks that systematics are under
 8012 control.

8013 17.3 Detector-related Systematic Uncertainties

8014 In this section we discuss the systematic error issues related to the Detectors, Electronics,
 8015 DAQ and the Offline Analysis. Table 17.1 lists the Gain and Pileup uncertainties and pro-
 8016 jections for improvements in the new $g-2$ experiment. The traditional T method analysis is
 8017 assumed because uncertainties can be reliably projected based on our considerable experi-
 8018 ence in these analysis efforts. Since the Q method is new, we have not included its positive
 8019 and partially independent impact on the final statistical result, nor are we presently able to
 8020 fully project associated systematics. This topic is an active study in the collaboration. One
 8021 key attractive feature of the Q method is pileup immunity; there is no correction necessary,
 8022 so that systematic uncertainty is absent. Comparing the analysis results using both T and
 8023 Q methods will provide a valuable confirmation that systematic errors are understood.

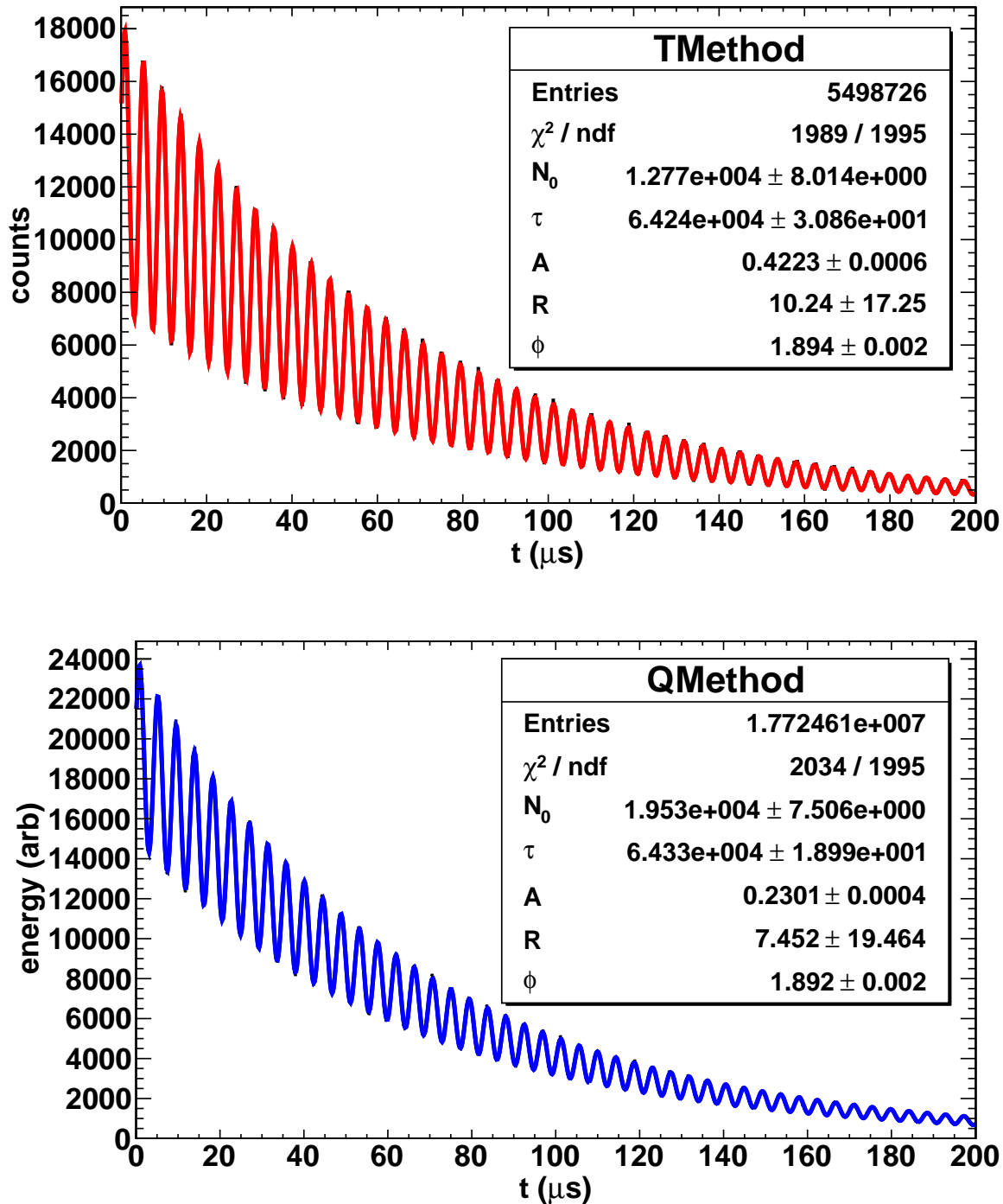


Figure 17.3: Top: Monte Carlo data analyzed using the T method with a threshold cut at $y = 0.6$. Bottom: Same data analyzed using the Q method. Detector acceptance is included. The asymmetry A is much higher for the T method; however, the Q method has many more events (N). The ω_a Monte-Carlo truth is $R = 0$ and the uncertainty in R is a measure of the precision, in ppm. Both methods give a similar statistical uncertainty and acceptable fit central values.

Table 17.1: Detector-specific systematic uncertainties in E821 and proposed upgrade actions and projected future uncertainties for E989.

E821 Error	Size [ppm]	Plan for the New $g-2$ Experiment	Goal [ppm]
Gain changes	0.12	Better laser calibration; low-energy threshold; temperature stability; segmentation to lower rates	0.02
Pileup	0.08	Low-energy samples recorded; calorimeter segmentation; Cherenkov; improved analysis techniques	0.04

17.3.1 Gain Changes and Energy-Scale Stability

The hardware gains of the E821 detectors [2] were determined to be stable to $\approx 0.15\%$ from early-to-late times within a storage ring fill. This limit was established by plotting the average energy for each $(g-2)$ period versus time after the PMTs were switched on. The gating circuitry in the tube base that allowed the PMTs to be turned off to avoid the initial burst of pions entering the ring also resulted in a small variation in the gain. For gain variations like this one, where the time constant is long compared to the $(g-2)$ oscillation period, the coupling to the ω_a frequency is small and, after correction, the residual systematic error is less than 0.02 ppm.

Several aspects of the current plan will be different. The first is that we will use silicon photo-multipliers (SiPMs), which can be saturated from a light burst and then recover with the same time constant as a low-light pulse. Each pixel is “on” or “off” and recovers with a common time constant. Importantly, we do not intend to switch off these devices during injection because the anticipated hadronic-based flash will be (largely) absent. The initial pion flux at the target location will be reduced by the factor $\exp(-x/173)$, where 173 m is the pion decay length for 3.1 GeV/ c . The path length, x , from target to storage ring, including 4 trips around the muon Delivery Ring (DR) is approximately 2000 m; thus primary pions are reduced by a factor of 10^5 ; thus a negligible rate into the ring. Similarly, beam protons—which travel slower than pions at 3.1 GeV/ c —will be eliminated in the DR using a kicker system timed to fire when the muon and proton bunches are well separated in space.

If the gain oscillates at a frequency ω_a , with an amplitude that varies in time, and with a phase that differs from that of the actual ω_a oscillation, then a direct error on the measured value of the anomalous precession frequency is produced. The average rate at which energy is deposited into the calorimeters oscillates with frequency ω_a , and therefore any rate dependence in the gain of the detectors produces gain oscillations. In E821, we were able to demonstrate that the gain dependence on rate was small enough that its effect on ω_a was typically less than 0.03 ppm. In the new experiment, the slightly increased beam rates will be offset by increased detector segmentation and our proposed monitoring system will be greatly improved compared to that employed in the past.

In E821, a UV-laser system was used to periodically pulse the scintillator in the detectors and thus monitor the complete gain and reconstruction chain during data collection against an out-of-beam reference counter. Unfortunately, the light distribution system included too many branches and not enough sub-branch reference detectors. Small fluctuations cascaded so that gain stability could be monitored to no better than a few tenths of a percent (im-

8058 pressive, but not quite good enough). The system being designed for E989 will use cascaded
8059 distribution systems having multiple monitors at each stage. This is described in Chapter 18,
8060 Section 18.3.3.

8061 The largest contribution to the gain systematic error in E821 came from analysis recon-
8062 struction induced gain oscillations at the ω_a frequency. The interpretation of the energy of
8063 a pulse from the fit to the waveform had a small bias. When a hardware signal rose above
8064 the waveform digitizer (WFD) trigger threshold, a pre-set minimum number of sequential
8065 samples was recorded. These data were fit offline to determine the peak height, time and
8066 the linear background under the pulse. However, if a trigger pulse was followed or preceded
8067 closely by another pulse, both pulses were fit together with a common background term,
8068 and the fitting region became longer compared to what is routinely used for a single pulse.
8069 In these pulses, the fitted energy was found to depend on the length of the fitting region,
8070 which was varying because of the hardware limitation. Because the data rate oscillates at
8071 frequency ω_a , and is higher at early than at late decay times, it follows that the fitting region
8072 length oscillated at frequency equal to ω_a and was, on average, longer at early times com-
8073 pared to late times. This produced a small, effective gain oscillation having an amplitude
8074 that decreases with time. A systematic error on ω_a results.

8075 Given the current capabilities in data throughput, the new electronics will record all
8076 samples rather than triggered, fixed-length isolated islands. This avoids the intrinsic bias
8077 in the recorded data and allows reconstruction routines to compensate for the waveform
8078 islands that have more than one pulse. In addition, we will have one other new tool that will
8079 provide powerful information related to energy scale and gain. As discussed in Chapter 19, a
8080 large-acceptance tracker system will be built just upstream of two calorimeter stations. This
8081 system will reside inside an unmodified vacuum chamber. It will be capable of providing
8082 high-precision tracking with good momentum definition these calorimeter stations, which
8083 will provide an absolute energy scale. The position information obtained will also inform
8084 the calorimeter cluster algorithm development. The energy scale obtained from the directly
8085 calibrated stations can be bootstrapped to other calorimeters by comparing the average
8086 energy distributions from decay positrons, which are expected to be similar. In summary,
8087 we expect that the largest of the gain systematic errors from E821 will be eliminated by
8088 the design of the electronics and data acquisition systems, combined with the verification
8089 from the tracker. The smaller contribution will be reduced by a more precise hardware gain
8090 monitoring system.

8091 **17.3.2 Pileup**

8092 The term “Pileup” refers to the overlap of events in the calorimeter that originate from
8093 separate muon decays, too close to each other in time and space to be resolved into individual
8094 pulses. When two pulses overlap, the result is that the two individual events are lost, and
8095 one event with the sum of their energies is gained. (Because there is, in general, a time
8096 offset between the two pulses, the pulse shape is widened so that the combined amplitude
8097 is somewhat less than the sum of the individual amplitudes.) Because the fraction of pileup
8098 events increases with rate, a component is introduced into the time spectrum that decays
8099 with half the nominal lifetime, or $32 \mu\text{s}$, preventing a precise fit to the five-parameter function
8100 in Equation 17.3.

8101 A more serious issue is that the muon spin precession phase varies with the energy of the
8102 pulse. A high-energy positron has a larger radius of curvature and therefore a longer time-
8103 of-flight to the calorimeter, so it carries the phase of a muon that decayed earlier than one
8104 that produced a low-energy positron. When two low-energy pulses are lost and an apparent
8105 high-energy pulse is gained, the high-energy pulse still has the phase of the low-energy pulses.
8106 The varying fraction of pileup over the fill causes an average early-to-late phase shift that
8107 directly distorts the fitted ω_a . Consequently, the (E, t) distribution of pileup pulses must be
8108 constructed and subtracted from the spectrum before it is fit.

8109 The pileup distribution can be constructed based on the assumption that the probability
8110 of a pulse at time t is, to a good approximation, the average of the probabilities that it is
8111 found at times $t + \delta t$ and $t - \delta t$, provided that δt is small compared to the precession period.
8112 Consequently, secondary pulses from the “shadow” just before or after a primary pulse can
8113 be added to the primary pulse to form a constructed pileup event. To the extent that all
8114 fills have equal initial intensities of stored muons, the probability of a pulse at time t in one
8115 fill is also nearly the same as the probability of a pulse at the same time t in a different fill;
8116 this can provide another independent source of “shadow” events.

8117 In E821, the construction of these distributions was complicated by the fact that only
8118 short islands around each pulse were stored, with a threshold of nearly 1 GeV required to
8119 store an island. The pileup distribution could only be fully reconstructed in a straightforward
8120 way at energies greater than twice this threshold. As described in the following Chapters on
8121 Electronics and Data Acquisition, in the new experiment, the full waveform for the entire fill
8122 will be available. It will therefore be possible to construct pileup down to a very low energy
8123 threshold.

8124 The unresolved pileup fraction scales linearly with rate in each segment of the detectors.
8125 The effective size of the segment depends on the geometric extent of the shower. Our
8126 simulations demonstrate that an array of PbF₂ crystals, having 54 independent segments
8127 (see Chapter 18), and a smaller Molière radius compared to the Pb/SciFi used in E821, will
8128 provide an effective three-fold reduction in the intrinsic pileup based on the implementation
8129 of a very simple and robust shower separation routine and a 9-element cluster algorithm.
8130 The simulation includes a representative stored muon ensemble in the ring and correct spin
8131 physics in precession and decay.

8132 While the final stored muon rate increase will depend on the actual implementation of
8133 several options, we work here with the expectation of a 50% increase compared to E821 and
8134 design for a range of up to a factor of 3 higher. We will use a factor of 3 below as it represents
8135 an upper limit of what might be expected.

8136 With a three-fold rate increase compared to BNL, the intrinsic pileup rate for the same
8137 two-pulse resolution time resolution of 5 ns is expected to be largely the same as in E821,
8138 owing to the segmentation. What can be improved is the uncertainty associated with the
8139 correction for unresolved pileup. After following the pileup subtraction procedure described
8140 above, we will be able to check the result using an applied artificial deadtime (ADT). The
8141 ADT is the time established in the analysis software below which two pulses are not resolved
8142 (even if they can be). The analysis proceeds by sorting data using a series of ADT values
8143 beginning with the intrinsic, device-specific constraints, and artificially extending to much
8144 larger values that exaggerate the pileup. The extraction of ω_a is then done for each data set,
8145 and ω_a will be plotted as a function of ADT. In principle, ω_a should not depend on ADT,

8146 but a small correction could be included by taking the deadtime-free value that occurs at
 8147 the zero-ADT extrapolation point. We have spent considerable laboratory bench time and
 8148 offline pulse-reconstruction efforts to determine and optimize the minimum hardware ADT
 8149 that our detectors will permit. Our laboratory tests demonstrate that pulses separated by
 8150 5 ns or more can be resolved easily for most pulse-amplitude ratios expected.

8151 In addition to the work that was done for E821, we have also carried out a precision
 8152 muon lifetime analysis with a pileup correction algorithm based on this pileup construction
 8153 and ADT extrapolation concept. The work is well documented [4, 3]. The algorithms will
 8154 be tested using the one station that has a high-resolution tracker (see Chapter 19) that can
 8155 resolve pileup events at the few mm level and provide the corresponding momentum of each.
 8156 Comparing identified pileup events from the tracker to the interpretation of the same events
 8157 by the calorimeter will give a great degree of confidence in the methods.

8158 We comment on what had been achieved in the past. The pileup systematic error of
 8159 0.08 ppm in the E821 experiment was obtained from three components listed below. The
 8160 first two were correlated and add linearly. The third is not correlated so it was added in
 8161 quadrature to the other two.

- 8162 1. Pileup efficiency, 0.036 ppm. This is due to an estimated 8% uncertainty in the ampli-
 8163 tude of the constructed pileup spectrum.
- 8164 2. Pileup phase, 0.038 ppm. This is the error due to the uncertainty in the phase of the
 8165 constructed pileup spectrum.
- 8166 3. Unseen pileup, 0.026 ppm. This is the error due to pulses so small that they cannot
 8167 be reconstructed and therefore they are not included in the pileup construction. In
 8168 general, the energy from these pulses cancels out, because they occur as often in the
 8169 pedestal, where they lower the fitted pulse energy, as under the pulse, where they raise
 8170 it. This error accounts for the potentially incomplete cancelation.

8171 We expect that the segmented detectors, better laser calibration, more complete waveform
 8172 record storage, verification of methods by using the tracker, and the use of our more mod-
 8173 ern extrapolation algorithms will lead to a comprehensive pileup correction with minimal
 8174 uncertainty. We assign up to 0.04 ppm here to account for any difficulties in the anticipated
 8175 analysis. As mentioned earlier, the Q method is complementary to the traditional T method
 8176 and has different sources of systematic errors. The most significant difference is the effect of
 8177 pileup—it will be greatly reduced for the Q method.

8178 17.4 Detector Systems Overview

8179 Three principle detector systems are central to the ω_a measurement: Calorimeter, Electron-
 8180 ics, Data Acquisition. They each have their own chapter in this report. The Tracker System
 8181 and Auxiliary detectors contribute to systematic uncertainty determination. Figure 17.4
 8182 illustrates the various subsystems within the direct ω_a measurement framework, organized
 8183 to illustrate how we define our work plans and distributed effort.

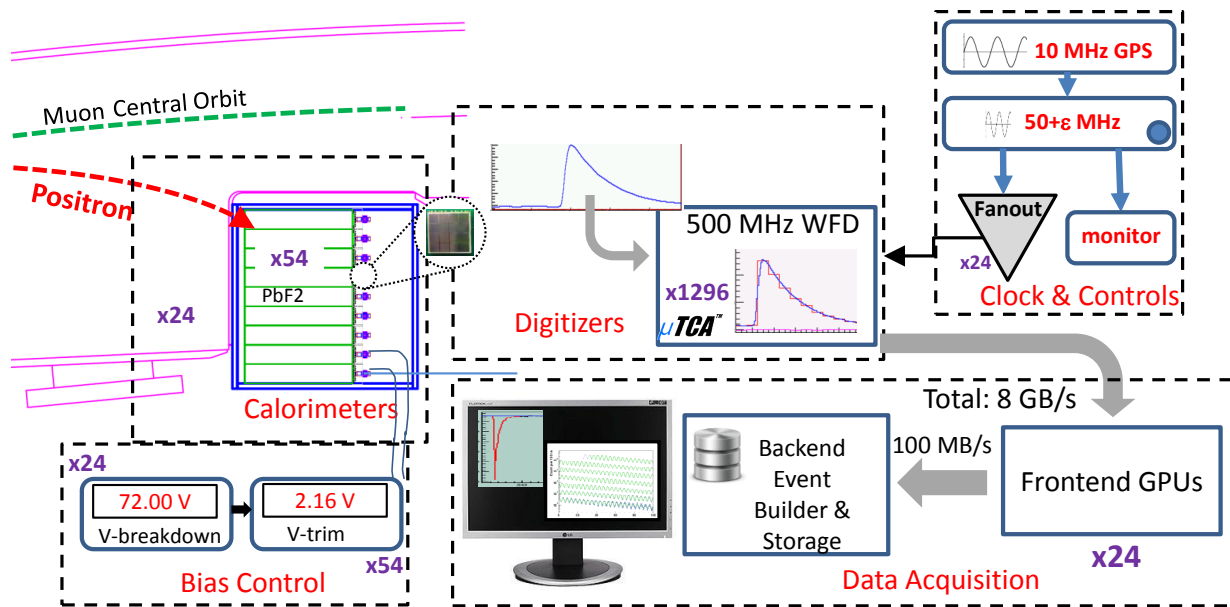


Figure 17.4: Schematic of the ω_a instrumentation organized by dedicated systems.

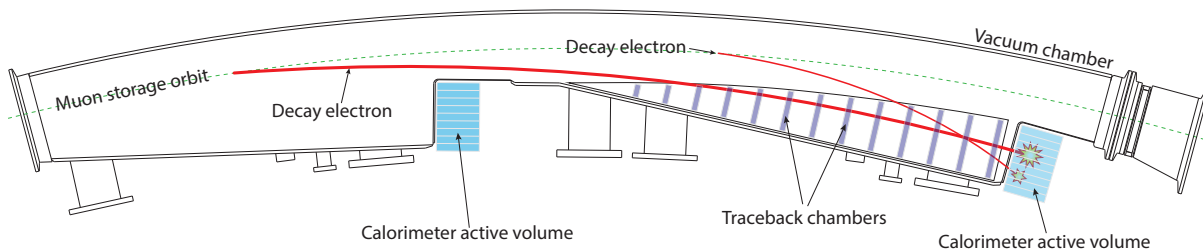


Figure 17.5: Scalloped vacuum chamber with positions of calorimeters indicated. A high-(low-) energy decay positron trajectory is shown by the thick (thin) red line, which impinges on the front face of the calorimeter array.

17.4.1 Calorimeter Subsystem Considerations

8184

8185 The decay positrons have momenta below the muon storage momentum and therefore they
 8186 curl to the inside of the ring through the opening in the C -shaped magnet. Electromagnetic
 8187 calorimeters are used to intercept the positrons and provide a measurement of energy and
 8188 time of detection, see Fig.17.5. Notice in the figure that the decay path, and consequently
 8189 the time of flight from decay to detection, depends on positron energy.

8190 The calorimeters will be placed adjacent to the storage ring vacuum chambers, and
 8191 located at 15 degree intervals around the ring. The 24 stations and their locations are
 8192 constrained by the plan to reuse the E821 vacuum chambers, see Fig. 17.5. These parameters
 8193 were optimized in a study preceding E821 construction and the conclusions remain valid for
 8194 E989.

8195 The number of emitted decay positrons vs. fractional energy is shown in the left panel

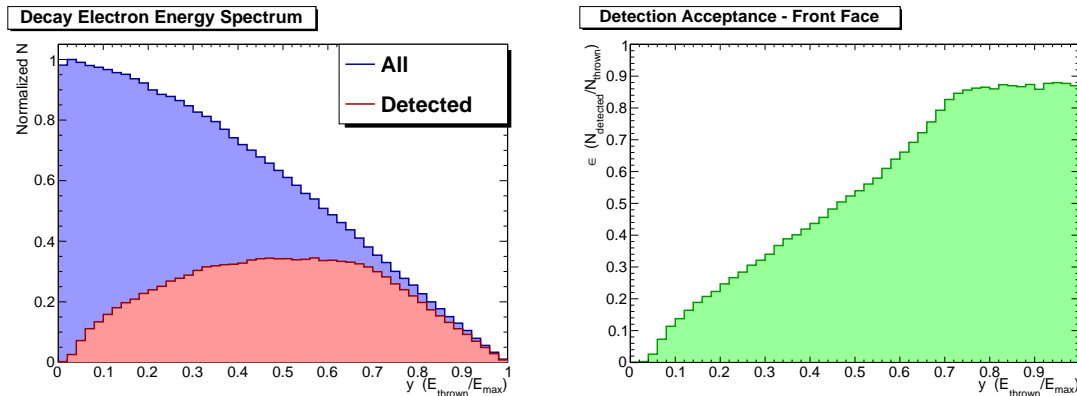


Figure 17.6: Left panel: Number of decay events vs. y in the laboratory frame (upper curve) and those that intercept the front face of a calorimeter (lower curve). Simulation uses full geometry, including pre-showering effects. Right panel: The differential acceptance of the 24 calorimeters vs. energy (the ratio of the two curves in the left panel). This is the fractional acceptance of events that hit the front face of the calorimeter array only.

8196 of Fig. 17.6. The upper curve is all decay positrons. The lower curve are only the positrons
 8197 that that strike the front face of one of the calorimeters. The right panel shows the ratio of
 8198 detected to thrown positrons vs. fractional energy. The geometry is designed to favor the
 8199 high-energy positrons that carry the maximum spin correlation information. Low-energy
 8200 positrons will often curl in between calorimeter stations and be lost. The design of the
 8201 new calorimeters is constrained by the unusual experimental demands. It is important to
 8202 emphasize that the relevant time scale for most systematic uncertainties is one $700 \mu\text{s}$ long
 8203 measuring period. The initial instantaneous event rate of several MHz drops by almost five
 8204 orders of magnitude during the $700 \mu\text{s}$ measuring period; thus, any rate-dependent detector
 8205 or readout response changes must be accurately known. The overall measurement system
 8206 must be extraordinarily stable for each short-term storage ring fill; however, long time scale
 8207 drifts can generally be tolerated. As an example, consider a gain function G that varies
 8208 from the beginning of a fill to the end of a fill; that is, $G \rightarrow G(t)$. When coupled to a
 8209 fixed energy threshold, the population of accepted events will then vary throughout the fill.
 8210 Because the asymmetry A and phase ϕ are functions of energy, the extracted ω_a will vary
 8211 throughout the fill. If this occurs systematically during each fill (as it might if the gain
 8212 change is coupled to rate), and is unaccounted for, then ω_a might be incorrectly determined.
 8213 Similarly, a time shift Δt owing to the clocking system or other influence can also change the
 8214 fitted frequency. Our experience in E821 established that the stability conditions that ensure
 8215 less than a 0.05 ppm shift to ω_a can be characterized by the requirement that $\Delta G < 0.1\%$
 8216 and $\Delta t < 10 \text{ ps}$ over a $200 \mu\text{s}$ interval.

8217 Two low-energy positrons, arriving close together in time, can be interpreted as one
 8218 equivalent high-energy positron, a type of “pileup” event. Because the low-energy positrons
 8219 have a shorter flight path to the detector compared to higher-energy positrons, they corre-
 8220 spond to muons having a slightly greater muon phase advance. Therefore, if such incorrect
 8221 interpretations of high-energy positrons are made more often early vs. late in a storage ring
 8222 fill, the ensemble average phase will shift, which is equivalent in the fit to a shift in ω_a .

8223 Unaccounted for, pileup will produce this effect, since the rate of fake high-energy positrons
 8224 coming from coincident low-energy positrons has a $\sim e^{-2t/\gamma\tau}$ time dependence. This means
 8225 the pileup rate falls twice as fast as the muon population decays. To minimize pileup, the
 8226 calorimeter response must be fast (few ns) and the readout system must record informa-
 8227 tion to enable the distinction between closely occurring pulse pairs, which strike the same
 8228 detector elements. This information should also provide a mechanism to correct the data,
 8229 on average, by removing the pileup events. Furthermore, if the detector segmentation is
 8230 optimized, many simultaneous lower-energy positrons will be recorded in independent area
 8231 of a calorimeter station and thus will not be interpreted as a pileup event. The goal in
 8232 the detector design is to reliably resolve same-element pulses separated by 5 ns or more, to
 8233 segment the detector to minimize pileup, and to accurately subtract unresolved pileup.

8234 The calorimeter resolution must be moderately good near 1.8 GeV (better than 10%)
 8235 to provide adequate energy discrimination. However, it also must be compact to avoid a
 8236 preponderance of positrons that strike the inside face of the detector. Usually higher density
 8237 materials imply lower resolution, so an optimization must be made. For E989, we are aiming
 8238 for a factor of 2 improvement in resolution compared to E821. This will aid in the pileup
 8239 analysis, but is not particularly critical to the simple T method threshold analysis in the
 8240 absence of pileup.

8241 17.4.2 Projected Rates in Calorimeter

8242 The model used for determining the rate in a calorimeter is as follows. The average number
 8243 of muons incident on a calorimeter for a fixed time interval is given in Equation 17.7. Here N_μ
 8244 is the number of stored muons and ϵ is the acceptance. The stored muons value is calculated
 8245 in Chapter 5 and shown in Table 5.1. The acceptance is given in Table 17.2. The calculation
 8246 was made by simulating the $g - 2$ ring and recording calorimeter hits. From these hits the
 8247 acceptance of the calorimeter was extracted. All calorimeters are treated identically in this
 8248 study.

$$\langle R_{\text{exp}} \rangle = N_\mu \epsilon \cdot \frac{1}{\tau_\mu} \exp\left(\frac{-t}{\tau_\mu}\right) \quad (17.7)$$

$$\langle R_{g-2} \rangle = \langle R_{\text{exp}} \rangle \cdot [1 + A \cos(\omega_a t)] \quad (17.8)$$

$$\langle R_{\text{FR}} \rangle = \langle R_{g-2} \rangle \cdot [1 + A_c \exp(-t/\tau_c) \cos(\omega_c t)] \quad (17.9)$$

8249 From the base of the simple exponential, which describes the muon lifetime, the spin
 8250 precession from ω_a is added producing Equation 17.8¹. Where A is the average asymmetry
 8251 of the oscillation. For larger values of the asymmetry a larger rate is observed. The final step
 8252 is to include the effects of the initial bunch structure of the incoming beam. At injection,
 8253 the ~ 120 ns wide muon bunch does not fill the storage ring, as shown in the temporal
 8254 profile in Fig. 7.6 and described in 7.3.1. The bunch rotates at the cyclotron frequency,
 8255 ω_c , with a period of 149 ns. Thus at each detector station, a large intensity oscillation is
 8256 imprinted on the distribution described by Eq. 17.8. Note that $\omega_c \gg \omega_a$. The fast rotation

¹For simplicity, we used the initial muon phase angle to be $\phi = 0$ in this discussion.

Table 17.2: Projected Rates in Calorimeters

Rate	ϵ		Instantaneous Rate (MHz) at $31 \mu\text{s}$	$\sim N_{\text{stored}}$
	$E > 0.1 \text{ GeV}$	$E > 1.8 \text{ GeV}$		
Full Calorimeter	0.0170	0.0050	16	linear
Cluster	0.0028	0.0008	2.7	linear
Hot Cluster	0.0057	0.0018	5.5	linear
Pileup	–	–	0.150	quadratic

8257 amplitude damps out as the momentum spread of the stored beam causes a redistribution
 8258 of the particles until the ring is effectively uniformly populated. The fast rotation can be
 8259 described by an amplitude, A_C , a damping time constant τ_c , and the cyclotron frequency ω_c .

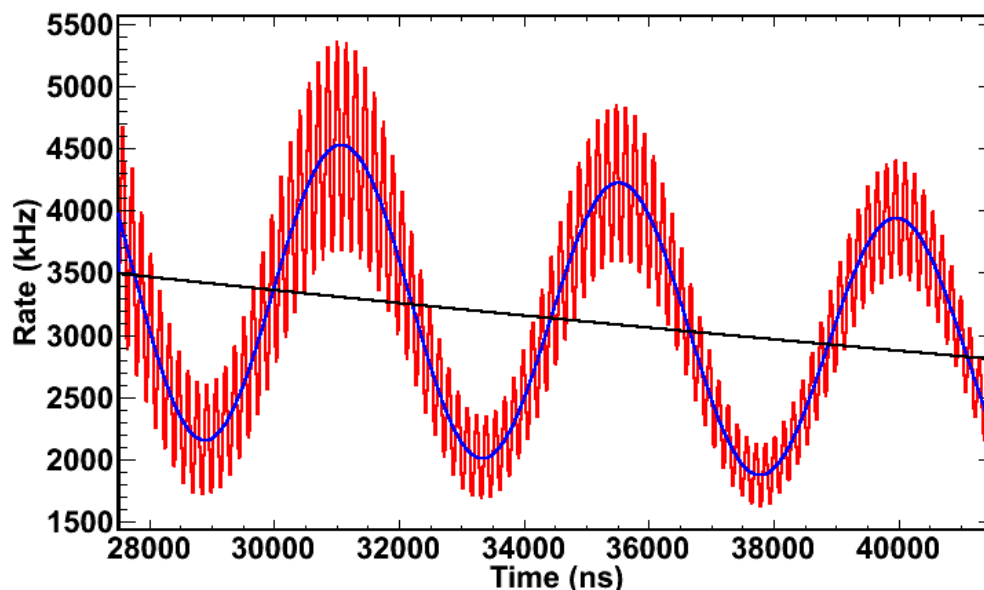


Figure 17.7: The three colored curves represent the instantaneous rate for: decaying muons (black), with ω_a oscillation (blue), and with fast rotation (red). This data was simulated the standard run conditions outlined in the CDR

8260 When all of these features are taken into account the maximum instantaneous rate in
 8261 a calorimeter can be evaluated. Figure 17.7 shows all three of these functions. By tuning
 8262 the parameters of the model to their expected values, the instantaneous rates are found,
 8263 as summarized in Table 17.2. “Full calorimeter” is the rate if the entire calorimeter were
 8264 readout as one monolith. “Cluster” represents a reduction in rate by the factor $9/54$, which
 8265 is the ratio of the size of a typical cluster to the full calorimeter. Finally “Hot Cluster” is
 8266 the cluster seeded in the region of the calorimeter where the maximum rate is expected. The
 8267 distribution of hits across the face of the calorimeter is not uniform, with larger radii (closer
 8268 to the storage volume) receiving more hits.

8269

Finally the rate of pileup is also calculated for the hot cluster. The pileup rate is

$$\langle R_{\text{pileup}} \rangle = \langle R \rangle^2 \cdot \Delta t \quad (17.10)$$

8270

where Δt is the resolving time of the calorimeter. Working with the rate in the Hot Cluster

8271

and a resolving time of 5 ns we calculate the maximum pileup rate to be 150 kHz. Also

8272

of interest is the maximum rate of pulses that an individual calorimeter segment can be

8273

expected to process. Figure 17.8 shows the instantaneous rate of hits over 25 MeV for each

8274

individual calorimeter crystal.

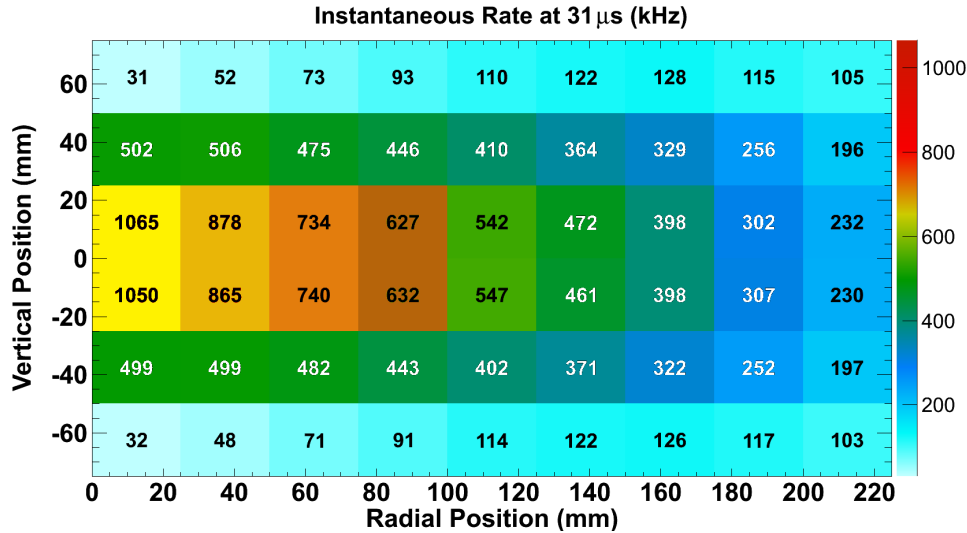


Figure 17.8: This histogram shows the projected instantaneous rate in each calorimeter crystal. The lower radial positions are closer to the muon storage region, hence the higher rate. This data set includes leakage of energy from one crystal to its neighbors. However there is no weight applied based on energy, all hits regardless of energy count as one hit. This data was simulated with g2MIGTrace and assumes the standard run conditions outlined in the CDR.

8275

17.4.3 Electronics and Data Acquisition Subsystems Considerations

8276

8277

To guarantee deadtime-free calorimetry readout, the signal from each of the 1296 active

8278

calorimeter channels will be continuously digitized for every 700 μs muon fill. Those wave-

8279

forms are then transferred to the DAQ system for data reduction – isolation of the time

8280

windows containing electromagnetic showers – and storage. The DAQ must apply an energy

8281

threshold to identify showers within a station, so the 54 waveforms from that station must

8282

be summed to keep the threshold independent of the incident positron position in a crystal.

8283

All 54 WFD waveforms must therefore be transferred to the same frontend DAQ system,

8284

which will use the waveform sum to perform data reduction on the digitization stream:

8285

identification of time islands with activity (T -method) and time rebinning of the waveform

8286

(Q -method).

8287 The energy range of interest for an individual calorimeter element is 25 to 3100 MeV
8288 for single events. Allowing pileup, suggests pushing the upper limit close to 5000 MeV. A
8289 digitizer with 12-bit depth (4096), is ideal. It will allow good pulse definition, important for
8290 the energy resolution requirements, and it will not saturate for the highest energy events.
8291 As discussed in Chapter 18, the pulse shape risetime is approximately 2-4 ns, and we are
8292 actively working to reduce it. The laboratory tests done to date suggest that a minimum of
8293 500 MHz sampling will be required to accurately fit the pulses, subject to optimizing pileup
8294 rejection. Therefore, each digitized waveform is corresponds to 350K 12-bit words for each
8295 muon fill.

8296 A precision oscillator (“clock”) will provide the timebase from which the ω_a frequency
8297 is measured. It must be controlled to provide negligible error compared to the anticipated
8298 0.1 ppm uncertainty on ω_a . In order to achieve this, the clock must have jitter that is
8299 significantly less than the 2 ns sampling period of the waveform digitizers. It must also have
8300 very low (< 10 ps) systematic shift across the time of a single fill. This latter requirement is
8301 important because of the large variation in event rate within a fill. A systematic time-slew
8302 that is correlated with muon or positron intensity would bias the result. The clock system
8303 must also enable a convenient blinding scheme such that the actual precise clock frequency
8304 cannot be known to the data analyzers.

8305 The data acquisition system must provide a deadtimeless readout of calorimeter segments
8306 using the waveform digitizers. Onboard memories in the digitizers will buffer the raw data
8307 and allow its asynchronous readout, thus decoupling the data acquisition cycles from storage
8308 ring fills. A frontend layer of multicore CPUs/GPUs will process the digitized records of each
8309 fill from every calorimeter segment into T -method, Q -method and other derived datasets. A
8310 backend layer of multicore CPUs/GPUs will handle the assembly of event fragments from
8311 the frontend layer and transfer of assembled events to the mass storage. Each stored event
8312 will represent a complete deadtime-free history of the entire activity in the detector system
8313 for every fill cycle.

8314

References

8315

[1] G. W. Bennett *et al.* [Muon G-2 Collaboration], Nucl. Instrum. Meth. A **579**, 1096 (2007).

8316

8317

[2] Sedykh S., et al. *Nucl. Instrum. Meth. A* 455:346 (2000).

8318

[3] V. Tishchenko *et al.* [MuLan Collaboration], Phys. Rev. D 87, 052003 (2013) arXiv:1211.0960 [hep-ex].

8319

8320

[4] D. Webber, *A part-per-million measurement of the positive muon lifetime and a determination of the Fermi constant*, doctoral thesis, University of Illinois at Urbana-Champaign (2010).

8321

8322

Chapter 18

Calorimeter

This chapter illustrates the design concept for the 24 electromagnetic calorimeters. The primary purpose of the electromagnetic calorimeter is to measure the energy and time of arrival of the daughter positrons from stored muon decay. The physics goals and subsequent requirements are reviewed. The recommended design for each subsystem – Absorber, Photodetection (SiPM), Bias Control, Laser Calibration, and Mechanical – is then presented. Finally, alternative designs, ES&H, risks, quality assurance, and value management are discussed.

18.1 Physics Goals and Requirements

The energy and timing information from the electromagnetic calorimeter introduces two potentially major sources systematic error to ω_a :

1. Unidentified pileup events, i.e. simultaneous positron showers in the same calorimeter station that cannot be resolved.
2. Rate-dependent effects that couple to the spin precession frequency (e.g. a rate-dependent gain change).

To meet the new FNAL E989 goal, the electromagnetic calorimeter must be able to resolve two showers by temporal or spatial separation. The calorimeters must provide 100% efficiency in the discrimination of two showers with time separations greater than 5 ns. Showers that occur closer in time than 5 ns must be further resolved spatially in more than 66% of occurrences. Therefore, the new calorimeter must have improved spatial resolution compared to the former E821 design [1].

The gain (G) stability requirement corresponds to a maximally allowed gain change of $\frac{\delta G}{G} < 0.1\%$ within a $200 \mu s$ time period in a fill. In addition, the arrival of a pulse should not affect the gain for a second pulse arriving a few nanoseconds later on the same channel, unless that change is understood and can be applied to the interpretation of a following pulse in a reliable manner. The long term gain stability ($>$ seconds) is more relaxed and we aim at $\frac{\delta G}{G} < 1\%$. To verify the overall gain stability, each of the 24 stations must be equipped with a calibration system that monitors the gain continually during the muon spills with a precision of $\frac{\delta G}{G} \sim 0.03\%$.

18.2 Evaluation Methodologies: Test Beams and Simulations

The recommended design builds upon extensive testing and simulation efforts. Prototype detectors were built. Various silicon photomultiplier (SiPM) and photomultiplier tube (PMT) candidates were tested. Several iterations of the electronics boards needed to operate the SiPMs were built and tested. Both laboratory and test beam studies were performed. We employed simulations to study detector performance, sensitivity to ω_a and pulse-shape fitting.

This laboratory and test beam work provided crucial results on pulse shape and energy resolution for different component choices. The tests provided direct results that we will present in detail below, and also validated and informed our simulation efforts. Our confidence that our baseline design will meet, in particular, the pile-up suppression goal stems directly from these efforts. A brief summary of this work is given next for context. The results of these efforts are described in line with the design recommendation topics.

The Fermilab Test Beam Facility (FTBF) was used several times to evaluate prototype calorimeters. In particular, our first effort in which 0.5-mm pitch tungsten plates alternated with 0.5-mm layers of scintillating fiber resulted in a publication [2]. A larger prototype was then built and tested, see Fig. 18.1. Finally, the recommended design based on PbF_2 crystals was tested using the 7-crystal array shown in Fig. 18.2. These crystals were compared directly to the W/SciFi detector and to a custom PbWO_4 crystal during the April 2012 FTBF period. The right panel of Fig. 18.1 shows the arrangement of PbF_2 crystals during assembly and Fig. 18.2 displays a front view of the full test setup. Various readout methods, wrappings and couplings were employed.

We also used simulation tools to evaluate performance and optimize parameters. GEANT-4 simulations were used to study light collection in crystals and to evaluate crystals shape, wrapping, and light yield. They were used to study array size and cluster formation. A realistic muon storage simulation was used to illuminate the calorimeters with positrons having the correct energy, spatial, and temporal distributions on the calorimeters. Finally, we developed custom software to build pulse-shape libraries from controlled lab tests, and then used the libraries to fit individual events and two-pulse events.

18.3 Recommended Calorimeter Design

The calorimeter system includes the following subsystems: absorber, photodetection, bias control, calibration, and mechanical. Over the past several years, the calorimeter design has gone through an extensive down-select process for absorber and readout technologies. Briefly, each of the 24 calorimeter stations will consist of a 6×9 array of lead-fluoride (PbF_2) Cherenkov crystals. Each crystal will be read out by a 16-channel Hamamatsu MPPC (Multi-Pixel Photon Counter, commonly dubbed “SiPMs” or silicon photomultipliers). Custom supporting electronics amplify the summed signal and convey it to the digitizers following a hardware pole-zero correction to shape the output. A photo of the prototype crystals and 16-channel surface-mount SiPM is shown in Fig. 18.3.

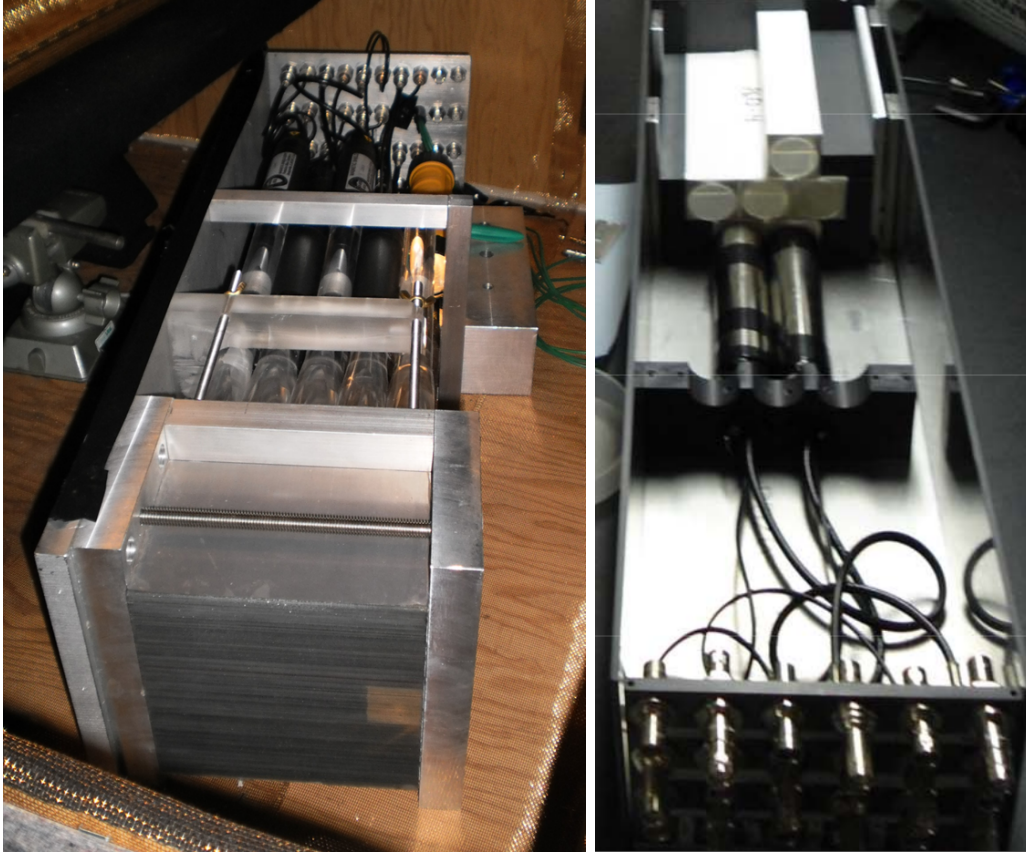


Figure 18.1: Left: Monolithic block of W/SciFi having 0.5 mm thick pure tungsten plates alternated with 0.5 mm diameter ribbons of blue scintillating fiber. The readout side is divided into 25 individual elements. Tapered lightguides direct the light from a $3 \times 3 \text{ cm}^2$ area to a PMT. Right: Crystals being prepared for test beam. Here, PMTs are used for the outer elements and a SiPM will be placed on the center crystal and alternatively a very fast Hamamatsu R9800 PMT for comparison.

8393 SiPM gains are very sensitive to bias and temperature, so a precise and stable bias volt-
 8394 age control system is under development and a temperature-stable operating environ-
 8395 ment has been designed. Both systems will help to maintain high gain stability, which addresses a
 8396 leading source of systematic uncertainty. A state-of-the-art laser-based distributed calibra-
 8397 tion system has been designed. It will permit precise monitoring of gain vs. time-in-fill for
 8398 the nearly 1300 crystals.

8399 Several factors that influenced the technology choice are:

- 8400 • Each of the 24 calorimeter stations will be located in the fringe field of the central
 8401 storage ring, directly adjacent to the muon storage volume in a cutout of a scalloped
 8402 vacuum chamber (see Fig. 17.5). The space is highly constrained vertically (17 cm)
 8403 and longitudinally (owing to vacuum interconnects and flanges). Strict limits exist on
 8404 the allowed magnetic field perturbation from the absorbers, electronics and mechanical
 8405 housings.

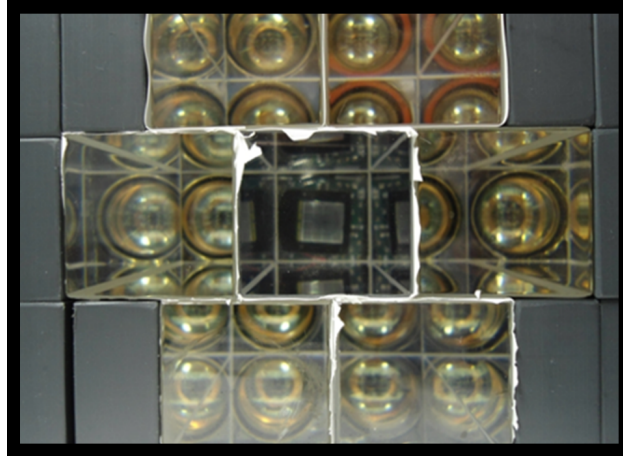


Figure 18.2: Front picture of the 7-crystal test array used in the FTBF. In this configuration, a SiPM is visible on the center channel, while PMTs are used on the remaining elements. These crystals were wrapped in white millipore paper.

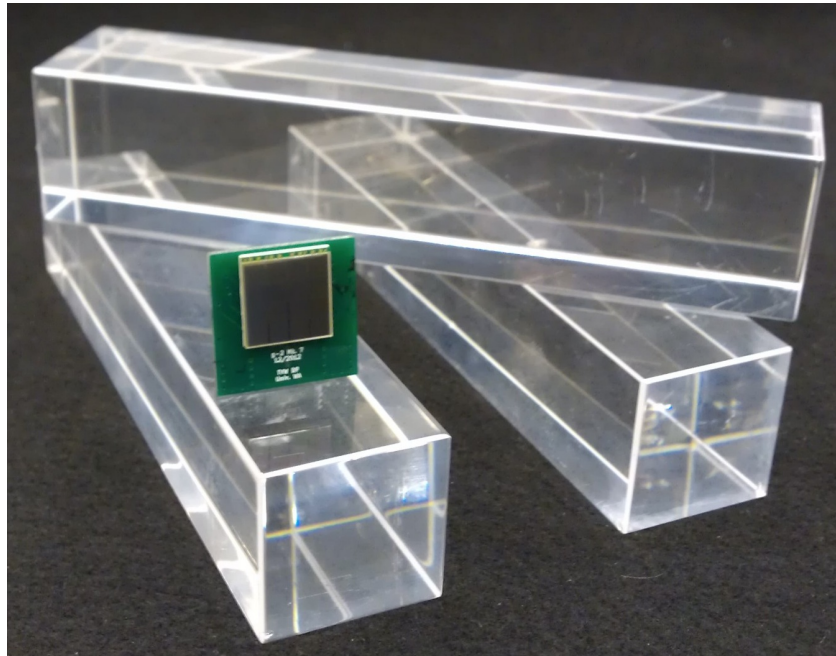


Figure 18.3: Sample $3 \times 3 \times 14 \text{ cm}^3$ PbF_2 crystals together with a 16-channel Hamamatsu SiPM mounted to our Mark VII, resistive summing, voltage amplifier board. (Note, these crystals are larger than in the conceptual design.)

8406

- The absorber must be dense to minimize the Molière radius and radiation length. A short radiation length is critical to minimize the number of positrons entering the side of the calorimeter while maintaining longitudinal shower containment.

8407

8408

8409

- The intrinsic signal speed must be very fast with no residual long-term tail, thus minimizing pileup.

8410

Table 18.1: Properties of lead-fluoride crystals

Crystal cross section	$2.5 \times 2.5 \text{ cm}^2$
Crystal length	14 cm ($> 15X_0$)
Array configuration	6 rows, 9 columns
Density of material	7.77 g/cm^3
Magnetic susceptibility	$-58.1 \times 10^{-6} \text{ cm}^3/\text{mol}$
Radiation length	0.93 cm
Molière radius R_M	2.2 cm
Molière R_M (Cherenkov only)	1.8 cm
$KE_{threshold}$ for Cherenkov light	102 keV
Expected photo-electron yield* / GeV (White wrapping)	1765
Expected photo-electron yield* / GeV (Black wrapping)	685

*using 1.2 cm^2 SiPM on rear face; light integrated over several crystals to have full shower containment

- 8411 • The resolution should be good—it is used to select events—but it need not be “excel-
8412 lent.” A resolution of $\approx 5\%$ at 2 GeV is the required benchmark and improves upon
8413 the E821 calorimeter system by a factor of 2.

8414 18.3.1 Absorber Subsystem

8415 The default material choice following an extensive comparative evaluation program (see
8416 Sec. 18.4) is lead-fluoride crystal (PbF_2). This crystal’s combination of good energy reso-
8417 lution and a very fast Cherenkov signal response outperformed the other absorber options
8418 that we considered (see Sec. 18.4). It has very low magnetic susceptibility, a radiation length
8419 of $X_0 = 0.93 \text{ cm}$, and a Molière radius of 1.8 cm. We used a precise ($\delta P/P \sim 1\%$) Frascati
8420 500 MeV electron beam to verify the resolution and light yield that had been documented
8421 [3] by the A4 collaboration from Mainz, that built a large PbF_2 array for their experiments.
8422 They found $\sigma/E \sim 3.5\%/\sqrt{E}$ and about 1.7 PE/MeV. Table 18.1 presents a summary of
8423 the properties of the crystals.

8424 The Shanghai Institute of Ceramics (SICCAS) provided the prototype crystals and a
8425 competitive quote for the 1350 elements required for the full system (plus spares). We
8426 own and have used instrumentation to measure the spectral response of the crystals over
8427 the range 230 nm to 800 nm, see Fig. 18.4. We have also made atomic force microscopy
8428 (AFM) measurements on a crystal to determine the surface quality so that we might properly
8429 represent it in our light-propagation simulations. The crystal procurement plan involves a
8430 1st-stage quality control check by the Shanghai University members of the collaboration,
8431 who are local to the vendor. Next, the crystals will be sent to the University of Washington
8432 team for wrapping and assembly. PbF_2 crystals are relatively easy to handle; they are only
8433 slightly hygroscopic.

8434 Detailed GEANT ray-trace simulations and direct laboratory measurements have been
8435 used to study the light collection efficiency of the crystals subject to various wrapping

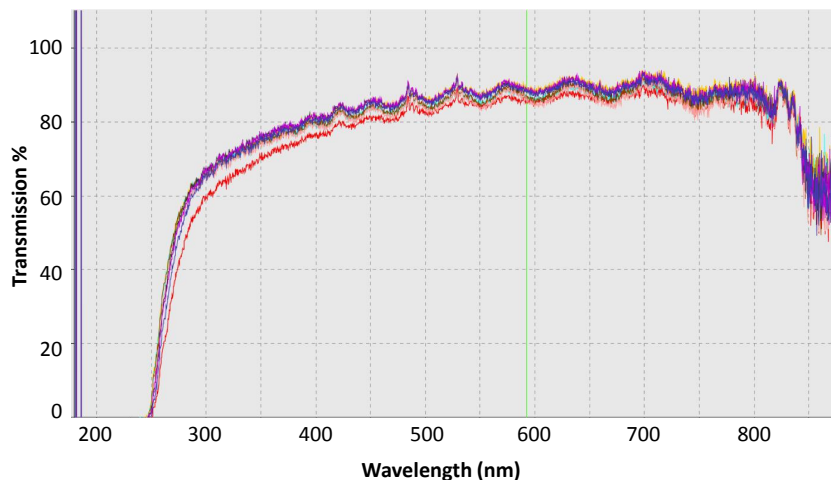


Figure 18.4: Transverse transmission efficiency vs. wavelength through a 3-cm-thick PbF_2 prototype crystal. The four curves correspond to rotations of the crystal with respect to the light source from an Ocean Optics spectrometer.

8436 schemes and couplings to the photo-sensitive readout. We have focussed on two extremes,
 8437 namely an all-black tedlar absorptive wrapping, and a diffuse reflective white millipore pa-
 8438 per wrapping. The black wrapping largely transmits only the direct Cherenkov light cone,
 8439 while the white wrapping allows light to bounce multiple times within the crystals, even-
 8440 tually leading to a higher overall photon yield. Both wrappings have advantages. For the
 8441 shortest pulse occupancy time, the black wrapping excels. For the greatest light yield, the
 8442 white wrapping is better. Shorter-duration pulses improve pileup rejection; higher light yield
 8443 improves energy resolution. We have evaluated both wrappings and an aluminum foil wrap-
 8444 ping in a test-beam using a standard 29-mm Photonis PMT for readout. The left panel of
 8445 Fig. 18.5 shows the results with the amplitudes normalized. The black wrapping (labeled
 8446 Tedlar in the figure) response shape reached the limit of the PMT response time. The right
 8447 panel compares PbF_2 to alternative design options discussed in Sec. 18.4. Here we observe
 8448 the true full width of 4 ns for the PbF_2 crystal as measured using a fast Hamamatsu R9800
 8449 PMT.

8450 Table 18.1 includes two entries that compare the absolute light yield in photo-electrons
 8451 as would be detected by our default photo-sensitive detectors. The simulation generates the
 8452 correct Cherenkov light distribution (by wavelength) from a 2 GeV incident positron and
 8453 it uses the correct crystal dimensions and surface reflectivity parameters. Optical-grease
 8454 coupling is assumed, as is the photo-detection efficiency of the readout device as a function
 8455 of wavelength. The yield of white paper wrapping is 2.5 times greater than the black paper,
 8456 which is consistent with laboratory tests we carried out with cosmic rays. The pulse duration
 8457 is also measured and largely agrees with the measurements. We intend to repeat the light
 8458 yield test with an improved calibration of PE/channel for the photo-sensitive readout.

8459 GEANT-4 simulations have been used to optimize the individual crystal size and the
 8460 array matrix configuration. A visualization of a typical 2 GeV positron shower is shown
 8461 in Fig. 18.6. A driving specification for an array of crystals is the reduction in pileup to
 8462 be realized by spatial separation. Candidate arrays of 5×7 and 6×9 (height by width)

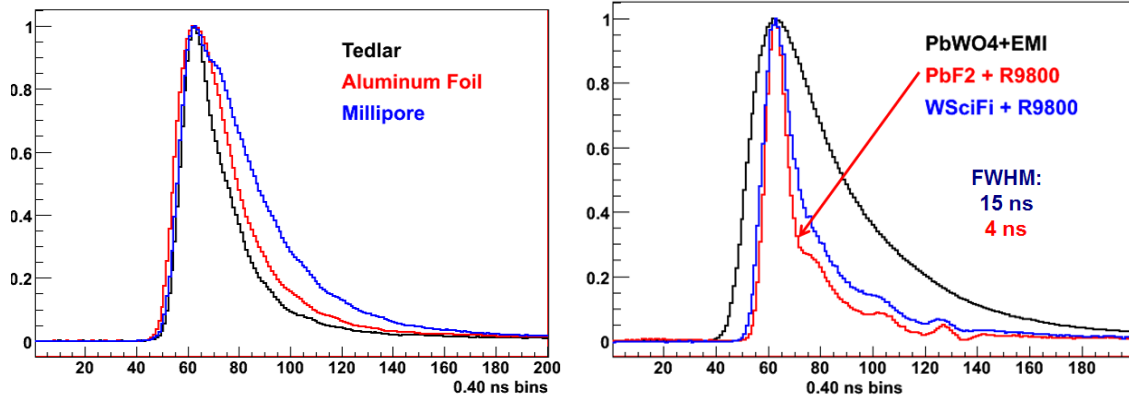


Figure 18.5: Left: Normalized response of PbF_2 crystal wrapped in absorptive black tedlar, reflective aluminum foil, and white millipore paper. A standard 29-mm Photonis PMT was used. Right: Comparison of three pulse shapes: PbF_2 using a very fast Hamamatsu R9800 PMT, W/SciFi using the same PMT, and PbWO_4 using an EMI PMT. The PbF_2 exhibits the fastest response (4 ns) indicated in red. The PbWO_4 is the slowest at 15 ns.

8463 segmentation using $3 \times 3 \text{ cm}^2$ or $2.5 \times 2.5 \text{ cm}^2$, $15X_0$ -deep crystals, respectively, will fit the
 8464 space constraints. A simulation with full showering and cluster reconstruction using a simple
 8465 and robust two-shower separation algorithm was used to choose the best arrangement. Not
 8466 surprisingly, the higher-granularity array is best. We find that it will provide at least a 3-fold
 8467 reduction in pileup compared to a monolithic design. These conclusions were arrived at from
 8468 a combination of simulation and direct measurement at the FTBF.

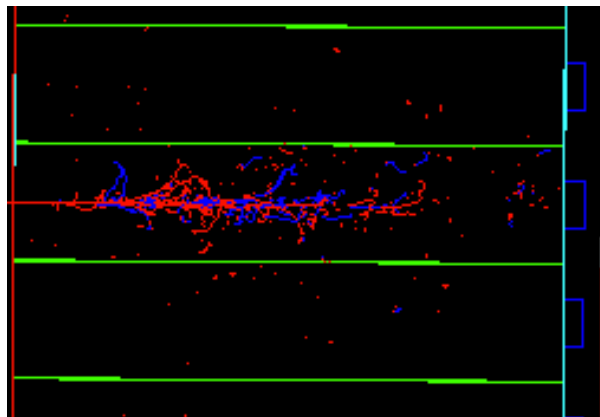


Figure 18.6: A single shower showing secondary positrons (blue) and electrons (red) in a $2.5 \text{ cm} \times 2.5 \text{ cm} \times 15X_0$ deep PbF_2 crystal, subject to a 2 GeV positron incident from the left. Photons have been removed for clarity.

8469 Energy sharing among neighbor crystals is shown in Fig. 18.7 for a shower that strikes
 8470 the center of the middle crystal. The simulation is calibrated against the test-beam measure-
 8471 ments in which an electron beam was directed into a crystal at various known positions and
 8472 the ratio of neighboring crystal responses was recorded. Fig. 18.7 also shows a histogram of
 8473 data vs. the simulation prediction. The agreement is excellent and verifies the model used

8474 to optimize array size and to evaluate pileup by shower separation.

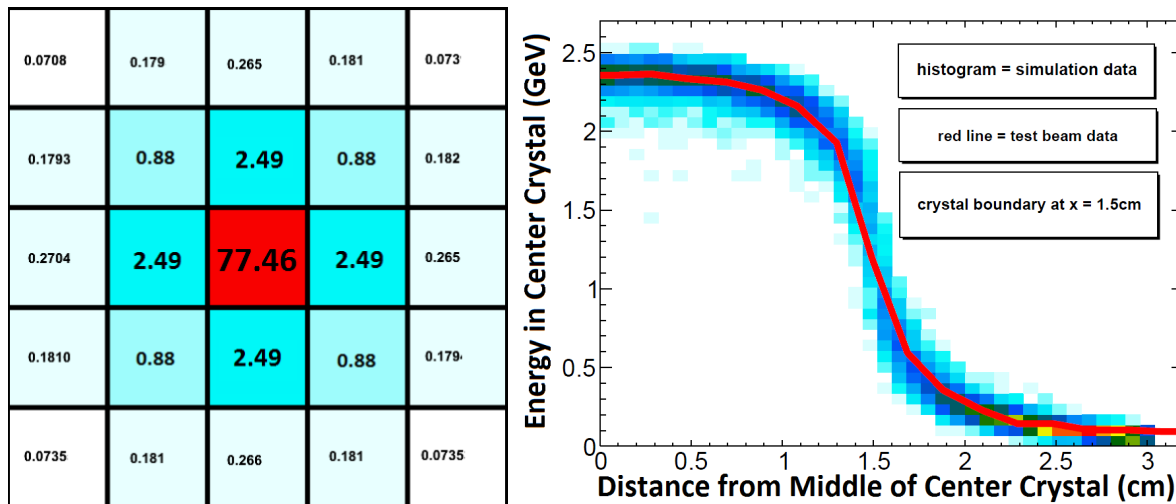


Figure 18.7: Left: Schematic representation of energy deposition in a section of the segmented electromagnetic calorimeter. Each cell is one crystal with dimensions ($2.5 \times 2.5 \times 14 \text{ cm}^3$). The numbers represent the percentage of the kinetic energy deposited in each crystal. This data was produced from a GEANT-4 simulation with an positron incident on the center of the central crystal. The results do not change for positrons in the range of 0.5 GeV to 3 GeV. Right: A comparison of test beam data and simulation data. This plot shows the shower leakage into neighboring crystals as a function of beam incidence position.

8475 The simulation was then used to study the spatial separation efficiency for two simul-
 8476 taneous showers. The left panel of Fig. 18.8 shows schematically the shower deposition by
 8477 color. The right panel is a systematic study of two-shower events as distributed on the
 8478 calorimeter based on the full muon storage and decay simulation. From the simulation we
 8479 see that the 6×9 configuration will allow identification of pileup events for 2/3 of the time,
 8480 so will provide our needed factor of three reduction in pileup relative to a monolithic array.

8481 18.3.2 Photodetection Subsystem – SiPM

8482 In the baseline design, silicon photomultipliers (SiPMs) read out the crystals. While chal-
 8483 lenging and relatively new devices, they are increasingly preferred over traditional PMTs in
 8484 many nuclear and particle physics applications. As such, the body of experience in their use
 8485 is growing rapidly and the variety of SiPM devices from many manufacturers is increasing.
 8486 They work as pixelated Geiger-mode counters. The default SiPM we are considering has
 8487 57,600 $50\text{-}\mu\text{m}$ -pitch pixels on a $1.2 \times 1.2 \text{ cm}^2$ device. When a photon strikes a pixel, it can
 8488 cause an avalanche that is summed together with the other struck pixels in a linear fashion
 8489 to produce the overall response. Quenching resistors are intrinsic to the device to arrest the
 8490 avalanche and allow the device to recover. The recovery time constant is typically 10's of ns.
 8491 Those pixels that are not struck, meanwhile, remain ready for a next pulse. In general, the
 8492 concept is to have a pixel count that greatly exceeds the highest photon count that would
 8493 strike the device. For example, for our crystals, a working number is 1 PE/MeV (for SiPM

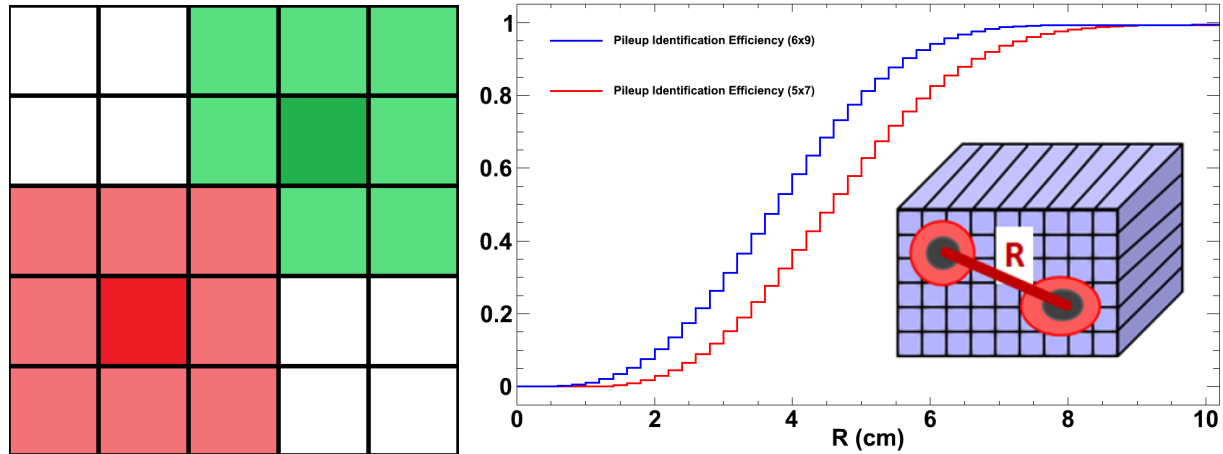


Figure 18.8: Left: Schematic representation of energy deposition in a section of the segmented electromagnetic calorimeter. Red represents the primary cluster reconstructed by the analysis software. Green represents the secondary cluster. The dark cells dictate the seed of each cluster. Right: Pileup separation efficiency curves for two different crystal segmentations, 6x9 (blue) and 5x7 (red), which correspond to 2.5 cm and 3 cm crystals, respectively. The variable R is the distance between the two incident positrons and is shown graphically in the inset.

8494 devices PE represents a converted photon). With a range of up to 3.1 GeV for single events,
 8495 the occupancy fraction remains no more than about 5%, which is in a near-linear regime and
 8496 allows for a good measurement of any closely trailing second pulse.

8497 The selection of SiPMs over PMTs is pragmatic. SiPMs can be placed inside the storage
 8498 ring fringe field, thus avoiding the awkward, long lightguides that would be needed for
 8499 remote PMTs. They have high photo-detection efficiency, they will not perturb the storage
 8500 ring field, and they can be mounted directly on the rear face of the PbF_2 crystals. The cost
 8501 of large-area SiPM arrays is rapidly falling and their performance characteristics continue to
 8502 improve. We have spent the last 2 years developing lab tests to evaluate these devices. The
 8503 collaboration has designed and built a series of custom pre-amplifier and summing amplifier
 8504 boards. The most recent version features low-power consumption and an intrinsic short pulse
 8505 when coupled to a pole-zero correction circuit that eliminates the long RC time-constant tail
 8506 of the device.

8507 Large-area SiPM devices are packaged as arrays of smaller individual channels. While
 8508 the market is constantly evolving, we are presently using a Hamamatsu surface-mount 16-
 8509 channel MPPC having 57,600 50- μm pixels in a $1.2 \times 1.2 \text{ cm}^2$ active area. It is reasonably
 8510 well-matched to the surface $2.5 \times 2.5 \text{ cm}^2$ crystal face. Figure 18.9 shows the Hamamatsu 16-
 8511 channel surface-mount MPPC (SiPM). This board is based on a the concept of a passive sum
 8512 and voltage amplifier. The output of a SiPM from a photo-electron event is a pulse of current,
 8513 with a fast rising, sub-ns, edge and a longer tail on the order of tens of ns. The current pulse
 8514 is converted to a voltage by a load resistor. Our present design follows the SiPM output
 8515 with two stages of voltage amplification provided by high-speed op amps. We continue
 8516 to improve our circuit and to follow the field to learn about new devices and techniques.

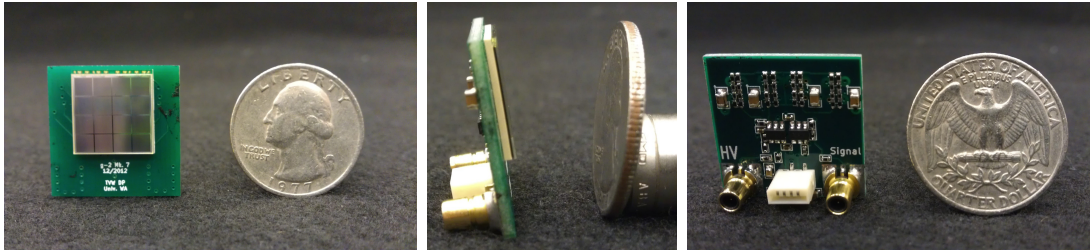


Figure 18.9: Surface-mount 16-channel MPPC. The coaxial connections represent the signal out and the common bias voltage in. The board low voltage is supplied through the white edge connector.

8517 Our development will likely cycle through 2 or more iterations prior to final purchase of
 8518 components in order to take advantage of the latest offerings. We have also begun a dialog
 8519 with University of Washington EE and Medical Physics research groups who are developing
 8520 an ASIC design having many overlapping features of common interest. Considering this
 8521 dynamic environment, the baseline conceptual design has been demonstrated to function
 8522 well enough for $g - 2$, but we are confident that improvements will be made based on
 8523 announcements of new products from the vendors and from the rapid advancement in the
 8524 electronics designs.

8525 One of the challenges of using SiPMs is their particular sensitivity to temperatures.
 8526 Figure 18.10 (left panel) shows the gain change of our SiPM device vs. temperature. The
 8527 gain change is 4% per $^{\circ}\text{C}$. Fortunately Hamamatsu claims this temperature dependance
 8528 is greatly reduced in their next generation of SiPMs. Once the next generation becomes
 8529 available for testing a comprehensive evaluation will be performed. In the meantime the
 8530 design is prepared to handle the temperature dependance currently observed. While short-
 8531 term shifts are unexpected, the overall SiPM environment must be maintained at a fairly
 8532 constant temperature in order to simplify the global calibration of gain during the running
 8533 period. The response of a SiPM is also quite sensitive to the bias voltage stability above
 8534 Geiger-mode breakdown threshold. The right panel of Fig. 18.10 shows a lab measurement
 8535 of our SiPM and voltage amplifier board output vs. bias voltage. The slope is steep near the
 8536 working bias of 72.5 V, leading to the need to have a separate bias control subsystem, which
 8537 we describe in Subsection 18.3.2.

8538 Given the working electronics board described above, simulations were carried out to
 8539 determine pulse-shape characteristics and, most importantly, two-pulse separation. We used
 8540 a 5 GSPS digitizer to record a series of pulses in which a SiPM was excited by a 600 ps
 8541 duration N_2 laser (337 nm) light pulse. The intrinsic fast risetime of a SiPM is slowed
 8542 somewhat by our circuit, while the exponential recovery time constant is determined by the
 8543 quenching resistance and internal capacitance. Because the pulse shape is predictive, a pole-
 8544 zero correction can be applied, post-amplifier, to produce the final recorded pulses. The left
 8545 panel of figure 18.11 shows the intrinsic raw SiPM pulse with its long recovery time. The
 8546 same pulse is seen with the pole-zero correction circuit applied. A series of pulses is used
 8547 to develop a pulse-shape library. The right panel then shows a representative single pulse
 8548 fit using the library template. This procedure is the basic element of our eventual analysis
 8549 method.

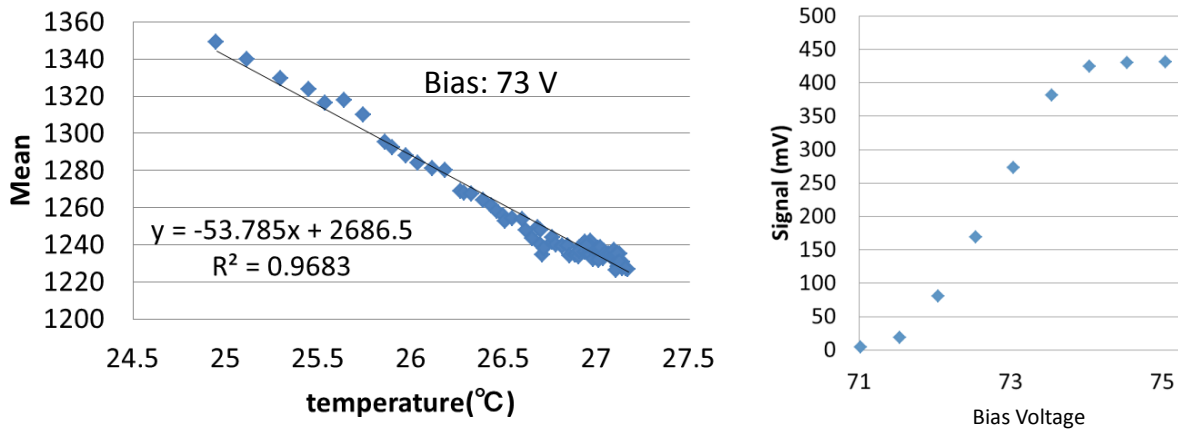


Figure 18.10: Left: Gain vs. temperature for 16-channel SiPM array. Right: Gain vs. bias voltage. The device response turn on above operating voltage is visible just above 71 V. Then there is a linear response region. Above 74V the response flattens. This is due to afterpulsing in the prototype SiPM. The next generation of SiPMs from Hamamatsu has drastically reduced the frequency of afterpulsing, permitting operation at higher overvoltages.

8550 The analysis of two-pulse waveforms is critical for pileup rejection. Both simulated and
 8551 measured studies were made, following many of the procedures we developed for the MuLan
 8552 1-ppm muon lifetime experiment. In that effort, unresolved pileup had to be corrected at the
 8553 10^{-3} level to avoid distortions to the lifetime [4]. It is less severe here, but still important. Our
 8554 two-pulse resolution software was adapted for the new $g - 2$ situation, which has different
 8555 pulse shapes and a much wider range of amplitude ratios for the two nearby pulses. At
 8556 present, we find that two pulses separated by 5 ns or more can be reliably separated. An
 8557 active area of our laboratory work is the systematic mapping of the two-pulse separation
 8558 function with varying pulse-to-pulse amplitude ratios and time separations. As an example,
 8559 Fig. 18.12 shows the waveform from laboratory tests in which the laser pulse was split with
 8560 one leg delayed by exactly 5 ns with respect to the second. The figure clearly shows resolved
 8561 pulses at a sampling rate of 698 MSPS. Chapter 21.1 presents another study in which the
 8562 pulses are sampled at the baseline 500 MSPS rate. The lab setup allows measurement of
 8563 the two pulses individually as well as their combination. Tests are ongoing to map the
 8564 efficiency of two-pulse resolution vs. Δt and R_{12} , the ratio of amplitudes for pulse 1 and
 8565 pulse 2. Additionally, we intend to map out the function $G2(\Delta t, R_{12})$, which is the change of
 8566 the second pulse amplitude versus the time separation and amplitude ratio. Because pixels
 8567 are struck (and therefore temporarily disabled) from the leading pulse, the trailing pulse
 8568 effectively see a “smaller” device, but in a predictable manner.

8569 Bias voltage system for the SiPMs

8570 Several possible approaches and technical implementations have been considered for the
 8571 SiPM Bias System; the following, most favored solution was chosen as the basis for our
 8572 cost and effort estimate. It is understood that as the design takes concrete shape and as
 8573 components are tested, it may be modified.

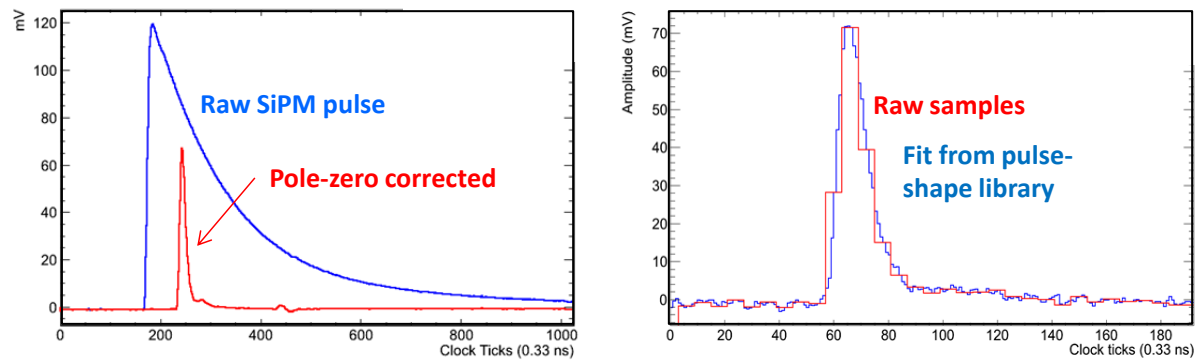


Figure 18.11: Left: Raw laboratory measurement of raw 16-channel SiPM pulse using voltage amplifier. Same pulse with post-amplifier, pole-zero circuit included. Right: Single pulse and fit using pulse-shape template library and current pulse-finding analysis software.

8574 The following requirements drove the baseline design presented below. The SiPM Bias
 8575 System must supply a bias voltage for each SiPM that is stabilized at the mV level, par-
 8576 ticularly over the critical $700\ \mu\text{s}$ time window. To meet this requirement, the control loop
 8577 for each channel must have a voltage resolution of at least 1 mV and a per-channel current
 8578 resolution of at least $50\ \mu\text{A}$. Each calorimeter must be gain-matched, so the system must
 8579 allow each channel to be set to an individual bias voltage. The expected operating voltage
 8580 range of the SiPMs is from 72 VDC to 73 VDC, so the bias voltage must be adjustable
 8581 over a broader nominal range. To allow use of alternative SiPMs, however, the overall offset
 8582 voltage should be easily adjustable to accommodate the new SiPMs operating range, such
 8583 as 30 – 35 VDC. To accommodate the baseline 6×9 crystal station and provide operational
 8584 spares, the Bias System will provide 64 channels per station. There will be 24 individual
 8585 SiPM Bias Systems, one for each calorimeter station, plus one additional spare.

8586 To control the voltage settings, the system must provide an interface compatible with
 8587 the experiment's choice of the Midas Slow Control Bus (MSCB). We will use RS-485 as the
 8588 physical layer for the MCSB communication so that optocouplers can be used to isolate the
 8589 SiPM Bias System.

8590 The system is also subject to several physical requirements. The SiPMs will be physically
 8591 1–2 meters from the 19-inch rack containing the 64-channel bias voltage supply. If possible,
 8592 twisted pair wire will connect each channel to each SiPM, but the system design will also
 8593 allow use of coaxial cable with SHV connectors. In the worst case, we will be required to
 8594 use triaxial cable with the return separated from the system ground. The vertical space for
 8595 the chassis will be very limited, so the system will be housed in a compact 1U (1.75") or 2U
 8596 (3.50") chassis.

8597 In addition to the chassis, internal power supplies and circuit boards, the final SiPM Bias
 8598 System may also need external components, such as 100 V capacitors on the bias voltage at
 8599 each SiPM.

8600 Based on the above requirements and restrictions, we have settled on the design shown
 8601 schematically in Fig. 18.13. A one-station system will be housed in a single 1U or 2U chassis
 8602 that contains four slots for daughterboards. Each daughterboard will power 16 indepen-

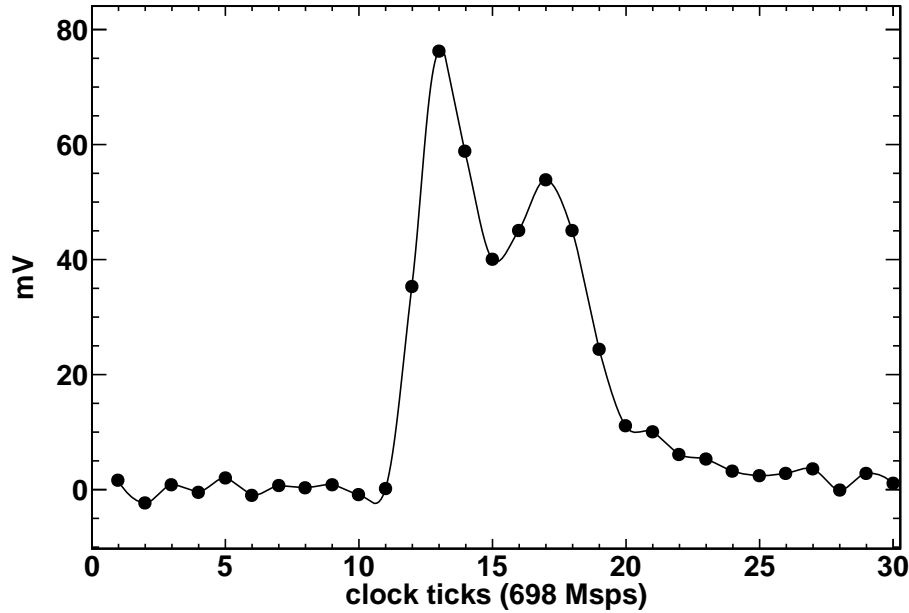


Figure 18.12: Digitized samples for a pair of pulses laser pulses striking the SiPM array 5 ns apart. The first pulse contained 1,250 photo-electrons and the second contained 800 photo-electrons.

8603 dently controllable channels. Each of these chassis will house a single 70V AC/DC power
 8604 supply, such as the 70EB04 (40 mA linear), and a single 5V AC/DC power supply like the
 8605 Acopian 5EB100 (1A linear). The 5V AC/DC supply will be floated above the reference
 8606 70V supply, and the Vss/GND terminal for logic circuits including the DAC will be floated
 8607 to 70VDC. Ground, 70V and 75V will be wired to the four internal boards (possibly using
 8608 screw terminals), but the ground will be used only as the ground for the bias voltage. Each
 8609 daughterboard will have an isolated, independent connection to the Midas Slow Control Bus.
 8610 The daughter boards could be arranged in either a 2×2 or a 4 stacked configuration.

8611 The SiPM bias system will monitor output voltages as described below. Specifically,
 8612 the measured bias voltage value for each individual SiPM channel will be compared to
 8613 the set voltage via the on-board microcontroller/MSCB bridge, with corrections applied
 8614 as necessary. The system will also provide for SiPM bias voltage corrections based on the
 8615 readout of the calorimeter (SiPM) temperature, should that be deemed necessary (the initial
 8616 implementation does not make explicit use of this feature).

8617 The key functions pertaining to the voltage setting and monitoring are provided by the
 8618 “System Monitor” circuit, on the one hand, and by the DAC–ADC tandem, on the other.
 8619 The “System Monitor” circuit shown in Fig. 18.13 will monitor the 70 VDC and 5 VDC
 8620 voltage levels in real time, and communicate them to the microcontroller and Midas Slow
 8621 Control frontend computer. The DAC, here represented by an Analog Devices AD5390, is
 8622 a 14-bit 16-channel unit which, in addition to the 16 individual channels of bias voltage,
 8623 also has an analog multiplexed (MUX) monitoring output. This output is connected to a
 8624 16-bit single-channel ADC, shown as TI ADS1100 in the figure, which reports the measured
 8625 value to the microcontroller. Depending on the final circuit design, we may choose to use an

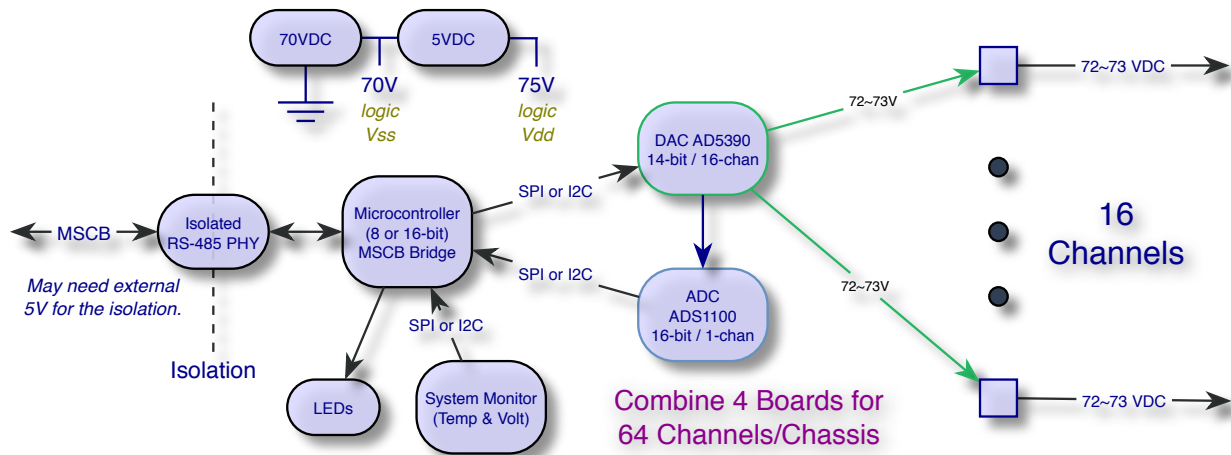


Figure 18.13: Schematic diagram of the working design for the SiPM Bias Voltage system (see text for details).

8626 integrated ADC instead of the ADS1100.

8627 The microcontroller combines the measurements of the 70 VDC (the floating ground of
8628 the circuit) and the ADC-reported increment, and regulates it, with possible additional
8629 inputs from the rest of the experiment via the MSCB, and from the on-board System Mon-
8630 itor if calorimeter temperature is used in the bias voltage regulation. The unit can work
8631 autonomously should the MSCB connection be severed.

8632 Overall, the comparative advantages of this approach win over the possible disadvantages
8633 of a system base, for example, on sixty-four independent 72–73VDC supplies. A common
8634 70V supply is cheaper than sixty-four 72–73VDC supplies. The system will also have a
8635 simpler overall circuit compared to solutions with completely independent supplies for each
8636 channel, and, for example, will eliminate the need for the debugging and maintenance of
8637 sixty-four separate power supply circuits. Finally, similar methods have been employed for
8638 other APD bias circuits, albeit with a more lenient ripple voltage tolerance than required
8639 for the $g - 2$ application.

8640 The potential disadvantages are comparatively minor, and we see them as acceptable
8641 tradeoffs. In particular, the ripple voltage may be higher in the system than for the indi-
8642 vidually controlled supply (perhaps at the 1 mV_{pp} level). Debugging of the system will also
8643 provide challenging since we must either isolate all test equipment from ground, or we must
8644 turn off the 70 VDC supply and shunted it to ground during debugging and testing.

8645 In testing and validation of the production units, we will ensure that all 64 channels
8646 can source the output voltage over the entire required range. We will also calibrate all 64
8647 channels so that the error between the programmed voltage setting and the actual voltage
8648 output is within our tight tolerance. The agreement shall be tested at several points across
8649 the output voltage range. We will also calibrate the internal sampling ADC for each of the 64
8650 channels to ensure that any discrepancy between the actual output voltage and the reported
8651 voltage from the internal ADC is also within our tolerances. This too will be tested at several
8652 points across the full output voltage range. Finally, we will measure the ripple voltage on
8653 each output and verify that it is within the requirements. We may want to perform this test

8654 on every channel or perhaps only on a subset of channels.

8655 We will also verify that the other basic functions of each board perform as intended. The
8656 current limit circuit on each channel must allow the required maximum current for proper
8657 SiPM operation, while limiting the current below the appropriate safety level. We may cali-
8658 brate the internal voltage monitor circuits or at least test that they read the internal voltages
8659 within an acceptable range of error. Finally, we will verify that the internal temperatures
8660 can be read and that the status LEDs function as expected.

8661 The actual tolerances and limits to be used in testing will be determined during the design
8662 phase. Since fewer than 30 systems are needed, a fully automated test and calibration system
8663 is not likely worth the extra cost of the automation equipment. However, we will implement
8664 some level of semi-automatic testing in order to minimize variations that can arise when
8665 different operators run the tests.

8666 We will likely want to create a custom board that breaks out the 37-pin connector into
8667 16 channels of banana jacks. An operator testing the equipment can then use a standard
8668 cable to connect the channel under test to an appropriate source meter and an oscilloscope
8669 (for ripple measurements), one channel at a time. For the oscilloscope, one that can be
8670 automated via LabView would be useful so that the operator moves the cables and clicks a
8671 button on the screen and LabView does the rest to capture and measure the ripple. For the
8672 voltage range and current range tests, we will use a source meter that can also sink current
8673 and voltage, such as the Keithley 2400 SourceMeter.

8674 The equipment needs for the production testing should be relatively modest: LabView
8675 running on a computer to control the SourceMeter and the Oscilloscope as well as to com-
8676 municate with the unit under test over Midas Slow Control. LabView would instruct the
8677 operator on which channel to connect, then it would perform the tests on that channel. It
8678 would then alert the operator when it is time to switch to the next channel and wait until
8679 the operator indicates that the next channel is connected. We could have at least one setup
8680 under ripple testing with the Keithley SourceMeter while another breakout board is used to
8681 perform simultaneous testing of a different 16-channel board with the oscilloscope.

8682 It might take a day to fully test a chassis which is more than fast enough for our needs.
8683 We are expecting students to be able to program the tests, with senior personnel available
8684 for guidance and questions.

8685 18.3.3 Laser Calibration Subsystem

8686 A high performance calibration system is required for the on-line monitoring of the output
8687 stability of each individual module in all calorimeter stations. It is estimated that the
8688 detector response must be calibrated with a relative accuracy at the sub-per mil level to
8689 achieve the E989 experimental goal of limiting the systematic uncertainty contributions
8690 from gain stability to 0.02 ppm. This is a challenge for the design of the calibration system
8691 because the desired accuracy is at least one order of magnitude higher than that of all other
8692 existing, or previous, calibration systems for calorimetry in particle physics.

8693 Almost 1,300 channels must be calibrated during data taking; the proposed solution
8694 is based on the method of sending simultaneous light calibration pulses onto the readout
8695 photo-detector through the active sections (crystals) of the calorimeter. Light pulses must
8696 be stable in intensity and timing to correct for systematic effects due to drifts in the response

8697 of the crystal readout devices. A suitable photo-detector system must be included in the
8698 calibration architecture to monitor any fluctuation in time of the light source intensity and
8699 beam pointing as well as any fluctuation of the transmitted light along the optical path of the
8700 light distribution system, which could occur due to mechanical vibrations or optics aging.

8701 Some guidelines are defined to select the light source(s) and to design the geometry of
8702 the light distribution and monitoring; the following criteria are adopted to select the light
8703 source type:

- 8704 • The luminous energy of the calibration pulses must be in the range of the electron
8705 deposit in the crystals, typically 1-2 GeV; this corresponds to a luminous energy on each
8706 module of a calorimeter station of about 0.01 pJ, or to about 0.013 nJ for simultaneous
8707 excitation of all calorimeter readout channels (1300). The numbers quoted above are
8708 merely indicative of the order of magnitude and they are derived by assuming that the
8709 readout of each crystal will produce up to 2 photo-electrons per MeV with 50% P.D.E.
8710 (Particle Detection Efficiency) for SiPMs and with 40% coverage of the crystal readout
8711 face.
- 8712 • Light wavelength must be in the spectral range accepted by the detector and deter-
8713 mined by the convolution of the spectral density of the Cherenkov signal produced by
8714 electrons in PbF₂ crystals with the spectral transmission of the crystals, and with the
8715 spectral quantum efficiency (Q.E.) of the photo-detector. The Q.E. is peaked around
8716 420 nm for SiPMs.
- 8717 • The pulse shape and time width must be suitable to infer on the readout capability
8718 in pile-up event discrimination; pulse rise/trailing time must be of the order of some
8719 hundred of picoseconds, the total pulse width should not exceed 1 ns. This implies
8720 a peak power per pulse at the source of about 1 Watt (1 nJ in a 1 ns wide pulse),
8721 assuming the conservative value of 1% for the total intensity transmission factor (T)
8722 of the calibration system.
- 8723 • The pulse repetition rate must be of the order of 10 KHz; this value will be tuned to
8724 obtain the best compromise between the need of having enough calibration statistics in
8725 the time interval (some tens of microseconds after the muon injection in the ring) when
8726 the maximum rate is achieved in the readout devices and the need to avoid saturation
8727 of the DAQ bandwidth.

8728 A number of commercial diode lasers satisfy the criteria listed above, and have been
8729 considered as a source for the calibration pulses. The final choice will be made after the
8730 completion of all tests required to quantify, in terms of light transmission and time stabil-
8731 ity, all other optical elements of the calibration system. Guidelines for designing the light
8732 distribution chain are listed below:

- 8733 • High sensitivity monitors of the transmitted light at the end-point of each individual
8734 section of the distribution chain must be used to ensure online control of the sys-
8735 tem stability and to have information for applying feed-back correction to the source
8736 operation parameters, if needed.

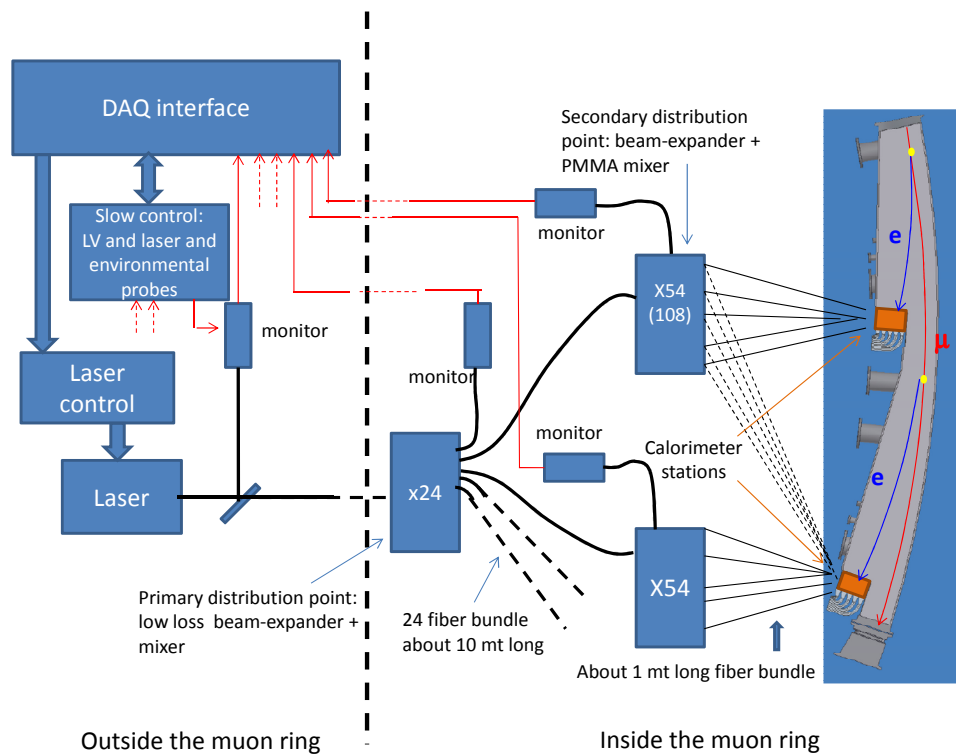


Figure 18.14: Calorimeter calibration system schematic diagram. There is a central light generation system (left side) that will then be distributed throughout the right (right side). At each stage the light levels will be monitored. Finally at the calorimeter level the light will be split and distributed to each module.

8737
8738
8739

- The optical path must be minimized in order to limit the light loss due to self-absorption in the optical fibers; the number of cascade distribution points must be also minimized to reduce the unavoidable light loss in the couplers between different sections.

8740
8741
8742
8743
8744
8745
8746
8747

- The laser source and its control electronics should be located outside the muon ring in order to avoid e.m. perturbations of the storage ring B-field induced by the current flow used to excite the laser. Consequently, a suitable geometry should include a primary light distribution point outside the ring, a bundle of fibers about 20 meter long that is used to feed light from the primary distribution point to the secondary ones, and secondary distribution points located close to each calorimeter station. From the secondary distribution points, short fibers, about 1 meter long, feed the light to the individual modules of each calorimeter station.

8748
8749
8750
8751

- Optical fiber selection: silica fibers (20 dB/km attenuation at 400 nm) are the best solution for long path light transmission and in terms of robustness against solarization or other aging affects due to large values of transmitted light intensity. For the shorter fiber bundles, where the transmitted intensity is at least one order of magnitude lower,

8752 PMMA clear fibers (200 dB/km attenuation at 400 nm) can also be considered to
8753 reduce costs.

8754 A possible geometry fulfilling all the requirements set by the guidelines listed above is
8755 shown in Figure 18.14; light generated by a laser source is fed onto a primary distribution
8756 device located in the center of the muon ring; quartz fibers (about 10 meter long, one
8757 per calorimeter station plus spares for monitoring purposes) route the light to secondary
8758 distribution devices located near the calorimeter stations, each distributor serving one or
8759 two close stations. A small fraction of the light exiting the source and the light distributors
8760 is routed to monitors whose analog signal is returned to the DAQ system for on-line checking
8761 of the system stability. An interface with the DAQ is also required for slow control signal
8762 recording. Communication with the timing signal controls is used to trigger the electronics
8763 of the laser driver.

8764 Qualification tests of the individual components will include comparison measurements
8765 of different options; apart the fiber type, alternative approaches are considered for:

- 8766 • laser source; as an alternative to a single, powerful laser light source, the possibility to
8767 use two or four lower power, synchronized, lasers can be considered; the latter solution
8768 would have the advantage that, in case of laser failure, calibration will not be disrupted
8769 during data acquisition; moreover, lower power lasers have, in general, better stability
8770 characteristics. An issue for the multi-source option is to demonstrate that the different
8771 pulses can be synchronized at the desired level, some tens of ps.

- 8772 • light distributors; the baseline solution uses custom designed beam-expanders with
8773 light mixers inside; this feature is required to guarantee intensity stability of the dis-
8774 tributed light against geometrical effects due to beam-pointing instabilities. Integrating
8775 spheres are an alternative and offer a high degree of output uniformity at the price of a
8776 higher factor in intensity loss (up to 100). Beam-splitters made with the linear circuit
8777 technology could also be considered if commercial devices, nowadays widely used only
8778 in the IR range for telecommunication, will be produced for the near-UV/visible range.

8779 18.3.4 Mechanical Subsystem

8780 Each calorimeter station will comprise a number of individual crystals that are made out of
8781 dense, usually brittle, material. In addition, the detector including the photo-sensitive device
8782 must be in a light tight encapsulation. A typical set of crystals and photo-detectors forming
8783 one calorimeter station weighs ≈ 40 kg. The housing must provide the light tightness, proper
8784 stability to carry the weight, feedthrough for cables, and a mechanism for easy lifting of the
8785 entire box and insertion into or out of the ring in the radial direction (e.g, rails).

8786 The locations of the 24 calorimeters in the experiment are fixed by the design of the
8787 scallop-shaped vacuum chambers. Several vacuum ports, bellows and the magnet's pole gap
8788 impose spatial limitations on the design. Specifically, the length of the calorimeter station
8789 along the positron's trajectory cannot exceed 38 cm. The pole gap limits each station to
8790 less than 17 cm. There are no tight limiting factors in the radial dimension that we can see
8791 would constrain the calorimeter station.

8792 For installation, maintenance and access to the vacuum chamber or the magnet, each
 8793 calorimeter station must be easily removable. We will determine later the degree of alignment
 8794 necessary, but a system of pins should allow for a reproducible position. The absolute position
 8795 is less critical. The calorimeter housing and retractable platform must allow for routing of
 8796 a variety of cables (detector signals, bias voltage, control signals, monitoring signals) and
 8797 service lines (e.g. water cooling pipes). The mechanical design must incorporate space
 8798 for the readout electronics crates to be placed on-board to be compatible with the moving
 8799 mechanism.

8800 A mechanical housing system was built for the test beam and a full-scale version has
 8801 been designed by CENPA engineers and costed for the experiment. It ensures a light-tight
 8802 environment, provides cooling as necessary, includes patch panels for cable runs and has a
 8803 front-end that will mate to the calibration interface plate described above. The housing has
 8804 serviceable doors that will allow easy access to the crystals and readout devices. Figure 18.15
 8805 shows three engineering drawings of the proposed system. Modifications will be made once
 8806 the decision on the signal and bias cabling is finalized. The front panel of the light-tight
 8807 housing holds the calibration plate. Figure 18.16 shows our current design in perspective.
 8808 This system will couple to the rest of the enclosure in a manner that allows easy removal for
 servicing.

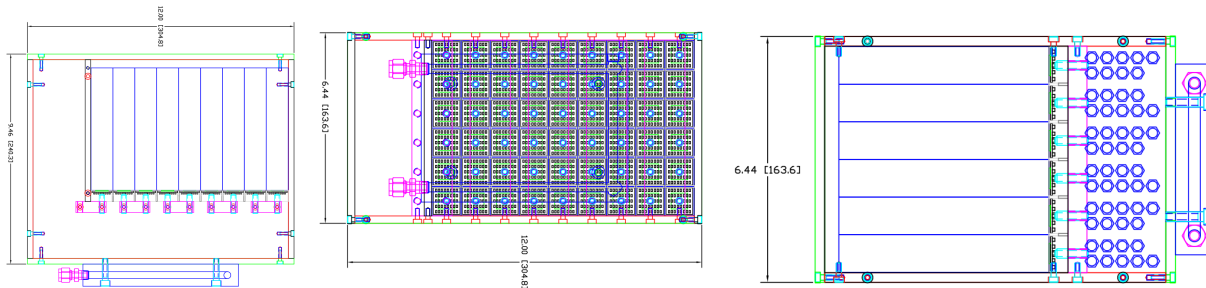


Figure 18.15: Proposed calorimeter light-tight housing. Left: Top view of 9 crystal columns. The storage ring is on the right. The extra space on the left side is used for panels, cooling, servicing. The rear part of the box includes a cooling channel. The front accommodates the calibration plate (not shown here). Middle: Side view of 6 rows of crystals. The conceptual plan for the signal feedthroughs is indicated. Right: Rear view showing the 54 SiPM pre-amplifier / amplifier summing boards.

8809

8810 18.4 Alternative Design Considerations

8811 Two alternative calorimeter material options and one alternative readout option were tested
 8812 using the Fermilab test beam facility. These included a home-built tungsten-scintillating
 8813 fiber sampling calorimeter, which is dense ($X_0 = 0.7$ cm), and has a fast-scintillator signal
 8814 response [2]. Unfortunately, it did not exhibit acceptable resolution in the as-built W:SciFi
 8815 50:50 ratio and necessary modifications would reduce the density. Next we tested a custom
 8816 undoped lead tungstate (PbWO_4) crystal. The idea was to reap the benefits of the higher
 8817 light yield of PbWO_4 , but to avoid the slow scintillator light component that is prohibitively

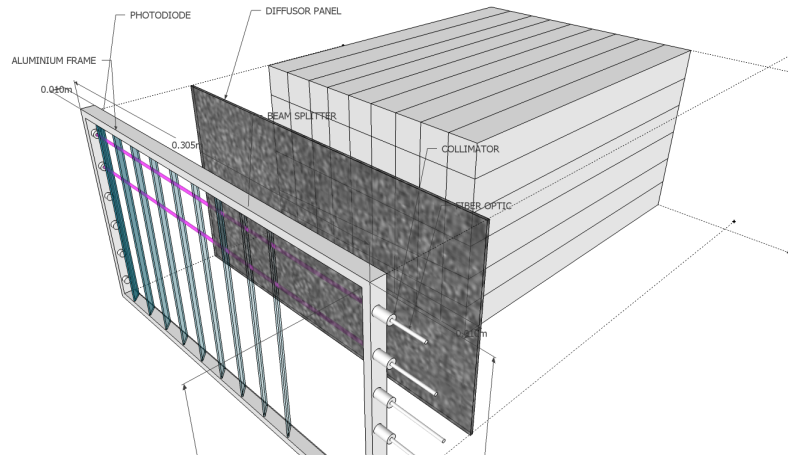


Figure 18.16: Proposed front calibration plate. Six optical fibers penetrate from the inner radial direction. The light is split using a series of beam splitter plates. A diffusor panel spreads the light across the crystal front faces. This system is being prototyped and is a possible alternative.

8818 long for our application. Although its resolution was excellent, the intrinsic pulse FWHM
 8819 of 15 ns greatly exceeds the 4 ns width measured for PbF_2 . There were no benefits of this
 8820 crystal from cost or other perspectives. A comparison of the pulse shapes from W/SciFi and
 8821 PbWO_4 to our default design of PbF_2 is shown in the right panel of Fig. 18.5.

8822 We also evaluated fast photomultiplier tubes as alternatives to SiPMs. The Hamamatsu
 8823 9800 is an excellent PMT, having a fairly compact footprint and intrinsic fast response. We
 8824 are using it regularly to benchmark the intrinsic light output time distribution from our
 8825 crystals. Unfortunately, it is not a good choice for full implementation in the experiment
 8826 owing to the need to place these PMTs at least 1.5 m from the calorimeter arrays. Because
 8827 of the rear-face readout from the geometry, the guides would require a rapid 90-degree bend
 8828 toward the radial direction and then a second bend to put the PMTs out of plane. The
 8829 high cost of the PMTs (about 5 times higher than the SiPMs) and the awkward lightguide
 8830 constraint were deemed to be major issues compared to the development of SiPMs that can
 8831 be located onboard the crystals.

8832 We are also actively evaluating SiPMs made by different companies, including the latest
 8833 blue sensitive SiPMs from SensL, STMicroelectronics and other vendors. Hamamatsu has
 8834 also announced new devices with attractive features such as silicon vias and lower quench
 8835 resistance. One option to increase the fractional readout area on the rear face of the crystals
 8836 (presently $144 \text{ mm}^2 / 625 \text{ mm}^2$ for the 16-ch MPPC) is to use larger area arrays of tileable
 8837 SMT packaged SiPMs on custom-designed PCBs. For example, an ideal 5×5 array of 3 mm^2
 8838 can be made using devices, which are competitively priced, from STMicroelectronics. Larger
 8839 area coverage would allow the use of smaller, thus faster pixels, while maintaining sufficient
 8840 overall photon detection efficiency. We are exploring these options prior to freezing the final
 8841 design.

8842 **18.5 ES&H**

8843 The 1300 SiPMs all receive a low-current ~ 70 V bias voltage, which is delivered to the
8844 enclosed housing through coax cables from a custom-built bias control system. A laser
8845 system will be used to distribute calibration pulses. Apart from the laser hut, the light will
8846 be entirely contained in optical fibers, with no possibility of escaping under normal use. The
8847 laser hut will be upstairs in the main MC-1 building and appropriate safety requirements
8848 will have to be developed to isolate the room and limit access to trained experts. The
8849 mechanical weight of the calorimeters is only 40 kg each and they will be supported on
8850 railed housings. There is no vacuum insertion, but these detectors will be placed near the
8851 storage ring magnetic field and, as such, care must be taken when servicing them to ensure
8852 that no magnetic tools are used (a general requirement for any access to the storage ring
8853 area).

8854 **18.6 Risks**

8855 **18.6.1 Performance Risks**

8856 If the gain stability of the system in actual use fails to meet the specifications, other analysis
8857 techniques will have to substitute. This situation happened in E821, where the laser system
8858 did not meet the performance goals. Instead, E821 was able to determine the stability of
8859 the gain from the data itself. It is not ideal, but did mitigate the risk.

8860 **18.6.2 Schedule Risks**

8861 An NSF Major Research Instrumentation proposal was submitted in February, 2013. This
8862 proposal would fund the costs of the detector, electronics and data acquisition systems. A
8863 substantial matching component was arranged from the domestic and international universi-
8864 ties involved. Separately, the Italian groups await approval from INFN for their production
8865 of the calibration subsystem. If either of these proposal fail, a greater burden on the Project
8866 budget will follow, with possible delays in the schedule.

8867 The production of large numbers of crystals and the procurement of SiPMs and the
8868 design and assembly of the bias control system all could encounter vendor or design delays.
8869 We do not anticipate this, given the quoted 18-month production time for the longest lead-
8870 time item (crystals), but any delay in funding, coupled with a slower production rate could
8871 impact the schedule. The demanding performance parameters applied to the bias control
8872 and laser gain monitoring system could require revision cycles that impact the schedule. We
8873 are mitigating the risk with an aggressive R&D program schedule that will accommodate
8874 several design iterations.

8875 **18.7 Quality Assurance**

8876 Our local Shanghai University collaborators will inspect the crystals at the factory before
8877 acceptance of the products. The crystals will then be shipped to the University of Washington

8878 where a sample of them will be tested for transmission efficiency. The crystals will then be
8879 wrapped. The SiPM boards will be built and then tested using a custom light scanner that
8880 can calibrate each device. Finally, the individual crystal-SiPM packages will be assembled
8881 into an array and tested with a calibrated laser front panel plate. We have a SiPM test
8882 laboratory at UW to evaluate the production SiPM boards and will prepare a program using
8883 undergraduate students to evaluate each piece in the assembly line.

8884 **18.8 Value Management**

8885 Competitive quotes have been obtained in order to prepare the MRI Proposal. Local fab-
8886 rication at universities with largely overhead-free labor will keep costs in check. We are
8887 continuing an aggressive program of SiPM vendor evaluations and board designs to obtain
8888 a higher fractional readout coverage at competitive cost.

8889 **18.9 R&D**

8890 We have used test beam opportunities repeatedly as necessary. We intend to use the new
8891 SLAC electron test beam to make final measurement of the light yield of crystals with two
8892 wrappings and the final SiPM device. In 2013, the Detector Team intends to build a 25-
8893 element array (5 x 5) and take it to the test beam for a full evaluation with all systems
8894 operational, including prototype digitizers and data acquisition.

8895 We continue to use our local laboratory tools to evaluate SiPM performance and have
8896 several student projects ongoing to map out gain functions and other performance charac-
8897 teristics.

8898 **References**

- 8899 [1] Sedykh SA, et al. *Nucl. Instrum. Meth. A* **445**:346 (2000).
- 8900 [2] R. McNabb, *et al.*, *Nucl. Instrum. Meth. A* **602**, 396 (2009) [arXiv:0910.0818
8901 [physics.ins-det]].
- 8902 [3] P. Achenbach, *et al.*, *Nucl. Instrum. Meth. A* **465**, 318 (2001).
- 8903 [4] V. Tishchenko *et al.* [MuLan Collaboration], *Phys. Rev. D* **87**, 052003 (2013)
8904 arXiv:1211.0960 [hep-ex].

Chapter 19

Tracking Detectors

19.1 Physics Goals

The primary physics goal of the tracking detectors is to measure the muon beam profile at multiple locations around the ring as a function of time throughout the muon fill. This information will be used to determine several parameters associated with the dynamics of the stored muon beam [1]. This is required for the following reasons:

- Momentum spread and betatron motion of the beam lead to ppm level corrections to the muon precession frequency associated with the fraction of muons that differ from the magic momentum and the fraction of time muons are not perpendicular to the storage ring field.
- Betatron motion of the beam causes acceptance changes in the calorimeters that must

Uncertainty	E821 value (ppm)	E989 goal (ppm)	Role of tracking
Magnetic field seen by muons	0.03	0.01	Measure beam profile on a fill by fill basis ensuring proper muon beam alignment
Beam dynamics corrections	0.05	0.03	Measure beam oscillation parameters as a function of time in the fill
Pileup correction	0.08	0.04	Isolate time windows with more than one positron hitting the calorimeter to verify calorimeter based pileup correction
Calorimeter gain stability	0.12	0.02	Measure positron momentum with better resolution than the calorimeter to verify calorimeter based gain measurement

Table 19.1: Systematic uncertainty goals for the Muon g-2 experiment. Information from the tracking detectors will be used to constrain these in several ways as indicated in the final column. For the first two rows, the tracker plays a primary role. For the last two, the tracker plays a supporting role.

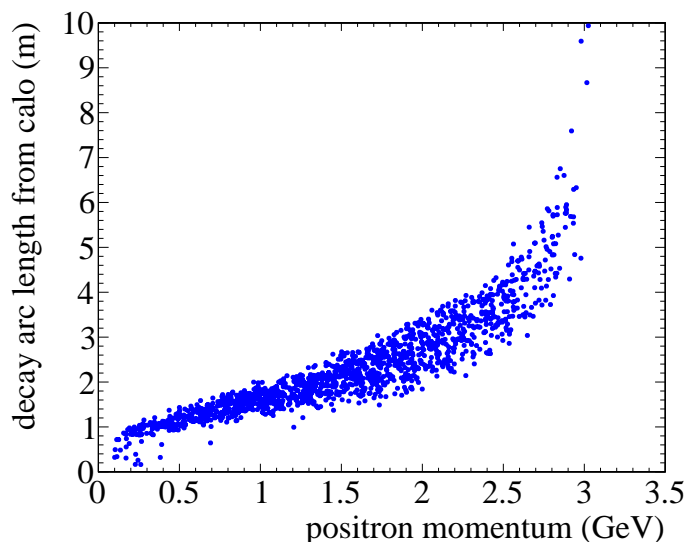


Figure 19.1: Arc length between the calorimeter and the muon decay point as a function of positron momentum.

8917 be included in the fitting functions used to extract the precession frequency.

- 8918 • The muon spatial distribution must be convoluted with the measured magnetic field
- 8919 map in the storage region to determine the effective field seen by the muon beam.

8920 The tracking detectors also play an important role in understanding systematic uncer-
 8921 tainties associated with the muon precession frequency measurement derived from calorime-
 8922 ter data. In particular, the tracking system will isolate time windows that have multiple
 8923 positrons hitting the calorimeter within a short time period and will provide an independent
 8924 measurement of the momentum of the incident particle. This will allow an independent val-
 8925 idation of techniques used to determine systematic uncertainties associated with calorimeter
 8926 pileup, calorimeter gain, and muon loss based solely on calorimeter data. The goals for
 8927 the systematic uncertainties that can be directly determined or partially constrained using
 8928 tracking information are listed in Table 19.1.

8929 The tracking detectors will also play a leading role in the search for a permanent electric
 8930 dipole moment (EDM) of the muon. A muon EDM causes the precession plane to tilt out
 8931 of the horizontal plane. This leads to a time dependent asymmetry in the positron vertical
 8932 angle with respect to the beam axis that can best be measured using a tracking detector [2].

8933 19.2 Requirements

8934 Requirements for the tracking detectors have been documented elsewhere [3] and are sum-
 8935 marized here. The DC nature of the muon beam requires that the tracker perform well over
 8936 a large momentum range and for muon decay positions up to 10 meters in front of the first

8937 tracking plane. The arc length between the calorimeter and the muon decay point as a func-
 8938 tion of positron momentum is shown in Fig. 19.1. The tracker must measure the vertical and
 8939 radial profile of the muon beam to much better than a centimeter, leading to requirements
 8940 of below 100 μm resolution per position measurement. The long extrapolation from the
 8941 tracking detector to the muon decay point requires that multiple scattering be minimized
 8942 and that the material associated with each tracking plane be below 0.5% radiation length.

8943 The trackers are required to reside in vacuum chambers in a vacuum of approximately
 8944 10^{-6} Torr and have either a vacuum load on the system below 5×10^{-5} Torr l/s or include
 8945 a local increase in pumping speed near the tracker. The readout electronics must also be
 8946 in the vacuum chamber to minimize the need for excessive feedthroughs. The tracker must
 8947 be located as close to the stored muon beam as possible without interfering with the NMR
 8948 trolley.

8949 Any perturbations to the magnetic field due to material or DC currents must be below
 8950 10 ppm at the center of the storage region over an azimuthal extent of greater than 2° .
 8951 Any perturbations due to transient currents on time scales below 1 ms must be below 0.01
 8952 ppm since these cannot be detected or monitored with NMR [4]. The requirements are
 8953 summarized in Table 19.2.

8954 19.3 Recommended Design

8955 The recommended design is an array of straw tubes with alternating planes oriented 7.5°
 8956 from the vertical direction. We refer to the plane with negative slope as the U plane and
 8957 the plane with the positive slope as the V plane with respect to the radial-vertical plane.
 8958 The DC nature of the beam requires a tracker with multiple planes spread out over as long
 8959 a lever arm as possible. The required number of planes, along with the need to minimize

Parameter	value	comments
Impact parameter resolution	$\ll 1$ cm	Set by RMS of the beam
Vertical angular resolution	$\ll 10$ mrad	Set by angular spread in the beam
Momentum resolution	$\ll 3.5\%$ at 1 GeV	Set by calorimeter resolution
Vacuum load	5×10^{-5} Torr l/s	assumes 10^{-6} Torr vacuum and E821 pumping speed
Instantaneous rate	10 kHz/cm ²	Extrapolated from E821
Ideal coverage	16×20 cm	Front face of calorimeter
Number of stations	≥ 2	Required to constrain beam parameters
Time independent field perturbation	< 10 ppm	Extrapolation from E821
Transient (< 1 ms) field perturbation	< 0.01 ppm	Invisible to NMR

Table 19.2: Summary of the major requirements and environmental considerations for the tracking detectors.

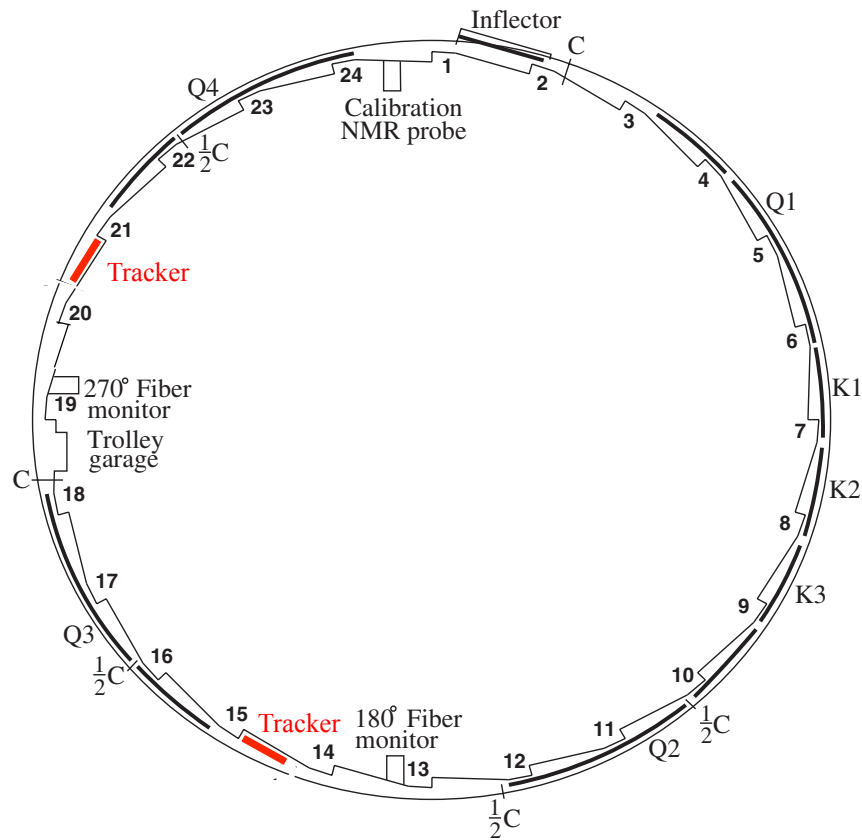


Figure 19.2: Placement of the tracking detectors in the muon storage ring. The detectors can be seen in front of calorimeter stations 15 and 21.

8960 multiple scattering lead to the choice of a gas based detector. The requirement to place the
 8961 detectors in the vacuum leads to the choice of straws since the circular geometry can hold
 8962 the differential pressure with minimal wall thickness.

Type	Straws	Stations	Spares	Total
Type-24	96	6	2	768
Type-16	64	5	2	448
Total per calorimeter				1216
Total for 2 calorimeters				2432

Table 19.3: Total number of straws in the stacking system. The first two rows are the numbers per calorimeter station.

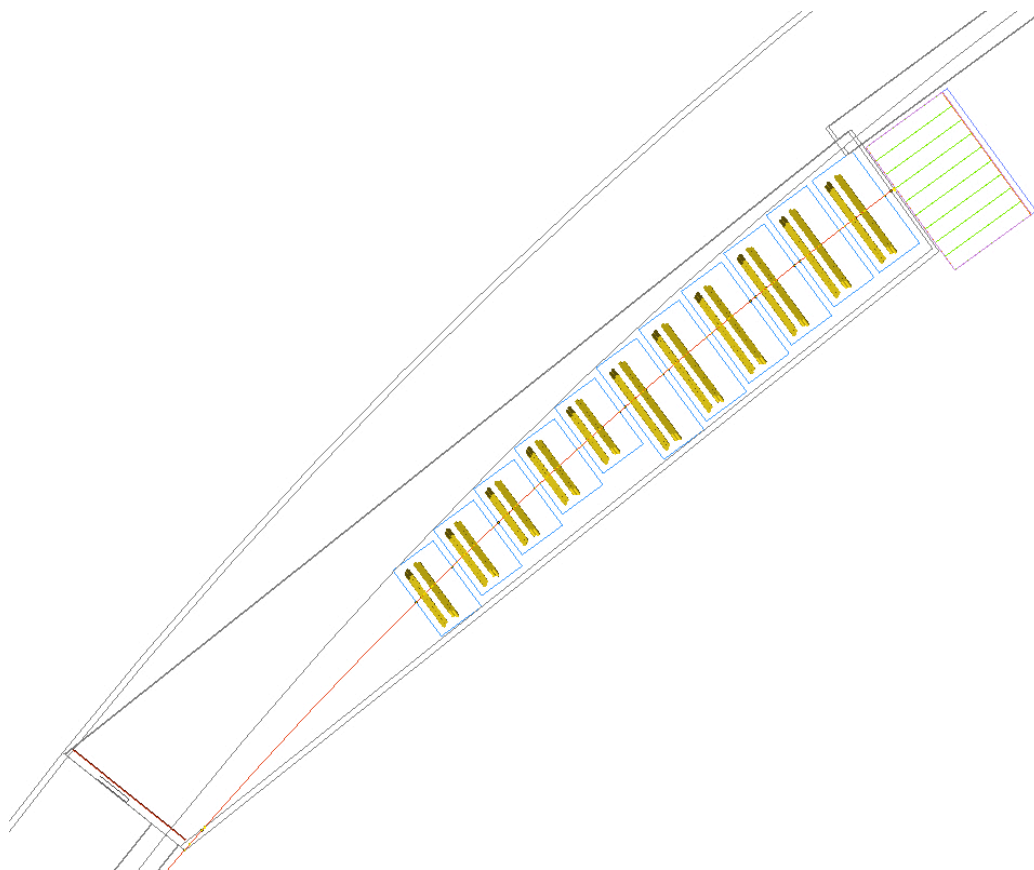


Figure 19.3: Placement of the straw tracking stations in the scallop region of the vacuum chamber. The side line is the a lost muon with momentum slightly below the beam energy of 3.1 GeV.

8963 19.3.1 Mechanical Design

8964 The design is to have two tracking detectors placed at approximately 180 and 270 degrees
 8965 from the injection point as shown in Fig. 19.2. These locations have a clear line of sight to
 8966 the muon beam. The vacuum chambers in these locations will be modified to contain large

Straw material	Aluminized Mylar
Straw wall thickness	15 μm
Wire	25 μm gold-plated tungsten
Straw length	12 cm
Stereo angle	$\pm 7.5^\circ$ from vertical
Gas	80:20 Argon:CO ₂
Pressure	1 Atm
Operating voltage	1400 V

Table 19.4: Summary of the properties of the tracking detectors.

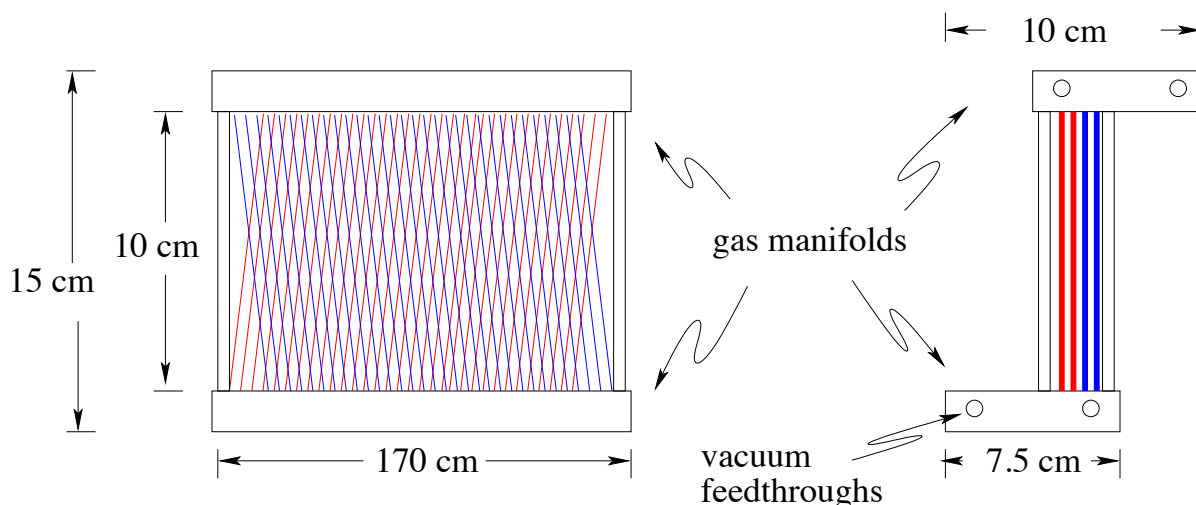


Figure 19.4: Diagram of the largest tracking station. The station is 24 straws wide. The figure on the left is the vertical-radial view. The figure on the right is the vertical azimuthal view.

8967 flanges that allow for installation and servicing of the tracking detectors.

8968 Each tracking detector consists of 11 tracking stations as shown in Fig. 19.3. Each
 8969 tracking station station has two planes of straws. The planes are in a UV configuration
 8970 oriented $\pm 7.5^\circ$ from the vertical direction. Each plane consists of a close-pack doublet of
 8971 straws.

8972 There are two types of station to account for the decreasing width in the scalloped region
 8973 of the vacuum chamber. The first station is 12 cm wide and contains 64 channels and is
 8974 referred to as a type-16 station (16 straw wide doublet x 2 views). The second type is 17 cm
 8975 wide and contains 96 channels and is referred to as a type-24 station (24 straw wide doublet
 8976 x 2 views). The total channel count including prototypes and spares is listed in Table 19.3.

8977 A diagram of the largest station is shown in Fig. 19.4. The active height of each station is

Material	Thickness	radiation Length (cm)	X/X_0 (%)
Gold	200 Å	0.3	6×10^{-4}
Aluminum	500+500 Å	8.9	1×10^{-4}
Adhesive	3 μm	17.6	2×10^{-3}
Mylar	6 + 6 μm	38.4	3×10^{-3}
Ar:CO ₂	5 cm	1×10^5	4×10^{-2}
Total per straw			0.05
Total per station			0.11
Tungsten	25 μm	0.35	0.7
Total after hitting 1 wire			0.82

Table 19.5: material budget in the active region of a station.

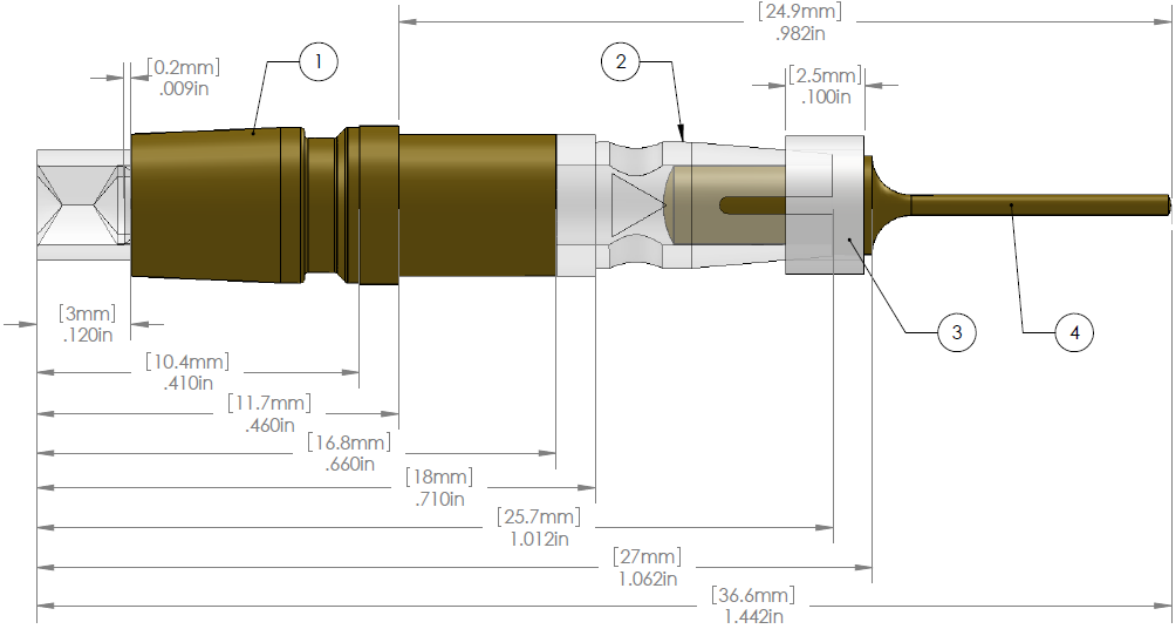


Figure 19.5: Straw terminations.

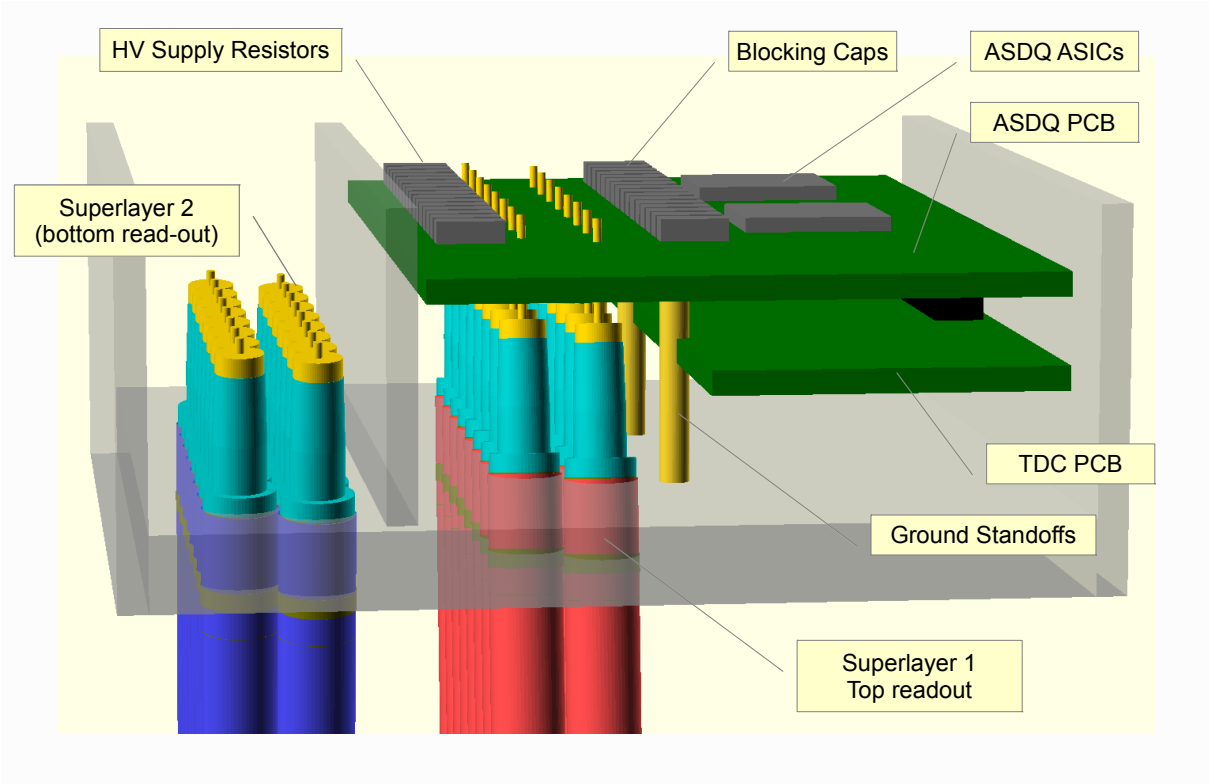


Figure 19.6: Gas manifold and electronics housing for the straws.

8978 10 cm. A 2.5 cm high gas manifold sits above and below the straws and houses the readout
8979 electronics. The stations are self supporting and sit on the bottom of the vacuum chamber
8980 on a thin aluminum plate that locks the stations in place controlling the station alignment.

8981 We have chosen a system based on Mu2e straws [5]. Each straw has a 5 mm diameter and
8982 is 12 cm long. The straw wall is made of two layers of 6 μm Mylar, spiral wound, with a 3 μm
8983 layer of adhesive between layers. The total thickness of the straw wall is 15 μm . The inner
8984 surface has 500 \AA of aluminum overlaid with 200 \AA of gold as the cathode layer. The outer
8985 surface has 500 \AA of aluminum to act as additional electrostatic shielding and improves
8986 the leak rate. The straws are attached to the manifolds at the ends and tensioned to 50
8987 grams to compensate for expansion under vacuum. The straw parameters are summarized
8988 in Table 19.4. The material budget in the active region of each station is given in Table 19.5.

8989 The sense wire is 25 μm gold-plated tungsten centered on the straw. The wire is tensioned
8990 to 10 grams and held in place by a pin and compression fitting in the end assembly of the
8991 straw, labeled as 3 and 4 in Fig. 19.5.

8992 The wire will be held at a voltage of 1400 V. The drift gas is 80:20 Argon:CO₂. The
8993 requirement of the best position resolution and the relatively low rates per straw allow us to
8994 not require a fast, flammable gas.

8995 The straw terminations, shown in Fig. 19.5, are an iteration of the terminations success-
8996 fully deployed by the Brookhaven E781 experiment [6] and consist of an aluminum collar with
8997 an injection molded ULTEM thermoplastic insulator. The insulator contains a V groove to
8998 position the wire and an aluminum pin crimps the wire in place and holds the wire tension.

8999 The straw is attached to the collar with a bead of silver epoxy to provide the electrical
9000 connection and a bead of standard epoxy to provide mechanical strength. A similar blend
9001 is used to connect the straw terminations to the manifolds.

9002 The gas manifolds for the straws are shown in Fig. 19.6. They are approximately 2.5
9003 cm high and contains separate gas paths for the U and V straws. The gas is brought into
9004 the manifold through a vacuum penetration through the flange on the vacuum chamber wall
9005 and the manifold. The gas flows through the straws and then over the readout electronics.
9006 The gas is required to dissipate approximately 5 Watts from the readout electronics. The
9007 gas then flows out a wide 5/8" (1.6 cm) tube that also carries 2 twisted pair cables that
9008 carry low voltage, high voltage and control signals to the readout electronics and carry the
9009 digitized signals out of the straws as described in more detail in the next section.

9010 19.3.2 Readout Electronics

9011 The basic instrumentation parameters which drive the design of the readout are given in
9012 Table 19.6. The readout electronics for a stereo layer pair consists of two stacked PC boards,
9013 a readout board and a TDC board. The readout board contains two or more ASDQ ASICs[7]
9014 which provide amplification, shaping, a discriminator and charge measurement for eight
9015 straws. The ASDQ outputs are digitized by a TDC implemented in a field-programmable
9016 gate array (FPGA).

9017 The tracker wire connection diagram is shown in Figure 19.8. The HV terminal provides
9018 high voltage (1400V nom.) to each tube through a 100k Ω current limiting resistor. HV
9019 is blocked by a 2kV SMT capacitor (value *t.b.d.*). A protection circuit consisting of four

Channels per readout board	32 or 48
Gas gain	4×10^4
Number of primary electrons (pe) for a typical track	41 pe
Signal amplitude for a typical track	256 fC
Operating threshold in pe	10 pe
Operating threshold	32 fC
Capacitance	1 pF

Table 19.6: Tracker Readout parameters

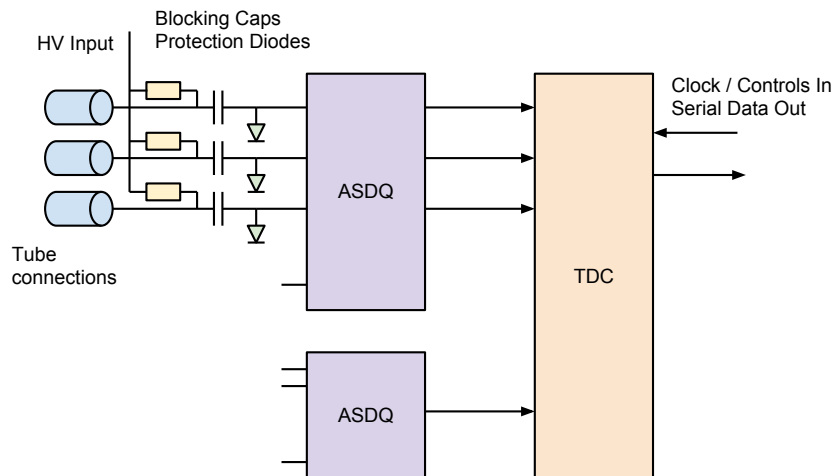


Figure 19.7: On-chamber electronics overview.

9020 Schottky diodes in a 2x2 mm DFN package provides bipolar protection for both the primary
 9021 and inverting ASDQ inputs. A 10 Ω series resistor limits peak current.

9022 The ASDQ provides eight channels of full analog signal processing between the chamber
 9023 and the TDC. Though developed for the CDF Central Outer Tracker, it provides a good
 9024 match to the Muon $g - 2$ tracking detector requirements. It provides fast charge collec-
 9025 tion (≈ 7 ns), good double pulse resolution of ≈ 30 ns, low power (≈ 40 mW/ch) and low
 9026 operational threshold (≈ 2 fC). Baseline restoration and ion tail compensation using the
 9027 pole-zero cancellation technique are provided. The output of each ASDQ is eight digital
 9028 differential signals, with leading edge representing the threshold crossing time and the pulse
 9029 width proportional to input charge.

9030 A 16-channel TDC with 625 ps LSB is implemented in an Altera EP3C5F256C6 FPGA,
 9031 with the initial design using about 50% of the FPGA logic resources. A reference clock
 9032 of 10 MHz is provided externally on an LVDS signal pair with multiplexed trigger and
 9033 control signals. The clock is multiplied internally to a four-phase 400 MHz clock for time
 9034 measurement and internal operation. Up to 2k TDC hits are stored on-chip and read out
 9035 over a single serial link at 25 MHz.

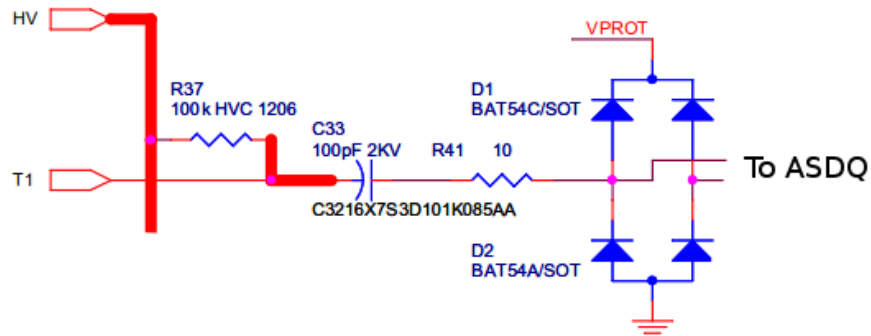


Figure 19.8: The connection of both the high voltage (HV) and the ASDQ chip input for a single straw wire (T1).

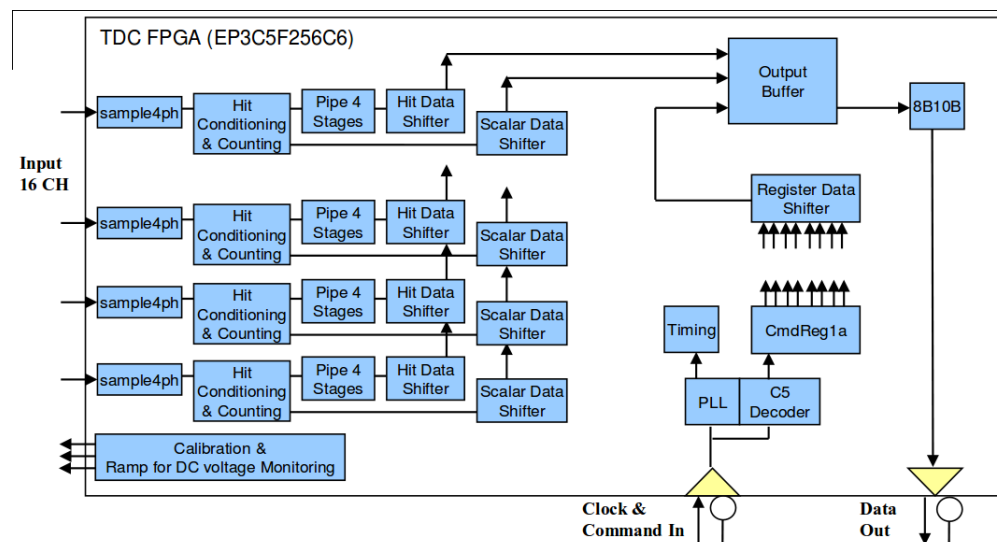


Figure 19.9: TDC block diagram

9036 Power, clock, control and readout for each chamber is provided by a tracker readout
 9037 module (TRM), implemented as an advanced mezzanine card[8] (AMC) and mounted in a
 9038 MicroTCA[9] crate. A block diagram is shown in Figure 19.10. An FPGA in the TRM
 9039 receives clock and control signals from the MicroTCA crate controller via the MicroTCA
 9040 backplane and distributes them to each station. DAQ data is received from the chambers
 9041 and decoded and buffered in the FPGA, which also provides a gigabit Ethernet interface via
 9042 the MicroTCA hub controller. Cables carry DC power from the TRM to the top and bottom
 9043 of each chamber's readout electronics, along with clock, control and readout signals. Power
 9044 for the on-chamber electronics is switched and current-limited on the TRM.

9045 Up to 12 TRM modules are mounted in a MicroTCA crate, as shown in Figure 19.11.
 9046 Control and configuration commands are provided to all modules by a commercial MicroTCA
 9047 hub controller (MCH) module via switched gigabit Ethernet and intelligent platform man-
 9048 agement bus (IPMB)[10] interfaces. A custom AMC13 module[11] developed for the CMS

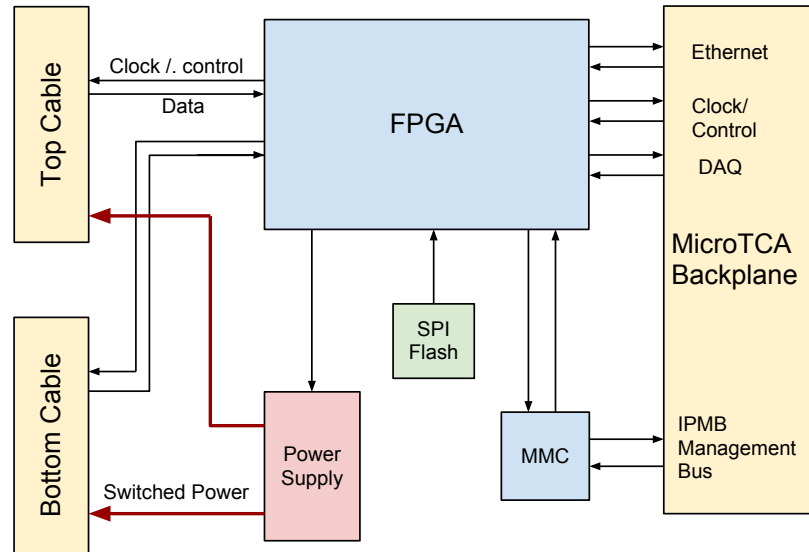


Figure 19.10: Tracker readout module block diagram

9049 experiment distributes clock and timing signals and reads out data from the TRMs.

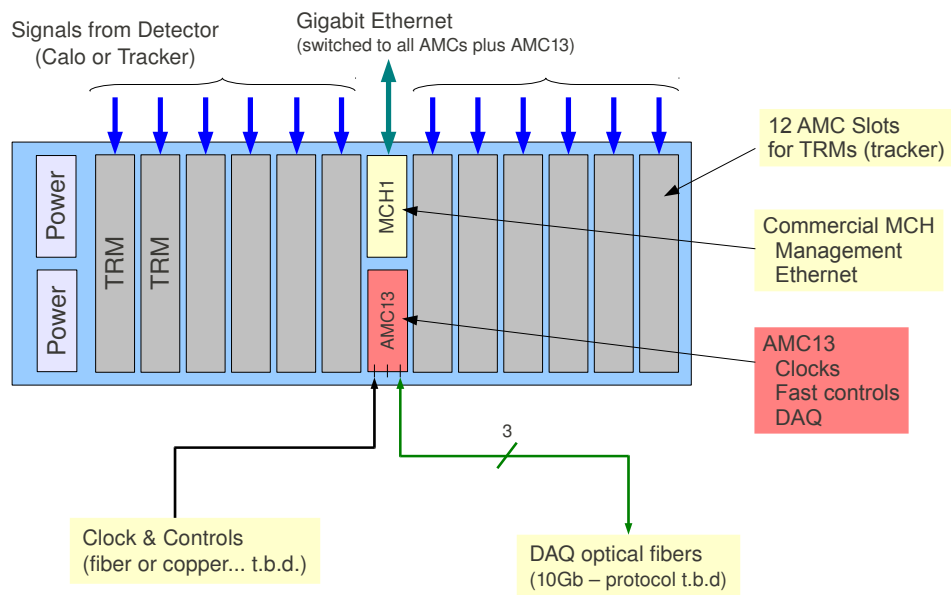


Figure 19.11: MicroTCA crate

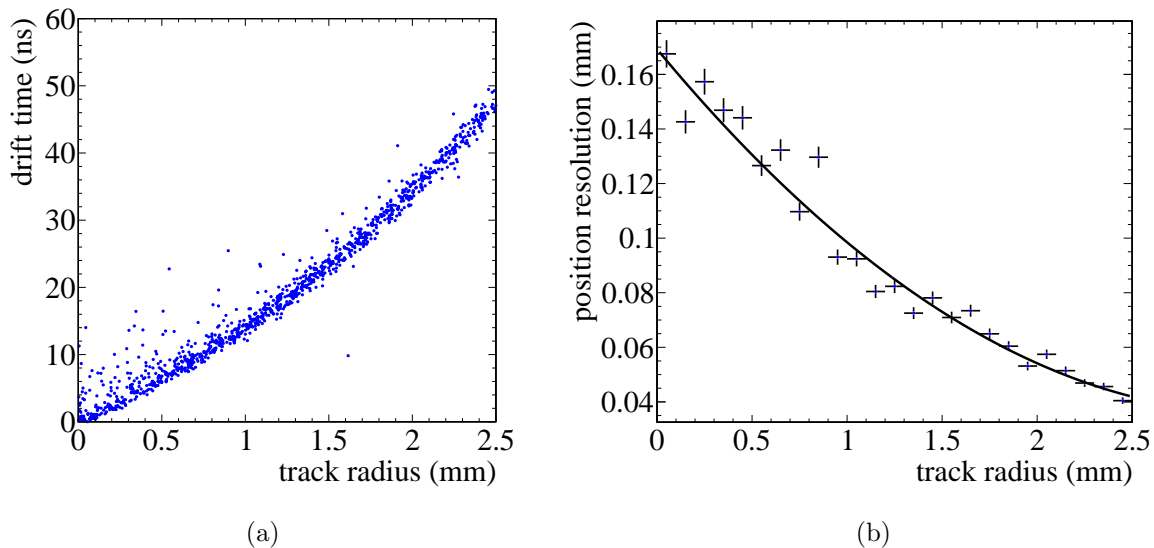
9050 **19.4 Performance**

Figure 19.12: (a): Time versus distance relation in a single straw predicted by GARFIELD. (b): The position resolution determined from GARFIELD for a single straw using the derived $x-t$ relation.

9051 The expected performance of the tracker conceptual design is determined by a simula-
 9052 tion. The performance of a single straw is determined using GARFIELD [12]. This program
 9053 simulates the propagation of electrons and ions in a gas in the presence of electric and mag-
 9054 netic fields. The geometry of the system is determined using a full GEANT4 [13] model of the
 9055 muon storage ring that includes the proper physics model to simulate muon storage, preces-
 9056 sion, and decay. The performance of the tracker is determined using a fast tracking software
 9057 package that takes the positron hit positions from the GEANT4 simulation, applies resolution
 9058 from GARFIELD and multiple scattering corrections, determines the positron trajectory, and
 9059 extrapolates back to the point of tangency to determine the muon decay position. The fast
 9060 simulation currently assumes a uniform magnetic field which is valid for the majority of the
 9061 tracking volume.

9062 The distance versus time ($x-t$) relation and single straw resolution determined from
 9063 GARFIELD are shown in Fig. 19.12. The average resolution is found to be approximately
 9064 $100\ \mu\text{m}$. The acceptance to reconstruct at least 5 hits as a function of momentum and as
 9065 a function of the muon decay distance is shown in Fig. 19.13. There is sufficient coverage
 9066 at all momenta that can be used to determine beam parameters. The loss of acceptance at
 9067 lower momenta is due to the fact that the lowest momentum positrons originate very close
 9068 to the calorimeter and the limited available space between the muon decay position and the
 9069 calorimeter limit the amount of tracker planes the positron can hit. The distance between
 9070 stations is currently dominated by the area necessary for the readout PCBs. In the final
 9071 design iteration we will investigate different geometries that could increase this efficiency.

9072 The momentum resolution, muon decay position, and positron vertical angle resolution
 9073 are shown in Figs. 19.14, 19.15, 19.16, and 19.17. The muon decay position resolution

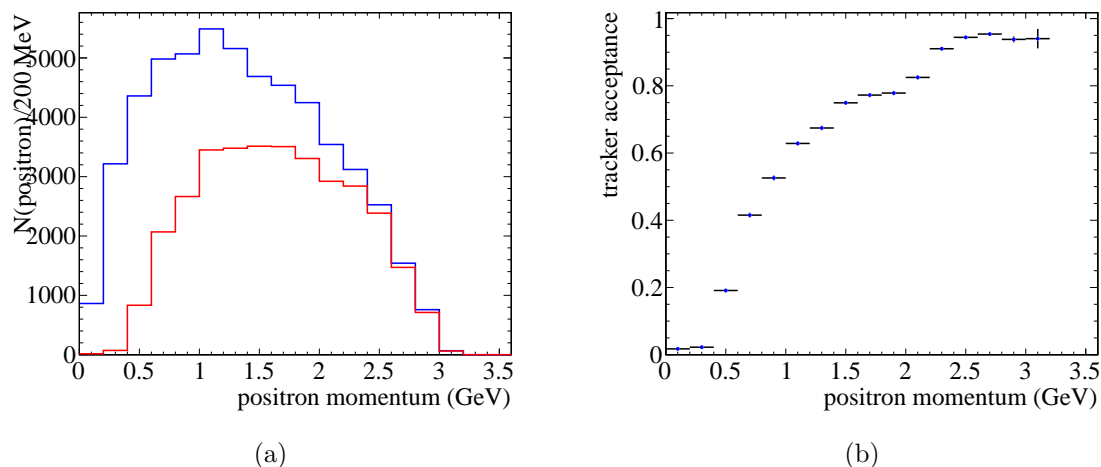


Figure 19.13: (a): The positron momentum spectrum for positrons incident on the front face of the calorimeter (blue) and also with sufficient hits in the tracking detector to form a track (red). (b): The ratio of the two distributions giving the relative efficiency between the tracker and the calorimeter as a function of positron momentum.

9074 is roughly 3 mm in the radial direction and 2 mm in the vertical direction. Both position
 9075 resolutions become significantly worse above 2.6 GeV. In this region, the muons are decaying
 9076 between 5 and 10 meters from the first tracking plane and the large lever arm makes a more
 9077 precise determination impractical. The momentum resolution is worse than for a typical
 9078 gas based system but is well below the resolution of the calorimeter which satisfies the
 9079 requirements. The vertical angle resolution is also well below the requirements.

9080 A single straw prototype has been constructed to verify key features of the GARFIELD
 9081 simulation and to gain experience with the assembly procedure. The straw is read out using
 9082 an ASDQ chip that has an analog output directly before the discriminator. The straw is
 9083 illuminated with an ^{55}Fe source with produces on average 230 primary electrons in our gas
 9084 mixture. The signal peak after amplification and shaping is shown in Fig 19.18. The turn-
 9085 over in the plot is due to clipping in the readout electronics. From this we expect that a
 9086 typical positron depositing 41 primary electrons will correspond to a signal peaking at about
 9087 16 mV at an operating voltage of 1400 V which should be well above the noise level.

9088 The mechanical integrity of the design is modeled using ANSYS. Particular attention was
 9089 given to the grounding plate in the manifold. The plate should be as thin as possible to
 9090 maximize the vertical acceptance of the detectors and the straw spacing should be as close
 9091 to the straw diameter as possible to avoid large gaps. However, the plate must be thick
 9092 enough to hold the straw tension and the 1 atm pressure differential.

9093 The stresses on the manifold are shown in Fig. 19.19. The model indicates that the
 9094 manifold can safely hold the stresses but the current deflection gradient needs to be reduced.
 9095 This will most likely be accomplished in the next design iteration by adding a rib structure
 9096 to the inside of the large manifold.

9097 The front end electronics are based on the ASDQ chip which has been used in several
 9098 experiments and the performance is well documented. A first version of the TDC code exists

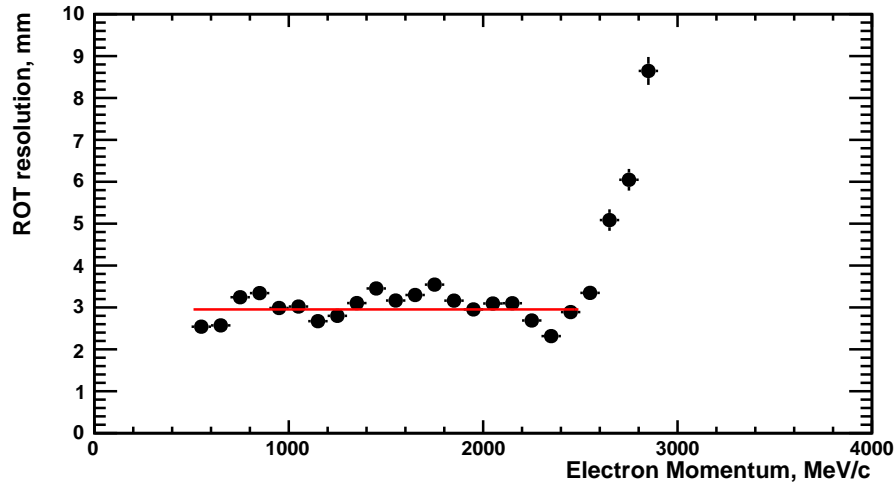


Figure 19.14: Resolution on the radius of the positron at the point of tangency to the central muon orbit as a function of positron momentum. The red line is a fit to the points in the region below 2.5 GeV.

9099 and an LSB of 0.6 ns has been achieved. The specifications for data size and transfer rates
 9100 are well below the limits of the micro-TCA crate specifications.

9101 The design of the tracker is driven by requirements for reducing systematic uncertainties
 9102 on the $g-2$ measurement. However, by measuring the positron vertical angle, the tracker will
 9103 also be able to limit the size of the muon's permanent electric dipole moment. Considering
 9104 only the acceptance of the recommended design and requiring at least three stations are
 9105 hit by the positron, we expect to increase the statistics with respect to the Brookhaven
 9106 EDM search [2] by approximately a factor of 200 per month and a factor of 3500 for the
 9107 full run. This gives us enough statistics to improve the limit on the EDM by an order of
 9108 magnitude very quickly and eventually approach a two order of magnitude improvement
 9109 assuming systematics can be properly constrained.

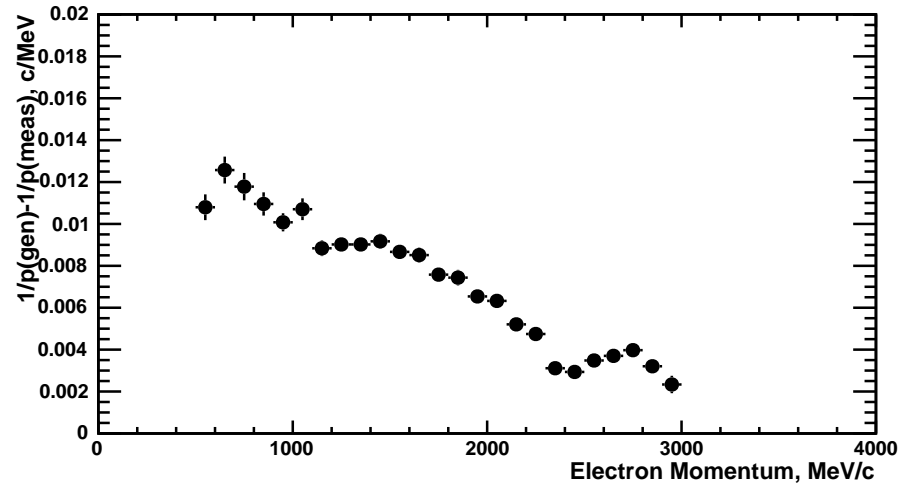


Figure 19.15: Resolution on the radius of the track curvature as a function of positron momentum. The momentum resolution at 1 GeV is 1%.

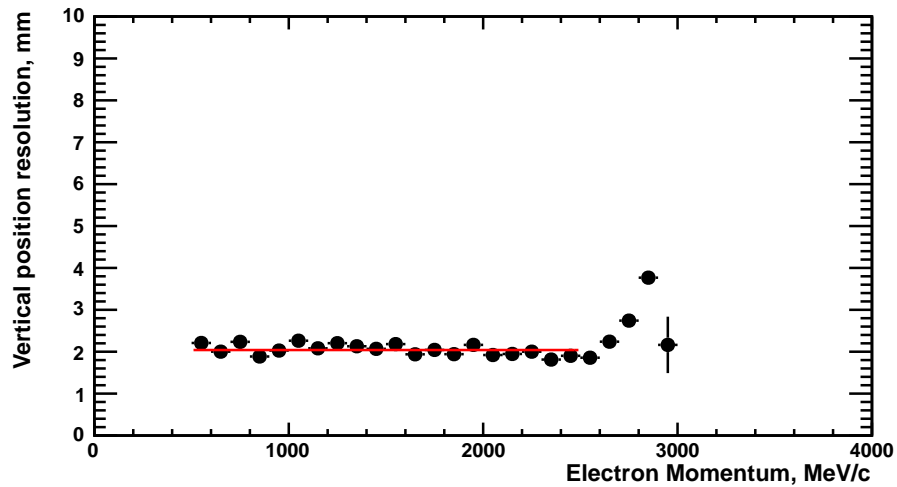


Figure 19.16: Resolution in the vertical muon decay position as a function of positron momentum. The red line is a fit to the distribution below 2.5 GeV.

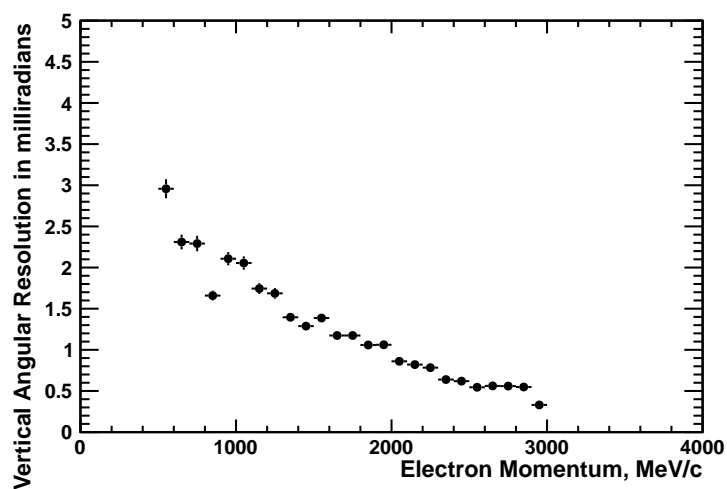


Figure 19.17: Resolution on the vertical positron angle as a function of positron momentum.

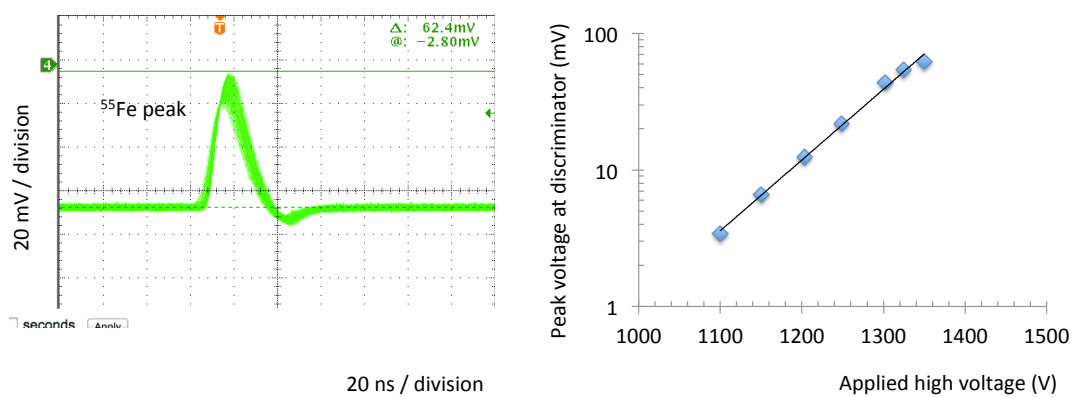


Figure 19.18: (a): The signal from a ^{55}Fe source after amplification and shaping corresponding to 230 primary electrons at an operating voltage of 1400 V. (b) The peak voltage of the ^{55}Fe signal as a function of applied voltage.

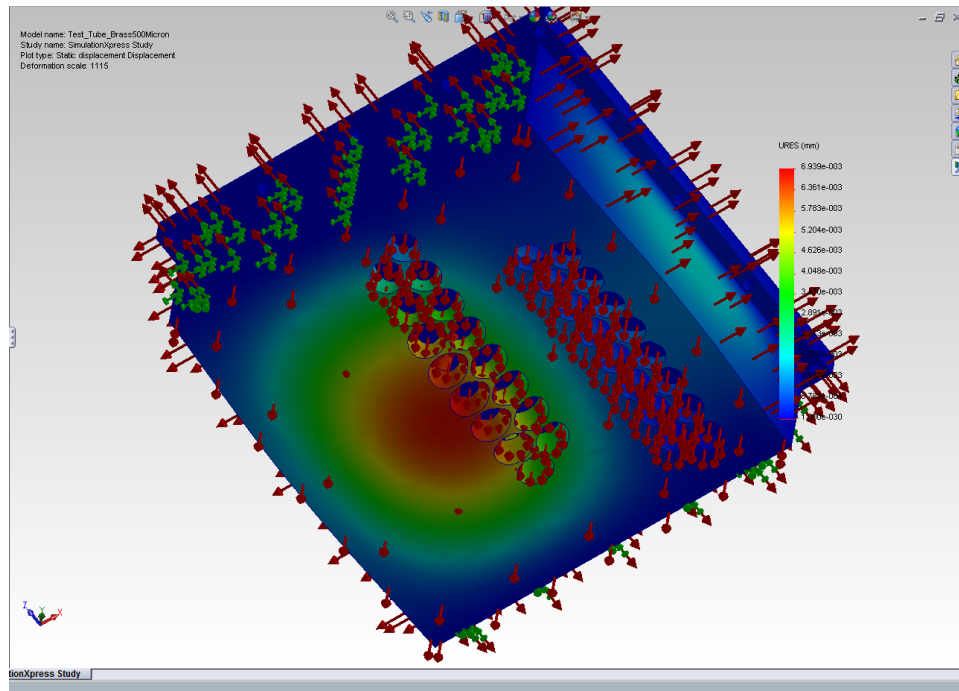


Figure 19.19: ANSYS model of the stresses in the gas manifold due to the straw and wire tension and the 1 ATM differential pressure.

19.5 Alternatives

The down selection of the recommended design has been an evolving process. We are confident that after thornily exploring all the alternatives listed below, we have converged on an optimal solution given the requirements and constraints. There are alternatives, mainly regarding geometry, that will be explored and settled in the preliminary design phase but we expect the main features to stay intact.

The two leading alternatives to a straw based system for the tracker are both silicon based. The first would use 300 μm Hamamatsu single sided strip sensors. These sensors were purchased for the DØ Run IIb detector upgrade [14] but never used. Sufficient sensors are in hand to build the $g - 2$ tracker. The readout would be based on the FSSRII chip [15] originally designed for BTeV and now being used for instrumentation upgrades for the JLab 12 GeV program. Tracking stations could be made with two sensors at a small stereo angle for a total material budget of 0.5% X_0 per station.

The second alternative would use the 50 μm thick Mimosa 26 pixel sensor [16] that has been developed with ILC R&D funding. There is about 25% dead space on the chip which would require a doublet structure to maintain adequate acceptance. Material is also needed in the active region for cooling and for flex cables. A thermal model of the device indicates that heat can be adequately dissipated if the two layers are mounted on blocks of 2.5 mm thick Si foam. After the Si foam and flex cables are added, the material budget is also close to 0.5% X_0 per station.

If we had a well defined interaction point and could build something like a 4 layer detector, either of these two alternatives would be preferable to straws. However, the DC nature of the beam requires us to have a multi layer device to sufficiently cover the momentum spectrum of the positrons. Building this out of the silicon options above would add far too much material and the effects of multiple scattering would severely compromise our ability to extrapolate the positron trajectories all the way back to the muon decay position.

For the amplifier, besides the ASDQ chip, we explored using discrete components or building an ASIC. Discrete components were ruled out due to space considerations and also due to power consumption. An ASIC is an expensive alternative particularly since the ASDQ chips are free, but it has the advantage that we could control all material used in the chip to avoid magnetic components such as tin. However we brought the ASDQ and FPGA chips to a 1.5 T test magnet at the Fermilab Technical division and determined that these chips have magnetic properties well within our specifications.

For the TDC, we considered commercially available products such as the 128 channel CAEN 767 or 1190 model multi hit TDCs. This would require bringing all signals out of the vacuum through some sort of feedthrough system. We investigated the feedthroughs being designed for liquid Argon TPC detectors that have the electronics placed inside the cryostat but these would have difficulty operating at the $g - 2$ vacuum of 10^{-6} Torr. The current design of an FPGA-based TDC is much more simple and cost effective.

For the station geometry, we considered a more close packed system that could be constructed using existing vacuum ports without requiring modifications to the existing vacuum chambers. A working solution was found for a detector that would have a total length of 0.5 meters. However, simulation indicates that the 1 meter lever arm length we have now is required to gain useful information on the higher momentum tracks that have the longest

9154 extrapolation back to the muon decay point.

9155 There are two alternatives still under consideration. The conceptual design calls for a
9156 closed packed doublet geometry with each layer offset by half a straw diameter. Once the
9157 required gap between straws is considered and the fact that the resolution is worst at the
9158 center of the straw, we would like to consider alternative offsets between layers. One option
9159 we will consider is having the two layers offset by one-third a straw diameter.

9160 The tracking simulation studies indicate that we have better resolution on the vertical
9161 parameters of the beam than the radial parameters. In general, the radial parameters have
9162 a greater effect on the $g - 2$ systematic uncertainties since they directly effect the accep-
9163 tance of the calorimeters. The original stereo angle was chosen based on calculations of the
9164 uncertainty on tracking parameters by hand. The full tracking simulation indicates that we
9165 may be able to reduce the stereo angle and improve the vertical resolution without adversely
9166 effecting the horizontal resolution.

9167 19.6 ES&H

9168 The $g - 2$ tracker is similar to other gas-based detectors that are commonly used at Fermilab
9169 and the $g - 2$ tracker is identical in many cases to the Mu2e system. Potential hazards
9170 include power systems and compressed gas. The gas will permeate at a small level inside the
9171 $g - 2$ vacuum and come in contact with the quadrupole high voltage. Any gas leak in the
9172 experimental hall will also bring the gas in contact with the high voltage stand-offs and feed-
9173 throughs of the kicker and quadrupoles. Because of this, and because using non-flammable
9174 gas appears to satisfy the performance requirements, we are precluding the use of flammable
9175 gas. These and all other hazards have been identified and documented in the Muon $g - 2$
9176 Preliminary Hazard Analysis [17].

9177 The detector requires power systems with both low voltages with high currents and high
9178 voltages. During normal operation, the tracker will be inaccessible inside the storage ring.
9179 Power will be distributed to the tracker through shielded cables and connectors that comply
9180 with Fermilab policies. Fermilab will review the installation prior to operation.

9181 Gas that will be used for the tracker will be kept in DOT compliant cylinders in quan-
9182 tities limited to the minimum required for efficient operation. The cylinders will be stored
9183 in a dedicated location appropriate to the type of gas being used. The storage area will be
9184 equipped with fire detection and suppression systems. The installation, including all associ-
9185 ated piping and valves, will be documented and reviewed by the Fermilab Mechanical Safety
9186 Subcommittee.

9187 The detector itself does not have any radioactive sources. However, Fe^{55} sources will be
9188 used to measure the gain of the straws before installation. Usage of radioactive sources will
9189 be reviewed to ensure adherence to Fermilab safety policy. In particular, the sources will be
9190 properly inventoried and stored and we see no opportunity for producing mixed waste.

9191 Solvents such as ethanol will be used to clean components before assembly and epoxy
9192 resins will be used in the assembly process. All chemicals will be clearly labeled and stored
9193 in approved, locked storage cabinets and will adhere to the Fermilab safety policy.

9194 19.7 Risks

9195 19.7.1 Performance Risk

9196 The performance of the system relies on the single straw resolution. Simulation indicates that
9197 the resolution is adequate to meet the goals of the experiment however the final performance
9198 will be a factor of many variables, particularly how well the system is assembled. This risk
9199 is being mitigated by performing cosmic tests of prototypes and a beam test of a full station
9200 prototype in Fall 2013. This will give a very good indication of the single straw resolution
9201 in a real system and will give us sufficient opportunities to make adjustments to the design
9202 before the project is baselined. Several quality control procedures will be put in place such
9203 as x-raying the detectors to determine proper positioning of the wires to ensure that the
9204 resolution is not compromised during assembly.

9205 The detector will require precise alignment with respect to the central muon orbit. Poor
9206 alignment could easily become the dominant source of uncertainty in the tracking measure-
9207 ment. The alignment can be determined in-situ using positrons but this can take a long time
9208 and can not be used to monitor alignment in real time. This risk will be mitigated by taking
9209 complete trackers to a beam test before final installation to determine the relative alignment
9210 between stations. Dedicated muon fills will also be taken on a regular basis where the muon
9211 losses are intentionally increased. These muons are essentially straight when they go through
9212 the tracker and can be used to verify the inter-station alignment as well as determine the
9213 alignment of the system with respect to the beam. We are also investigating adding 3-D
9214 Hall probes inside the gas manifolds for the tracking stations. The precision field is known
9215 well enough so that any change in the Hall probe readout would constitute a change in the
9216 tracking station position.

9217 The tracker has been designed assuming a maximum instantaneous rate of 10 kHz/cm².
9218 This value is extrapolated from measurements at the Brookhaven experiment. The Brookhaven
9219 experiment had significant contamination from pions that led to a large hadronic flash at
9220 the beginning of the fill. This pion contamination has been removed from the Fermilab ex-
9221 periment but there is still a possibility that there will be some unaccounted for background
9222 that leads to unacceptable rates. The straws have been designed to operate with CF₄ so a
9223 faster gas could be used to deal with this. We are also investigating using a circuit to reduce
9224 the gain of the straws during injection. This is complicated and would require electrical
9225 engineering resources to design if we are required implement this.

9226 The system of collimators used to scrape the muon beam after injection is partially in
9227 the line of sight of the tracking detectors. This would limit the acceptance of the tracker and
9228 potentially cause high backgrounds early in the fill. To mitigate this risk, we are performing
9229 studies to determine alternative locations for the collimators and working closely with the
9230 groups associated with the collimator system.

9231 19.7.2 Technical and Operational Risk

9232 The greatest technical risk is that the tracking system will in some way affect the precision
9233 magnetic field of the storage ring. This risk is being mitigated in several ways:

- 9234 • All scientists, engineers, technicians, students, and vendors involved in the design and

9235 construction of the system are educated on the importance of the magnetic properties
9236 of the system.

9237 • The specifications are clearly stated in terms of the static and dynamic effects on the
9238 field. These have been documented and agreed on by the collaboration.

9239 • Individual components are taken to an existing 1.5 T test magnet and their static
9240 magnetic properties are verified to be within specifications.

9241 • Full magnetic simulation of the detector using OPERA [18] will be added to the existing
9242 storage ring OPERA simulation to verify that any static effects can be shimmed out of
9243 the field using the existing shimming kit.

9244 • The full detector will be tested in a test solenoid that is being shipped from LANL to
9245 Fermilab specifically for this purpose.

9246 • A fast coil will be designed to measure the size and time structure of any transient
9247 magnetic fields being produced by the electronics.

9248 The vacuum specifications for the g-2 storage ring are set by the electrostatic quadrupoles
9249 inside the storage ring. The combination of the electric field from the quads and the mag-
9250 netic field from the g-2 magnet leads to regions where photoelectrons can be captured in
9251 Penning traps. These electrons can eventually interact with residual gas molecules, lead-
9252 ing to avalanche and sparking. This is the primary factor influencing the lifetime of the
9253 quadrupole plates.

9254 For μ^+ operation, a vacuum of 10^{-6} Torr is required. If μ^- running is required or if the
9255 quadrupoles are operated at a greater HV to move to a different tune point, the vacuum may
9256 need to be improved to 10^{-7} Torr. The leak rate of the straws has been measured by Mu2e
9257 and indicates that 10^{-6} Torr can be achieved. To mitigate the risk of needing to operate
9258 at a higher vacuum we are designing the ability to add higher capacity to the pumping
9259 speed near the tracking detectors. We are also investigating adding a $25\ \mu\text{m}$ secondary
9260 containment barrier using aluminized Mylar. This would greatly increase the efficiency of
9261 any local pumping but adds material in front of the detector. This will be included in the
9262 full simulation to quantify the effects on the system performance.

9263 Contaminated gas is a serious risk for any drift chamber. This risk is mitigated in several
9264 ways. First, Ar:CO₂ is one of the least prone gasses to harmful contaminants. Second, we
9265 will perform a detailed analysis on each batch of gas before it is incorporated into the system.
9266 Finally, spare chambers in test stands will use the same gas and will be illuminated with
9267 radioactive sources to monitor gain and give early warning of problems.

9268 A broken wire will cause an entire plane of a station to be inoperable. A broken straw will
9269 cause an entire station to be inoperable. To mitigate this risk, the system is being designed
9270 in a way so that a damaged station can be easily removed and replaced with a spare with
9271 approximately 1 day lost to reestablishing the vacuum. We anticipate breaking vacuum at
9272 least once every several months to service the NMR trolley so as long as the frequency of
9273 problems is much less than this, there is no risk to the run schedule.

9274 19.8 Quality Assurance

9275 Proper quality assurance is essential to construct a tracking detector that meets the Muon
9276 $g - 2$ requirements for performance and reliable operation. Quality assurance will be inte-
9277 grated into all phases of the tracker work including design, procurement, fabrication, and
9278 installation.

9279 Individual straws must be leak tight, straight, and be held at the proper wire tension.
9280 The straws will be leak tested before being installed. The straws will be connected to a clean
9281 gas system and over-pressured. The leak rate will be measured over an appropriate time
9282 interval by measuring the pressure drop. After the assembly of a station, the entire station
9283 will be leak tested again.

9284 The straws must maintain their shape and be mounted at the proper stereo angle to op-
9285 erate efficiently and to maintain an appropriate distance between the wire and the grounded
9286 Mylar surface to avoid breakdown. Straws will first be visually inspected for roundness and
9287 straightness before assembly. Flawed straws that escape detection during visual inspection
9288 can be identified by non-uniform gas gain and resolution. This will be done as part of the
9289 wire position measurement.

9290 The appropriate tension must be applied and maintained in a straw for efficient, stable
9291 operation. Tension is applied through calibrated mechanical force but can be lost through
9292 relaxation mechanisms. Both wire and straw tension will be measured after assembly using
9293 vibrational resonance techniques appropriate to our short straws.

9294 All electronics components will be tested prior to installation on the tracking stations
9295 including a suitable burn-in period. The high voltage circuits will be tested for leakage
9296 current. The threshold characteristics of each channel will be tested with a threshold scan.
9297 A noise scan will be performed for various threshold settings to identify channels with large
9298 noise fractions. The FPGA TDCs will be validated by comparing their output to commercial
9299 TDC devices with higher resolution.

9300 19.9 Value Management

9301 The tracker technology for Muon $g - 2$ is well established and has been implemented in
9302 other high energy and nuclear physics experiments. Value management principles have been
9303 applied over time during the development of the technology. Value management moving for-
9304 ward is mainly related to labor costs since the straw tracker assembly will be labor intensive.
9305 We have identified collaborating institutions with students who can perform a large fraction
9306 of the assembly work at minimal cost. This requires more work up front in engineering to
9307 design parts that do not require highly skilled technicians for assembly but this is in any
9308 case part of best practice engineering.

9309 We are subcontracting engineering to university engineering departments and using Fer-
9310 milab engineering resources to perform independent design reviews before production or
9311 procurement. This keeps the overall engineering costs low while maintaing the standards of
9312 Fermilab engineering.

9313 We are also in the process of performing a full analysis of determining the beam paramete-
9314 rs from the tracking system. While the default configuration calls for two tracking stations

9315 around the ring separated by 90 degrees, this study may indicate we need more than two
9316 stations or that the information from one station is sufficient.

9317 The back-end readout electronics and data acquisition for the tracker are equivalent to
9318 those used for the calorimeters. This simplifies the design and operation of the system.
9319 However, once the final specifications are known, we will investigate possible cost savings by
9320 using different system components. Current FPGA technology is sufficient to meet the needs
9321 of the tracker electronics. These will be purchased once they are no longer the most current
9322 devices which should lead to significant cost savings. Sufficient spares will be purchased to
9323 ensure the stock for the lifetime of the experiment.

9324 The straw terminations require injection molded pieces. The cost of these pieces is almost
9325 entirely driven by the cost of the mold and so design iterations are costly. To mitigate this,
9326 we intend to first produce all injection molded pieces with a 3-D printer and construct straws
9327 with the printed pieces to validate the design before the molds are procured.

9328 **19.10 R&D**

9329 Work is well underway on straw termination, tensioning, and alignment procedures. Three,
9330 4 to 8 channel prototypes have been constructed to gain experience with proper handling
9331 and assembly procedures. A full 32 channel (type-8) station is currently under construction
9332 that will include a prototype ASDQ readout board and an FPGA evaluation board. The 3D
9333 model of the prototype is shown in Fig. 19.20. This will be tested in-vacuo using cosmics
9334 and in a beam test scheduled for January 2014.

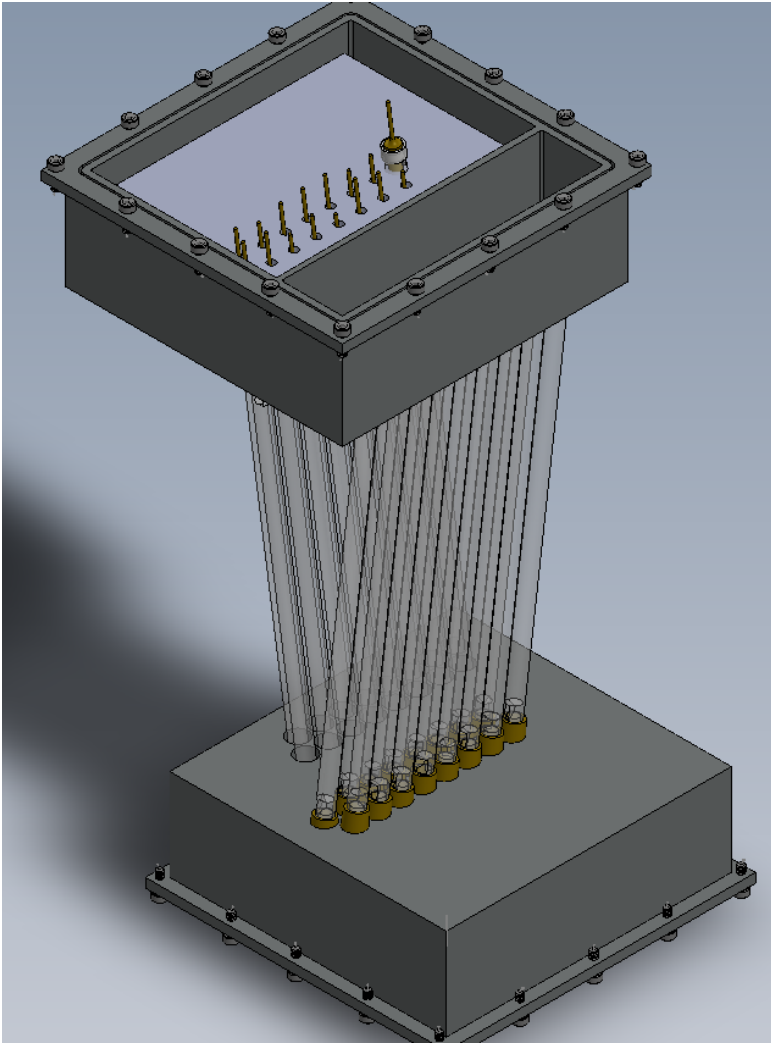


Figure 19.20: 3D model of the 32 channel prototype now under construction.

References

9335

- 9336 [1] G. W. Bennett *et. al.* (Muon $g - 2$ Collaboration) Phys. Rev. D 73, 072003 (2006).
- 9337 [2] G. W. Bennett *et. al.* (Muon $g - 2$ Collaboration) Phys. Rev. D 80, 052008 (2009).
- 9338 [3] B.C.K. Casey, GM2-doc-512-v1.
- 9339 [4] B.C.K. Casey, D. Kawall *et. al.* Field specification in preparation.
- 9340 [5] R.E.Ray, Mu2e-doc-1169-v21
- 9341 [6] S. Graessle *et. al.*, Nucl. Inst. Meth. A 367, 138 (1995).
- 9342 [7] T. Affolder *et. al.*, Nucl. Inst. Meth. A 526, 249 (2004).
- 9343 [8] “AdvancedMCTMMezzanine Module” AMC.0 Rev 2.0, PICMG.
- 9344 [9] “MicroTCA[®]” Rev MTCA.0 Rev 1.0, PICMG.
- 9345 [10] Intelligent Platform Management Interface.
- 9346 [11] Evolving design.
- 9347 [12] The appropriate reference for Garfield.
- 9348 [13] S. Agostinelli *et. al.* Nucl. Inst. Meth. A 506, 250 (2003).
- 9349 [14] D. S. Denisov, S. Soldner-Rembold, Fermilab-Proposal-0925, Fermilab-Design-2001-02,
9350 (2001).
- 9351 [15] R. Yurema *et. al.*, IEEE 52, 799 (2005).
- 9352 [16] R. De Masi *et. al.*, PoS (HEP-EPS 2009), 157 (2009).
- 9353 [17] K. W. Merrit. Hazard analysis document in preparation.
- 9354 [18] OPERA. Cobham Technical Services, Vector Fields Software, 1984-2012.

Chapter 20

Auxiliary detectors

20.1 Fiber beam monitors

20.1.1 Requirements

The fiber beam monitor system is designed to serve three purposes:

- As a commissioning instrument, to determine the position (x, y) and angle (x', y') of the beam at injection,
- To monitor the evolution of these beam properties during the kick and scraping phases, and
- To observe and directly characterize periodic beam motion, notably the modulation of beam centroid position and width by coherent betatron oscillations.

On the other hand, the fiber beam monitor is not suited to a determination of the equilibrium radius of the stored beam. A GEANT4 simulation showed that energy loss in the fibers moves the average radius inward by $\sim 0.1 \text{ mm}/\mu\text{s}$, so the radius will be altered before equilibrium can be established. Even an order of magnitude less energy loss would still be unacceptable for this measurement, so it is not plausible that any system that intercepts the beam would be useful for it.

In order to serve these purposes, the fiber beam monitor system is subject to the following requirements:

- The pulse width and deadtime must be much less than one cyclotron period of 150 ns, by at least one order of magnitude.
- The system must be able to characterize a muon beam whose intensity ranges from 5% to 200% of the expected 7000 muons per fill.
- The spatial resolution of each detector must be sufficient to observe the transition from x' to x and from y' to y over a 90° phase advance.
- The detector must be able to reside in a vacuum of 10^{-6} Torr, with a vacuum load of less than 5×10^{-5} Torr L/s.

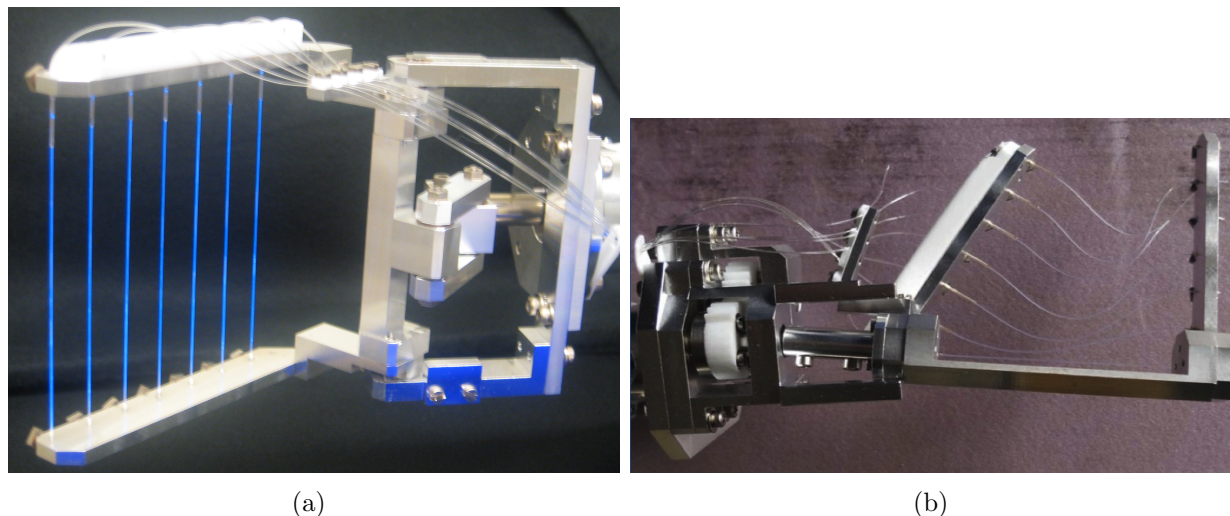


Figure 20.1: (a) The 180° x profile monitor, glowing under ultraviolet illumination in the laboratory. (b) The 270° y profile monitor, which was found to be damaged when it was removed from the Brookhaven E821 storage ring.

- 9382 • The detector must be able to function in a 1.5 T magnetic field.
- 9383 • The detector must perturb the local magnetic field by less than 10 ppm. There must
- 9384 be no transient field perturbations of less than 1 ms duration except during special
- 9385 runs when the detector is activated and inserted.

9386 20.1.2 Recommended Design

9387 The fiber beam monitors were originally built for E821 by a group at KEK that is not part
 9388 of the Fermilab collaboration [2, 3]. We intend to refurbish and reuse all components from
 9389 the existing system that remain suitable.

9390 Each fiber beam monitor holds a “harp” of seven scintillating fibers of 0.5 mm diameter,
 9391 each 90 mm long and separated from its neighbors by 13 mm, as shown in Figure 20.1(a).
 9392 Each scintillating fiber is bonded to a standard optical fiber that connects it to a vacuum
 9393 feedthrough. There are a total of four devices, and they are deployed near the 180° and 270°
 9394 positions in the ring. The 180° fiber beam monitor should observe an image of the beam
 9395 as it was injected at the inflector, while the 270° fiber beam monitor should map x' and y'
 9396 at the inflector into x and y there. At each location, one fiber beam monitor has the fibers
 9397 suspended vertically to measure in x , and the other arranges them horizontally to measure
 9398 in y . The fibers stay inside the beam vacuum, and they can be plunged into the beam path.
 9399 As shown in Figure 20.2, they can be also rotated into a horizontal plane, where all fibers see
 9400 the same beam, for calibration, or upright for measurement. Because ferromagnetic material
 9401 cannot be placed this close to the precision magnetic field, aluminum motors and actuators
 9402 driven by compressed air are used for this motion.

9403 All of the fiber beam monitors have been dismantled from E821, and three of the four
 9404 appear to be in good condition. One fiber beam monitor was found to be damaged, with

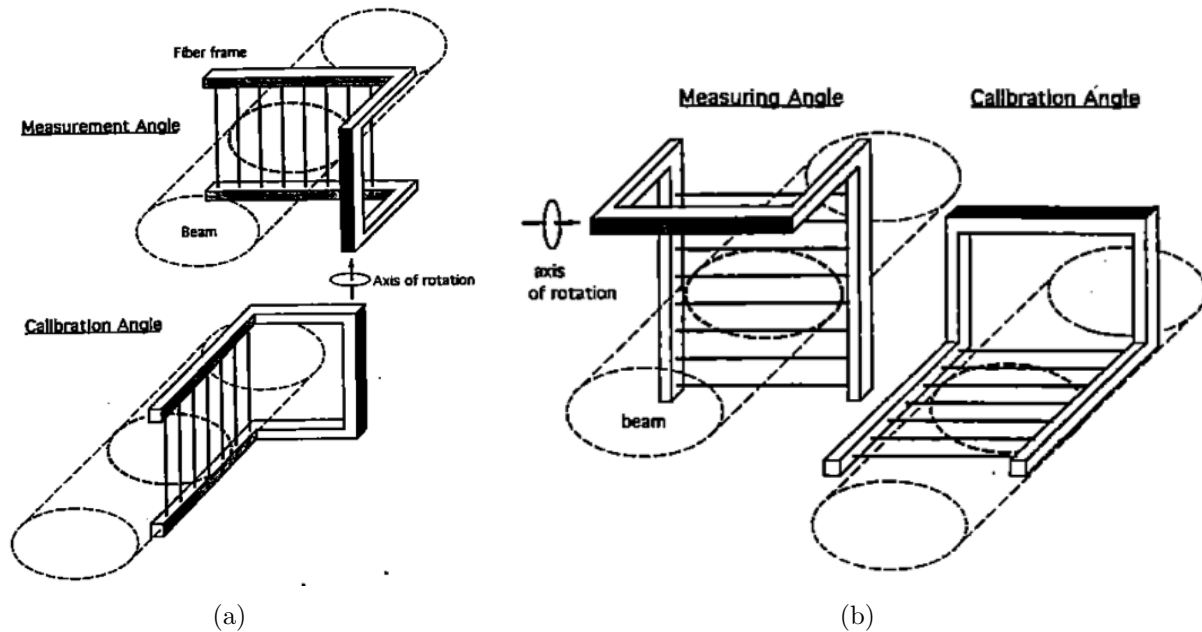


Figure 20.2: Rotational motion corresponding to the calibration and measurement positions for (a) x and (b) y . This figure is reproduced from [3].

9405 a snapped fiber and some bent frame components, as shown in Figure 20.1(b). The unex-
 9406 pectedly high observed muon loss rate in E821 when the fiber harps were inserted suggests
 9407 that this damage may have existed at that time. At a minimum, this frame will need to be
 9408 straightened and realigned, and the broken fiber will need to be re-bonded.

9409 We will clean and lubricate the parts of the system that were outside the vacuum, and
 9410 we will test the compressed-air driven motion control system, making any necessary repairs.
 9411 Similarly, we will test and assure the vacuum integrity of the system.

9412 In E821, the fibers were read out with conventional photomultipliers in a remote location,
 9413 at the end of a long fiber, where the magnetic field was reduced. Replacement by SiPMs
 9414 mounted directly on the fiber harps will allow the long fiber to be eliminated. SiPMs also have
 9415 higher photon detection efficiency than conventional photomultipliers. Initial SiPM tests
 9416 have been conducted with the Hamamatsu S10362-11-050C, for which we have developed a
 9417 readout board with a simple two-stage voltage preamplifier. It has a $1 \times 1 \text{ mm}^2$ area that
 9418 is suitable for fiber readout applications. It also seems to be an appropriate match to the
 9419 estimated number of photoelectrons. An initial GEANT4 simulation indicated that the most
 9420 probable energy deposit is 0.06 MeV in each interaction, leading to approximately 6 photons
 9421 at the SiPM. This SiPM, with $\sim 65\%$ quantum efficiency and 61.5% fill factor, would therefore
 9422 yield 2.4 photoelectrons per interaction. Approximately 1% of stored muons should interact
 9423 with a typical fiber in each turn. Extrapolating from E821, we anticipate approximately
 9424 7000 stored muons in each fill, which would lead to 170 photoelectrons. This is comfortably
 9425 near the center of the dynamic range of 400 available pixels on the SiPM. The maximum
 9426 dark count rate of 800 kcps would give one photoelectron of noise every 8 fills.

9427 We have acquired a quantity of 30 of this model of SiPM from unused spares from a

9428 previous project at Argonne National Laboratory, more than the 28 that are required. We
9429 will refine the readout board so that one printed circuit board will provide both mechanical
9430 support and preamplification for all seven SiPMs on each device.

9431 **20.2 Entrance counters**

9432 **20.2.1 Requirements**

9433 The time at which the muon bunch enters the ring must be subtracted from the time of
9434 each decay positron in order to align data from different fills properly. The relative intensity
9435 of each fill is also monitored. An entrance counter, positioned just outside the inflector, is
9436 needed to record the time and intensity of each fill. The cyclotron “fast rotation” structure
9437 is removed by adding a randomly generated number on the order of the cyclotron period of
9438 150 ns to the entrance time of each bunch. This procedure sets the requirement on the time
9439 resolution of the entrance counter:

- 9440 • The counter must be able to determine the mean time of each muon bunch with a time
9441 resolution that is much less than the cyclotron period of 150 ns, by at least one order
9442 of magnitude.
- 9443 • The counter must be able to adequately characterize a beam whose intensity ranges
9444 from 5% to 200% of the expected 7000 muons per fill.

9445 In E821, “flashlets” of beam that leaked from the AGS onto the target during the mea-
9446 suring period led to a potential systematic error. Muons arrived at the experiment at the
9447 cyclotron period of the AGS, produced by protons from a bunch that had not been cleanly
9448 kicked. It is difficult to envision how this phenomenon could arise at Fermilab; any out-of-
9449 time muons would somehow need to be stored in the delivery ring without being kicked in.
9450 Nevertheless, it worthwhile to be prepared with an extinction monitor to verify the absence
9451 of these out-of-time muons. Such a monitoring detector must satisfy this requirement:

- 9452 • Following a pulse of up to 200% of the expected 7000 muons per fill, after a delay of
9453 10 μ s, the counter must be able to detect a single isolated muon.

9454 The 10 μ s delay is set by the circumference of the recycler ring, which would give any
9455 “flashlets” a period of 10.9 μ s.

9456 **20.2.2 Recommended design**

9457 In E821, the primary entrance (“T0”) counter consisted of a 1 mm thick, 10 cm diameter
9458 volume of Lucite that produced Cerenkov light. It was coupled to a two-inch Hamamatsu
9459 R1828 photomultiplier. This existing T0 counter appears to be in good condition. It will be
9460 tested and repaired as needed. Because it will be among the only traditional photomultipliers
9461 in the experiment, a single-channel high voltage supply will need to be procured for it.

9462 The flashlet counter was a plastic scintillation detector that was only used in early runs
9463 of E821. The photomultiplier was configured to be gated off at the primary beam injection

9464 time by reversing the voltages on two dynodes. Consequently, the gain could be set to
9465 observe small amounts of beam entering at later times. This detector is also believed to be
9466 in working condition and to require only a suitable high voltage power supply. It will also
9467 be tested and repaired as needed.

9468 **20.3 Performance**

9469 The existing fiber beam monitors and entrance counters were used in E821. They fulfilled
9470 the requirements of that experiment, which were very similar to those proposed here.

9471 The SiPM upgrade to the fiber beam monitors should further increase the number of
9472 detected photons and therefore improve the signal-to-noise ratio. However, the performance
9473 was already sufficient to directly observe and characterize the coherent betatron motion,
9474 which was published as Figure 21 in [1].

9475 In E821, the fiber beam monitors were typically not prepared for the first day of the run.
9476 We will We will also ensure that all of these detectors are ready for the first day of muon
9477 beam operation so that they can fulfill their requirements as beam commissioning devices.

9478 **20.4 Alternatives**

9479 Initially, we evaluated reusing the conventional photomultipliers that were used with the
9480 fiber beam monitors in E821. In that experiment, a ~ 3 m long fiber connected each of
9481 the fibers from the feedthrough to an Amperex XP2202/B photomultiplier tube that was
9482 located in a cable tray above the storage ring in a location where the magnetic fringe field
9483 could be shielded with mu-metal. The signals were small enough that various models of
9484 LeCroy linear amplifiers in an adjacent NIM crate were needed to drive the long cables to
9485 the counting room. The photomultipliers and voltage divider bases that were used in E821
9486 had already been reused from a previous project, and they are clearly aging devices that are
9487 in need of replacement. An initial inspection showed that they were in poor condition and
9488 unsuitable for future use. It would have been necessary to develop a new light conversion
9489 system, whether or not we moved to SiPM technology. Given the collaboration's familiarity
9490 with SiPMs from their extensive use in the calorimeter development, their compactness, and
9491 their comparatively low cost, there was a clear choice.

9492 We also briefly considered diagnostic devices that would remain continuously deployed
9493 in the storage ring. However, any detector that intercepts the muons, even a low-mass
9494 wire chamber, would degrade the beam lifetime unacceptably, as shown in Figure 20.3. and
9495 the E821 experience with pickup electrodes was unsatisfactory; they were paralyzed by the
9496 pulsed high voltage devices.

9497 In E821, the primary method of monitoring the rate of flashlets was to suppress the
9498 firing of the electrostatic quadrupoles periodically, preventing the injected muon bunch from
9499 being stored. The number of suppressed fills could be varied, but it was typically one out
9500 of 25. Any signals that appeared in the calorimeters during these fills were presumed to
9501 be from flashlets, which was verified by observing the cyclotron period of the AGS in the
9502 time structure of the signals. While this method is effective, it unnecessarily discards a few
9503 percent of the data.

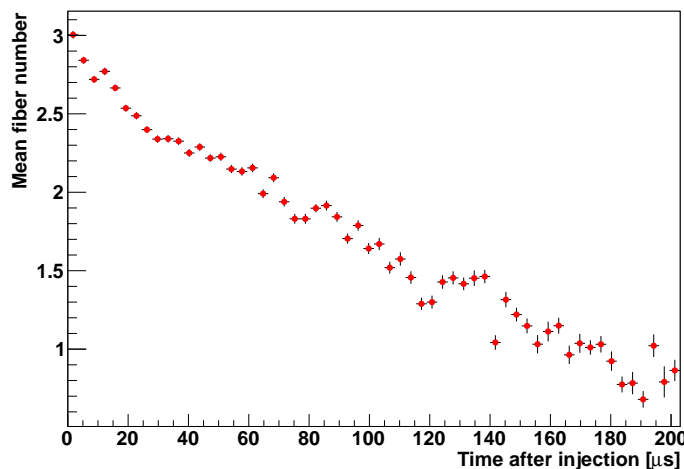


Figure 20.3: Simulated radial beam centroid position, in units of fiber number (7 mm), when the fiber harps are inserted. Energy loss in the fibers causes the beam to shift radially inward.

9504 20.5 ES&H

9505 The most significant hazards associated with the auxiliary detectors are electrical. The bias
 9506 voltages needed for the SiPM readout of the fiber beam monitors will be approximately 70 V.
 9507 To mitigate this hazard, a current-limited power supply will be used, with the current limit
 9508 set to the lowest value that allows the devices to operate. The photomultipliers required by
 9509 the entrance counters require a voltage of approximately 2000 V. Again, an appropriately
 9510 current-limited high voltage supply will be used. All electrical devices will be subject to
 9511 Fermilab's standard design review and operational readiness clearance processes.

9512 The fiber beam monitors will be powered by compressed air at less than 150 psi. Require-
 9513 ments for appropriate personal protective equipment, such as eye protection, when working
 9514 around compressed air lines will be determined in consultation with Fermilab ES&H experts.
 9515 Similarly, the fiber beam monitors interface with the ultra high vacuum system, and they
 9516 are within the large fringe field of the storage ring magnet. We will work with Fermilab
 9517 ES&H to establish appropriate procedures to mitigate these hazards.

9518 20.6 Risks

9519 There is a risk of hidden damage, or degradation over time, to the fiber beam monitors that
 9520 might require more repair work than anticipated. This damage may not be discovered until
 9521 mechanical, vacuum, and light output tests are completed. There is also a risk that, after
 9522 testing, we may find that the SiPMs that we were able to acquire at no cost are not suitable
 9523 for the application and that we need to procure another model.

9524 However, the only risk that would be expected to have a noticeable impact on the total
 9525 project cost would be the destruction or damage beyond repair of one or more of the existing

9526 fiber harp devices by an accident in shipping, storage, or testing. Because much of the original
9527 knowledge of the system has been lost, to re-create a fiber beam monitor from scratch would
9528 require a significant level of unplanned engineering cost in addition to the precision machining
9529 work.

9530 Because the fiber beam monitors interface with the ultra high vacuum system, any leak
9531 could cause downtime for the experiment. The motion control system could potentially fail
9532 in a way that would not allow them to be retracted, which would also cause downtime,
9533 requiring the entire storage ring to be brought up to atmospheric pressure to remove them.
9534 We intend to minimize these risks by careful testing before installation.

9535 **20.7 Quality Assurance**

9536 We will test the motion and vacuum integrity of the fiber beam monitors with extensive
9537 exercises in a test chamber in the laboratory before they are installed in the storage ring.
9538 We will also check the output of each fiber, and therefore the functionality of each SiPM
9539 channel, with a set of light pulsers and radiation sources.

9540 **20.8 Value Management**

9541 The auxiliary detectors represent a successful application of value management principles.
9542 All components that are suitable for reuse from Brookhaven E821 will be reused. The
9543 primary upgrade to the fiber beam monitor devices will be a SiPM readout system. For that
9544 installation, suitable unused SiPM devices (spares from a previous project) were identified
9545 and made available by Argonne National Laboratory.

9546 **20.9 R&D**

9547 Extensive R&D work on the auxiliary detectors will begin in earnest in summer 2013. Sev-
9548 eral undergraduate students will have summer research projects related to the fiber beam
9549 monitors. One will develop an improved version of our SiPM readout circuit and will use it
9550 to test the light output from each fiber. Another will re-establish the motion of the devices
9551 and will set up a vacuum test stand to check for leaks. A third student will begin to define
9552 the interface between the motion controller and the MSCB-based slow control system.

9553 **References**

- 9554 [1] G.W. Bennett et al. ($g - 2$ Collaboration), Phys. Rev. D, 73 072003 (2006).
- 9555 [2] Y. Mizumachi and T. Sato, E821 Muon $g - 2$ Internal Note No. 192 (1994).
- 9556 [3] Design Report, BNL E821, A New Precision Measurement of the Muon ($g - 2$) Value at
9557 the level of 0.35 ppm. 3rd edition, D.H. Brown et al. B.L. Roberts Editor, March 1995.

Chapter 21

Calorimeter Backend Electronics

21.1 Backend Electronics

The calorimeter backend electronics for E989 encompass the systems for the distribution of the clock and synchronization signals to the experiment, and for the digitization of the waveforms from each channel of electromagnetic calorimetry. The backend electronics for the tracker and the auxiliary detectors are discussed within those sections. The calorimeter and tracker backend electronics use a common readout platform.

21.1.1 Physics Goals

The clock system must provide a frequency stabilized and blinded clock signal that provides the time basis for determination of ω_a and a second frequency-stabilized clock, tied to the same master clock, for the precision magnetic field measurement.

As section 17 discusses, the calorimeter backend electronics contributes to three fundamental areas in the determination of ω_a : the determination of the positron arrival time at the calorimeter, the determination of the positron energy, and the separation two positrons proximate in time (pile-up). Given the continuous distribution that the muons reach in the storage ring and the random decay probability, waveform digitizers (WFDs) best fulfill these roles. The SiPM output response is deterministic, so fits to the digitized wave form can determine the arrival time, the energy and can resolve overlapping signals. Furthermore, there is no need for the electronics to recover after detection of an electron, as an ADC would require. The WFDs therefore also eliminate a source of deadtime and efficiency that would be correlated with muon intensity and would introduce a systematic uncertainty that is difficult to control at the sub-ppm level.

The WFD must convert the analog waveforms to digital while retaining the signal fidelity necessary to meet the calorimetry requirements on energy resolution and pileup differentiation. The system must convert the distributed clock frequency to the required sampling frequency range while maintaining the timing requirements, without allowing circumvention of the experimental frequency blinding. The digitized waveforms must be transferred without loss to the DAQ front ends for data reduction. The system must also provide the support and infrastructure to capture samples for pedestal determination, gain monitoring and correction, and for stability cross checks of the gain monitoring system.

Table 21.1: Summary of the clock and digitization requirements for the calorimeter backend electronics.

Feature	Driving Consideration	Requirement
Digitization rate	Pile-up identification	≥ 500 MSPS
bandwidth	Pile-up identification	≥ 500 MHz
Bit depth	Energy resolution	12 bits
Station readout rate	Fill length and rep. rate	≥ 3 Gbit/s (avg.)
Clock stability over fill	negligible ω_a systematic contribution	< 10 ps over $700 \mu\text{s}$
Clock jitter	Signal fidelity for time extraction	≤ 200 ps

21.1.2 Requirements

Clock and synchronization distribution

To avoid systematic biasing of ω_a , the distributed clock must be held stable against systematic phase shifts or timing drifts to under 10 ps over the 700 μs fill [1]. To help maintain signal fidelity, and subsequent extraction of the electron arrival time from fits to the digitized waveform, the random timing jitter should be smaller than the ADC signal sampling window (the ADC's aperture delay), which is of order 100 – 200 ps for the required digitization rates. The frequency up-conversion within the WFDs must maintain these requirements.

Synchronization signals such as start-of-fill and reset must be distributed to each front-end electronics channel. These signals must perform two distinct functions. First, to allow precise time alignment of signals from each channel within a calorimeter to allow for rapid summation on the DAQ front-end data reduction algorithms, they should be delivered to each channel within a calorimeter with a relative precision commensurate with the ADC aperture delay.

Second, across the entire experiment, the synchronization signals will flag the specific clock cycle on which to begin data acquisition for each muon fill. This requires signal delivery to the detector stations within a time window somewhat smaller than the digitization period.

Waveform Digitization

Signal requirements The energy resolution budget (5% near the 1.5 GeV threshold for fitting) determines the waveform digitizer (WFD) minimum bit depth. Assuming a typical 3×3 array of crystals summed to determine the energy, having 8 bits at 1.5 GeV would already contribute 1.2% to the energy resolution. This energy is about 1/2 the maximum energy range, and the system should have the overhead for complete study of the pileup energy distribution, which requires 10 effective bits. The effective number of bits is typically between 1 and 2 bits lower than the physical ADC bits. We therefore requires a digitization depth of at least 12 bits.

The signal separation characteristics will be determined by a combination of the crystal wrapping, the choice of which the GEANT4 Cherenkov light simulation (Section 18.3.1) shows can cause the rise time to vary from 1 to 3 ns, the SiPM and amplifier response (see Figure 18.11), and the total cable and WFD bandwidth. The WFD bandwidth must be large enough to avoid significant stretching of the pulse shapes, with the rise time remaining

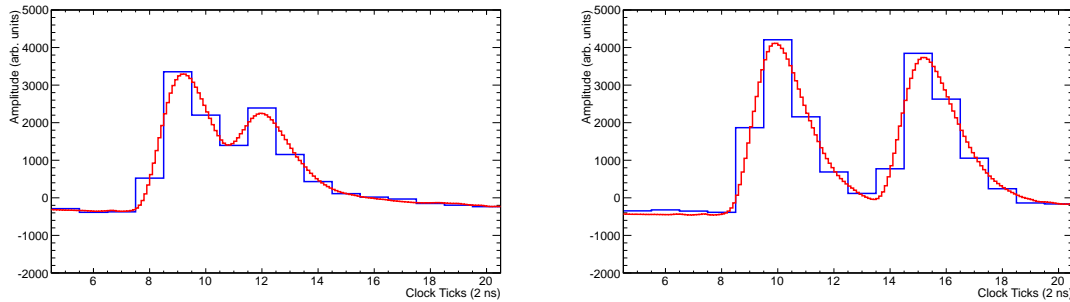


Figure 21.1: Fits to test data (see Section 18.3.1) with two pulses separated by 5 ns (left) and 10 ns (right) with a 500 MSPS sampling rate. The fits (red) clearly resolve the two peaks in the data (blue), even for the 5 ns separation.

9620 under 2 ns (if the final wrapping choice allows). The overall pileup requirement for the
 9621 experiment (see Section 18.1), that the system must be able to distinguish pulses separated
 9622 by 5 ns, drives the specification for the digitization sampling rate. Laboratory tests at 700
 9623 megasamples per second (MSPS) show clear separation of pulses with this separation (see
 9624 Figure 18.12). Figure 21.1 shows the fits for two pulses measured in the lab with 5 and 10
 9625 ns separations at 500 MSPS sampling rate. We can clearly resolve even the 5 ns separation
 9626 at 500 MSPS, but we will lose fidelity at lower sampling rates. We still have some headroom
 9627 to separate pulses separated less than 5 ns, which will help ensure our pileup separation
 9628 requirement, and therefore require a minimum digitization rate of 500 MSPS.

9629 **Physical requirements** The WFD crates will be located about 1 - 1.5 m from the dipole
 9630 field of the storage ring, where the fringe field is of order 100 gauss. Ideally, the resulting
 9631 magnetization of the materials in each WFD station would perturb the storage ring field by
 9632 well under a part per million. We can make rough limit on magnetic materials assuming a
 9633 magnetized sphere of material in a uniform magnetic field with static perturbations under
 9634 10^{-7} . A predominantly aluminum chassis would be no problem – 15 kg would result in a
 9635 perturbation under 0.1% of this limit. For ferromagnetic materials, however, the total mass
 9636 must kept under about 200 g, which may require the power supplies to be located farther
 9637 away. WFD prototype studies will determine whether shielding will be required to suppress
 9638 dynamical field perturbations.

9639 **DAQ requirements** During experimental running, muons will be stored in the storage
 9640 ring for 700 μ sec fills. The basic fill structure will be four groups of four fills, with the fills
 9641 within a group occurring at 12 ms intervals and the groups of four occurring at 132 ms
 9642 intervals. This basic structure repeats every 1.3 s, for an average fill rate of 12 Hz.

9643 To eliminate dead-time, the 700 μ s waveform for each calorimeter channel will be digitized
 9644 and transferred to the DAQ front-end system for data reduction. Each WFD station must
 9645 provide adequate buffering and throughput to support the average data rate, assuming a 500
 9646 MSPS digitization rate, of 3 Gbit / s. The rates will require high speed serial lines, which
 9647 must be quiet during each fill to avoid introducing potentially rate-dependent noise. There
 9648 must therefore be a begin-of-fill synchronization signal that arrives early enough to allow
 9649 any WFD \rightarrow AMC13 block data transfers to complete before the fill starts.

21.1.3 Recommended Design

Clock distribution

The Clock System will distribute a high-precision clock and synchronization signals to each front-end crate. It will provide timing that is fully independent of accelerator timing to insure that the ω_a measurement is not biased by synchronous events.

The Clock System follows a similar strategy to that which was used in E821 [2] and MuLan [3]. This system will primarily consist of off-the-shelf components. The primary clock signal will be produced by a Meridian Precision GPS TimeBase, a GPS-disciplined oscillator. We have recently purchased an initial module and are currently evaluating its properties. The Meridian module will be supplemented by their “Low-Phase-Noise” output module to minimize jitter. The GPS TimeBase will be used as the clock source for both the ω_a and ω_p measurements. The utilization of the clock in the ω_p measurement is described in Sect. 16.2.6. The GPS clock produces a 10 MHz output signal. This will be fed to a Fluke 6160B frequency synthesizer that will shift the ω_a clock to 50 MHz plus a small offset that will be blinded. The $50 + \epsilon$ MHz clock, where ϵ is the blinded offset that will be kept constant, will then be distributed to the back end crates. An AMC13 board, originally designed for the CMS μ TCA, in each calorimeter μ TCA crate will receive the clock signal and put it on the μ TCA backplane. Once received by each waveform digitizer, the clock frequency will be shifted up to the 500 MHz sampling frequency.

To minimize pickup from other sources, particularly sources that might be synchronous with the fill structure, the clock will be delivered to each front end crate on double-shielded RG-142 cable.

Monitoring of the clock system will occur at several stages. We will continuously monitor the source and frequency synthesizer for any systematic shifts in frequency. At the receiving end, the AMC13 will verify clock functionality with an internal counter compared to a local oscillator. Further, direct tests on time slewing and other systematic effects will be performed using the clock signals as seen by the waveform digitizers.

The Clock System will also receive and distribute timing signals from the Fermilab accelerator system. For example, the “Recycler Ring beam sync” signal will identify the time of Recycler beam extraction. This signal, after time-alignment, will serve as the “begin fill” signal that will synchronize all front ends (provide a common $t = 0$) and initiate data acquisition. We will deliver accelerator synchronization signals to each calorimeter crate differentially on shielded, twisted pair cable.

In order to perform system testing at all sites developing the detector hardware and electronics, we will construct a μ TCA “Test Clock” emulator board that will deliver a realistic set of clock and synchronization signals to the AMC13 board. The Test Clock will not have the timing precision of the final system, but it will permit development and testing to go on at remote sites under realistic DAQ system conditions. This increases the likelihood of a smooth transition to full scale system assembly at Fermilab.

Waveform digitization

The proposed system draws heavily on the hadronic calorimeter and DAQ upgrade [4] underway for the CMS experiment at the Large Hadron Collider (LHC), which utilizes μ TCA

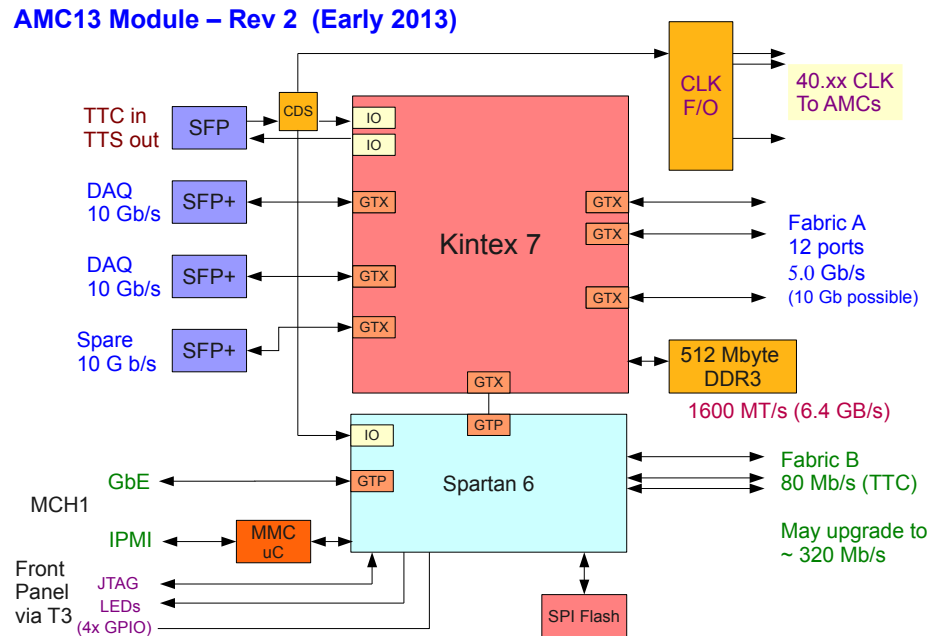


Figure 21.2: Block diagram of the CMS-designed AMC13 μ TCA card that will control the $g-2$ WFD readout.

9692 technology. The WFDs for each calorimeter station will reside in a single Vadatech VT892
 9693 μ TCA crate as a set of 5 channel Advanced Mezzanine Cards (AMCs). The crate accommodates
 9694 12 full height AMC cards. Eleven AMCs will instrument the 54 calorimeter channels
 9695 for one calorimeter station, leaving one channel for the pin diode signal that monitors the
 9696 laser calibration intensity delivered to the station. A twelfth WFD AMC will reside in the
 9697 crate as a hot spare. The μ TCA choice brings a robust system designed for remote operation
 9698 and monitoring, with cooling, power distribution and clock distribution capabilities already
 9699 designed in.

9700 CMS has already prototyped the AMC13 as part of its hadronic calorimeter DAQ upgrade
 9701 (Figure 21.3), and Cornell has begun assembling a μ TCA test bench for the WFD AMC
 9702 development.

9703 Readout will be controlled by a CMS-designed AMC card that replaces a second (re-
 9704 dundant) μ TCA Carrier Hub (MCH) in the μ TCA crate. This AMC13 card [5] is shown
 9705 in block diagram form in Figure 21.2. The μ TCA backplane connects each of the 12 WFD
 9706 AMC cards in a star topology (Figure 21.4). These connections, managed by the Kintex 7
 9707 FPGA, allow parallel readout of the 12 WFDs at rates up to 5 Gbit / second. The current
 9708 CMS firmware introduces overhead that maintains backwards compatibility with some of
 9709 their subdetectors, but currently limits the throughput to 2.5 Gbit / second. This overhead
 9710 will be eliminated through reprogramming of the Kintex 7, with no hardware modifications.

9711 The AMC13 itself can provide buffering of several seconds of calorimeter waveform data
 9712 on its 512 MB on board memory the AMC13 by taking advantage of lossless encoding /



Figure 21.3: Left: VadaTech 892 with CMS AMC13 under testing for CMS HCAL DAQ upgrade. Right: Core μ TCA equipment under setup at Cornell to begin testing for $g-2$.

9713 decoding. This encoding can easily be accommodated by the Kintex 7 on the fly. This
 9714 buffering alone will allow the AMC13 to communicate with the external DAQ system at
 9715 the average data rate of 3 Gbit / second, though the individual WFD channels will provide
 9716 deeper buffering. The AMC13 includes 3 10 Gbit optical links for communicating with the
 9717 DAQ front-end computers, though $g-2$ needs only one of these links. We will support a
 9718 TCP/IP protocol on standard 10 Gbit ethernet, so the DAQ system will communicate with
 9719 the WFD system via a standard 10 Gbit optical NIC.

9720 The AMC13 has substantial on-board processing capability in the Kintex 7 device which
 9721 could be used to form time islands for the T method or accumulate histograms for the Q
 9722 method. This would substantially reduce the required bandwidth between the AMC13 and
 9723 the DAQ front ends, as well as relieving processing requirements on the DAQ, if needed.

9724 The baseline WFD design is centered on the TI ADS5463, a 500 MSPS 12 bit ADC with
 9725 an input bandwidth of 300 MHz, and will be based on the successful 300 MSPS design [6]
 9726 (see Fig. 21.5) used for the CESR-TA project at the Cornell Electron Storage Ring (CESR).
 9727 The block diagram for the five-channel AMC card is also shown in Fig. 21.5. Each channel
 9728 will have a Kintex 7 FPGA to control the data flow out of the ADC and to / from an 64M
 9729 x 16 bit SDRAM memory buffer. At an average 12 Hz fill rate, this buffer can hold over 15
 9730 seconds of data.

9731 A sixth Kintex-7 FPGA provides the interface to the μ TCA fabric. The BU engineering
 9732 group, which has designed the AMC13 for CMS, will provide the FPGA firmware block that
 9733 supports the 5 Gbit/s transfer link from our WFD AMC to the AMC13 Kintex-7. This
 9734 Kintex-7 will transfer data out of the five channels sequentially, communicating with the
 9735 each channel's FGPA over a dedicated high speed serial line. For the 500 MSPS 12 bit
 9736 baseline design, the data from one fill can be transferred from the five-channel card in 4
 9737 msec over the 5 Gbit link.

9738 The AMC card must frequency lock on the distributed $50 + \varepsilon$ MHz clock and upconvert
 9739 to a near-500 MHz clock for the ADCs. The WFD cards will receive the 50 MHz clock
 9740 via the μ TCA backplane, which is distributed by the AMC13 via the FPGA-free LVDS

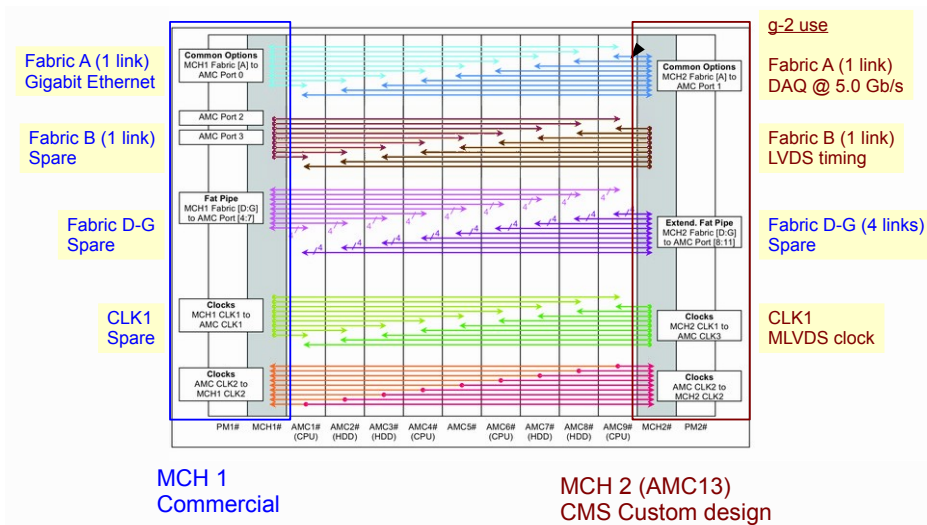


Figure 21.4: Dual-star backplane configuration for use with g-2 AMC13. High speed data transfers proceed over Fabric A. Timing and synchronization proceed via Fabric B.

9741 clock path shown in Fig. 21.6. The full clock path will need significant testing to verify
 9742 that it will have a highly stable duty cycle, slew and wander within the phase stability
 9743 specifications over a fill, and no differential nonlinearities. The engineer responsible for the
 9744 clock for operation of the Cornell Electron Storage Ring (CESR), which also has stringent
 9745 timing requirements, does not anticipate any intrinsic difficulty in meeting the $g-2$ stability
 9746 specification. On timescales of several hundred μsec , a more important issue is typically
 9747 environmental noise. We must ensure, for example, that the clock supplied to the ADC will
 9748 be immune in particular to noise sources correlated with the fill structure, such as the firing
 9749 of the kicker. Because environmental noise is an issue, we are planning a single package clock
 9750 management, based on the TI LMK04010 or similar chip, rather than a discrete component
 9751 solution. This chip can up convert the 50 MHz input clock to the 500 MHz range, distribute
 9752 it over five output channels with a programmable delay on each line. The programmable
 9753 delay will allow correction of channel by channel timing differences in signal path lengths
 9754 from the photodetectors at the sub-clock-cycle level. The single package device will be far
 9755 less immune to external noise than a discrete component solution, and has much better
 9756 overall jitter specifications (under 200 fs) than a discrete component solution.

9757 We will operate the WFDs following the CESR-TA implementation: the ADC chips
 9758 will sample continuously, and data collection will be gated during the fill, triggered by the
 9759 synchronization signal. There will also be options for dedicated operation to collect pedestal
 9760 and gain data.

9761 Bench testing the clock distribution from the AMC13 to the ADC will be the highest
 9762 priority testing we will launch with the one-channel prototype under development. These
 9763 studies will include sensitivity to environmental noise sources. We are also considering
 9764 design options for the final system that would incorporate monitoring of the final ADC
 9765 clock. Options could include onboard comparison to a second independent stabilized clock
 9766 signal generated locally on each station's MCH.



Figure 21.5: Left: A single-channel 300 MSPS ADC mezzanine card with on board buffering developed for the CESR-TA program. Right: Block diagram of the five-channel WFD AMC card.

9767 21.1.4 Performance

9768 The proposed baseline will meet the basic energy, pulse separation, readout rate and random
 9769 jitter requirements. As noted above, the level of control of systematic timing trends over the
 9770 700 μs fill times with the expected fill structure must still be characterized, but we do not
 9771 expect a serious problem.

9772 The proposed solution also provides the experiment with significant flexibility. The sys-
 9773 tem is capable of readout of the data from a fill in the 11 msec inter fill period, even at a 1
 9774 GSPS sampling rate. Should the opportunity arise, for example, for a higher average rate of
 9775 muon fills, there is no intrinsic limitation from the μTCA -based solution outlined here.

9776 With the TI ADC, we expect each station to consume approximately 500 W of power,
 9777 which is safely below the maximum power of the 792 W power module available for the
 9778 VadaTech crate

9779 The μTCA solution also provides a natural platform for the tracker readout boards 19.

9780 21.1.5 Alternatives and Value Engineering

9781 We considered a PCIe-based system to host the WFD's as an alternative to μTCA . Under
 9782 this scenario, the WFD's would become PCIe cards that plug either directly into a PCIe-
 9783 based motherboard or into a PCIe expansion chassis. We would need to engineer all of
 9784 the timing, cooling, power, mechanical and remote monitoring elements that are already
 9785 engineered into a COTS μTCA system, escalating the risk. Data throughput rates would
 9786 require a PCIe backplane with enough 16 lane slots to accommodate all of the WFDs, which
 9787 were difficult to locate. Finally, the solution did not scale easily from the 35 channel (5×7)
 9788 calorimeter considered early on to the 54 channel (6×9) baseline. As our initial estimates
 9789 indicated that the solution was only about 10% less expensive, but carried significantly more
 9790 risk, particularly for the 54 channel calorimeter.

9791 We also considered COTS waveform digitizers. When approaching Struck, however, the

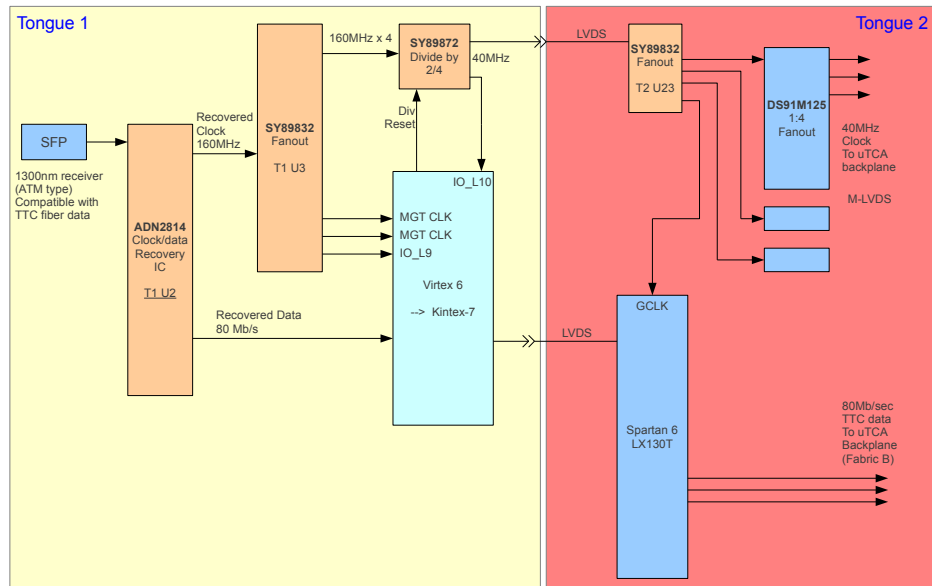


Figure 21.6: Right: Timing paths through the AMC13 for the LHC. The $g-2$ experiment will utilize the FPGA-free LVDS path, which distributes the 40 MHz clock shown for CMS, but in principle can support any frequency in the range from 10 to several hundred MHz. The $g-2$ baseline design utilizes 50 MHz.

9792 reply we received was “For an application in the 1500 channel count I tend to assume, that
 9793 a custom card may be advised to optimize performance and cost to the application.” We
 9794 continued on the path of developing our own.

9795 We considered two other 12 bit 500 MSPS ADC chips as alternatives to the TI ADS5463,
 9796 the e2v AT84AS001 and the Analog Devices AD9434-500. All chips had a similar cost /
 9797 part. The e2v AT84AS001 has a much larger footprint than the other chips, which would
 9798 complicate the layout in an already dense board, so we eliminated it from consideration. The
 9799 TI chip had slightly better noise and bandwidth specifications, while the AD chip consumed
 9800 considerably less power and space. We may have opted for the AD9434-500, all else being
 9801 equal, but TI offered to donate all 1600 ADCs needed for prototype WFD development and
 9802 final WFD production.

9803 We also explored the 1 GSPS versus 500 MSPS digitization rate. From our test beam
 9804 and simulation studies, it is clear that, not surprisingly, a 1 GSPS digitization rate would
 9805 provide better performance. The 500 MSPS does meet our requirements in the baseline
 9806 design, however, and with the baseline design the 1 GSPS option would not deliver a full
 9807 additional factor of two gain in pileup separation. A 1 GSPS option would significantly
 9808 increase the cost of the electronics. Currently, the price differential for native 1 GSPS ADCs
 9809 alone would double the cost of the WFD system, even before considering the additional
 9810 engineering required for the increased clock stability and higher rate data movement between
 9811 ADC and buffer memory. Interleaving two 500 MSPS TI chips would also essentially double
 9812 the WFD system cost. The power requirement would almost double, and we are already
 9813 near the maximum we would consider given the power the crate can deliver. Hence we would

9814 need two μ TCA crates per system, as well as additional parts and FPGAs. Interleaving the
9815 AD ADCs is feasible from a power perspective, but would forego the TI donation. The
9816 incremental system cost would exceed \$500,000 in that scenario.

9817 The ongoing R&D for the SiPM devices and associated amplifier may result in a very
9818 fast pulse that will require the 1 GSPS sampling rate. We will explore options, based for
9819 example on the TI ADC12D1000, for moving to the increased digitization rate.

9820 We have investigated discrete component circuitry on the WFD AMC card based on the
9821 AD9510 or another similar clock synthesizer. The design included a clock delay line for each
9822 channel that can correct for differences in signal path lengths from the photodetectors at
9823 the sub-clock-cycle level. Such a design would have significantly more inherent jitter, several
9824 tens of picoseconds, and would have greater sensitivity to environmental noise.

9825 As we move forward, we will continue to evaluate performance / cost issues for emerging
9826 μ TCA MCH options, component options for the WFD AMC cards, for power supplies for
9827 the μ TCA crates, and elsewhere as the opportunity arises.

9828 For the Clock System, we have considered alternate clock sources. The clock for E821
9829 was disciplined by the LORAN-C signal which is now obsolete. Undisciplined Rubidium
9830 oscillators would likely deliver the precision necessary, however the GPS disciplined oscillator
9831 provides long term stability as well as additional features like time-stamps which are of
9832 particular use to the field measurement. Options for the frequency synthesizer are limited
9833 by the 50 MHz signal necessary for the WFD.

9834 **21.1.6 ES&H**

9835 The μ TCA crate for each calorimeter station will weigh approximately 30 pounds and will be
9836 supported by the calorimeter housing (see section 18.5). Power to each crate will be supplied
9837 by a 60 – 70 V supply that connects to an in-crate power module that maintains the stable
9838 48 V on the backplane. When fully populated with the WFDs, the each station will draw
9839 approximately 500 W of power. If the magnetic field requirements allow, the power supply
9840 will be resident on the crate. If not, the supplies will be located more centrally in the ring,
9841 with a few meter cable run and the supply voltage closer to 70 V.

9842 The latter configuration in particular involves high voltage with several amps of current.
9843 We will ensure that all our equipment and installation conforms to the Operational Readiness
9844 Clearance criteria.

9845 **21.1.7 Risks**

9846 The largest risk in the WFD project regards the distribution of the clock signal through the
9847 AMC13 and μ TCA backplane, and in particular, whether that path will meet the frequency
9848 and phase drift requirements. To mitigate risk to the project, we will design the WFD AMC
9849 cards to allow timing and synchronization inputs via the front panel. We can then engineer
9850 a standalone distribution system to the AMC modules that meets the final specifications.
9851 This alternative would also require a modified clock fan-out and cabling scheme. Total
9852 differential cost to the experiment should be under \$40K for engineering and production.
9853 Biases in the clock translate directly into biasing of ω_a , so the clock must meet its stability
9854 requirements. We plan to incorporate in-situ monitoring of the final up-converted clocks on

9855 the AMC modules, and will also periodically test the distributed signals at each crate to
9856 ensure that they have remained synchronized.

9857 The μ TCA crate will reside about one meter from the storage ring, where the residual
9858 magnetic field is approximately 100 gauss. The crate, electronics and power supply can
9859 potentially perturb the precision field, both statically and dynamically. The main concern
9860 for the static perturbation is the presence of ferromagnetic materials, which must be limited
9861 to a several hundred grams at the proposed location. VadaTech has previous experience in
9862 migrating other μ TCA chassis from their standard steel-based configuration to an aluminum
9863 chassis. They will provide us with a custom aluminum chassis for the full order, and will
9864 send us preliminary versions of the chassis for magnetics characterization before filling the
9865 full order. They are currently working with us to identify and control other areas of the
9866 crate and modules that contain ferromagnetic materials. The largest unknown is the power
9867 supply, a 3rd party supply that VadaTech installs. If that supply is problematic, the supply
9868 for each crate can be relocated towards the center of the storage ring and the voltage applied
9869 by means of a shielded cable.

9870 We will assess the magnetic field perturbations induced by fields at the precision magnet
9871 that will be established at Fermilab, and use our OPERA 3D simulations to extrapolate
9872 observed perturbations in the test magnet to the behavior in the fringe field of the storage
9873 ring. We will also use pickup coils to assess the dynamical perturbations, and shield the
9874 crate as necessary to minimize these.

9875 If these mitigations are insufficient, we can always locate the crates somewhat farther, at
9876 the expense of modest increases in the signal cable length.

9877 Longer term drifts in the frequency will in principle cancel in the ω_a/ω_p ratio since both
9878 the ω_a and the magnetic field measurements are tied to the same master clock. Reliance
9879 upon this cancellation would, however, require some care in the procedure that weights the
9880 magnetic field measurements with the muon fill statistics. The GPS stabilization of the
9881 master clock will minimize this drift and therefore also minimize our need to rely upon strict
9882 cancellation of any time dependence in the ratio.

9883 Further development on the SiPM pulse shapes, in particular if they narrow further,
9884 could necessitate a shift to a higher digitization rate, such as 1 GSPS. Unless there is a
9885 significant price decrease in the 1 GSPS ADCs, there would be a significant hardware cost
9886 increase (of order \$500,000) as well as an increased development time. This risk is somewhat
9887 mitigated in that the changes would be local to the WFD AMC boards. The AMC13-based
9888 μ TCA readout has more than sufficient throughput capacity to absorb the increased data
9889 volume, and the on-board buffering would still accommodate over 5 seconds of data.

9890 21.1.8 Quality Assurance

9891 Cornell is establishing a test station to assess the performance of the μ TCA platform, of the
9892 AMC13 modules and the WFD AMCs themselves. We plan two major stages of prototyping:
9893 and initial one channel design to verify the fundamental per channel performance without
9894 facing the board density issue simultaneously. The second stage will move the one channel
9895 design to the full five channel design with the denser component layout. The plans for each
9896 stage include two versions of AMC prototype, and both versions will undergo significant
9897 testing to assure that the baseline requirements for $g-2$ are met.

9898 We will produce enough of the second five channel prototype to fully populate the μ TCA
9899 crate, as planned for the experiment, so that we can ensure the entire system under full load
9900 can meet the specifications, and that we do not encounter unanticipated cross talk or clock
9901 biasing with the full system. This system will also be deployed in the 25 channel test beam
9902 planned to stress test the entire calorimeter through DAQ design.

9903 Production of the WFD AMC modules and delivery of the μ TCA crates should complete a
9904 year in advance of the start of the experiment. Burn-in and stress-testing of the production
9905 components will continue at Cornell as we receive the components, and can continue for
9906 several months thereafter before moving the equipment to FNAL for installation.

9907 The Illinois group will test and evaluate each component of the clock system prior to
9908 installation. In addition, we will perform detailed in-situ timing for each path in the final
9909 experimental configuration. This “timing-in” is necessary to insure that the synchronization
9910 signals are delivered to each location simultaneously.

9911 References

- 9912 [1] R. Carey and J. Miller, E821 Muon $g - 2$ Internal Note No. 165, 1(1993).
- 9913 [2] G.W. Bennett, et al., Phys. Rev. D 73, 072003 (2006).
- 9914 [3] V. Tishchenko *et al.* [MuLan Collaboration], Phys. Rev. D 87, 052003 (2013)
9915 arXiv:1211.0960 [hep-ex].
- 9916 [4]
- 9917 [5] J. Mans *et al.* [CMS Collaboration], *CMS Technical Design Report for the*
9918 *Phase 1 Upgrade of the Hadron Calorimeter*, CERN-LHCC-2012-015, CMS-TDR-10,
9919 <http://cds.cern.ch/record/1481837?ln=en>.
- 9920 Amc13 development project, <http://www.amc13.info>.
- 9921 [6] N.T. Rider, J.P. Alexander, J.A. Dobbins, M.G. Billing, R.E. Meller, M.A. Palmer,
9922 D.P. Peterson, C.R. Strohman, *Development of an X-Ray Beam Size Monitor with*
9923 *Single Pass Measurement Capability for CESRTA*, Proceedings of the 2011 Particle
9924 Accelerator Conference (PAC 11) , 687 (2011).

Chapter 22

Data Acquisition System

22.1 Physics Goals

The data acquisition system must read, process, monitor and store the data produced by the various detector systems in the muon $g-2$ experiment. Most importantly, the DAQ must provide a distortion-free record of the detector signals originating from the decay positrons during the 700 μs -long spills from the muon storage ring. Additionally, the system must record all data required to perform the corrections from effects such as pulse pileup, gain instabilities and beam dynamics. Furthermore, the system must permit the monitoring needed to guarantee the overall integrity of data taking and record-keeping needed to document the experimental conditions during data taking.

22.2 Overall Requirements

The DAQ must handle the accelerator-defined time structure of the data readout from the detector systems. Under normal operations we anticipate a 12 Hz average rate of muon spills that comprises sequences of four consecutive 700 μs spills with 11 ms spill-separations for each booster batch received by the muon $g-2$ experiment. The procedures for reading, processing, monitoring and storing these data must not introduce time-dependent losses or time-dependent distortions of the detector signals during the muon spills.

The DAQ must handle the readout, processing, monitoring and storage of the data obtained from the 1296 channels of 500 MSPS, 12-bit, waveform digitizers instrumenting the individual PbF_2 crystals of the twenty four calorimeters. For each spill the raw data will consist of 1296 channels of 700 μs -long streams of continuously-digitized ADC samples. The DAQ must process these raw data into derived datasets including: T-method data (*i.e.* individual islands of digitized pulses), Q-method data (*i.e.* accumulated histograms of calorimeter spectra), and other calibration, diagnostic and systematic data. At a 12 Hz spill rate the readout (*i.e.* raw) data rate will be about 8.2 GB/s and the stored (*i.e.* derived) data rate will be about 50 MB/s.

The DAQ must also handle the readout, processing, monitoring and storage of the data obtained from the two positron tracking stations. This system consists of roughly 2000 channels of straw tubes with associated amplifier-discriminator-TDC electronics. The raw

9955 data – consisting of time stamps and spill numbers from individual straw tubes – is expected
9956 to yield a roughly 2 MB/s time-averaged data rate.

9957 Additionally, the DAQ must handle the readout, processing, monitoring and storage of
9958 data from the auxiliary detector systems. These systems include the muon entrance detector,
9959 fiber harp detectors and electric quadrupole monitors and involve both instrumentation that
9960 is operated during normal data taking (the muon entrance detector) and instrumentation
9961 that is operated during dedicated data taking (the fiber harp detectors). The read out for
9962 the muon entrance detector, fiber harp detectors and electric quadrupole monitors will use
9963 an existing system of custom-built, fast-sampling, VME-based, waveform digitizers. The
9964 expected data rates from auxiliary detector systems are: (i) 17 MB/s during dedicated data
9965 taking with the fiber harp detectors and (ii) 3 MB/s during normal data taking with the
9966 muon entrance detector and the electric quadrupole monitors.

9967 The DAQ must coordinate the acquisition of data by the frontend readout processes with
9968 the accelerator-defined spill cycles. This coordination involves both readout systems where
9969 data is transferred synchronously with spill cycles (direct memory transfer from VME-based
9970 electronics) and readout electronics where data is transferred asynchronously with spill cycles
9971 (network packet transfer from micro TCA based electronics).

9972 The DAQ must assemble the individual fragments of spill-by-spill data from networked
9973 readout processes into complete, deadtime-free records of each muon spill. This includes
9974 assembling the data banks of T-method and other datasets from the twenty four calorimeter
9975 stations as well as the data from the two tracker stations and the auxiliary detector sys-
9976 tems. In total the event builder must match and assemble the fragments originating from
9977 roughly thirty frontend processes at an expected rate of about 50 MB/s. The resulting
9978 fully-assembled spill-by-spill events must be transferred to the Fermilab computing facilities.

9979 The DAQ must provide the local / remote run control for data taking as well as facilities
9980 for configuration and readback of configuration parameters such as digitizer settings, multihit
9981 TDC settings *etc.* The system must provide the monitoring of data integrity and data quality
9982 and a comprehensive database of the experimental conditions and configuration parameters
9983 during data taking. The system must additionally provide for local storage of sufficient data
9984 for online analysis tasks.

9985 **22.3 Recommended Design**

9986 The major challenge for the data acquisition is the combination of the high data rates with the
9987 requirement of avoiding any time-dependent losses or time-dependent distortions of detector
9988 signals during muon spills. In addition, the system must provide: the monitoring of data
9989 integrity, cataloging of experimental conditions, and flexibility for diagnostics measurements.

9990 The DAQ will acquire data in deadtime-free blocks that correspond to individual muon
9991 spills from the storage ring. Each event will represent a complete deadtime-free history of the
9992 entire activity in the detector systems for a complete spill – rather than events corresponding
9993 to individual positrons. This scheme will utilize the on-board memories in waveform digitizer
9994 and multi-hit TDCs to temporarily buffer the recorded data before its data transfer to the
9995 data acquisition. The design will be implemented as a modular, distributed computer system
9996 on a parallel, layered array of networked, commodity processors with graphical processing

9997 units (GPUs). The DAQ group has developed and operated very similar architectures [1]
9998 for the MuLan, MuCap and MuSun experiments at the Paul Scherrer Institute.

9999 The data acquisition system is depicted schematically in Fig. 22.1. It shows a frontend
10000 processor layer responsible for readout and processing of waveform digitizer and multihit
10001 TDC data, a backend layer responsible for event assembly and data storage, a slow control
10002 layer responsible for control and read-back, and a data analysis layer responsible for monitor-
10003 ing data integrity. The DAQ hardware will comprise a networked cluster of high performance
10004 processors running Scientific Linux. The DAQ software will be based on the MIDAS data
10005 acquisition package [2], ROOT data analysis package [3], and NVIDIA's parallel computing
10006 platform CUDA [4]. To maximize bandwidth, one network will handle traffic between the
10007 frontend layer and the backend layer and another network will handle traffic between the
10008 backend layer and the analysis layer.

10009 The calorimeter readout consists of one frontend processor per calorimeter station. Each
10010 frontend processor will read out the 54 waveform digitizer channels associated with the 9×6
10011 PbF_2 crystals of a single calorimeter station. Each group of 54 waveform digitizer channels
10012 will occupy a single micro TCA crate. The digitizers are configured and read out via combi-
10013 nation of a commercial MCH controller [5] with a 1 GbE link and a custom AMC13 controller
10014 [6] with a 10 GbE link. For each spill the raw calorimeter data will consist of $24 \times 54 = 1296$
10015 channels of 700 μs -long streams of continuously-digitized, 500 MSPS, 12-bit, ADC samples –
10016 a total of 680 MB per spill or 8.2 GB per second. The processors are designed to provide the
10017 necessary performance to compress the continuously-digitized ADC samples into the T-/Q-
10018 method datasets at the software level in the frontend CPU/GPUs. The T-method datasets
10019 will consist of individual “islands” of above-threshold calorimeter signals and the Q-method
10020 datasets will consist of histograms of consecutive spills of continuously-digitized samples.
10021 The algorithms for constructing the T-/Q-method datasets involve copying, masking and
10022 summing data arrays and therefore are well suited to GPU-based parallelization using stan-
10023 dard algorithms. The scheme will offer the flexibility to implement other datasets – such as
10024 pile-up datasets (*e.g.* by summing fills before storing islands) and diagnostic datasets (*e.g.*
10025 by storing prescaled fills of fully-digitized samples) – as needed. Each calorimeter frontend
10026 process will finally zip, pack and dispatch the various derived datasets as MIDAS-format
10027 databanks over the frontend network to the event builder.

10028 The positron tracking system consists of two tracking stations that each comprise about
10029 1000 individual channels of straw tube detectors. The raw data – derived from amplifier-
10030 discriminator-TDC electronics that instrument each straw tube detector – are transferred to
10031 custom AMC modules housed in a single micro TCA crate for each tracking station. The
10032 AMC modules are configured and read out via a commercial MCH controller with a 1 GbE
10033 link. Each tracker frontend process will receive the raw data – *i.e.* hits defined by a time
10034 stamp and a spill index – and then compress, pack and dispatch the tracking station data
10035 as MIDAS-format databanks over the frontend network to the event builder.

10036 The auxiliary detector systems comprise the muon entrance detector, fiber harp detectors
10037 and electric quadrupole monitors. Their read out will be based on existing electronics of
10038 custom-built, high-speed, 8-bit, waveform digitizers with 512 kByte on-board FIFO memories
10039 [1]. These digitizers are configurable for different sampling rates and different triggering
10040 / gating modes and therefore suitable for the readout of the different detector systems.
10041 The digitizers are housed in 6U VME crates and read out using Struck Innovative Systeme

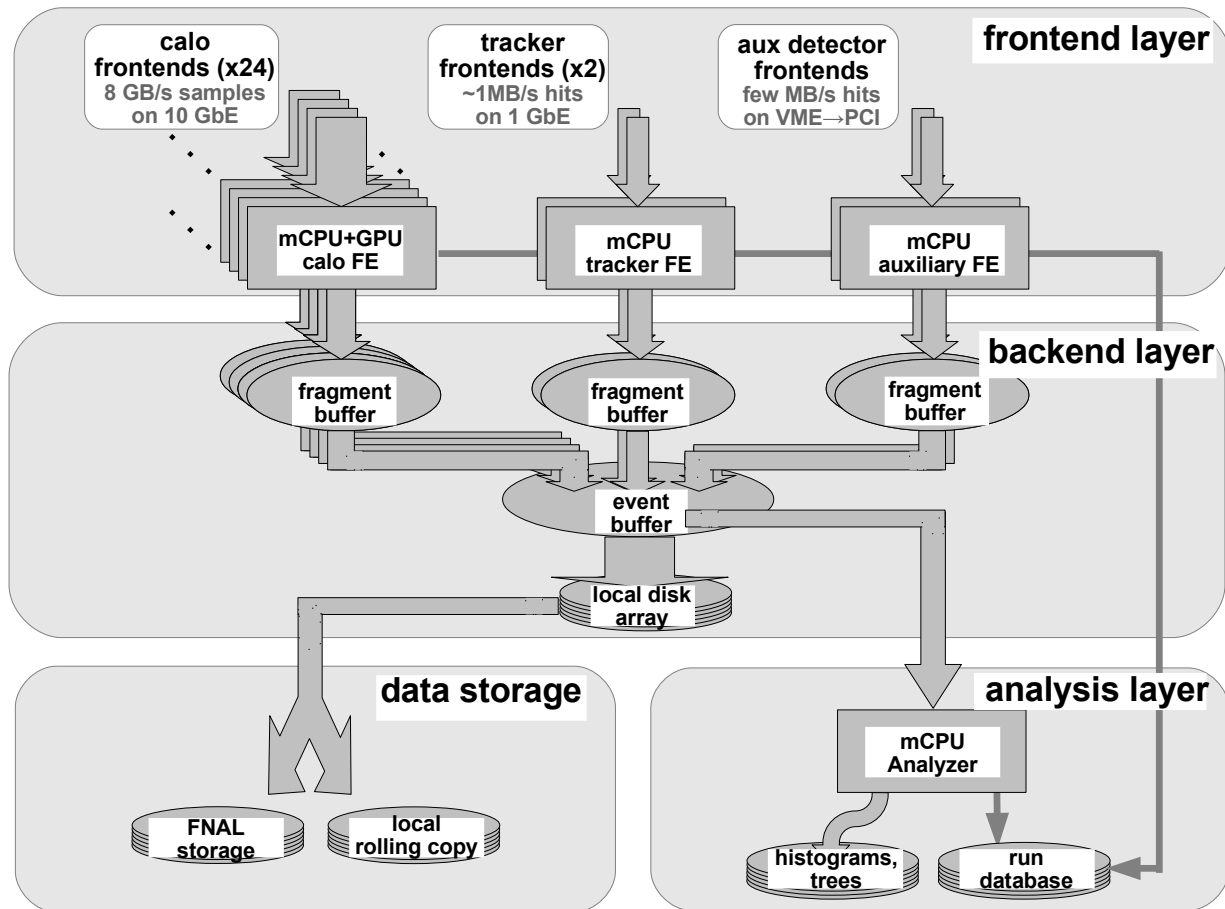


Figure 22.1: Conceptual design of the $g-2$ data acquisition. The figure shows: (i) the frontend layer for readout and processing of data from the calorimeter stations, tracking stations and auxiliary detector systems, (ii) the backend layer for event building and data storage, (iii) the analysis layer for monitoring data quality and recording run-by-run experimental conditions, configuration parameters, *etc.*, and (iv) data storage. The layers comprise arrays of networked commodity processors.

10042 SIS3100/1100 VME-to-PCI interfaces. The muon entrance readout will use a single digitizer
 10043 channel operating at 500 MSPS sampling rate to record continuous ADC samples. The fiber
 10044 harp detector readout will use 28 channels of waveform digitizers operating at a 500 MSPS
 10045 sampling rate with an external gate signal to record continuous streams of ADC samples
 10046 during the initial 100 μ s of the muon spill. The electric quadrupole monitors will be read
 10047 out using 32 channels of waveform digitizers operating at a 25 MSPS sampling rate with an
 10048 external gate signal to record continuous streams of ADC samples during the entire 700 μ s
 10049 of the muon spill.

10050 The DAQ design incorporates a master frontend process and hardware control logic in
 10051 order to synchronize the data acquisition readout cycles with the accelerator-defined spill
 10052 cycles. Importantly, the master frontend and control logic must accommodate both the spill-

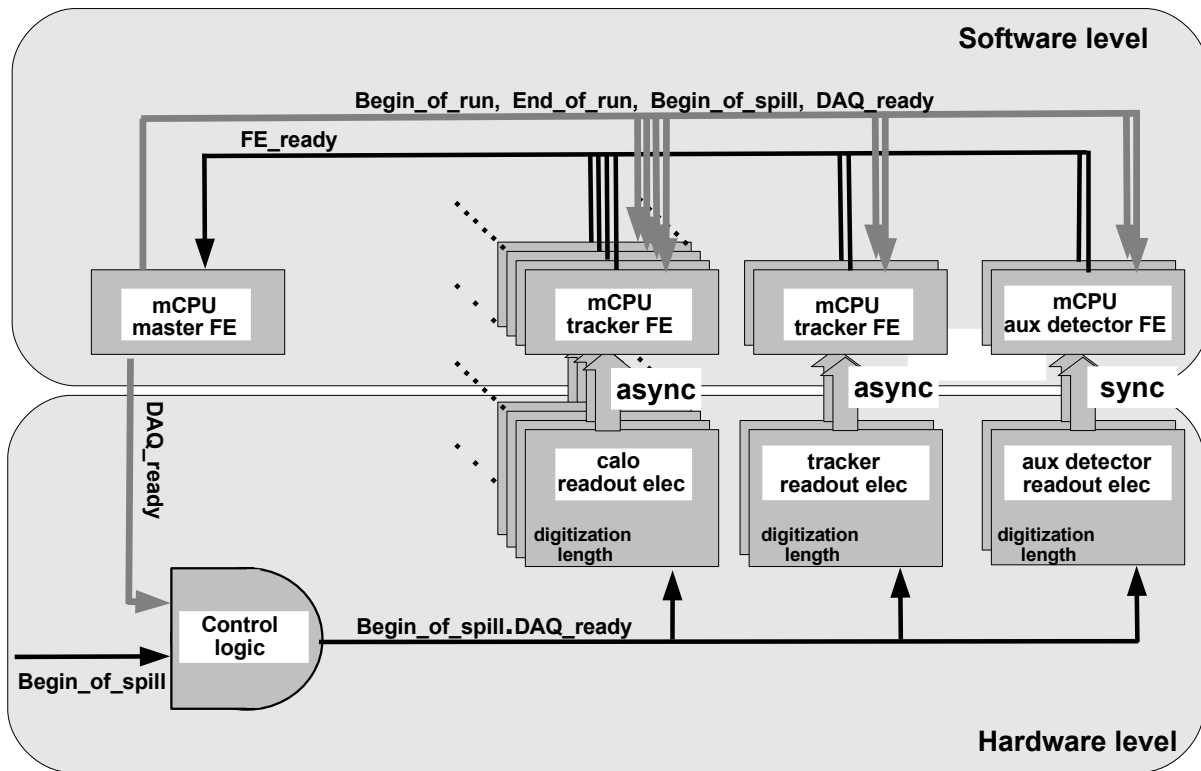


Figure 22.2: Conceptual design of the $g-2$ control logic. The controls signals involve an accelerator-defined *begin-of-spill* signal and a process-defined *DAQ_ready* signal. Control signals are distributed across the readout processes by remote procedure calls (the upper software level) and across the readout electronics by the control logic module (the lower hardware level).

10053 synchronous data transfer from the VME crates via Struck SIS 3100/3300 interface modules
 10054 and the spill-asynchronous data transfer from the micro TCA crates via 1/10 GbE network
 10055 links.

10056 The conceptual design of the logic to coordinate the fill cycles and readout cycles is given
 10057 in Figs. 22.2 and 22.3. The design involves two control signals – a *begin-of-spill* signal and
 10058 *DAQ_ready* level – that are distributed to the readout electronics via the hardware control
 10059 logic and distributed to the frontend readout processes by the master frontend process. On
 10060 starting a run (see Fig. 22.3), each enabled readout process after completing initialization
 10061 functions will transmit a *FE_ready* signal via a remote procedure call to the master frontend
 10062 process. On receipt of all *FE_ready* signals the master processes sets the *DAQ_ready* level
 10063 “high” in the control logic. The next *begin-of-spill* signal then: (i) propagates through the
 10064 control logic to initiate the digitization by the readout electronics, (ii) propagates to the

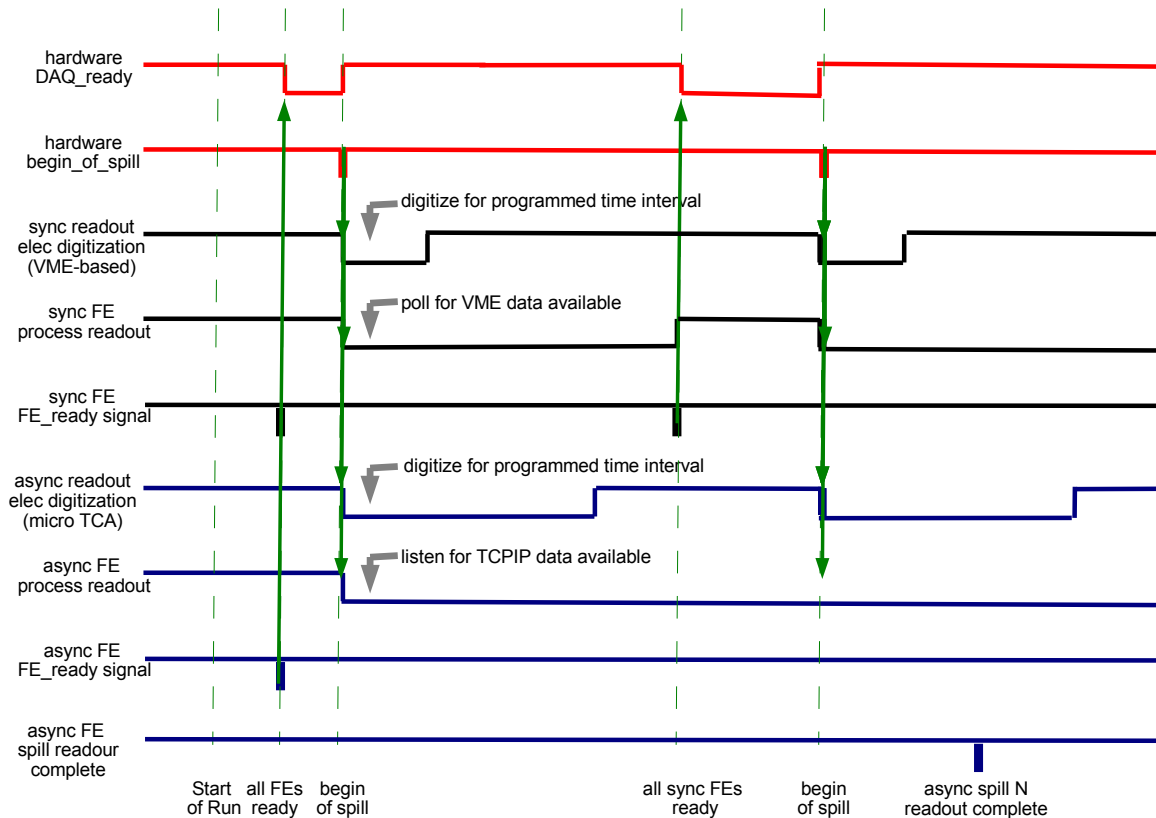


Figure 22.3: Timing diagram for the $g-2$ control logic. In solid red are indicated the hardware control signals (the *begin_of_spill* from the accelerator and *DAQ_ready* from the acquisition system). In solid black are indicated the sequence of digitization and readout for the VME-based, synchronous readout systems and in solid blue are indicated the sequence of digitization and readout for the micro TCA-based, asynchronous readout systems. The readout processes for the VME-based electronics will poll the VME modules for data. The readout processes for the micro TCA-based electronics will listen for TCPIP packets of data.

10065 readout processes to initiate software *begin_of_spill* functions, and (iii) resets the *DAQ_ready*
 10066 level “low”. The digitization time range for each detector system is a configuration parameter
 10067 in the readout electronics that is set by the DAQ. The VME-based synchronous frontend
 10068 processes, which require the readout of all data before acquiring the next spill, will identify
 10069 the availability of data by a polling scheme and report the readout completion via a *FE_ready*
 10070 remote procedure call. Asynchronous frontend processes, that listen for TCPIP packets of
 10071 data from the frontend electronics, do not require the readout of all data before acquiring the
 10072 next spill.¹ After receiving the *FE_ready* signals from all synchronous readout processes, the

¹As indicated in Fig. 22.3, the completion of spill-by-spill events from asynchronous frontend processes will be monitored to prevent the overflow of the data buffers in the event builder. The data buffers for event

10073 master processes again sets the *DAQ_ready* level “high” in the control logic – thus continuing
10074 the data taking. Note we plan to use a PCI-based GPS synchronization card [8] to GPS
10075 timestamp the digitized spills to facilitate later coordination between the detector system
10076 readout and the magnetic field readout.

10077 Each frontend readout process will transmit its spill-by-spill data fragments as MIDAS-
10078 format databanks across the frontend network to the backend processor. Initially, the data
10079 fragments from the twenty four calorimeter processes, two tracking system processes and
10080 various auxiliary detector processes, are transferred to individual shared memory segments
10081 on the backend machine. After matching the MIDAS serial numbers and muon spill indexes
10082 of event fragments the event builder process assembles all data fragments into single events
10083 representing a complete record of each spill. The spill events are then written by the event
10084 builder process to a final memory segment known as the system memory segment and are
10085 available for data storage tasks, data analysis tasks, *etc.*

10086 The backend layer will use a two step procedure to permanently store a full copy of the
10087 data on the Fermilab Computing facilities and temporarily store a rolling copy of the recent
10088 data on our analysis layer. First, the data will be transferred from the system memory
10089 segment to a temporary disk file on a local redundant disk array on the backend processor.
10090 Next, the temporary data files on the backend processor will be asynchronously migrated to
10091 both the Fermilab computing facilities for permanent storage and the DAQ analysis layer
10092 for local analysis projects. This approach will minimize any delays in data taking due to
10093 latencies associated with the permanent archiving of the experimental data and make the
10094 current data available for local analysis projects.

10095 The DAQ analysis layer will provide both integrity checking and online histogramming.
10096 The online analyzer will receive events over the network from the system memory segment on
10097 the backend layer. These events will be received “as available” in order to avoid introducing
10098 any delays into the readout or the data storage. The online analysis will utilize the MIDAS
10099 analyzer package and a modular, multistage approach to the analysis tasks. Specifically, the
10100 different analysis tasks will be implemented as individual analyzer modules and switched on /
10101 off as needed. Each analysis module will have access to a global structure that contains both
10102 the raw MIDAS databanks from the readout processes and any derived MIDAS databanks
10103 from the preceding analysis modules. Low-level modules will be responsible for unpacking
10104 the databanks and checking their integrity. Intermediate-level modules will be responsible
10105 for various histogramming tasks to ensure the correct operations of detector systems. High-
10106 level modules will be responsible for online “physics” analysis such as fits to the precession
10107 signal.

10108 The data acquisition system will incorporate database support to provide a comprehen-
10109 sive run-by-run record of the experimental conditions, configuration parameters, *etc.*, during
10110 the entire experiment. The run-by-run database will store information derived from the MI-
10111 DAS online database such as run start time, run stop time, operator run-time comments, the
10112 number of events, and hardware settings including the high voltage setting, digitizer config-
10113 uration parameters, multihit-TDC configuration parameters, *etc.* In addition, the database
10114 will record such quantities as detector gains, pedestals, *etc.*, fitted frequencies, lifetimes, *etc.*,
10115 that are derived from the analysis layer. These metadata are foundations for the offline data

building are sufficient to store the entire data from one 1.33 second cycle of beam delivery.

10116 analysis.

10117 The DAQ will be housed in the computer room in the MC-1 building. 10 GbE optical
10118 fiber links (64 cables) and 1GbE copper Ethernet (48 cables) will provide the connections
10119 between the detector sub-systems in the experimental hall and the data acquisition in the
10120 control room. The DAQ will require clean, uninterruptible power of roughly 50 kiloWatts
10121 total power with appropriate power distribution for roughly thirty rackmount computers and
10122 associated network switches, mass storage devices, *etc.* The control room will require air
10123 circulation for appropriate temperature and humidity control with temperature, humidity
10124 and air velocity sensors with digital readout. It will require a reliable, fast network connection
10125 between the MC-1 computer room and the Fermilab data storage facilities that is capable
10126 of a sustained data rate of roughly 100 MB/s.

10127 **22.4 Design Performance**

10128 The DAQ is designed to operate at 12 Hz average spill rate with muon spills that comprises
10129 sequences of four consecutive 700 μ s spills with 11 ms spill-separations. It must handle
10130 the readout, processing and storage of the raw data rates from the twenty four calorimeter
10131 stations, two tracking station, and the auxiliary detector systems

10132 During normal data taking at 12 Hz spill rate, the time-averaged data rate of raw
10133 calorimeter ADC samples will be 340 MB/s per individual station and 8.2 GB/s for all
10134 twenty four stations. Overall – to achieve both manageable rates and reasonable volumes of
10135 stored data – the data processing by calorimeter frontends must achieve at least a 100-fold
10136 compression of continuously-digitized ADC samples into T-/Q- and other method datasets.
10137 During normal data taking at 12 Hz spill rate, the tracking system raw data rate is expected
10138 to be roughly 2 MB/s and the auxiliary detector systems raw data rates are expected to be
10139 roughly 3 MB/s.

10140 The experiment will require the Fermilab data storage facilities to handle a sustained
10141 data rate of up to 80 MB/s during the operating periods of the g -2 experiment. Based on
10142 roughly one year of total running time, the experiment will require a permanent data storage
10143 capacity from Fermilab data storage facilities of 1-2 Petabytes.

10144 **22.5 Alternatives**

10145 The collaboration considered two alternative data acquisition frameworks: the CODA DAQ
10146 package [10] that is used at JLab and the artdaq DAQ package [11] that is under development
10147 at Fermilab. One advantage of using the MIDAS is that collaboration members have already
10148 developed very similar DAQ architectures with the MIDAS framework for other experiments.
10149 The g -2 DAQ can therefore profit from the software/hardware development for the earlier
10150 experiments. Another advantage of MIDAS is the availability of an extensive range of DAQ
10151 tools including an event builder, an analysis framework, a slow control system, a data alarm
10152 system, data storage and database tools, as well as large collections of device drivers for
10153 readout hardware. MIDAS has an active community of software developers and is widely
10154 used at numerous nuclear and particle laboratories.

10155 Several alternatives were considered for processing the raw calorimeter data into T-, Q-
10156 and other method datasets. In particular, the collaboration considered the possibilities of
10157 deriving the T-/Q- method datasets at either the software level in the frontend processors
10158 or the hardware level in the digitizer FPGA electronics. An advantage of the software
10159 implementation is the greater flexibility to modify or add new datasets or analysis algorithms
10160 as needed during the design, commissioning and running phases of the experiment. An
10161 advantage of the firmware implementation is the lower data rates from the readout electronics
10162 to the frontend processors.

10163 Different architectures and parallelization schemes were also considered for the calorime-
10164 ter frontend processors. In one parallelization scheme using multicore CPUs the frontends
10165 process individual spills in separate CPU threads in order to achieve the necessary data
10166 compression bandwidth. In another parallelization scheme using many core GPUs the fron-
10167 tends process individual samples in separate GPU threads in order to achieve the necessary
10168 data compression bandwidth. The GPU-based approach is better suited to paralleling the
10169 tasks involved in deriving T-/Q-method datasets and takes advantage of general purpose
10170 algorithms for such operations.

10171 Two different NVIDIA GPU architectures – the newer Kepler architecture and the older
10172 Fermi architecture – will be evaluated for the frontend processors. The Kepler architecture
10173 may permit faster data transfer between the CPU and the GPU and thereby improve the
10174 rate performance for data compression.

10175 In addition to T-/Q-method data compression we plan to evaluate the loss-less com-
10176 pression of digitizer data using standard libraries (*e.g.* ZLIB library [9]). For continuously-
10177 digitized ADC samples that consist of occasional pulses the loss-less algorithms should offer
10178 efficient compression.

10179 **22.5.1 ES&H**

10180 The components of the data acquisition do not involve either hazardous materials or unusual
10181 electrical / mechanical hazards. The system will comply with safety standards for power
10182 distribution and will require appropriate temperature, humidity and air velocity sensors.

10183 **22.6 Risks**

10184 The largest risk in the data acquisition system is the corruption or the distortion of the
10185 positron time spectra (the calorimeter readout involves computation of derived T-/Q-method
10186 datasets from continuously digitized ADC samples). These risks are mitigated by DAQ in-
10187 tegrity testing using DAQ test stands (see Sec. 22.7).

10188 A further risk is insufficient performance of the data acquisition – in particular the deriva-
10189 tion of T-/Q-method datasets – that would impact rates of data accumulation during data
10190 taking. This risk is mitigated by the possibility of moving some tasks in the dataset deriva-
10191 tion from the GPU hardware to the Kintex 7 FPGA in the AMC13 interface module. Also,
10192 the combined memory of the digitizer modules and the AMC13 interface module, can buffer
10193 about 13 seconds of consecutive spills and help mitigate any DAQ bottlenecks.

10194 A further risk is the possibility of a change from the planned 500 MSPS digitization to a
10195 faster 1 GSPS digitization in the calorimeter readout electronics. The change would double
10196 both the input raw data rate and the output T-method data rate at the calorimeter frontend.
10197 The change would require additional DAQ processing power, DAQ network bandwidth, and
10198 Fermilab permanent storage capacity.

10199 Another risk is delays in the software development of the data acquisition that would
10200 impact schedules for detector commissioning and data taking. The DAQ is assembled from
10201 commodity computing hardware, so procurement and delivery is not a risk.

10202 22.7 Quality Assurance

10203 Kentucky has established a test stand for DAQ development, testing and quality assurance.
10204 Our first stage of prototyping for calorimeter readout and event building is underway using
10205 simulated data. A second stage of prototyping will begin this summer with the acquisition
10206 of micro TCA crate with MCH/AMC13 cards and continue this fall with the acquisition of
10207 a single prototype digitizer. Other DAQ groups at UIUC and Oxford will also establish test
10208 stands for DAQ development, testing and quality assurance for the tracker readout and the
10209 DAQ control system.

10210 An important milestones for DAQ development is a single calorimeter test run planned
10211 for SLAC in spring 2014 and a tracker sub-system test run planned for Fermilab in fall
10212 2013. Stress tests and integrity tests of the DAQ components will be conducted using the
10213 test stands at the various institutions. Software and support will be provided to other
10214 institutions responsible for readout electronics and detector systems.

10215 22.8 R&D

10216 The collaboration has conducted a number of R&D projects to test the design components.
10217 In particular, a number of R&D projects were conducted on the hardware / software imple-
10218 mentation of the: (i) frontend processing of raw calorimeter ADC samples into T-/Q-method
10219 datasets, (ii) event builder tasks of event fragment matching and event fragment assembly,
10220 and (iii) coordination between the accelerator-controlled spill cycles and the the computer-
10221 controlled readout cycles. In addition, a DAQ system was developed for beam tests of
10222 calorimeter prototypes and evaluation tests of waveform digitizer systems.

10223 The MIDAS-based DAQ platform for R&D projects is shown in Figs. 22.4 and 22.5. It
10224 comprises a network of three frontend processor and one backend processors. The backend
10225 processor hosts the MIDAS server process MSERVER that manages inter-process commu-
10226 nications, the MIDAS web daemon MHTTPD that provides run control, the MIDAS event
10227 builder MEVB, as well as MIDAS data storage and analysis tools. Frontend processor FE01
10228 comprised two quad-core Intel Xeon X5550 CPUs and a 240-core, NVIDIA Tesla C1060 GPU.
10229 A calorimeter emulator – running as a separate thread on the processor FE01 – was used for
10230 development work on GPU-based T-/Q-method processing of continuously-digitized ADC
10231 samples. A GbE interface to two 12-bit, 4-channel, 500 MSPS Struck SIS3350 waveform
10232 digitizer modules [7] is being used for both DAQ development work and prototype calorime-

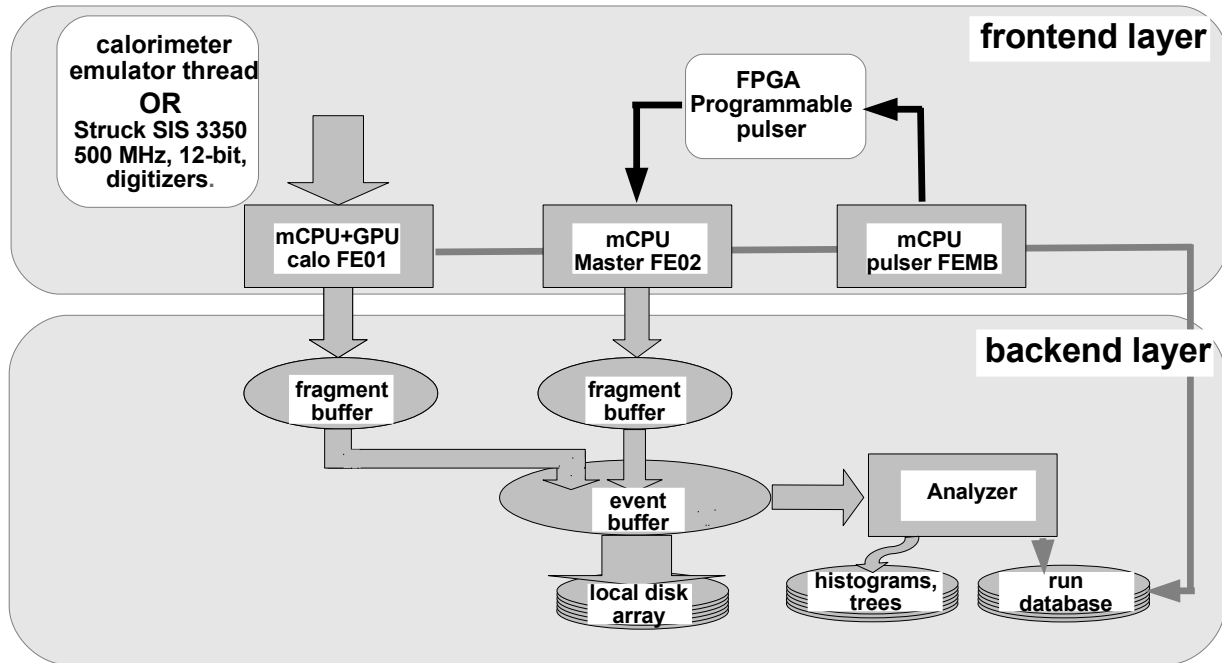


Figure 22.4: Layout of MIDAS-based DAQ-platform for R&D projects. The frontend FE01 incorporates both readout of emulated continuously-digitized ADC samples from a calorimeter simulation thread and real continuously-digitized ADC samples from a Struck SIS3350 digitizer system. The frontend FEMB emulates the Fermilab accelerator control signals and the frontend FE02 provides the software synchronization of spill-by-spill readout. The system also includes an event builder layer and data monitor layer.

10233 ter tests. Another frontend processor FEMB was connected to a Xilinx FPGA-based pro-
 10234 grammable pulser and used to emulate the accelerator-defined spill cycles. Another frontend
 10235 processor FEMB was used for the synchronization between the spill cycles and the readout
 10236 cycles. The platform was arranged as a local network of disk-less, frontend processors with
 10237 a backend server.

10238 Fig. 22.6 shows a typical spill of simulated data – *i.e.* 3.5×10^5 ADC samples of $700 \mu\text{s}$
 10239 continuous-digitization – that was Monte-Carlo generated by the calorimeter emulator. In
 10240 building streams of ADC samples, the decay positrons were generated with the appropriate
 10241 energy-time distributions for $3.094 \text{ GeV}/c$ decays and the calorimeter hits were generated
 10242 with appropriate x-y distributions and pulse shapes. The raw data were read out and
 10243 processed into T-/Q-method datasets in the DAQ frontend layer and then analyzed and



Figure 22.5: Photograph of the DAQ test stand at the University of Kentucky.

10244 histogrammed in the DAQ analysis layer. Representative plots of T-method energy and
10245 time distributions of decay positrons are shown in Fig. 22.7.

10246 Results from frontend timing tests of the GPU-based, T-/Q-method processing of the
10247 simulated calorimeter data are shown in Fig. 22.8. After completing the readout of each
10248 spill of ADC samples the raw data are transferred from the CPU memory to the GPU
10249 memory. The GPU then initiates a sequence that involves: derivation of the segment-
10250 summed calorimeter samples from the individual crystal segment samples, identification of
10251 the T-method above-threshold pulses in the summed calorimeter samples, assembly islands of
10252 the T-method above-threshold islands with pre-/post-samples, and transfer of the resulting
10253 T-method data from the GPU memory to the CPU memory. Additionally, a Q-method
10254 dataset was constructed by summing consecutive blocks of 32 ADC samples of digitizer data
10255 and then copied from the GPU memory to the CPU memory. Finally, the T-/Q-method
10256 datasets are packaged into MIDAS databanks and transferred to the backend layer.

10257 Also conducted were timing tests of event building on simulated databanks in the back-
10258 end layer of the data acquisition. The tests showed the rate limitations in event building
10259 were largely governed by memory copy operations during event fragment assembly. For the

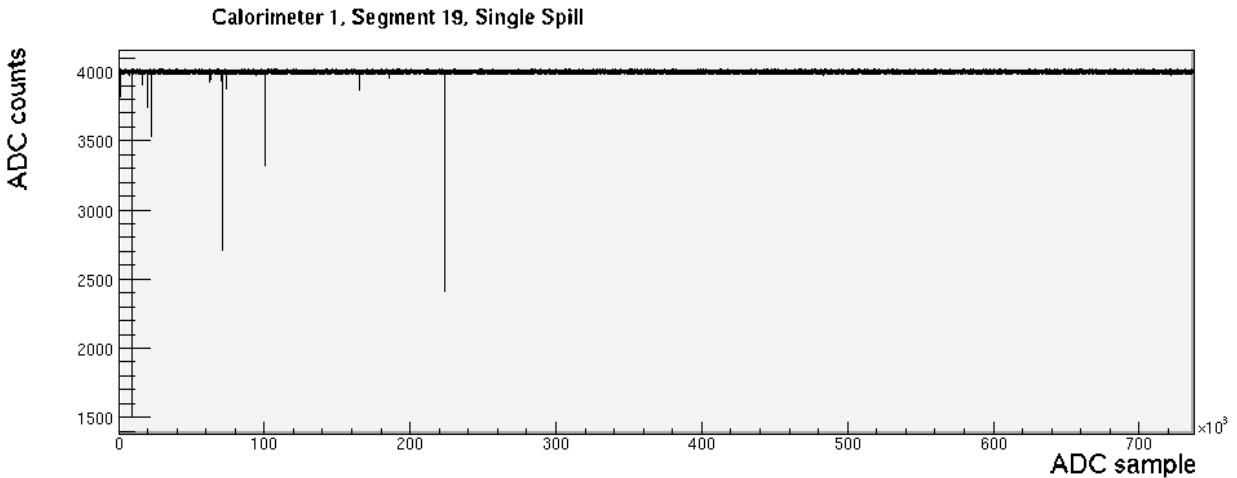


Figure 22.6: A representative single spill of simulated data generated by the calorimeter emulator. The data correspond to 3.5×10^5 ADC samples of $700 \mu\text{s}$ continuous-digitization for one segment of one calorimeter.

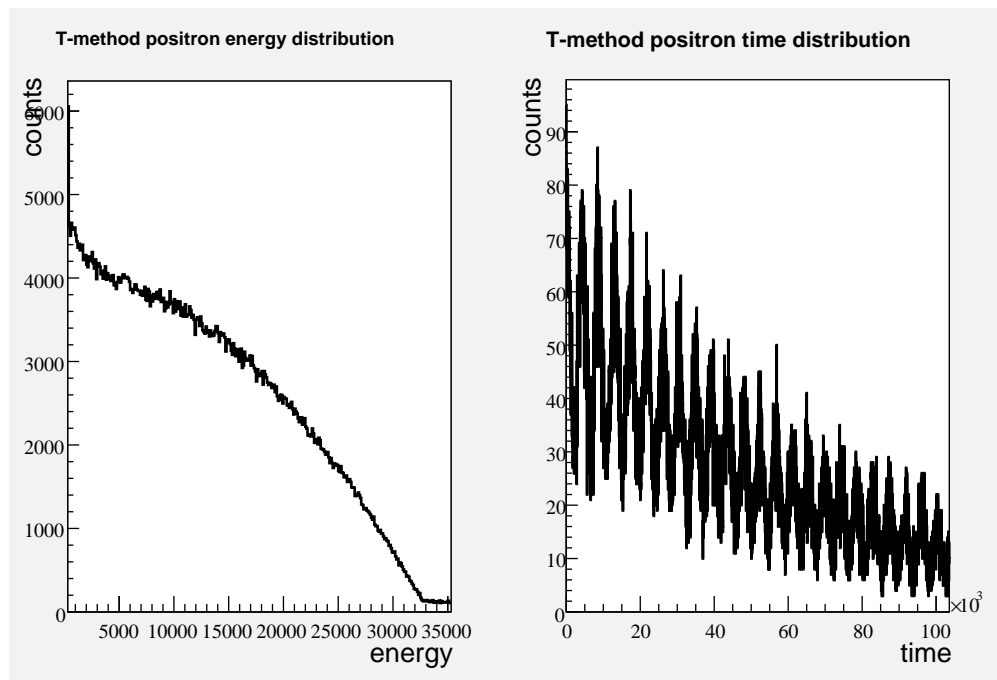


Figure 22.7: Energy distribution (lefthand plot) and time distribution (righthand plot) of energy / times of positron hits. The data were generated as continuous-digitization spills by the calorimeter emulator, were processed into T-Method datasets in the calorimeter, and histogrammed in the analysis layer. The energy distribution shows the positron endpoint energy and the time distribution shows the anomalous precession frequency.

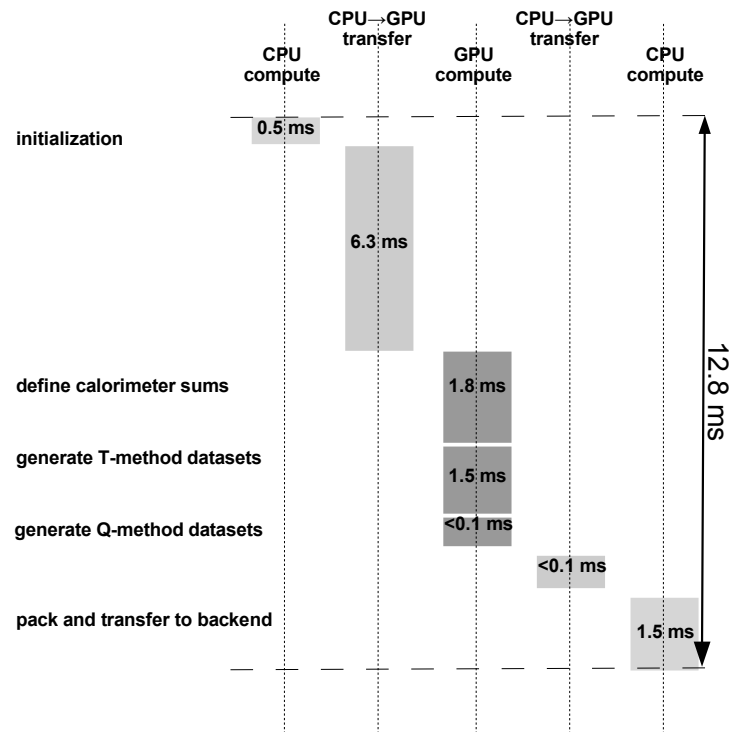


Figure 22.8: Schematic diagram of frontend processing of T-/Q-method datasets from simulated data of continuously-digitized ADC samples.

10260 backend processor in the R&D test stand – a six core, Intel i7 processor with 8 GBytes of
 10261 high-bandwidth DDR3 memory – the DAQ was able to handle a 80 MB/s data rate of event
 10262 building without introducing time delays.

References

10263

- 10264 [1] V. Tishchenko, S. Battu, S. Cheekatmalla, D. B. Chitwood, S. Dhamija, T. P. Gor-
10265 ringe, F. Gray and K. R. Lynch *et al.*, Nucl. Instrum. Meth. A **592**, 114 (2008)
10266 [arXiv:0802.1029 [nucl-ex]].
- 10267 [2] E. Frlez *et al.*, Nucl. Instrum. Meth. **A526** (2004) 300; see also <http://midas.psi.ch/>.
- 10268 [3] Rene Brun and Fons Rademakers, Nucl. Instrum. Meth. **A389** (1997) 81; see also
10269 <http://root.cern.ch/>.
- 10270 [4] Jason Sanders and Edward Kandrot, CUDA by Example: An Introduction to
10271 General-Purpose GPU Programming, Addison-Wesley, ISBN-10: 0131387685. Also
10272 <http://docs.nvidia.com/cuda/index.html>
- 10273 [5] V. Rose Microsystems, VRM-MCH Micro TCA Carrier Hub,
10274 <http://www.vrosemicrosystems.com/product-159.htm>
- 10275 [6] Eric Hazen, CMS AMC13 hub card, [http://joule.bu.edu/hazen/CMS/AMC13/](http://joule.bu.edu/hazen/CMS/AMC13/AMC13_Short_Spec_05Oct2012.pdf)
10276 [AMC13_Short_Spec_05Oct2012.pdf](http://joule.bu.edu/hazen/CMS/AMC13/AMC13_Short_Spec_05Oct2012.pdf)
- 10277 [7] Struck Innovative System, Harksheider Str. 102A, 22399 Hamburg, Germany; see also
10278 <http://www.struck.de/>.
- 10279 [8] Spectracom Corporation, 1565 Jefferson Road, Suite 460, Rochester, NY 14623, .
10280 <http://www.spectracomcorp.com/ProductsServices/TimingSynchronization>.
- 10281 [9] D. A. Huffman, Proceedings of the Inst. of Radio Engineers, **40** (1952) 1098; see also
10282 <http://www.zlib.net/>.
- 10283 [10] Jefferson Laboratory Data Acquisition Group CODA Wiki,
10284 https://coda.jlab.org/wiki/index.php/Main_Page
- 10285 [11] Kurt Biery, artdaq: An event filtering framework for fermilab experiments, Real Time
10286 Conference (RT), 2012 18th IEEE-NPSS, 9-15 June 2012,

Chapter 23

Slow Controls

23.1 Overview and general requirements

The $g - 2$ is a complex system that involves many subsystems for which adequate sensing and control during normal operation is required. The purpose of the slow controls and its associated data acquisition system is to set and monitor parameters such as voltages, currents, gas flows, temperatures etc. These tasks are essential for operation of the experiment over many months of data taking. The immediate online feedback allows the monitoring of the quality of the incoming data and reaction to changes in the data taking. For example, unprecedented gain stability via precise control of bias voltages for the silicon photo-multiplier readout of the electron calorimeter is required to meet the systematic uncertainty budget for ω_a . While the gain stability of these photo-detectors will be monitored at the 10^{-3} level or better via a dedicated laser calibration system, immediate feedback on the two parameters (bias voltage and temperature) determining the gain of these devices is achieved via such continuous monitoring. There are plenty of other cases where such external parameters will be useful in this high precision measurement to establish a full understanding of all systematic uncertainties.

For setting and read-back of parameters, the slow control system must provide sufficient sensors or control units which will either be directly integrated into the design of new subsystems or come as external devices. Most of these systems will connect to the slow control DAQ via the Midas Slow Control Bus (MSCB) which is a cost effective field bus developed at the Paul Scherrer Institute (PSI), Switzerland. This very mature system has been successfully employed in other similar experiments and allows for easy integration into the envisioned data acquisition framework MIDAS [1]. The slow control DAQ will also include communication interfaces to other external systems like the main $g - 2$ storage ring (iFix [2]) and the Fermilab accelerator (ACNet [3]). Other external devices like the μ TCA crates for the readout electronics of the electron calorimeter will be interfaced and monitored.

The demand and read-back values for all parameters controlled by the slow control system need to be stored in a convenient database such as MySQL or PostgreSQL. While a local copy of the data will be available for online monitoring and analysis, the copy will be transferred to a Fermilab database server for long-term storage. For efficient usage of the read-backs during data taking, user friendly visualization tools have to be provided in order to easily

10319 access the stored database information. A web browser based framework will be developed
10320 to display the large amount of different channels monitored by the system. Such script based
10321 tools are easy to expand and offer an interface for users without the need of installation of
10322 special software tools.

10323 Critical subsystems of the detectors might require special handling in case of unsafe
10324 running conditions. A stand-alone alarm system will provide necessary interlocks and other
10325 measures for such situations. For example, the gas flow of the straw tracker will be monitored
10326 and shutdown in case of flow read-backs that are outside normal ranges. Other critical
10327 systems like the cryogenic and vacuum controls of the $g - 2$ ring will be embedded in a
10328 special PLC system (see section 15.1). In the current design, no direct communication
10329 between the two systems has been designed but it is anticipated that the two systems might
10330 be interlinked.

10331 **23.2 Recommended Design**

10332 **23.2.1 Software and hardware architecture**

10333 The slow control system will comprise a variety of sensors and control units described in
10334 more detail in the following section. Some of these systems will be purchased as single units
10335 (like power supplies) and interfaced via serial or parallel standard (like RS232, GPIB). Other
10336 subsystems will be custom-built and their design requires integration of an appropriate slow
10337 control interface. The usage of field buses like CAN, Profibus and LON are not justified as
10338 their integration requires significant effort. Instead, we will employ the Midas Slow Control
10339 Bus (MSCB [4]) which is a field bus developed at PSI. This system was optimized for the
10340 environment of a typical physics experiment and for cost-efficiency (typically \$20 per node).
10341 In addition, it conveniently integrates into the MIDAS data acquisition system which is the
10342 basic design choice for the slow control computing infrastructure.

10343 The MSCB is the default choice for all sensors and control units that are custom built
10344 for the $g - 2$ experiment. The MSCB is based on the RS485 protocol which is similar to
10345 RS232 except for employing differential signals for superior noise immunity. RS485 is a
10346 multidrop half duplex communication standard so that many nodes can be connected to
10347 the same bus but only one can send data at a time. A single submaster can facilitate the
10348 communication between the MIDAS host computer and up to 256 individual MSCB nodes.
10349 In fact, by employing a layer of repeaters up to 65536 nodes can be operated on a single bus
10350 with up to a few km long cables. The MSCB requires two signal wires for the differential
10351 signal and a ground wire. Three additional lines provide power (+5 V, ± 12 V). The usage
10352 of a 10-wire flat ribbon cable provides four additional digital lines for application specific
10353 usage. Figure 23.1(a) shows one of the available submasters that can be purchased from PSI.
10354 Given the simple MSCB protocol, a typical node remains relatively compact like the SCS100
10355 shown in Fig. 23.1(b) that contains DACs, ADCs and an integrated temperature sensor
10356 for the on-board micro-controller. For $g - 2$ specific applications, the development of new
10357 nodes is a viable option which we will employ for some systems in the $g - 2$ setup (e.g. the
10358 bias voltage module for the electron calorimeter). The alternative is to purchase the more
10359 integrated SCS2000 unit with appropriate MSCB daughter cards for various applications.

10360 This possibility will be explained in more detail in the section 23.2.2 below.



(a) MSCB ethernet submaster



(b) SCS100 MSCB node with DACs, ADCs and integrated temperature sensor.

10361 The MSCB protocol is byte oriented and uses bit 9 from RS232 for addressing purposes.
 10362 As this bit usually cannot be switched on and off fast enough in the UART (universal
 10363 asynchronous receiver/transmitter) of a PC, simply using RS232-RS485 converters is not
 10364 sufficient. This can be overcome by employing a submaster on the computer side with a
 10365 micro-controller to provide the handshake with the PC and enough memory to avoid data
 10366 loss. In this scheme, bit rates of up to 345600 bits/s are sustainable.

10367 As mentioned before, the MIDAS software framework will be used for the slow control
 10368 data acquisition computer(s). Straightforward integration of MSCB-based hardware is al-
 10369 ready provided by appropriate drivers integrated into the software package. The end user has
 10370 to provide an application specific frontend module to control the specific sensor or control
 10371 unit, i.e. to set and readout parameters of the hardware system. Setting of the parameters
 10372 such as detector voltages or the readout rates of sensors are handled by corresponding set-
 10373 tings in the online database (ODB) on the slow control computer. A backend main server
 10374 will handle the collection of the readout data with an adapted event builder provided in the
 10375 MIDAS software. The assembled MIDAS events from all slow control subsystems are then
 10376 handed off to a data logger module which will store the data in an SQL based database
 10377 locally as well as transfer it to the Fermilab long-term storage server.

10378 Figure 23.1 shows the basic layout of the slow control system in the $g - 2$ experiment
 10379 indicated by the solid colored boxes. A single slow control backend host (brown box) manages
 10380 the communication with all MSCB nodes (blue boxes) via the MSCB submaster (green box).
 10381 Non-MSCB based sensor and control nodes (purple boxes) will communicate directly with the
 10382 backend server via appropriate interfaces (e.g. USB, RS232, ...). During the development
 10383 phase of the $g - 2$ experiment, we expect several institutions to setup their own MIDAS
 10384 and MSCB host computers for testing of individual components (e.g. the MSCB interface
 10385 for the SiPM bias voltage control). Although a single main PC and submaster would be
 10386 sufficient to handle all MSCB nodes in the $g - 2$ experiment, these additional available host
 10387 computers with their MSCB submaster and nodes could be easily integrated into the slow

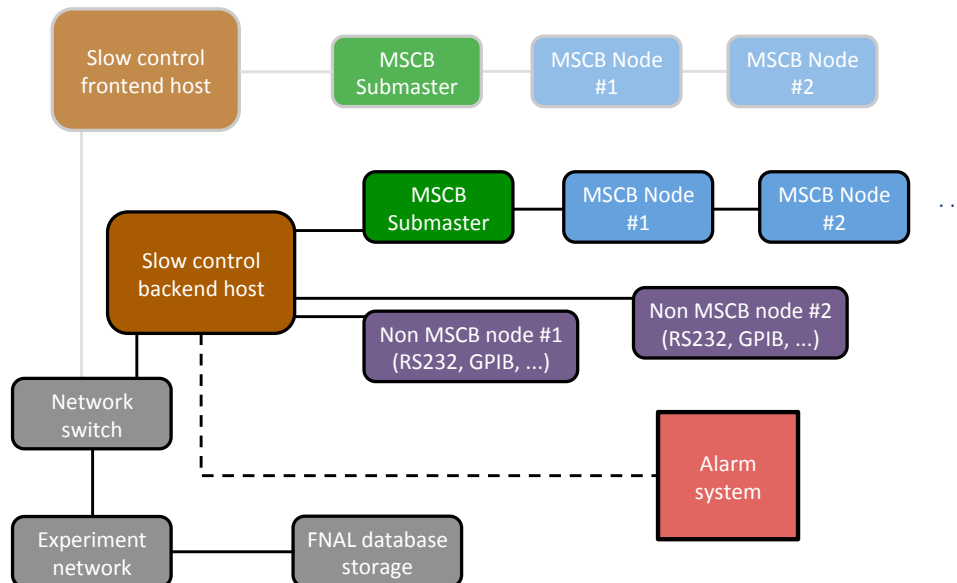


Figure 23.1: Slow control system for the $g - 2$ experiment: The basic layout includes a backend host (brown box) which manages the communication with all MSCB nodes (blue boxes) via the MSCB submaster (green box). Non-MSCB nodes (purple boxes) directly connect to the backend via the appropriate interface (USB, RS232, ...). Lightly shaded boxes refer to possible frontend computer(s) with their own MSCB bus and nodes for dedicated applications which would communicate and exchange data with the backend server via ethernet network. The stand-alone alarm system (red box) will provide adequate measures to handle unsafe running conditions.

10388 control system. Therefore, the final implementation in E989 might involve additional MSCB
 10389 frontend hosts to control special subsystems as indicated by the light shaded chain of boxes
 10390 in Fig. 23.1. Data exchange between a frontend computer and the slow control backend
 10391 computer happens via ethernet network. This scheme adds redundancy to the system in case
 10392 of maintenance or failure of one of the computers since MSCB nodes and their appropriate
 10393 MIDAS software frontend can be easily moved from one to another computer. The system
 10394 is completed by a stand-alone alarm system (red box) to provide appropriate actions in case
 10395 of unsafe operating conditions of various subsystems.

10396 In the following subsection, we will describe the sensors and control units, their require-
 10397 ments and the institutional responsibility. Thereafter, the conceptual design of the alarm
 10398 system, the backend server and the data storage are outlined.

10399 **23.2.2 Sensors and controls**

10400 The $g - 2$ experiment will employ a variety of systems to facilitate the overall measurement
 10401 of the muon anomalous magnetic moment. Figure 23.2 displays the current required func-
 10402 tionality for a variety of systems (as depicted by the individual nodes). Solid boxes denote

10403 systems that are currently known to have direct interfacing to the slow control whereas
 10404 lightly shaded nodes are currently interfaced by the fast calorimeter DAQ system (see 22).

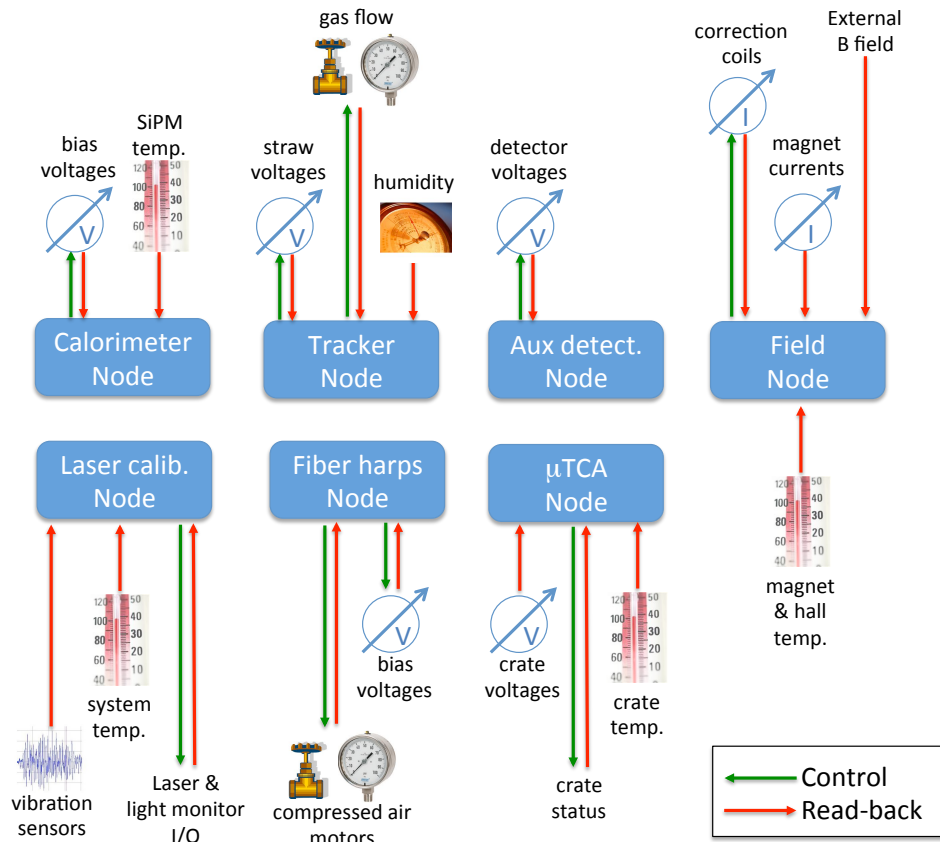


Figure 23.2: Schematic breakdown of the individual slow control nodes with individual control of parameters and sensor read-backs.

10405 The corresponding table 23.1 lists the actual parameters set and monitored via the slow
 10406 control. The read-back precision, rates and channel counts are preliminary estimates and are
 10407 subject to change with advancing design of each system. The photo-readout of the electron
 10408 calorimeter for the spin precession frequency will be based on silicon photo-multipliers (see
 10409 section 18). The design incorporates a surface mount SiPM on a readout board integrating
 10410 the bias voltage supply and an amplification of the readout signal. Since the experiment
 10411 requires high gain stability, a stabilization and monitoring of the two external parameters
 10412 that determine the SiPM gain, namely the bias voltage and temperature, is required. While
 10413 the bias voltage of each SiPM channel is set and monitored separately for each channel, the
 10414 temperature sensors will only be placed at a few locations inside each calorimeter station.
 10415 The associated laser calibration system which monitors absolute gain changes will require
 10416 a monitoring of the laser intensity and light distribution system's temperature at several
 10417 locations. Due to the usage of diffusing spheres for the laser distribution and their sensitivity
 10418 to small mechanical movement, a vibration monitor is most likely needed during operations.
 10419 It would consist of a 3-axis inclinometer and be integrated over a second so that readout

10420 rates of the order of less than 1 Hz are required. In order to control and enable the system,
 10421 a few I/O channels will be necessary. Depending on the final implementation of the laser
 10422 system the total number is expected to be less than 96. Finally, some of the available lasers
 10423 under consideration have a serial (USB, RS232) interface to control and read-back the laser
 10424 status.

10425 The tracker system comprises two stations of in-vacuum straws located in two scallop
 10426 regions. The slow control will provide readings for ambient temperature, humidity, and
 10427 pressure at the two locations. It will also monitor the gas flow and temperature as well as
 10428 currents and high voltages for the 36 individual substations. The system will provide the
 10429 setting of the high voltage demand values as well as their read-backs. The stand-alone alarm
 10430 system (see section 23.2.4) will provide interlocks for immediate shutdown of gas and HV in
 10431 case of irregular running conditions.

Table 23.1: List of control and read-back parameters in $g - 2$ handled by the slow control unit with anticipated read-back precision and rates, channel counts and the institutional responsibility for the implementation of the actual devices.

Parameter	Read-back precision	Read-back rate	Channel count	Responsibility
Calorimeter				
SiPM bias voltage	\sim mV	0.1 Hz	1300	UVa, JMU
preamp voltage	0.1 V	0.01 Hz	24	UVa, UW
SiPM temperature	0.1° C	0.1 Hz	\sim 75	ANL, UW
Laser calibration				
Laser temperature	$< 0.5^\circ$ C	< 1 Hz	< 10	INFN, ANL
Vibration monitor		< 1 Hz	~ 10	INFN
Output signals (enable)			< 48	INFN
Input signals			< 48	INFN
Serial laser interface	–		< 10	INFN
Tracker				
Voltage	~ 1 V	< 1 Hz	36	FNAL
Current		< 1 Hz	36	FNAL
Amb. pressure		< 1 Hz	2	FNAL, ANL
Amb. temperature	$< 0.5^\circ$ C	< 1 Hz	2	FNAL, ANL
Amb. humidity		< 1 Hz	2	FNAL, ANL
Gas flow		< 1 Hz	36	FNAL
Gas temperature		< 1 Hz	36	FNAL
Fiber harps				
SiPM bias voltage	few mV	0.01 Hz	2	Regis
preamp voltage	0.1 V	0.01 Hz	2	Regis
SiPM temperature	0.1° C	0.1 Hz	4	ANL
Motor control	-	-	4	Regis, ANL
Entrance counter				
PMT HV	~ 1 V	0.01 Hz	2	Regis
General				

Table 23.1 – *Continued from previous page*

Yoke temperature	< 0.5 °C	< 0.01 Hz	~ 20	ANL
Hall temperature	< 0.5 °C	< 0.01 Hz	~ 5	ANL

10432 The fiber harp detectors will be equipped with high and low voltage power supplies that
 10433 have some serial interface for the communication so that remote control and read-back of the
 10434 voltages is possible. As the SiPMs for the readout of the fibers are grouped in 4 rows of 7, we
 10435 anticipate monitoring the SiPM temperatures with one probe per row so that four sensors
 10436 are required. As the fiber harps are rotated into the beam by compressed air actuators, 2
 10437 control channels and read-backs of these must be available.

10438 The auxiliary detectors node in Fig. 23.2 includes all future additional counters that
 10439 might be added to the $g - 2$ setup. At this moment, it only comprises the so-called t_0
 10440 entrance counter which is a scintillator paddle with standard PMT readout that requires a
 10441 single channel HV power supply with a serial interface for remote communication.

10442 The μ TCA node comprises the communication between the slow control DAQ and the
 10443 μ TCA crates via the Remote Management Control Protocol to monitor the status of each
 10444 crate. As we are mainly reading status parameters provided by the crate, most likely no
 10445 additional sensors will be required. Some more details about this communication interface
 10446 will be covered in the following section 23.2.3.

10447 The field node in Fig. 23.2 includes possible readouts of the main magnet and the
 10448 correction coil currents as well as external fluxgate monitors. While these read-backs will
 10449 be recorded, they are currently not explicitly listed in Table 23.1 since it is most likely that
 10450 these are stored by the DAQ for the fixed NMR probes.

10451 Many of the systems described above include temperature readout channels. In addition,
 10452 we will monitor the ambient hall and magnet yoke temperatures at approximately 25 addi-
 10453 tional locations. Since changes in the magnet temperature are the main driver for changes
 10454 in the field homogeneity, a monitoring of the temperature will allow detection of any irreg-
 10455 ular temperature trends which could be caused by a deterioration of the magnet insulation.
 10456 Overall, we expect a total of ~ 100 temperature probes with a read-back precision of at most
 10457 0.1°C . Since we are mostly sensitive to temperature changes, the absolute accuracy is of
 10458 less importance. For the implementation of these temperature sensors, we plan to use the
 10459 available general purpose SCS2000 unit¹ shown in Fig. 23.3(a). The SCS2000 provides the
 10460 MSCB communication over Ethernet via the MSCB submaster with the PC. The unit has
 10461 an on-board programmable logic device (CLPD, Xilinx XC2C384) which handles the MSCB
 10462 protocol on one side. On the other end, there are slots for 8 independent MSCB daughter
 10463 cards which are each accessed by the CLPD via a 2-lane SPI and a parallel 8-bit bus. The
 10464 available daughter cards come with a multitude of different functions. Examples are shown in
 10465 Fig. 23.3(b) and the complete set of these daughter cards comprises functions like standard
 10466 I/O channels, 24-bit ADCs, current sources, valve controls, and many more. This system is
 10467 successfully employed in the MEG experiment at PSI and therefore, the set of typical slow
 10468 control functionality is available. Because the MSCB protocol and communication is handled
 10469 by the central programmable logic device in the SCS2000, the daughter cards only require a

¹At the time of the expected purchase, the successor SCS3000 will be available which provides the same functionality but adds a graphics display for direct user interaction and immediate status feedback.

10470 simple design and the whole package offers a relatively cost-efficient solution. For the above
 10471 mentioned ~ 100 temperature channels, we plan on using an existing 8-channel temperature
 10472 daughter card based on the Analog Device AD590 2-terminal temperature transducer. Since
 10473 each channel senses the current in the AD590, long cables of more than 10 m can be used so
 10474 that the SCS2000 unit(s) may be located at the center of the ring. Unused card slots in the
 10475 two SCS2000 can be used for additional other functionality.

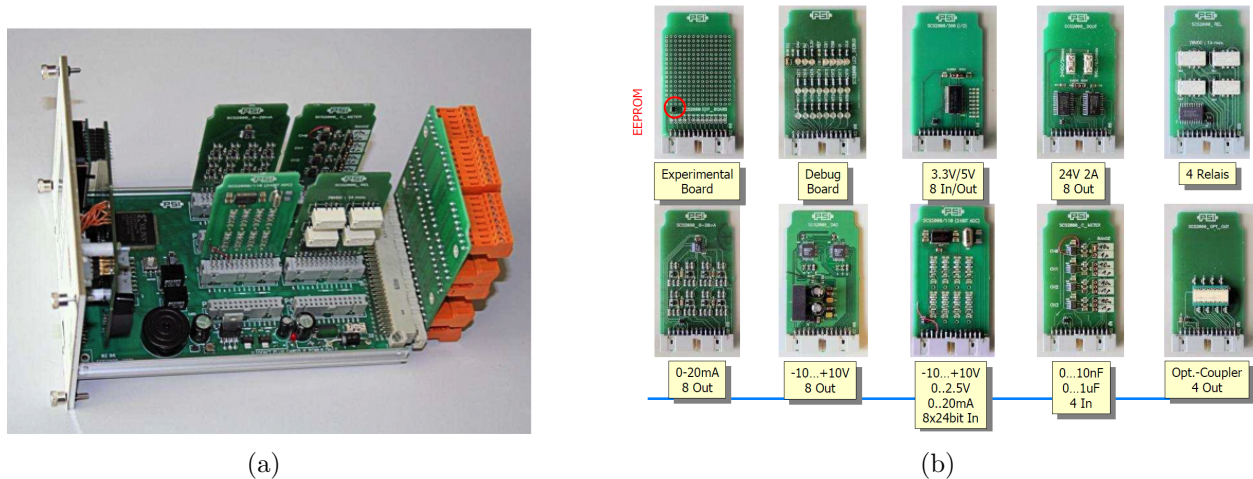


Figure 23.3: a) SCS-2000 general purpose control unit. b) Examples of available SCS2000 daughter cards.

23.2.3 Communication with external systems

10476 **23.2.3 Communication with external systems**
 10477 The slow control DAQ will not only retrieve data from the various sensors described above
 10478 but also communicate with other systems in the $g-2$ experiment and the Fermilab accelerator
 10479 infrastructure. As of now, there are a total of three such systems. Communication will need
 10480 to be established with the main ring control system, the Fermilab accelerator complex, and
 10481 the μ TCA crates for the readout of the electron calorimeter stations. In the following we will
 10482 shortly describe some more details about the three communication methods to the extent
 10483 relevant for the conceptual design of the slow controls.

10484 The ring control system for the cryogenics and vacuum is based on PLC interfaces which
 10485 are accessed via the human machine interface iFix. Figure 23.4 shows the schematic layout
 10486 for this complex system. As can be seen in the figure, the communication path (thick double
 10487 arrow) between the iFix server and the slow control DAQ system will be facilitated via an
 10488 OLE for Process Control (OPC) server integrated into iFix. The communication on the
 10489 slow control DAQ side is handled by an OPC client which is available as commercial or
 10490 open-source products for the Linux based system.

10491 During the $g-2$ operation, some parameters of the accelerator (like magnet currents,
 10492 beam intensities, status of other beam elements) will be stored in the output datastream.
 10493 This information can be retrieved via a data broker from the accelerator network (ACNet).
 10494 Retrieval of accelerator related parameters is already implemented at Fermilab in the larger

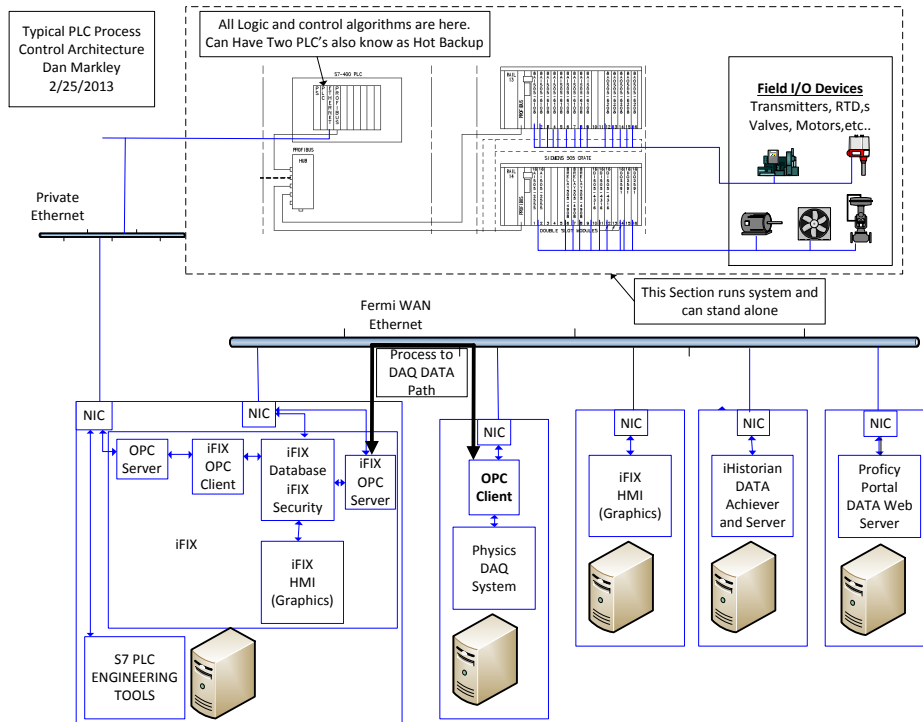


Figure 23.4: Schematic layout of the PLC-based main ring controls and the interface via the iFix to the slow control DAQ.

10495 context of a beam database for the intensity frontier experiments (IFbeam) and we will be
 10496 able to benefit from this existing implementation by adapting it to our needs and software
 10497 infrastructure. The data is usually stored in PostgreSQL format and can be integrated into
 10498 our experimental condition database.

10499 A third system that we want to establish communication with are the μ TCA crates for
 10500 the readout of the electron calorimeters and possibly other electronics in the experiment.
 10501 These crates typically provide internal status parameters (e.g. temperature, fan speeds,
 10502 error indicators etc.) that are useful to monitor to quickly identify hardware problems or
 10503 failures. System management and monitoring is achieved by means of software solutions
 10504 based on the Intelligent Platform Management Interface (IPMI), a standardized computer
 10505 system interface. A variety of user interfaces can be employed such as web-based GUIs or
 10506 programmatic interfaces. The latter comprise the Simple Network Management Protocol, an
 10507 industry standard and the Remote Management Control Protocol (RMCP) which supports
 10508 the IPMI commands over IP. For now we anticipate establishing an RMCP based client on
 10509 the slow control side to establish the required monitoring and communication with these
 10510 central electronics infrastructure in the $g - 2$ experiment.

10511 23.2.4 Alarm system

10512 A stand-alone alarm system will serve the purpose of allowing quick and safe shutdown of
10513 certain elements of the $g - 2$ detectors. Similar functionality via the slow control software by
10514 changing the demand values of high voltages or a valve status is typically not immediate and
10515 for some components of the experiment, the availability of hardware interrupt is preferable. It
10516 should be noted that there will be a separate PLC-based system handling the more critical
10517 components like the cryogenics of the magnet as well as vacuum controls. The system
10518 described here will deal with detector components which are not critical in the sense of life
10519 threatening unsafe conditions. The interrupts provided by the alarm system are mainly
10520 for protection of the detector components and other systems. While this functionality will
10521 ideally be unused during operations, it could be beneficial of having such a system readily
10522 available in case of unforeseen changes in the experimental conditions.

10523 At this moment, we plan to provide hardware interlocks for the high voltages and the
10524 non-flammable gas for the straw detectors which are located inside the vacuum. Scenarios
10525 necessitating shutdown of voltages and gas flow could be vacuum leaks in the ring vacuum
10526 chambers, overheating or high fluctuations in the straw current that could indicate a devel-
10527 oping problem. An interlock for the laser calibration system might be useful to protect the
10528 system in case of overheating or abnormal parameters. Similarly, hardware interlocks for the
10529 SiPM bias voltages could be provided in the same scheme if the request for it arises.

10530 Given the experience with other similar experiments, such an alarm system typically
10531 is expanded over time because additional useful interlocks are identified during the design,
10532 testing and implementation of detector systems. Therefore, we will adopt a simple basic
10533 concept using relays for the various interlock mechanisms. Figure 23.5 shows the schematic
10534 design for the system. Components that form a group and are interlocked at the same time
10535 will be connected to their own relay (Double Pole Double Throw type). The relay's actuator
10536 for such a group is triggered by different sources like the backend computer or a direct
10537 hardwired signal. For example, the straw tracker gas flow and high voltage system might be
10538 shutdown if the vacuum exceeds a defined threshold. As the vacuum control and read-back
10539 happens in the PLC, the actuator trigger might come directly from an output channel of
10540 the PLC system (see section 15). On the other hand, an interlock of the laser system might
10541 only be required if the read-back temperature of this system rises above a threshold. As this
10542 presumably is a slow process and not time critical, the interlock signal can come from the
10543 slow control computer monitoring these temperature read-backs.

10544 The interlocks for each groups are actually activated by the first internal relay switch
10545 (contacts 11, 12, 14). The second relay switch (contacts 21, 22, 24) can be used to form a
10546 serial loop monitored by the slow control computer's parallel port (acknowledge channel). A
10547 triggered actuator of any of the serialized relays would then trigger an alarm on the computers
10548 in the $g - 2$ control room. Depending on the criticality of each system, a triggered relay
10549 interlock might also include to set off an alarm siren and flashing light. The details of these
10550 alarm feedbacks have to be decided for each system. If necessary, one can setup multiple
10551 computer feedback loops by adding parallel port interfaces. The concept is very modular
10552 and easily expandable.

10553 It should be noted that the basic concept will be based on the underlying general layout
10554 that systems need positive approval (i.e. a running computer, powered PLC system etc.) in

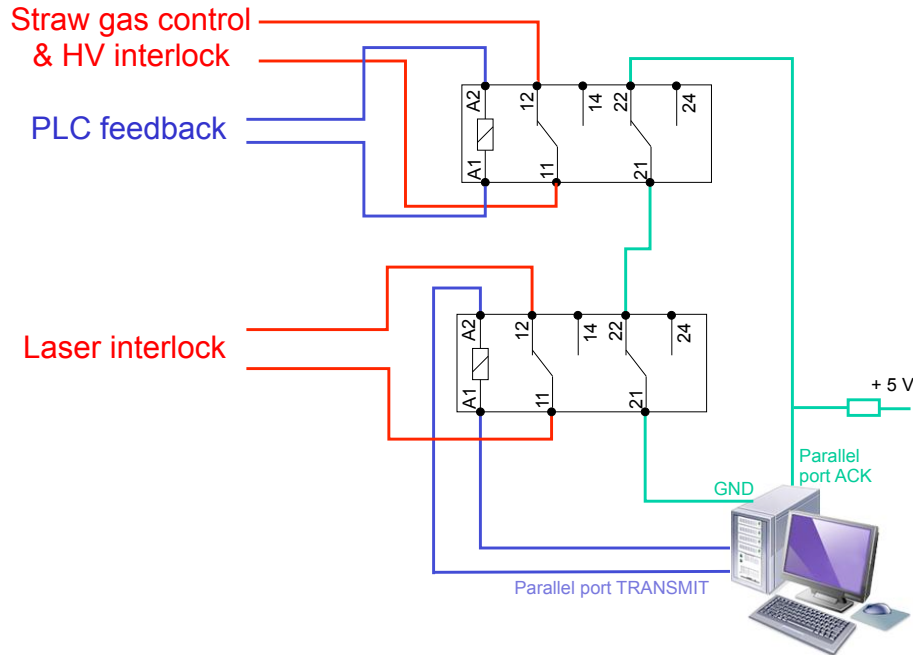


Figure 23.5: Basic conceptual design for the stand-alone slow control alarm system with two exemplary interlock groups (straw detector and laser).

10555 order to be functional.

10556 23.2.5 Backend server

10557 The backend server is the central computer in the slow control DAQ to communicate with
 10558 the various control units and sensors and retrieve all read-backs. Since data rates on the
 10559 slow control backend server are low (less than 1 MB/s), a standard modern Linux desktop is
 10560 sufficient. It should provide enough interfaces (RS232, USB, MSCB) for the external devices.
 10561 As mentioned above, we will work within the MIDAS software framework to coordinate the
 10562 different tasks. The various sensors and controls can be accessed individually by independent
 10563 frontend programs which run in parallel within the main MIDAS server. Each frontend has
 10564 its specific functionality to set experimental parameters (like high voltages for each SiPM),
 10565 read-back parameters, and allow to change read-back rates. For MSCB devices, the necessary
 10566 hardware drivers are provided by MIDAS so that the actual implementation of the frontends
 10567 is simplified. For other hardware connecting to the backend over RS232 or USB, MIDAS
 10568 also includes software components that will make integration of these subsystems into the
 10569 slow control easier. Such frontend code has been developed previously like for the MuLan
 10570 [5] and MuCap [6] experiments at PSI by some of the current E989 collaborators. Therefore,
 10571 the implementation of the various frontends for all sensors and controls should not pose a
 10572 major effort.

10573 **23.2.6 Data storage and access tools**

10574 For the data storage of slow control parameters, we will use a SQL-based database format
10575 (MySQL or PostgreSQL). While MIDAS has already built in options for MySQL handling,
10576 Fermilab's preferred choice is PostgreSQL which is the current anticipated choice for E989.
10577 Integration of PostgreSQL capabilities into the MIDAS framework should be feasible with
10578 minimal effort. The backend server will have standard ethernet network connection(s) for the
10579 communication with external systems (see section 23.2.3) and synchronization of the local
10580 database with the remote long term storage at Fermilab. We will employ the automated
10581 script-based mechanisms developed at Fermilab for this purpose. Overall, the database
10582 handling and storage is expected to nicely integrate into the existing infrastructure.

10583 From table 23.1 one can deduce that the anticipated maximal channel count for the slow
10584 control is about 2000 read out at most with 1 Hz rate. If we recorded for every single channel
10585 three float values (4 bytes) in form of a timestamp, demand and current read-back value,
10586 we therefore can deduce a conservative upper limit of the expected data rate of 24 kB/s or
10587 2 GB per day. Given the standard storage sizes of more than 1 TB today, the overall slow
10588 control data for the entire $g - 2$ data taking period will be easily storable and does not pose
10589 any major challenge.

10590 Any data acquisition requires a well designed interface for the online monitoring and
10591 during the offline analysis. For example, a user friendly visualization interface to inspect
10592 the large number of different channels (the calorimeter alone has 1300 channels) is very
10593 essential during data taking. Based on past developments for muon precision experiments
10594 at PSI and current other Intensity Frontier experiments at Fermilab, we will have a variety
10595 of options to establish such tools. The IFbeam software tools incorporate the python based
10596 Web Server Gateway Interface and subsequent Google Charts to access and display database
10597 information in the web browser. The experiments at PSI, MuLan and MuCap, used custom
10598 developed web browser based tools to query and display the database information as well as
10599 standalone graphics displays within the ROOT framework [7]. At this point, it is not clear
10600 which exact tools we will use for E989. In general, usage of a single tool will increase user
10601 friendliness but it could be advantageous to have optimized tools for various different data
10602 streams. However, the specific implementation will profit from extensive former experience
10603 which will guide the collaboration in making the final decisions in the future.

10604 **23.3 Alternative Design Considerations**

10605 The information recorded by the slow digitization DAQ is quite independent from any other
10606 DAQ system in $g - 2$. Therefore, we have investigated the usage of alternative software
10607 packages like the ORCA system. The collaboration has used this system in the ongoing
10608 SiPM tests at UW in order to gain practical experience with this system. Another option is
10609 the EPICS software which is well supported at the Advanced Photon Source at ANL and at
10610 FNAL. However a careful comparison of the three systems has revealed that MIDAS is our
10611 best choice for the software framework for the slow control DAQ. Its major advantages are
10612 the fact that several of the $g - 2$ collaborators have many years of experience with this system.
10613 It has been used successfully by a variety of experiments at PSI and other laboratories. We

10614 also have a good relationship with the main developers of MIDAS at PSI. Last but not least,
10615 synergies with the fast detector DAQ are obvious as it is based on the same framework. The
10616 amount of maintenance and debugging reduces and collaborators on shifts will only need to
10617 familiarize themselves with the subtleties of one system.

10618 The default choice of the MSCB for hardware components is tightly connected to the
10619 decision for using the MIDAS framework as the latter has easy integration of MSCB compo-
10620 nents. In addition, the MSCB is optimized for cost efficiency. We have looked into the usage
10621 of more commercial products (e.g. National Instruments hardware with possible integration
10622 into LabVIEW) but such systems would simply increase the cost. In addition, some of our
10623 systems require custom built components (e.g. the extremely stable low voltage power sup-
10624 ply for the SiPM) and therefore, we can profit from the simplicity of the MSCB protocol.
10625 Finally, the MIDAS and MSCB framework is very open and we have good connections to one
10626 of the experts of this system at the Paul Scherrer Institute, Switzerland. We are therefore
10627 confident, that development of new modules should be feasible with limited effort. It should
10628 also be noted, that we can still rely on non-MSCB off-the-shelf components if it turns out
10629 that they are an optimal choice to control or monitor some of our subsystems. Communica-
10630 tion with such devices via typical standards of RS232 or USB is available within the MIDAS
10631 framework. Our default choice is therefore very modular and expandable but comes at a
10632 quite optimal cost.

10633 The alarm system is based on a simple relay concept. There has been good experience
10634 with this concept in the muon capture experiment MuCap at PSI where it was used to
10635 interlock critical detectors in a similar way as proposed. The stand-alone design (i.e. separate
10636 form the main PLC-based control system, see section 15) has the advantage that we can
10637 operate detector systems separately which might be very useful during beam tests before
10638 the real data taking. However, while the design of the subsystems evolves, it might turn
10639 out that this basic concept is inadequate for some of our applications. In that case, we have
10640 the alternative to integrate the monitoring and interlock functionality into the PLC-based
10641 system described in section 15. This will most likely require additional hardware in form
10642 of control and sensor boards, i.e. more channels for the system. Due to the more complex
10643 nature of this system, the costs per channel are significantly higher than in the current
10644 default design and the implementation of this alternative was dismissed.

10645 **23.4 ES&H**

10646 The slow control system will involve sensor and control units that mainly need low voltages
10647 and currents for operations. If high voltages (like for the SiPM bias voltage or the PMT
10648 voltage) are involved, adequate protection (shielded cables, enclosed and fused electronic
10649 components) will be employed to comply with Fermilab's safety rules. The components for
10650 the slow control do not require any hazardous materials and there are no mechanical hazards
10651 since the components are typically small.

10652 The alarm system included in the design of the slow control will interlock non-critical
10653 components to prevent direct damage to the hardware. It does not include any life-threatening
10654 hazards.

23.5 Risks

The default design of slow control relies on the mature MSCB system that has been successfully employed in several experiments. Therefore, there is only a small risk that components will not work appropriately to the specified requirements. Certainly, the exact design and implementation of the stringent bias voltage system for the SiPMs in the calorimeter is crucial in succeeding to meet the gain stability. This specific risk is considered in the calorimeter section (see Sec. 18). Other sensors (like temperature, voltage, currents etc.) are readily available and should be sufficient to meet the requirements in the E989 experiment. If not, a design of an appropriate component would require additional resources. Since the design of a new MSCB node is not too complex, the associated cost risk is rather small.

A failure in meeting the specified requirements for controlling devices and read back of performance parameters potentially causes an inability of detecting a loss in the data quality during the experiment. This could result in the necessity of dismissing data from the analysis and could result in the need of longer data taking to acquire the full statistics.

During the design phase of various subsystems, it could be found that the current design of the alarm system based on a simple relays layout is inadequate. Examples for such a diagnosis could be that the systems is not reliable enough, that it is not compliant with safety rules that require a more complex system to interlock detectors, that the response is not fast enough. In that case, we might need to integrate its functionality into the more complex PLC-based main control system (see section 18). The probability for this risk is very low since we already have good experience with the current scheme from the muon capture experiment at PSI. However, if realized it would certainly increase the costs as we would need additional labor resources to transfer the functionality to the different system and come up with an adequate design. In addition, we would need to purchase necessary hardware channels to control, monitor and interlock the systems appropriately.

Any components installed close to the precision magnetic field (especially electronics circuits with time-varying currents) can cause a static or dynamic distortion to the homogeneity of the field and possibly decrease the precision in its measurement. Mitigation of this risk is achieved by using non-magnetic materials close to the field region and by testing all components for their magnetic properties in a 1.45 T test magnet and with specially designed pickup coils for transient fields.

23.6 Quality Assurance

The implementation of the slow control system relies on well established software in the form of the MIDAS framework. In addition, we will employ the very matured MSCB hardware whenever possible or purchase commercially available systems. Quality assurance measures are therefore mainly limited to verifying that custom-built sensors and control units meet the requirements that all systems work properly and comply with all safety regulations. We will extensively test individual components and the full system in dedicated bench tests before the final installation in the experimental hall. As outlined in the risks, these tests will include the verification of the stringent magnetic requirements for components installed in the vicinity of the precision magnetic field of the storage ring. In addition, several institutions across the

10696 collaboration will have their own small slow control system to develop individual components.
10697 This will help identifying any problems and debugging the system's functionality.

10698 Since the slow control provides an online monitoring of the status of many systems in the
10699 $g - 2$ experiment, care will be taken to properly design the appropriate visualization tools
10700 providing easy access to all parameters. This will be an important component in detecting
10701 any changes in the quality of the collected data during the experiment.

10702 **23.7 Value Management**

10703 The usage of freely available open-source MIDAS software and the specifically cost-optimized
10704 MSCB hardware is key in keeping the slow control systems overall cost low. Some compo-
10705 nents that cannot be readily purchased (like the SiPM bias voltage supply with its stringent
10706 requirements, see section 18.3.2) and need to be custom-built. Most of these will be designed
10707 and implemented by collaborators at universities and outside the US in order to keep the
10708 overall cost low. At the same time, the centralized integration of all components at Argonne
10709 will allow verification of the full system and detection of any interference of different sensors
10710 or control units.

10711 **23.8 R&D**

10712 Necessary R&D for custom-built components that will be integrated in the slow control
10713 system is performed by some of the collaborating institutions and will be described in the
10714 appropriate sections in this document. Examples for these are the SiPM bias voltage supply
10715 (section 18.3.2) or the laser calibration system (section 18.3.3).

10716

References

10717 [1] E. Frlez *et al.*, Nucl. Instrum. Meth. **A526** (2004) 300; see also <http://midas.psi.ch/>.

10718 [2] <http://www.ge-ip.com/products/proficy-hmi-scada-ifix-5-5/p3311>

10719 [3] <http://www-bd.fnal.gov/controls/consoles/userguide.html>

10720 [4] <http://midas.psi.ch/mscb>

10721 [5] V. Tishchenko *et al.*, Phys. Rev. **D87**, 052003 (2013)

10722 [6] V.A. Andreev *et al.*, Phys. Rev. Lett. **110**, 012504 (2013)

10723 [7] Rene Brun and Fons Rademakers, Nucl. Instrum. Meth. **A389** (1997) 81; see also
10724 <http://root.cern.ch/>.